FRACTURE TOUGHNESS DETERMINATION USING CONSTRAINT ENHANCED SUB-SIZED SPECIMENS

Glynn Rothwell

A thesis submitted in partial fulfilment of the requirements of
Liverpool John Moores University for the degree of Doctor of Philosophy

January 2003

ABSTRACT

Failure of a material subjected to an essentially tensile load by fast fracture under conditions of limited crack tip plasticity is governed by the material fracture toughness, the value of which for a given material at a particular temperature is heavily dependent on the thickness of the material and level of crack tip constraint. As a consequence, for tough materials, the specimen size required to provide acceptable fracture toughness values under test conditions is often excessively large.

The work presented in this thesis investigates the possibility of using constraint enhanced sub-sized specimens to provide essentially plane strain results. Two types of specimen are investigated, the side grooved reduced thickness compact tension specimen and the circumferentially cracked round bar specimen.

Linear elastic fracture mechanics analysis of aluminium alloy specimens was undertaken in order to establish the effects of side groove depth and geometry on crack front stress intensity factor and constraint for full thickness specimens. It was concluded that Vee grooves with a depth of 30% of the specimen thickness provided an optimum configuration. Analytical and experimental support was also given to Freed and Krafft's idea of effective thickness with the exponent, m, being evaluated by finite element analysis to be between 0.62 and 0.66, and experimentally to be 0.71 for the specimen configuration in question.

A two parameter fracture mechanics investigation based on J-Q theory was used to investigate crack tip constraint in sub thickness side grooved specimens manufactured from EN24 steel, this involved finite element modelling of a range of plain and side grooved sub thickness specimens together with an extensive experimental programme. Good agreement was obtained between the finite element predictions and the experimental results. The investigation concluded that side grooves were very effective at increasing the level of constraint along the crack front, to the extent that near minimum fracture toughness values could be expected from specimens of one fifth the recommended thickness.

The results obtained from a similar investigation of circumferentially cracked round bar specimens indicated that they are not suitable for linear elastic fracture mechanics testing and that their use should be limited to elastic-plastic fracture mechanics.

ACKNOWLEDGEMENTS

I would like to express my gratitude to my supervisor, Dr Ian Graham, for his guidance throughout the project. Also thanks to Prof Ben Mills and Prof Neil Barlow for their help and advice.

I would also like to thank the engineering workshop technicians at JMU for machining the test specimens and particularly Steve Gotts, Colin Peters and Tony Cunningham for their assistance with pre-cracking and testing of the specimens.

Finally, I am very grateful for the patience and support shown by my wife Janet and daughter Amy throughout, and to Janet for taking on the considerable task of typing the manuscript.

CONTENTS

NOMENCLATURE

α	Ramberg Osgood fit parameter
δ_i	Crack tip opening at initiation
δ_{IC}	Critical crack opening displacement
δ_t	Crack opening displacement
ε	Strain
ε_f	Material fracture strain
ε_{nom}	Engineering strain
ε_o	Yield strain
$\tilde{\varepsilon}_{ij}$	Normalised strain function of θ
$\bar{\varepsilon}_p$	Equivalent plastic strain
$\bar{\varepsilon}_f^*$	Critical local fracture strain
γ_e	Elastic surface energy
η	Natural co-ordinate, Dimensionless constant dependent on geometry
η_{el}	Elastic dimensionless constant dependent on geometry
η_{pl}	Plastic dimensionless constant dependent on geometry
θ	Angle
ρ	Root radius
σ	Stress
σ_f	Critical stress to cause instability, Critical tensile failure stress
σ_{FB}	Stress associated with a crack in a finite body
σ_m	Hydrostatic stress
σ_{nom}	Engineering stress
σ_o	Yield stress
σ_{TSP}	Tensile strength at fatigue pre-cracking temperature
σ_Y	Yield stress
σ_y	Stress in y direction
σ_{YS}	0.2% Proof stress at test temperature
σ_{YSP}	0.2% Proof stress at fatigue pre-cracking temperature
$\tilde{\sigma}_{ij}$	Normalised stress function of θ
$\bar{\sigma}$	Equivalent (or effective) stress
$(\sigma_{ij})HRR$	HRR stress field
$(\sigma_{ij})SSY$	Small scale yielding stress field
$(\sigma_{ij})diff$	Difference stress field

ν	Poissons ratio
ξ	Natural co-ordinate
[K]	Global stiffness matrix
{f}	Nodal load vector
{u}	Displacement vector
a	Crack length
A_{FB}	Area associated with a crack in a finite body
B	Specimen thickness, Levers and Radon biaxiality parameter
B_N	Specimen thickness at root of side groove
C	Uncracked ligament, Compliance
d	Side groove depth
d_p	Distance between void initiating particles
E	Young's modulus
E'	$= E/\left(1-\upsilon^2\right)$ in plane strain and E in plane stress
F	Work performed by external forces
F	Probability of failure
$\bar{f}_{ij}$	Dimensionless combination of material parameters
f_{ij}	Dimensionless combination of material parameters
G	Energy release rate, Material shear modulus
G_C	Critical energy release rate
G_{IC}	Critical mode I energy release rate
g_{ij}	Dimensionless combination of material parameters
G_{NOM}	Nominal strain energy release rate obtained from a side grooved specimen
h_{ij}	Dimensionless combination of material parameters
I_n	HRR dimensionless constant
J	Rice J integral
J_{el}	Elastic part of J integral
J_{FB}	J associated with a crack in a finite body
J_{IC}	Fracture toughness
J_{pl}	Plastic part of J integral
K	Stress intensity factor
k	Yield shear stress
K_C	Critical stress intensity factor
K_{ff}	Material constant relating to flat fracture area
K_{IC}	Critical mode I stress intensity factor
K_{IQ}	Predicted fracture toughness
K_{NOM}	Nominal fracture toughness value obtained from a side grooved specimen

K_{PS}	Plane strain fracture toughness
K_Q	Provisional value of fracture toughness from test
K_{SL}	Material constant relating to shear area
L	Length
l_o	Characteristic distance
m	Side grooving exponent
N	Shape function
n	Strain hardening exponent
P	Potential energy, load
P_Q	Preliminary failure load
R	Radius
r_o	Initial blunted radius
r_Y	Plastic zone radius
$\bar{r}$	$r/(J/\sigma_o)$ evaluated ahead of a crack tip at $\theta = 0$
S_{ij}	Deviatoric stress
T	Traction vector, Elastic T stress
t	Specimen thickness
t_o	Critical specimen thickness for 100% shear lip formation
u	Displacement
$\tilde{u}_{ij}$	Normalised displacement function of θ
U	Total Energy
U_γ	Change in elastic energy caused by the formation of new surfaces
U_a	Change of elastic energy by introducing a crack
U_c	Energy in a cracked body
U_o	Elastic energy of an uncracked plate
U_t	Total energy
v	Load line displacement
$V(\sigma_1)$	Cumulative volume over which the principal stress is greater than σ_1
v_c	Contribution to load line displacement of the presence of a crack
v_t	Total load line displacement
v_{uc}	Load line displacement of an uncracked specimen
W	Specimen width, Strain energy density
w	Side groove width

CHAPTER 1

INTRODUCTION

Failure of a material subjected to an essentially tensile load by fast fracture under conditions of limited crack tip plasticity is governed by the material fracture toughness, the value of which for a given material at a particular temperature is heavily dependent on the thickness of the material and level of crack tip constraint. Minimum, hence conservative, values of fracture toughness are obtained for a particular material when deep cracks are present and the thickness is sufficient to ensure conditions of plane strain along the majority of the crack front.

It follows therefore that fracture toughness testing must be undertaken under essentially plane strain conditions and with deeply cracked specimens. Both British and American standards relating to fracture testing demand that these conditions are met before measured values obtained from test specimens can be designated as true material properties. A consequence of this approach is that, for tough materials, the specimen size required to provide plane strain values is excessively large and often the demands in terms of testing machine load capacity are prohibitive.

The work presented in this thesis investigates the possibility of using constraint enhanced sub-sized specimens to provide essentially plane strain results. Two types of specimen are investigated, the side grooved reduced thickness compact tension specimen and the circumferentially cracked round bar specimen. Constraint enhancement is provided in the side grooved specimen by the interaction of the crack front stress field with that of the root of the side groove. In the case of the circumferentially cracked round bar specimen constraint is provided by the fact that the circumferential crack tip has no free surface and that the required crack depth and minimum diameter need only to ensure that the crack tip plastic zone is not influenced by the free surface of the cylinder or the specimen axis of symmetry.

The successful use of these specimens would also provide benefit to many industries where, due to the materials employed, it is often not possible to provide specimens of the standard thickness required by current fracture toughness test methods.

In order to fully investigate the implications of using sub-sized specimens a single parameter characterisation of the crack front stress fields by the use of stress intensity

factor, or J integral, alone is not sufficient. Although they are both a measure of the intensity of the near crack tip deformation and stress fields, in practice the extent to which these parameters dominate is largely dependent on the amount of constraint at the crack tip.

In order to allow the effects of constraint to be fully investigated a detailed finite element study of the crack front stress fields has been undertaken together with a two parameter fracture mechanics approach. Where possible this theoretical treatment of the problem has been supported by an extensive experimental programme.

CHAPTER 2

FRACTURE MECHANICS – BACKGROUND THEORY

2.1 INTRODUCTION

Engineering failures can, in general, be yield dominated or fracture dominated. If they are fracture dominated then failure occurs by catastrophic crack growth emanating from a material defect or crack. Due to the spectacular nature of some of these failures a great deal of interest and research effort has been directed into the field of fracture over the past fifty years.

Several outstanding texts relating to the general development of the subject of fracture mechanics (see refs. [1 – 4]) have been published over the past twenty years, hence a detailed review will not be presented. The purpose of this chapter is to describe the major developments that have taken place and that are relevant to the work presented in this thesis.

2.2 THE GRIFFITH THEORY

Griffith formulated his energy balance approach in the 1920's whilst using glass to study the failure of brittle solids [5, 6]. He considered an infinite plate of unit thickness containing a through crack of length $2a$ and subjected to a uniform tensile stress σ, see fig. 2.1. The total energy U of the cracked plate is given by:

$$U = U_o + U_a + U_\gamma - F \quad .....(2.1)$$

where:

$U_o =$ elastic energy of the loaded uncracked plate (constant).

$U_a =$ change in the elastic energy caused by introducing the crack in the plate.

$U_\gamma =$ change in elastic surface energy caused by the formation of the crack surfaces.

$F =$ work performed by external forces (this must be subtracted in equation (2.1) since this is not part of the internal energy of the plate).

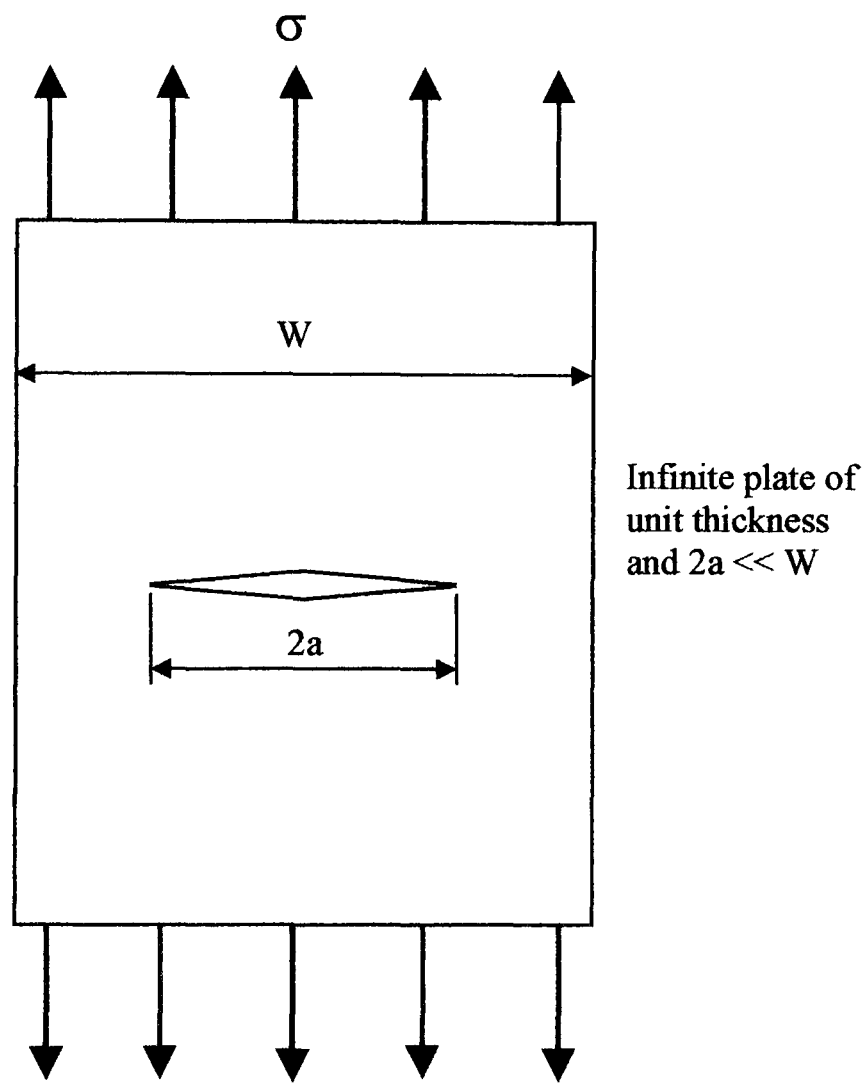

Fig. 2.1 Centre cracked plate

Griffith used expressions developed by Inglis [7] for the elastic strain energy per unit thickness of an infinite plate containing a central crack given by:

$$|U_a| = \frac{\pi\sigma^2 a^2}{E} \quad (plane\ \ stress) \quad .....(2.2)$$

$$|U_a| = \frac{\pi(1-\nu^2)\sigma^2 a^2}{E} \quad (plane\ \ strain) \quad .....(2.3)$$

where:

σ = applied stress perpendicular to the crack

E = Young's Modulus.

υ = Poisson's Ratio

The elastic surface energy, U_γ, per unit thickness is equal to the product of the elastic surface energy of the material γ_e and the new surface area of the crack.

$$U_\gamma = 4a\gamma_e \quad .....(2.4)$$

Griffith reasoned that unstable crack growth would occur when the energy release rate was at least equal to the rate of energy absorption due to the creation of new surfaces and considering that U_o is constant, hence dU_o/da is zero, the condition for instability is given by:

$$\frac{d}{da}(U_a + U_\gamma - F) = 0 \quad .....(2.5)$$

For the case where no work is done by external forces, $F = 0$, and considering the change in elastic energy due to the introduction of the crack to be negative, equation (2.5) becomes:

$$\frac{d}{da}(-U_a + U_\gamma) = 0 \quad .....(2.6)$$

Substituting equations (2.3) and (2.4) into equation (2.6) gives (for plane strain):

$$\frac{d}{da}\left(-\frac{\pi(1-\nu^2)\sigma^2 a^2}{E} + 4a\gamma_e\right) = 0 \quad .....(2.7)$$

hence:

$$\frac{\pi a\sigma^2(1-\nu^2)}{E} = 2\gamma_e \quad ..... (2.8)$$

which leads to the Griffith relation:

$$\sigma_f = \sqrt{\frac{2\gamma_e E}{\pi a(1-\nu^2)}} \quad .... (2.9)$$

where σ_f is the critical stress required to cause instability.

The Griffith approach is only strictly applicable to brittle solids and as such is precluded from consideration for real engineering structures. In recognition of the limitations of Griffith's theory both Irwin [8] and Orowan [9] independently proposed modifications to account for a limited amount of plastic deformation at the crack tip. The modification involved the inclusion into equation (2.9) of a plastic work term γ_p, which because of its magnitude effectively replaces γ_e.

2.3 STRAIN ENERGY RELEASE RATE

Irwin [8] also proposed another modification to the original Griffith theory and suggested that crack propagation will occur when *du/da* reaches a certain critical value. The energy release rate is designated as G with the critical value at fracture being G_c the material fracture toughness. Hence, from equation (2.9) the energy release rate can be defined from:

$$\sigma_f = \sqrt{\frac{G_c E}{\pi a(1-\nu^2)}} \quad .....(2.10)$$

2.4 STRESS INTENSITY FACTOR APPROACH

Despite modifications to the original Griffith approach its application to practical problems is severely limited. As a result of these difficulties Irwin [10] proposed a stress intensity approach which represented a major advance in fracture mechanics. Using the method and results of a previous analysis by Westergaard [11] for stress functions for crack problems Irwin derived expressions for the stress distribution ahead of a crack tip, this being:

$$\sigma_{ij} = \frac{K}{\sqrt{2\pi r}} . f_{ij}(\theta) \quad .....(2.11)$$

where r and θ are as defined in fig. 2.2 and K is known as the ***stress intensity factor*** corresponding to one of the three cracking modes as shown in fig. 2.3.

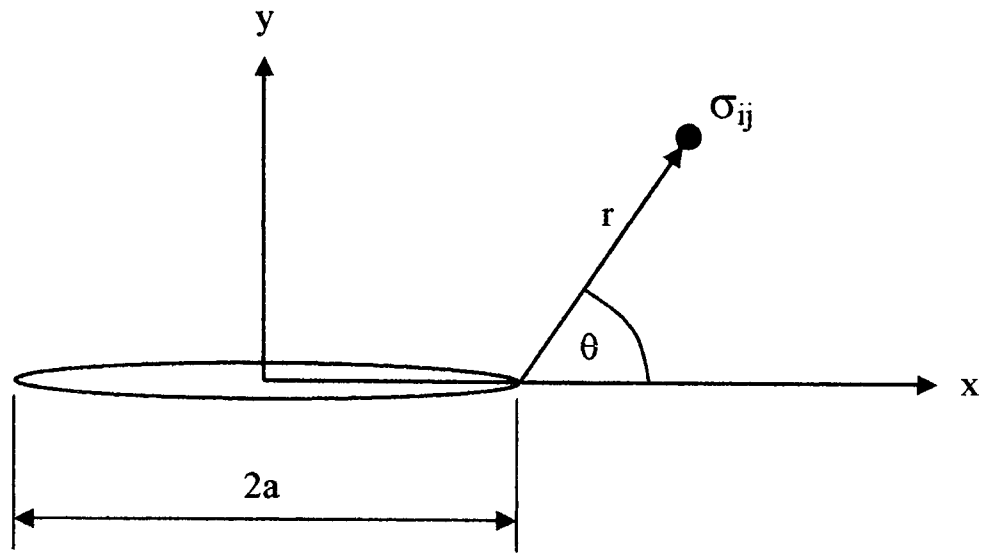

Fig. 2.2 Stresses at a point ahead of a crack tip

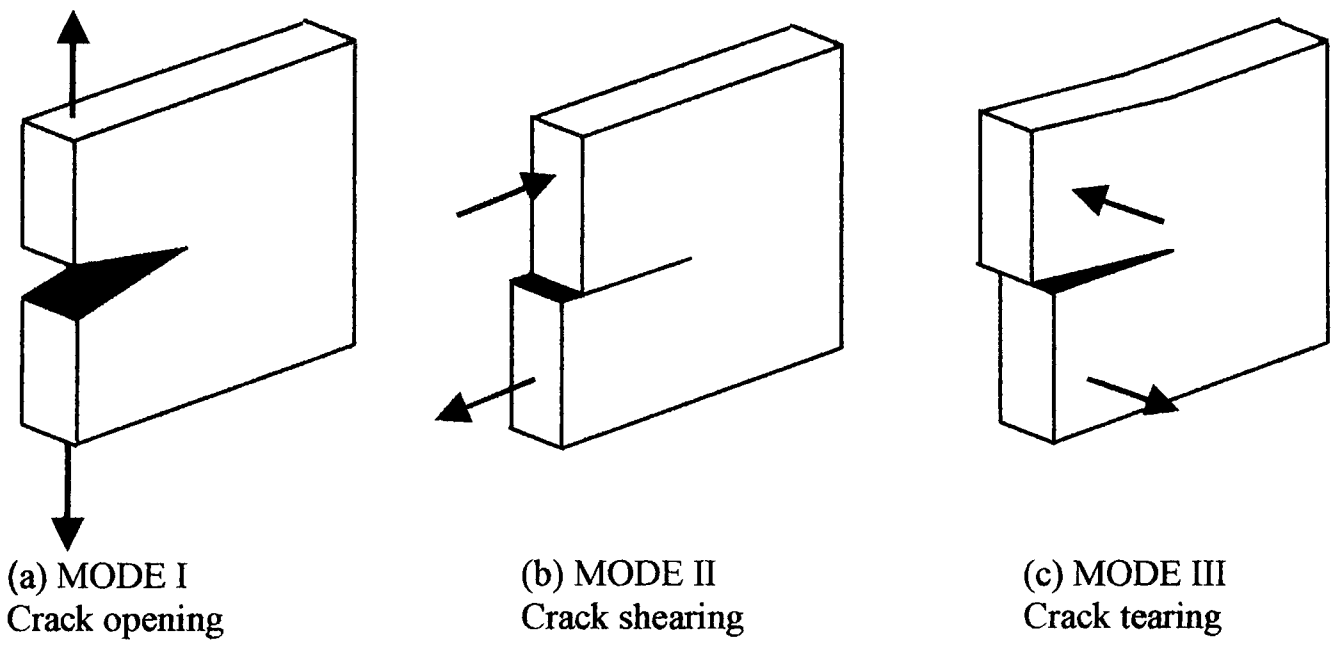

Fig. 2.3 Modes of fracture

These three fundamental modes of fracture are defined as:

Mode I, crack opening, see fig. 2.3(a)

Mode II, crack shearing, see fig. 2.3(b)

Mode III, crack tearing, see fig. 2.3(c)

As can be seen from equation (2.11) the crack tip stress field has a $\frac{1}{\sqrt{r}}$ singularity and the stress intensity factor K is the only parameter that relates the crack tip stress field to the loading and geometry of the system.

The form of the stress intensity factor is given by:

$$K = \sigma\sqrt{\pi a}.f\left(\frac{a}{W}\right) \quad .....(2.12)$$

where $f\left(\frac{a}{W}\right)$ is dimensionless and is dependent upon the geometry of both the specimen and the crack. As with the energy balance approach, for failure to occur K must exceed a critical value K_C. K_C is a material property but is dependent on the mode of crack loading. For mode I loading the critical stress intensity factor is designated K_{IC} and is the material fracture toughness.

The stress intensity factor and strain energy release rate concepts are related by the following equivalence relationships.

$$K^2 = \frac{EG}{(1-\nu^2)} \quad (plane\ strain) \quad .....(2.13)$$

$$K^2 = EG \quad (plane\ stress) \quad .....(2.14)$$

Expressions for K have been evaluated by a variety of methods for a large range of geometries and loading situations and have been well published in the past (see ref. [12]).

2.5 PLASTIC ZONE SIZE/SHAPE

The elastic stress distribution at the crack tip is such that there is a stress singularity. However, because the material will deform plastically at stresses above the yield stress, in practice this leads to the formation of a plastic zone which means that the elastic solution is not applicable.

Irwin [13] considered the plastic zone to be circular and of diameter $2r_Y$ and developed the following expressions for the size of the zone, for plane stress equation (2.15) and for plane strain equation (2.16).

$$r_Y = \frac{1}{2\pi}\left(\frac{K_I}{\sigma_Y}\right)^2 \quad .....(2.15)$$

$$r_Y = \frac{1}{2\pi}\left(\frac{K_I}{C\sigma_Y}\right)^2 \quad .....(2.16)$$

He also showed that the crack can be viewed as having a notional tip a distance r_Y ahead of the real tip, see fig. 2.4.

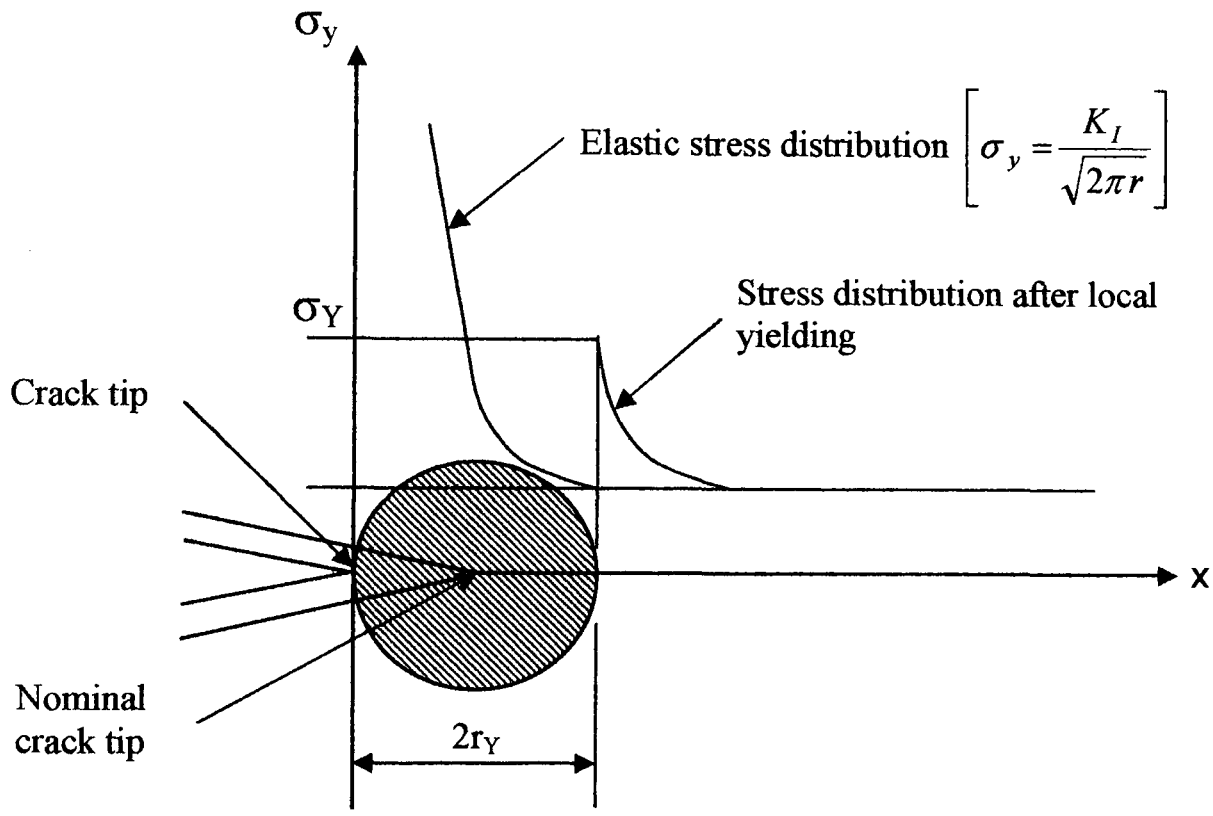

Fig. 2.4 The Irwin plastic zone size

The arguments presented above make the assumption that the plastic zone is of circular shape, centred at the crack tip. This is a gross simplification and by considering the yield condition for θ angles different to zero, a better impression of the real shape of the plastic zone can be obtained [13, 14]. [θ being measured anti-clockwise from the direction of crack growth at the crack tip].

Plastic zone shapes according to the von-Mises yield criterion are shown in fig. 2.5 for plane stress and plane strain conditions. In practice, the true shape of the plastic zone is greatly affected by material thickness, with plane strain conditions prevailing in the interior of the material and plane stress conditions at the surface.

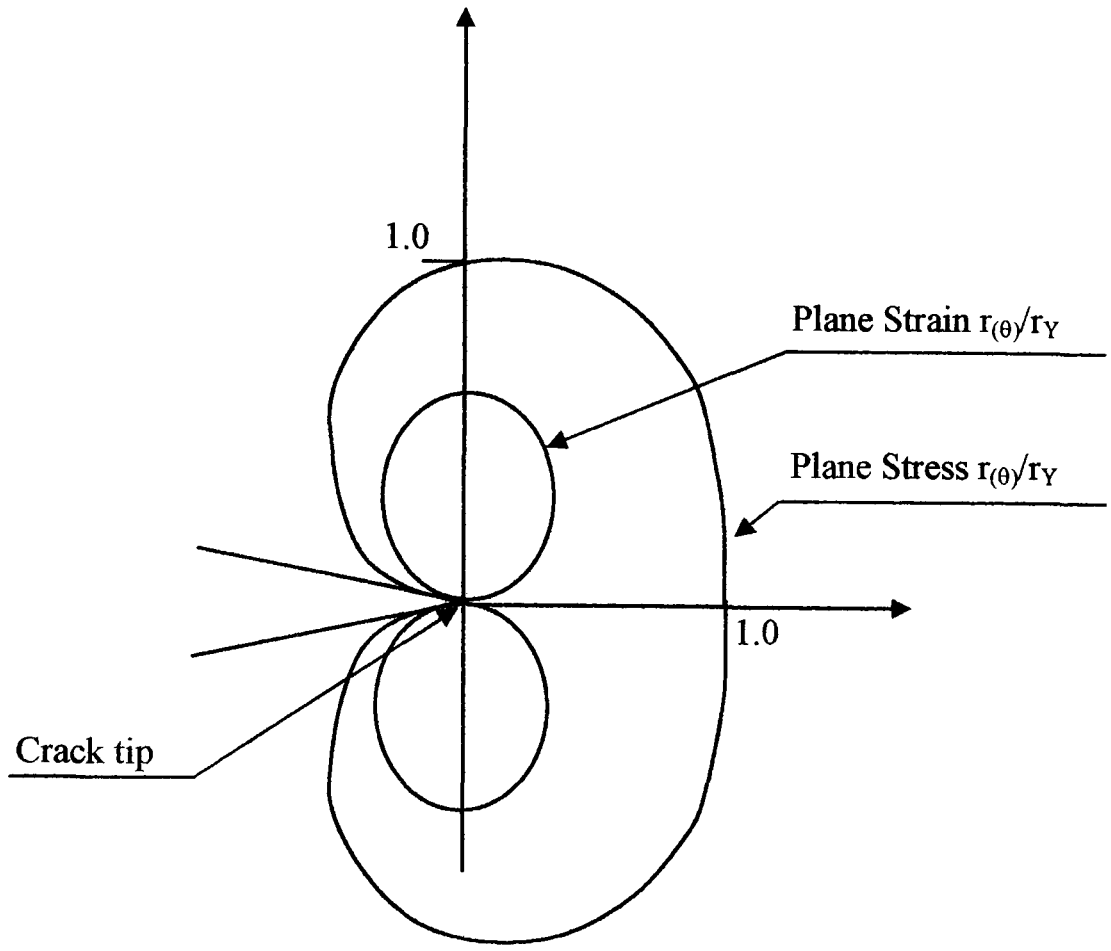

Fig. 2.5 Dimensionless plastic zone shape from von-Mises criterion

This can be explained to a certain degree by considering a through thickness crack in a plate.

By combining equations (2.11) and (2.12), the elastic stresses will be given by:

$$\sigma_{ij} = \frac{\sigma\sqrt{\pi a}}{\sqrt{2\pi r}} . f_{ij}(\theta) \quad .....(2.17)$$

For small values of r both σ_x and σ_y will exceed the material yield stress and hence lead to the formation of the plastic zone. If there is no strain hardening then the material within the plastic zone should be capable of plastic flow and hence will contract in the thickness direction. However, within the interior the surrounding elastic material cannot contract to the same extent, leading to tensile through thickness stresses at the elastic plastic boundary. This corresponds to a condition of plane strain and the setting up of a triaxial stress situation. At the plate surface the material within the plastic zone is capable of some contraction and there are no stresses in the thickness direction. Hence, the stress field is biaxial in nature and can be considered to be plane stress. When

considering the plastic zone size variation through the thickness of the plate, it can be seen from fig. 2.6 that there is an intermediate zone slightly in from the surface where the plastic zone size varies between plane stress conditions at the surface to plane strain conditions in the interior.

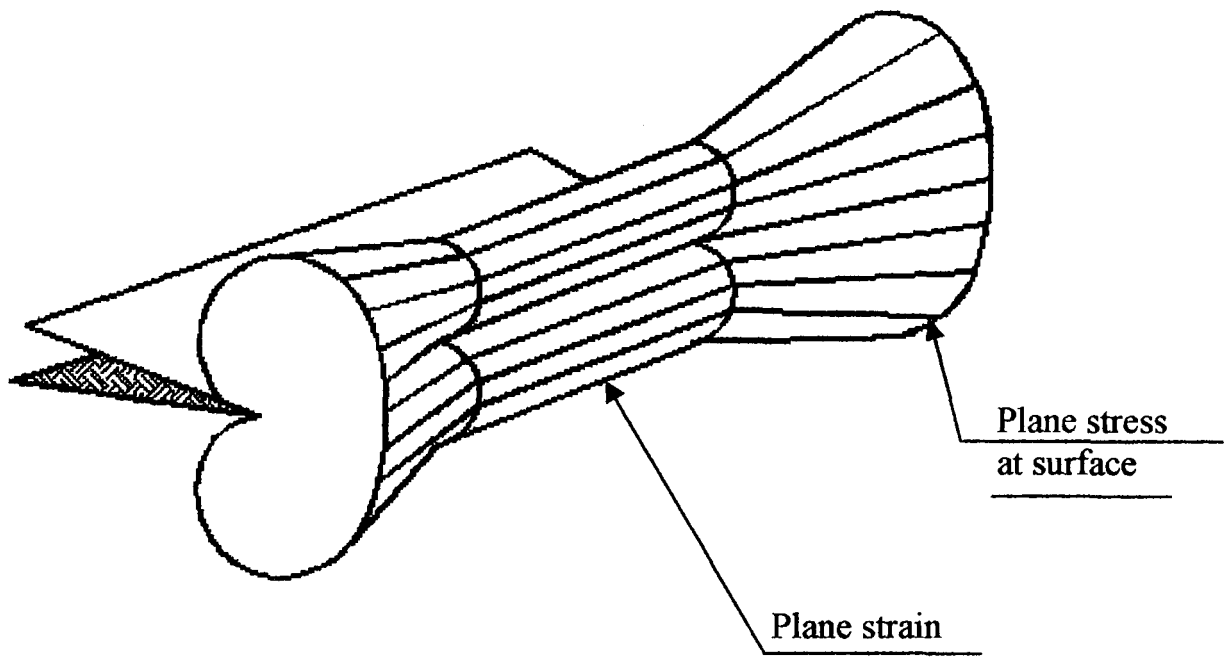

Fig. 2.6 Through thickness plastic zone in a plate of intermediate thickness

2.6 CRACK OPENING DISPLACEMENT

In the preceding sections only the elastic fracture case has been considered, together with the effects of very limited plasticity. However, where ductile materials are involved that exhibit a large amount of plastic deformation the use of linear elastic fracture mechanics is not sufficient. Instead elastic plastic fracture mechanics must be used. One approach proposed by Wells [15] is that of crack opening displacement, COD. In situations where significant yielding occurs at the crack tip then there will be some separation of the crack faces prior to crack growth. Hence fracture will occur when a critical value of COD is reached which is a reflection of the amount of plastic strain at the crack tip at failure.

Burdekin and Stone [16] used the Dugdale strip yield model [17] to develop an expression for COD as follows:

$$\delta_t = \frac{8\sigma_Y a}{\pi E} \ln\left[\sec\left(\frac{\pi a}{2\sigma_Y}\right)\right] \quad .....(2.18)$$

where;

δ_t = crack opening displacement

σ_Y = material yield stress

It was also shown that under linear elastic fracture mechanics conditions that there are direct relations between δ_t and K_I as follows:

$$\delta_t = \frac{K_I^{\,2}}{\sigma_Y E} \quad (plane\ stress) \quad .....(2.19)$$

$$\delta_t = \frac{K_I^{\,2}(1-\nu^2)}{\sigma_Y E} \quad (plane\ strain) \quad .....(2.20)$$

2.7 THE RICE CONTOUR INTEGRAL

An alternative to COD was developed by Rice [18] in the form of a contour integral of the type developed by Eshelby [19]. The contour integral, termed the J integral, follows a path around a crack tip shown in fig. 2.7 and is path independent provided that the start and finish points of the contour Γ are on opposite faces of the crack and that the contour contains the crack tip. The J- integral is defined as:

$$J = \int_{\Gamma}\left(Wdy - T\frac{\partial u}{\partial x}ds\right) \quad .....(2.21)$$

where:

$x, y =$ rectangular co ordinates normal to the crack front

$ds =$ increment along the contour

$T =$ stress vector acting on the contour

$u =$ displacement vector

$W =$ strain energy density $= \int \sigma_{ij} dE_{ij}$

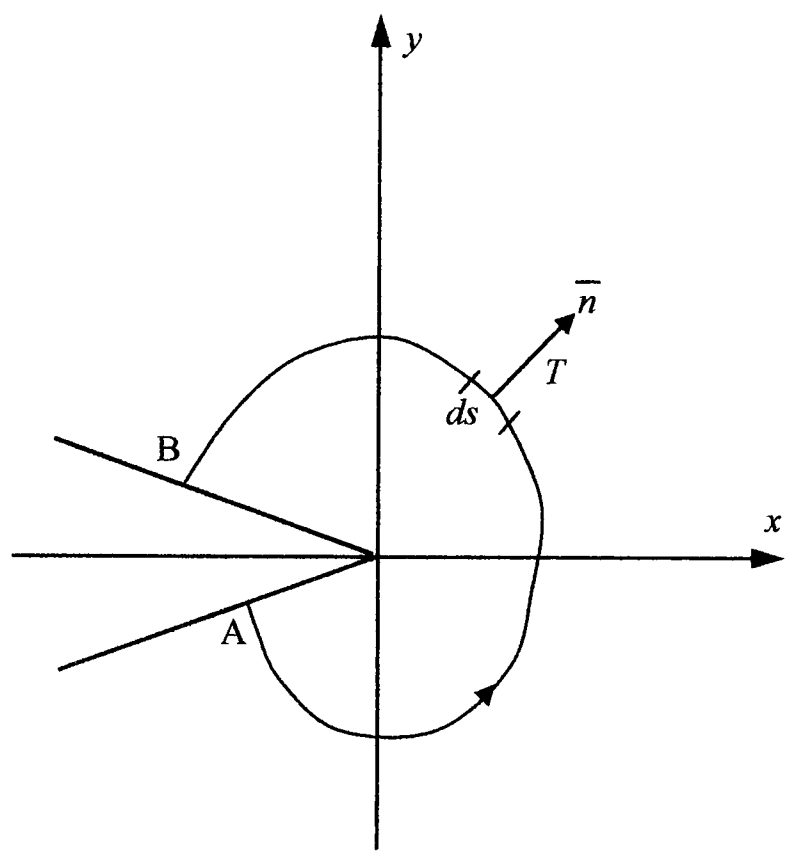

Fig. 2.7 J integral path around a crack tip

Rice also showed that the J integral when taken around a closed path containing the crack tip represents the change of potential energy for a virtual crack extension da, hence:

$$J = -\frac{du}{da} \quad .....(2.22)$$

Hence for the linear elastic case the J integral is directly equivalent to G. Hence:

$$J = G = \frac{K^2}{E}(1-\nu^2) \quad (plane\ strain) \quad .....(2.23)$$

It is important to understand that the *J* integral concept is actually based on a non linear elastic system which can only be used to model the plastic behaviour of a material providing that no unloading occurs, since the actual plastic part of the deformation is irreversible.

2.8 EFFECTS OF THICKNESS

When fracture surfaces are examined on failed test specimens it is seen that two distinct regions are present. Generally in the interior of the material the fracture surface is flat and extends directly from the root of the crack. Towards the surfaces of the material, however, the fracture surfaces tend to be at 45^0 to the principal loading direction, this is illustrated in fig. 2.8.

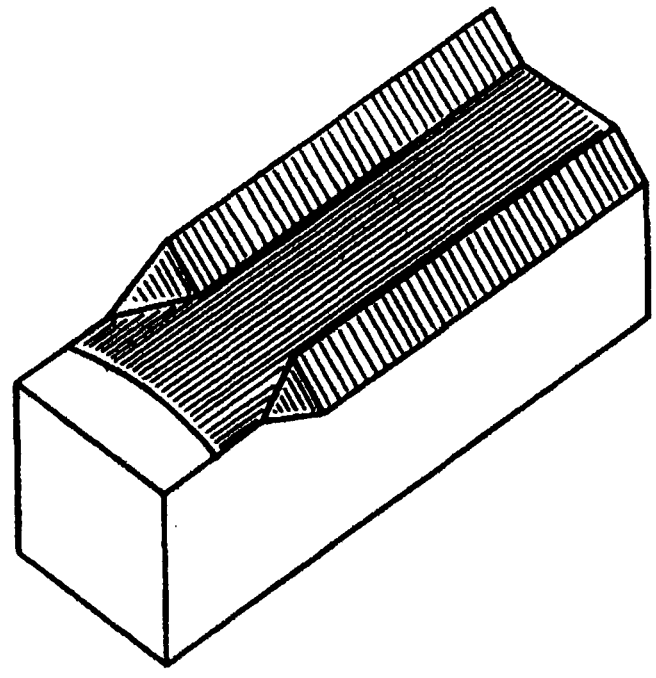

Fig. 2.8 Typical fracture surfaces

This behaviour can be explained by considering the stress states through the thickness of the material. It was argued in section 2.5 that highly triaxial stress states are developed in the interior of the material but not at the surface where the stress state is essentially biaxial. Due to high triaxial stresses in the interior there is no driving force for slip to occur and hence the absence of shear. The situation at the surface, however, is very

different with shear being the dominant failure mode due to the highly biaxial stress field.

As a consequence of the above it has been observed by many investigators that material thickness has a profound effect on measured values of K_{IC} obtained from standard test specimens. Material yield stress also has an effect on the material behaviour observed in the transitional region between plane stress and plane strain this, together with the effects of thickness, is illustrated in fig. 2.9.

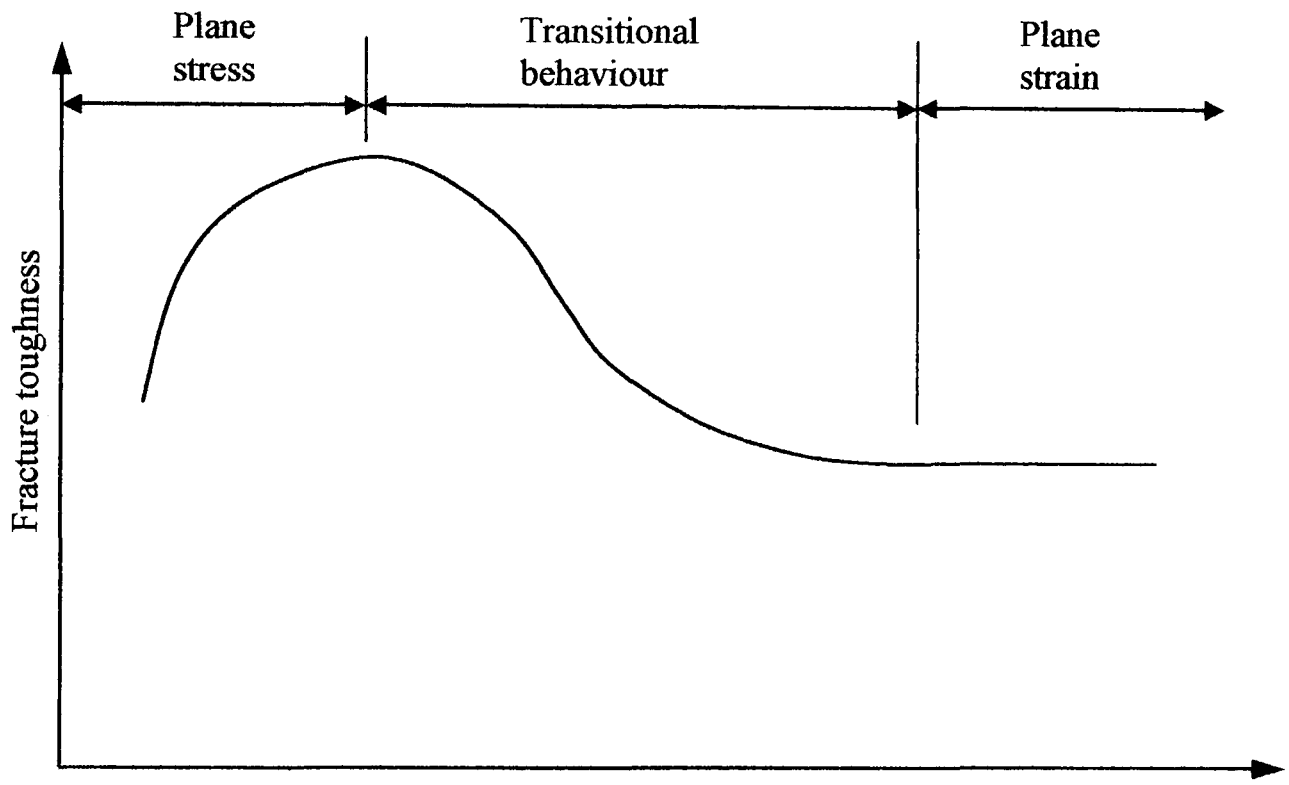

Fig. 2.9 Variation of fracture toughness with thickness

Although the effect of thickness on measured values of fracture toughness is understood in qualitative terms not many quantitative models exist.

Bluhm [20] proposed a quantitative model based on the assumptions that:

i) The shear lip size at fracture is independent of thickness.
ii) Flat fracture is a surface phenomenon and shear lip formation is volumetric in nature.

Assumption (i) above implies that the transition from plane strain in the specimen interior to plane stress at the surface always occurs in the same volume of material.

Hence, the shear lip size is equal to half the maximum thickness in which full plane stress develops. Hence the fracture energy for the shear regions is given by:

$$dW = \frac{1}{2} K_{SL} t^2 da \quad t \le t_o \quad \text{.....(2.24)}$$

and

$$\left.\begin{aligned} dW &= \frac{1}{2} K_{SL} t_o^{\,2} da \\ dW &= K_{ff}(t - t_o)\, da \end{aligned}\right\} \quad t \ge t_o \quad \text{.....(2.25)}$$

where:

t = specimen thickness

t_o = critical thickness for 100% shear lip formation

K_{SL} = a material constant relating to the shear area

K_{ff} = a material constant relating to the flat fracture area

The critical energy release rate $G_{IC} = dW/tda$ therefore equations (2.24) and (2.25) lead to:

$$\left.\begin{aligned} G_{IC} &= \frac{1}{2} K_{SL}\, t_o \left(\frac{t}{t_o}\right) \quad if \quad \left(\frac{t}{t_o}\right) < 1 \\ G_{IC} &= \frac{1}{2} K_{SL}\, t_o \left(\frac{t_o}{t}\right) + K_{ff}\left(1 - \frac{t_o}{t}\right) \quad if \quad \left(\frac{t}{t_o}\right) > 1 \end{aligned}\right\} \quad \text{.....(2.26)}$$

By considering that t_o is approximately equal to twice the plastic zone size as given by equation (2.15) it follows that:

$$\frac{K_{IQ}}{K_{IC}} = \sqrt{1 + \left(\frac{EK_{SL}}{6\pi\sigma_Y^2} - 1\right)\frac{t_o}{t}} = \sqrt{1 + q\frac{t_o}{t}} \quad \text{.....(2.27)}$$

Substitution of appropriate material properties for E, K_{SL} and σ_Y in equation (2.27) does not show good agreement with test data hence the generalisation to include the term q to fit test data.

Bluhm used the above analysis on the experimental results of Repko et al [21] with a reasonable degree of success, the results are reproduced in fig. 2.10.

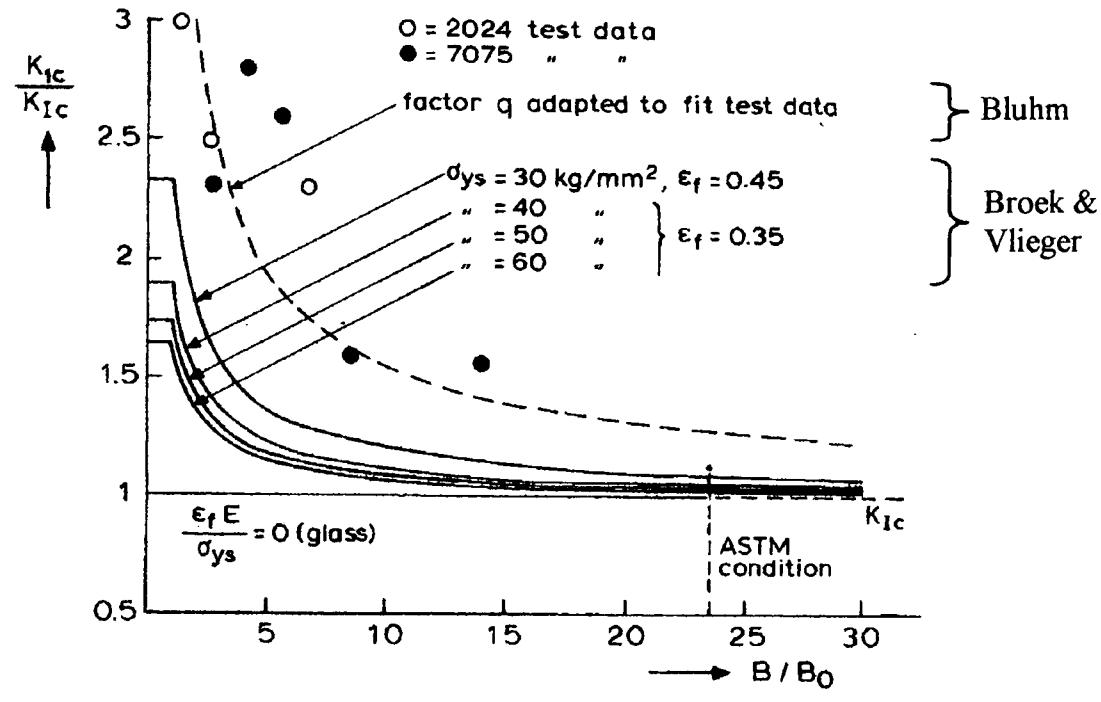

Fig. 2.10 Thickness models of Bluhm, and Broek and Vlieger. After Broek [2]

Similar results have been obtained from Broek and Vlieger's [22] extension of a model developed by Isherwood and Williams [23] which, with some simplifying, assumptions with respect to the plastic zone led to the following expression.

$$\frac{K_{IQ}}{K_{IC}} = \sqrt{1 + \frac{\varepsilon_f E}{24\sigma_Y} \cdot \frac{t_o}{t}} \quad \text{.....(2.28)}$$

where:

ε_f = the true fracture strain of the material

σ_Y = the material yield strength

Examination of equation (2.28) shows that K_{IQ} gradually approaches K_{IC} for large thickness values. However, at the ASTM limit condition of $2.5\,(K_{IC}/\sigma_Y)^2$ the predicted K_{IQ} still has a slight error in the order of a few percent when compared to measured values. The error depends largely on the material properties.

Other thickness models have been presented by Shih and Hartranft [24] and Anderson [25] who took a simplistic view that the transitional behaviour could be represented by a linear decrease from a maximum value to the ASTM thickness limit of $2.5\,(K_{IC}/\sigma_Y)^2$ value. Although the model of Anderson is applicable in design it does not predict thickness effects with any degree of accuracy.

With the above in mind both British and American standards [26, 27] call for fracture testing to be undertaken using specimens of minimum thickness $B \geq 2.5(K_Q/\sigma_Y)^2$ where K_Q is an estimated value of K_{IC}.

2.9 INFLUENCE OF SIDE GROOVING ON THICKNESS EFFECTS

In order that the effects of shear lips can be reduced, side grooves can be machined into the specimen along the line of expected crack growth.

Among the first researchers to investigate the effects of side grooving on measurements of plane strain fracture toughness were Freed and Krafft [28], who conducted an experimental investigation of side grooving using single edge notched tension specimens. Work was undertaken on 7178-T6 Aluminium Alloy, with 60 degree V notch side grooves and root radii between 0.002 and 0.005 ins., to attempt to establish if the data would be of the form:

$$K_{IC} = K_{NOM}\left(\frac{B}{B_N}\right)^m \quad \ldots\ldots (2.29)$$

where:

$B =$ specimen thickness

$B_N =$ specimen thickness at root of side groove

and evaluate the side groove sensitivity exponent m, which theoretical predictions [28, 29] suggest lies in the range of 0.5 – 1. The results from this work established that $m = 0.56$ for the material and side groove geometry tested, see fig. 2.11.

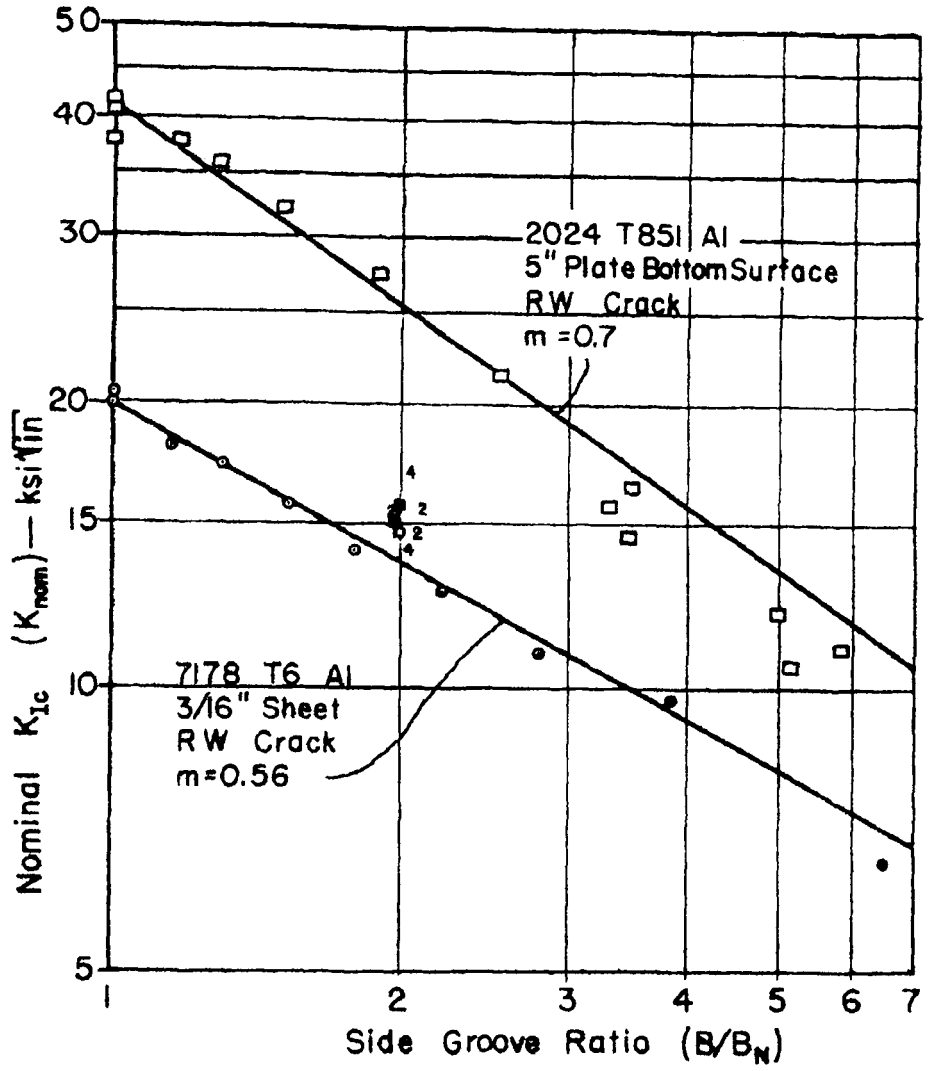

Fig. 2.11 Side groove sensitivity exponent, m, for two aluminium alloys. After Freed and Krafft [28]

Freed and Krafft also attempted to determine the size requirements for side grooved specimens in order to obtain representative K_{IC} measurements. The conclusion of this work was that side grooving may restore the detectability of crack initiation at specimen thickness as low as $5r_\gamma$.

MacDonald and Pajot [30] have recently given analytical support for Freed and Krafft's concept of effective thickness by using three dimensional, elastic finite element analysis of various smooth and 20% side grooved specimens. The results of this work indicated that the concept of effective thickness is slightly conservative in the form of the equation given in the British and American standards.

Another important work in the area of the elastic plastic analysis of side grooving was undertaken by Delorenzi and Shih [31] who built on the work of other investigators [32, 33] that had shown that the plain strain load displacement curve can be obtained from smaller specimens than called for by British and American standards, providing they were side grooved.

Shih et al [34] had earlier analysed the elastic stress and strain fields in the vicinity of the crack with varying depths of side grooves and shown that the optimum side groove depth was in the order of 25%. At this depth, the plain strain constraint and stress intensity factor are almost uniform across the crack front and only differ slightly from the 2D plane strain value.

Resulting from this earlier investigation, 25% side grooved compact tension specimens were used for the elastic-plastic analysis and a review of the linear elastic analysis. Finite element analysis repeated for the linear elastic case gave the results indicated in fig. 2.12 and fig. 2.13 when plotted as stress intensity ratio against distance from specimen edge. It was also observed that the stress intensity factor is higher all along the crack front in the side grooved specimen than the standard specimen by an average of about 3%. Also the stress intensity factor is constant across the section in the side grooved specimen but falls away towards the edge in the standard specimen.

Delorenzi and Shih also investigated the variation of plane strain constraint, $\sigma_z/(\sigma_x + \sigma_y)$, along the crack front. Plane strain constraint falls off considerably towards the edge of the standard specimen, fig. 2.14, but for side grooved specimens the plane strain constraint is much more uniform and drops only slightly at the side groove, see fig. 2.15.

2.10 FINITE ELEMENT ANALYSIS OF FRACTURE

The finite element method has over the past twenty years become established as a method of determining stress intensity factors in the practical analysis of fracture mechanics problems.

Several authors (see refs. [35 – 37]) have presented excellent reviews of the finite element method applied to fracture mechanics. The purpose of this section is to review only those aspects of the method that are relevant to the work presented in this thesis.

In order that finite elements can be used effectively for fracture mechanics analysis two considerations are important.

i) That the crack tip stress/strain singularity is correctly modelled.

ii) That the relevant fracture parameter, stress intensity factor or J integral, can be calculated.

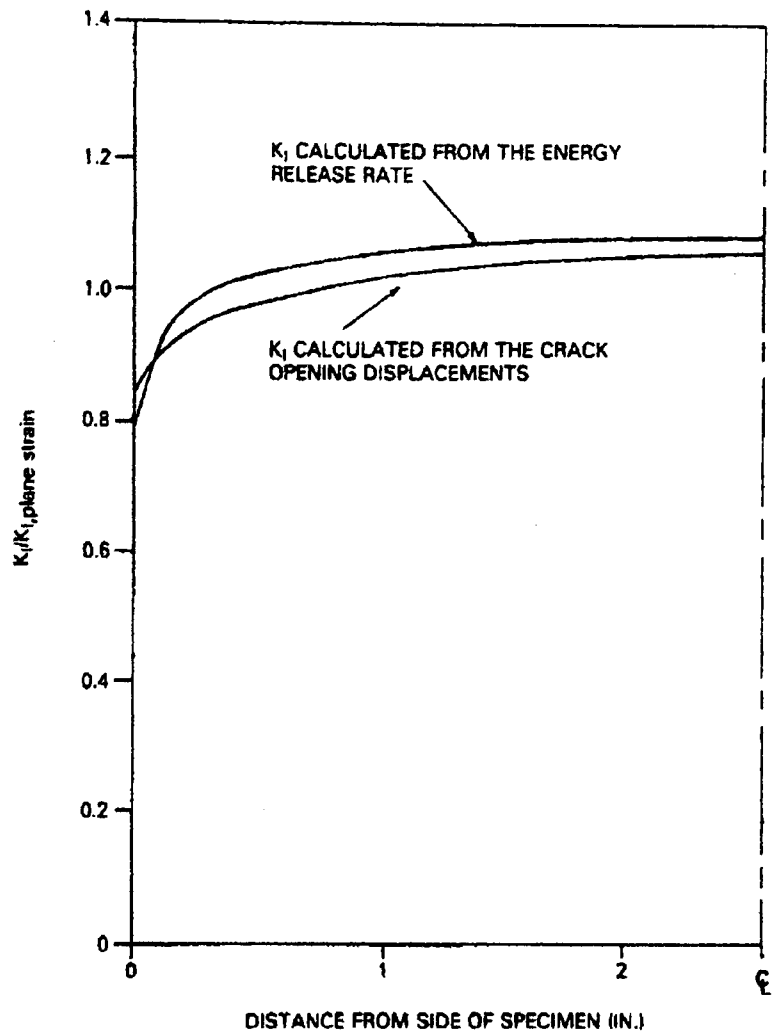

Fig. 2.12 Variation of stress intensity factor along crack front for a smooth compact specimen for a power law hardening material with $E/\sigma_0 = 500$, $\nu = 0.3$, $n = 10$ and $\alpha = 0.05$. After deLorenzi and Shih [31]

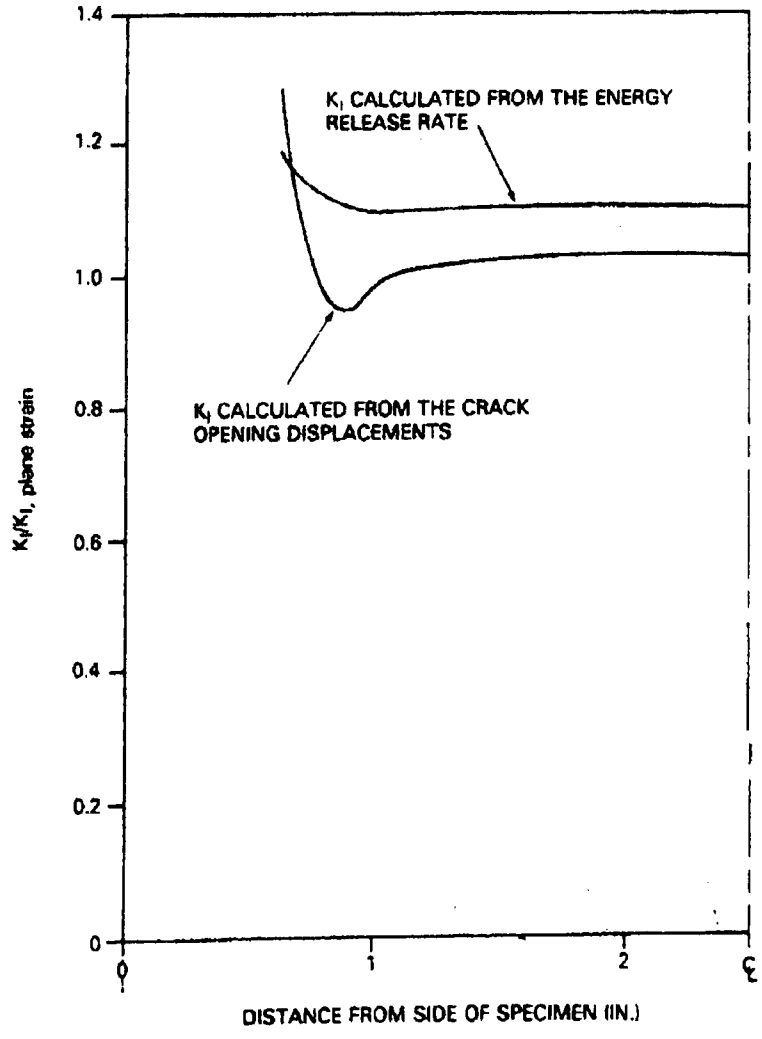

Fig. 2.13 Variation of stress intensity factor along crack front for a side grooved compact specimen for a power law hardening material with $E/\sigma_0 = 500$, $\nu = 0.3$, $n = 10$ and $\alpha = 0.05$. After deLorenzi and Shih [31]

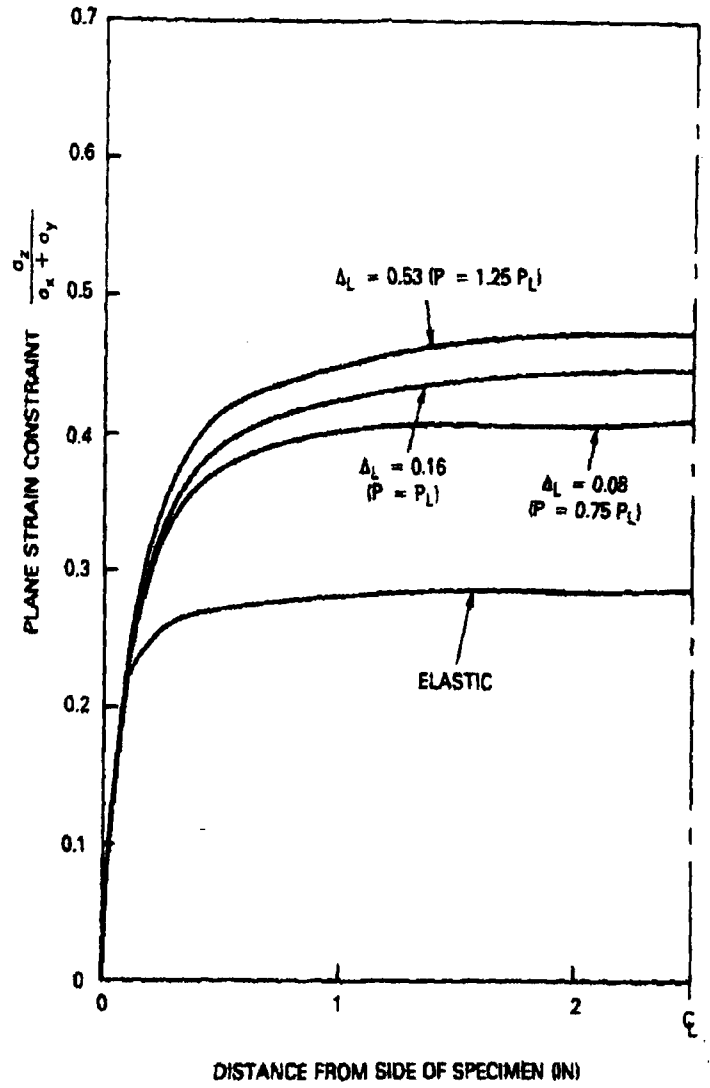

Fig. 2.14 Variation of plane strain constraint along crack front for a smooth compact specimen for a power law hardening material with $E/\sigma_0 = 500$, $\nu = 0.3$, $n = 10$ and $\alpha = 0.05$. After deLorenzi and Shih [31]

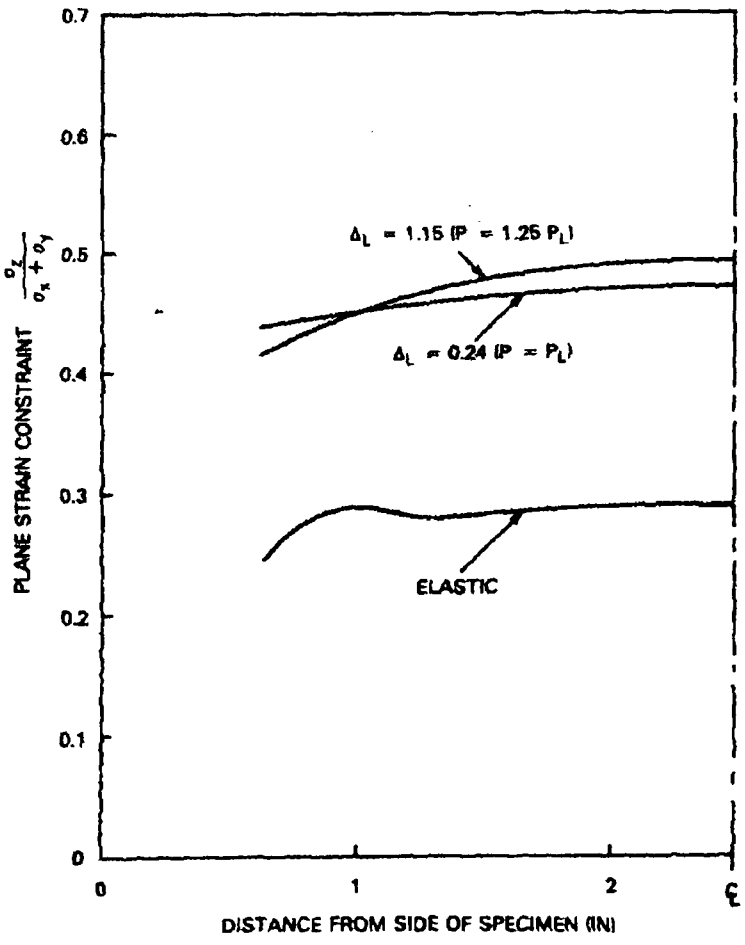

Fig. 2.15 Variation of plane strain constraint along crack front for a side grooved compact specimen for a power law hardening material with $E/\sigma_0 = 500$, $\nu = 0.3$, $n = 10$ and $\alpha = 0.05$. After deLorenzi and Shih [31]

2.10.1 CRACK TIP SINGULALRITY MODELLING

Early attempts to undertake fracture mechanics analysis used very fine meshes consisting of conventional elements, (see ref. [38]) in order to obtain the correct stress/strain field. In some instances, particularly when a very detailed prediction of the stress field ahead of the crack is required, this method is still used with blunted crack models.

Tracey [39] first introduced a $\frac{1}{\sqrt{r}}$ singularity into a finite element by employing a polynominal displacement field within a triangular element. This was then generalised into a family of elements by Tracey and Cook [40]. Blackburn [41] also formulated a singular triangular element whilst Benzley [42] introduced supplementary terms into the displacement field of a quadrilateral element to model the singularity. All of the element formulations so far have meant that special elements need to be placed around the crack tip. Major advances were made independently by Barsoum [43] and Henshell and Shaw [44] who introduced a $\frac{1}{\sqrt{r}}$ singularity simply by manipulation of the mid side nodes of a standard quadratic isoparametric element.

Consider the quadratic isoparametric element shown in fig. 2.16. The required strain singularity can be obtained at node 1 by moving the mid side nodes 2 and 8 to a position one quarter of the distance along the edge of the element as shown. For edge 1 – 3 defined in local co ordinates by $\eta = -1$ the shape functions are:

$$N_1 = -\frac{1}{2}\xi(1-\xi)$$
$$N_2 = (1-\xi^2)$$
$$N_3 = \frac{1}{2}\xi(1+\xi) \quad .....(2.30)$$

With the isoparametric element formulation a co ordinate in x can be written as:

$$x = \sum_{i=1}^{3} N_i x_i = -\frac{1}{2}\xi(1-\xi)x_1 + (1-\xi^2)x_2 + \frac{1}{2}\xi(1+\xi)x_3 \quad .....(2.31)$$

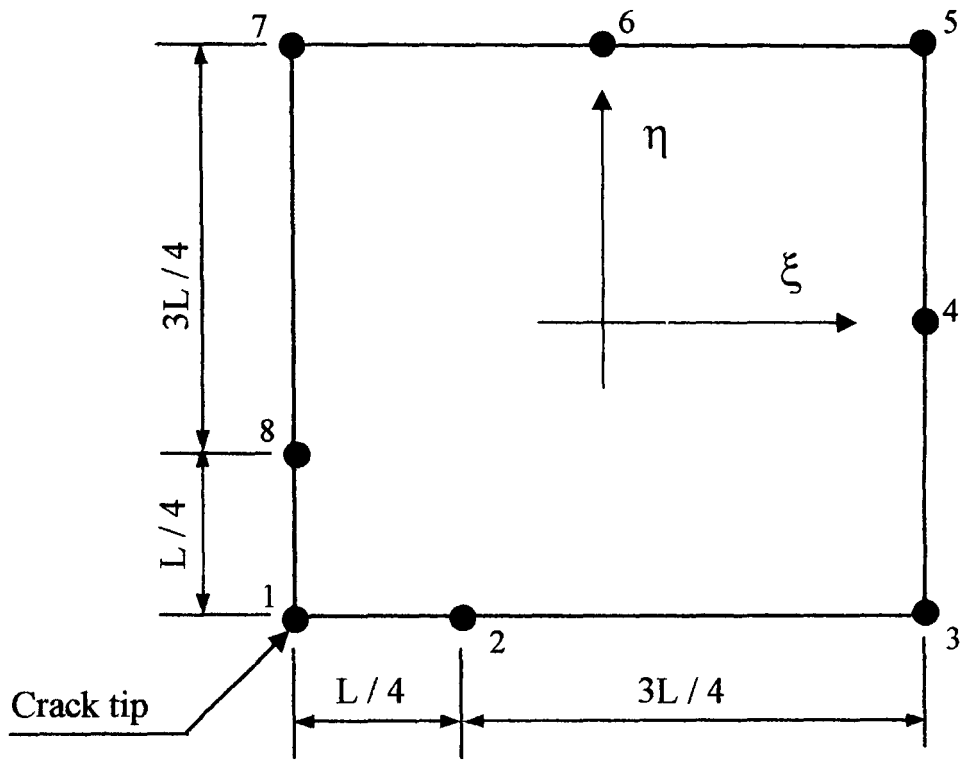

Fig. 2.16 Quadrilateral isoparametric element

substituting $x_1 = 0$, $x_2 = \frac{L}{4}$ and $x_3 = L$ into (2.31) gives:

$$x = \frac{1}{2}\xi(1+\xi)L + (1-\xi^2)\frac{L}{4} \quad \text{.....(2.32)}$$

hence:

$$\xi = -1 + 2\sqrt{\frac{x}{L}} \quad \text{.....(2.33)}$$

Again for the isoparametric element displacements are given as:

$$u = \sum_{i=1}^{3} N_i u_i = -\frac{1}{2}\xi(1-\xi)u_1 + (1-\xi^2)u_2 + \frac{1}{2}\xi(1+\xi)u_3 \quad \text{.....(2.34)}$$

substituting for ξ from (2.33) gives:

$$u = -\frac{1}{2}\left(-1+2\sqrt{\frac{x}{L}}\right)\left(2-2\sqrt{\frac{x}{L}}\right)u_1 + 4\left(\sqrt{\frac{x}{L}}-\frac{x}{L}\right)u_2$$

$$+\frac{1}{2}\left(-1+2\sqrt{\frac{x}{L}}\right)\left(2\sqrt{\frac{x}{L}}\right)u_3 \qquad \text{.....(2.35)}$$

The direct strain in the x direction is then given by:

$$\varepsilon_x = \frac{\partial u}{\partial x} = \frac{\partial \xi}{\partial x}\cdot\frac{\partial u}{\partial \xi} =$$

$$-\frac{1}{2}\left[\frac{3}{\sqrt{xL}}-\frac{4}{L}\right]u_1 + \left[\frac{2}{\sqrt{xL}}-\frac{4}{L}\right]u_2 + \frac{1}{2}\left[-\frac{1}{\sqrt{xL}}+\frac{4}{L}\right]u_3 \qquad \text{.....(2.36)}$$

Hence the strain singularity along edge 1 – 3 is of the correct order $\frac{1}{\sqrt{r}}$. It can also be shown that this is the case for edge 1 – 7, rays within the element emanating at node 1 do not give the correct singularity. The correct condition can be obtained by collapsing the element into a triangle and coalescing the nodes at the crack tip, that is, nodes 1, 7 and 8 in fig. 2.17. Again the mid side nodes are moved to the quarter position and it can be seen that the local co ordinates $\xi + \eta$ have now become directly related to the polar co ordinates r and θ respectively. Along the $\eta = 0$ axis the shape functions become:

$$N_1 = N_3 = N_5 = N_7 = -\frac{1}{4}\left(1-\xi^2\right)$$

$$N_2 = N_6 = \frac{1}{2}\left(1-\xi^2\right)$$

$$N_4 = N_8 = \frac{1}{2}\left(1-\xi\right) \qquad \text{.....(2.37)}$$

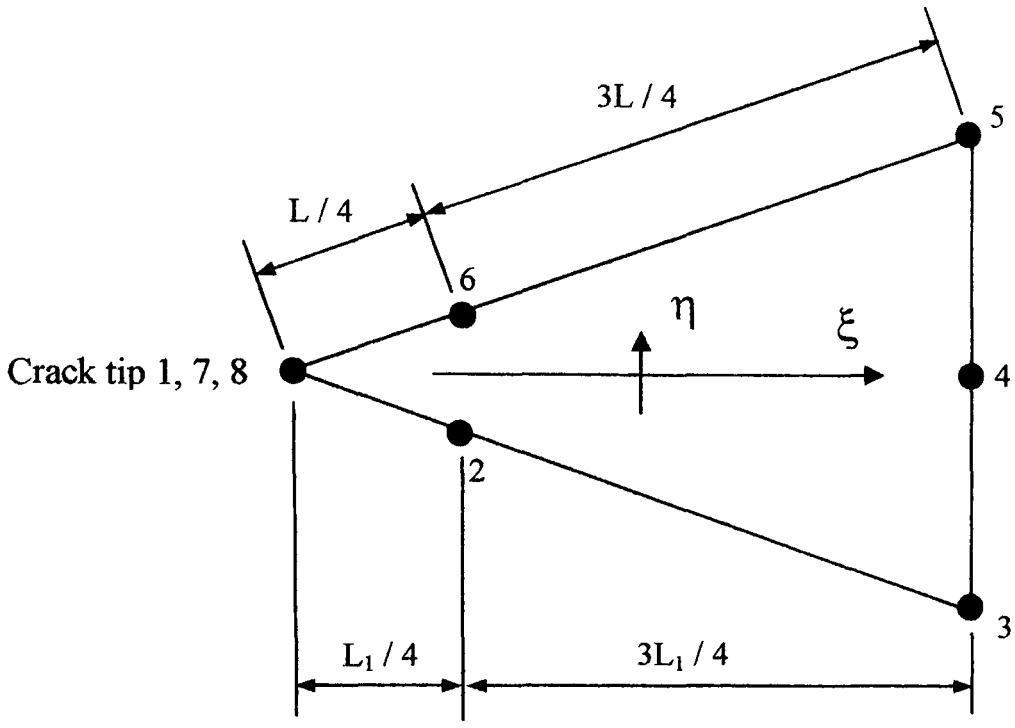

Fig. 2.17 Collapsed isoparametric element

If the crack tip is located at node 1 then:

$$x_1 = x_7 = x_8 = 0$$

$$x_2 = x_6 = \frac{L_1}{4}$$

$$x_3 = x_4 = x_5 = L_1 \quad \ldots\ldots (2.38)$$

Again with the isoparametric formulation x and y co ordinates can be written as:

$$\begin{bmatrix} x \\ y \end{bmatrix} = \sum_{i=1}^{n} \begin{bmatrix} N_i & 0 \\ 0 & N_i \end{bmatrix} \begin{bmatrix} x_i \\ y_i \end{bmatrix} \quad \ldots\ldots (2.39)$$

substituting (2.37) and (2.38) into (2.39) gives:

$$x = \frac{L_1}{4}(1+\xi)^2 \quad \ldots\ldots (2.40)$$

hence:

$$\xi = -1 + 2\sqrt{\frac{x}{L}} \quad \text{.....(2.41)}$$

which is identical to equation (2.33). The displacement along the axis becomes:

$$u = -\frac{1}{4}(1-\xi^2)(u_1 + u_3 + u_5 + u_7) + \frac{1}{2}(1-\xi^2)(u_2 + u_6)$$
$$+\frac{1}{2}(1-\xi)(u_4 + u_8) \quad \text{.....(2.42)}$$

and the strain distribution can now be directly calculated from:

$$\varepsilon_x = \frac{\partial \xi}{\partial x} \cdot \frac{\partial u}{\partial \xi} = \frac{1}{L_1}(2u_1 + u_3 + u_5 - 2u_2 - 2u_6)$$
$$-\frac{1}{2\sqrt{L_1 x}}(3u_1 + u_3 + u_4 + u_5 - 2u_2 - 2u_6) \quad \text{.....(2.43)}$$

Again it can be seen that the strain distribution exhibits a $\frac{1}{\sqrt{r}}$ singularity at the crack tip. It can also be shown that any ray emanating from the crack tip exhibits the same singularity.

2.10.2 STRESS INTENSITY FACTOR EVALUATION

Having established the correct strain singularity at the crack tip, stress intensity factors can now be obtained by a variety of methods as follows:

Crack Tip Opening Displacement

This method is derived from the general displacement extrapolation method [35]. The displacement field around a crack tip can be characterised as follows:

$$v = K_I \cdot \frac{\sqrt{2\pi r}}{8G\pi}\left[(2k+1)\sin\frac{\theta}{2} - \sin\frac{3\theta}{2}\right] \quad \text{.....(2.44)}$$

where:

$G =$ material shear modulus

$k =$ $3 - 4v$ for plane stress

$k =$ $(3 - v)/(1 + v)$ for plane strain

Hence the nodal displacement field can be determined by finite element analysis using crack tip elements as shown in fig. 2.18. Then for any particular radial line emanating from the crack tip K_I can be plotted against r. Results can then be extrapolated to $r = 0$ to give the stress intensity factor at the crack tip.

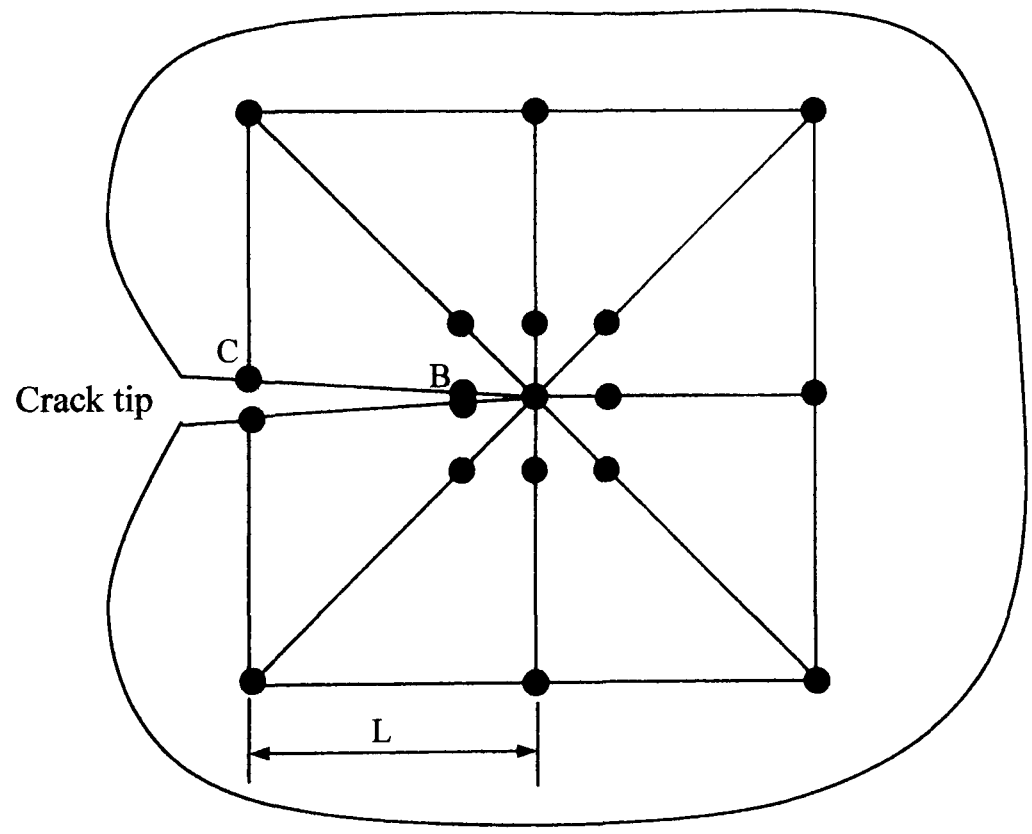

Fig. 2.18 Arrangement of crack tip elements

Particularly, by consideration of equation (2.44), for displacements along the crack face and the y component of the displacement field (v), Shih et al [45] showed that the mode I stress intensity factor K_I is given by:

$$K_1 = \frac{2G\sqrt{2\pi}\left(4V_B - V_C\right)}{\left(k+1\right)\sqrt{L}} \quad \ldots\ldots (2.45)$$

Hence the stress intensity factor can be calculated directly from knowledge of the crack tip opening displacement.

Strain Energy Release Rate

As was shown in section 2.3 when a crack of length a is extended by an amount δa it is accompanied by a release of strain energy δu such that the strain energy release rate is:

$$G = \frac{\delta u}{\delta a} \quad \text{.....(2.46)}$$

The stress intensity factor can then be calculated directly from equation (2.13) and (2.14). Hence by performing two finite element analyses for two crack lengths that differ by an amount δa and evaluating the change in strain energy δu the strain energy release rate and hence stress intensity factor can be calculated.

Virtual Crack Extension

The virtual crack extension method is a variant of the strain energy release rate method outlined above and was first proposed by Parks [46] and Helen [47]. Although the method is based on energy release rate its implementation does not require a second finite element solution with a slightly different crack length. For simplicity, the method is presented for a linear elastic two dimensional problem of unit thickness. Upon completion of a finite element analysis the form of the solution is a vector of nodal displacement $\{u\}$, the potential energy may be expressed as:

$$P = \frac{1}{2}\{u\}^T [K]\{u\} - \{u\}^T \{f\} \quad \text{.....(2.47)}$$

where:

$[K]$ is the global stiffness matrix

$\{f\}$ is the vector of prescribed nodal loads.

We can differentiate (2.47) with respect to crack length to obtain the energy release rate, i.e:

$$\left.\frac{-\partial P}{\partial l}\right|_{load} = \frac{-\partial\{u\}^T}{\partial l}\left[[K]\{u\}-\{f\}\right]-\frac{1}{2}\{u\}^T\frac{\partial[K]}{\partial l}\{u\}+\{u\}^T\frac{\partial\{f\}}{\partial l} \quad \text{..... (2.48)}$$

The global stiffness matrix [K] is symetric and the term $\left[[K]\{u\}-\{f\}\right]$ has been made exactly zero by the finite element solution. For plane strain:

$$\left.\frac{-\partial P}{\partial l}\right|_{load} = K_I{}^2\frac{(1-\nu^2)}{E} = \frac{-1}{2}\{u\}^T\frac{\partial[K]}{\partial l}\{u\}+\{u\}^T\frac{\partial\{f\}}{\partial l} \quad \text{..... (2.49)}$$

The matrix $\frac{\partial[K]}{\partial l}$ is the change in the global stiffness matrix per unit crack advance. Consider fig. 2.19, crack advance is produced by rigidly translating all nodes on and within a contour Γ_0 about the crack tip by a small amount Δl in the x direction. All other nodes remain in their original position. Hence the global stiffness matrix [K], which depends only on individual element geometries, displacement functions and elastic material properties, remains unchanged in the regions interior to Γ_0 and exterior to Γ_1. The only contributions to (2.49) come from the band of elements between the two contours. The global stiffness matrix is the sum over all the element stiffness matrices, hence:

$$-\frac{1}{2}\{u\}^T\frac{\partial[K]}{\partial l}\{u\} = -\frac{1}{2}\{u\}^T\sum_{i=1}^{N_C}\frac{\partial[K_i^C]}{\partial l}\{u\} \quad \text{..... (2.50)}$$

where $[K_i^C]$ is the element stiffness matrix of an element between contours Γ_0 and Γ_1 and N_C is the number of elements.

If the structure loading is due to forces outside the crack tip elements then the load vector $\{f\}$ is independent of crack advance and equation (2.49) reduces to:

$$K_I{}^2\frac{(1-\nu^2)}{E} = -\frac{1}{2}\{u\}^T\frac{\partial[K]}{\partial l}\{u\} \quad \text{..... (2.51)}$$

However, if body forces and/or crack face loadings are to be included then the full form of equation (2.49) needs to be considered, for a description of the method see ref. [46].

The terms in equation (2.47) are obtained and post processed directly from the finite element analysis results. Parks [48] later extended the analysis to include plasticity effects.

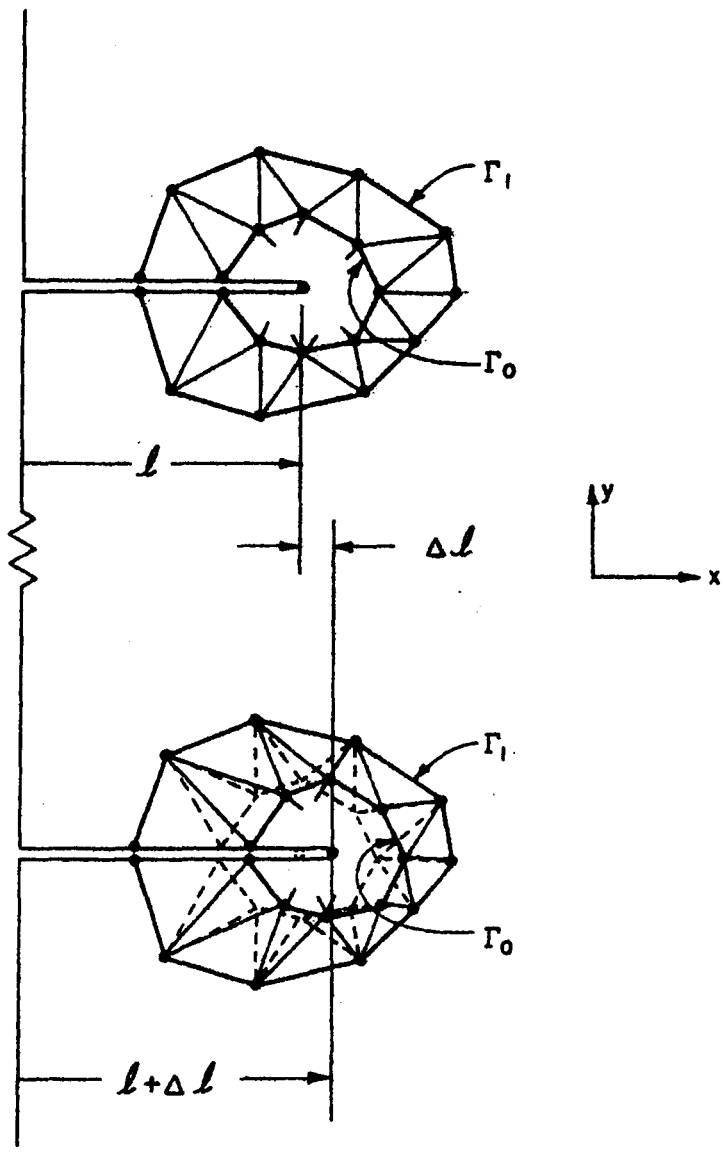

Fig. 2.19 Accommodation of crack tip extension by advancing nodes. After Parks [46]

CHAPTER 3

TWO PARAMETER FRACTURE MECHANICS – A REVIEW

3.1 INTRODUCTION

The previous chapter outlined the background theoretical considerations relevant to the work presented in this thesis. What was described was a single parameter representation in terms of K or J, which are both a measure of the intensity of the near crack tip deformation and stress fields. In practice the extent to which these parameters dominate is largely dependent on the amount of constraint at the crack tip.

In situations where high levels of crack tip constraint are not present a single parameter representation is no longer adequate and a two parameter approach is required. This chapter outlines the principles of non linear fracture mechanics and some recent approaches to two parameter fracture mechanics that will be put to use later in the thesis.

3.2 NATURE OF CRACK TIP STRESS FIELDS

The underlying theory behind non linear fracture mechanics for materials under monotonic loading is the J integral as defined in section 2.7. From a physical point of view J is a measure of the intensity of near tip deformation. Solutions to the governing equations based on power law hardening materials for crack tip stress fields were first presented, independently, by Hutchinson [49, 50] and Rice and Rosengren [51, 52]. The solutions are asymptotic and are based on the assumption that the crack remains sharp. The resulting singularity fields are commonly referred to as the HRR fields and together with the J integral form the theoretical basis of non linear fracture mechanics.

The HRR fields are based on a power law hardening material model, a convenient form of which is the Ramberg–Osgood equation:

$$\frac{\varepsilon}{\varepsilon_o} = \frac{\sigma}{\sigma_o} + \alpha\left(\frac{\sigma}{\sigma_o}\right)^n \quad \ldots\ldots (3.1)$$

where σ_o is the effective yield stress, $\varepsilon_o = \frac{\sigma_o}{E}$ and α and n are parameters chosen to fit data. Typical values of n for metals are in the range 5 for high levels of hardening to 50 for low levels of hardening. Within the immediate vicinity of the crack tip the elastic strains are negligible in comparison to the plastic strains hence only the plastic part of the Ramberg–Osgood equation needs to be considered, equation (3.1) becomes:

$$\frac{\varepsilon}{\varepsilon_o} = \alpha\left(\frac{\sigma}{\sigma_o}\right)^n \quad .....(3.2)$$

If J_2 deformation theory (von-Mises) is used, equation (3.2) can be extended to multiaxial states resulting in the following:

$$\frac{\varepsilon_{ij}}{\varepsilon_o} = \frac{3}{2}\alpha\left(\frac{\sigma_e}{\sigma_o}\right)^{n-1}\frac{S_{ij}}{\sigma_o} \quad .....(3.3)$$

where:

$$\sigma_e = \left(\frac{3}{2}S_{ij}\,S_{ij}\right)^{\frac{1}{2}} \quad .....(3.4)$$

and S_{ij} is the deviatoric stress.

With reference to polar co ordinates HRR [49 – 51] showed that the asymtotic crack-tip stress, strain and displacement fields are:

$$\sigma_{ij} = \sigma_o\left(\frac{J}{\alpha\sigma_o\varepsilon_o I_n r}\right)^{\frac{1}{n+1}}\tilde{\sigma}_{ij}(\theta,n) \quad .....(3.5)$$

$$\varepsilon_{ij} = \alpha\varepsilon_o\left(\frac{J}{\alpha\sigma_o\varepsilon_o I_n r}\right)^{\frac{n}{n+1}}\tilde{\varepsilon}_{ij}(\theta,n) \quad .....(3.6)$$

$$u_i - \tilde{u}_i = \frac{J}{I_n\sigma_o}\left(\frac{\alpha\sigma_o\varepsilon_o I_n r}{J}\right)^{\frac{1}{n+1}}\tilde{u}_i(\theta,n) \quad .....(3.7)$$

The stress distribution ahead of the crack tip as given by equation (3.5) is illustrated in fig. 3.1. Further details of the fields are given in [49 – 51] and have been extended to mixed mode problems by Shih [53].

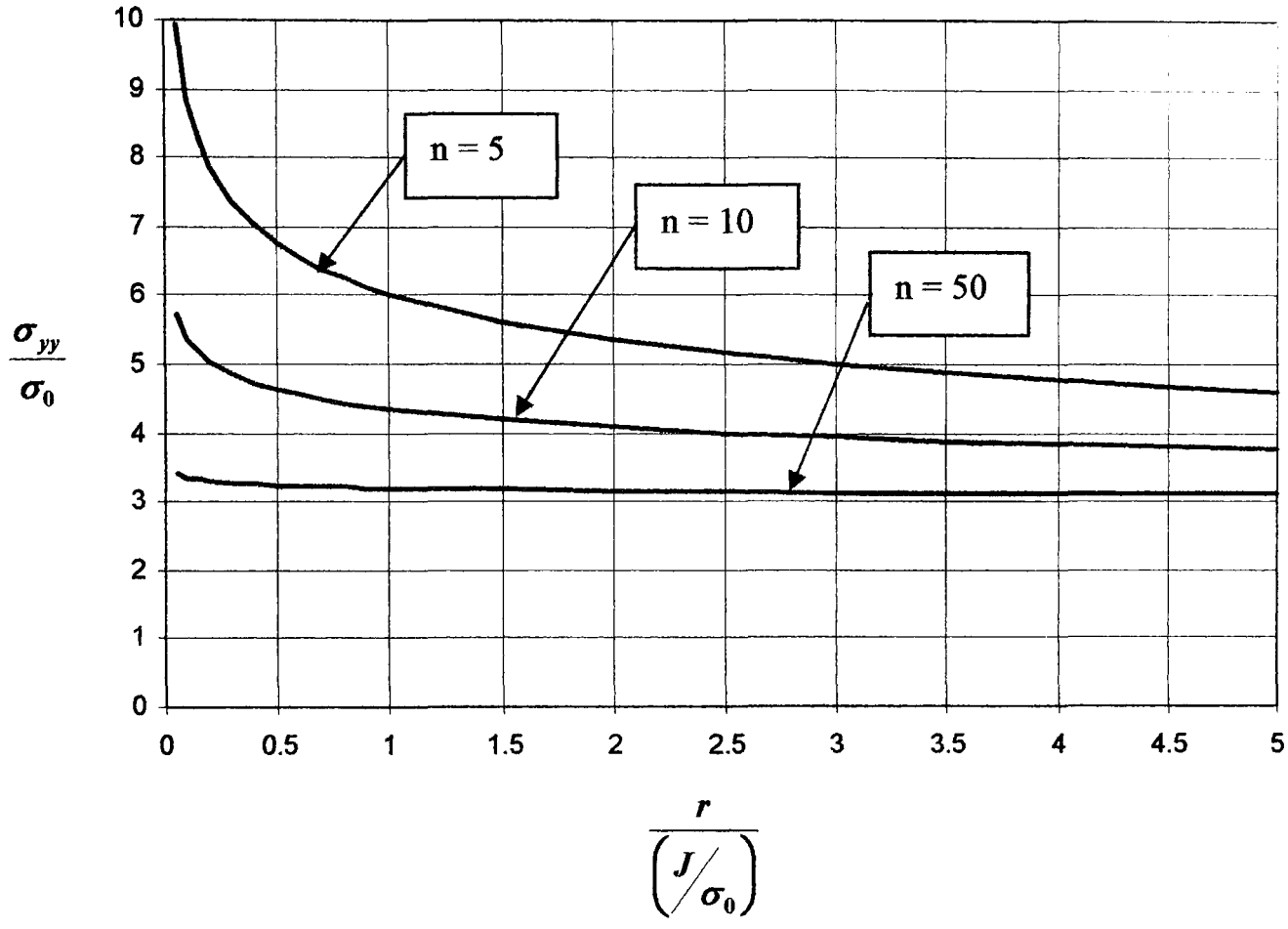

Fig. 3.1 HRR stress fields for n = 5, 10 and 50, $E/\sigma_0 = 300$ materials

The dimensionless θ variations $\tilde{\sigma}$, $\tilde{\varepsilon}_{ij}$ and $\tilde{u}_{ij}$ depend on the crack opening mode, n, and whether plane strain or plane stress in assumed as does the normalising constant I_n. These variations are normalised in [49] and [53] by setting the maximum θ variation of the effective stress $\tilde{\sigma}_e$ to unity. Tabulated results for $\tilde{\sigma}_{ij}$, $\tilde{\varepsilon}_{ij}$, $\tilde{u}_{ij}$ and I_n are given by Shih in [54].

3.3 MECHANISMS OF FAILURE

Macroscopic fracture behaviour based on K or J does not necessitate any understanding of the fracture events that occur on a microscopic scale. However, in order to fully understand fracture processes, it is essential to review the various mechanisms of fracture that occur on such a microscopic scale.

Failure of metals can occur in a number of ways that can be generally grouped as being either ductile or brittle in nature. In some cases, as with ferritic steels in the ductile/brittle transition, the fracture processes can be complex with ductile tearing and cleavage fracture competing.

3.3.1 CLEAVAGE FRACTURE

Many models have been proposed for cleavage fracture some involving statistical considerations, others not. In the context of the work being presented in this thesis one particular cleavage failure model will be considered, this being due to Ritchie, Knott and Rice [55], hence being known as the RKR model.

The model relates the critical value of tensile stress (σ_f) ahead of a crack for unstable cleavage fracture to fracture toughness K_{IC} and is based on the cleavage cracking model of Smith [56, 57] and accurate elastic plastic stress solutions ahead of a sharp crack by Rice and Johnson [58].

Earlier work by Orowan [59] and Knott [60] had shown that for slip induced cleavage fracture the local stress, σ_{yy}, ahead of a stress concentrator had to exceed a critical value, σ_f, with values of σ_f being calculated from slip line field theory using rigid plastic solutions for notched bars in plane strain bending.

Such a solution, due to Hill [61] is shown in fig. 3.2 with the maximum value of σ_{yy} being achieved when the plastic zone size reaches a critical radius r_Y' as:

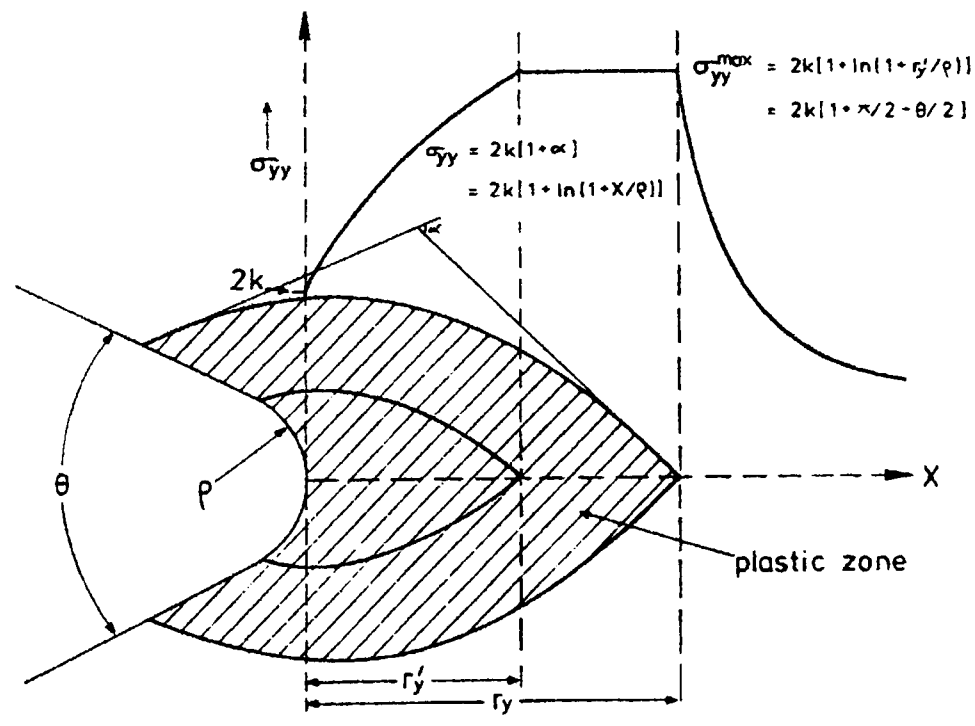

Fig. 3.2 Schematic longitudinal stress (σ_{yy}) distribution ahead of a rounded notch at general yield based on Hill's rigid/plastic slip-line field solution [61], after Ritchie *et. al.*[55]

$$\sigma_{yy}{}^{max} = 2k\left[1+\ln\left(1+r_Y'/\rho\right)\right] \quad \ldots\ldots (3.8)$$

where:

k is the shear yield stress

ρ is the root radius

r_Y is the plastic zone dimension

This value being assumed to be approximately constant up to the plastic elastic interface.

RKR extended this work by considering the HRR asymptotic stress fields together with the approximate modified stress distribution allowing for progressive crack tip blunting of Rice and Johnson, see fig. 3.3.

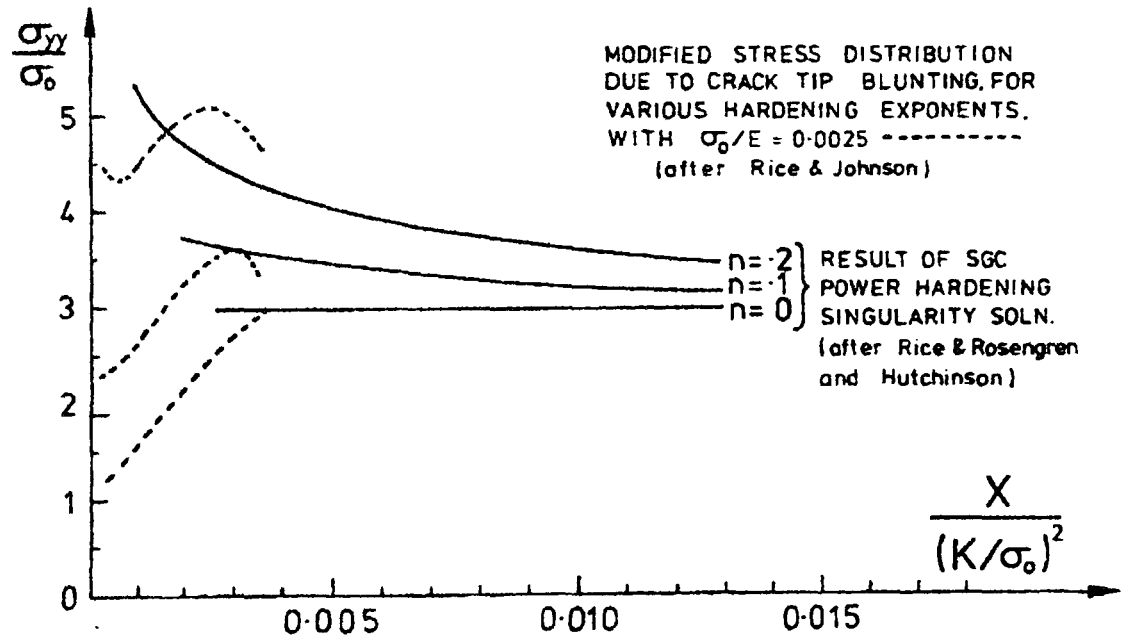

Fig. 3.3 Distribution of longitudinal stress (σ_{yy}) ahead of a sharp crack under plane strain and small scale yielding conditions from the singularity solution for a hardening material due to HRR (solid lines) and modified due to crack tip blunting due to Rice and Johnson [58], after Rice and Johnson [58]. After Ritchie and Thompson [62]

It is clear that the maximum stress intensification possible at a crack tip can be much larger than that predicted for a rounded notch by slip line field theory. Also the maximum stress occurs not at the elastic plastic interface but much closer to the crack tip. Hence if the cleavage failure criterion for a sharp crack were simply

that σ_{yy} be sufficiently large to exceed some critical value σ_f then fracture could be produced by vanishingly small loads.

RKR found it necessary, therefore, to supplement this earlier theory by the additional requirement that the critical stress needs to be achieved over some microstructurally significant distance ahead of the crack tip.

Using the HRR field as defined by equation (3.5) [62] to define the stress field the RKR model implies [55, 63, 64] that:

$$K_{IC}\alpha\left[\frac{(\sigma_f)^{\frac{(1+n)}{2}}}{(\sigma_o)^{\frac{(1-n)}{2}}}\right]l_o^{\frac{1}{2}} \quad .....(3.9)$$

where:

σ_o is the effective yield stress

n is the strain hardening index

l_o is a characteristic distance

By comparison of calculated results with experimental data for the variation of K with temperature, RKR found very close agreement when l_o was set equal to two grain diameters. The principles of the RKR model are shown in fig. 3.4a.

3.3.2 DUCTILE FRACTURE

The mechanism of ductile fracture is essentially one of microvoid coalescence which tends to be more complex in nature than that of cleavage fracture.

Microvoids nucleate at various internal discontinuities such as intermetallic particles and precipitates and also at grain boundaries. As local stress increases these microvoids grow, coalesce and eventually form a fracture surface that is dimpled in appearance. Dimple shape is strongly influenced by loading type with uniaxial tensile loading resulting in the formation of equiaxed dimples. Shear will produce elongated or parabolic shaped dimples that point in opposite directions

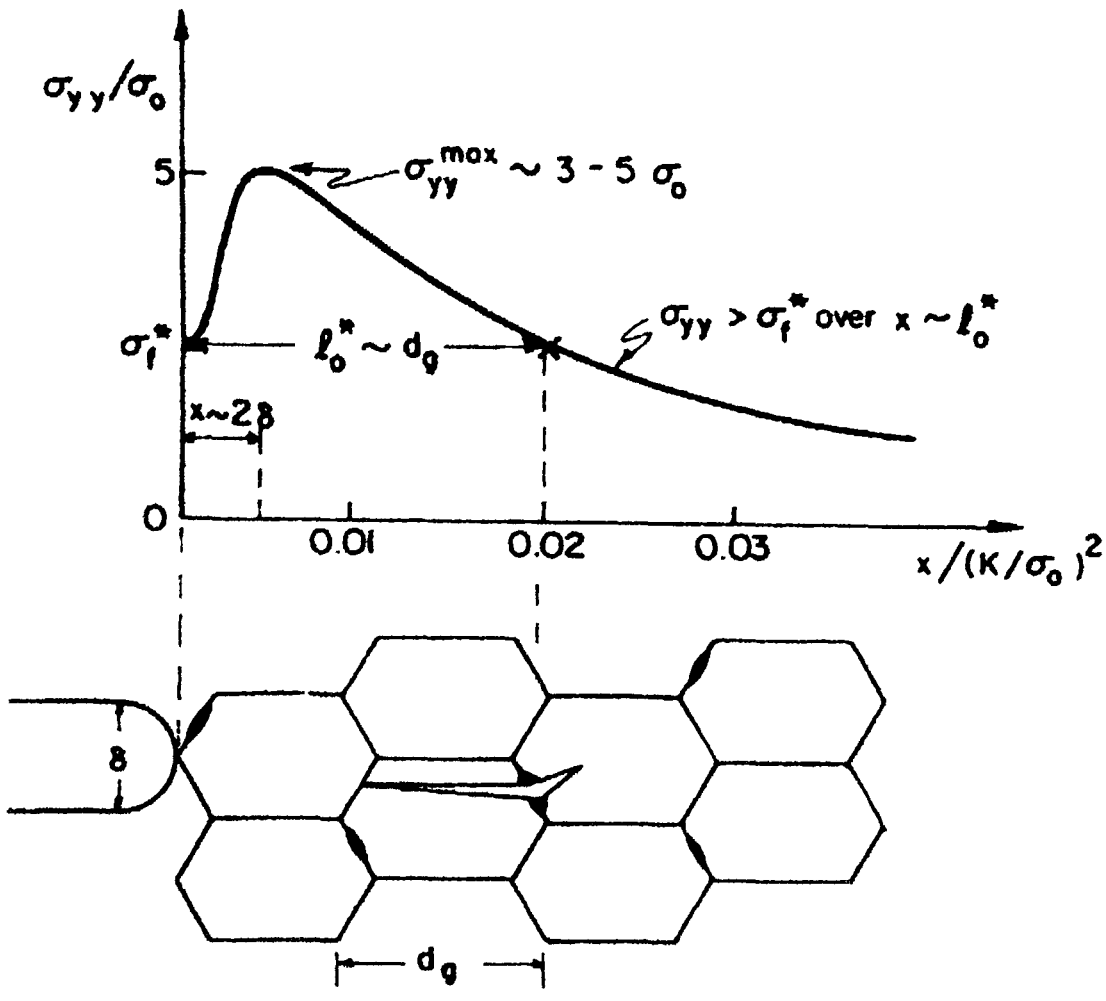

Fig. 3.4 Schematic idealisation of microscopic fracture criteria pertaining to (a) critical stress-controlled model for cleavage fracture (RKR) and (b) critical stress-modified critical strain-controlled model for microvoid coalescence. After Ritchie and Thompson [62]

on the two fracture surfaces, whilst tensile tearing produces elongated dimples that point in the same direction on the two fracture surfaces.

For ductile fracture initiation by microvoid coalescence several authors [65, 58, 66] considered that the critical crack tip opening displacement must exceed half of the mean void initiating particle spacing. By considering non hardening materials this criterion is fulfilled when the void sites are enveloped by the intense strain region at the crack tip, i.e. at a distance of approximately 2δ from the tip. The model implies that:

$$\delta_i = \delta_{IC} \approx (0.5 \; to \; 2) d_p \quad \ldots\ldots (3.10)$$

where:

δ_i is the crack tip opening displacement at initiation

δ_{IC} is the critical crack tip opening displacement

d_p is the distance between void initiating particles.

The main limitation with this model is that it also implies that:

$$J_{IC} \approx \sigma_o l_o \quad \ldots\ldots (3.11)$$

It is unusual to find a practical case where the fracture toughness increases directly with increasing yield strength.

The problem has been overcome by the approach of McClintock [67], Mackenzie et al [68] and others [64, 70] who have proposed a stress modified critical strain criterion. In this approach the equivalent plastic strain $\bar{\varepsilon}_p$ must exceed a critical fracture strain or ductility $\bar{\varepsilon}_f^* \left(\frac{\sigma_m}{\bar{\sigma}} \right)$, specific to the relevant stress state over a characteristic distance l_o. The characteristic distance is comparable to the mean spacing of the void initiating particles d_p. The principles of the model are shown in fig. 3.4b.

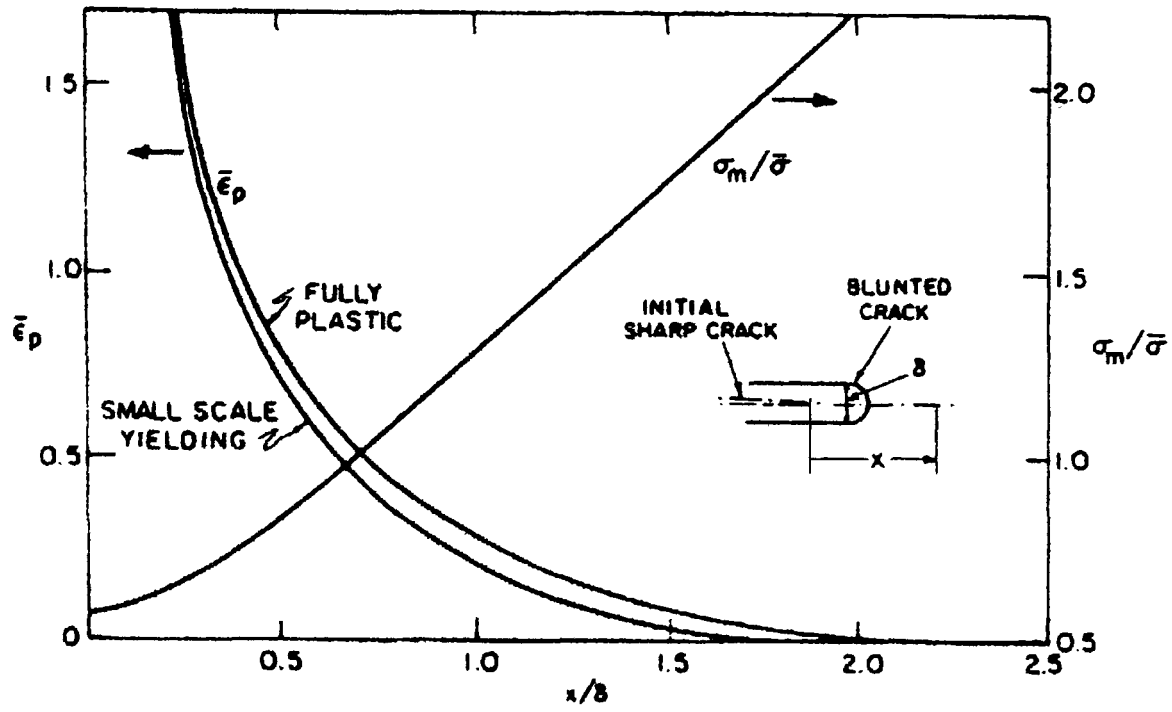

Fig. 3.5 Distribution of local equivalent plastic strain $\bar{\varepsilon}_p$ as a function of distance x, normalised with respect to δ the CTOD, directly ahead of a crack tip under plane strain conditions together with the corresponding variation of stress state $(\sigma_m/\bar{\sigma})$. Solutions based on finite geometry blunting solutions of Rice and Johnson [58] and Mc Meeking [69] for both small-scale yielding and fully plastic conditions. After Ritchie and Thompson [62]

Richie et al [64] considered the near-tip strain distribution shown in fig. 3.5 in terms of x/δ and showed that:

$$\bar{\varepsilon}_p \, \alpha \left(\frac{J}{\sigma_o r}\right)^{\frac{1}{n+1}} \approx C_1 \left(\frac{\delta}{x}\right) \quad .....(3.12)$$

where C_1 is a constant of order unity. Hence the initiation criterion of $\bar{\varepsilon}_p > \bar{\varepsilon}_f^* \left(\frac{\sigma_m}{\bar{\sigma}}\right)$ over $x = l_o \approx d_p$ at $J = J_{IC}$ implies a ductile fracture toughness of:

$$\delta_i = \delta_{IC} \approx \bar{\varepsilon}_f^* l_o \quad .....(3.13)$$

or

$$J_{IC} \approx \sigma_o \bar{\varepsilon}_f^* l_o \quad .....(3.14)$$

and

$$K_{IC} = \sqrt{J_{IC} E'} \approx \sqrt{E' \sigma_o \bar{\varepsilon}_f^* l_o} \quad .....(3.15)$$

Equation (3.15) now implies that J_{IC} for ductile fracture is proportional to strength times ductility which is more physically realistic. Also in terms of critical plastic zones size for Mode I fracture, r_{Yi} [62]:

$$r_{Yi} \approx \frac{1}{\pi} \cdot l_o \cdot \frac{\bar{\varepsilon}_f^{\,*}}{\varepsilon_o} \quad \ldots\ldots (3.16)$$

where ε_o is the yield strain (σ_o/E) and α is taken to be 0.5.

Although there is no conceptual difficulty with the term $\bar{\varepsilon}_f^{\,*}$ its definition as a material constant is difficult in practice. For a review of recent techniques for determining $\bar{\varepsilon}_f^{\,*}$ see [62].

3.4 J DOMINANCE

As previously stated in section 3.2 the J integral is a measure of the intensity of the near tip deformation. Solutions for power law hardening materials as given by the HRR fields in the crack tip region depend upon a high degree of crack tip constraint. If this high level of constraint is present then the HRR fields are valid and a single character parameterisation of the materials fracture behaviour is given by the J integral.

In practice the extent to which the HRR fields dominate over a length scale which is larger than the fracture process zone is termed J dominance. Early work by Begely and Landes [71] denoted the radius of the zone of J dominance as R, see fig. 3.6, which depends strongly on specimen geometry and hardening, particularly for low-hardening materials. In order to ensure the above conditions, Paris [72] suggested that in addition to the size of the uncracked ligament C, another important parameter is the specimen thickness B, giving a minimum value for J dominance of:

$$B, C \geq M \frac{J_{IC}}{\sigma_o} \quad \ldots\ldots (3.17)$$

Paris suggested that for thickness considerations a value of $M = 50$ should be used.

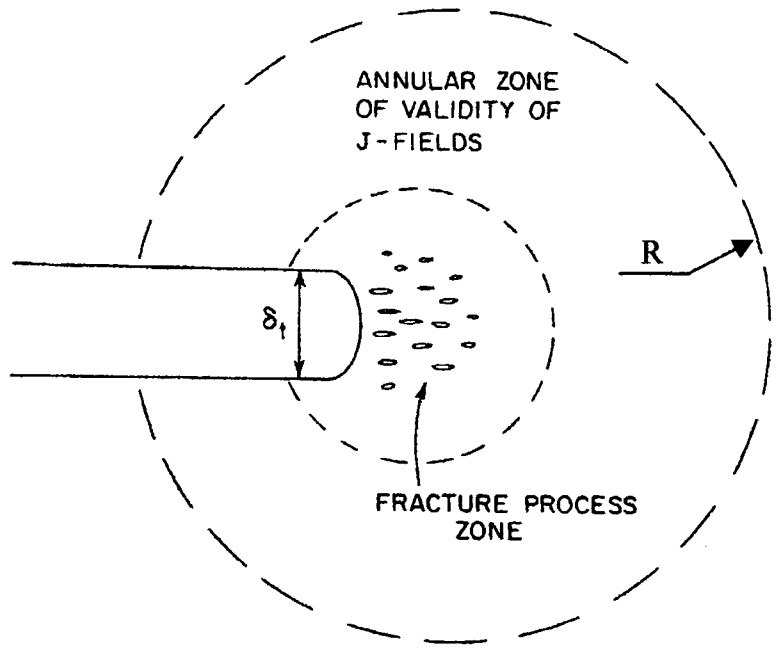

Fig. 3.6 Schematic of near-tip behaviour under J-dominance conditions

McMeeking and Parks [73] carried out a careful plane strain finite element study of edge cracked bend specimens and centre cracked plates for low hardening materials based on a finite deformation formulation. They concluded that to ensure valid J tests using centre cracked plates a conservative estimate of $M = 200$ can be used for the uncracked ligament length.

Shih and German [74] used finite element analysis based on small strain theory to evaluate detailed crack tip stress and strain fields again for edge cracked and centre cracked plate geometries. The result of this work was to validate the results of McMeeking and Parks.

In order to attempt to overcome the restrictions of a single parameter approach to elastic plastic fracture mechanics several authors have examined the possibility of using a two parameter approach. In the context of work presented in this thesis two such approaches are relevant, the T stress approach and J-Q theory both of which are described in the next two sections.

3.5 T STRESS

The elastic crack tip stress field was expressed by Williams [75] as an asymptotic series in cylindrical *(r, θ)* co ordinates about the crack tip, i.e:

$$\sigma_{ij} = A_{ij}(\theta)r^{-1/2} + B_{ij}(\theta) + C_{ij}(\theta)r^{-1/2} + \quad .....(3.18)$$

Restricting interest to the first two terms of the expansion, i.e., neglecting small order effects it can be seen that the first term is singular at the crack tip and forms the basis of linear elastic fracture mechanics when expressed in the form of equation (2.11).

Larsson and Carlsson [76] demonstrated that the second term in the series has a significant effect on the size and shape of the plastic zone at the crack tip. Using the notation of Rice [77] the second term is denoted as the T stress and can be regarded as a uniaxial tensile or compressive stress parallel to the crack flanks. In matrix form the first two terms can be written:

$$\begin{bmatrix} \sigma_{11} & \sigma_{12} \\ \sigma_{21} & \sigma_{22} \end{bmatrix} = \frac{K}{\sqrt{2\pi r}} \begin{bmatrix} f_{11}(\theta) & f_{12}(\theta) \\ f_{21}(\theta) & f_{22}(\theta) \end{bmatrix} + \begin{bmatrix} T & O \\ O & O \end{bmatrix} \quad .....(3.19)$$

The magnitude of the T stress can be defined through a biaxiality parameter B, introduced by Leevers and Radon [78] as:

$$B = \frac{T\sqrt{\pi a}}{K} \quad .....(3.20)$$

Alternatively T can be expressed simply as a stress concentration factor $\left(\frac{T}{\sigma}\right)$, hence T can be obtained by multiplying an applied stress by a tabulated constant.

Following the work of McMeeking and Parks [73] and Shih and German [74], Betegon and Hancock [79] investigated the effects of T stress on J dominance. They first used a plane strain boundary layer formulation involving both K and T terms which they later

correlated with full field solutions for centre cracked plate and edge cracked bar geometries exhibiting positive and negative T stresses.

Du and Hancock [80] examined the effects of T stress on crack tip constraint and plastic zone development ahead of a crack tip whilst Al-Ani and Hancock [81] also examined the effects of T stress on J dominance of short cracks in tension and bending. Refs. [79-81] are discussed in detail as follows:

3.5.1 TWO PARAMETER CHARACTERIZATION OF ELASTIC-PLASTIC CRACK-TIP FIELDS, After Betegon and Hancock [79], 1991

In this work the crack-tip deformation was first modelled by a boundary layer formulation using focused meshes as shown in fig. 3.7. The meshes consisted of 240 eight-noded isoparametric elements arranged in 20 rings of 12 elements concentric with the crack tip. The crack tip consisted of 25 independent but initially coincident nodes. The radius ratio between the first ring of elements and the outer ring of elements was 1:1000. Displacement boundary conditions were imposed on the outer boundary which corresponded to the displacements associated with a K field and various levels of T stress. The material was described by the Ramberg-Osgood power law hardening model as defined by equation (3.1) with n set to *3, 13* and ∞. Poisson's ratio was set to *0.3* and α = *3/7*, while the ratio of yield stress σ_o to the elastic modulus E was *0.002*. The analysis was based on small strain flow plasticity theory and carried out using the ABAQUS finite element package.

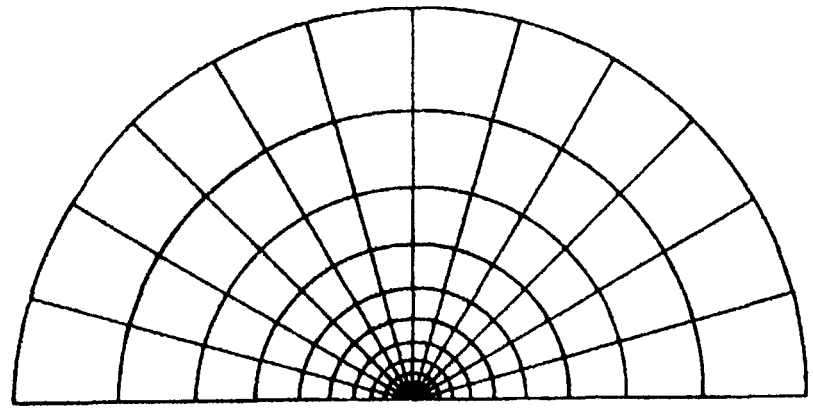

Fig. 3.7 Boundary layer formulation mesh, after Betegon and Hancock [79]

Analysis results for B = -1.06, 0 and +1.06 with $n = \infty$ and 13 are shown in fig. 3.8, where B is defined by equation (3.20).

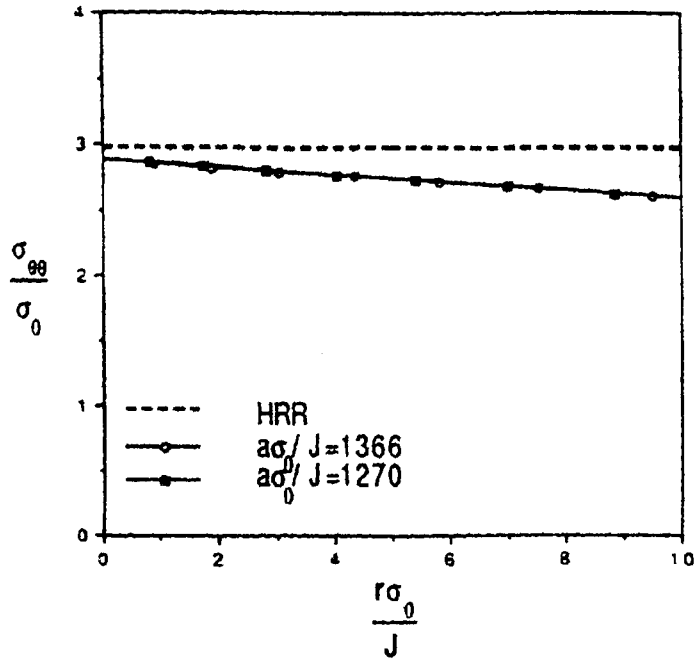

(a) Tangential stress ahead of a crack in a non-hardening plastic boundary layer formulation, B = 0, n = ∞

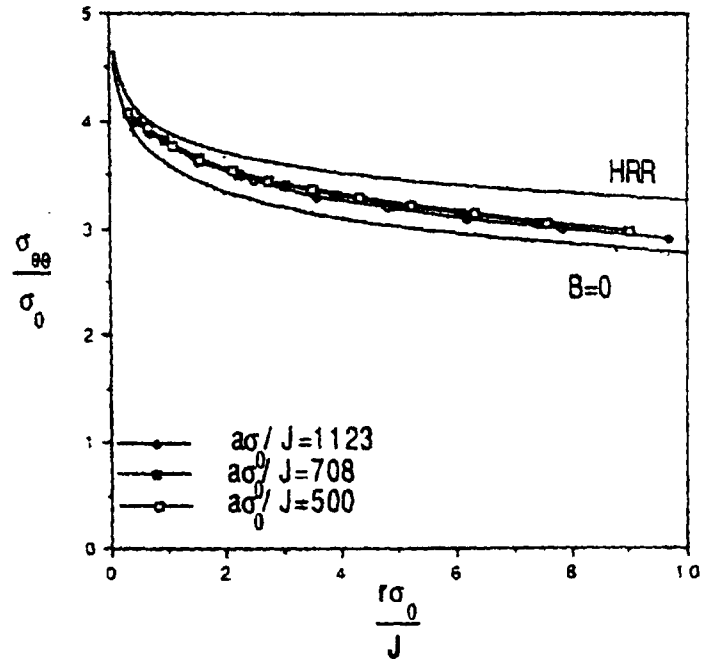

(b) Tangential stress ahead of a crack in a modified boundary layer formulation, B = +1.06, n = 13

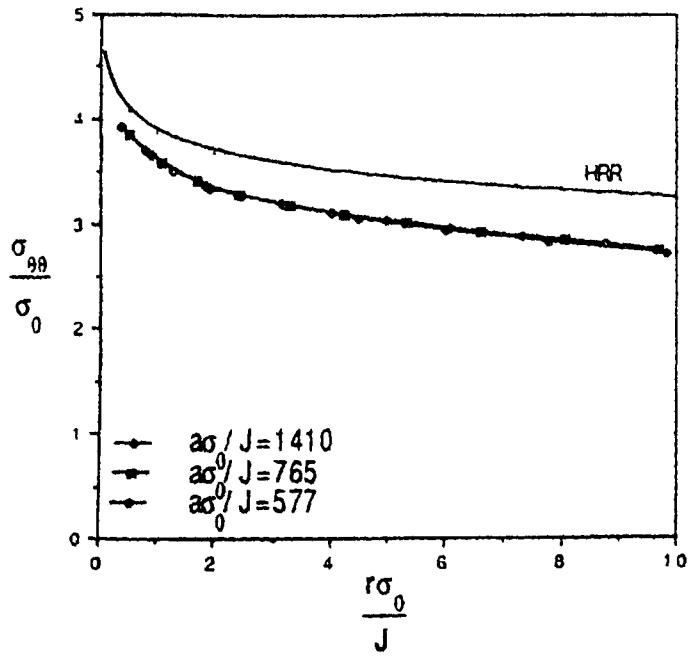

(c) Tangential stress ahead of a crack in a modified boundary layer formulation, B = 0, n = 13

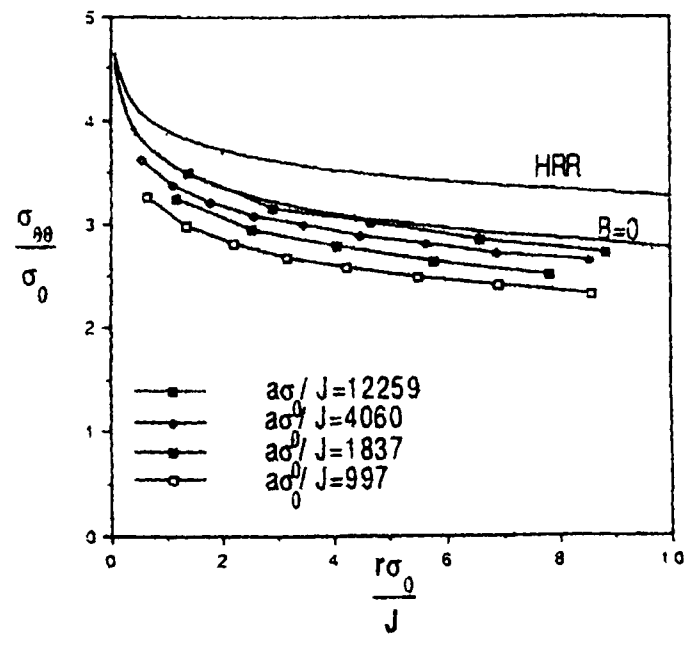

(d) Tangential stress ahead of a crack in a modified boundary layer formulation, B = -1.06, n = 13

Fig. 3.8 Stress distributions ahead of a crack tip at different levels of T stress. After Betegon and Hancock [79]

Figures 3.8a and 3.8c show tangential stress $\sigma_{\theta\theta}$ directly ahead of the crack $(\theta = 0)$ for both hardening and non hardening formulations in which the T stress is zero $(B = 0)$. The stresses are normalised by the yield stress σ_o and the radial distance from the crack tip is normalised by J/σ_o. As can be seen the data is self similar in that it is insensitive to the level of K with all data falling on the same curve but below the HRR stress field as determined by equation (3.5).

Consideration of fig. 3.8b illustrates the effect of a positive biaxiality parameter $B = +1.06$ which produces tensile T stresses which increase with deformation. Further examination of the data indicates that the stress fields are not quite self similar and lie above the $B = 0$ field but below the HRR field.

Finally figure 3.8d illustrates the effect of a negative biaxiality parameter $B = -1.06$ which produces a compressive T stress. As can be seen the stresses are initially close to the $B = 0$ data for small T stresses but as T becomes progressively more negative the stresses fall significantly below both the HRR and $B = 0$ fields.

The data shown in fig. 3.8 is combined with other data in fig. 3.9 as a family of curves which are functions of T stress but independent of B for $n = 13$. The effects of positive and negative T stress can be clearly seen.

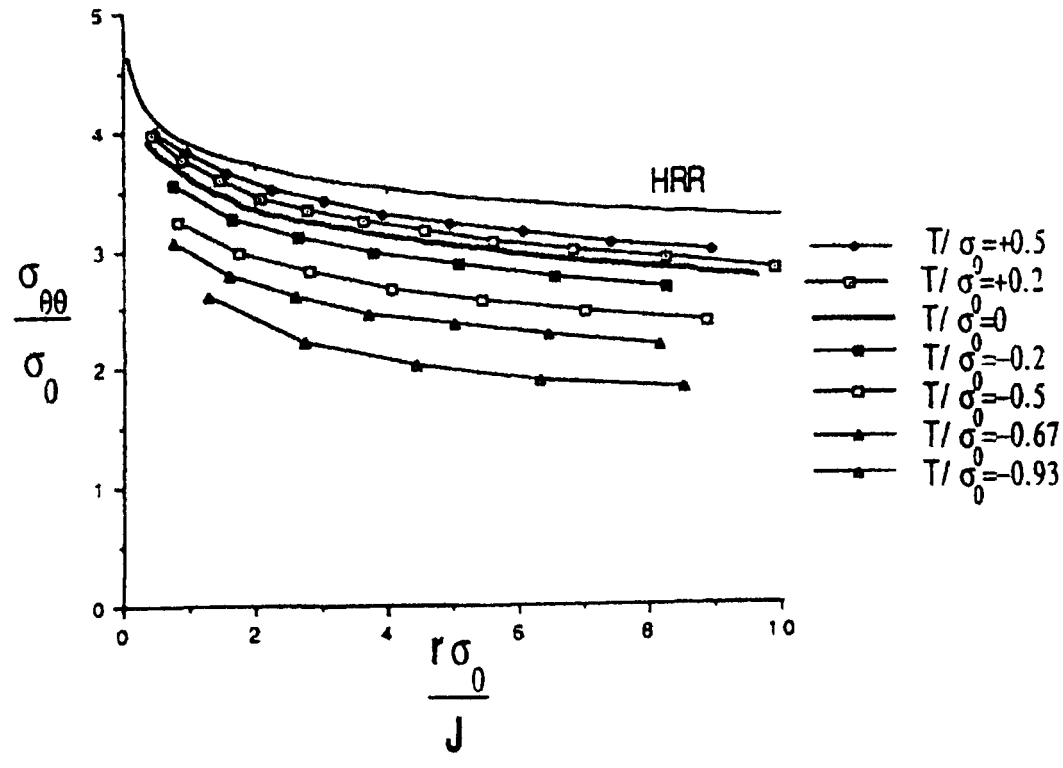

Fig. 3.9 The tangential stress field ahead of a crack in boundary layer formulations at different levels of T stress, n=13.
After Betegon and Hancock [79]

The authors continued to examine full field solutions for geometries representative of positive, zero and negative T stresses. Analyses were performed on a centre cracked panel under uniaxial tension to give negative T stress, a single edge notched bar with $a/W = 0.9$ to give positive T stress, whilst the results of an analysis by Al-Ani and Hancock [81] on a single edge notched bar with $a/W = 0.3$ were used to give the zero T stress condition. The results of these analyses can be seen in figs. 3.10 – 3.12.

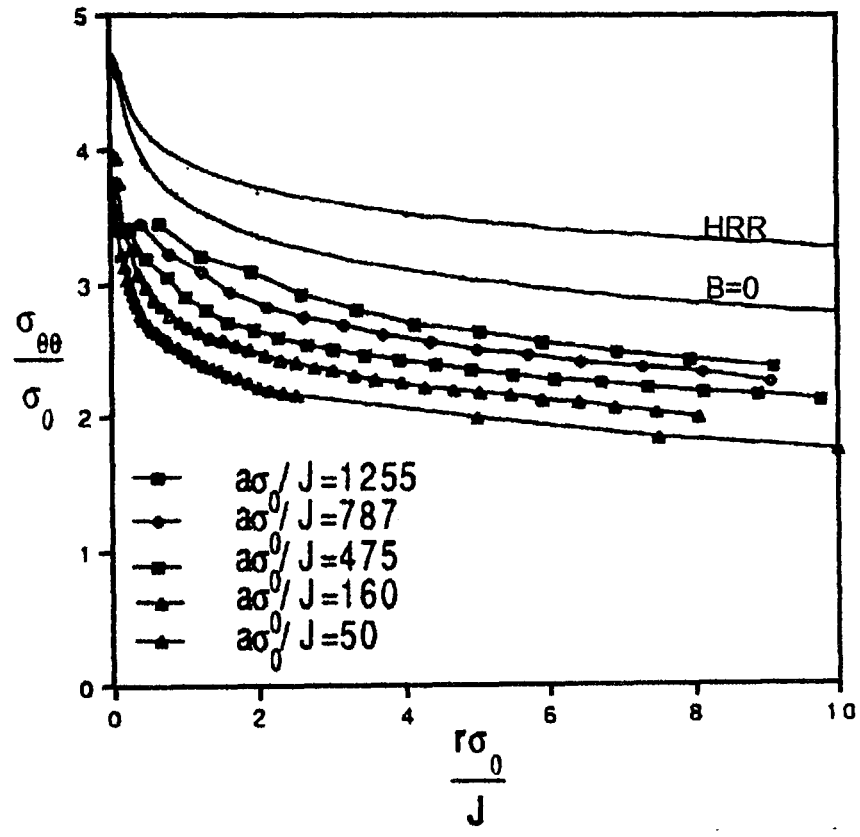

Fig. 3.10 The tangential stress field ahead of a crack in a centre cracked panel under uni-axial tension, n=13.
After Betegon and Hancock [79]

Comparison of the full field solutions with the boundary layer formulations indicated close agreement at corresponding levels of T stress.

In conclusion the work showed that for a single parameter characterisation of the fracture process, J dominance is achieved if the T stress is zero or positive. For situations of negative T stress J dominance is lost and a two parameter characterisation is necessary.

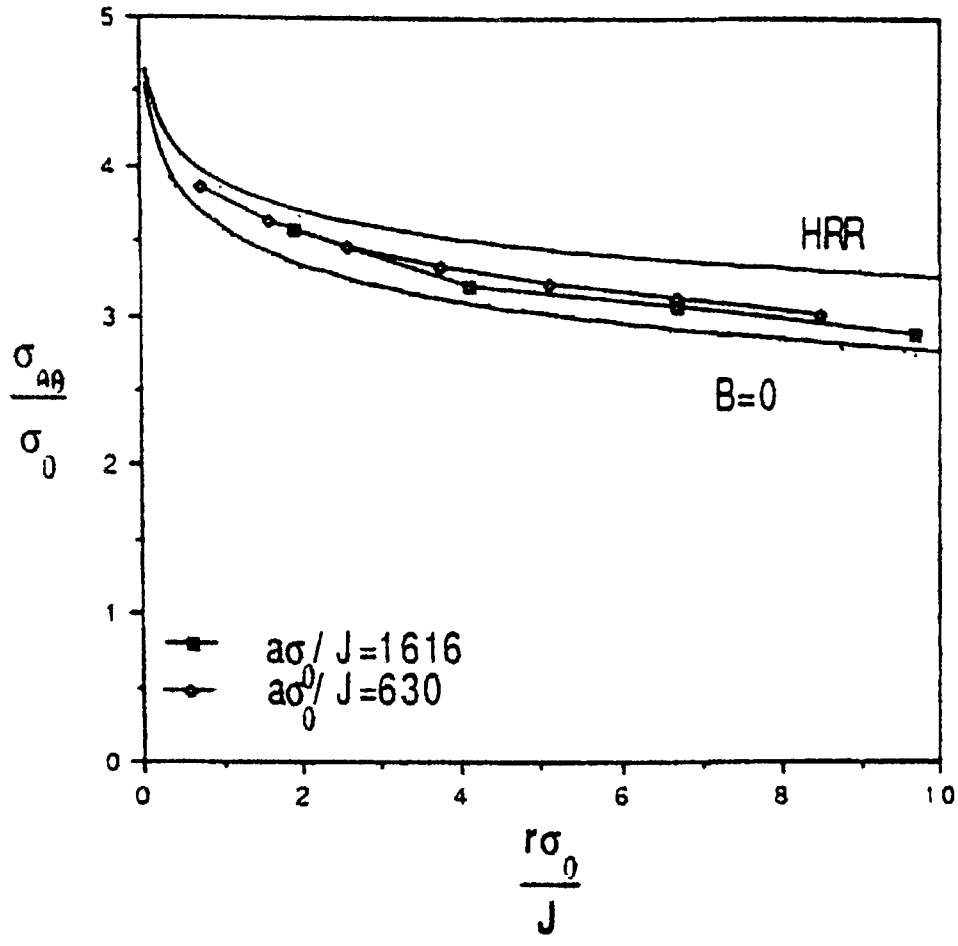

Fig. 3.11 The tangential stress directly ahead of a crack tip in a single-edge notched bend bar, a/W = 0.9, n = 13.
After Betegon and Hancock [79]

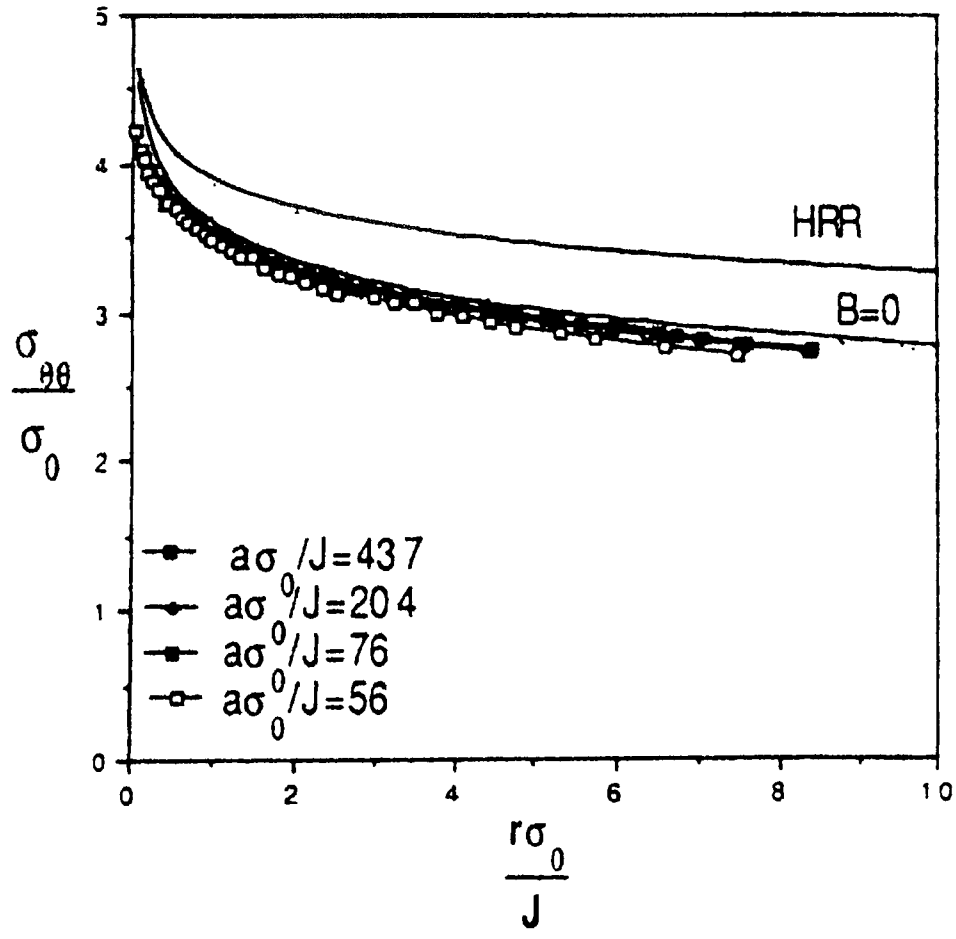

Fig. 3.12 The tangential stress directly ahead of a crack tip in a single-edge notched bend bar, a/W = 0.3, n = 13.
After Al-Ani and Hancock [81]

3.5.2 THE EFFECT OF NON-SINGULAR STRESSES ON CRACK-TIP CONSTRAINT, After Du and Hancock [80], 1991

Again crack tip deformation was modelled by boundary layer formulation using a focussed mesh similar but slightly coarser than that shown in fig. 3.7. The material response was based on non hardening J_2 flow plasticity, in order to avoid numerical problems the elastic response used a value for Poisson's ratio of *0.3* with a small number of solutions being obtained with a Poisson's ratio of *0.49* to investigate the effects of compressibility.

The shapes of the plastic zones obtained are shown in fig. 3.13. Compressive T stress enlarged the maximum radius of the plastic zone and caused the plastic lobes to move forward. Tensile T stress caused the plastic lobes to decrease in size and rotate backwards. The von-Mises stress was extrapolated along radial lines back to the crack tip at regular intervals in order to examine the angular extent of yielding, however, an elastic wedge was found on the crack flanks for compressive and zero T stress. In the absence of T stress plasticity at the crack tip extended to an angle close to 130^0, the effect of compressive T stress was to give a larger elastic wedge, whilst tensile T stress reduced the elastic wedge. At a tensile T stress of $+0.446\ \sigma_o$ plasticity was observed in the elements of the crack flank and the elastic wedge had disappeared.

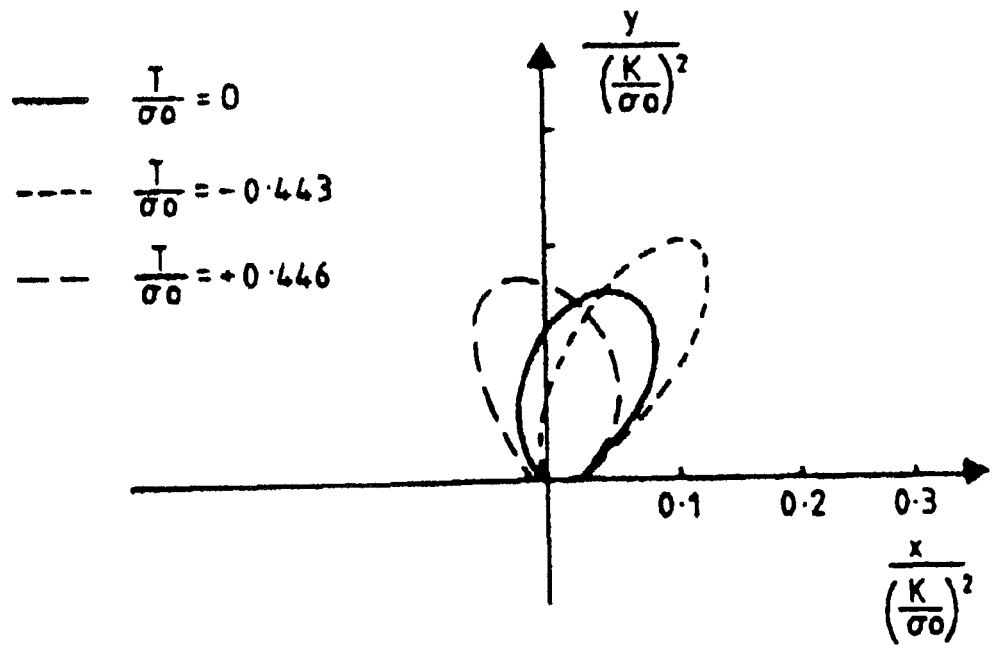

Fig. 3.13 The effect of T-stress on the non-dimensionalized plastic zone shapes. After Du and Hancock [80]

Although the numerical solutions presented do not apply to a rigid plastic incompressible solid the authors found it appropriate to interpret the stresses in the context of slip line theory. This interpretation of the effect of T stress on the slip line field solutions for a perfectly plastic material, hence plastic zone size and shape can be seen in fig. 3.14.

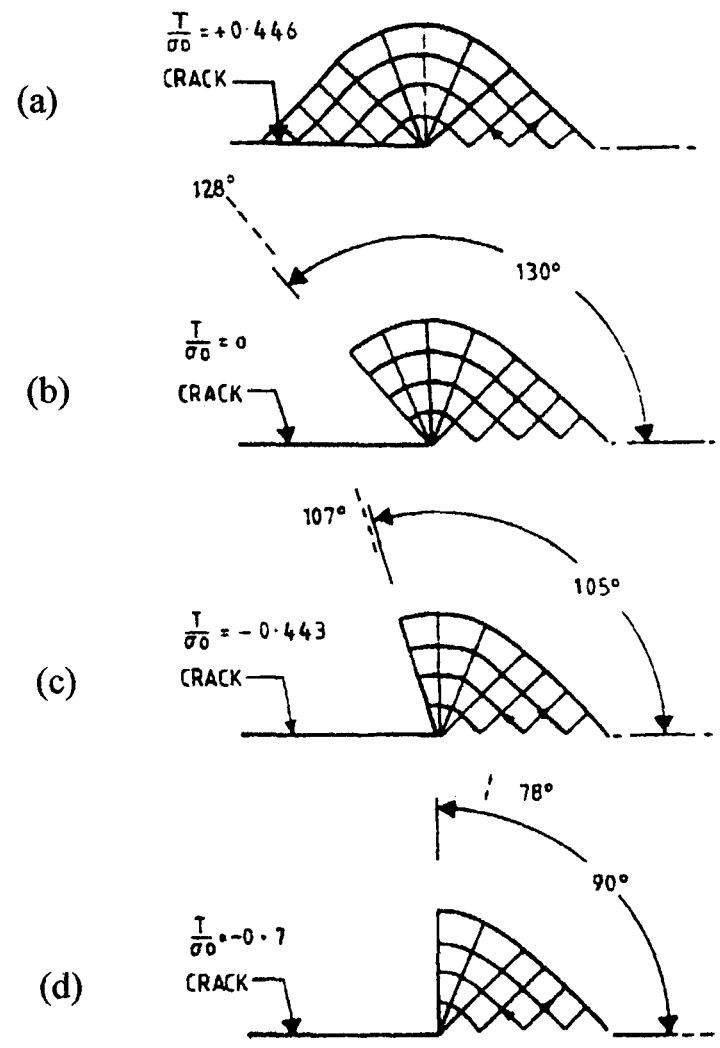

Fig. 3.14 A slip line field representation of the crack tip stress field for (a) $T/\sigma_o = +0.446$, (b) $T/\sigma_o = 0$, (c) $T/\sigma_o = -0.443$, (d) $T/\sigma_o = -0.7$. After Du and Hancock [80]

Fig. 3.15 shows the level of triaxial stress on a function of angle *(θ)* around the crack tip, whilst the results directly ahead of the crack tip *($r = 0$, $\theta = 0$)* are shown in fig. 3.16. As can be seen the effect of positive T stress is to maintain a high level of stress triaxiality in front of the crack tip and J dominance will exist. Negative values of T stress, however, give significantly reduced levels of stress triaxility and hence a loss of J dominance.

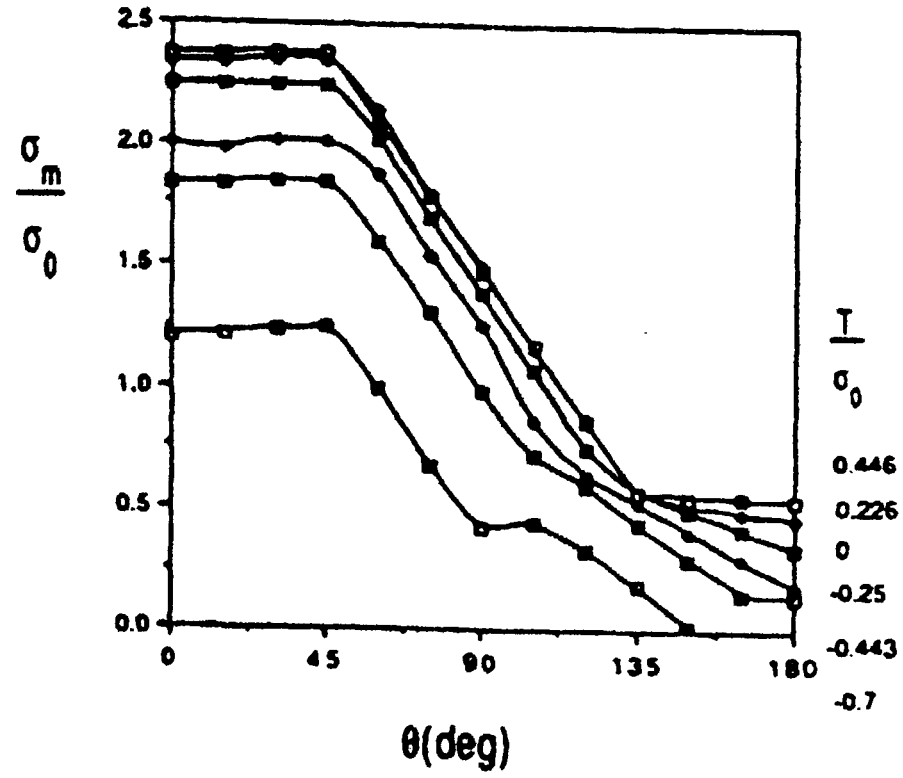

Fig. 3.15 Mean stress at the crack tip as a function of angular co-ordinate θ. After Du and Hancock [80]

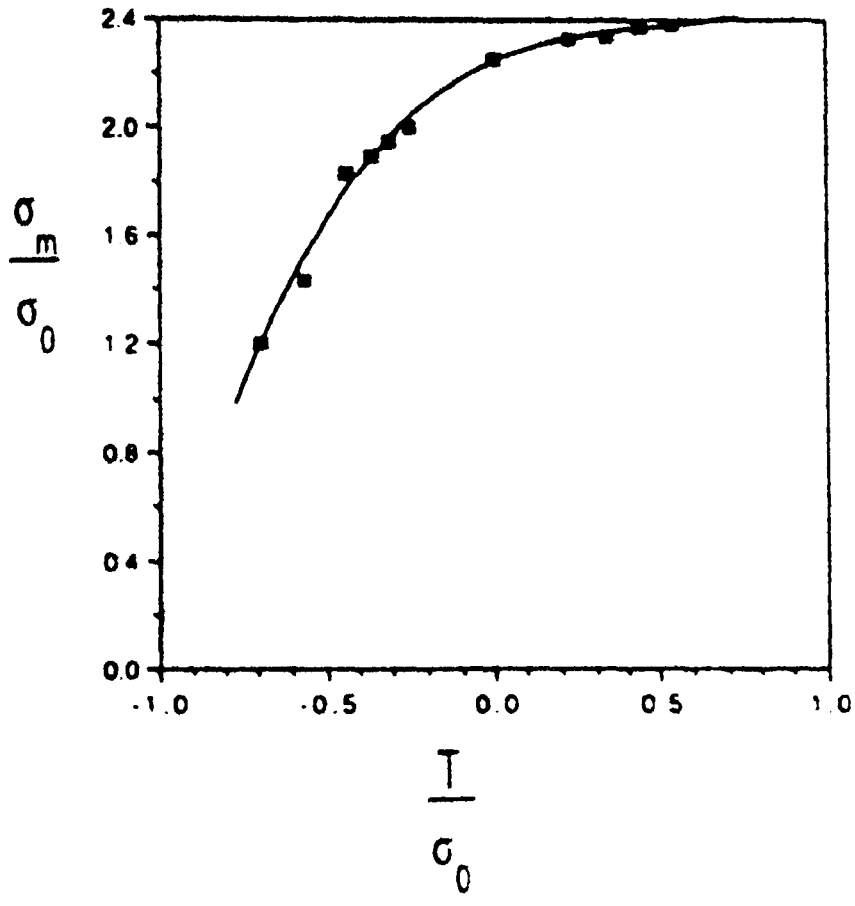

Fig. 3.16 Mean stress ahead of the crack tip (θ = 0, r = 0) as a function of T/σ_o. After Du and Hancock [80]

3.5.3 *J*-DOMINANCE OF SHORT CRACKS IN TENSION AND BENDING, After Al-Ani and Hancock [81], 1991

Al-Ani and Hancock [81] carried out a detailed full field finite element analysis using both small geometry change and large geometry change formulations of short cracks in tension and bending.

Loss of *J* dominance was associated with the development of plasticity to the cracked face, whilst retention of *J* dominance was associated with the development of plasticity through the ligament without spreading to the cracked face.

Results for crack tip stress fields for a single edge notched bar in bending with $a/W = 0.3$ were given in fig. 3.12 whilst those for $a/W = 0.1$ are given in fig. 3.17. As can be seen for an $a/W = 0.1$ the stresses fall considerably below the HRR field and reduce with increased deformation, in contrast for $a/W = 0.3$ there is no fall off due to increased deformation with the stress fields remaining essentially self similar.

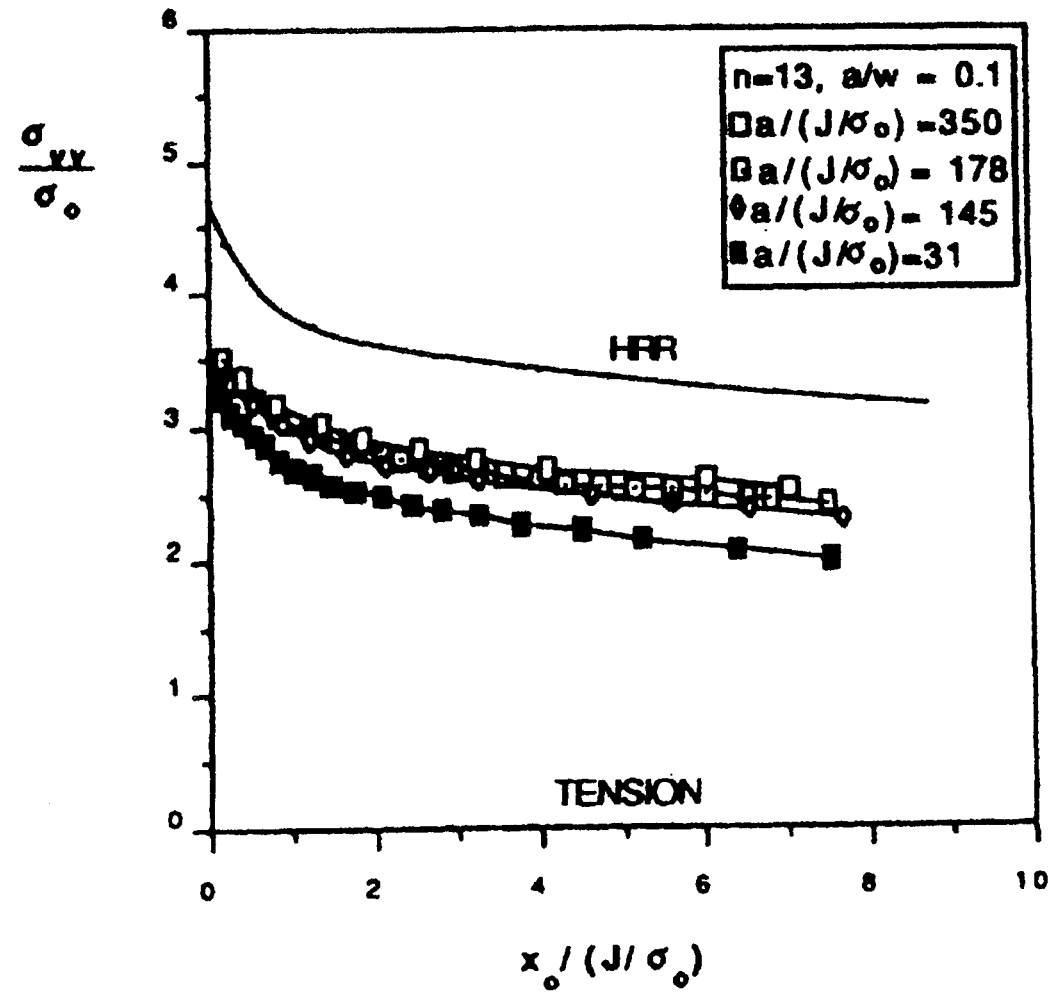

Fig. 3.17 The tangential stress directly ahead of a crack tip in a single-edge notched bend bar, a/W = 0.1, n = 13.
After Al-Ani and Hancock [81]

Plastic zone development for both crack depths are shown in fig. 3.18 where it can be seen clearly that the plastic zone extends to the cracked face at high loading for the $a/W = 0.1$ case, whilst plasticity is contained within the ligament for the $a/W = 0.3$ case.

This work supplements that of Du and Hancock [80] and supports the argument that even though the T stress concept is an elastic phenomenon it can be extended into large scale yielding situations.

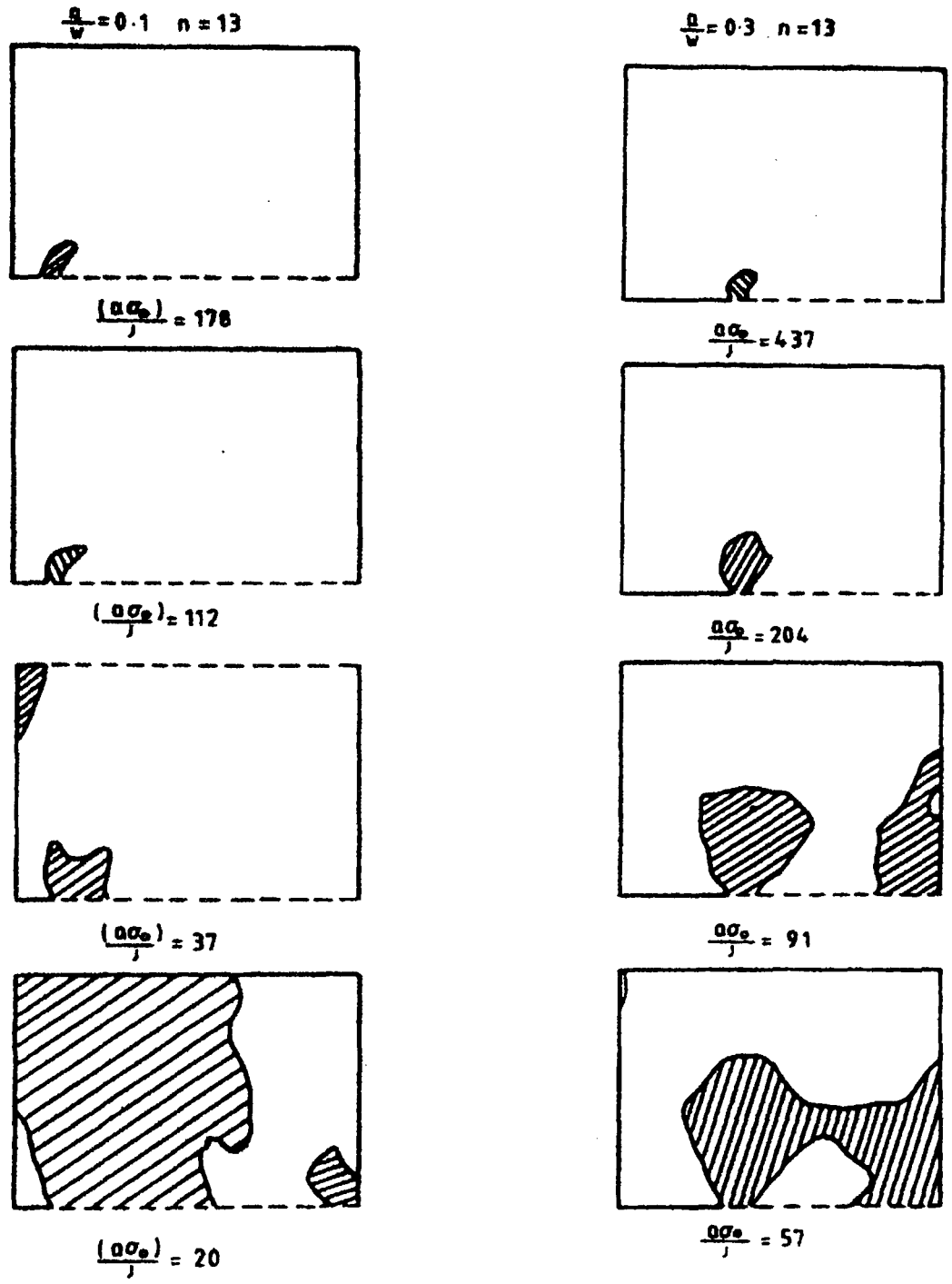

Fig. 3.18 The development of the plastic zone for a shallow-cracked bar in bending (a) a/W = 0.1, n = 13 and (b) a/W = 0.3, n = 13
After Al-Ani and Hancock [81]

3.6 *J-Q* THEORY

J-Q theory is based on a two parameter fracture mechanics approach by O'Dowd and Shih [82, 83], Shih et al [84] and Xia et al [85] and a similar approach by Li and Wang [86] and Sharma and Aravas [87]. Essentially the stress distribution ahead of a crack is obtained by detailed finite element analysis and then compared with a high constraint reference field such as the HRR field or a small scale yielding solution again obtained by finite element analysis.

An excellent review of the theory is given in [88] and is summarised as follows:

Consider a boundary layer formulation in which the boundary displacements are given by equation 3.19. Using different combinations of the loading parameters K_I and T will give near-tip plastic fields of different magnitudes. From dimensional considerations, these fields can be organised into a family of crack tip fields parameterised by T/σ_o, i.e:

$$\sigma_{ij} = \sigma_o \tilde{f}_{ij}\left(\frac{r}{J/\sigma_o}, \theta; T/\sigma_o\right) \quad .....(3.21)$$

However, O'Dowd and Shih [82, 83] claimed that because the T stress is essentially an elastic condition it is increasingly violated with the progression of plastic flow. Hence they identified members of the family fields by the parameter Q which arises from the plasticity analysis, i.e:

$$\sigma_{ij} = \sigma_o f_{ij}\left(\frac{r}{J/\sigma_o}, \theta; Q\right)$$

$$\varepsilon_{ij} = \varepsilon_o g_{ij}\left(\frac{r}{J/\sigma_o}, \theta; Q\right)$$

$$u_i = \frac{J}{\sigma_o} h_i\left(\frac{r}{J/\sigma_o}, \theta; Q\right) \quad .....(3.22)$$

where f_{ij}, g_{ij} and h_I depend upon dimensionless combinations of material parameters.

The results of several finite element analyses performed by O'Dowd and Shih [88] are illustrated in fig. 3.19, which shows the hoop and radial stress distribution directly ahead of a crack tip for several values of T/σ_o (n = 10 material, E/σ_o = 500, ν = 0.3). They considered the difference field as defined by:

$$(\sigma_{ij})_{diff} = (\sigma_{ij})_{SSY} - (\sigma_{ij})_{HRR} \quad .....(3.23)$$

where $(\sigma_{ij})_{HRR}$ is the HRR field and $(\sigma_{ij})_{SSY}$ is the small scale yielding field. They also systematically investigated the difference fields within the forward sector, $|\theta| < \pi/2$, of the annulus $J/\sigma_o < r < 5J/\sigma_o$ since this zone encompasses the microstructurally significant length scales for both brittle and ductile fracture [62].

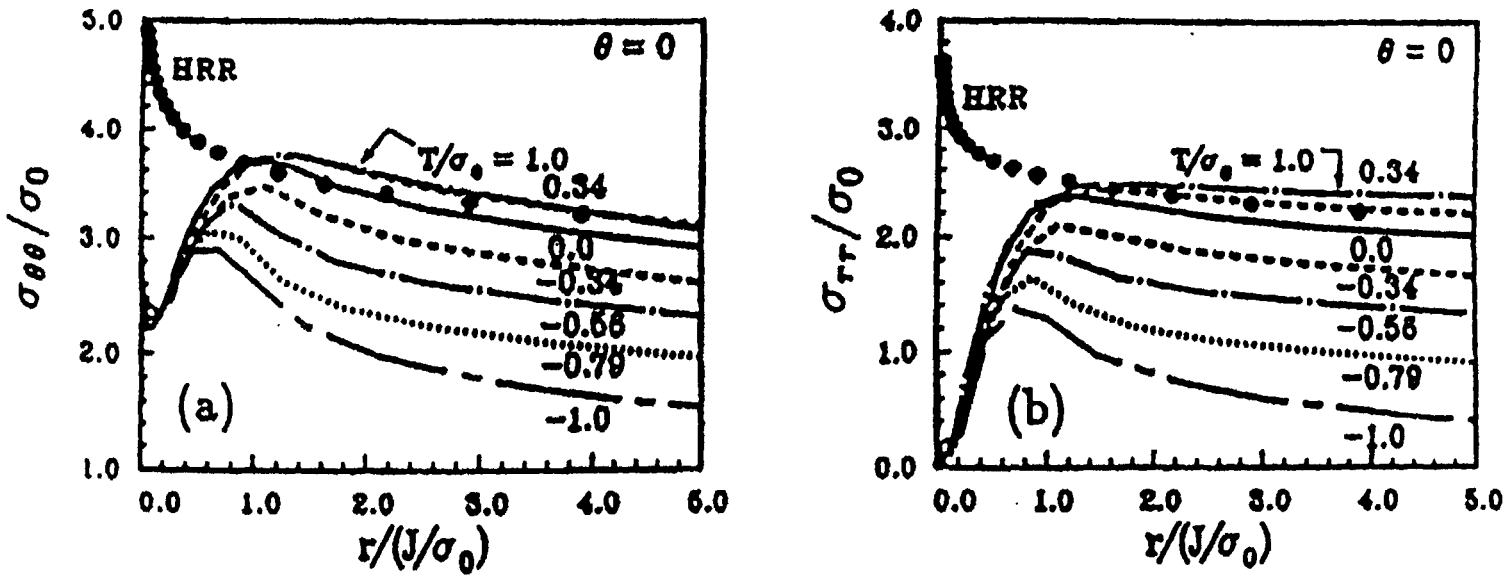

Fig. 3.19 Distribution of hoop and radial stress directly ahead of a crack tip for several values of T/σ_0, n = 10 material (E/σ_0 = 500, ν = 0.3). After O'Dowd and Shih [88].

The difference fields in the forward sector exhibited minimal dependence on r, and therefore can be expressed as:

$$(\sigma_{ij})_{diff} = Q\sigma_o\hat{\sigma}_{ij}(\theta) \quad .....(3.24)$$

where the angular functions $\hat{\sigma}_{ij}$ are normalised by requiring $\hat{\sigma}_{\theta\theta}(\theta = 0)$ be unity. The calculations also showed that $\hat{\sigma}_{rr} \approx \hat{\sigma}_{\theta\theta}$ *and* $|\hat{\sigma}_{r\theta}| \le |\hat{\sigma}_{\theta\theta}|$ thus indicating that Q is essentially a stress triaxiality parameter.

Thus difference fields within the section, $|\theta| < \pi/2$ and $J/\sigma_o < r < 5J/\sigma_o$, correspond to spatially uniform hydrostatic stress states. Therefore, Q defined by:

$$Q \equiv \frac{\sigma_{\theta\theta} - (\sigma_{\theta\theta})_{HRR}}{\sigma_o} \text{ at } \theta = 0, r = 2J/\sigma_o \quad \text{.....(3.25)}$$

is a measure of near-tip stress triaxiality, or crack tip constraint relative to a reference high triaxiality stress state. The distance chosen for Q lies just outside the finite strain blunting zone.

O'Dowd and Shih [88] also considered the difference field relative to a reference stress field given by the standard small scale yielding solution $(\sigma_{ij})_{SSY;T=0}$, which is driven by K alone, i.e:

$$(\sigma_{ij})_{diff} = (\sigma_{ij})_{SSY} - (\sigma_{ij})_{SSY;T=0} \quad \text{.....(3.26)}$$

In this case the resulting forward sector difference field matches a spatially uniform hydrostatic stress state even more closely, hence leading to an alternative definition of Q as:

$$Q \equiv \frac{\sigma_{\theta\theta} - (\sigma_{\theta\theta})_{SSY;T=0}}{\sigma_o} \text{ at } \theta = o, r = 2J/\sigma_o \quad \text{.....(3.27)}$$

The choice of reference field does slightly affect the value of Q obtained, however, in practice it does not matter which reference field is used so long as it is applied consistently. An advantage of using $(Q_{\theta\theta})_{SSY,T=0}$ as the reference field is that the actual stress strain relation for the material under consideration can be used rather than the limitation of a power-law hardening definition if $(\sigma_{\theta\theta})_{HRR}$ is used.

Q can also be defined at any radius as:

$$Q(\bar{r}) = \frac{\sigma_{\theta\theta}(\bar{r}) - [\sigma_{\theta\theta}(\bar{r})]_{SSY,T=0}}{\sigma_o} \quad \text{.....(3.28)}$$

where $\bar{r} = r/(J/\sigma_o)$ evaluated ahead of the crack ($\theta = 0$).

The mean gradient of Q over distances $1 < \bar{r} < 5$,

$$Q' = \frac{Q(\bar{r}=5) - Q(\bar{r}=1)}{4} \quad .....(3.29)$$

can be used to monitor changes in the spatial distribution of hoop stress that do not conform to a spatially uniform difference field.

3.7 EQUIVALENCE OF *J-T* AND *J-Q* APPROACHES

Q can be shown to depend on T alone within the modified boundary layer formulation, i.e:

$$Q = F(T/\sigma_o; n) \quad .....(3.30)$$

Curves of Q vs T/σ_o for n = 5, 10, 20 and ∞ materials (E/σ_o = 500, ν = 0.3) are given in fig. 3.20.

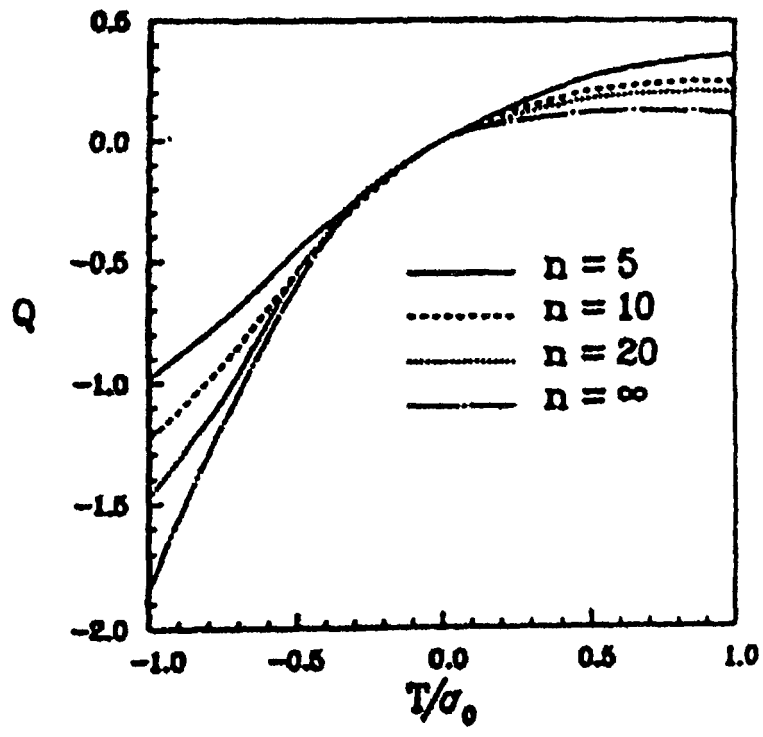

Fig. 3.20 Q v T/σ_0 for n = 5, 10, 20 and ∞ materials. After O'Dowd and Shih [88].

A description of near tip stress states by J and Q is strictly equivalent to a description in terms of K and T when small scale yielding conditions apply. It also follows that a two parameter description of near tip stress states based on J and T is equivalent to that based on J and Q, however, this equivalence does not hold under fully yielded conditions.

3.8 *J-Q* MATERIAL TOUGHNESS LOCUS

J-Q theory provides a quantitative framework that can be used to characterise a materials fracture resistance over a range of crack-tip stress triaxiality. The experimental determination of the *J-Q* toughness locus have been discussed by Dodds et al [89] as follows:

The fracture resistance of ferritic steels in the ductile to brittle transition region gives rise to competing fracture mechanisms. These being cleavage and ductile tearing. Fracture by cleavage normally demands high crack tip constraint whilst ductile tearing can develop at low constraint. This is illustrated in fig. 3.21 by two distinct segments to the toughness locus shown. Due to the amount of scatter generally observed in fracture mechanics testing both upper and lower bounds to the toughness locii are indicated which define bands for brittle and ductile fracture.

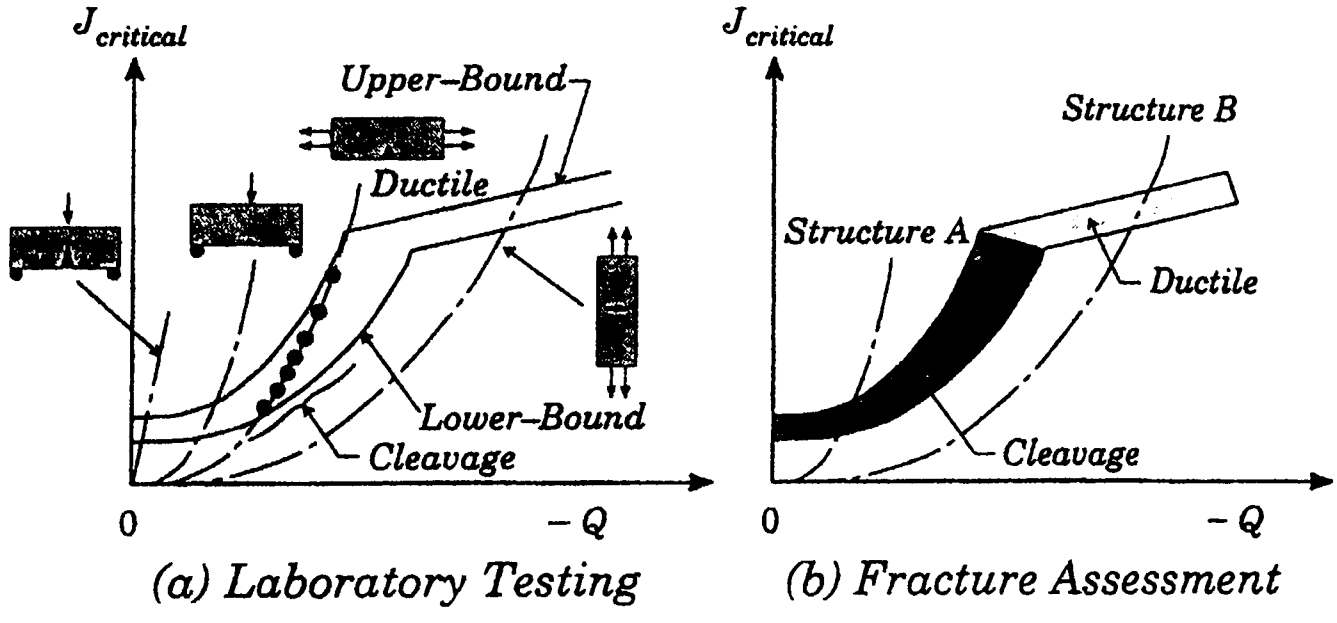

Fig. 3.21 The application of J – Q theory in fracture assessments. After Dodds et. al. [89].

In order to construct the toughness locus toughness values over the full range of crack-tip constraints fracture toughness values can be measured using test specimens of appropriate geometry as shown in fig. 3.21a. High constraint geometries such as deeply cracked bend specimens produce driving force curves which raise steeply and produce a toughness locus within a well defined narrow band on the *J-Q* diagram. In contrast, centre cracked panels and single edge cracked panels loaded in tension provide low constraint situations. They produce driving force curves which are much shallower and provide a broad zone on the *J-Q* diagram due to the amount of scatter observed in experimental results.

Once constructed the *J-Q* toughness locus can be used to predict a materials fracture resistance under service conditions as illustrated in fig. 3.21b. Structure *A* exhibits a steep driving force curve and hence will fail due to cleavage fracture, whilst structure *B* exhibits a shallow curve indicating failure by ductile tearing.

3.9 MICROMECHANICS BASED CONSTRAINT CORRECTION – AREA SCALING

Dodds et al [90] and Anderton and Dodds [91] have shown that by using a micromechanics approach the effects of size on fracture toughness can be quantitatively predicted. The method utilises the RKR model [55] and considers the attainment of a critical stress over a microstructurally relevant volume to the appropriate micromechanical failure criterion. Hence the probability of fracture in a cracked specimen can be expressed as:

$$F = f[V(\sigma_1)] \quad .....(3.31)$$

where F is the probability of failure, σ_1 is the maximum principal stress at a point and $V(\sigma_1)$ is the cumulative volume over which the principal stress is equal to or greater than σ_1. The form of equation (3.31) applies to any failure process controlled by maximum principal stress. The method does not attempt to predict absolute values of J_c from metallurgical parameters but predicts the variation of fracture toughness with constraint changes by scaling to a reference solution.

Modification of equation (3.22) leads to:

$$\frac{\sigma_1}{\sigma_o} = f_1\left(\frac{r}{J_o/\sigma_o}, \theta; Q\right) \quad .....(3.32)$$

where J_o is the J to which the SSY model must be loaded to achieve the same stressed volume and thereby the same likelihood of cleavage fracture as in a finite body.

Rearrangement of equation (3.32) gives an expression for distance r as a function of θ and σ_1/σ_o as:

$$r = \frac{J}{\sigma_o} g_1(\theta; \sigma_1/\sigma_o, Q) \quad .....(3.33)$$

For a particular stress level of principal stress σ_1/σ_o the area A over which the principal stress is greater than σ_1/σ_o is given by:

$$A = \frac{J^2}{\sigma_o^{\,2}} h(\sigma_1/\sigma_o; Q); \quad h = \frac{1}{2}\int_{-\pi}^{\pi} g_1^2(\theta; \sigma_1/\sigma_o, Q)\, d\theta \quad .....(3.34)$$

If A_o and J_o designate the area and J associated with the $Q = O$ field and A_{FB} and J_{FB} designate the area and J associated with a crack in a finite body with $Q \neq O$, then:

$$A_o = \frac{J_o^{\,2}}{\sigma_o^{\,2}} h_o(\sigma_1/\sigma_o); \quad h_o = \frac{1}{2}\int_{-\pi}^{\pi} g_1^2(\theta; \sigma_1/\sigma_o, Q = O)\, d\theta \quad .....(3.35)$$

and

$$A_{FB} = \frac{J_{FB}^{\,2}}{\sigma_{FB}^{\,2}} h_{FB}(\sigma_1/\sigma_o); \quad h_{FB} = \frac{1}{2}\int_{-\pi}^{\pi} g_1^2(\theta; \sigma_1/\sigma_o, Q)\, d\theta \quad .....(3.36)$$

The model requires the attainment of equivalent stressed volumes (A_{FB} x thickness) for cleavage fracture in different specimens. Hence the ratio of applied J in a finite body and the $Q = O$ stress state that generate equivalent stressed volumes is found by equating areas in (3.25) and (3.26) to give:

$$\frac{J_{FB}}{J_o} = \sqrt{\frac{h_o(\sigma_1/\sigma_o)}{h_{FB}(\sigma_1/\sigma_o)}} \quad .....(3.37)$$

Fig. 3.22 shows the results of finite element modelling [89] of a single edge notched bend bar with $a/W = 0.15$ and $n = 10$. As can be seen the area enclosed by the principal stress contours for $\sigma_1/\sigma_o = 3$ is smaller than that for the $Q = O$ case, and decreases with increased deformation.

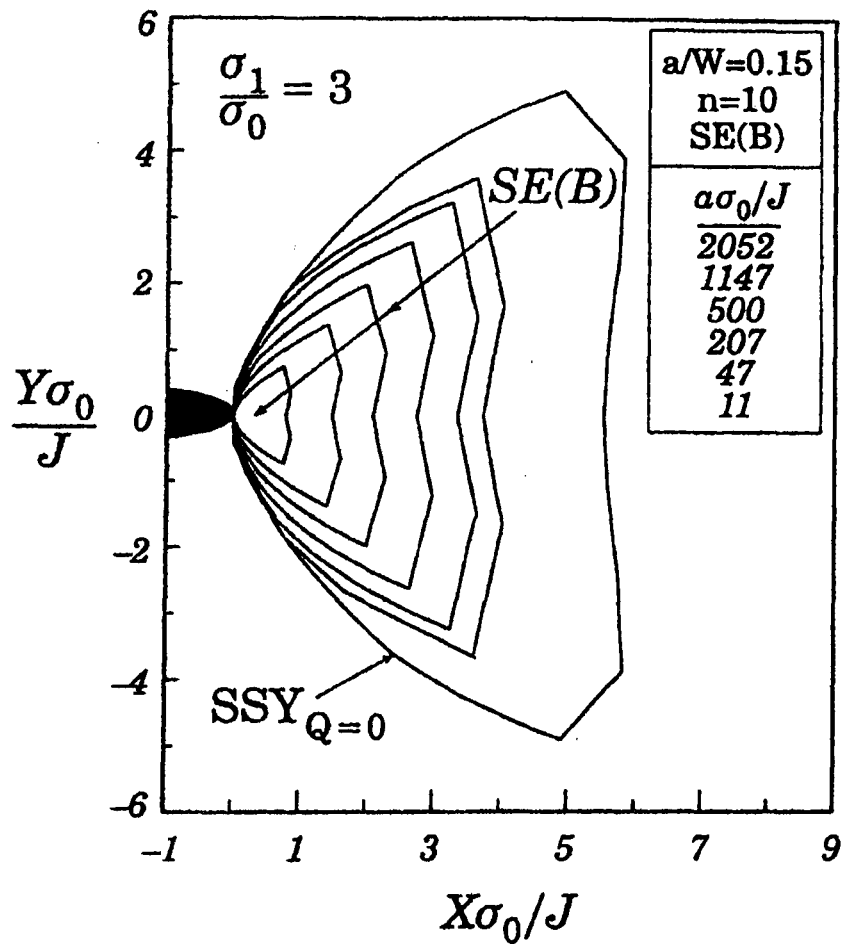

Fig. 3.22 Comparison of principal stress contours for Q = 0 and a/W = 0.15, n = 10 SE(B) specimen. After Dodds et. al. [89].

Dodds et al [89] also investigated the effect of choice of σ_1/σ_o and concluded that the area ratios are relatively insensitive to the chosen level of σ_1/σ_o until deformations become excessive, this is illustrated in fig. 3.23. Similarly the influence of specified critical stress ratio on the prediction of fracture toughness variation is insensitive to the chosen level of σ_1/σ_o, this is illustrated in fig. 2.24.

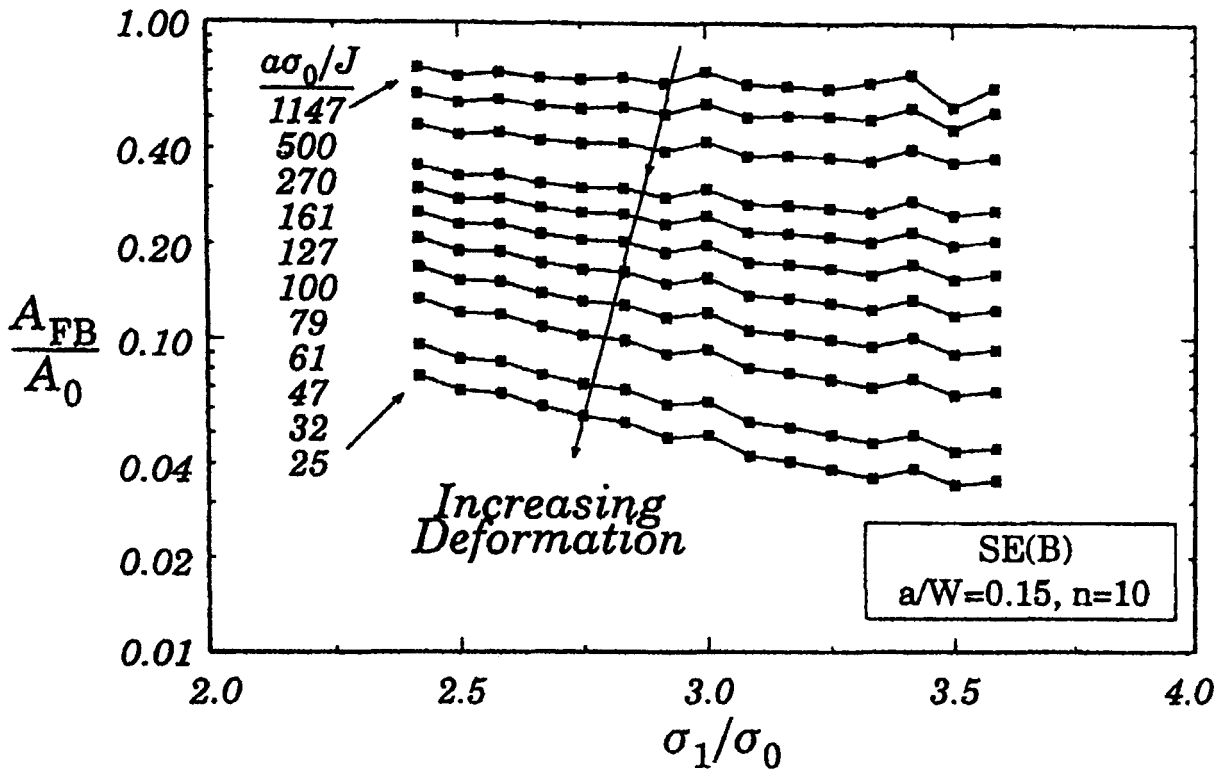

Fig. 3.23 Areas within principal stress contours for an a/W = 0.15, n = 10 SE(B). Values are normalised by area within contour for $SSY_{Q=0}$ at same J value. After Dodds et. al. [89].

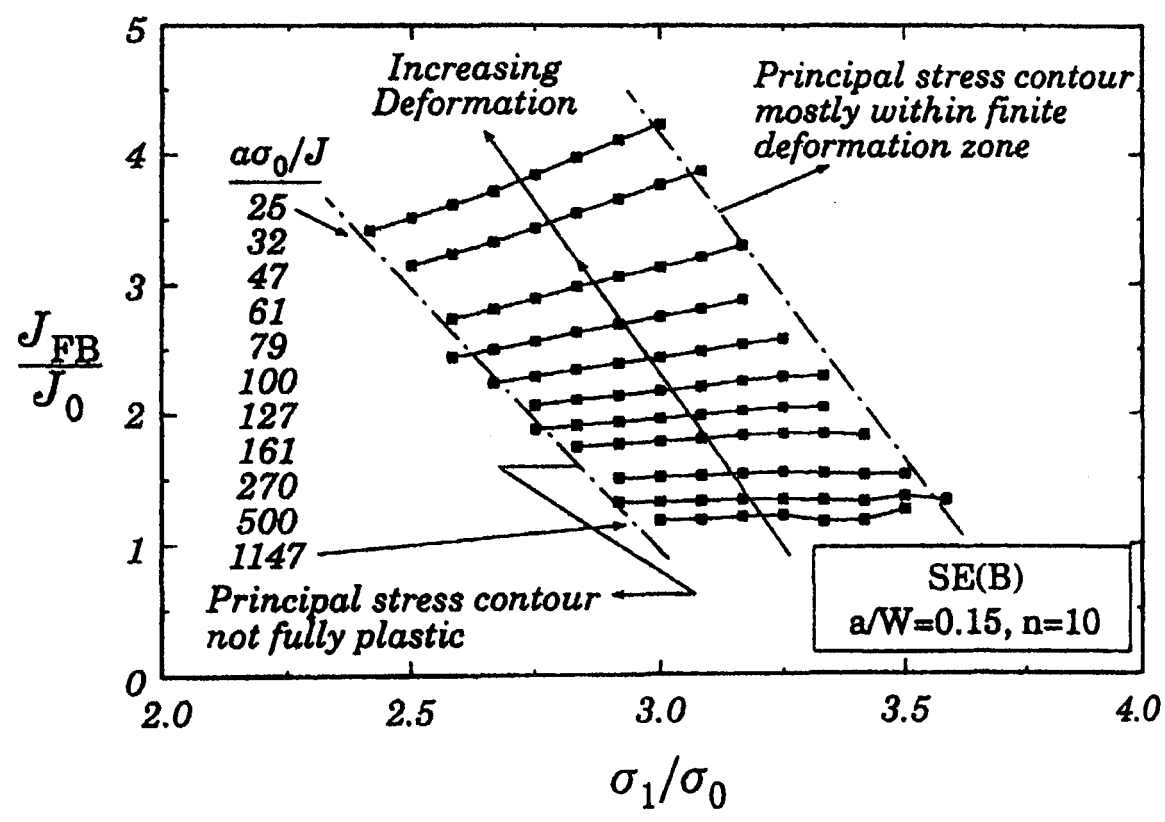

Fig. 3.24 Influence of specified critical stress on the micromechanics prediction of fracture toughness variation with constraint for an a/W = 0.15, n = 10 SE(B). After Dodds et. al. [89].

3.10 CLOSURE

The principles of two parameter fracture mechanics outlined in this chapter provide a basic methodology by which the effects of specimen thickness and side grooving can be evaluated on a quantitative basis. In particular, *J-Q* theory and the area scaling method will be used to evaluate constraint effects and provide estimates of fracture toughness values that can be expected from non-standard test specimens. Both of these methods have been implemented using finite element analysis to provide such estimates.

CHAPTER 4

THE INFLUENCE OF SIDE GROOVING ON AN ALUMINIUM ALLOY

4.1 INTRODUCTION

This first section of work is concerned with an investigation of the influence of side groove depth and shape on materials characterised by linear elastic fracture mechanics. Standard compact tension specimens with a range of Vee, U and square side grooves have been modelled using three dimensional finite element analysis. The finite element analysis was backed up by an experimental programme which investigated the effects of side groove depth for Vee grooves in an aluminium alloy specimen. The finite element and experimental results show good agreement and provide support for the concept of effective thickness as originally proposed by Freed and Krafft [28].

4.1.1 AIMS AND OBJECTIVES

The aims and objectives of the work are as follows:

1. To investigate the effect of side groove depth on the fracture behaviour of a material characterised by linear elastic fracture mechanics using finite element analysis.

2. To investigate the effect of side groove shape on the fracture behaviour of a material characterised by linear elastic fracture mechanics using finite element analysis.

3. To experimentally investigate the effect of side groove depth for Vee grooves in an aluminium alloy specimen that is characterised by linear elastic fracture mechanics.

4. To provide further analytical support for the concept of effective thickness as originally proposed by Freed and Krafft [28].

4.2 SPECIMEN GEOMETRY AND PREPARATION

Specimen geometry requirements for fracture toughness testing in the linear elastic fracture mechanics regime are defined by both British and American standards [26 and 27]. Both standards recommend K_{IC} specimens as illustrated in fig. 4.1. The specimens must be fatigue pre-cracked and meet minimum size requirements if valid K_{IC} results are to be obtained as follows:

$$a \geq 2.5 \left(\frac{K_{IC}}{\sigma_Y}\right)^2 \quad .....(4.1)$$

$$B \geq 2.5 \left(\frac{K_{IC}}{\sigma_Y}\right)^2 \quad .....(4.2)$$

$$W \geq 5.0 \left(\frac{K_{IC}}{\sigma_Y}\right)^2 \quad .....(4.3)$$

where σ_Y is the material yield strength.

It is generally accepted that predominantly plane strain behaviour may be expected when the calculated size of the plane stress plastic zone, i.e. $2r_Y$ in equation (2.15) is no larger than one tenth the specimen thickness. For $K_I = K_{IC}$, substitution of equation (2.15) into equations (4.1 – 4.3) shows that the minimum thickness, B, is only about eight times the plane stress plastic zone size. However, experience shows that the minimum size requirements given in equations (4.1 – 4.3) yield minimum values of K_{IC}.

In this study an aluminium alloy was used to investigate the effect of side grooving. The mechanical properties of the material were found by experiment (see section 4.4) to be as follows:

0.05% proof stress – 475 MPa
Young's Modulus, E – 72GPa
Fracture toughness, K_{IC} – 22 MPa $m^{0.5}$

Consideration of the above material properties leads to a minimum specimen thickness of 6 mm with all other dimensions being as defined in fig. 4.1.

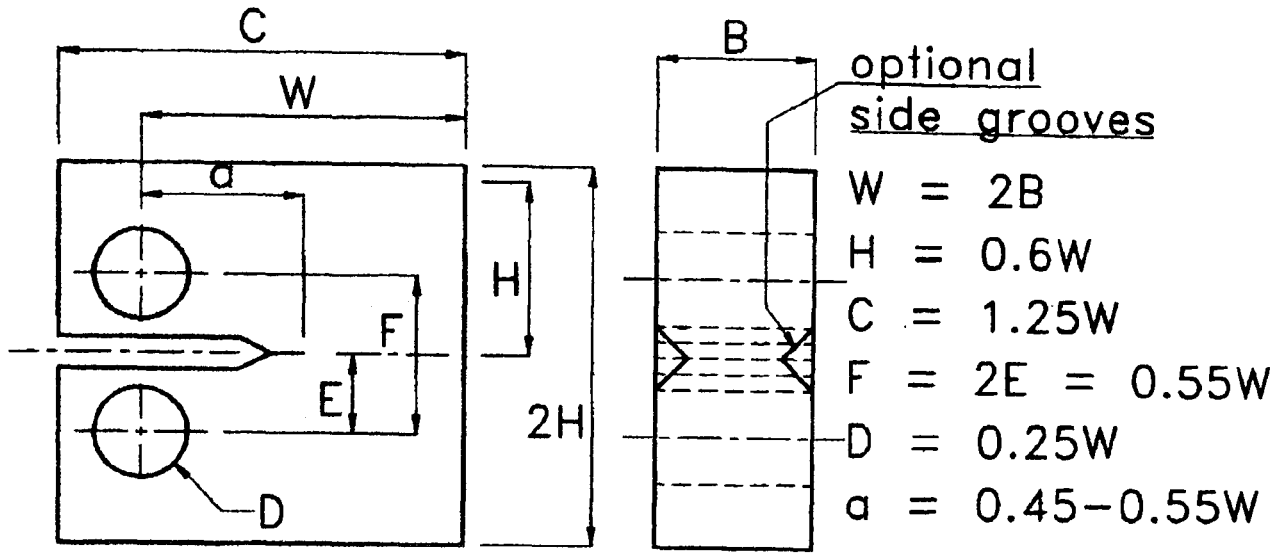

Fig. 4.1a Standard compact tension specimen

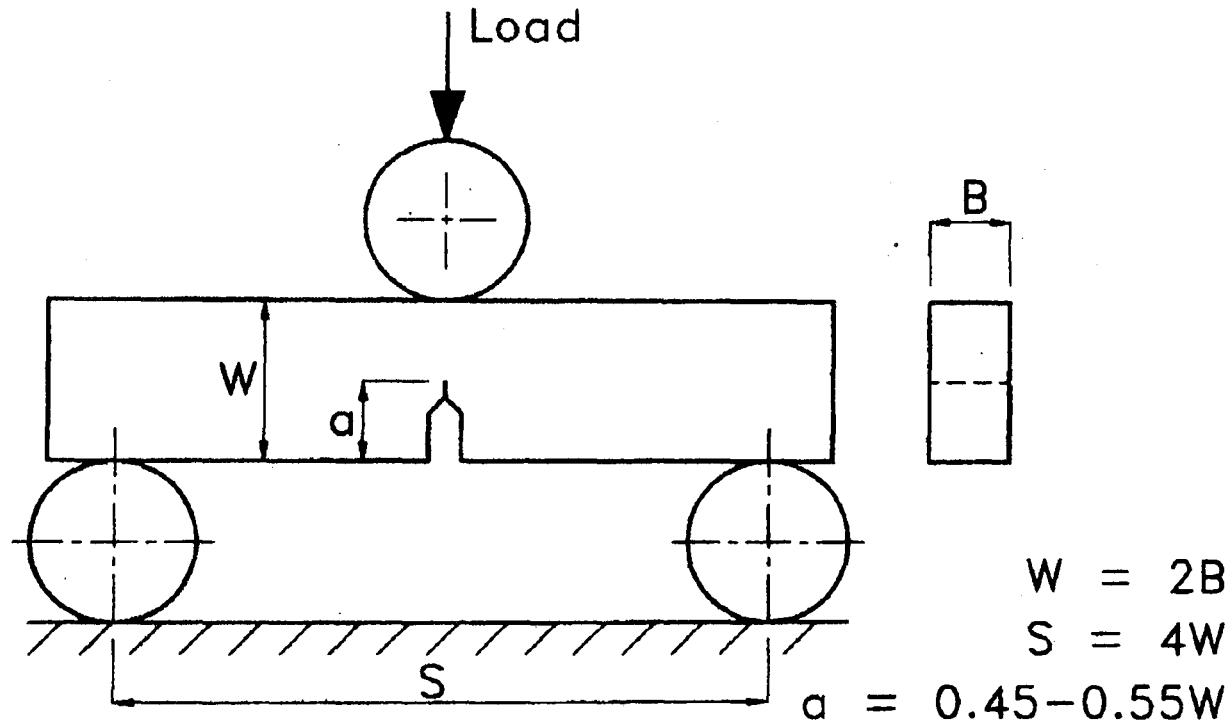

Fig. 4.1b Standard three point bend specimen

An actual specimen thickness of 10 mm was used for both analysis and testing. The reason for this decision was due to the fact that the machining of side grooves was much easier at this increased thickness.

A variety of Vee, U and square side grooves have been considered to a depth of 40% where the percentage side grooving is defined as $100(B - B_N)/B$ where B and B_N are as defined in equation (2.9).

4.3 FINITE ELEMENT ANALYSIS

The finite element analysis was performed using the NISA finite element package [92] together with the ENDURE fracture/fatigue post processor [93].

NISA is a general purpose finite element package capable of a wide range of analysis types. It is modular in construction with separate modules being available for static, dynamic, heat transfer analysis etc. The STATIC module was used for all of the analysis undertaken in this chapter. Stress intensity factors were obtained using the ENDURE post processor. The ENDURE module reads the results file of a STATIC analysis and determines stress intensity factors based on either crack tip opening displacement (CTOD) or virtual crack extension (VCE) as previously described in section 2.10.2. A limitation of the ENDURE package at the time that the work was undertaken was that it would only provide solutions for a linear elastic STATIC analysis. This did not constitute a problem for the work presented in this chapter, but was a limiting factor in the choice of analysis package for subsequent elastic-plastic analysis.

Pre and post processing of the finite element models was carried out using the DISPLAY III graphical pre/post processor [94].

4.3.1 BENCHMARKING

Prior to modelling of the aluminium alloy compact tension specimens, two NAFEMS benchmarks [95] were analysed using the NISA/ENDURE packages. The reason for benchmarking in this way was twofold, firstly to gain experience using the packages and secondly to test the package against benchmark problems with known solutions. The two benchmarks chosen were those of a centre cracked plate in tension, as illustrated in fig. 2.1, and a standard compact tension specimen modelled in 2D as shown in fig. 4.1. All the models were built using 8 noded isoparametric elements with the nodes at the crack tip being moved to the quarter point position to ensure correct modelling of the crack tip singularity. The results obtained are summarised in table 4.1.

		Centre cracked plate in tension	Compact tension specimen
Theoretical Solution	K_O	$\sigma[\pi a]^{1/2}$	$P/t(W)^{1/2}$
	K_I/K_O from NAFEMS benchmark	1.325	9.659
NISA Solution (CTOD)		1.339	9.629
Difference		1.05%	0.31%
NISA Solution (VCE)		1.335	9.737
Difference		0.7%	0.8%

Table 4.1 – Benchmark analysis results

As can be seen from table 4.1 the NISA results are good when compared to the benchmark solutions. This gave encouragement that good accuracy could be achieved from 2D and 3D finite element analysis of compact tension specimens.

4.3.2 TWO DIMENSIONAL ANALYSIS OF COMPACT TENSION SPECIMENS

In order to theoretically predict the effect of side grooving on the fracture performance of materials it was necessary to undertake three dimensional finite element analysis of a variety of compact tension specimens with a variety of side grooves. Meshing of the 3D finite element models in the region of the intersection of the crack front with the side groove is difficult, particularly considering the conflicting requirements of accuracy of results and reasonable solution times. Due to the different side groove configurations different meshes are required, particularly at the crack front-side groove intersection.

In order to assess the suitability of these different mesh configurations and perform some refinement of the mesh a series of two dimensional plane strain templates were produced for each 3D mesh. All models used eight noded isoparametric elements, with the crack tip nodes being moved to the quarter point position to ensure the correct modelling of the crack tip singularity. Template

meshes were judged to be suitable in terms of their refinement when successive refinements agreed within 3% in terms of calculated K_I results.

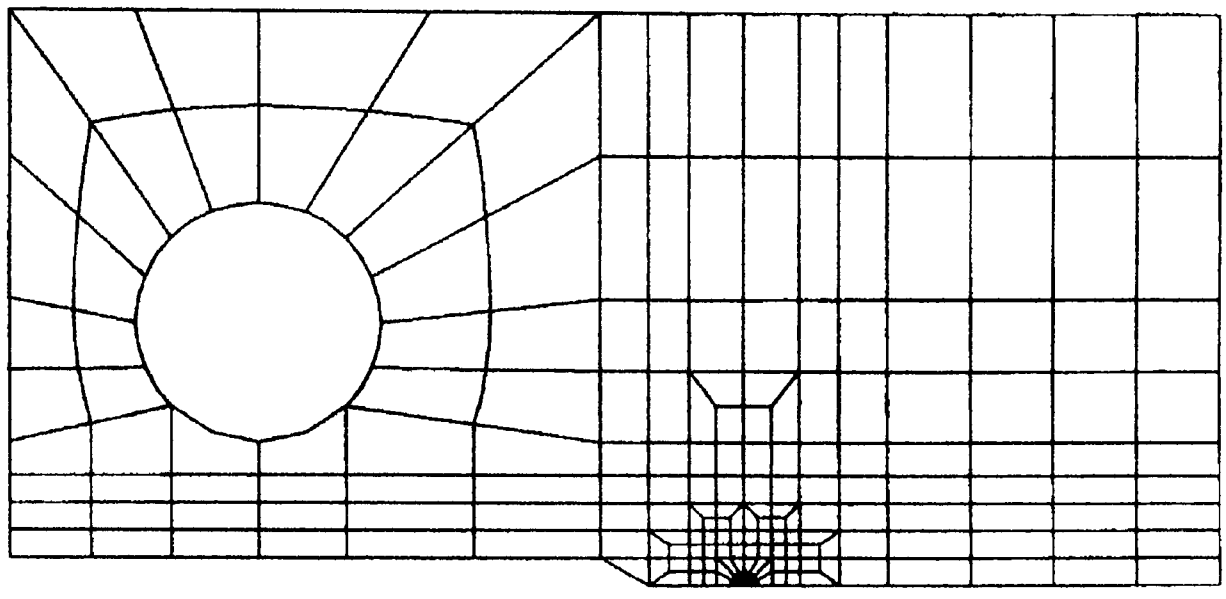

Fig. 4.2 Typical 2D mesh

A typical 2D mesh is shown in fig. 4.2. Only half of the compact tension specimen was modelled due to symmetry conditions. Y symmetry constraints were added to the uncracked ligament along the crack plane and an X direction constraint was applied to a single node at the top of the clevice pin hole to prevent rigid body motion. The models were loaded by the application of a pressure to the top of the clevice pin hole. The analysis results were also compared with the standard stress intensity factor solution for a compact tension specimen, which is given as [96]:

$$K_I = \frac{P_Q}{BW^{0.5}} \cdot f\left(\frac{a}{W}\right) \quad \ldots\ldots (4.4)$$

where P is the applied load and a, B and W are as defined in fig. 4.1a, and $f\left(\frac{a}{W}\right)$ is given as:

$$f\left(\frac{a}{W}\right)=\frac{\left(2+\frac{a}{W}\right)\left[0.886+4.64\left(\frac{a}{W}\right)-13.32\left(\frac{a}{W}\right)^{2}+14.72\left(\frac{a}{W}\right)^{3}-5.6\left(\frac{a}{W}\right)^{4}\right]}{\left(1-\frac{a}{W}\right)^{\frac{3}{2}}} \quad \ldots\ldots (4.5)$$

Results from the 2D finite element analysis are compared with the theoretical solutions given by equation (4.4) and (4.5) in table 4.2.

Examination of table 4.2 shows that the maximum difference between the finite element and theoretical solutions for Vee grooved templates is 1.8% for the CTOD result with template 3. The maximum difference between the finite element and theoretical solutions for all templates being 3.4% for the CTOD result obtained with template 6 which relates to U and square grooved specimens. It was considered that the results obtained from the 2D analysis provided a series of mesh templates that would provide 3D finite element meshes that would give an acceptable balance between accuracy of results and solution time.

2D Template	Related 3D model		K_I (FE)/K_I theoretical	
	SG type	Depth	CTOD	VCE
Template 1	Vee	20% & 40%	0.983	0.996
Template 2	Vee	10%	0.987	0.995
Template 3	Vee	30%	0.982	0.995
Template 4	U & Square	10%	0.976	0.977
Template 5	U & Square	20%	0.971	0.977
Template 6	U & Square	30%	0.966	0.977

Table 4.2 – Comparison of 2D FE results with equation (4.4)

4.3.3 THREE DIMENSIONAL ANALYSIS OF COMPACT TENSION SPECIMENS

Having established a series of two dimensional templates that gave favourable results when compared to standard plane strain solutions, as given by equations (4.4) and (4.5), modelling progressed firstly to consider three dimensional FE analysis of a plain sided CT specimen and then the analysis of CT specimens with a variety of side groove geometries and depths.

All models were again based on the material outlined in section 4.2. Only full thickness specimens were modelled (i.e. 10 mm thick) as required by BS 7448. This enabled the effects of side groove geometry and depth to be investigated without the need to consider effects from thickness changes.

All models were built from 20 noded collapsed isoparametric elements with all the nodes along the crack front being moved to the quarter point position to ensure correct modelling of the crack front singularity. In all cases only a quarter of the specimen was modelled because of symmetry conditions. On average the models contained approximately 1200 elements, 6200 nodes and 18000 degrees of freedom. The models were loaded by the application of a pressure to the top of the clevice pin hole. The applied loads and boundary conditions are shown in fig. 4.3.

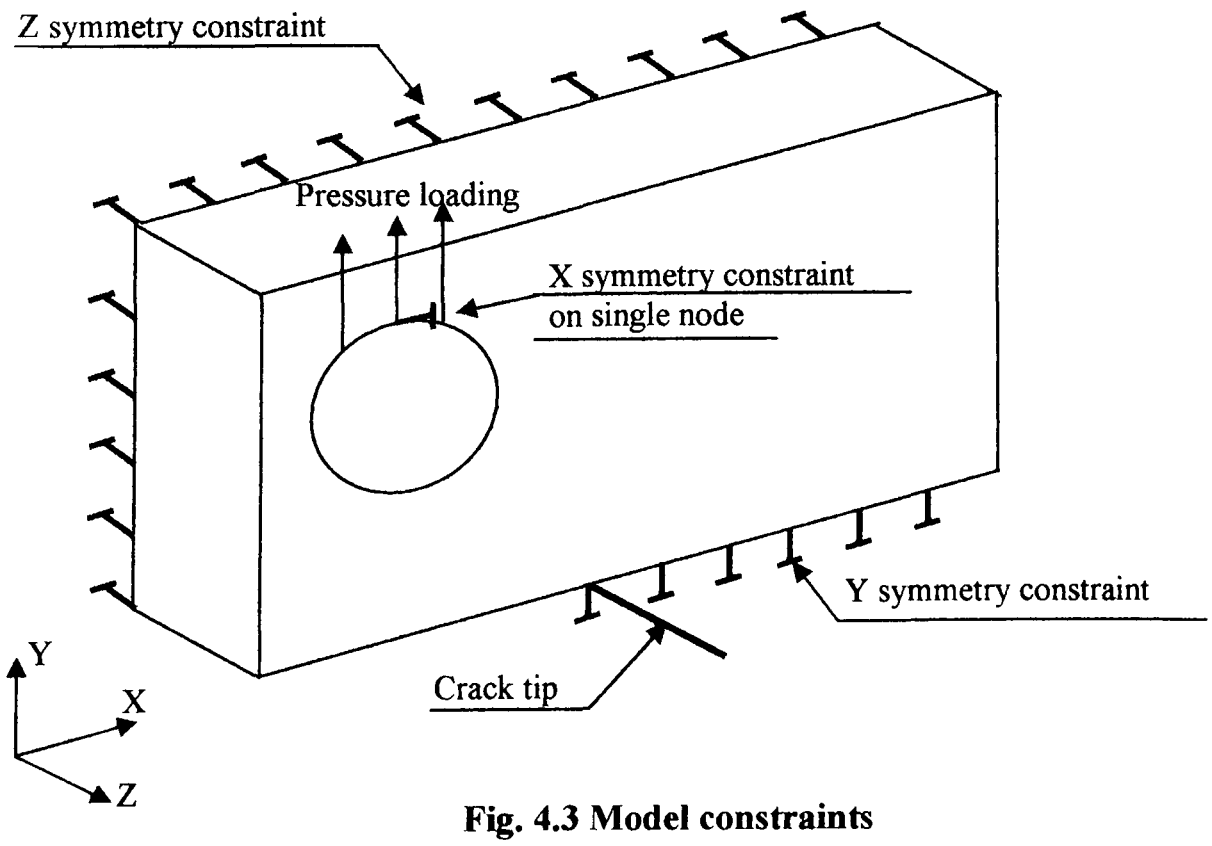

Fig. 4.3 Model constraints

The average processing time was in the order of 2-3 hours on a PC 486 DX 266.

Typical meshes for a plain sided and a 20% U side grooved specimen are illustrated in fig. 4.4.

Plain Specimen Results

Results from the plain specimen analysis can be seen in figs. 4.5 and 4.6. The variation of K_I along the crack front is shown in fig. 4.5 for both CTOD and VCE. The centre line value of K_I given by CTOD is 5% higher than the plane strain value given by equations (4.4) and (4.5) whilst that given by VCE is only 0.34% higher. The average value of K_I across the crack front is lower than the centre line value in the case of both CTOD and VCE due to the fact that the stress intensity factor falls away at the edge of the specimen. In the case of CTOD calculations the average value across the crack front is 99.6% of the plane strain value, whilst for VCE calculations the average value in 95.6% of the plane strain value. For CTOD the stress intensity factor falls off at the edge of the specimen to approximately 17% below the centre line value, for VCE this fall off is approximately 15%.

The elevation of the stress intensity factor over the plane strain value at the centre of the specimen has been reported by several authors. De Lorenzi and Shih [31] obtained an elevation of 7% based on energy release rate calculations.

Crack tip constraint is also important when considering the fracture behaviour of materials. In this study the constraint is quantified using the ratio $\sigma_{zz}/\nu(\sigma_{xx}+\sigma_{yy})$ which equals one for plane strain conditions. All stress values were taken from element Gauss points closest to the crack tip for all elements across the crack front. The variation of crack tip constraint defined in this way can be seen in fig. 4.6. Again the centre line value of 0.957 can be seen to fall off to a minimum value of 0.804 at the specimen edge, the average value across the crack front is 0.935.

These observations are typical of what would be expected for a plain sided specimen and can be used to explain the fracture appearance of such specimens as argued in section 2.8.

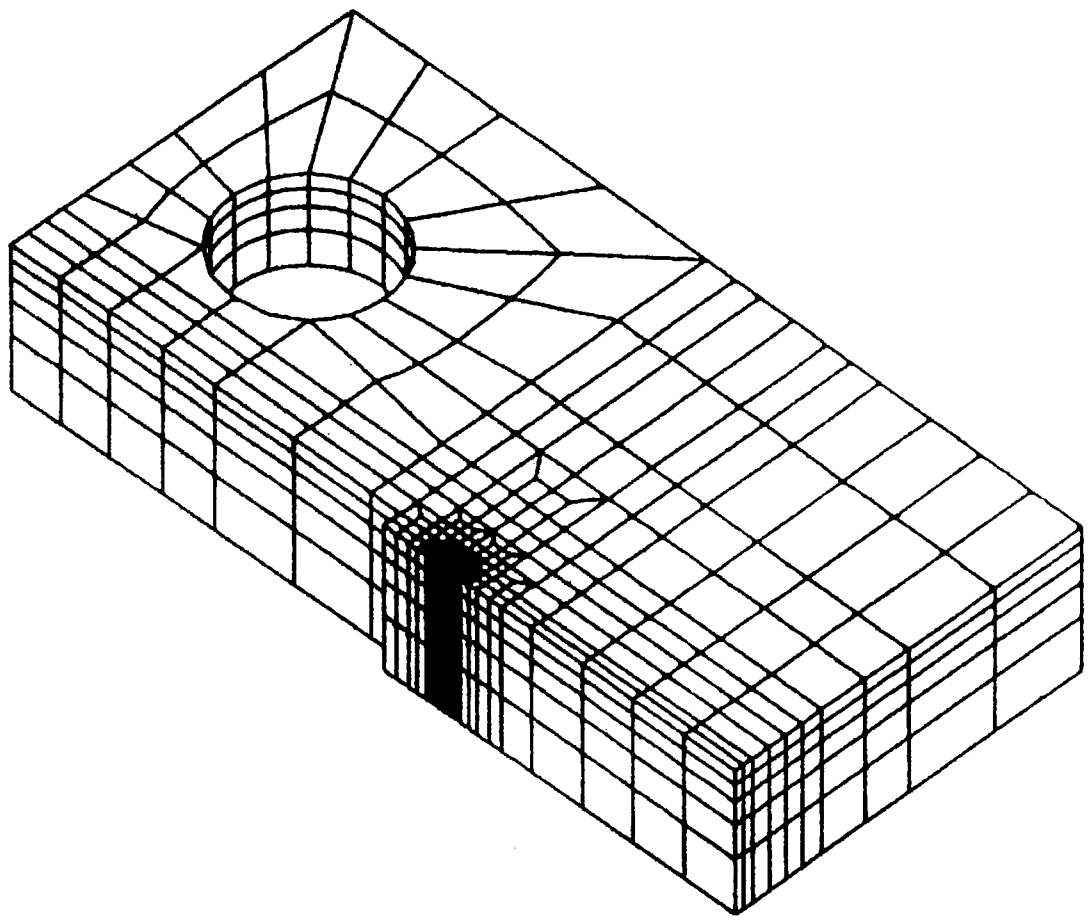

Fig. 4.4a Plain sided specimen

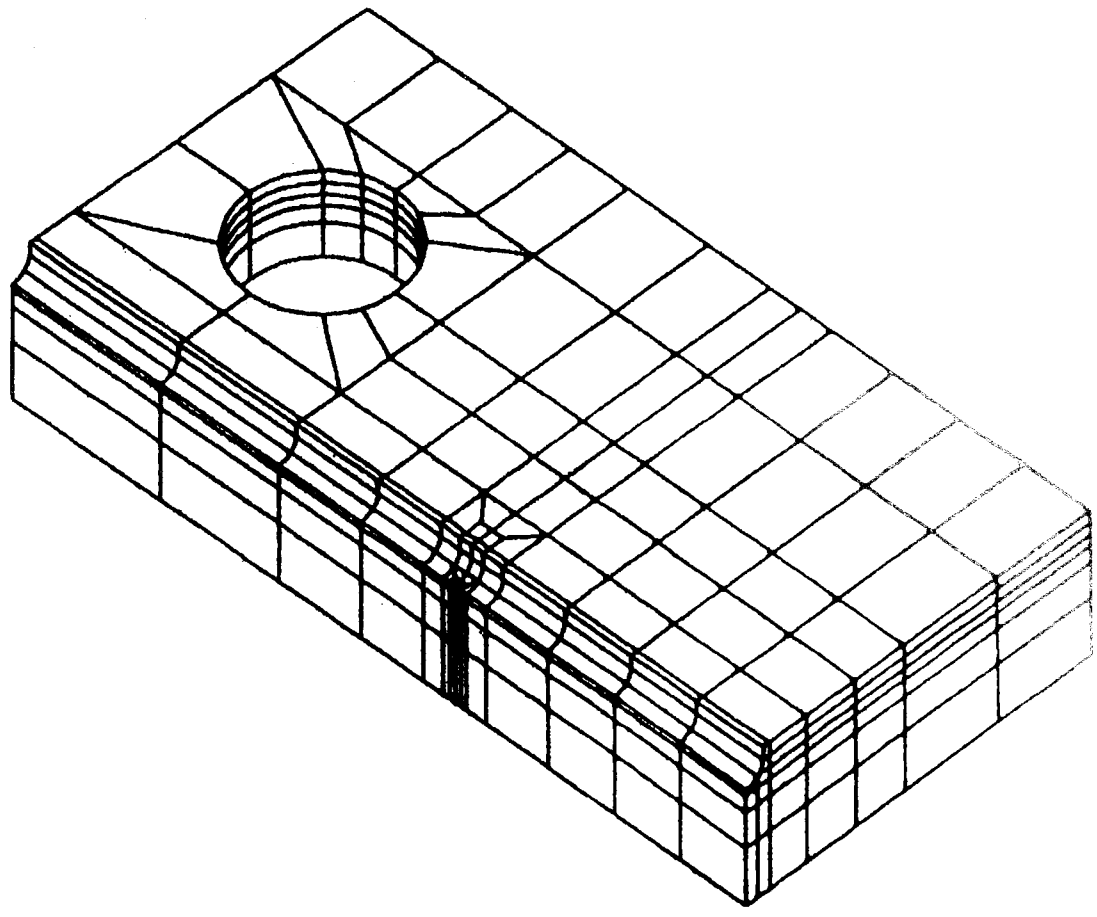

Fig. 4.4b 20% U grooved specimen

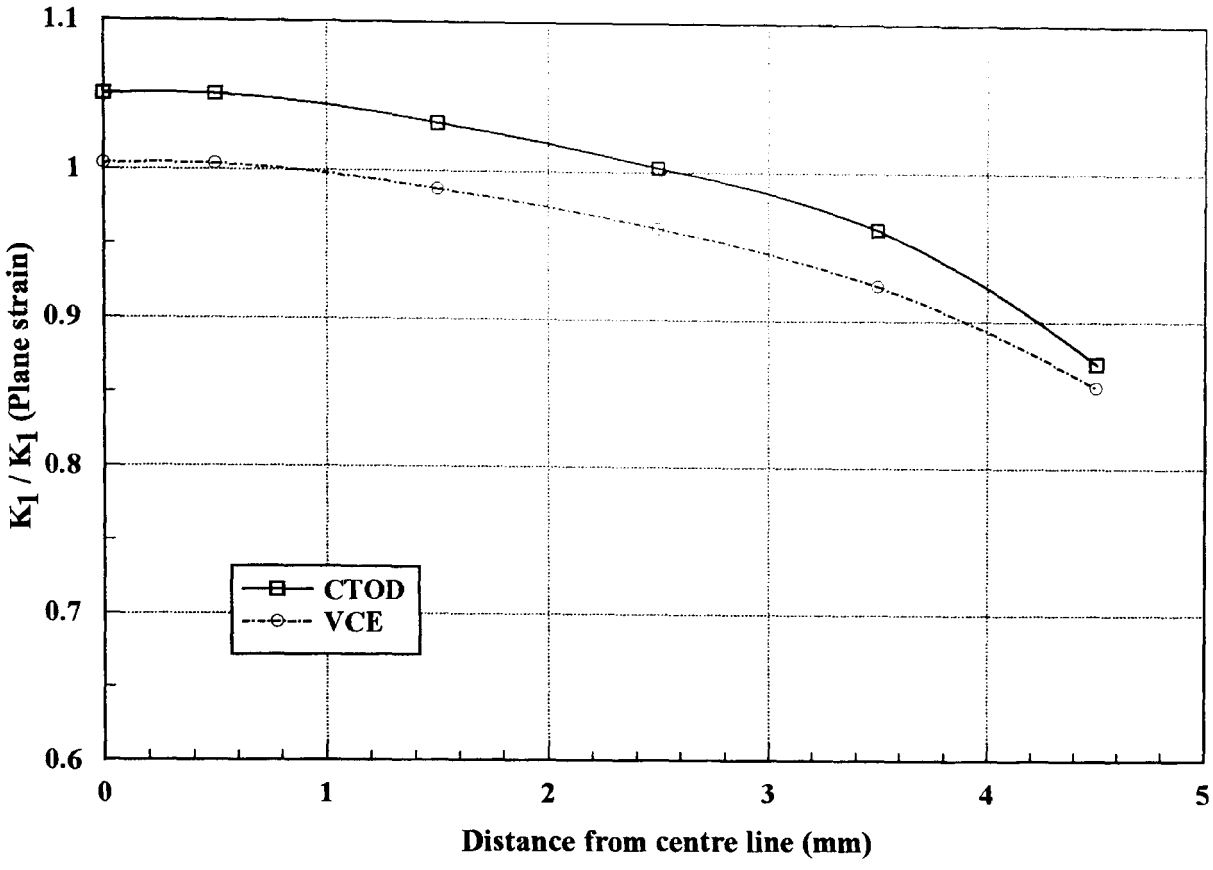

Fig. 4.5 Variation of K_I through specimen thickness – plain sided specimen

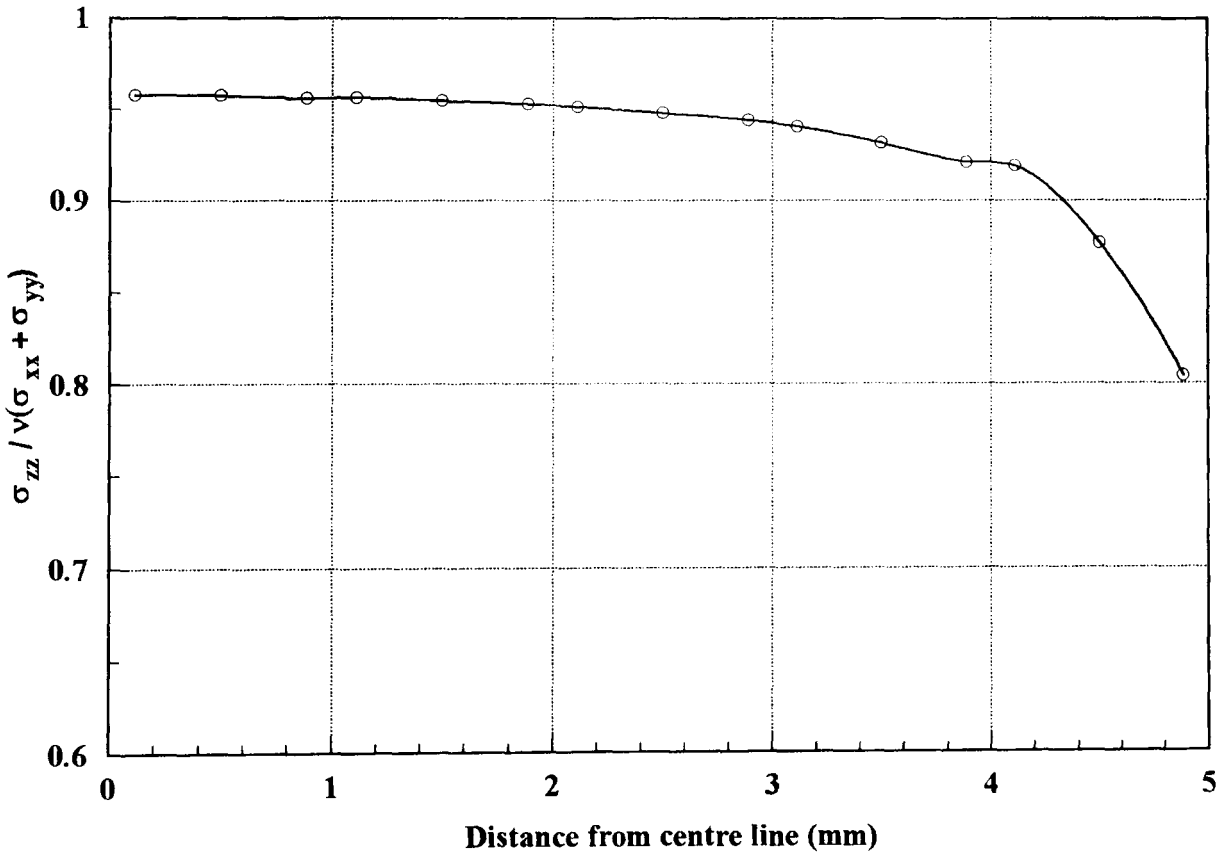

Fig. 4.6 Variation of constraint through specimen thickness – plain sided specimen

Side Grooved Specimen Analysis

Three different side groove geometries and four depths were considered, these being Vee, U and Square grooves at depths of 10%, 20%, 30% and 40% with a range of different aspect ratios for the U and Square grooved specimens.

The U and square groove profiles are based on giving the same aspect ratio as for a standard 60^0 Vee groove, i.e. d/w = 0.87. However, in order to fully establish the effect of both side groove depth and geometry other aspect ratios of d/w = 1.16, 1.29, 1.73, 2.59 and 3.47 were considered, these aspect ratios being generated by varying the groove depth between 10 - 40% for the widths provided by consideration of 10 – 40% Vee grooves. In all 24 different side groove geometry depth combinations were studied.

The variation of K_I along the crack front for all depth/geometry combinations is shown in figs. 4.7 to 4.10 for CTOD calculations and figs. 4.11 to 4.14 for VCE calculations. The variation of crack tip constraint in terms of the ratio $\sigma_{zz}/\nu(\sigma_{xx}+\sigma_{yy})$ along the crack front is shown if figs. 4.15 to 4.18.

Table 4.3 presents centre line and average values for K_I and crack tip constraint for all specimens.

Analysis results for both CTOD and VCE exhibit some similar trends across the full range of geometries and depth combinations studied. In all cases the centre line value for K_I is higher by some degree than the value obtained for the plain specimen, as is the average value across the crack front. Also there is a dramatic increase in the value of K_I at the root of the side groove. The only exceptions to this observation are the VCE results for Vee grooves, which do not exhibit a rise in K_I at the root of the side groove but provide a much flatter variation across the crack front. This is likely to be due to the mesh refinement in the through thickness direction at the root of the side groove being unable to correctly model the large stress/strain gradients that are present in the case of the Vee groove.

Consideration of all the results presented in figs. 4.7 to 4.14 and summarised in table 4.3 indicates that the effect of groove depth is to increase the centre line value of K_I in all cases. This would be expected as the same load was applied to

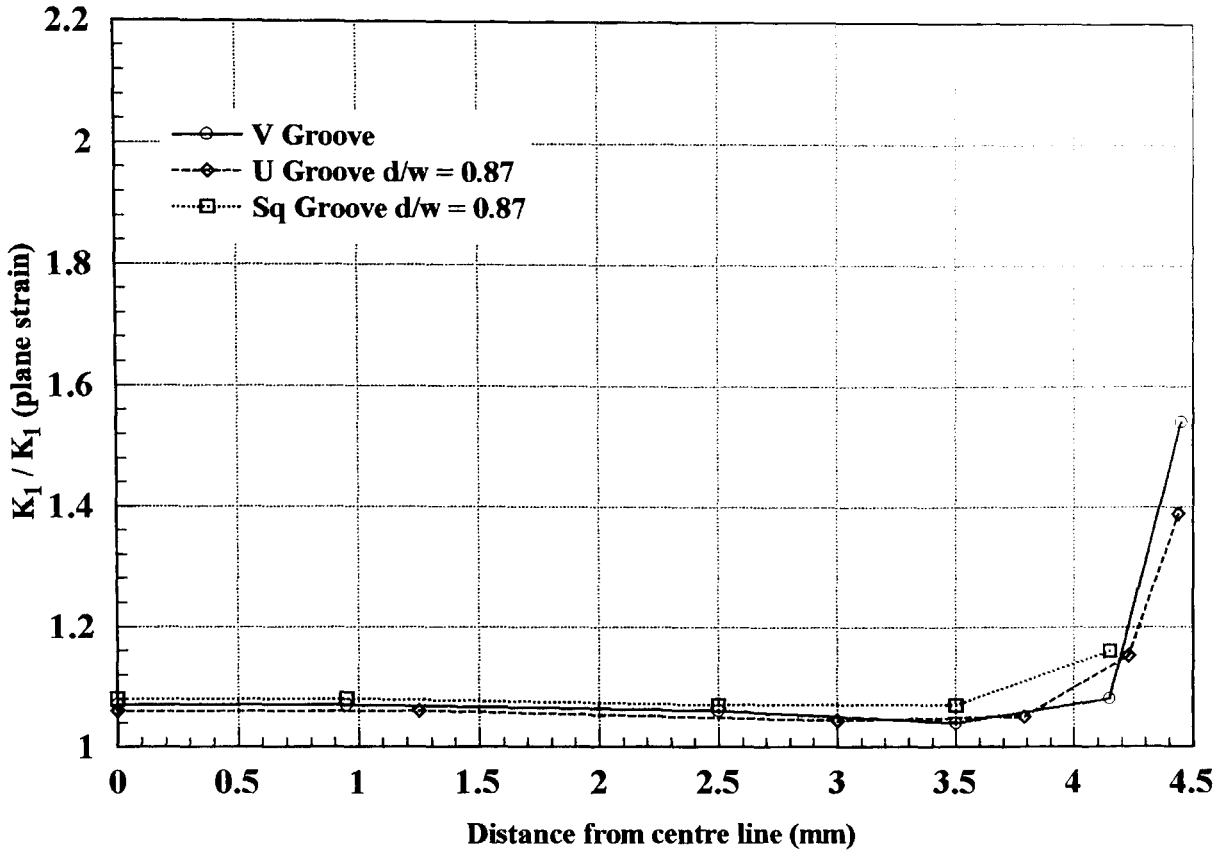

Fig. 4.7 Variation of K_I through specimen thickness – 10% side grooved specimen (CTOD)

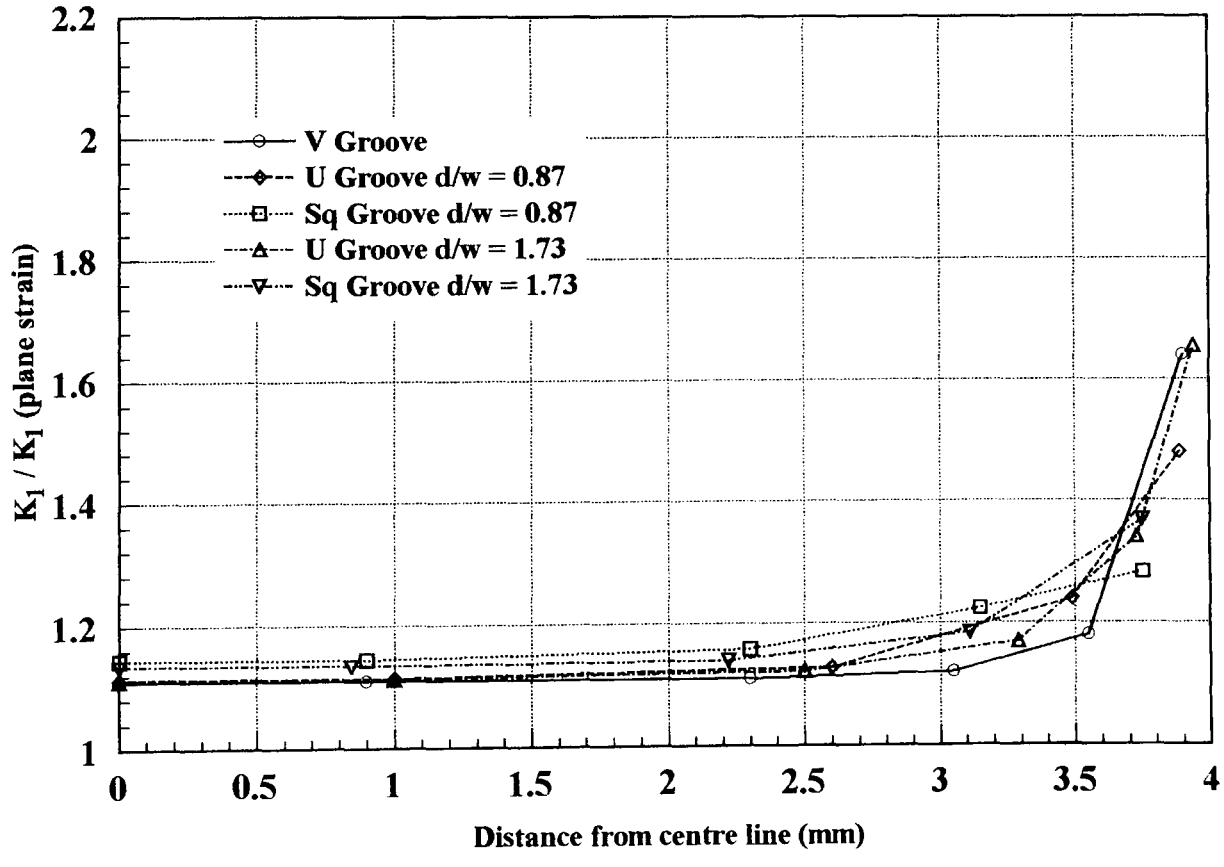

Fig. 4.8 Variation of K_I through specimen thickness – 20% side grooved specimen (CTOD)

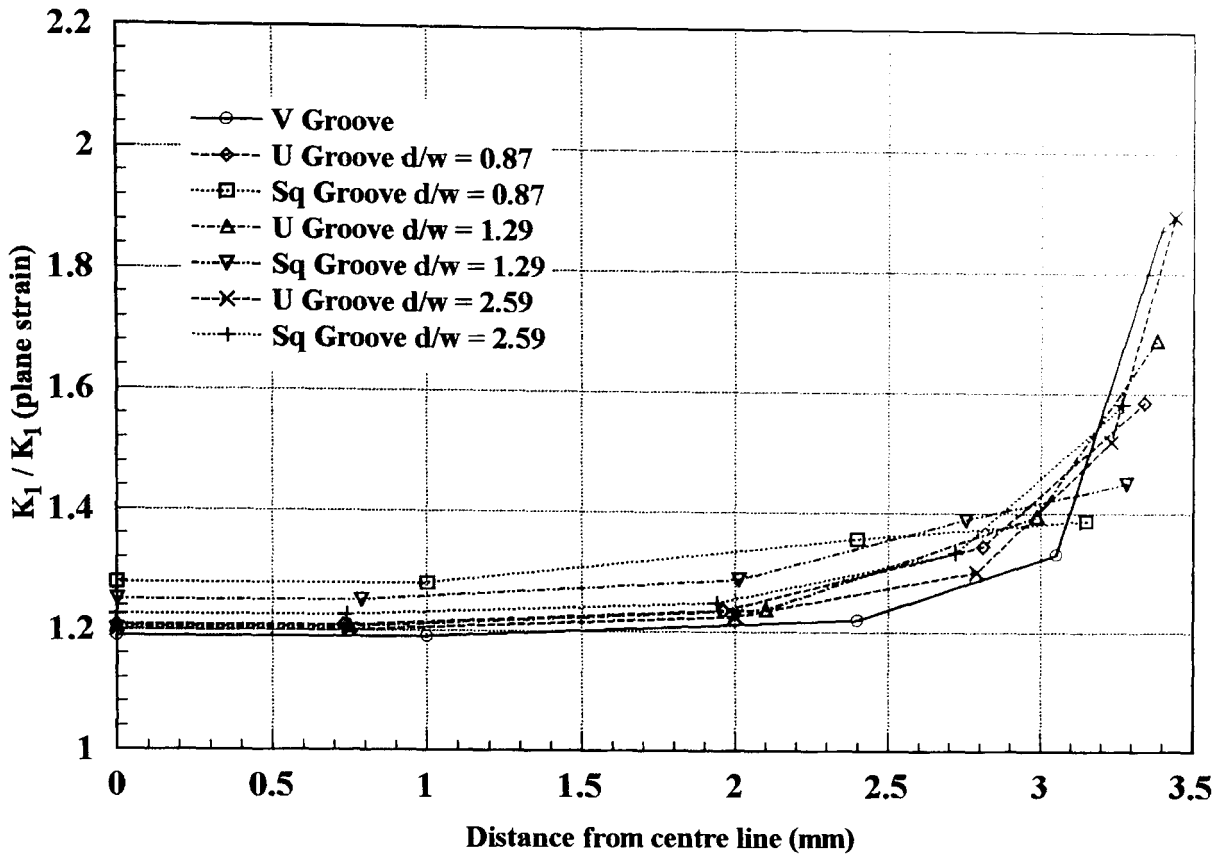

Fig. 4.9 Variation of K_I through specimen thickness – 30% side grooved specimen (CTOD)

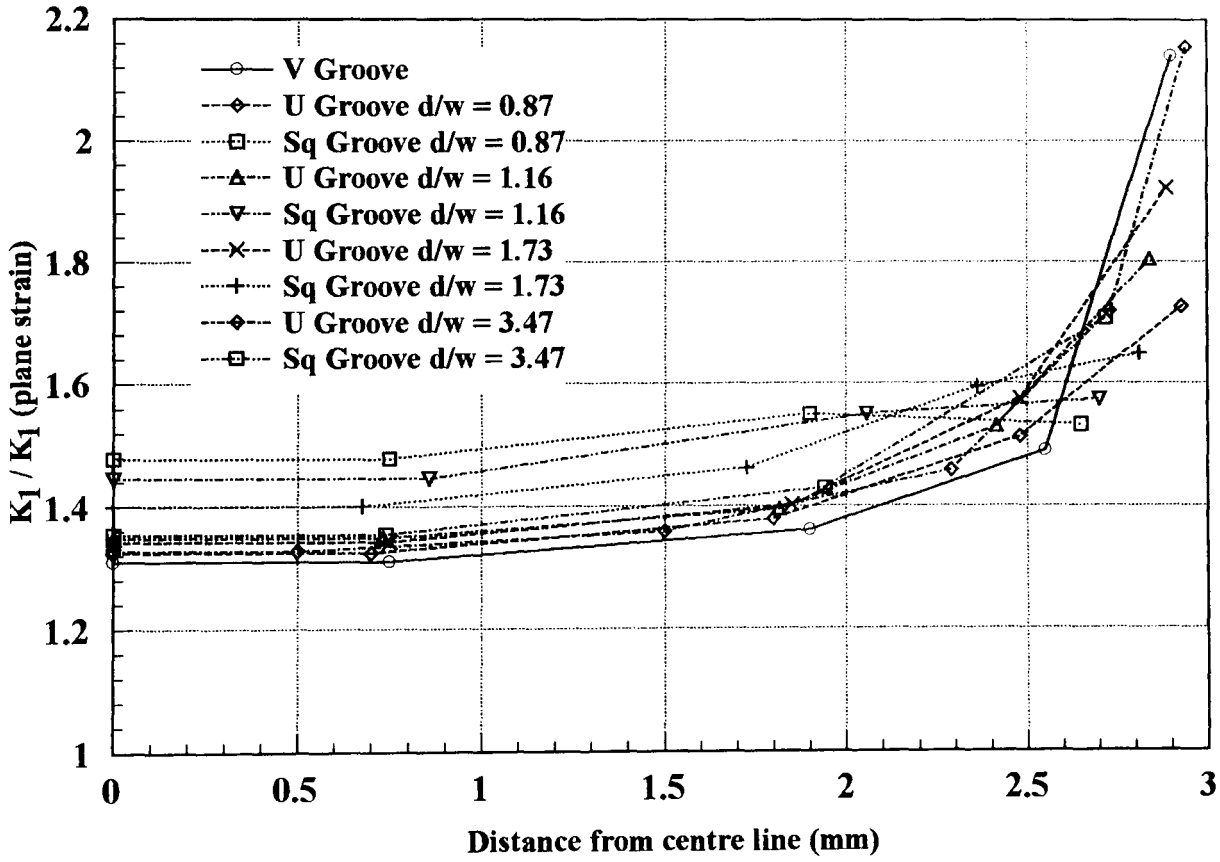

Fig. 4.10 Variation of K_I through specimen thickness – 40% side grooved specimen (CTOD)

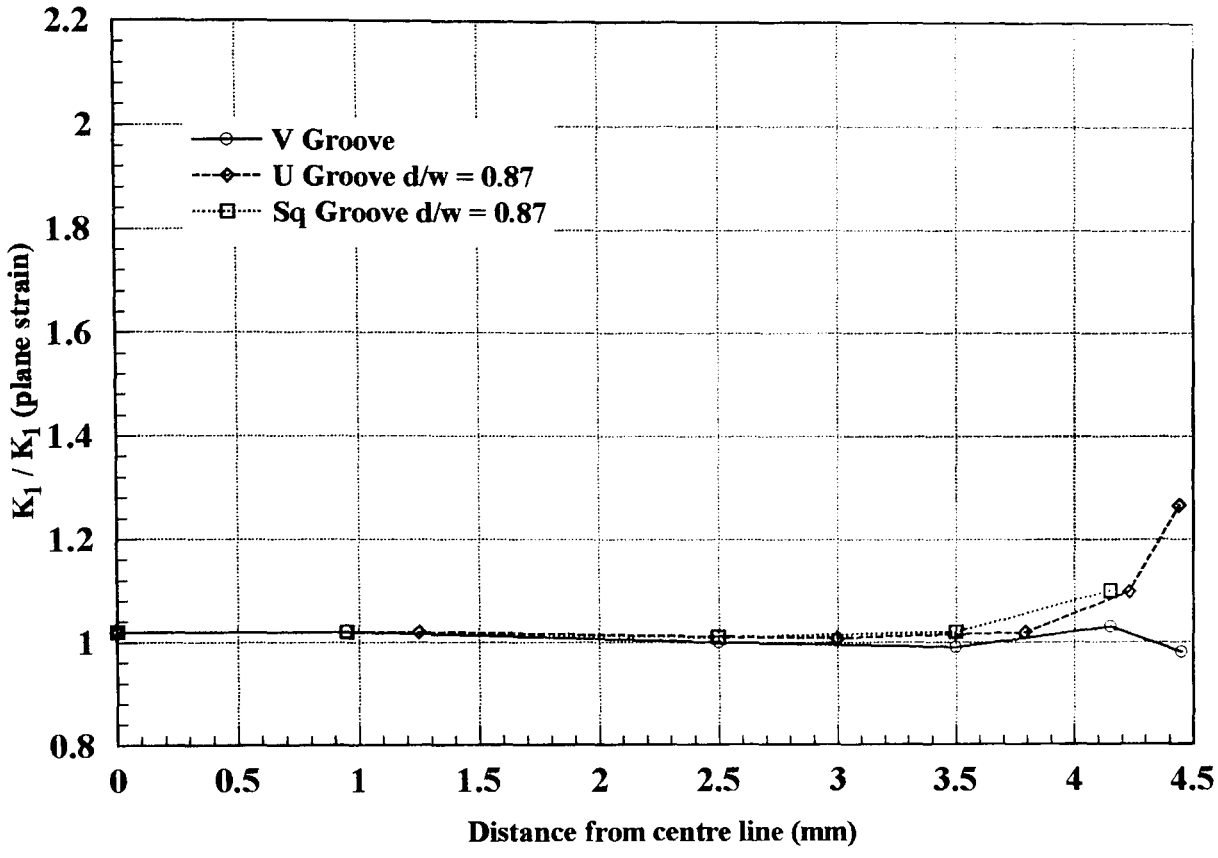

Fig. 4.11 Variation of K_I through specimen thickness – 10% side grooved specimen (VCE)

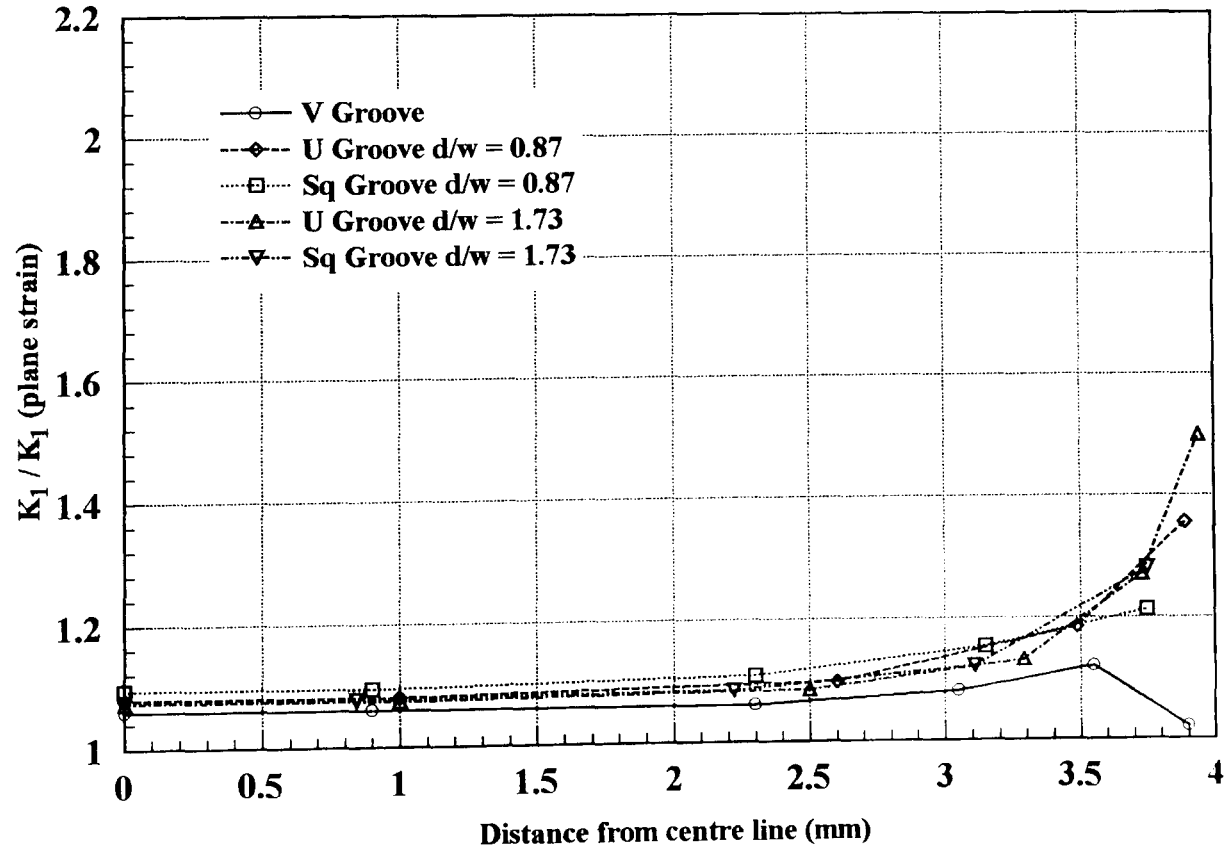

Fig. 4.12 Variation of K_I through specimen thickness – 20% side grooved specimen (VCE)

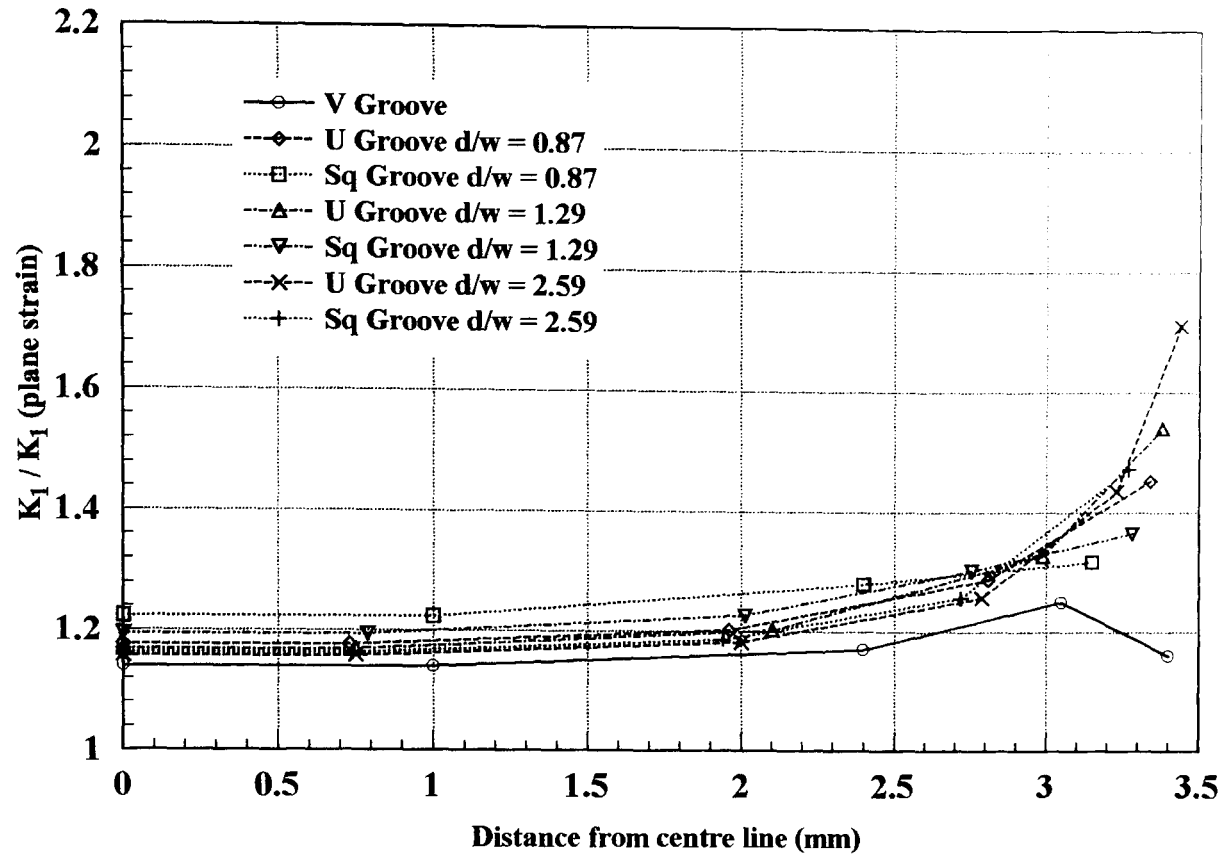

Fig. 4.13 Variation of K_I through specimen thickness – 30% side grooved specimen (VCE)

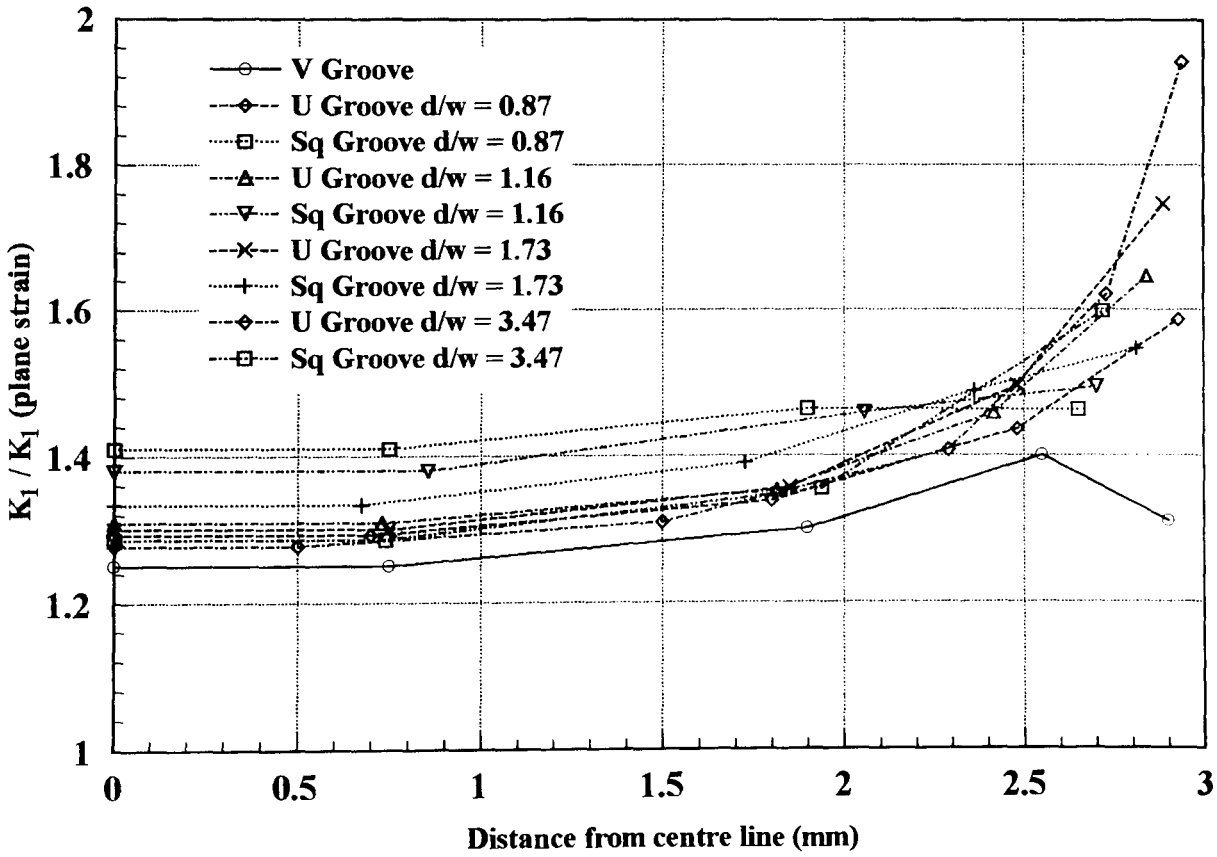

Fig. 4.14 Variation of K_I through specimen thickness – 40% side grooved specimen (VCE)

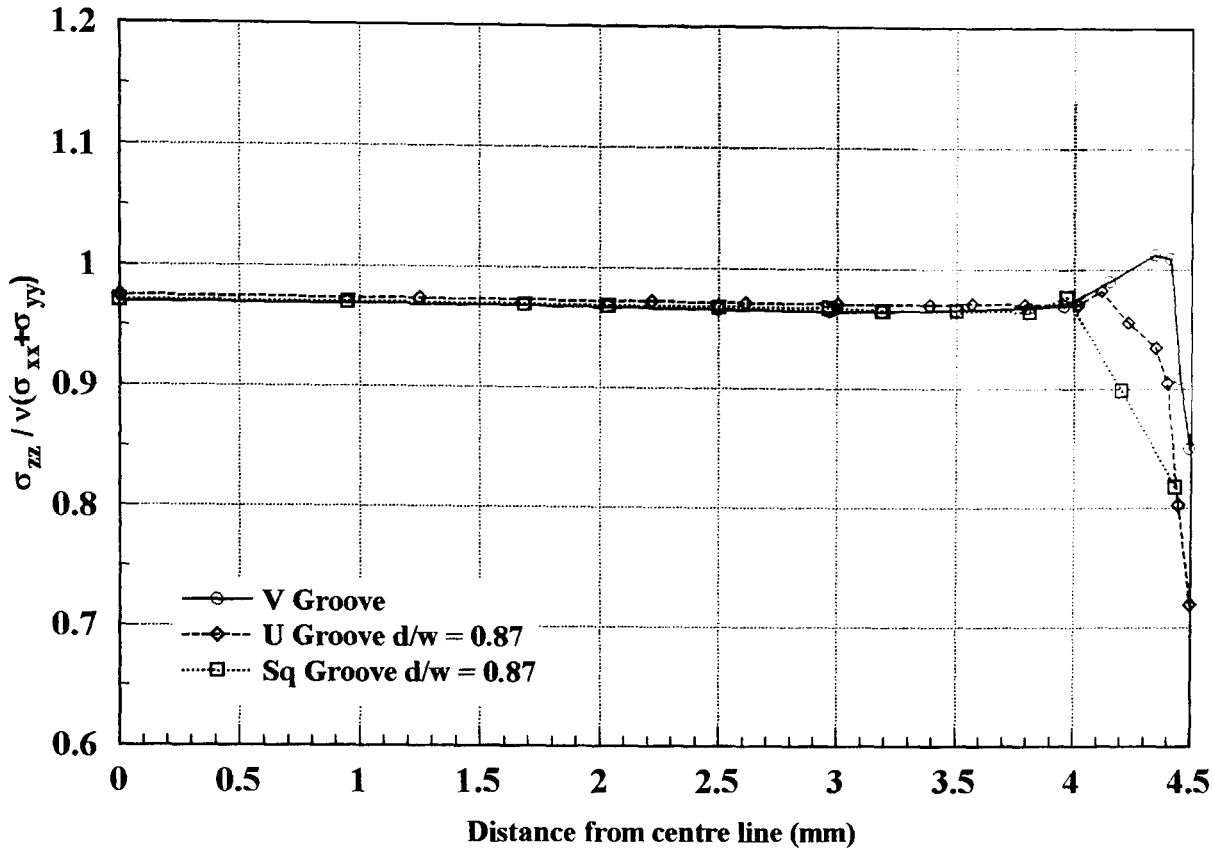

Fig. 4.15 Variation of constraint through specimen thickness – 10% side grooved specimen

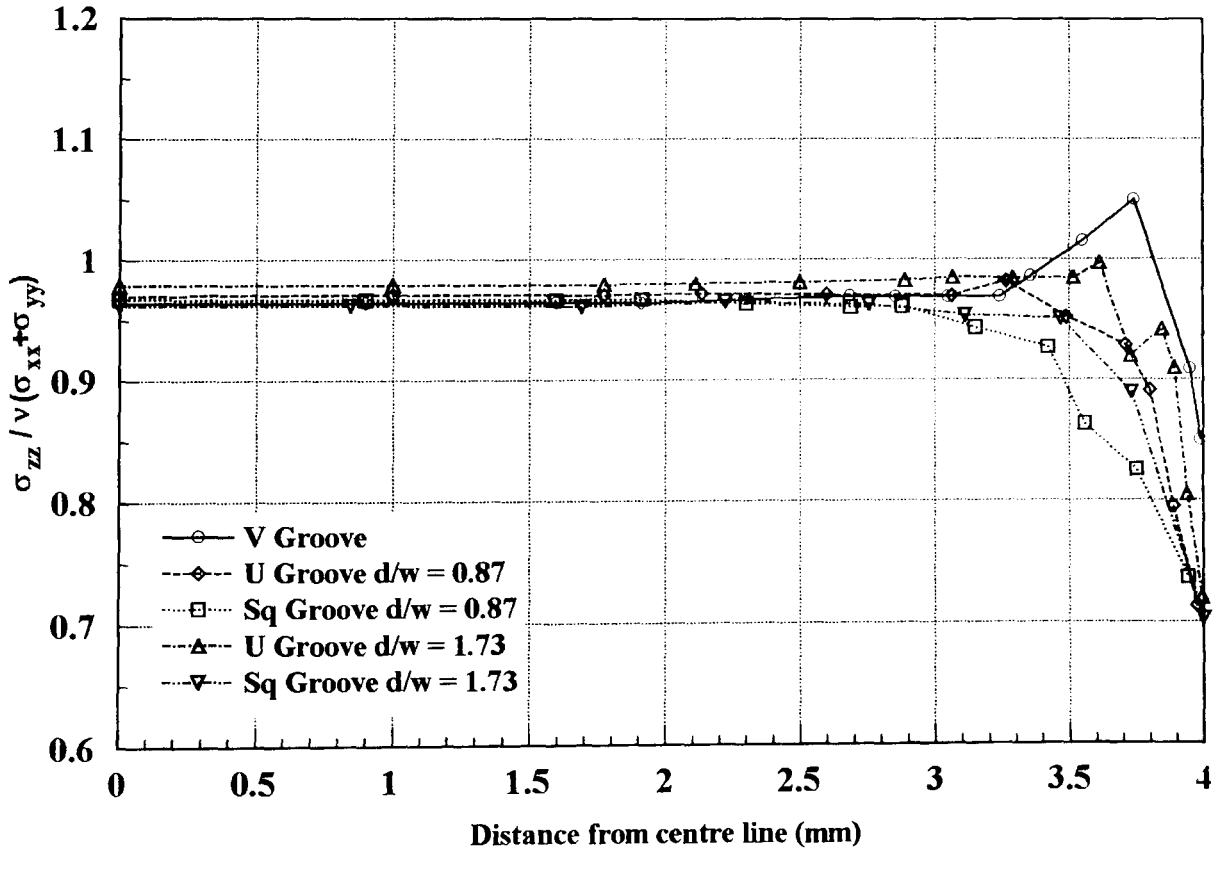

Fig. 4.16 Variation of constraint through specimen thickness – 20% side grooved specimen

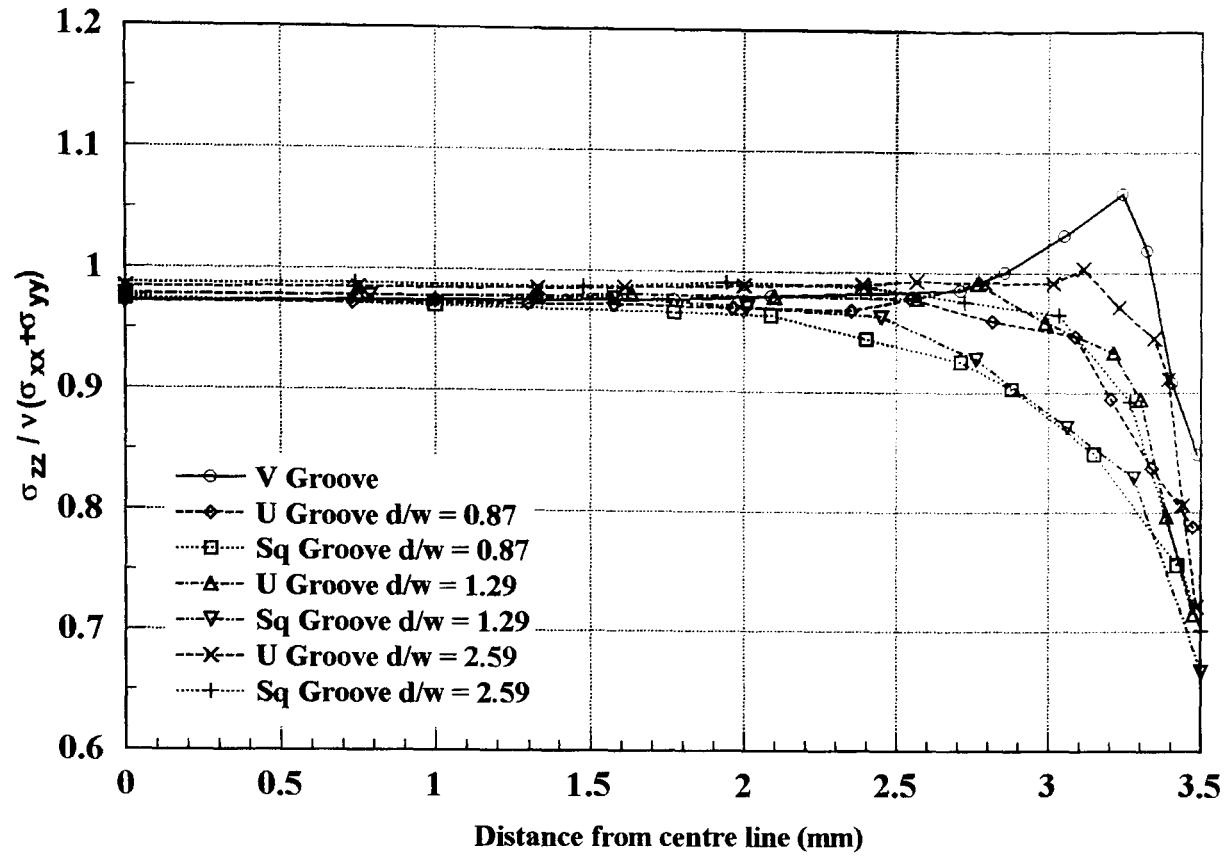

Fig. 4.17 Variation of constraint through specimen thickness – 30% side grooved specimen

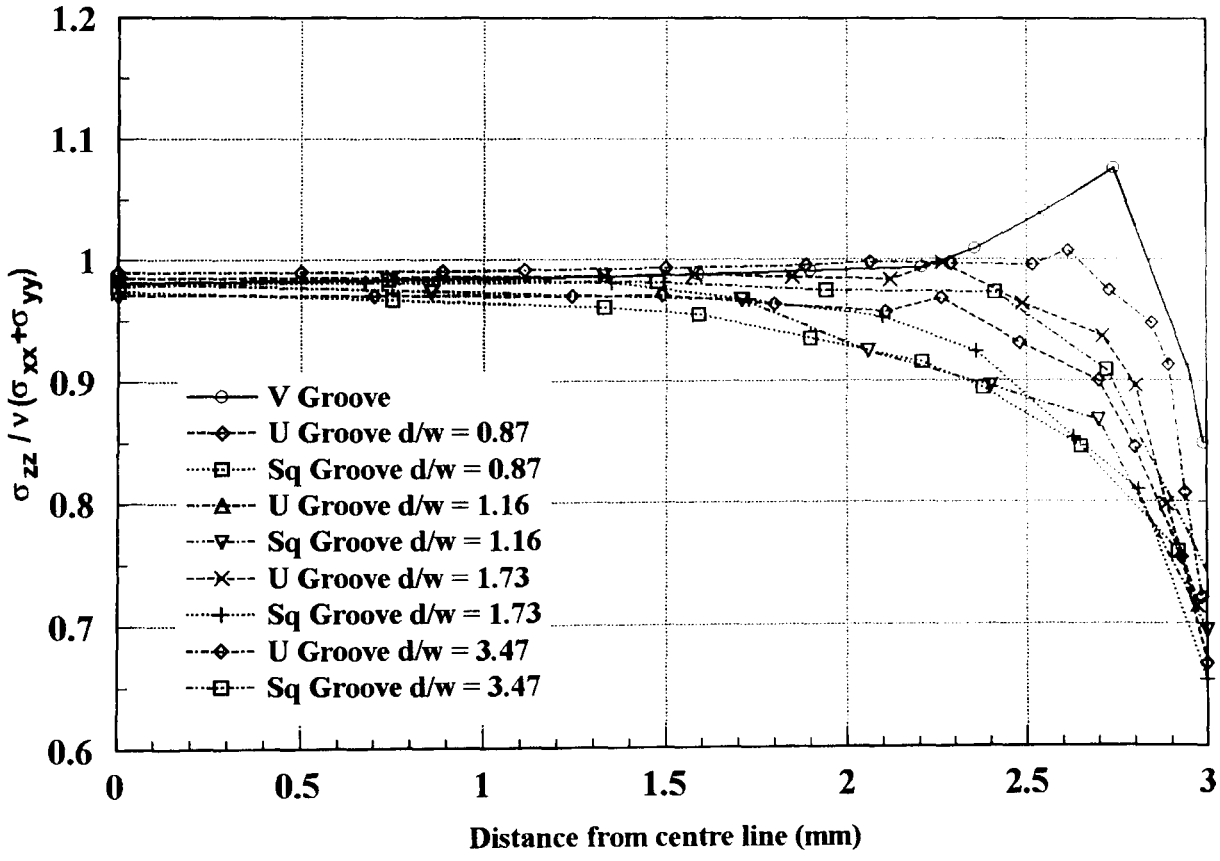

Fig. 4.18 Variation of constraint through specimen thickness – 40% side grooved specimen

each model irrespective of the depth of side groove. Vee grooves show less tendency to elevate the centre line value of K_I than other geometries and provide a flatter variation of K_I across the crack front. For depths up to 30% Vee grooves provide an almost constant value of K_I across 70% of the crack front, again this is consistent with the results obtained by De Lorenzi and Shih [31]. At a depth of 40% the variation of K_I is constant over only 30% of the crack front for Vee grooved specimens. Other groove geometries provide constancy across slightly less of the crack front than Vee grooves.

The ratio of K_I (Ave)/K_I (CL) is also given in table 4.3, as can be seen the effect of all of the side groove depth/geometry combinations considered was to give a ratio of between 0.8% to 8.2% above the plane strain value. In comparison the result obtained for the plain specimen was 0.4% below the plane strain value based on CTOD calculations and 4.5% below the plane strain value based on VCE calculations. This ratio clearly demonstrates the effectiveness of side grooving in terms of reducing the fall off of stress intensity factor at the specimen edge.

In order to fully establish the effects of side grooving on the fracture characteristics of materials, crack tip constraint is also an important consideration. The variation of $\sigma_{zz}/\nu(\sigma_{xx}+\sigma_{yy})$ along the crack front is shown in figs. 4.15 to 4.18, with summary information again being provided in table 4.3. In all cases the effect of the side grooving is to increase both the level of constraint at the centre line and the average value across the crack front above that obtained for the plain specimen. In the case of the Vee groove, an increase in constraint of between 4% and 9.5% over the centre line value is observed at a position slightly in board from the root of the side groove. This behaviour is not observed for other side groove geometries where constraint tends to fall away towards the edge of the specimen as is the case with the plain specimen. Consideration of the results obtained for U grooves suggests that the aspect ratio is important in producing a flat variation of constraint through the thickness of the specimen. Average constraint values given in table 4.3 indicate that U grooves with large aspect ratios perform well and are almost as effective as Vee grooves. Least favourable with regard to providing a flat variation of crack tip constraint were the square grooves with average constraint values falling significantly below those of Vee and U grooves.

Specimen Type	%age SG	SG Depth mm	SG Width mm	d/w	K/K (Plane Strain) Centre Line CTOD	K/K (Plane Strain) Average CTOD	K(Ave) / K(CL) CTOD	K/K (Plane Strain) Centre Line VCE	K/K (Plane Strain) Average VCE	K(Ave) / K(CL) VCE	Contraint Centre Line	Contraint Average
Plane Strain					1.000	1.000	1.000	1.000	1.000	1.000	1.000	1.000
Smooth					1.050	1.046	0.996	1.003	0.958	0.955	0.957	0.935
	10	0.5	0.577	0.87	1.070	1.078	1.007	1.020	1.008	0.988	0.969	0.967
	20	1.0	1.154	0.87	1.110	1.143	1.030	1.060	1.067	1.007	0.964	0.968
Vee	30	1.5	1.731	0.87	1.190	1.255	1.055	1.140	1.166	1.023	0.972	0.978
	40	2.0	2.308	0.87	1.310	1.407	1.074	1.250	1.295	1.036	0.981	0.989
	10	0.5	0.577	0.87	1.060	1.069	1.008	1.020	1.027	1.007	0.974	0.966
	20	1.0	1.154	0.87	1.114	1.158	1.039	1.080	1.116	1.033	0.970	0.954
	20	1.0	0.577	1.73	1.113	1.157	1.040	1.074	1.113	1.036	0.978	0.972
	30	1.5	1.731	0.87	1.208	1.274	1.055	1.176	1.228	1.044	0.972	0.950
U	30	1.5	1.154	1.30	1.206	1.280	1.061	1.169	1.230	1.052	0.977	0.958
	30	1.5	0.577	2.60	1.200	1.276	1.063	1.157	1.225	1.059	0.984	0.976
	40	2.0	2.308	0.87	1.324	1.408	1.063	1.292	1.356	1.050	0.971	0.946
	40	2.0	1.731	1.16	1.348	1.428	1.059	1.309	1.373	1.049	0.976	0.951
	40	2.0	1.154	1.73	1.342	1.442	1.075	1.300	1.384	1.065	0.984	0.961
	40	2.0	0.577	3.47	1.327	1.436	1.082	1.277	1.375	1.077	0.989	0.980
	10	0.5	0.577	0.87	1.080	1.081	1.001	1.020	1.023	1.003	0.970	0.947
	20	1.0	1.154	0.87	1.145	1.175	1.026	1.094	1.119	1.023	0.967	0.931
	20	1.0	0.577	1.73	1.135	1.166	1.027	1.077	1.105	1.026	0.962	0.947
	30	1.5	1.731	0.87	1.279	1.318	1.030	1.223	1.253	1.025	0.974	0.938
Square	30	1.5	1.154	1.30	1.250	1.304	1.043	1.193	1.230	1.031	0.977	0.944
	30	1.5	0.577	2.60	1.226	1.284	1.047	1.162	1.214	1.045	0.987	0.969
	40	2.0	2.308	0.87	1.478	1.511	1.022	1.410	1.436	1.018	0.974	0.931
	40	2.0	1.731	1.16	1.445	1.496	1.035	1.380	1.420	1.029	0.981	0.935
	40	2.0	1.154	1.73	1.400	1.476	1.054	1.334	1.397	1.047	0.981	0.941
	40	2.0	0.577	3.47	1.354	1.432	1.058	1.286	1.355	1.054	0.978	0.959

Table 4.3 Centre line and average K_I and crack tip constraint

A summary of the potential usefulness of the three side groove types considered with regard to improving the fracture performance of test specimens is as follows:

i) Vee grooves provide a flat variation of K_I and crack tip constraint over a significant proportion of the specimen net thickness. However, both the stress intensity factor and level of crack tip constraint are high at the root of the side groove. In brittle materials this could encourage the crack to propagate preferentially from the root of the side groove rather than evenly across the crack front. It is more likely, however, that side grooving would be used with more ductile materials in which case the high local constraint at the root of the side groove will tend to lead to a more even crack growth rather than tunnelling as is often observed. Vee grooves have excellent potential for inducing favourable fracture conditions in sub thickness specimens.

ii) U grooves also provide a reasonably flat variation of K_I and crack tip constraint over a significant proportion of the specimen net thickness. They do not exhibit a significant increase in crack tip constraint at the root of the side groove and, therefore, remove any incentive for preferential crack growth at the root, as is the case with the Vee grooves.

iii) The performance of Square grooves is highly dependent on the groove aspect ratio. From the results presented it is likely that only very narrow grooves could provide useful results.

4.3.4 THEORETICAL SPECIMEN EFFECTIVE THICKNESS DETERMINATION

As stated in section 4.1 an objective for this chapter was to provide analytical support for the concept of specimen effective thickness as originally proposed by Freed and Krafft [28]. For a side grooved specimen Freed and Krafft suggested that the plane strain fracture toughness could be obtained from equation (2.29), which is repeated below for clarity.

$$K_{IC} = K_{NOM}\left(\frac{B}{B_N}\right)^m \quad \ldots.(2.29)$$

where:

K_{IC} = Material plane strain fracture toughness.

K_{NOM} = Fracture toughness obtained when the failure load is assumed to act on a specimen of full thickness.

B = Full specimen thickness.

B_N = Thickness at the root of the side groove.

Freed and Krafft examined extreme cases of sensitivity to side grooving which can be reasoned from basic fracture mechanics theory based on previous work by Irwin and Kies [97] and Paris and Sih [98]. The argument presented in [28] can be summarised by first considering a very thick plain sided fracture specimen in which the fracture energy rate can be considered to be of a uniform (average) value, $G_A = G_I$, across the majority of the crack front thickness, B. If this were the case then it would be reasonable to assume that the crack would advance normal to the original crack front. The elastic energy released during crack advance, du, would be equal to that which would be stored up again in re-closing the crack with local forces. This is directly reflected in an increase in overall compliance of the specimen which may be measured [97]. Hence:

$$\frac{du}{da} = G_A = G_{IC} = \frac{1}{2}\cdot\frac{P^2}{B}\cdot\frac{dC}{da} \quad \ldots..(4.6)$$

where P is the total load, C is the total compliance but G and du/da are on a unit thickness basis.

Now consider a side grooved specimen. If crack advance was normal to the original crack front as before then it would still be reasonable to assume that this was because G was still the same at all locations across the crack front. However, the energy release would only be expended over B_N and B_N can be substituted for B giving:

$$G_{IC} = \frac{B}{B_N} \cdot G_{NOM} \quad .....(4.7)$$

where G_{NOM} is the nominal value of G_{IC} calculated using equation (4.6) as though no side groove was present. It is reasonable to assume that the reduction in thickness due to the side grooves has little effect on the absolute value of dC/da. Hence G_{NOM} can be calculated using plain specimen calibration and then calibrated for the effects of side grooving in terms of the stress intensity factor.

$$K_{IC} = K_{NOM} \left(\frac{B}{B_N} \right)^{1/2} \quad .....(4.8)$$

An alternative to the assumption that the crack advances uniformly across the width of the specimen would be to assume that initiation would be strongly influenced by the locally more intense stress near the junction of the crack front and side groove. Irwin [97] suggested an analogy with a deep notched specimen which is cited as eq58 in [98], i.e.

$$K = \frac{\sigma_N}{2\sqrt{2}} \sqrt{\pi B_N} \quad .....(4.9)$$

To calculate the local (net) stress, σ_N, he averaged the y direction stress singularity of the main crack to the distance $B_N/2$ back from its front, i.e.

$$\sigma_N = \frac{8}{\pi B_N^{\,2}} \int_0^{B_N/2} \frac{K_{NOM}}{\sqrt{2\pi r}} \cdot B \, dr = \frac{8B}{\pi B_N^{\,2}} K_{NOM} \sqrt{\frac{B_N}{\pi}} \quad .....(4.10)$$

substitution into equation (4.9) yields:

$$K = \frac{4}{\pi\sqrt{2}} \; K_{NOM} \left(\frac{B}{B_N} \right)^1 \quad \ldots\ldots (4.11)$$

It is expected, therefore, that the value of m will be between 0.5 and 1.0 as predicted above.

Finite element analysis data has been used to verify equation (2.28) and to evaluate m. Fig. 4.19 and 4.20 are log log plots of K_{NOM} against thickness ratio B/B_N for CTOD and VCE based calculations respectively, the slope of which should be –m.

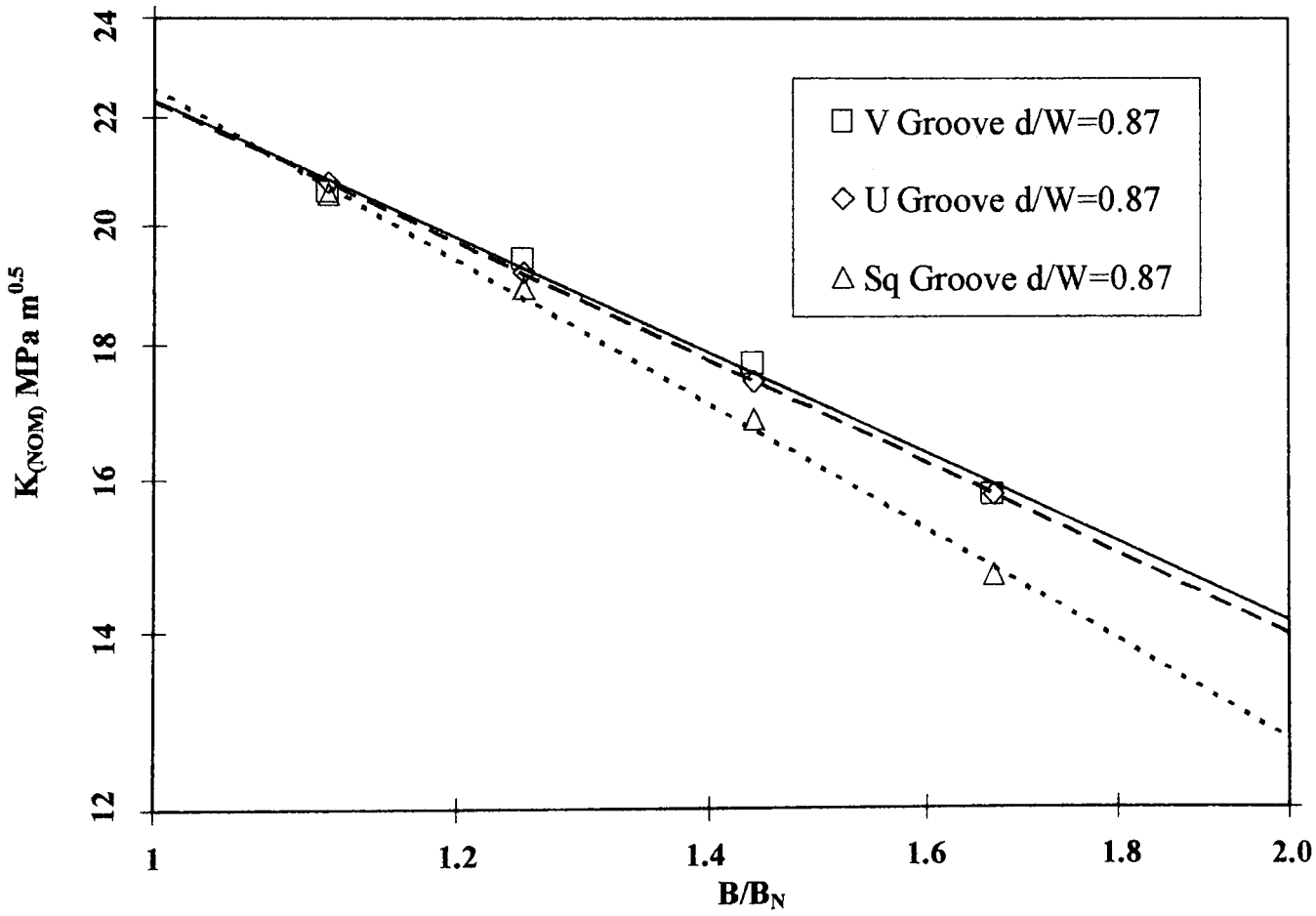

Fig. 4.19 $K_{(NOM)}$ from FE (CTOD) v B/B_N based on equation 4.4

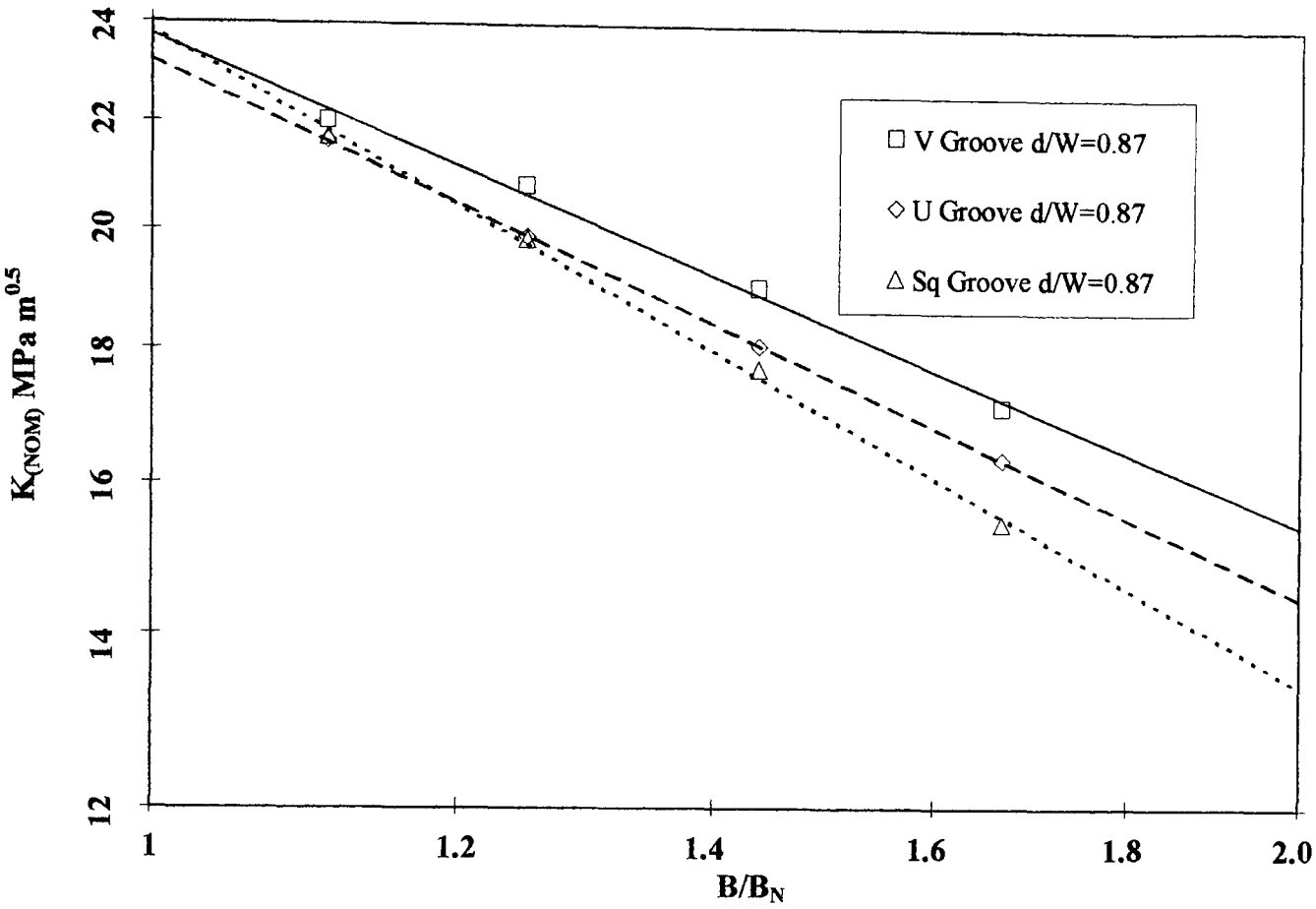

Fig. 4.20 $K_{(NOM)}$ from FE (VCE) v B/B_N based on equation 4.4

The values of K_{NOM} were determined for each side grooved model by using the average value of K_I across the crack front to establish a failure load based on the experimental value obtained for the material fracture toughness of 22 MPa $m^{0.5}$. This failure load was then used in equation (4.4) together with an f(a/W) value obtained from equation (4.5) for a/W = 0.5 to give a nominal K value based on a full thickness plain sided specimen. Results for all specimens considered are presented in table 4.4 and plotted in figs. 4.19 for CTOD based calculations and 4.20 for VCE based calculations for side grooves with an aspect ratio of 0.87.

Specimen Type	%age SG	SG Depth mm	SG Width mm	d/w	B/B_N	K/K (Plane Strain) Average CTOD	K / unit load $MPa.m^{0.5}$ / kN	Failure Load (FE) kN	K_{NOM} BS7448	K/K (Plane Strain) Average VCE	K / unit load $MPa.m^{0.5}$ / kN	Failure Load (FE) kN	K_{NOM} BS7448
Plane Strain						1.000	6.829	3.254	22.227	1.000	6.829	3.254	22.227
Smooth					1.000	1.046	7.143	3.111	21.249	0.958	6.542	3.397	23.201
Vee	10	0.5	0.577	0.87	1.110	1.078	7.361	3.018	20.618	1.008	6.883	3.228	22.050
	20	1.0	1.154	0.87	1.250	1.143	7.805	2.847	19.446	1.067	7.286	3.050	20.831
	30	1.5	1.731	0.87	1.438	1.255	8.570	2.593	17.710	1.166	7.962	2.791	19.062
	40	2.0	2.308	0.87	1.667	1.407	9.608	2.313	15.797	1.295	8.843	2.513	17.163
U	10	0.5	0.577	0.87	1.110	1.069	7.300	3.044	20.792	1.027	7.013	3.168	21.642
	20	1.0	1.154	0.87	1.250	1.158	7.908	2.810	19.194	1.116	7.621	2.916	19.916
	20	1.0	0.577	1.73	1.250	1.157	7.901	2.812	19.210	1.113	7.600	2.924	19.970
	30	1.5	1.731	0.87	1.438	1.274	8.700	2.554	17.446	1.228	8.386	2.650	18.100
	30	1.5	1.154	1.30	1.438	1.280	8.741	2.542	17.364	1.230	8.399	2.645	18.070
	30	1.5	0.577	2.60	1.438	1.276	8.713	2.550	17.419	1.225	8.365	2.656	18.144
	40	2.0	2.308	0.87	1.667	1.408	9.615	2.311	15.786	1.356	9.260	2.400	16.391
	40	2.0	1.731	1.16	1.667	1.428	9.751	2.279	15.565	1.373	9.376	2.370	16.188
	40	2.0	1.154	1.73	1.667	1.442	9.847	2.257	15.414	1.384	9.451	2.351	16.060
	40	2.0	0.577	3.47	1.667	1.436	9.806	2.266	15.478	1.375	9.389	2.366	16.165
Square	10	0.5	0.577	0.87	1.110	1.081	7.382	3.010	20.561	1.023	6.986	3.181	21.727
	20	1.0	1.154	0.87	1.250	1.175	8.024	2.769	18.916	1.119	7.641	2.908	19.863
	20	1.0	0.577	1.73	1.250	1.166	7.962	2.791	19.062	1.105	7.546	2.945	20.114
	30	1.5	1.731	0.87	1.438	1.318	9.000	2.469	16.864	1.253	8.556	2.597	17.739
	30	1.5	1.154	1.30	1.438	1.304	8.905	2.495	17.045	1.230	8.399	2.645	18.070
	30	1.5	0.577	2.60	1.438	1.284	8.768	2.534	17.310	1.214	8.290	2.680	18.308
	40	2.0	2.308	0.87	1.667	1.511	10.318	2.153	14.710	1.436	9.806	2.266	15.478
	40	2.0	1.731	1.16	1.667	1.496	10.216	2.175	14.857	1.420	9.697	2.292	15.652
	40	2.0	1.154	1.73	1.667	1.476	10.079	2.205	15.059	1.397	9.540	2.329	15.910
	40	2.0	0.577	3.47	1.667	1.432	9.779	2.272	15.521	1.355	9.253	2.401	16.403

Table 4.4 Determination of K_{NOM} to BS7448 from FE results

Trend lines were added to the graphs for each side groove type in order to evaluate the slope and intercept and hence obtain m and the value K given by the regression analysis. The results are given in table 4.5 below.

	CTOD		VCE	
Specimen Type	**m**	**Intercept Fracture Toughness MPa $m^{0.5}$**	**m**	**Intercept Fracture Toughness MPa $m^{0.5}$**
Vee	0.66	22.21	0.62	23.26
U	0.67	22.22	0.68	23.12
Sq	0.82	22.49	0.83	23.73

Table 4.5 – Specimen effective thickness results

As can be seen from table 4.5 all of the values for m lie between 0.5 and 1.0 as would be expected.

Vee and U grooves perform almost identically, however, the value obtained for Vee grooved specimens from VCE is approximately 7% lower than that obtained from CTOD. This observation is due to the very flat distribution of K across the specimen thickness illustrated in figures 4.11 to 4.14 and discussed in section 4.3.3.

Interestingly the m value obtained for Square grooved specimens is considerably higher than that obtained for either Vee or U grooves. Further consideration suggests that this should be expected, particularly for small d/w ratios, in the limit as d/w $\rightarrow$ o then the specimen would become a plain specimen of thickness B_N and hence would have a full power dependency with regard to the value obtained for K_I, i.e.. m $\rightarrow$ 1.

4.4 FRACTURE TOUGHNESS TESTING

Results from the finite element analysis indicate that both Vee and U grooved specimens offer potential for further investigation. However, due to reasons associated with manufacture, it was decided that the test programme should concentrate on Vee grooved specimens of varying depth. Manufacture of Vee grooved specimens is relatively easy using Vee shaped side and face milling cutters whereas U grooved specimens require profiled cutters.

Testing was also limited to side grooves of 20% and greater because preliminary work suggested that due to high scatter normally associated with fracture testing, the effects of shallow side grooves was difficult to detect.

Testing was undertaken using an Instron servo-hydraulic test machine of 50 KN dynamic and 100 KN static load capacity. The material used for fracture toughness testing was an aluminium alloy of chemical composition 3.8-4.8% Cu, 0.2-0.8% Mg, 0.5-0.9% Si, 0.3-1.2% Mn, 0.7% Fe with a 0.05% proof stress obtained by test of 475 MPa, a UTS of 517 MPa and E = 72 GPa. Preliminary tests had shown that valid K_{IC} results could be obtained for a specimen thickness of 10 mm at a load of approximately 3 KN, which meant that the material could be tested within the capacity of the Instron machine. A stress-strain curve for the material can be seen in figure 4.21.

All fracture testing was carried out in accordance with BS 7448, part 1, 1991 [26].

4.4.1 SPECIMEN PREPARATION

All specimens were prepared in accordance with BS 7448 , part 1, 1991 [26], section 6. The specimens were first machined to a plain sided state then fatigue pre-cracked to give the ratio of a/W between 0.45 – 0.55. Crack length during the pre-cracking process was monitored by the use of a travelling microscope. Ideally the specimens would have been side grooved prior to pre-cracking, however, this was not done because of the difficulty in determining the fatigue crack length at the root of the side groove. Consequently the side grooves were machined after pre-cracking.

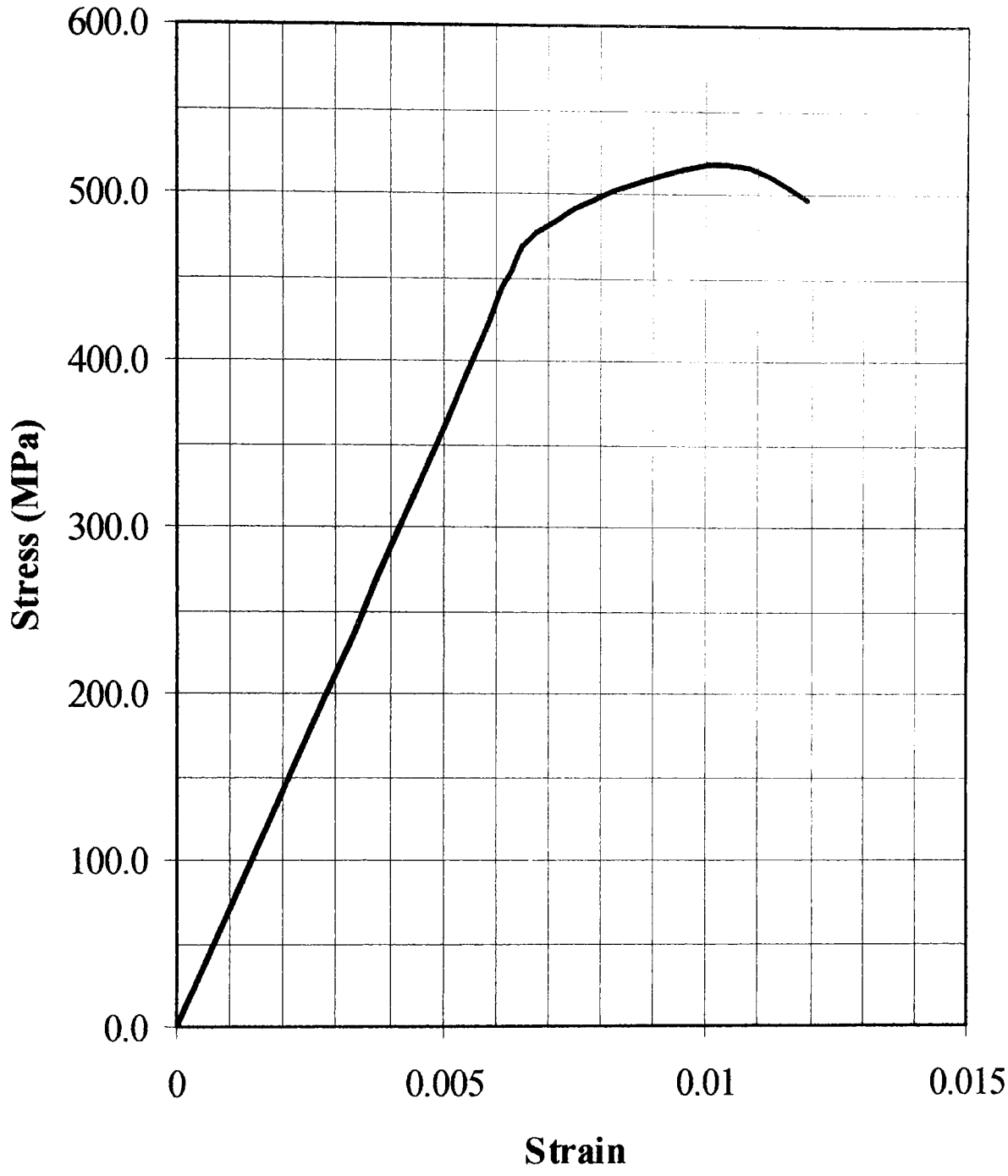

Fig. 4.21 Aluminium alloy stress – strain curve

Clause 6.4.6 of BS 7448 [26] states that the maximum pre-cracking force F_f, during the final 1.3 mm or 50% of pre-crack extension, whichever is less, shall be the lower of:

a) $$F_f = \frac{0.2B(W-a)^2\left(\sigma_{YSP} + \sigma_{TSP}\right)}{(2W-a)} \quad \text{.....(4.12)}$$

b) a force such that $\frac{\Delta K}{E} = 3.2 \times 10^{-4} m^{0.5}$ ..... (4.13)

c) $F_f = \frac{K_f BW^{0.5}}{f\left(\frac{a}{W}\right)}$ ..... (4.14) in tests that give valid K_{IC} values.

where:

$$K_f = 0.6\left[\frac{\sigma_{YSP}}{\sigma_{YS}}\right] K_Q \quad \text{..... (4.15)}$$

σ_{YS} = 0.2% proof strength at the temperature of the fracture test.

σ_{YSP} = 0.2% proof strength at the temperature of fatigue pre-cracking.

σ_{TSP} = tensile strength at the temperature of fatigue pre-cracking.

K_Q = the provisional value of fracture toughness from test.

a = an assumed crack length ≤ the crack length in the subsequent fracture test.

$f\left(\frac{a}{W}\right)$ is given by equation 4.5.

Table 4.6 gives details of all pre-cracking data and maximum pre-cracking force conditions according to clause 6.4.6 of BS 7448 [26]. All of the requirements of clause 6.4.6 were met by all of the specimens under consideration.

Further conditions as laid down by clause 6.4.7 (a) and (b) of BS 7448 [26] which states that the maximum stress intensity factor during initial fatigue pre-crack extension shall not exceed 1.3 K_f and that the fatigue force ratio shall be in the range 0 to 0.1 were also satisfied by all specimens. Clause 6.4.7(c), (d) and (e) which relate to pre-crack shape and size were also satisfied.

Specimen No	Side Groove Type	Pre-cracking Data								Pre-cracking force conditions		
		Initial Cycles				Final Cycles				F_f(kN)	Condition	F_f(kN)
		Mean Load (kN)	Amplitude (kN)	No of Cycles	Crack length (mm)	Mean Load (kN)	Amplitude (kN)	No of Cycles	Crack length (mm)	eq 4.12	eq 4.13	eq 4.14
1	Plain	1.40	1.35	2258	0.56	0.80	0.60	25359	1.96	6.18	1.39E-07	1.84
2	Plain	1.40	1.35	3109	0.34	0.80	0.60	29900	2.60	5.75	1.49E-07	1.73
3	V 20%	1.00	0.80	22000	1.00	0.80	0.60	30000	2.27	5.54	1.54E-07	1.67
4	V 20%	1.00	0.80	18811	1.00	0.75	0.65	33782	2.00	6.18	1.39E-07	1.84
5	V 30%	1.00	0.80	23500	0.76	0.75	0.65	30908	1.60	5.96	1.44E-07	1.78
6	V 30%	1.00	0.80	14200	0.70	0.75	0.65	35602	1.79	6.61	1.31E-07	1.96
7	V 30%	1.00	0.80	17000	0.80	0.75	0.65	45400	1.72	6.18	1.39E-07	1.84
8	V 30%	1.00	0.80	12000	0.80	0.75	0.65	20000	1.75	7.06	1.23E-07	2.08
9	V 40%	1.00	0.80	11703	0.70	0.75	0.65	34500	1.60	6.18	1.39E-07	1.84
10	V 40%	1.00	0.80	16000	0.70	0.75	0.65	57000	1.70	5.96	1.44E-07	1.78
11	V 40%	1.00	0.80	13210	0.75	0.75	0.65	31197	1.75	5.96	1.44E-07	1.78
12	V 40%	1.00	0.80	22000	0.70	0.75	0.65	29000	1.70	6.18	1.39E-07	1.84
13	V 50%	1.00	0.80	19500	0.65	0.75	0.65	36000	1.70	6.39	1.35E-07	1.90
14	V 50%	1.00	0.80	25500	0.68	0.75	0.65	43000	1.98	5.75	1.49E-07	1.73
15	V 50%	1.00	0.80	21000	0.70	0.75	0.65	31000	1.70	5.96	1.44E-07	1.78
16	V 50%	1.00	0.80	13600	0.70	0.75	0.65	28500	1.70	5.96	1.44E-07	1.78

Table 4.6 Pre-cracking data

4.4.2 TEST PROCEDURE

All specimens were tested under displacement control such that a nominal loading rate of 1.0 $MPa\sqrt{m}/s$ was achieved for all specimens based on a nominal a/W of 0.5, this ensured that the limit laid down in clause 8.5 of BS 7448 of loading between 0.5 and 3.0 $MPa\sqrt{m}/s$ was met.

The specimen geometry was of the straight notched compact tension type as illustrated in fig. 4.1a. Crack mouth opening displacement was measured by a standard Instron clip gauge mounted on outward facing knife edges of thickness 0.5 mm as illustrated in fig. 4.22.

All other aspects of the test procedure were in accordance with clause 8 of BS 7448 [26].

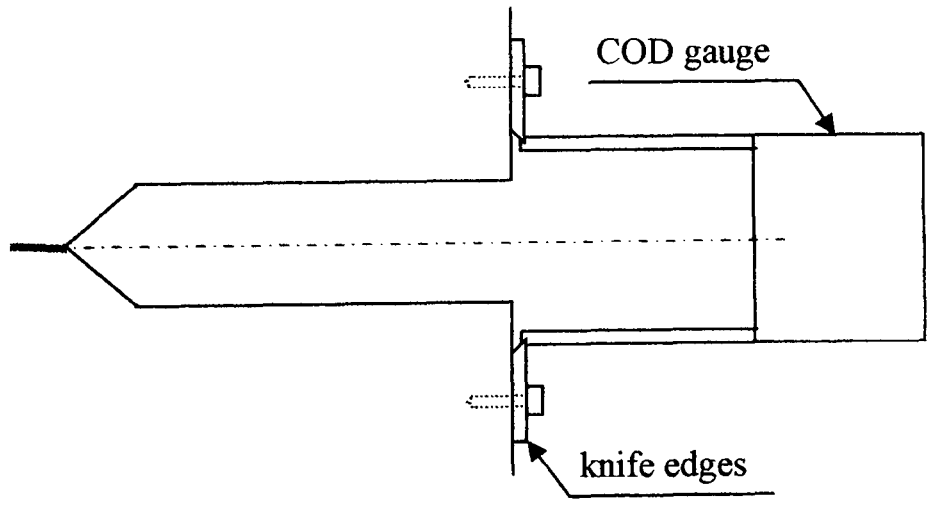

Fig. 4.22 Knife edge and COD gauge arrangement

4.4.3 TEST RESULTS

A typical test record, obtained for specimen 1, is illustrated in fig. 4.23. This was typical of all the test records obtained for both plain and side grooved specimens. P_Q was calculated by using the 5% offset rule specified in clause 9.2.2 of BS 7448 [26], this procedure is performed automatically within the K_{IC} Instron program but a few test records were checked manually and found to be correct.

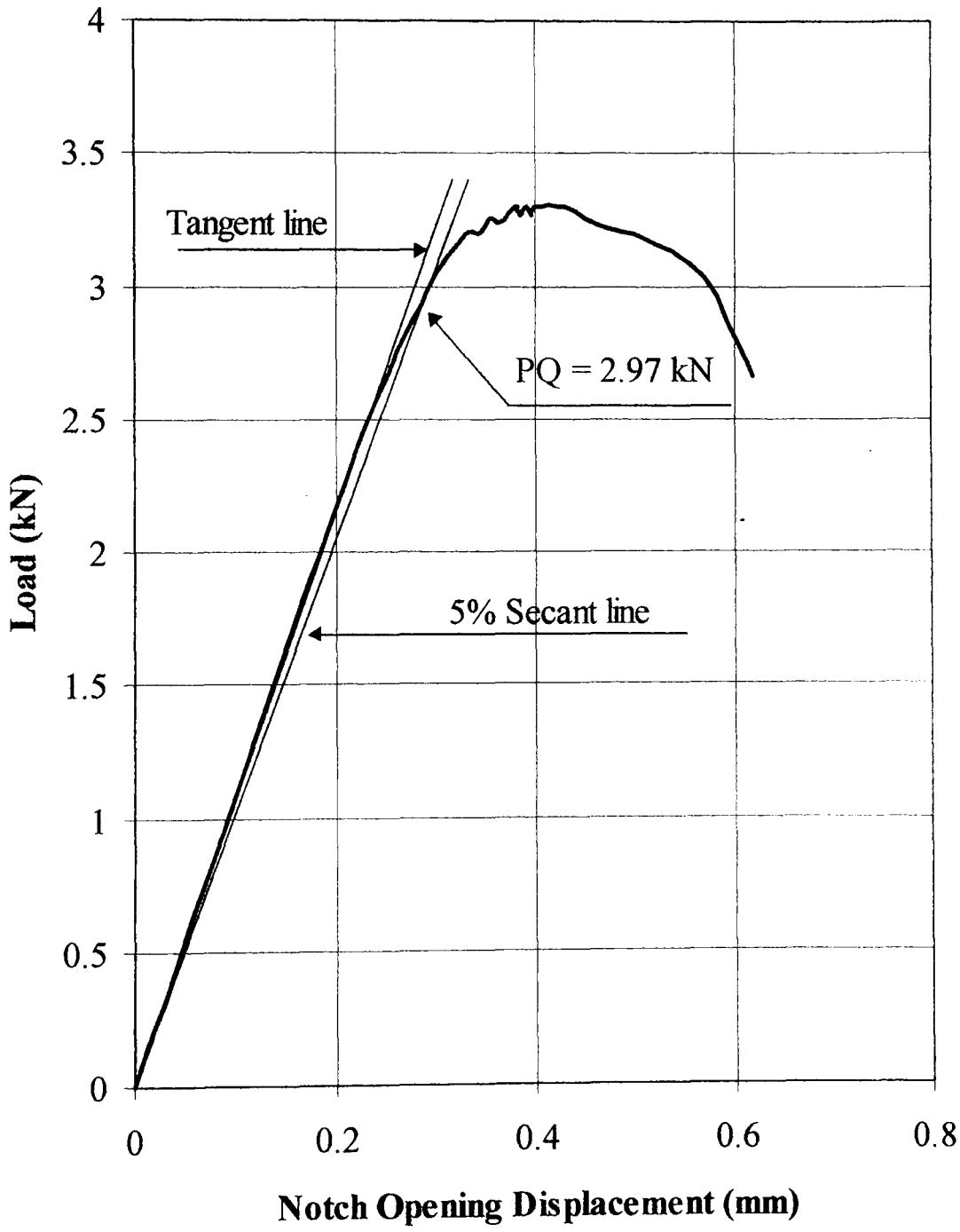

Fig. 4.23 Load v notch opening displacement test record - specimen 1

Typical fracture surfaces are illustrated in fig. 4.24 for plain, 20%, 30% and 50% side grooved specimens. There was no evidence of stable crack growth in any of the specimens tested. The final fatigue pre-crack length was determined by the use of a travelling microscope fitted with vernier scales in accordance with clause 8.7.2 in BS7448 [26]. K_Q was calculated from P_Q in accordance with equation (4.4) and (4.5) and post fracture validity checks were performed in accordance with clause 10 in BS 7448 [26]. Hence, for the plain specimen tests K_Q became K_{IC} the fracture toughness for the material. In the case of the side grooved specimens the value of K_Q could not be designated as a K_{IC} value for obvious reasons. Values of P_Q and K_Q can be seen for all test specimens in table 4.7.

Specimen No	**Side Groove Type**	**a/W**	**Failure Load P_Q (kN)**	**K_Q MPa $m^{0.5}$**
1	Plain	0.52	2.97	21.28
2	Plain	0.54	2.96	22.65
3	V 20%	0.55	2.24	17.73
4	V 20%	0.52	2.67	19.13
5	V 30%	0.53	2.34	17.32
6	V 30%	0.50	2.44	16.42
7	V 30%	0.52	2.45	17.56
8	V 30%	0.48	2.68	16.98
9	V 40%	0.52	2.19	15.69
10	V 40%	0.53	2.11	15.62
11	V 40%	0.53	2.05	15.17
12	V 40%	0.52	2.14	15.34
13	V 50%	0.51	2.03	14.09
14	V 50%	0.54	1.65	12.63
15	V 50%	0.53	1.77	13.10
16	V 50%	0.53	1.78	13.18

Table 4.7 Experimental results

4.4.4 EXPERIMENTAL SPECIMEN EFFECTIVE THICKNESS DETERMINATION

Data from the test programme has been used to establish the effective thickness for Vee grooved specimens in a similar way to the theoretical effective thickness determination presented in section 4.3.4. Fig. 4.25 is a log log plot of K_{NOM} against thickness ratio B/B_N the slope of which will be –m in equation (2.29). The nominal fracture toughness K_{NOM} was taken as the value of K_I produced

(a) Plain specimen

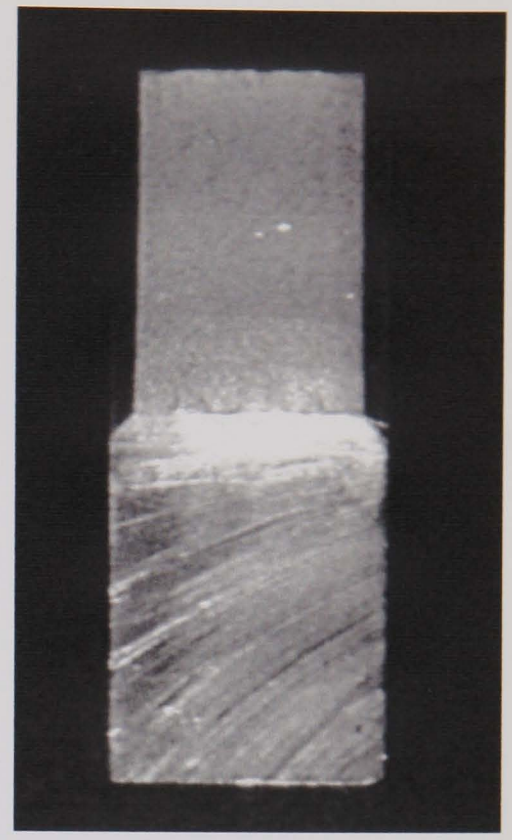

(b) 20% side grooved specimen

(c) 30% side grooved specimen

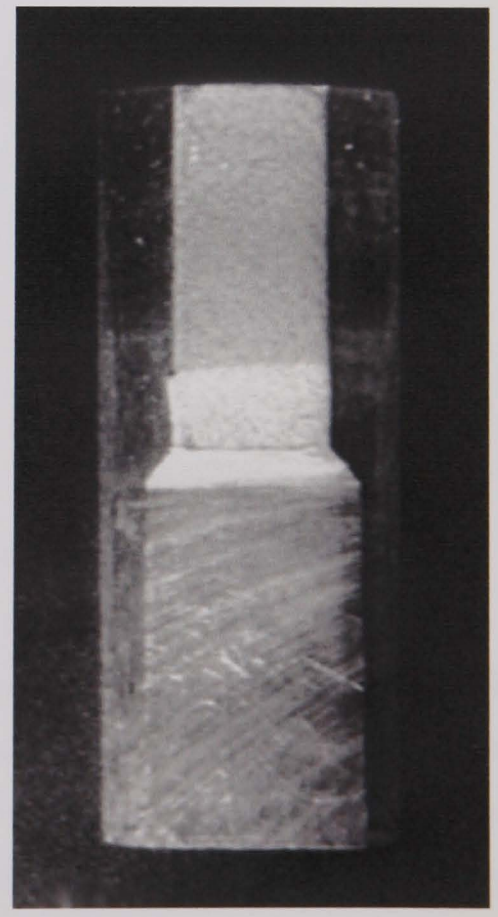

(d) 50% side grooved specimen

Fig 4.24 Typical fracture surfaces

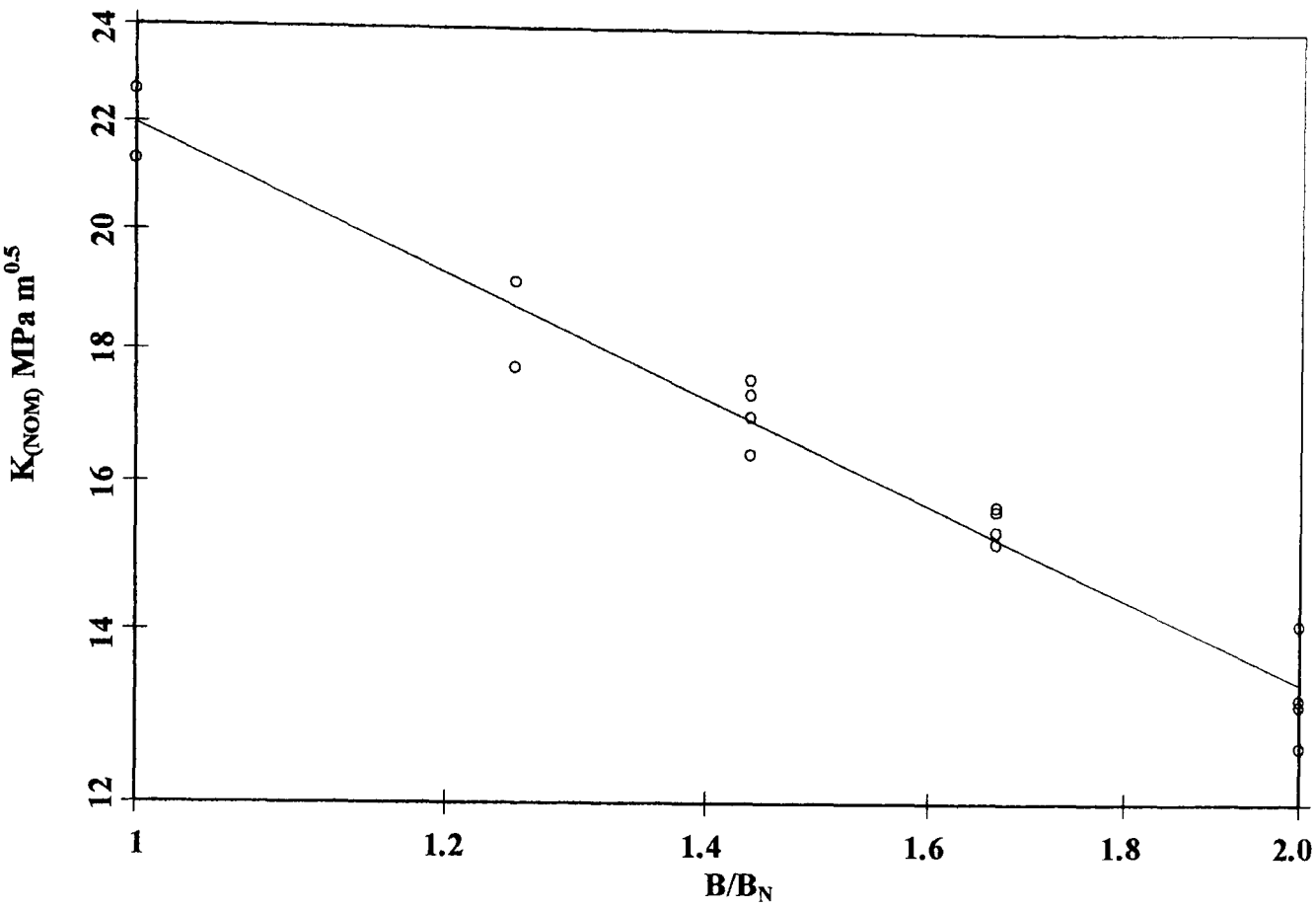

Fig. 4.25 Experimental $K_{(NOM)}$ v B/B_N Vee grooved specimen

when the failure load was considered to apply to a full thickness specimen. As with the theoretical results a trend line was added in order to evaluate the slope and intercept and, hence, obtain m and the value of fracture toughness given by the regression analysis. The results obtained were a value of m = 0.71 and a fracture toughness value of 22 MPa $\sqrt{m}$.

4.5 DISCUSSION OF RESULTS AND CLOSURE

The results presented in this chapter demonstrate the effectiveness of side grooves of varying depth and geometry in increasing both stress intensity factor and crack tip constraint above that expected for plain sided specimens. Potentially this increase could lead to essentially plane strain fracture toughness results being obtained from sub-sized specimens which are side grooved. One drawback of the approach taken however is that only qualitative judgements of the performance of different side groove depth/geometry combinations have been possible by the independent consideration of stress intensity factor and crack tip constraint.

Particularly interesting are the results obtained for both the theoretical and experimental determination of effective thickness in accordance with equation (2.29). The result obtained for the exponent m from the finite element analysis was 0.66 based on CTOD and 0.62 based on VCE, whilst the result obtained from experiment was 0.71. These results compare favourably to the results of Freed and Krafft [28] who tested two aluminium alloys, 2024-T851 (chemical composition – Cu, 4.5%; Mg, 1.5%; Mn, 0.6%; balance Al), 0.2% yield strength 67ksi (460 MPa), for which they obtained a value for m experimentally of 0.7 and 7178-T6 (chemical composition – Zn, 6.8%; Mg, 2.7%; Cu, 2.0%; Cr, 0.3%; balance Al), 0.2% yield strength 79ksi (543 MPa), for which they obtained a value for m experimentally of 0.56.

Results obtained from the experimental programme indicate that side grooves of less than 20% deep do not yield useful results due to the effects of scatter. Also, there does not seem to be an incentive to use excessively deep side grooves, the optimum depth would seem to be in the order of 30%.

The work presented in this chapter now needs to be extended to examine the effects of plasticity and the effects of side grooving on sub thickness specimens.

CHAPTER 5

MODIFIED BOUNDARY LAYER ANALYSIS

5.1 INTRODUCTION

The previous chapter outlined the difficulties in establishing the fracture behaviour of plain and side grooved specimens when only a qualitative model of the crack tip constraint is available. The work presented in this chapter introduces a two parameter approach based on the evaluation of Q [82 – 88] and the use of area scaling [89 – 91] as previously described in sections 3.6 – 3.9.

Firstly, analysis results obtained from modified boundary layer loading are presented for a range of power law hardening materials. This allows the results obtained to be directly compared with results published in open literature.

Following on from the general analysis of power law hardening materials results are presented for a specific material, EN24 steel. Results presented in the previous chapter, for an aluminium alloy characterised by linear elastic fracture mechanics, considered the effects of side groove depth and geometry on full thickness specimens only. In order that an evaluation of the effects of side grooving on sub thickness specimens could be undertaken, an alternative material was required that would allow an experimental programme to be undertaken. The specimens used in the work reported in the previous chapter were 10 mm thick at the full thickness required to give valid K_{IC} results.

Clearly it was not a practical proposition from a manufacturing and testing standpoint to manufacture side-grooved specimens from this material that were of a significantly reduced thickness. Hence it was decided that EN24 steel should be used for the next phase of work involving sub thickness specimens. EN24 is a low-nickel, low-chromium, molybdenum steel with a typical chemical composition of 0.4% C, 0.55% Mn, 1.5% Ni,1.1% Cr, 0.3% Mo which can be heat treated to give a wide range of properties, see section 5.3, with valid K_{IC} results being obtained from 25 mm thick specimens and fracture loads being within the range of the available Instron testing machine. Failure is essentially ductile by microvoid coalescence at room temperature and brittle at lower shelf temperatures where the failure mode is cleavage. The J-Q approach described in chapter 3.6 is valid for both failure mechanisms, whereas the area scaling approach described in chapter 3.9 is applicable only when cleavage is

the dominant failure mechanism. Although in the work presented here it was only possible to undertake material tests at room temperature the finite element analysis still considered the use of the area scaling method as an indicator of lower shelf performance.

Both Q determination and area scaling depend upon the accurate prediction of the stress field ahead of the crack tip. Hence, the principal focus of the work presented in this chapter was to produce an optimal 2D finite element mesh that could be carried forward to the 3D analysis of the EN24 compact tension fracture specimens. Also as a result of the work a small scale yielding solution was obtained for the EN24 material that would subsequently produce the reference stress field from which the Q stress could be evaluated.

5.1.1 AIMS AND OBJECTIVES

The aims and objectives of the work described in this chapter were as follows:

1. To undertake a modified boundary layer analysis of a range of power law hardening materials.

2. To obtain relevant material properties for EN24 that could be used in the finite element analysis.

3. To investigate mesh design in the crack tip region in order that accurate stress field predictions could be made using a boundary layer formulation.

4. To obtain a small scale yielding solution for EN24 which would provide a reference stress field from which Q stress could be evaluated.

5. To develop a post processor capable of determining Q from finite element results.

6. To develop a post processor capable of establishing the area within principal stress contours obtained by finite element analysis for use in an area scaling analysis.

5.2 MODIFIED BOUNDARY LAYER ANALYSIS OF POWER LAW HARDENING MATERIALS

In order to perform the modified boundary layer analysis detailed post yield finite element analysis of the crack tip region was required. The finite element fracture post processor that had been used for the work on linear elastic fracture mechanics presented in the previous chapter, ENDURE, was not capable of J integral evaluation for non linear analysis. Hence the ABAQUS finite element package was used for the modified boundary layer analysis and all subsequent finite element analysis.

ABAQUS [99] is a general purpose finite element package capable of a wide range of linear and non-linear analysis types. J integral estimates can be obtained directly from the ABAQUS package which uses a domain integral method to evaluate the contour integral along a user defined path around the crack tip.

Pre and post processing of the finite element models was carried out using the FEMGV graphical pre/post processor [100] and ABAQUS post [101].

The modified boundary layer analysis was undertaken by modelling a near crack tip region as a semi-circular domain of outer radius R as shown in fig. 5.1. The crack tip

$$u_i = \frac{K_I}{E}\sqrt{\frac{R}{2\pi}}\, f(\theta,\nu) + \frac{T}{E} R\, g(\theta,\nu)$$

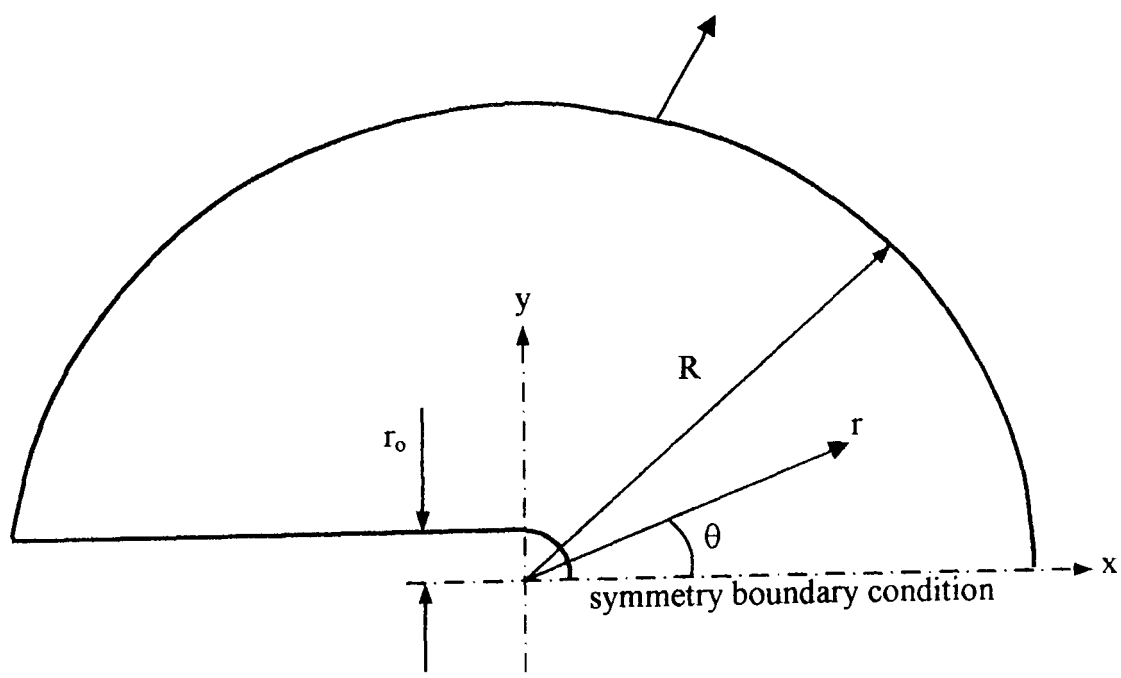

Fig. 5.1 Modified boundary layer domain with blunted crack tip

was blunted with an initial radius, r_o, of 10^{-5} times the distance to the model boundary. Symmetry boundary conditions were applied along the crack line as illustrated in fig. 5.1. Many authors have performed similar analysis with a variety of meshes and crack tip conditions, these are summarised in table 5.1.

Author	**Mesh details**	**Crack tip condition**	**Analysis package**
Betegon and Hancock [79]	240 eight noded elements arranged in 20 rings of 12 elements concentric with crack tip.	25 independent but initially coincident nodes.	ABAQUS
O'Dowd and Shih [82]	1000 four noded elements.	Blunted crack tip with initial radius of 10^{-5} times distance to boundary where tractions are applied.	BESPOKE
Wang and Parks [102]	1119 plane strain reduced integration elements arranged in 40 rings of 28 elements circumferentially (first ring had 22 elements).	Blunted crack tip to simulate finite strain zone with initial radius of 2×10^{-6} times distance to boundary.	ABAQUS
Anderson and Dodds [91]	720 four noded elements arranged in 40 rings of 18 elements concentric with crack tip. .	Not specified	Not specified

Table 5.1 – Comparison of boundary layer meshes.

The mesh used in the analysis was similar to that of Anderson and Dodds [91] consisting of 40 rings of 18 eight noded plane strain reduced integration elements concentric to the crack tip, the element size being arranged in an approximate geometric progression getting coarser away from the crack tip, the mesh can be seen in fig. 5.2.

Displacement boundary conditions were imposed as indicated in fig. 5.1 in accordance with equation 5.1 [102].

$$u_i = \frac{K_I}{E}\sqrt{\frac{R}{2\pi}} \cdot f(\theta,\upsilon) + \frac{T}{E} \cdot R \cdot g(\theta,\upsilon) \quad \text{.....(5.1)}$$

where f (θ, υ) are the angular variations of the cartesian displacement components of the plane strain elastic singular field and g (θ, υ) are the angular variations of the displacement component from the plane strain T stress term.

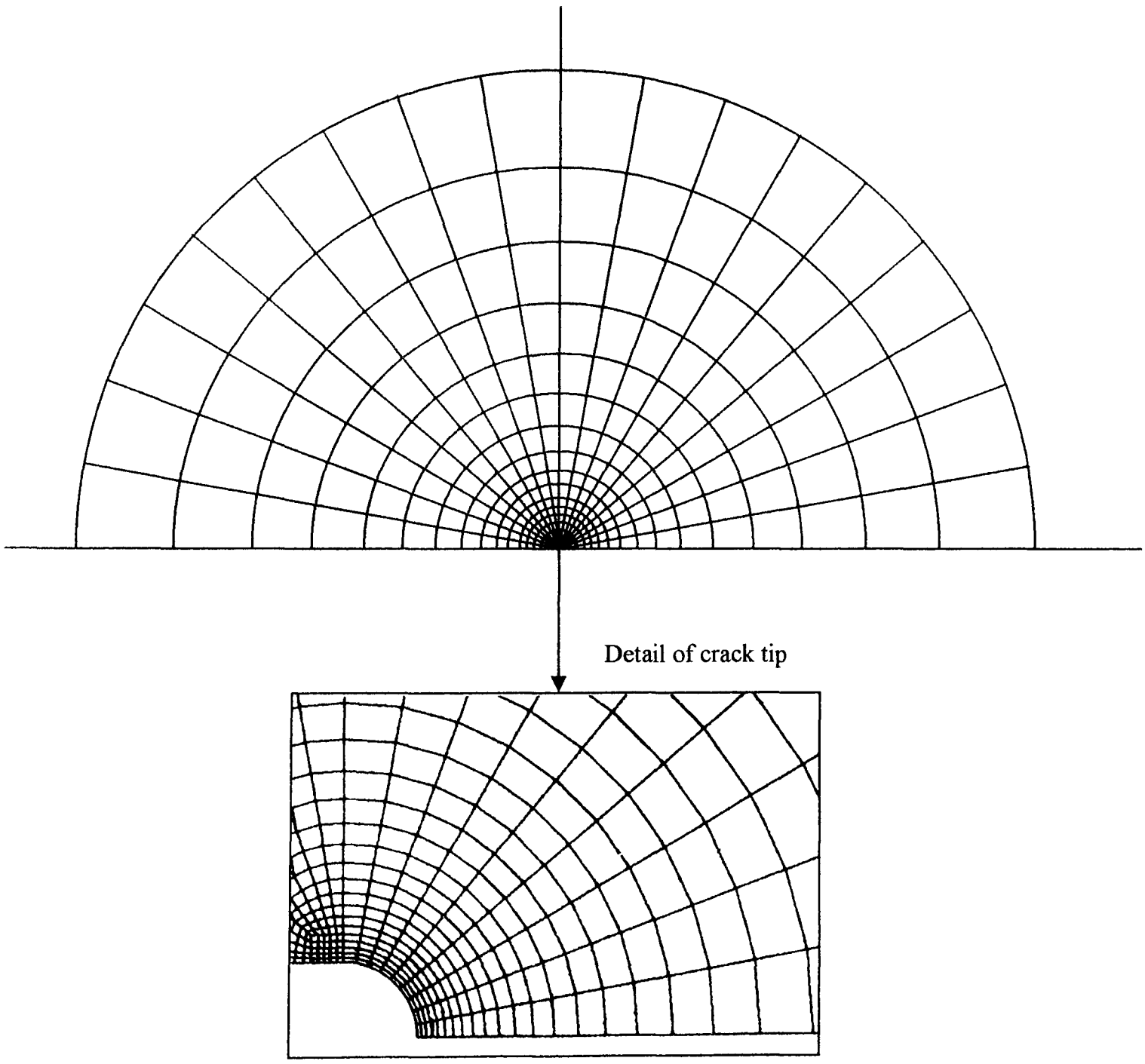

Fig. 5.2 Modified boundary layer analysis mesh

The exact expressions for f (θ, υ) and g (θ, υ) are listed in table 5.2 [102].

Field	x component	y component
f	$(1+\upsilon)(3-4\upsilon-\cos\theta)\cos(\theta/2)$	$(1+\upsilon)(3-4\upsilon-\cos\theta)\sin(\theta/2)$
g	$(1-\upsilon)(1+\upsilon)\cos\theta$	$-\upsilon(1-\upsilon)\sin\theta$

Table 5.2 – Functional forms of f (θ, υ) and g (θ, υ)

The material stress-strain behaviour was modelled using a Ramberg-Osgood power law expression as given in equation (5.2) which was implemented directly as a deformation plasticity material model within ABAQUS.

$$\frac{\varepsilon}{\varepsilon_o} = \frac{\sigma}{\sigma_o} + \alpha\left(\frac{\sigma}{\sigma_o}\right)^n \quad \text{.....(5.2)}$$

where ε is strain, σ is stress, σ_o is the yield stress, $\varepsilon_o = \sigma_o/E$ and α is a yield offset used to fit data. The values of $\alpha = 1.0$, $\varepsilon_o = 0.002$ and $\sigma_o = 400$ MPa were chosen to give $E/\sigma_o = 500$ which is broadly consistent with the values used by Anderson and Dodds [91]. Values of n = 5, 10 and 50 were used to correspond to high, medium and low work hardening.

A small strain formulation was used throughout the analysis. This is justified when considering the results presented by O'Dowd and Shih [82] where small strain and finite strain results were shown to be in good agreement outside the blunting zone. Betegon and Hancock [79] also used a small strain formulation to evaluate the effect of T stress on the tangential stresses ahead of a crack tip. The use of small strain analysis is further justified in terms of computational time when considering that the ultimate goal is to develop three dimensional solutions based on the outcomes of this section of work. Further, the evaluation of Q can be based on a number of reference stress fields, i.e. HRR, small scale yielding. Hence, if the same analysis is used to evaluate the reference stress field under small scale yielding boundary layer displacement as for the subsequent analysis of test specimens then for distance scales appropriate to the evaluation of Q the approach is justified.

Results from the analysis in terms of normalised crack opening stresses are presented in figs. 5.3 – 5.5 for each value of hardening exponent, n, and a variety of T stresses, i.e. $T/\sigma_o = 0$ (small scale yielding), $T/\sigma_o = -0.5$, $T/\sigma_o = -1.0$ and $T/\sigma_o = -1.5$.

The results presented in figs. 5.3 – 5.5 compare well with published data [79, 82, 91 and 102]. For all levels of hardening the crack opening stresses lie below the HRR field even for the small scale yielding (T = 0) condition. As the value of T stress becomes progressively more negative, the stresses fall significantly below those provided by both the HRR and small scale yielding solution.

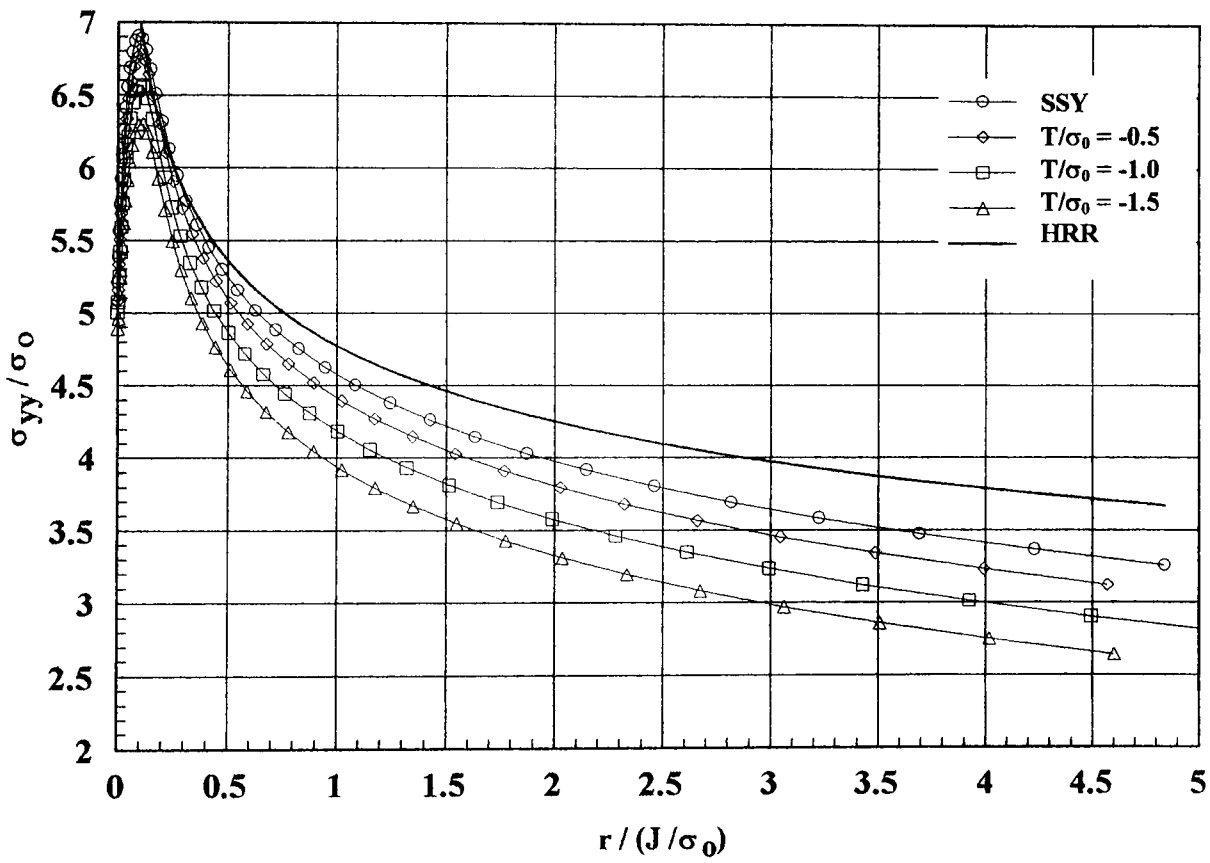

Fig. 5.3 Stress distribution normal to crack plane for n=5

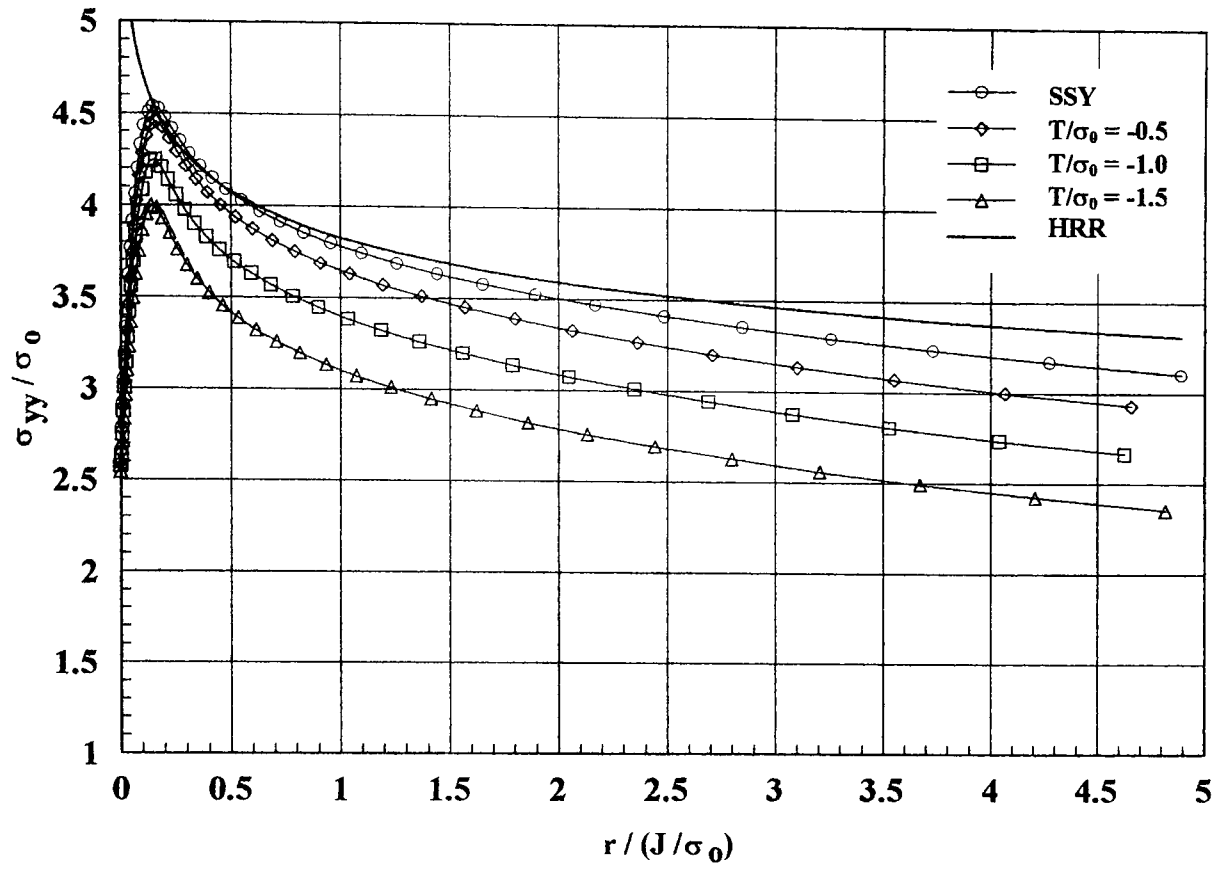

Fig. 5.4 Stress distribution normal to crack plane for n=10

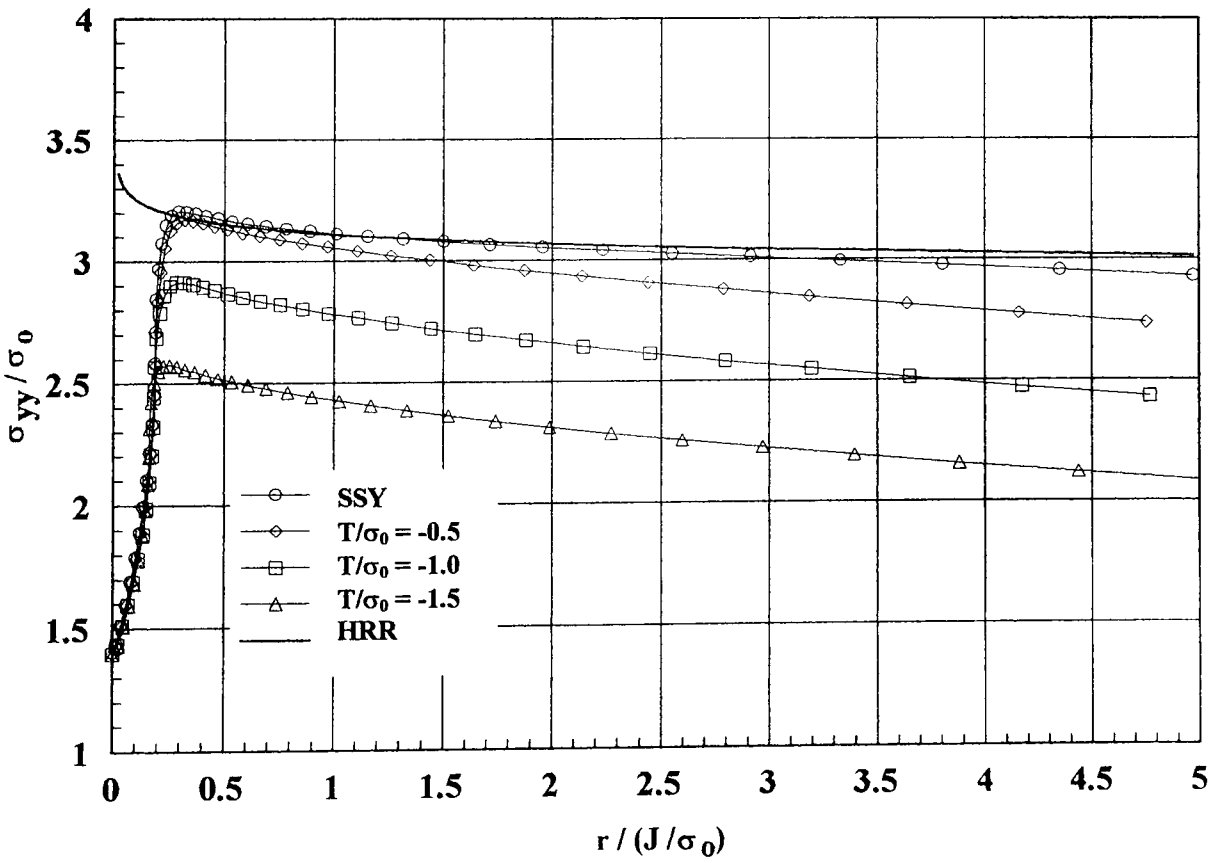

Fig. 5.5 Stress distribution normal to crack plane for n=50

The work presented in this section clearly provides a strong basis for the modified boundary layer analysis of the EN24 material that will subsequently be used in the side groove evaluation.

5.3 MATERIAL PROPERTY EVALUATION OF EN24

Before a modified boundary layer analysis and subsequent side grooving evaluation could be undertaken material properties had to be obtained.

EN24 material was obtained in the form of 110 mm diameter bar section in a soft condition. The bar was carefully marked to establish a datum that would allow specimens to be machined with consistent orientation.

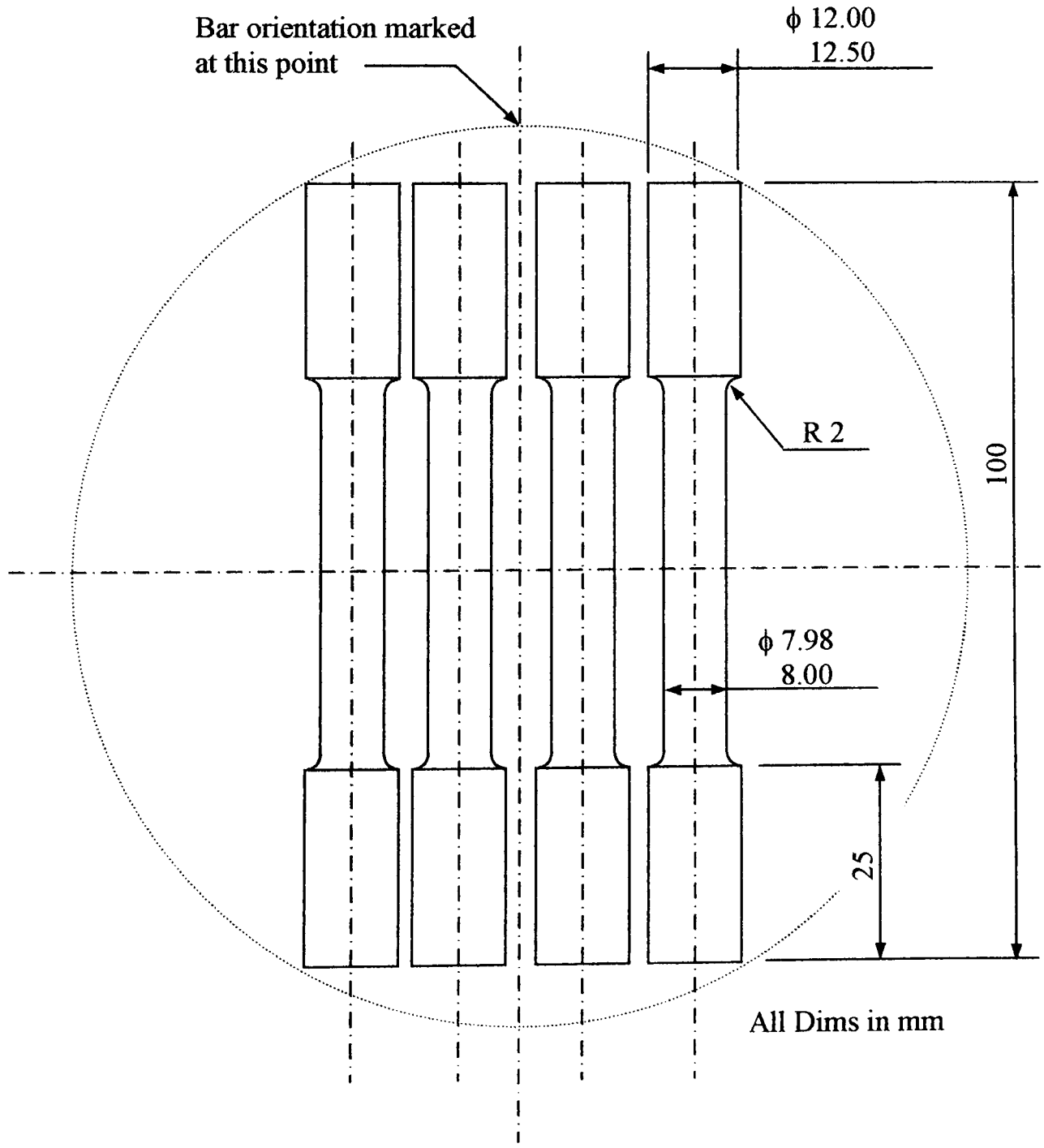

Fig. 5.6 EN24 Tensile specimens

Firstly, tensile specimens were cut from the bar as shown in fig. 5.6. Four specimens per diametral slice were obtained and in total 16 specimens were cut for testing. In order to investigate the effects of heat treatment on the material properties, all of the specimens were heated to 835° C and then oil quenched. This initial hardening treatment was followed by tempering at different temperatures between 450° C and 625° C for 30 minutes followed by still air cooling.

The heat treatment given to all of the specimens can be seen in table 5.3 together with hardness values prior to and subsequent to heat treatment.

Sample	**Initial hardness Rockwell C**	**Final hardness Rockwell C**	**Temper temp °C**	**Temper hardness Rockwell C**
1	24	52	450	35
2	22	50	475	33
3	21	52	500	31
4	21	50	525	29
5	25	51	550	29
6	23	52	575	30
7	22	50	600	26
8	24	53	625	24
9	22	51	450	37
10	20	52	475	35
11	24	51	500	35
12	24	52	525	34
13	22	52	550	29
14	22	51	575	29
15	23	50	600	28
16	24	52	625	27

Table 5.3 - Specimen Heat Treatment

The resulting nominal stress-strain curves obtained for each level of heat treatment can be seen in fig. 5.7. In order that the stress strain data can be input to the finite element package true stress–true strain data must be used.

Fig. 5.8 shows the true stress-true stain curve for each heat treatment, as obtained from equations 5.3 and 5.4.

$$\varepsilon = \ln(1 + \varepsilon_{nom}) \quad \ldots\ldots (5.3)$$

$$\sigma = \sigma_{nom}(1 + \varepsilon_{nom}) \quad \ldots\ldots (5.4)$$

Preliminary fracture toughness tests on the material yielded a plane strain fracture toughness for a 450° temper temperature of 74 MPa √m and for a 625° temper

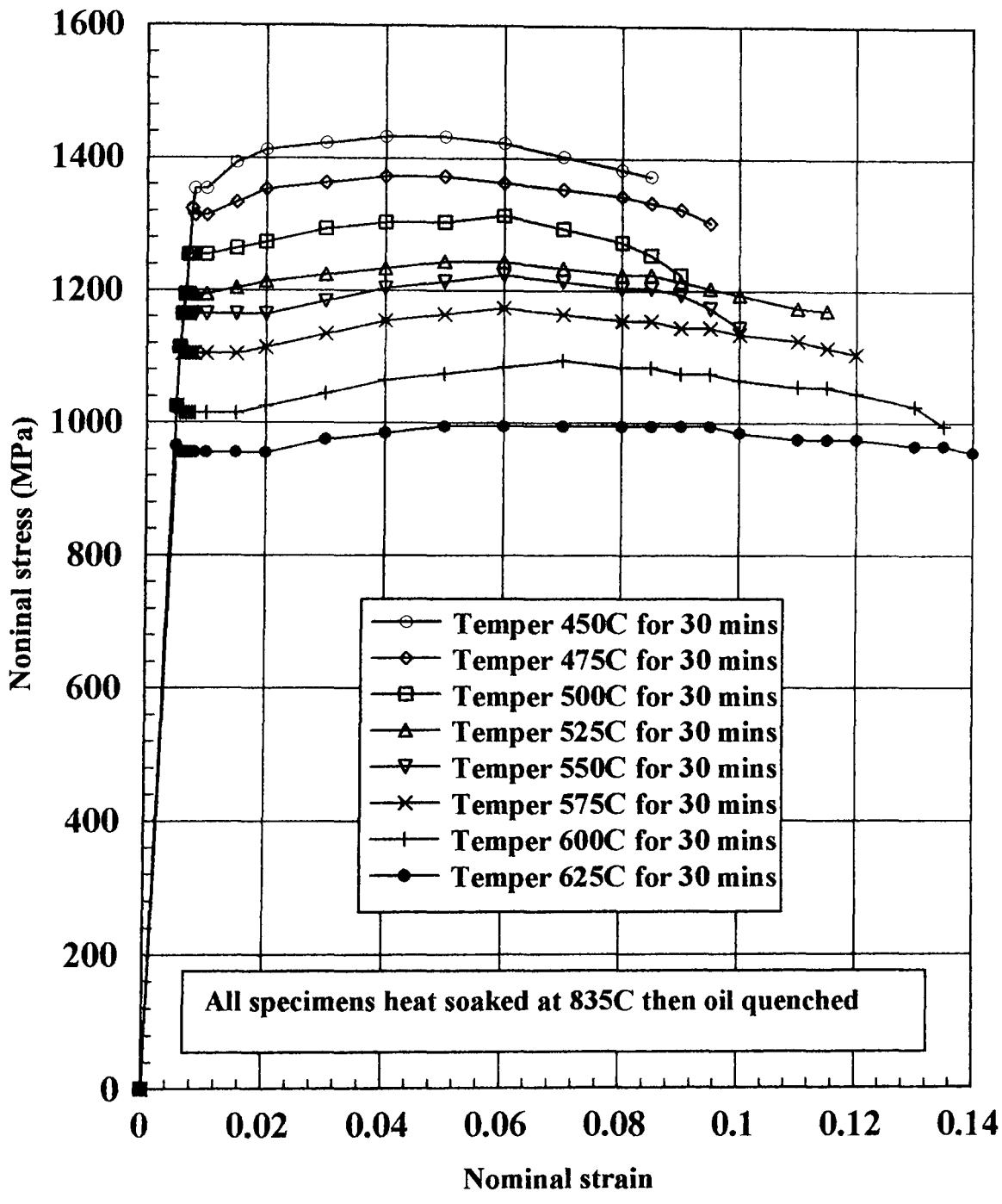

Fig. 5.7 Nominal stress – strain data for EN24

temperature of 95 MPa √m. Some preliminary fracture toughness tests were also carried out on sub thickness specimens of various tempers in order to gain an appreciation of the fracture behaviour of thin specimens. As a result of these tests it was decided that a tempering temperature of 625°C held the best potential for examining the effects of side grooving on transitional thickness effects and the formulation of shear lips.

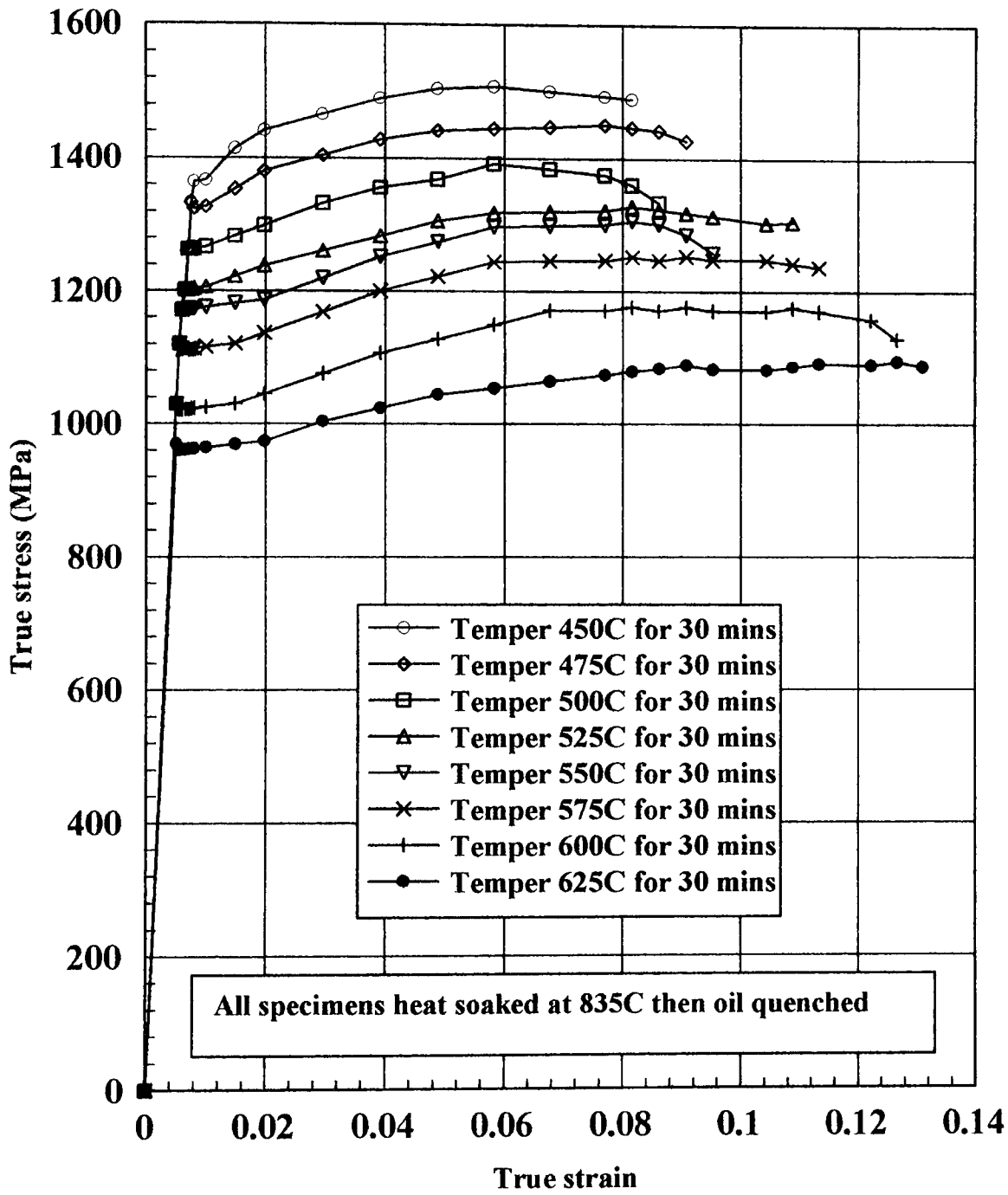

Fig. 5.8 True stress – strain data for EN24

Two plasticity models exist within the ABAQUS package, these being an incremental plasticity model where the stress strain behaviour is specified by a segmented multi-linear model and a deformation plasticity model based on the Ramberg Osgood model. The latter is provided specifically for fracture mechanics analysis in order that handbook solutions for power law hardening materials can be developed. Since all of the

subsequent models were to be statically loaded with no potential for unloading, and to allow comparison with published data it was decided to use a deformation plasticity model.

The Ramberg Osgood material description was in accordance with equation 5.2, where values of n = 50, $\alpha = 0.15$, $\varepsilon_0 = 0.0048$, $\sigma_0 = 970$ MPa and E = 200GPa were chosen to fit data. The resulting stress-strain curve together with the relevant true stress-strain curve extracted from fig. 5.8 can be seen in fig. 5.9.

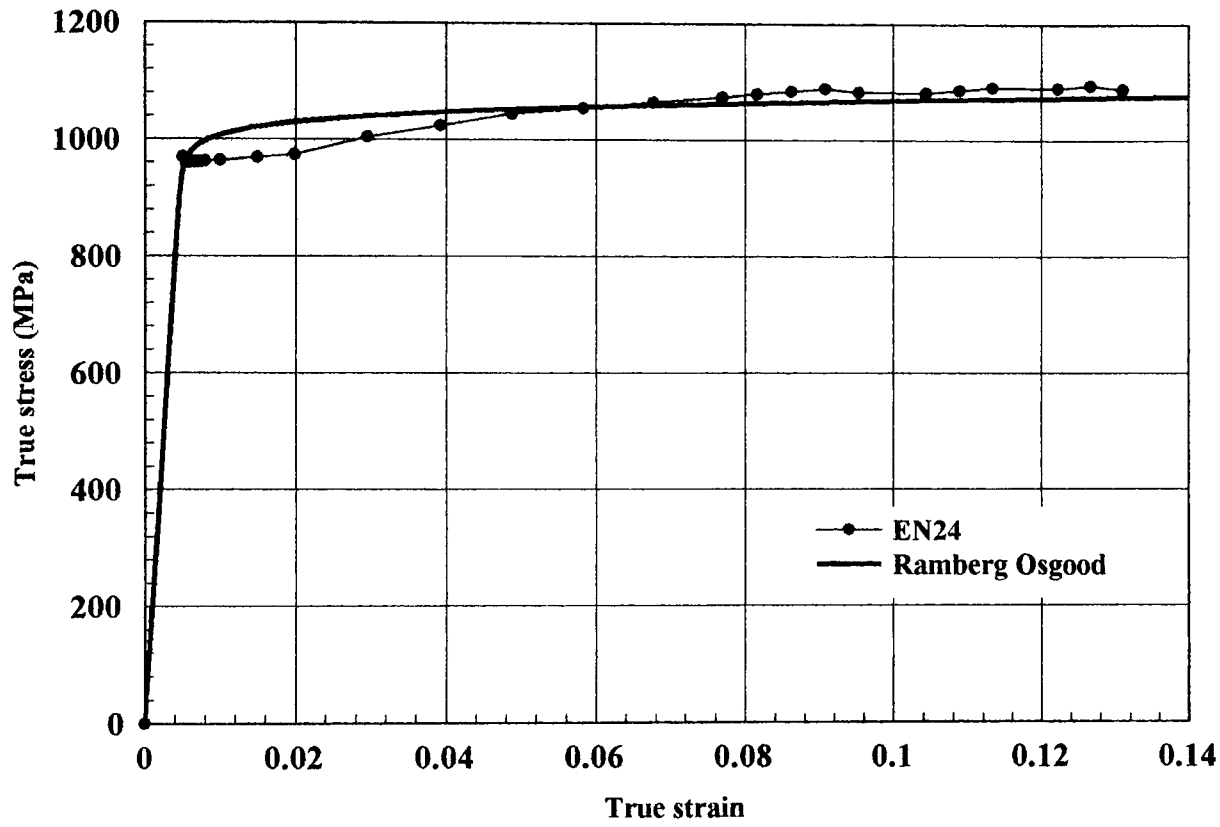

Fig. 5.9 Ramberg –Osgood fit to EN24

As can be seen from fig. 5.9 the Ramberg Osgood model provides a good fit to the elastic part of the stress strain curve and a reasonable fit to the plastic part of the curve. By varying the values given to α and n it is possible to improve the fit in the plastic region but only at the expense of the fit in the elastic region. O'Dowd [103] undertook an extensive survey with regard to curve fit performance in elastic-plastic fracture mechanics and concluded that in order to provide reasonable estimates of both J and Q it is important to accurately model the elastic portion of the stress-strain curve even at high loads. This would seem to be particularly important in this work, as plasticity is likely to be well contained within regions of elastic material.

5.4 MODIFIED BOUNDARY LAYER ANALYSIS OF EN24

The modified boundary layer analysis of EN24 proceeded exactly as described for power law hardening materials in section 5.2, using the material description developed in section 5.3. Initially, the same mesh was used as for the models described in section 5.2. However, it was clear from the outset of the analysis that, if such a fine mesh were to be extruded into 3D for the subsequent analysis of compact tension specimens, computer run times could be excessive and in all likelihood not achievable on the computers available at the time the analysis was undertaken. Several further mesh designs were tested with a view to obtaining an optimised mesh design that could be incorporated into subsequent 3D models of compact tension specimens. The final mesh consisted of 120 eight noded plane strain elements arranged in 15 rings of eight elements, again the element size was arranged to fit approximately to a geometric progression getting coarser away from the crack tip. As with the models used in section 5.2 the crack tip itself was blunted with an initial radius of 10^{-5} times the distance to the model boundary. A comparison of the results obtained in terms of normalised crack opening stresses from this mesh with results obtained for the mesh described in section 5.2 can be seen in fig. 5.10 for the EN24 material model.

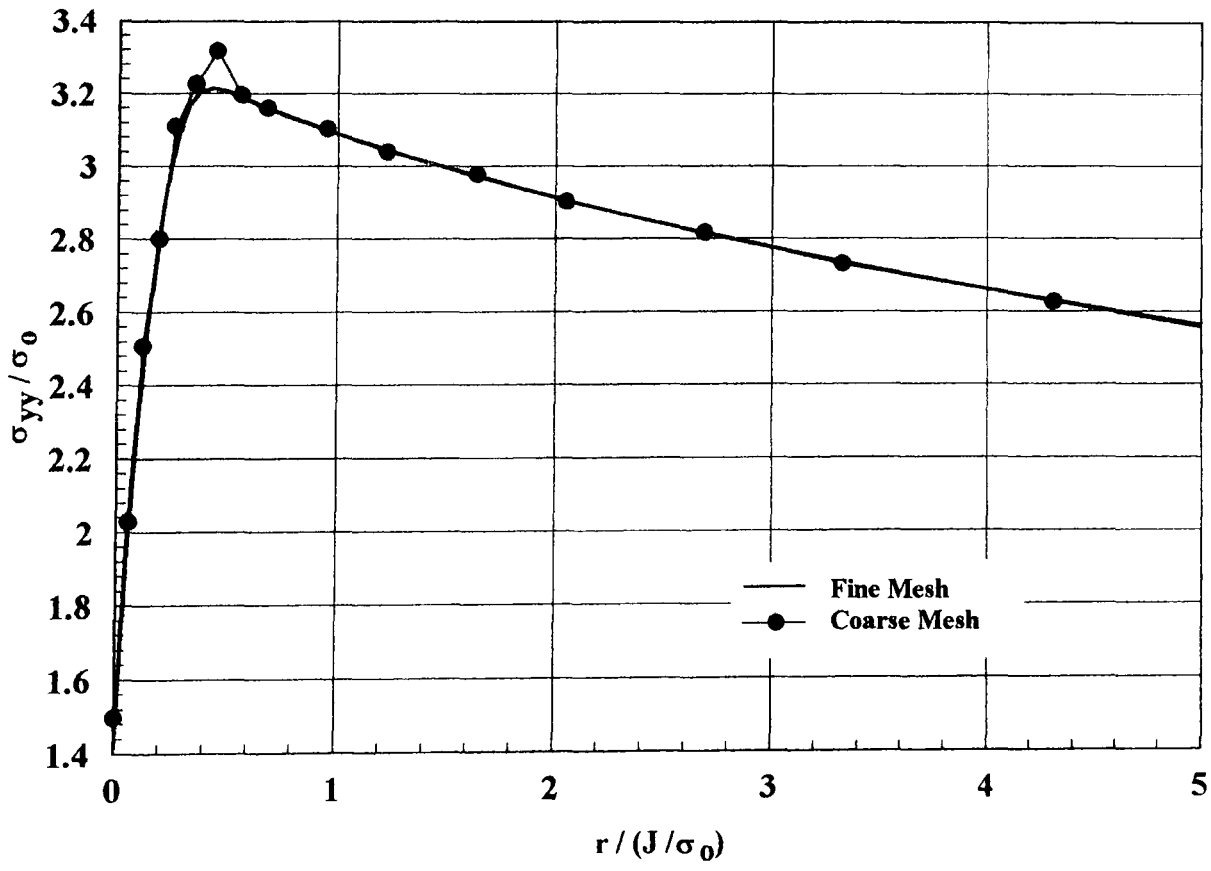

Fig. 5.10 Stress distribution normal to crack plane for EN24 comparison of fine and coarse meshes

Consideration of fig. 5.10 reveals that the curves produced by both the fine and coarse meshes lie one on top of the other with the exception of the peak stress value at $r/(J/\sigma) = 0.4$ where the coarse mesh gives a normalised stress approximately 3% higher than the fine mesh. Since this discrepancy occurs essentially within the blunting region it is not seen as important, at distances where Q and Q′ are evaluated the curves are coincident. It was considered that this mesh could provide a good compromise between accuracy of results and computer run time when incorporated into the subsequent 3D models. The final mesh can be seen in fig. 5.11.

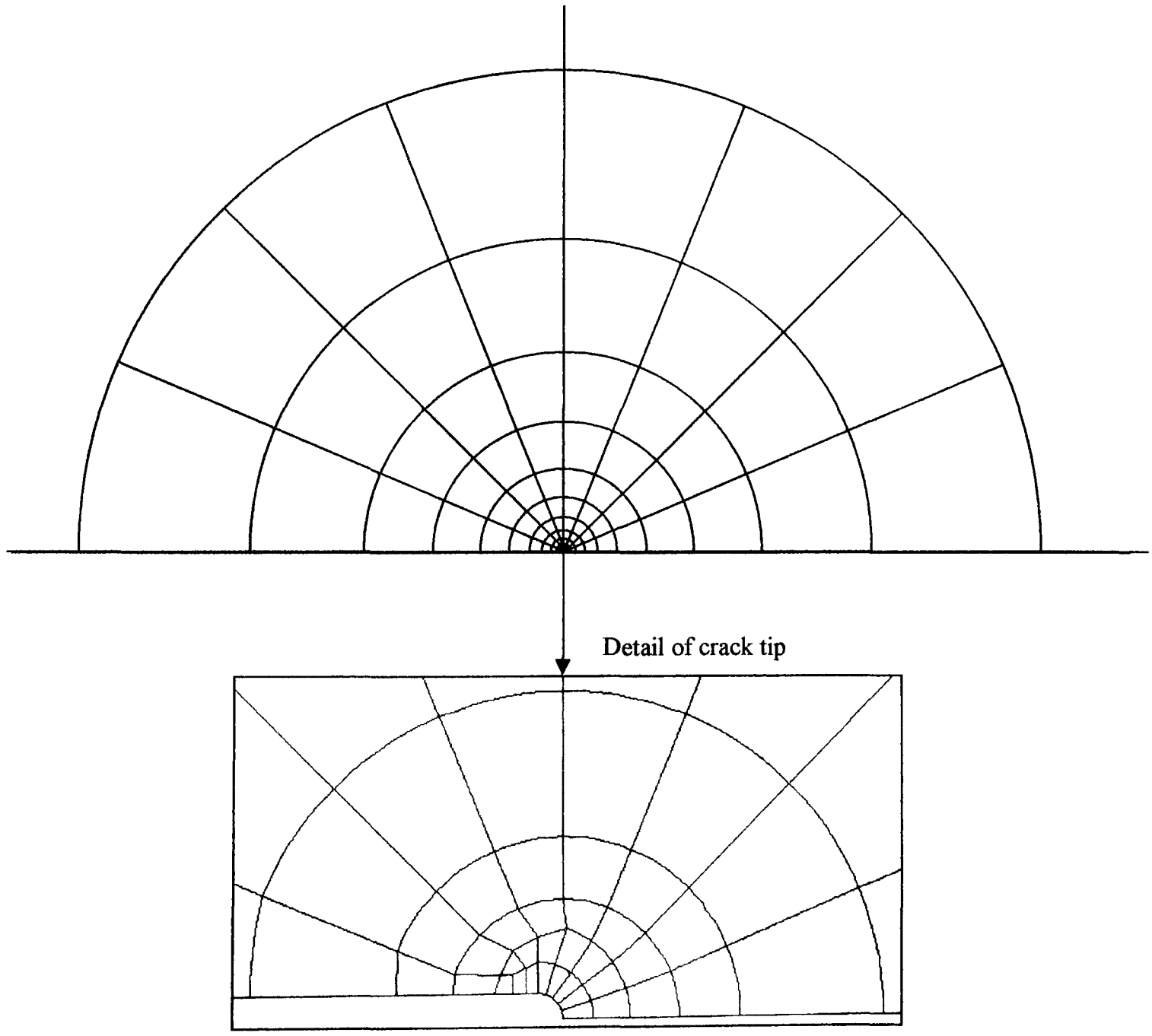

Fig. 5.11 Final EN24 boundary layer analysis mesh

Results from the modified boundary layer analysis can be seen in fig. 5.12 in terms of opening mode stress on the crack line for a variety of T stresses, i.e. $T/\sigma_0 = 0$ (small scale yielding), $T/\sigma_0 = -0.2$, -0.4, -0.6, -0.8, -1.0 and -1.5. The applied K at the model boundary was consistent with the fracture toughness of EN24, i.e. 95 MP $\sqrt{m}$. Again as the value of T stress becomes progressively more negative, the opening mode stresses fall significantly below the small scale yielding solution.

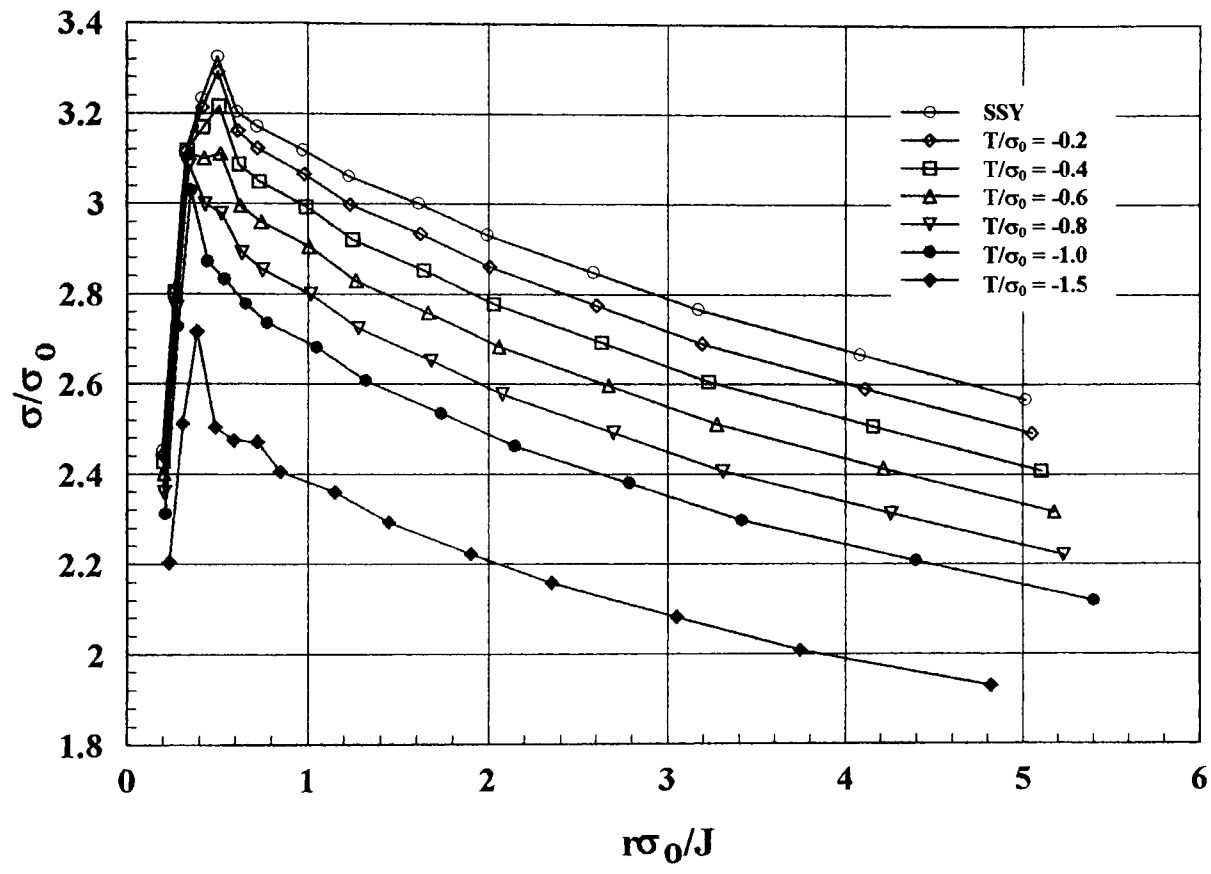

Fig. 5.12 Stress distribution normal to crack plane for EN24

5.4.1 AREA SCALING

The area scaling method of Dodds et al [90] and Anderton and Dodds [91] was introduced in section 3.9. The method predicts the ratio of J_{FB} required to cause failure in a finite body to a reference quantity J obtained for a small scale yielding SSY solution by using areas within principal stress contours to make the prediction in accordance with equation (3.37).

The area contained within principal stress contours is not readily obtainable from the ABAQUS package, hence there was a necessity to write a post processor to calculate the principal stress areas from the finite element results. Due to the fact that the mesh in the crack tip region had been optimised for use with 3D models, with the intention that this part of the mesh should remain the same throughout, it was decided to write a post processor based on this fixed arrangement so as to provide simplicity of programming. Averaged nodal stresses were output from the ABAQUS package in the form of an ASCII text file (.dat file) which was subsequently cut and pasted into two data files, lcoord(n).dat and layer(n).dat, where (n) is a integer that allows layer identification for subsequent 3D analysis.

lcoord(n).dat contains nodal position data in the format [Node number, x co-ord, y co-ord, z co-ord].

layer(n).dat contains averaged nodal stress data in the format [Node number, maximum principal stress, σ_{xx}, σ_{yy}, σ_{zz}].

This matrix format was ideal for reading into the MATLAB programming environment which was used for post processing. Three MATLAB (m) files can be found in Appendix 1 which contains full listings of the programmes used for post processing. A brief description of each programme is given below:

SORT3DPLAIN.m

This programme reads the lcoord.dat and layer.dat files and combines them into a single matrix in the format [Node number, x co-ord, y co-ord, max principal stress]. The nodes are then renumbered in accordance with a predefined 2D template to give the correct format for contour plotting.

CONT3DPLAIN.m

This programme first calls the nodal sorting programme SORT3DPLAIN.m in order to obtain the correct format for contour plotting. User defined values for material yield stress, J integral and required stress contour level are then input to the program to allow the appropriate axis scaling. Points lying on the principal stress contour are then determined by simple linear interpolation of the averaged nodal stresses in the global x and y directions. The interpolated points are then

ordered to provide a smooth contour for the stress level requested. Finally, the area contained within the contour is calculated based on space co-ordinates and normalised co-ordinates ($X\sigma_0/J$ and $Y\sigma_0/J$) using a simple trapezium rule. Plots are also generated based on space and normalised co ordinates and the plot data written to an ASCII file for subsequent plot manipulation.

Q3DPLAIN.m

This programme allows the evaluation of Q at a distance from the crack tip of $2\sigma_0/J$ as defined by equation (3.27) and of Q′ in accordance with equation (3.29). The first part of the programme is identical to SORT3DPLAIN.m and rearranges the input data into the correct format for Q evaluation. User defined values for material yield stress and J integral are then input to the programme to allow appropriate axis scaling. Reference values for $Q_{2\sigma_o/J}$, $Q_{\sigma_o/J}$ and $Q_{5\sigma_o/J}$ are set within the programme listing but can be changed to reflect the SSY solution for the material and deformation level under consideration. Crack opening stress at the relevant positions, i.e. $r = 2\sigma_0/J$, σ_0/J and $5\sigma_0/J$ is then found by linear interpolation of the input data to allow calculation of Q and Q′.

Finally, plots were generated and plot data written to an ASCII file for subsequent plot manipulation.

An equivalent set of MATLAB programs [CONT3DGROOVE.m, SORT3DGROOVE.m and Q3DGROOVE.m] based on a refined mesh which was used for side grooved specimens were also written. When the 3D work was undertaken with side grooved specimens this in-plane refinement was found to be required in order to keep element aspect ratios acceptable considering the through thickness mesh refinement requirements at the root of the side groove, see section 6.

5.4.2 AREA SCALING RESULTS FOR MODIFIED BOUNDARY LAYER ANALYSIS

The results obtained from the modified boundary layer analysis in terms of the areas contained within specific stress contours can be seen in fig. 5.13.

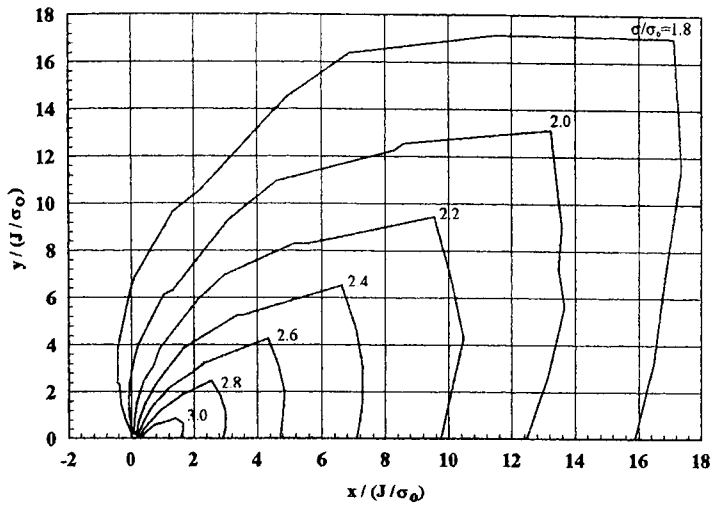

(a) small scale yielding

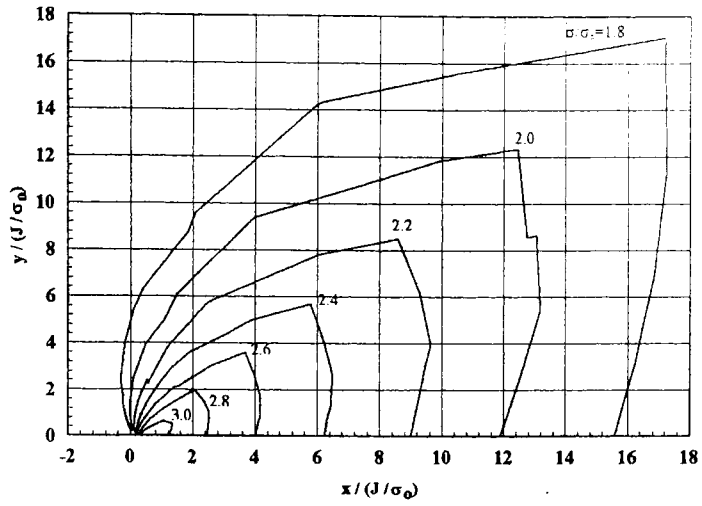

(b) $T / \sigma_o = - 0.2$

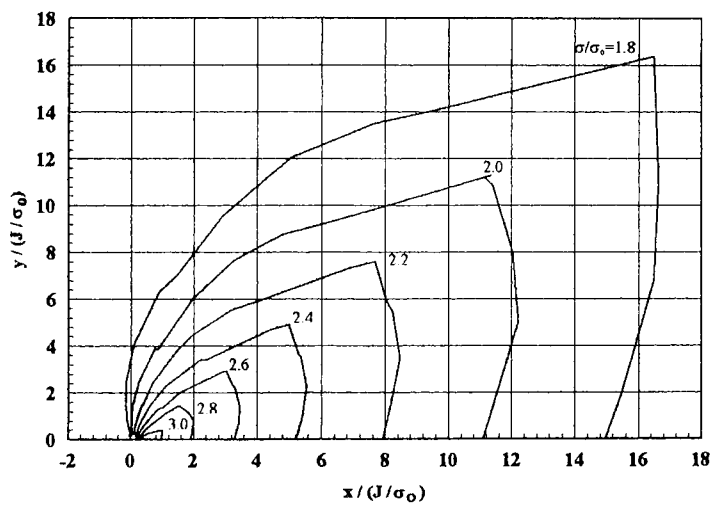

(c) $T / \sigma_o = - 0.4$

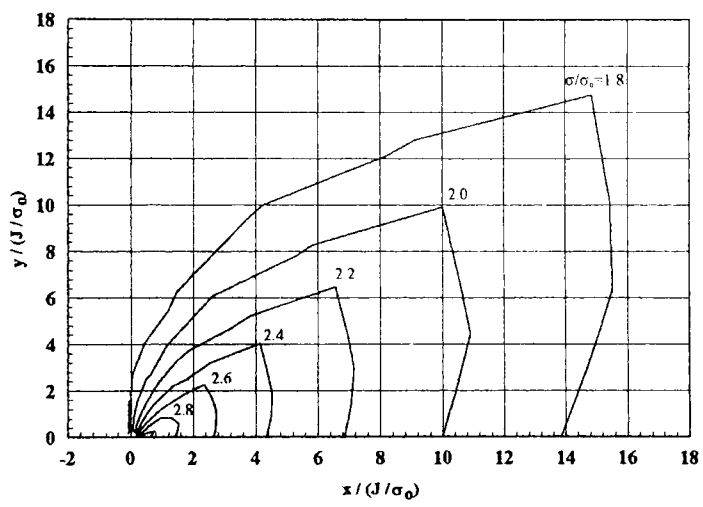

(d) $T / \sigma_o = - 0.6$

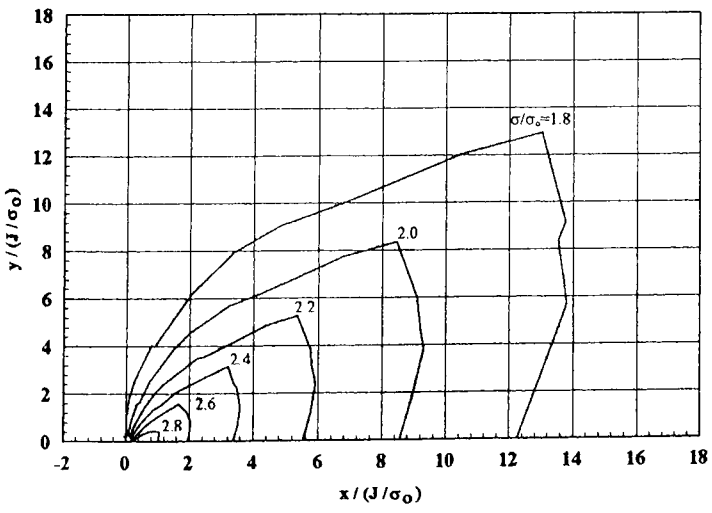

(e) $T / \sigma_o = - 0.8$

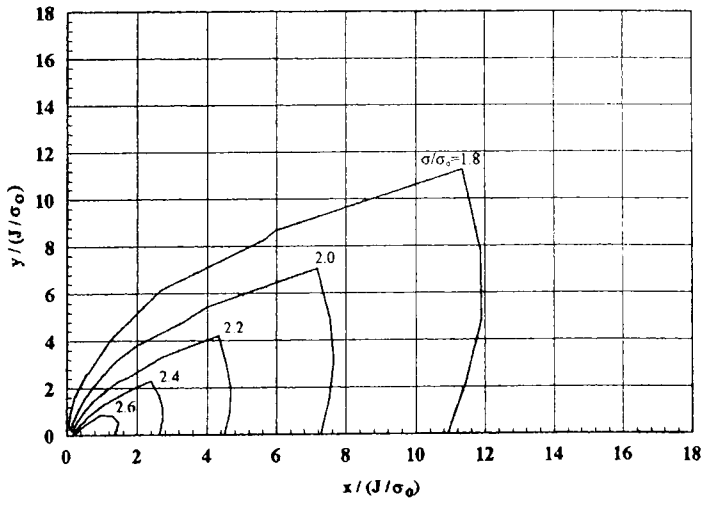

(f) $T / \sigma_o = - 1.0$

Fig. 5.13 Principal stress contours for various levels of T stress – EN24

As would be expected the area contained within the principal stress contours is reduced as the applied T stress becomes progressively more negative. The effect of choice of area ratio on the area contained within principal stress contours is shown in fig. 5.14. The ratio of the area contained within the principal stress contour divided by the area contained under small scale yielding at the same deformation level is plotted against the ratio of principal stress divided by the material yield stress. Consideration of fig. 5.14 suggests that the selection of principal stress ratio is important when using the area scaling method to predict failure due to cleavage. This is supported by fig. 15.15 which shows the predicted value of J by the use of equation 3.3.7 plotted against principal stress divided by the material yield stress. As can be seen the influence of the chosen principal stress level at which to evaluate the enclosed area has an effect on the J integral result. This effect is weak for $T / \sigma_o = - 0.2$ but becomes stronger as the T stress becomes progressively more negative.

It can be concluded, therefore, that the choice of principal stress level when considering finite bodies is important for EN24 material.

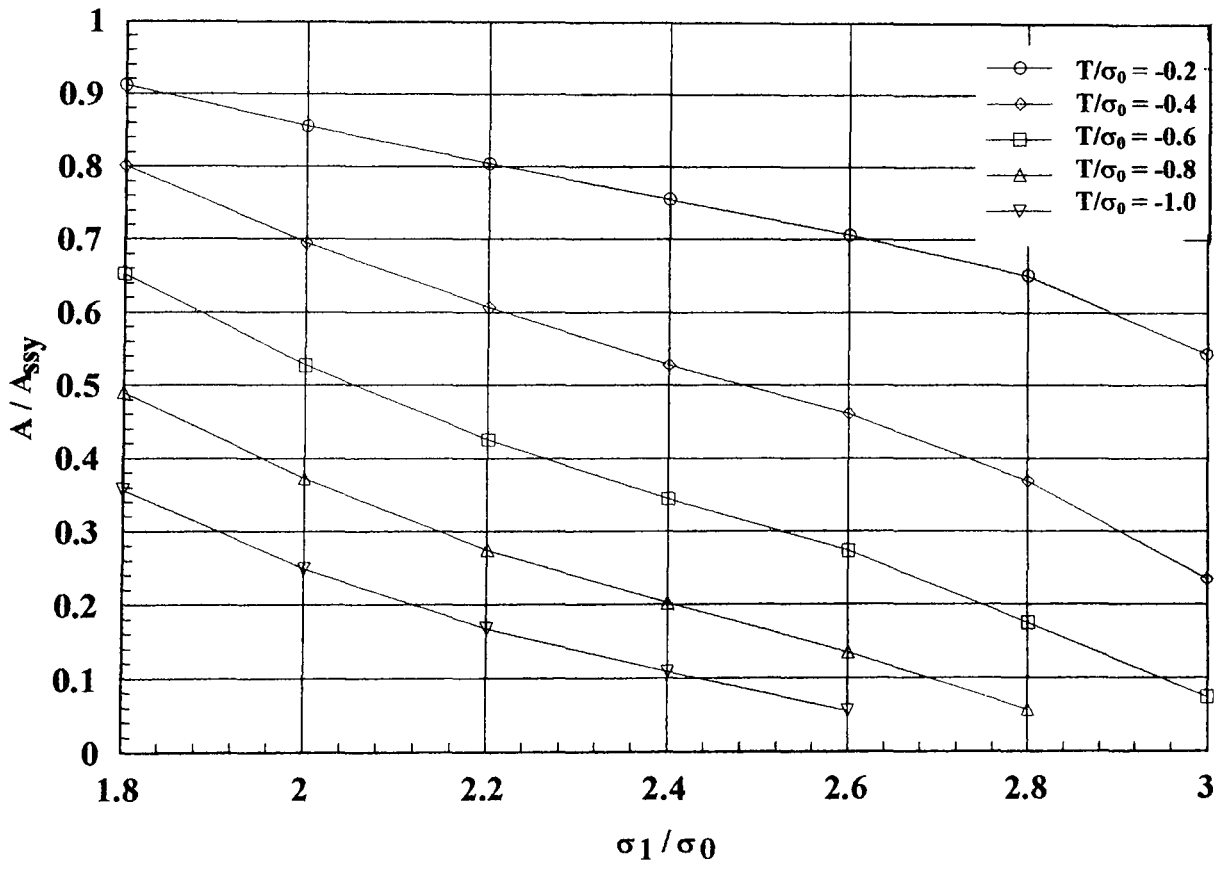

Fig. 5.14 Areas within principal stress contours

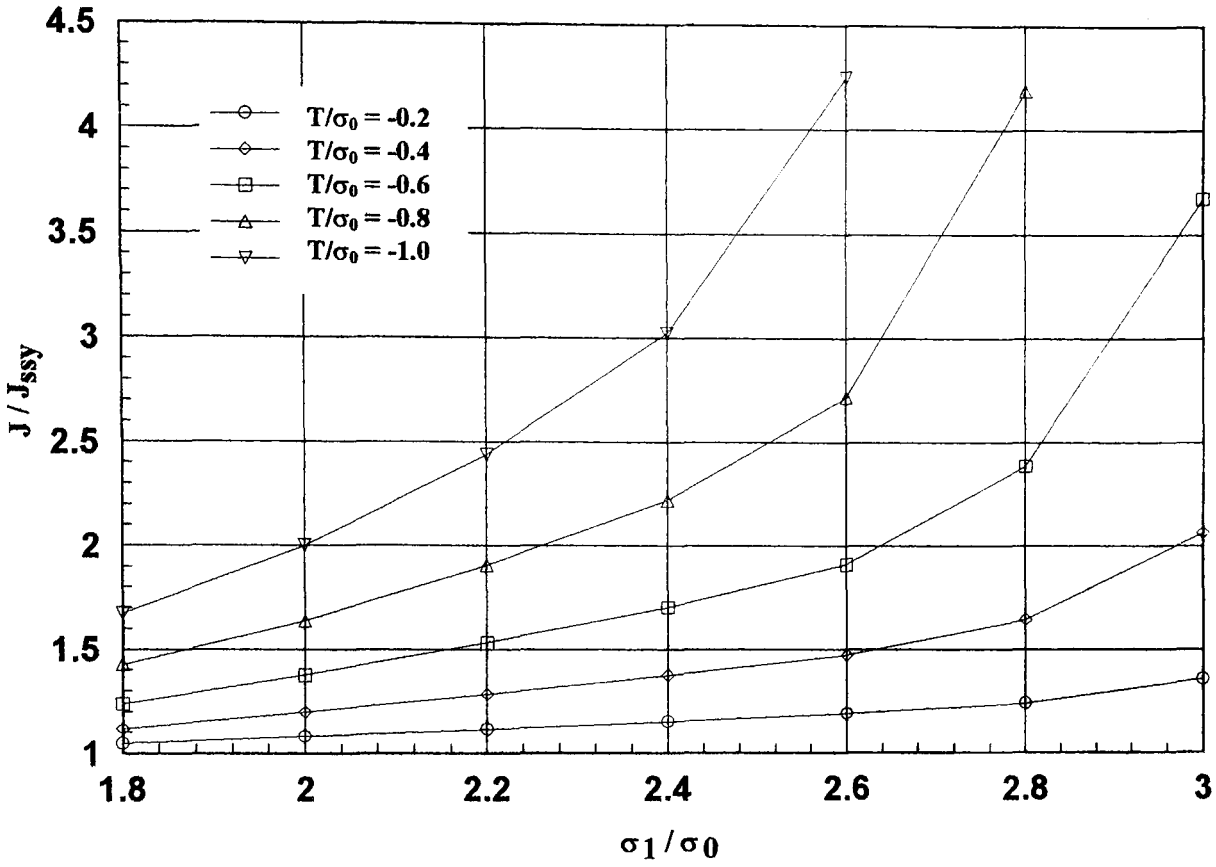

Fig. 5.15 Influence of specified principal stress on fracture toughness prediction

5.5 DISCUSSION OF RESULTS AND CLOSURE

The results presented in this chapter establish methodologies based on Q and area scaling that can be carried forward to evaluate the effects of side-grooving on the fracture performance of sub thickness compact tension specimens. A small scale yielding solution has also been obtained for the EN24 material that can be used for Q evaluation in the subsequent analysis of 3D plain and side grooved compact tensions specimens.

In order to evaluate both Q and the area within user specified crack opening mode stress levels MATLAB based post-processing programmes have been developed. Again these will be particularly useful when evaluating the performance of 3D geometries.

The results obtained from the area scaling analysis have shown that the correct selection of principal stress contour levels will be important if good predictions of fracture performance are to be obtained for the EN24 material being considered under cleavage conditions.

CHAPTER 6

THE INFLUENCE OF THICKNESS AND SIDE GROOVING ON EN24 STEEL

6.1 INTRODUCTION

The previous chapter developed methodologies, based on a two parameter fracture mechanics approach, which allow the effects of crack tip constraint on fracture performance to be established in a quantitative manner. The work presented in this chapter extends this approach to investigate the effect of thickness and 30% Vee side grooving on the fracture behaviour of EN24 steel.

Again finite element analysis has been used to provide theoretical predictions of the fracture performance of sub-thickness specimens manufactured from EN24 steel. The properties of the EN24 material have been fully defined in the previous chapter, together with the idealisation required for the finite element analysis in terms of a Ramberg Osgood material model. The finite element results are supported by experimental results for full and sub-thickness specimens which were both plain sided and side grooved.

The theoretical predictions obtained from the finite element analysis show reasonable agreement with experimental observations.

6.1.1 AIMS AND OBJECTIVES

The aims and objectives of the work described in this chapter are as follows:

1. To investigate the effect of thickness on the fracture behaviour of EN24 steel using finite element analysis.

2. To investigate the effect of side grooving on the fracture behaviour of sub-thickness specimens manufactured from EN24 steel using finite element analysis.

3. To experimentally investigate the effect of thickness on the fracture behaviour of EN24 steel.

4. To experimentally investigate the effect of side grooving on the fracture behaviour of sub-thickness specimens manufactured from EN24 steel.

6.2 SPECIMEN GEOMETRY AND PREPARATION

The specimen geometry used for this section of the work differed slightly from that used for the aluminium alloy specimens reported in chapter 4 in that they were stepped notch compact tension specimens rather than straight notch compact tension specimens. The reason for the change was due to the fact that specimens that were considerably below the thickness required to give plane strain results were to be tested, hence requiring J rather than K determination. The type of specimen selected is acceptable for both J and K determination whereas the straight notch compact tension specimen used previously can only be used for K determination. Again the specimen geometry requirements are defined by both British and American standards [26 and 27] as shown in fig. 6.1.

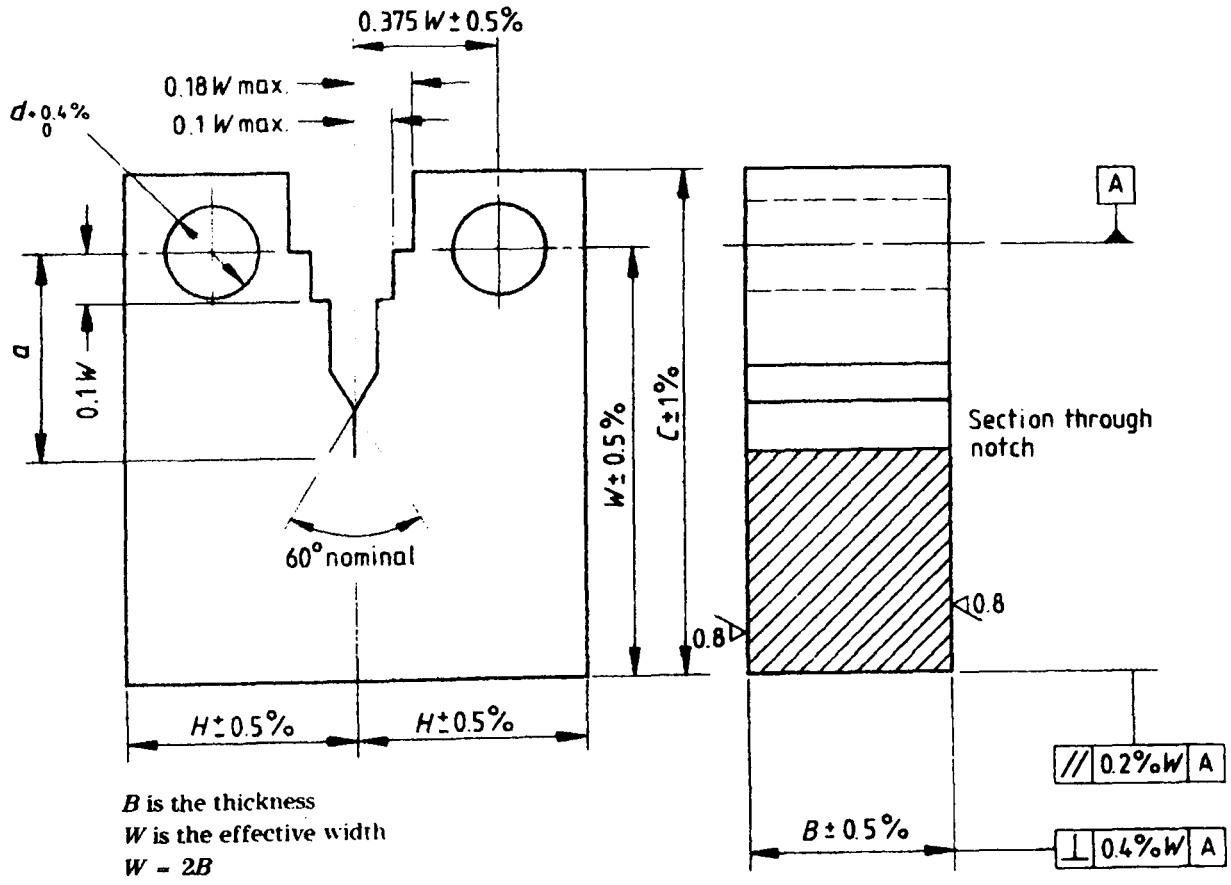

Fig. 6.1 Stepped notch compact tension specimen

The specimens must be pre-cracked and meet minimum size requirements as defined by equations (4.1), (4.2) and (4.3) if valid K_{IC} results are to be obtained. The specimen size requirements for valid J_{IC} testing as laid down in E813-88 [104] are much more lenient than those required for K_{IC} testing primarily because the J integral is better suited to non linear material behaviour. The minimum specimen dimensions for valid J_{IC} testing are:

$$B, b \geq \frac{25\, J_{IC}}{\sigma_Y} \quad \ldots\ldots \quad (6.1)$$

where B is the specimen thickness and b is the uncracked ligament length (W – a).

The material properties of the EN24 steel used were defined in section 5.3 to be as follows:

Yield strength – 970 MPa
Young's modulus, E – 200 GPa
Preliminary fracture toughness, K_{IC} – 95 MPa $\sqrt{m}$

Consideration of the above material properties leads to a minimum specimen thickness for valid K_{IC} results of 24 mm, based on only preliminary fracture toughness tests, hence it was decided that the specimen design should be based on a thickness of 25 mm.

In addition to the full thickness specimen of 25 mm a range of sub-thickness specimens were also analysed/tested in both plain and side grooved forms. Specifically, thicknesses of 25 mm, 15 mm, 10 mm, 5 mm, 3.75 mm, 2.5 mm and 1.25 mm.

6.3 FINITE ELEMENT ANALYSIS

As with the modified boundary layer analysis the ABAQUS finite element package [99] was used together with the FEMGV graphical pre/post processor [100] and ABAQUS post [101].

The optimised crack tip mesh developed for the modified boundary layer analysis as described in section 5.4 needed to be extended into 3D in order to obtain a detailed stress analysis of the crack tip region. However, such detailed refinement of the whole compact tension specimen even allowing for a transition to a coarser mesh away from the crack tip region was not feasible due to the resulting computational demands in

terms of runtimes and hard disc usage. In order to overcome this problem it was decided that a sub modelling technique should be used. A sub model of the crack tip region was produced with a refined mesh based on the optimised mesh developed for the modified boundary layer analysis. The boundary of the sub model was driven by an interpolation of the solution from a global model of the compact tension specimen which was produced to a much coarser refinement.

Sub modelling is a standard technique available within the ABAQUS package and is useful when an accurate, detailed solution is required for a local region but where the detailed modelling of the local region has negligible effect on the overall solution. The response at the boundary of the local region is determined by the solution of the global model which determines the solution in the sub model. The technique does rely on the global model defining the sub model boundary response with sufficient accuracy. The sub model is run as a separate analysis with the only link between the sub model and the global model being the transfer of time dependent values of variables to the boundary nodes of the sub model. There is no requirement within the ABAQUS package that the boundary nodes on the sub model coincide with nodes within the global model. Neither is there a requirement of the load incrementation regime to be the same within the sub model and the global model. However, to ensure consistency of results between the global and sub model, the sub model boundary nodes did coincide with nodes within the global model and the same load incrementation scheme was applied.

Typical meshes, for both the global and sub model, can be seen in figs. 6.2 and 6.3 (for the 25 mm thick plain sided specimen).

The global models of the compact tension specimens were built from 20 noded isoparametric elements, in all cases only a quarter of the specimen was modelled because of symmetry conditions. All of the elements along the crack front were collapsed to form degenerate elements but the nodes along the collapsed edge, although coincident, were allowed to retain their individual degrees of freedom so as to allow some degree of crack-tip blunting that would be expected in an elastic-plastic analysis. This approach also ensured the correct $^{1}/r$ singularity at the crack tip required for elastic-plastic J integral evaluation.

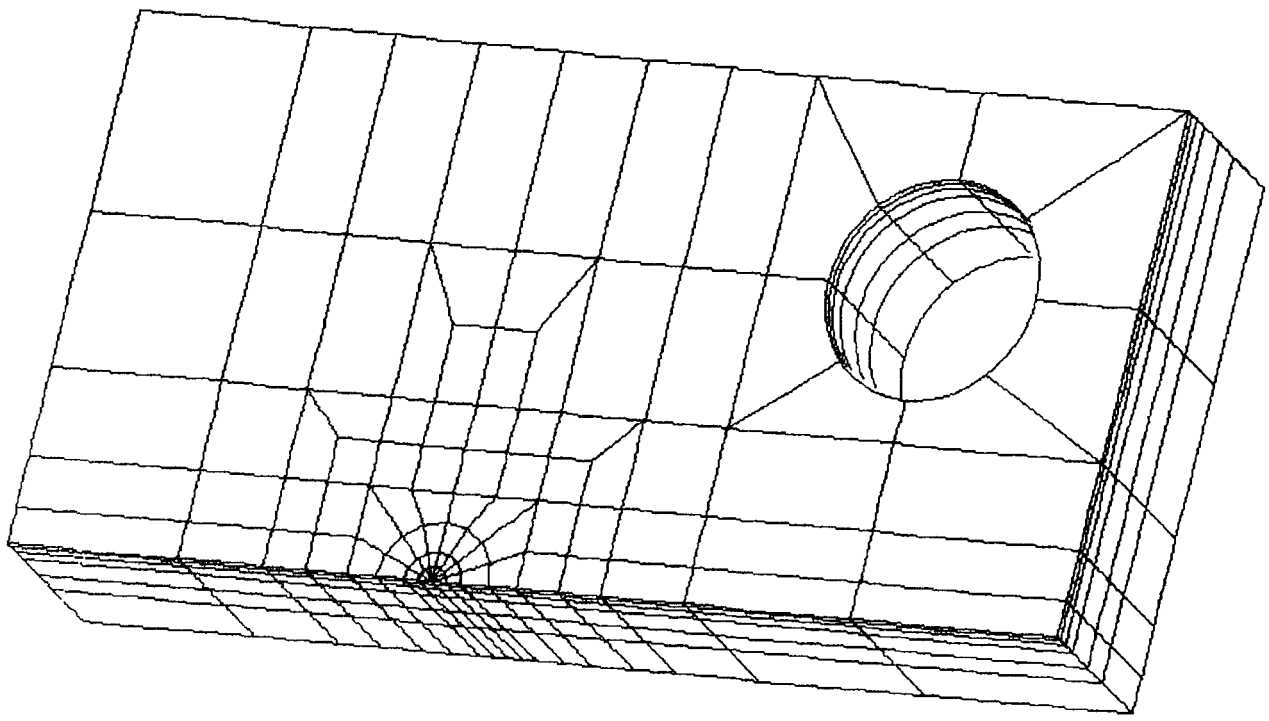

Fig. 6.2 Global model of a 25 mm thick plain sided specimen

The number of elements varied from model to model depending on the thickness of the specimen being analysed, so giving average element and node counts is meaningless. As an example, the 25 mm thick plain sided model shown in fig. 6.2 contained 657 elements and 3,085 nodes with six elements through the specimen thickness biased to give refinement at the specimen edge. The boundary conditions were identical to those used for the aluminium specimen analysis and illustrated in fig. 4.3. The models were loaded by the application of a pressure to the top of the clevice pin hole, with the load being applied in two load steps. The first load step consisted of 5 load increments up to 90% of the expected specimen failure load based on preliminary estimates of the material fracture toughness. The second load step consisted of a further 4 load increments up to 110% of the expected specimen failure load.

The analysis was carried out on a Pentium 133 with 96 MB RAM available to ABAQUS and processing times varied between 1 – 3 hours depending on the specimen thickness.

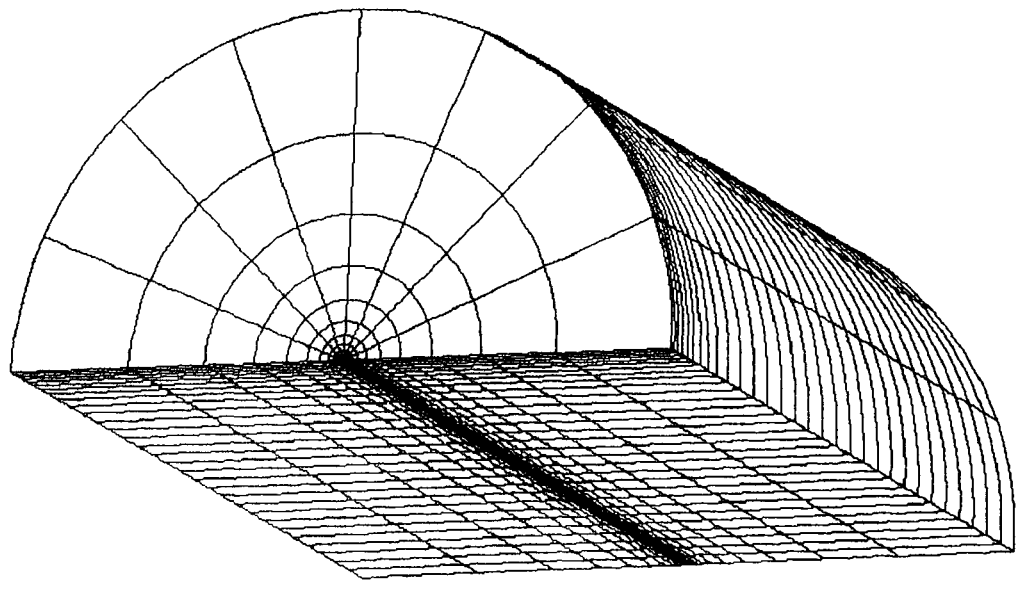

Fig. 6.3 Crack tip sub-model for a 25 mm thick plain sided specimen

The sub models were again built from 20 noded isoparametric elements with only a quarter of the specimen being modelled due to symmetry conditions. The mesh was simply an extended form of that used for the modified boundary layer analysis and illustrated in fig. 5.11. As with the global models the number of elements varied from model to model depending on specimen thickness. Again, by way of example, the 25 mm thick plain sided model shown in fig. 6.3 contained 6,966 elements and 45,233 nodes with 31 elements through the specimen thickness again biased to give refinement at the specimen edge. The load incrementation scheme was exactly the same as that for the global models to ensure consistency of results.

Again the analysis of the plain specimens and some of the side grooved specimens was undertaken on a Pentium 133 with 96 MB RAM available to ABAQUS with processing times for the plain sided specimens varying between approximately 12 and 84 hours depending on specimen thickness.

All of the plain sided specimens were successfully processed as described above; however difficulties with respect to model convergence were experienced for the side grooved specimens. The problems were associated with the determination of the steep stress gradients at the intersection of the side groove root and crack tip. The solution adopted was to significantly increase the through thickness mesh refinement at the root of the side groove. In order to maintain a reasonable aspect ratio for the elements in this

region the mesh in the plane of the specimen was also refined slightly from that used for the modified boundary layer and plain specimen analysis.

Typical meshes can be seen for both the 25 mm thick global and sub models in figs. 6.4 and 6.5.

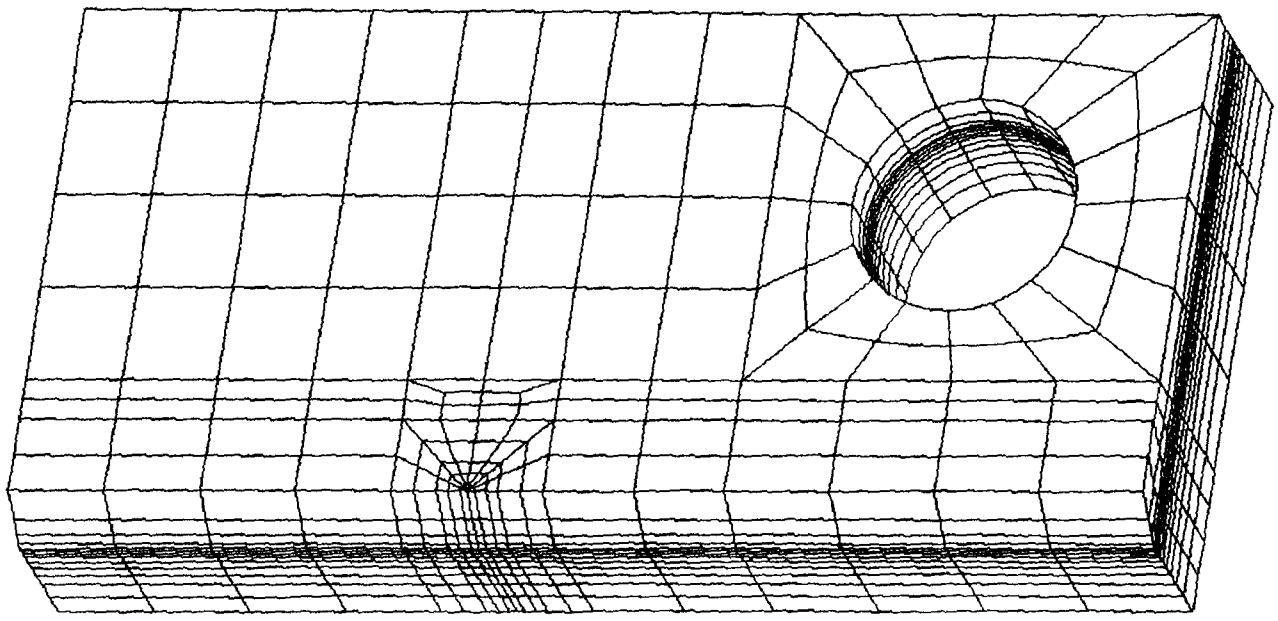

Fig. 6.4 Global model of a 25 mm thick side grooved specimen

The increase in mesh refinement meant that, for example, the 25 mm thick side grooved global model contained 3,085 elements and 8,000 nodes with 12 elements through the thickness. The corresponding sub model consisted of 9,975 elements 46, 076 nodes and 45 elements through the thickness which were biased towards the side groove. As a consequence of this refinement the 10, 15, and 25 mm thick specimens were processed using a SUN Ultra 10 workstation with 512 MB RAM available to ABAQUS.

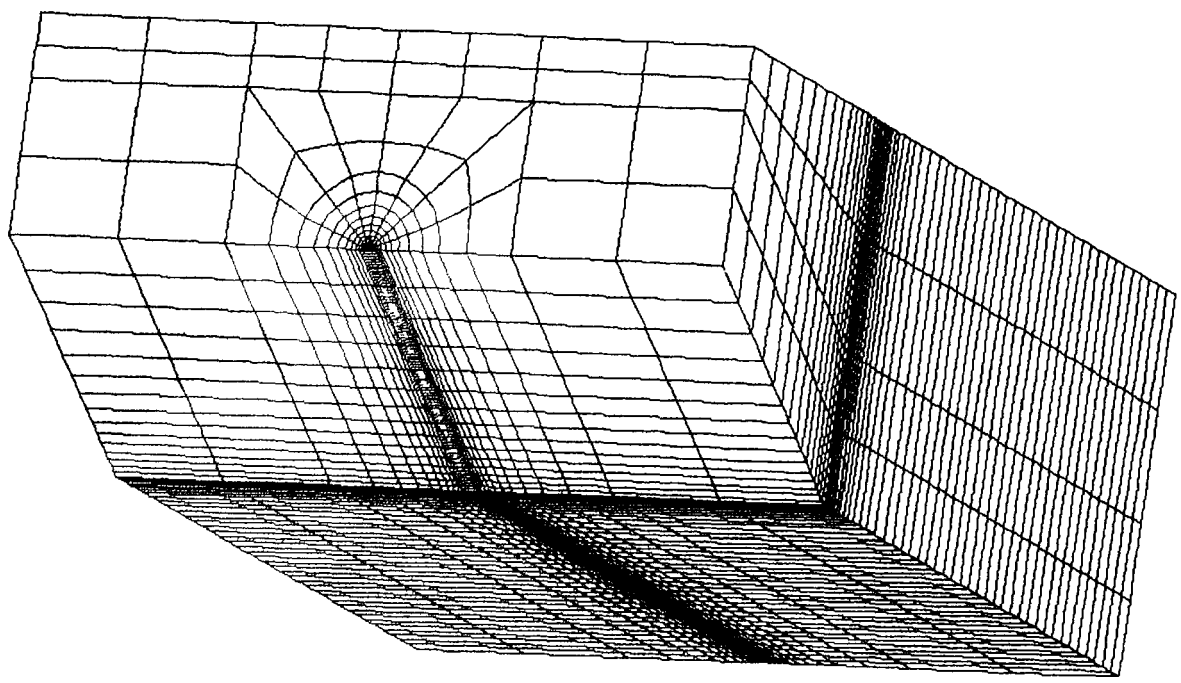

Fig. 6.5 Crack tip sub-model for a 25 mm thick side grooved specimen

6.3.1 FINITE ELEMENT ANALYSIS RESULTS

The results from the finite element analysis for both plain sided and side grooved specimens can be seen in figs. 6.6 – 6.32.

Results for J variation through the specimen thickness can be seen in figs. 6.6 – 6.12 for the full range of plain sided specimens. In all cases the variation of J is plotted for a load range of between 90% and 110% of the expected failure load for the specimen, based on preliminary fracture tests. Consistent with the results obtained from the linear elastic analysis presented in chapter 4 for the through thickness variation of K, the value of J falls away significantly at the specimen edge when compared with the centre line value. This fall off becomes more pronounced as the load level increases for all specimen thicknesses.

Consideration of fig. 6.6. shows that J is relatively constant across a significant proportion of the crack front at all load levels for full specimen thickness. A good indicator of this is the ratio of the average J across the crack front to the centre line value which varies between 0.931 at the lowest deformation level and 0.927 at the highest deformation level. Both the 15 mm and 10 mm thick specimens

exhibit similar behaviour in terms of J variation as the 25 mm thick specimen with the ratio of average J to centre line J for the 10 mm thick specimen being 0.930 at the lowest deformation level and 0.909 at the highest deformation level. Specimens below 10 mm thick show a larger variation of J across the crack front with the ratio of average to centre line J values varying from 0.894 at the lowest deformation level of the 5 mm thick specimen to 0.693 for the highest deformation level of the 1.25 mm thick specimen.

In comparison, the results obtained for through thickness J variation in the side grooved specimens can be seen in figs. 6.13 - 6.19. Again results are plotted for a load range between 90% and 110% of the expected failure load for the specimen based on preliminary fracture tests. The effect of side grooving is to significantly elevate J in the region of the side groove and to provide a relatively constant value of J over a significant proportion of the specimen thickness even for specimens which are significantly below the minimum thickness demanded by British and American standards [26 and 27] in order to obtain valid tests results. The ratio of average J to centre line J for the 25 mm thick specimen is 1.140 at the lowest deformation level and 1.130 at the highest deformation level. Indeed the ratio remains above unity for all specimens except the 1.25 mm thick specimen which has a ratio of 0.990 at the lowest deformation level and 0.954 at the highest deformation level.

In all side grooved cases the J values obtained adjacent to the side groove showed some oscillation, this is most likely to be due to the finite element mesh being unable to accurately model the corner singularity at the root of the side groove. Oscillation was also present to a lesser extent in the plain sided models at the free surface and has been observed by several other authors [30, 105]. The effect has been described in detail by Nakumara and Parks [106]. Due to the fact that only a very small distance in from the root of the side groove is involved it should not have an adverse affect on the results obtained or observations made.

Results from the two parameter fracture mechanics investigation can be seen in figs. 6.20 – 6.26 for plain sided specimens and figs. 6.27 – 6.33 for side grooved specimens. In each case (a) shows principal stress contours for $\sigma/\sigma_0 = 2$ at various locations through the specimen thickness, whilst (b) shows the crack line opening mode stress at various locations through the specimen thickness together with the SSY solution. J-Q trajectories are shown in (c) at specific locations

through the specimen thickness, for plain specimens of 3.75 mm thick and above the trajectory locations are at the specimen centre line and at approximately 60%, 80% 90% and 95% of the distance from the centre line to the specimen edge. For plain specimens below 3.75 mm thick the trajectory locations are at the specimen centre line and approximately 20%, 55% 70% and 80% of the distance from the centre line to the specimen edge. For side grooved specimens trajectory locations are at the specimen centre line and approximately 60%, 80%, 90% and 95% of the distance from the centre line to the side groove root for all specimens. The variation of Q through the specimen thickness is shown in (d) for all specimens. Q is calculated at the J level approximately corresponding to the fracture toughness of the material.

Consideration of the through thickness Q variation reveals that for the full thickness, 25 mm thick, plain specimen Q is constant and slightly positive for a significant proportion of the crack front. Positive Q is maintained over some portion of the crack front for specimen thicknesses down to 10 mm, below this Q is negative at all positions along the crack front. Average crack front Q values are given in table 6.1. The average Q value for the full thickness specimen is positive, whilst all other thicknesses exhibit a negative average value of Q, getting progressively more negative as the thickness reduces. For specimens of 10 mm thick and above the Q value remains close to zero, i.e. –0.07868 for the 10 mm thick specimen. Below 10 mm thick the average value of Q falls considerably.

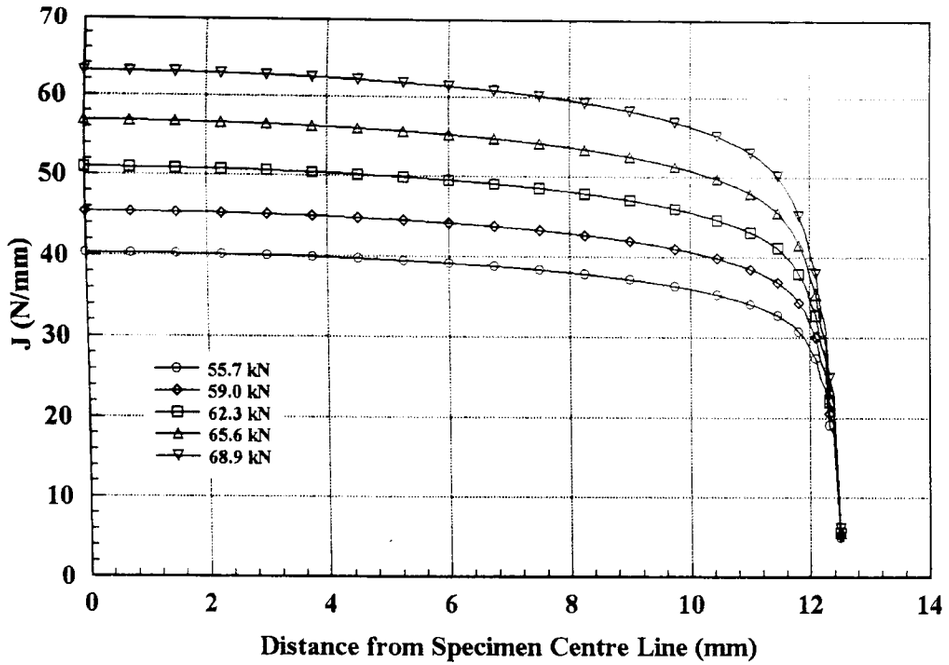

Fig. 6.6 Variation of J through specimen thickness
25 mm thick plain specimen

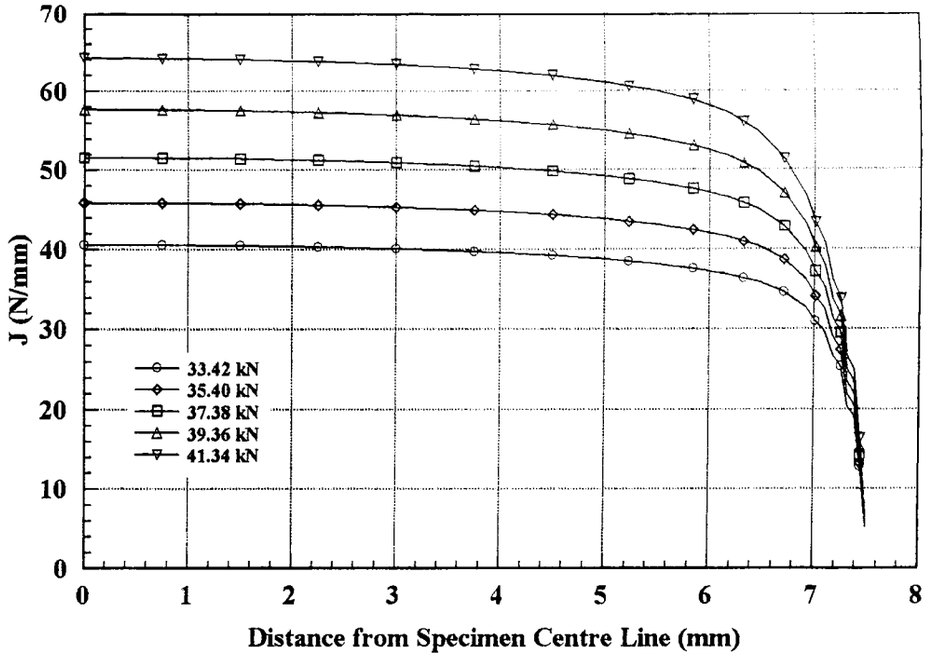

Fig. 6.7 Variation of J through specimen thickness
15 mm thick plain specimen

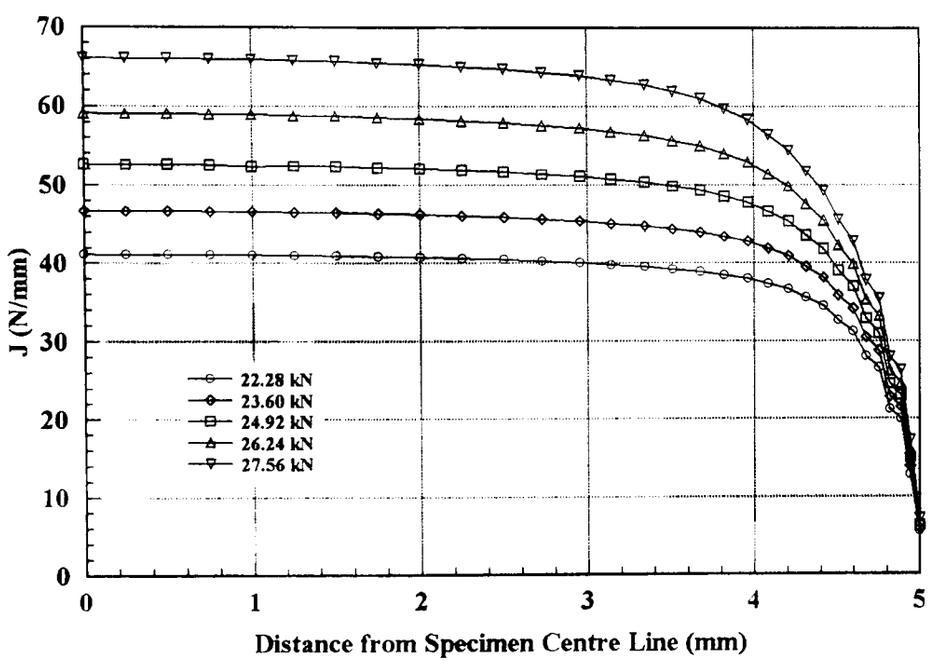

Fig. 6.8 Variation of J through specimen thickness
10 mm thick plain specimen

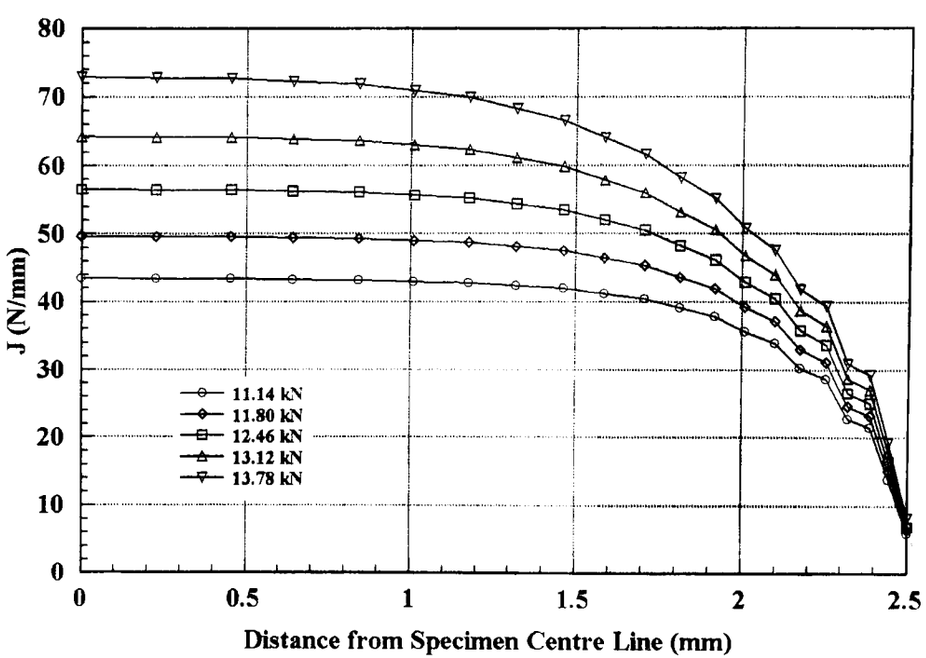

Fig. 6.9 Variation of J through specimen thickness
5 mm thick plain specimen

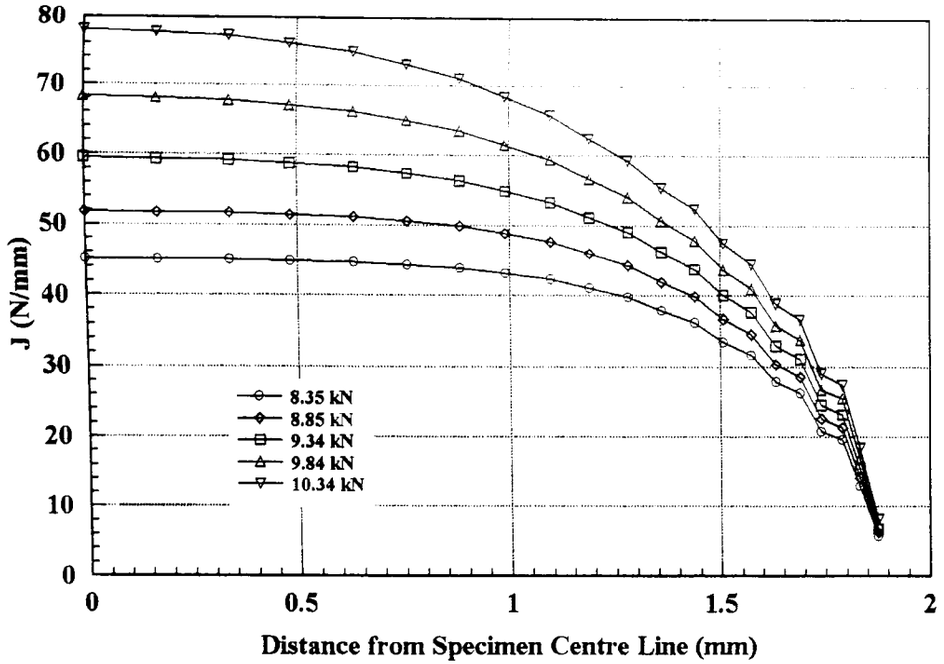

Fig. 6.10 Variation of J through specimen thickness 3.75 mm thick plain specimen

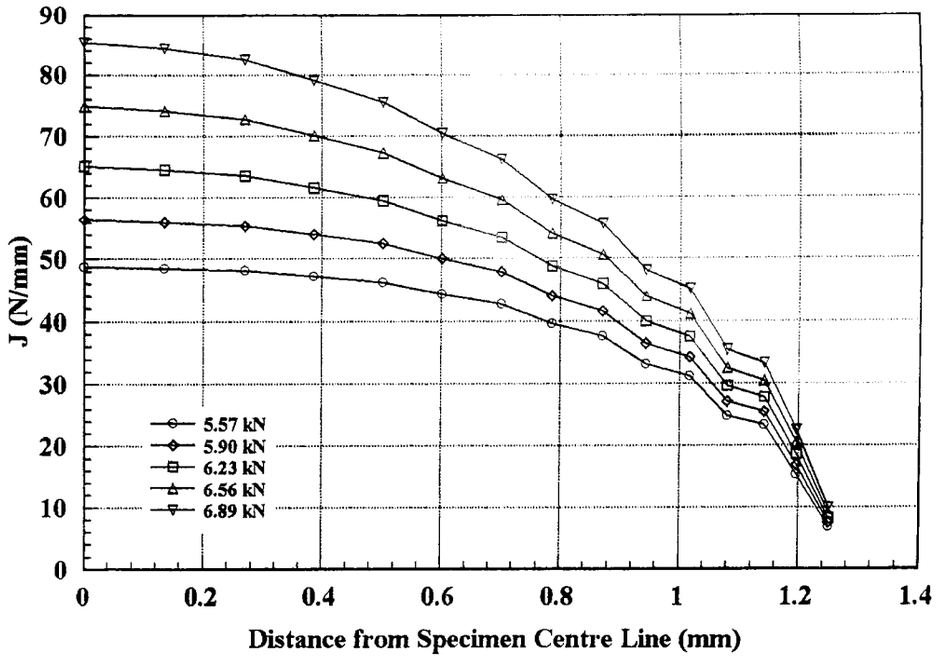

Fig. 6.11 Variation of J through specimen thickness 2.5 mm thick plain specimen

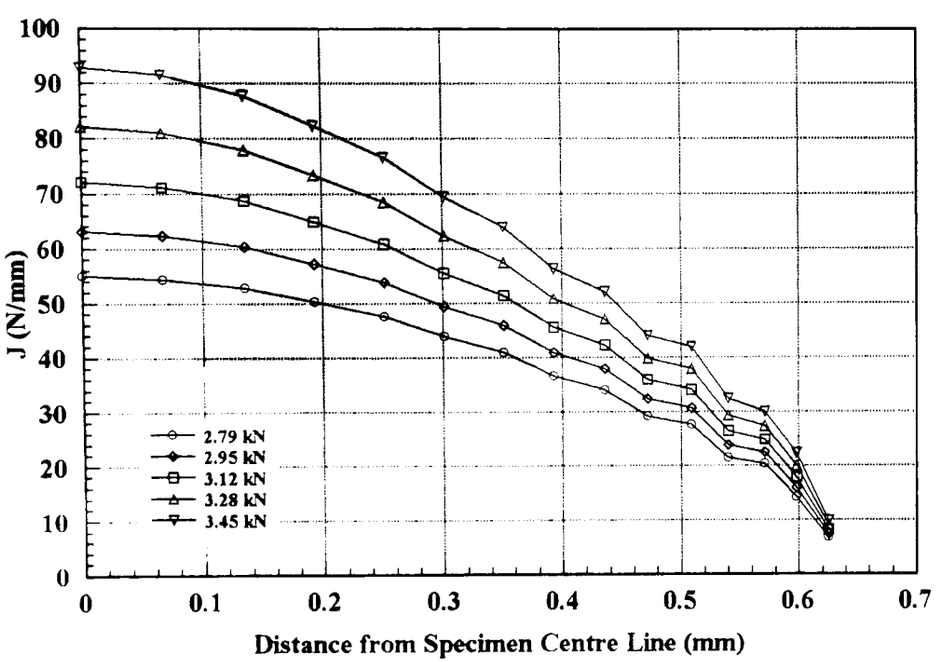

Fig. 6.12 Variation of J through specimen thickness 1.25 mm thick plain specimen

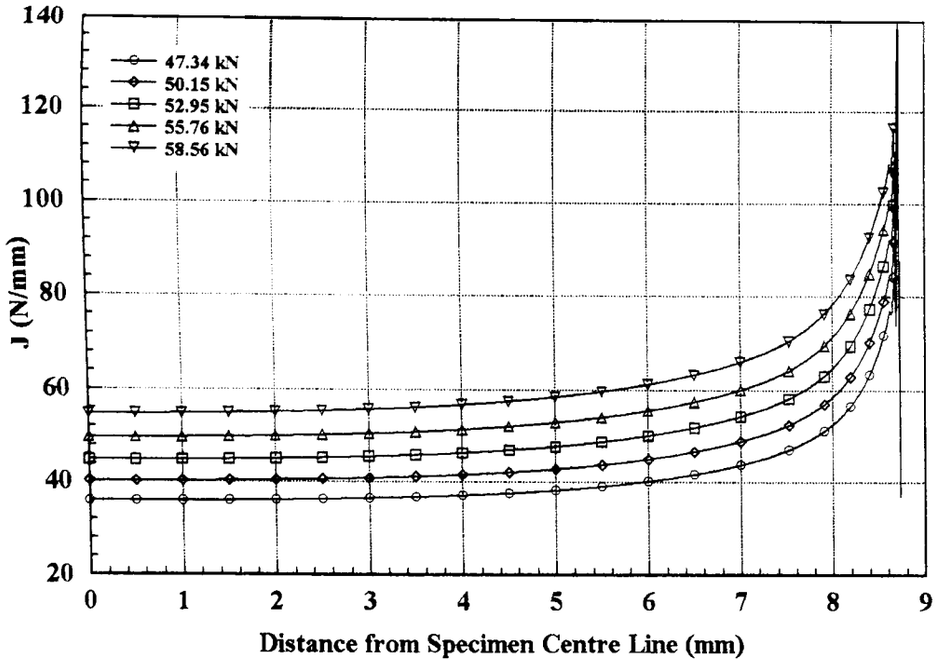

Fig. 6.13 Variation of J through specimen thickness
25 mm thick side grooved specimen

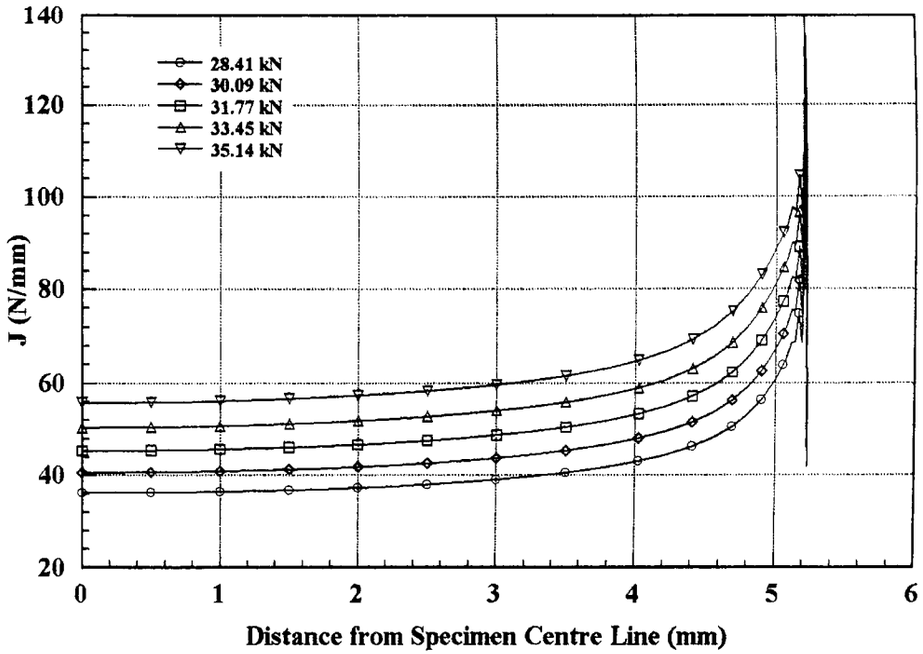

Fig. 6.14 Variation of J through specimen thickness
15 mm thick side grooved specimen

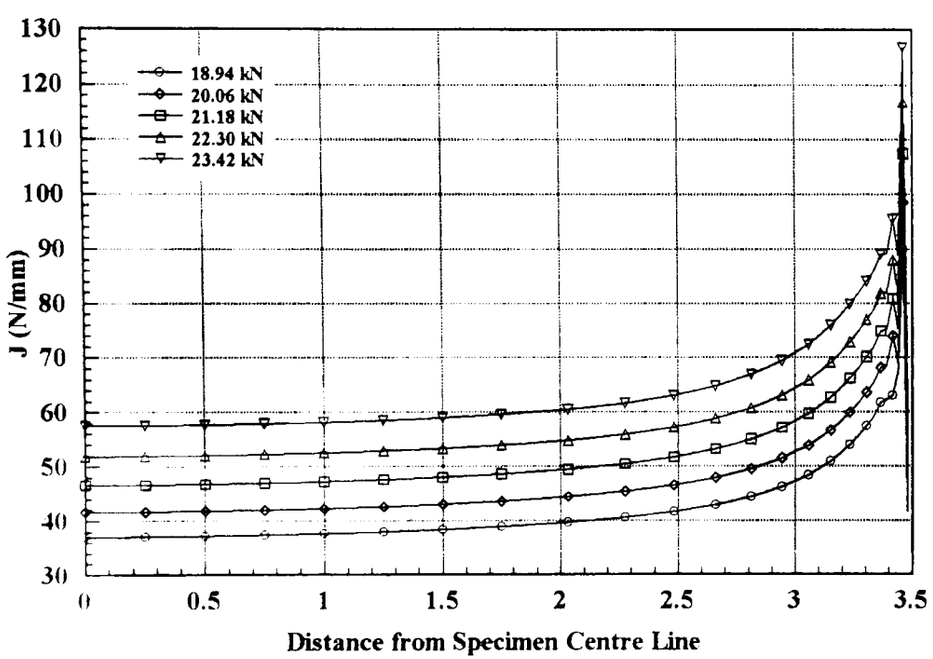

Fig. 6.15 Variation of J through specimen thickness
10 mm thick side grooved specimen

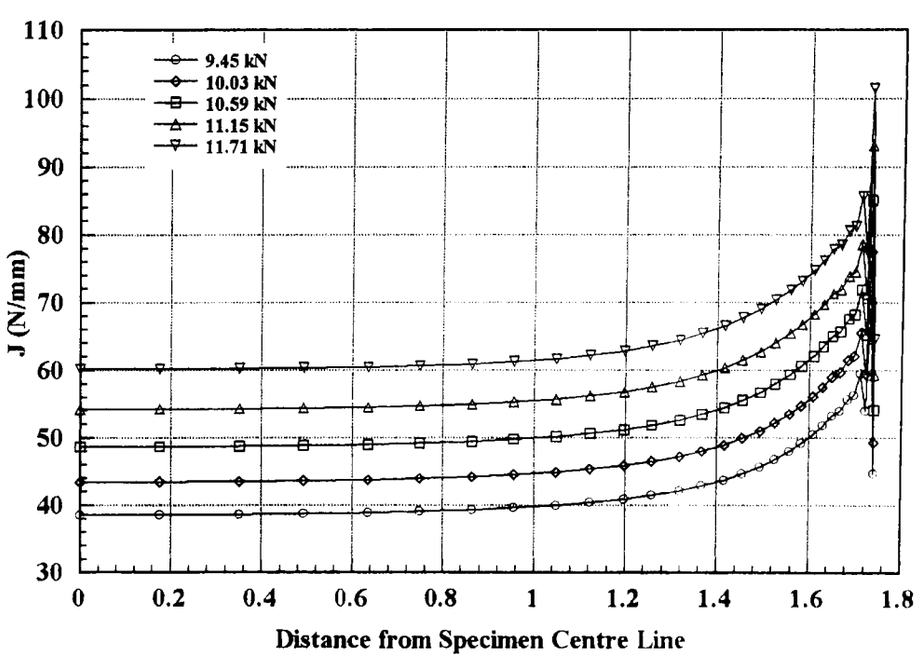

Fig. 6.16 Variation of J through specimen thickness
5 mm thick side grooved specimen

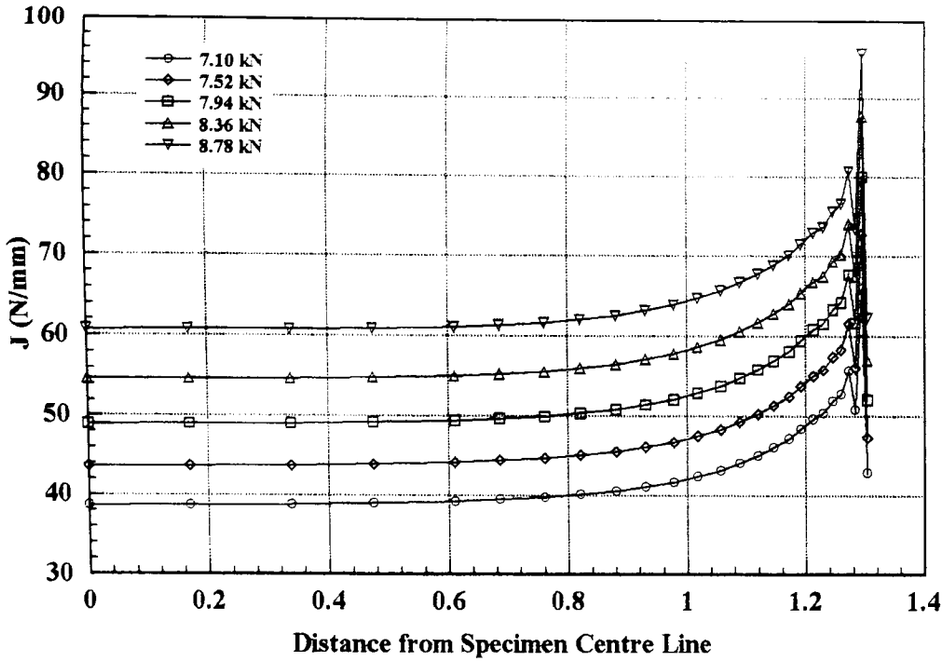

Fig. 6.17 Variation of J through specimen thickness 3.75 mm thick side grooved specimen

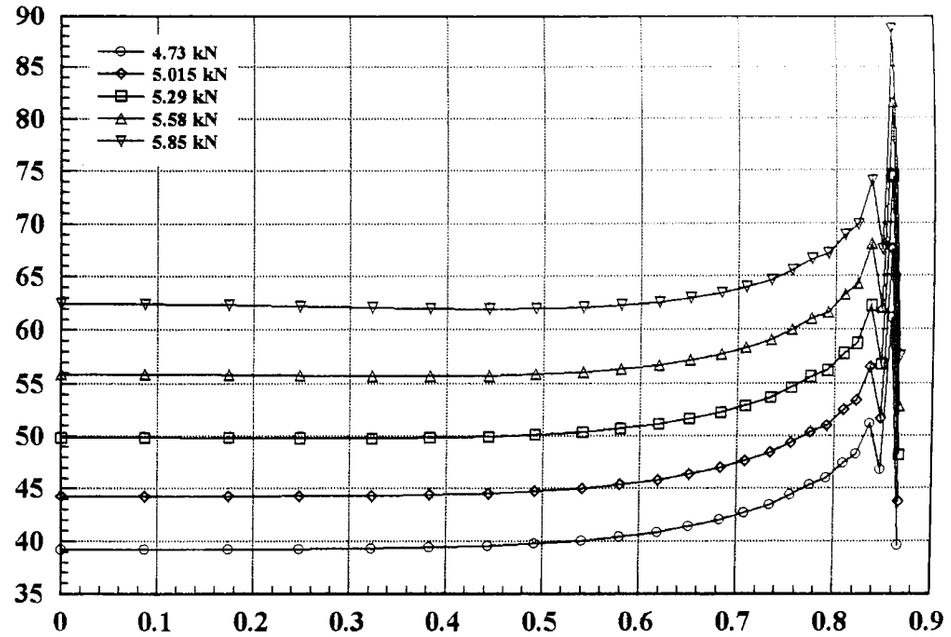

Fig. 6.18 Variation of J through specimen thickness 2.5 mm thick side grooved specimen

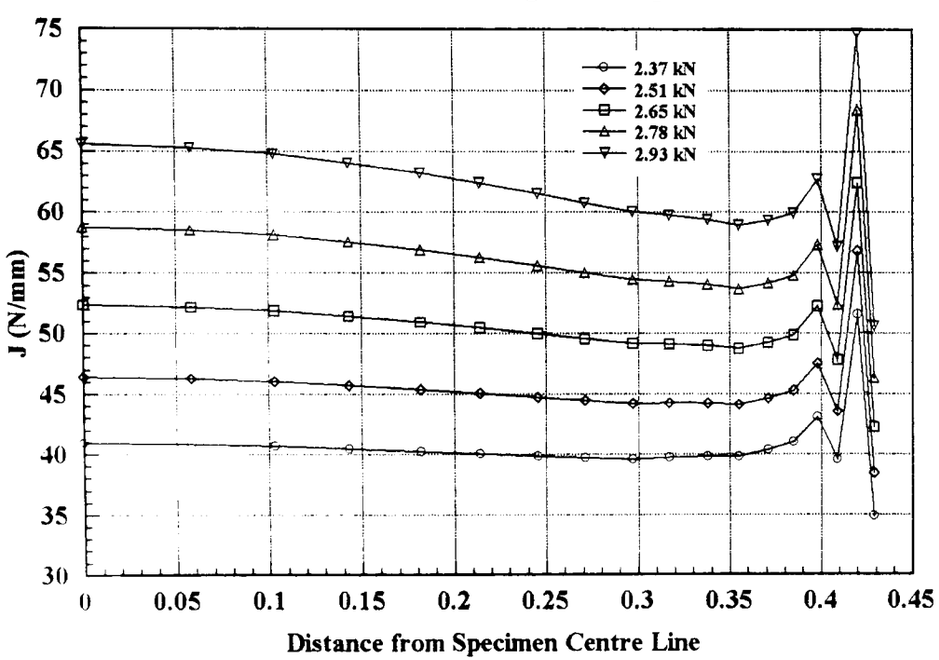

Fig. 6.19 Variation of J through specimen thickness 1.25 mm thick side grooved specimen

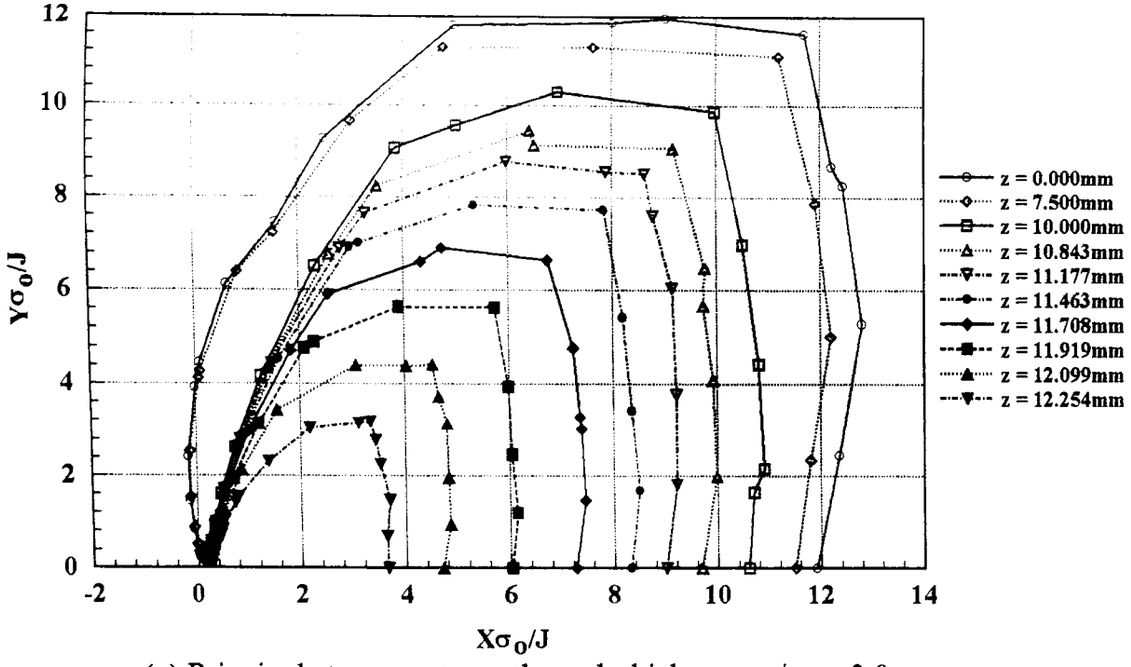

(a) Principal stress contours through thickness; $\sigma/\sigma_o = 2.0$

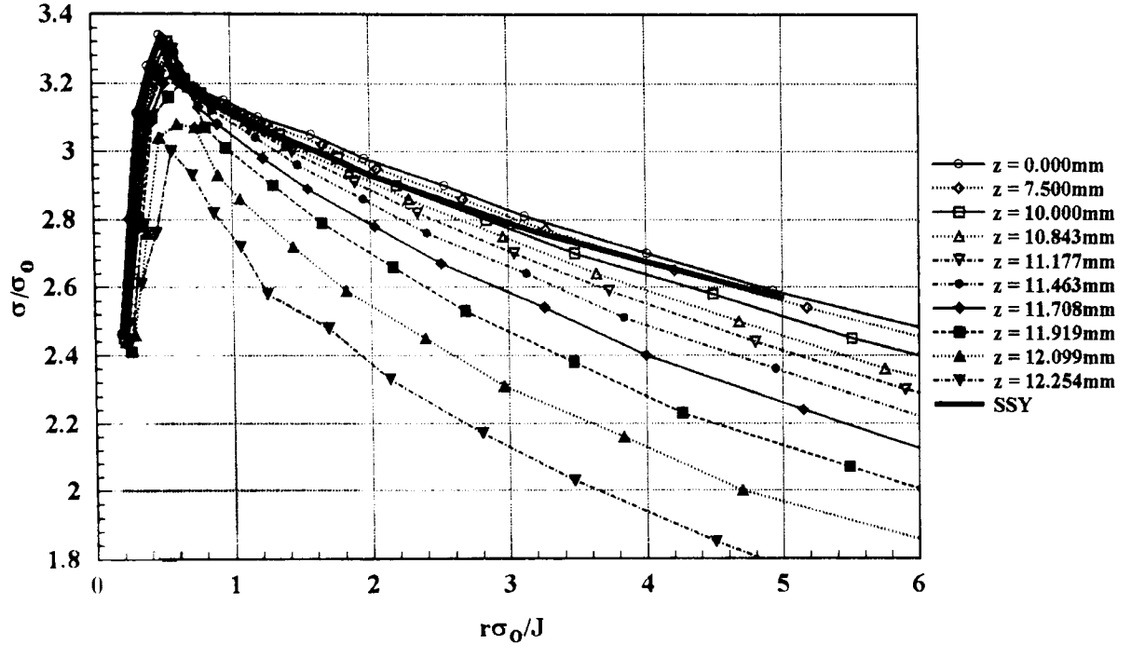

(b) Crack line opening mode stress

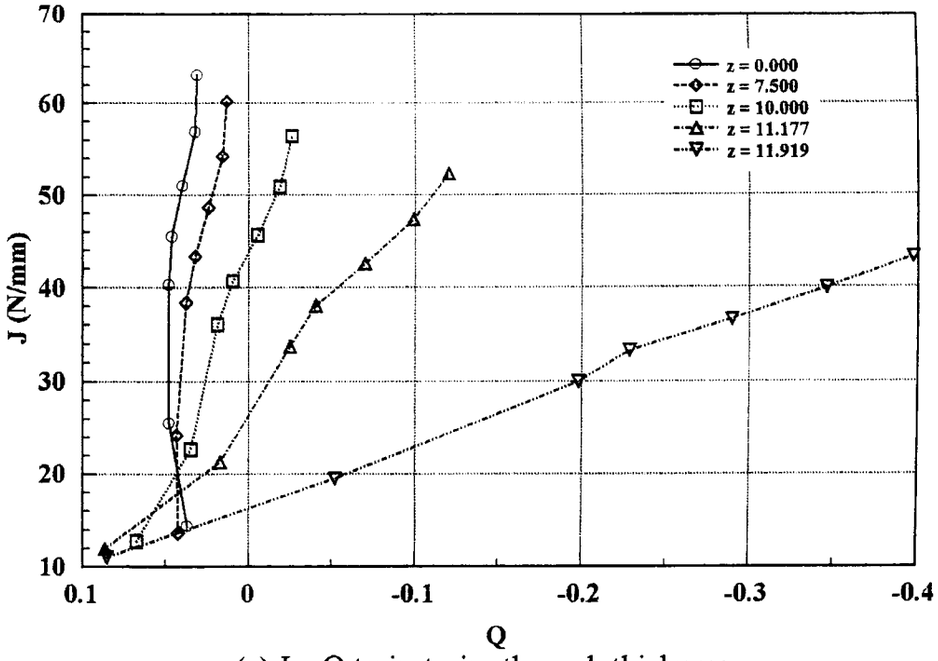

(c) J – Q trajectories through thickness

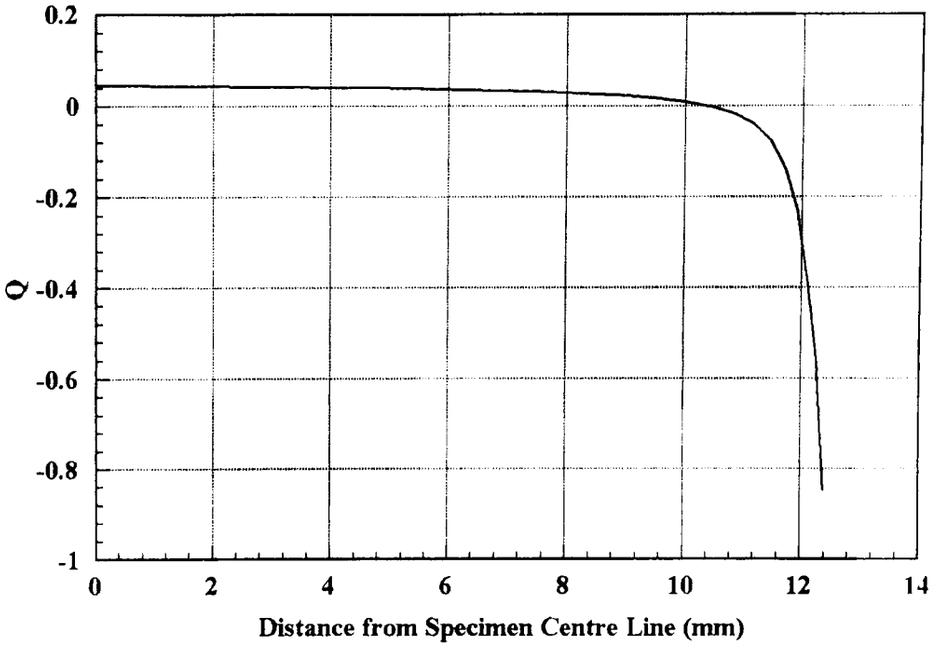

(d) Variation of Q through thickness

Fig 6.20 Analysis results 25 mm thick specimen

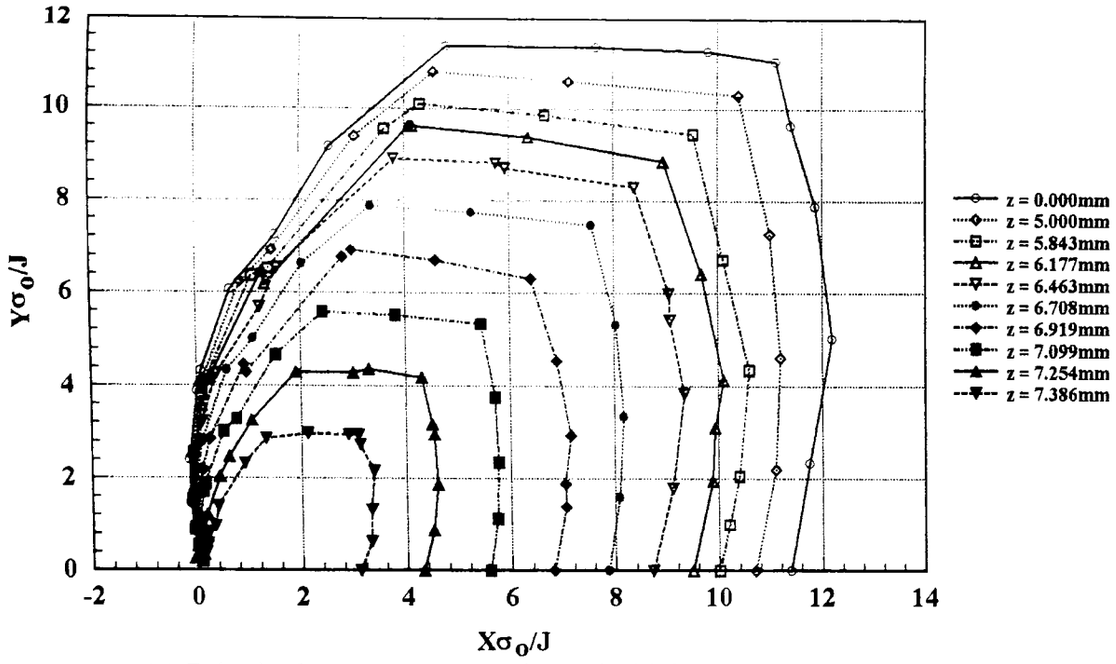

(a) Principal stress contours through thickness; $\sigma/\sigma_o = 2.0$

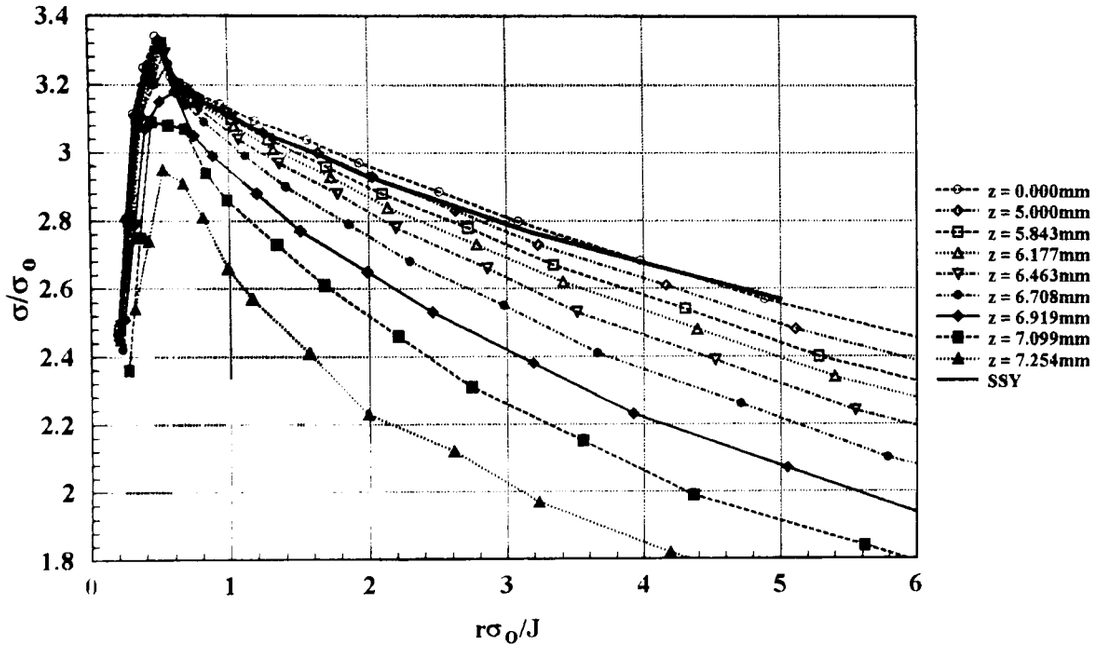

(b) Crack line opening mode stress

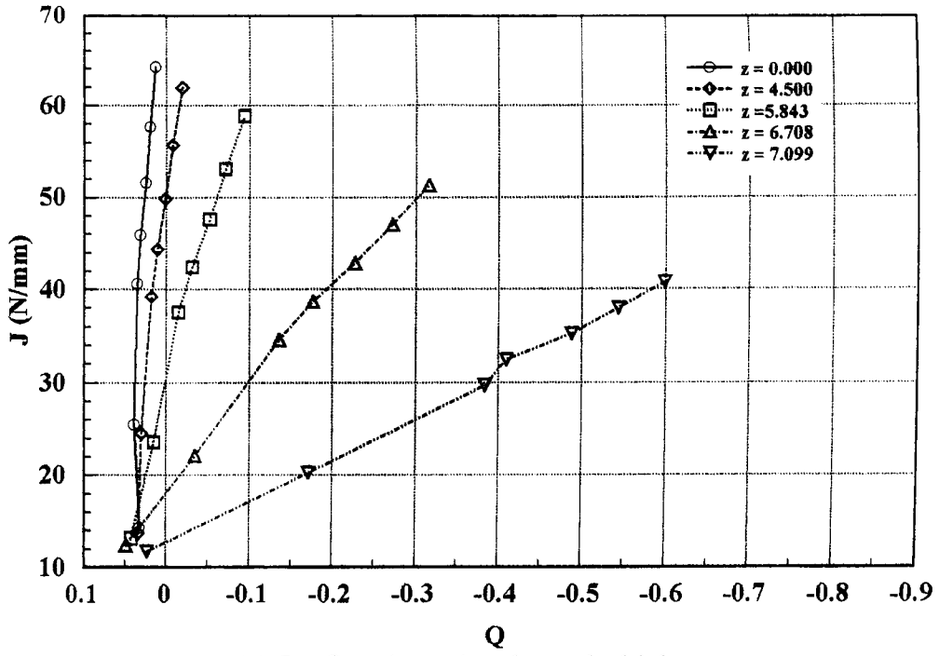

(c) J – Q trajectories through thickness

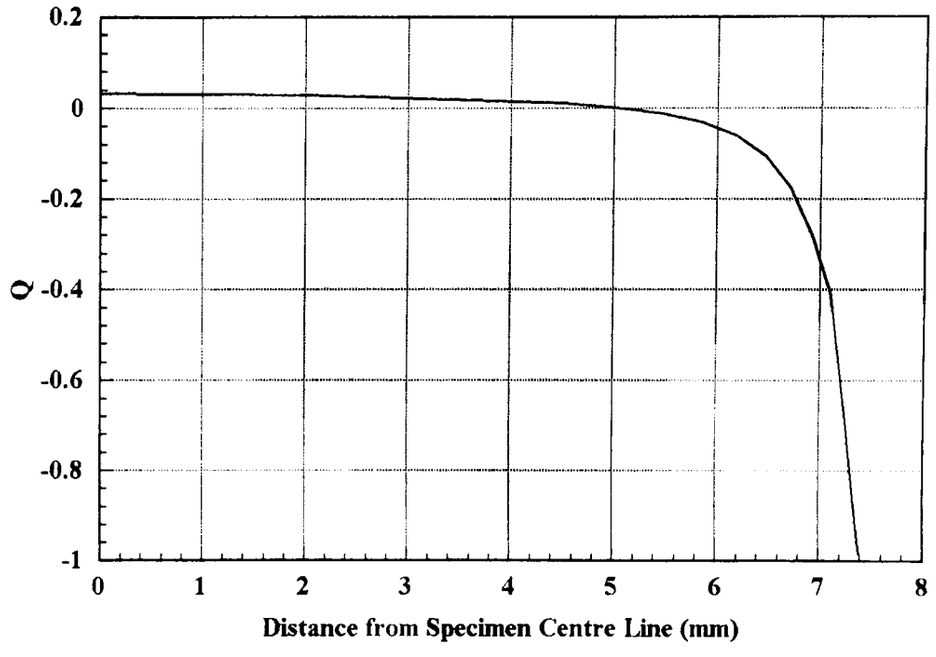

(d) Variation of Q through thickness

Fig 6.21 Analysis results 15 mm thick specimen

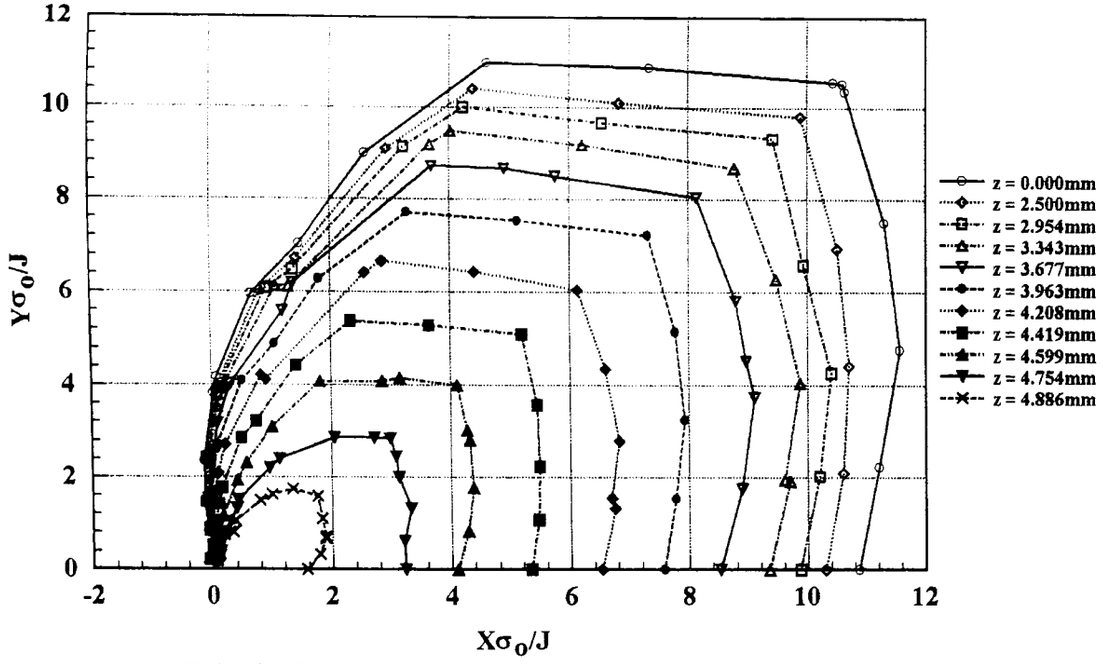

(a) Principal stress contours through thickness; σ/σ_o = 2.0

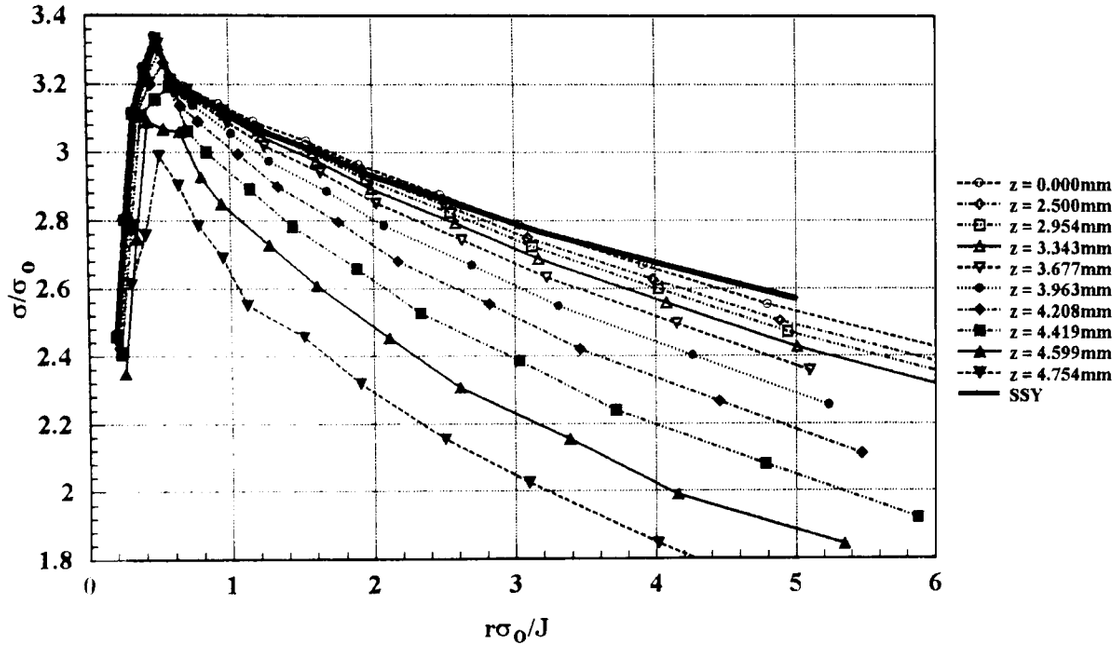

(b) Crack line opening mode stress

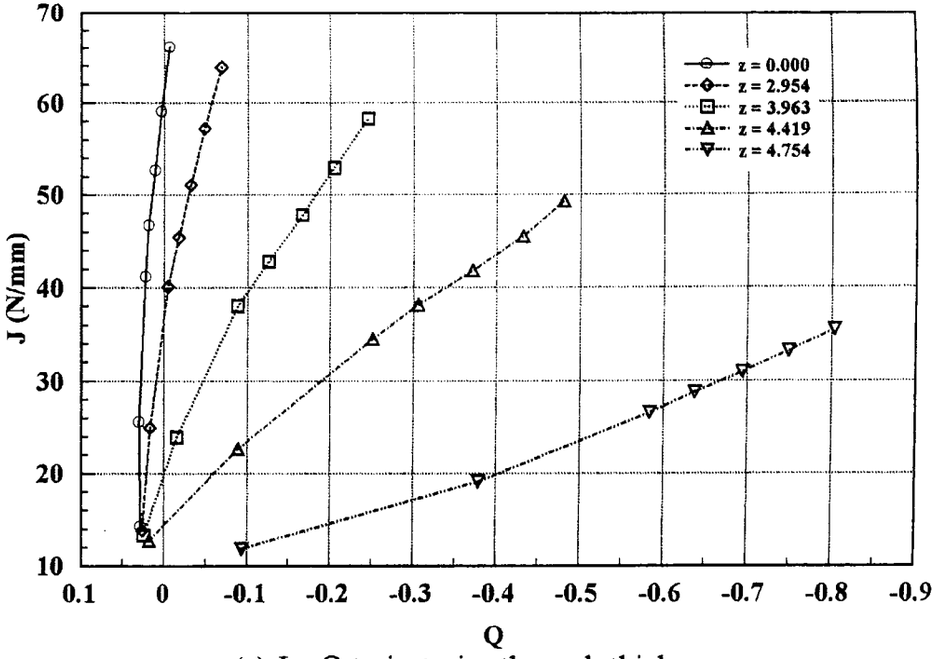

(c) J – Q trajectories through thickness

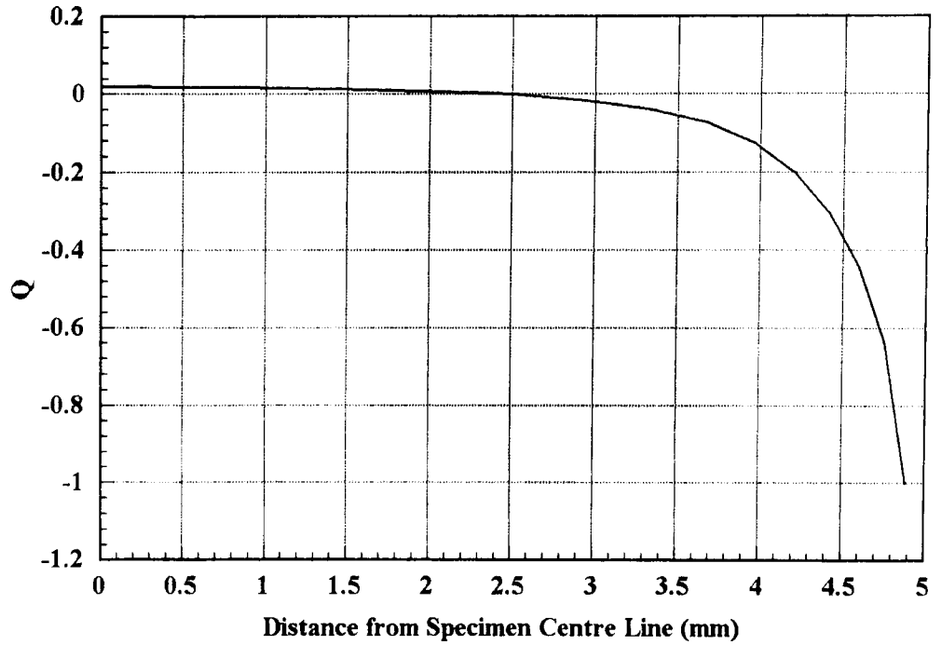

(d) Variation of Q through thickness

Fig 6.22 Analysis results 10 mm thick specimen

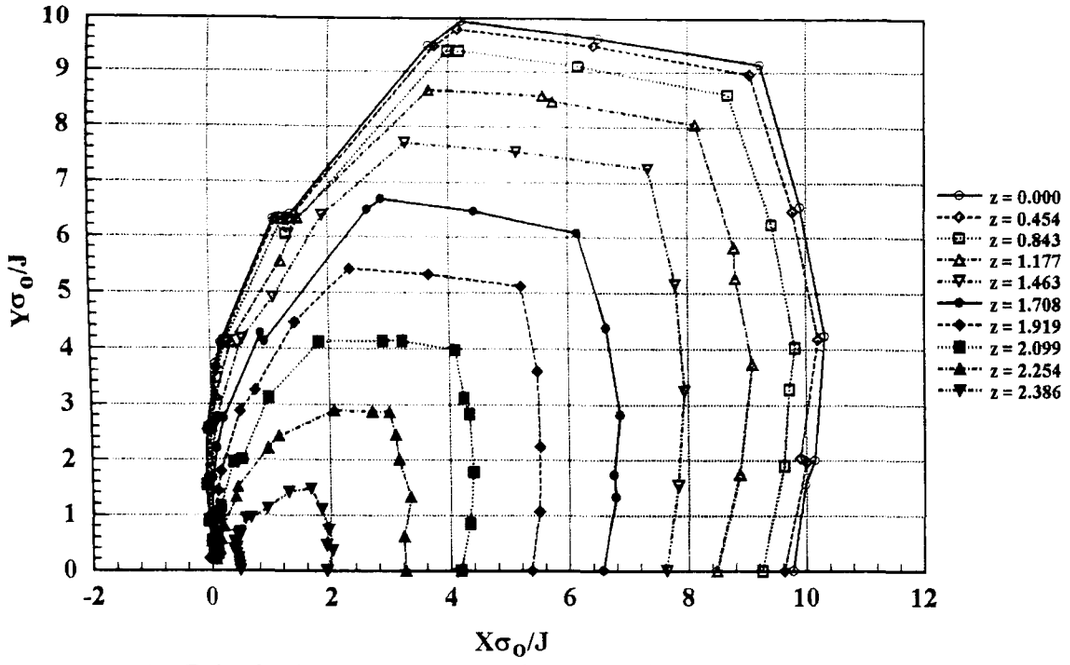

(a) Principal stress contours through thickness; $\sigma/\sigma_o = 2.0$

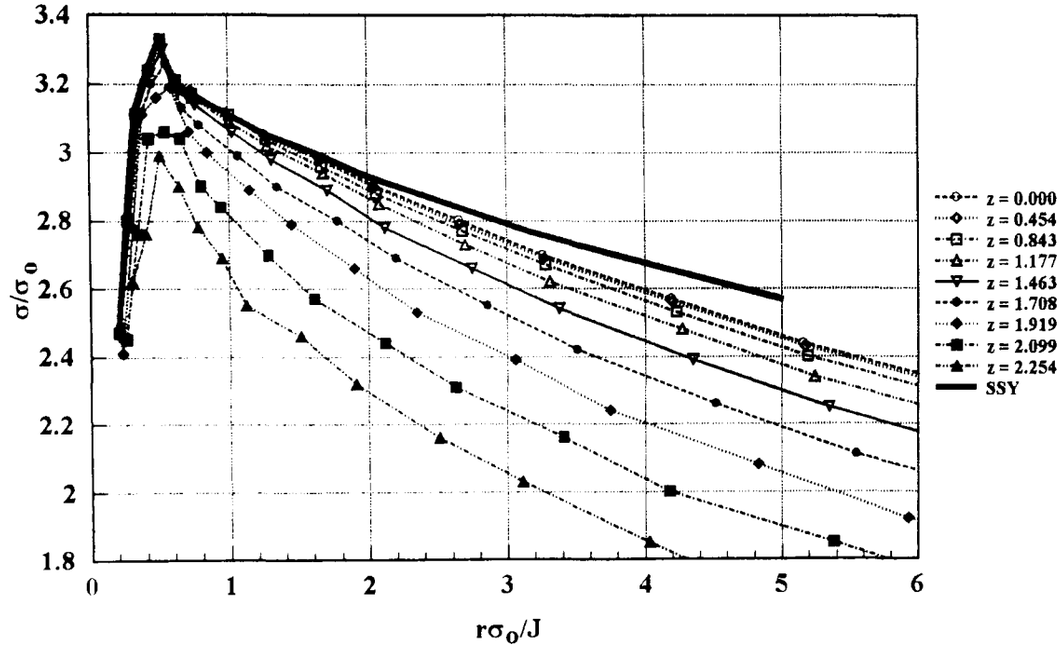

(b) Crack line opening mode stress

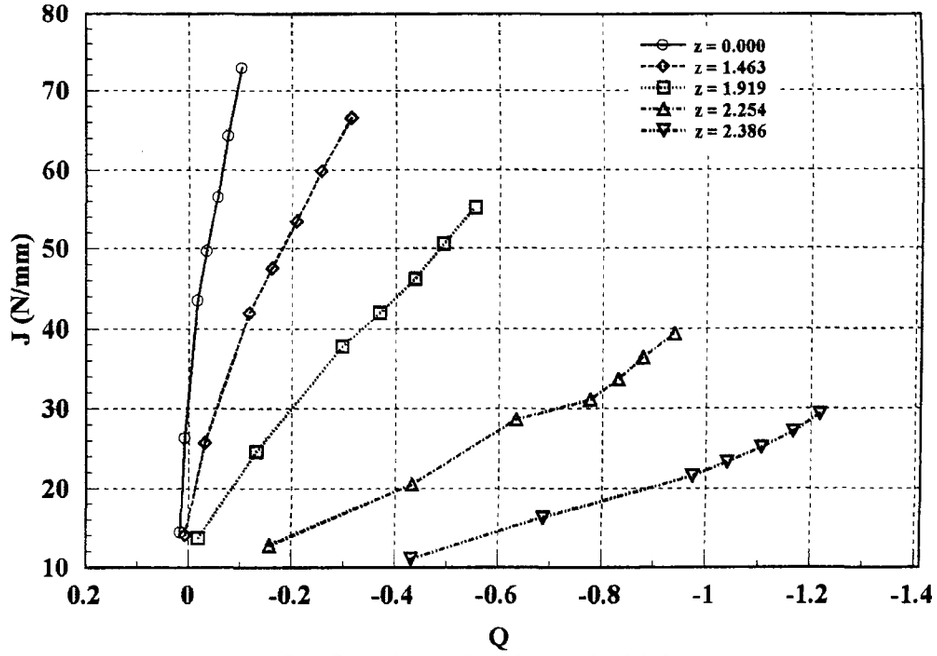

(c) J – Q trajectories through thickness

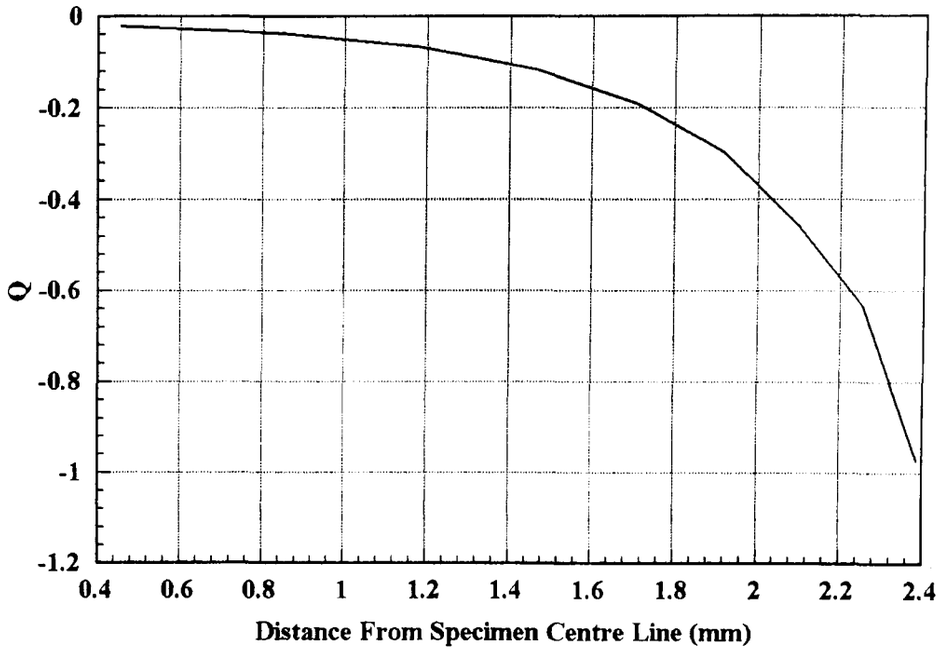

(d) Variation of Q through thickness

Fig 6.23 Analysis results 5 mm thick specimen

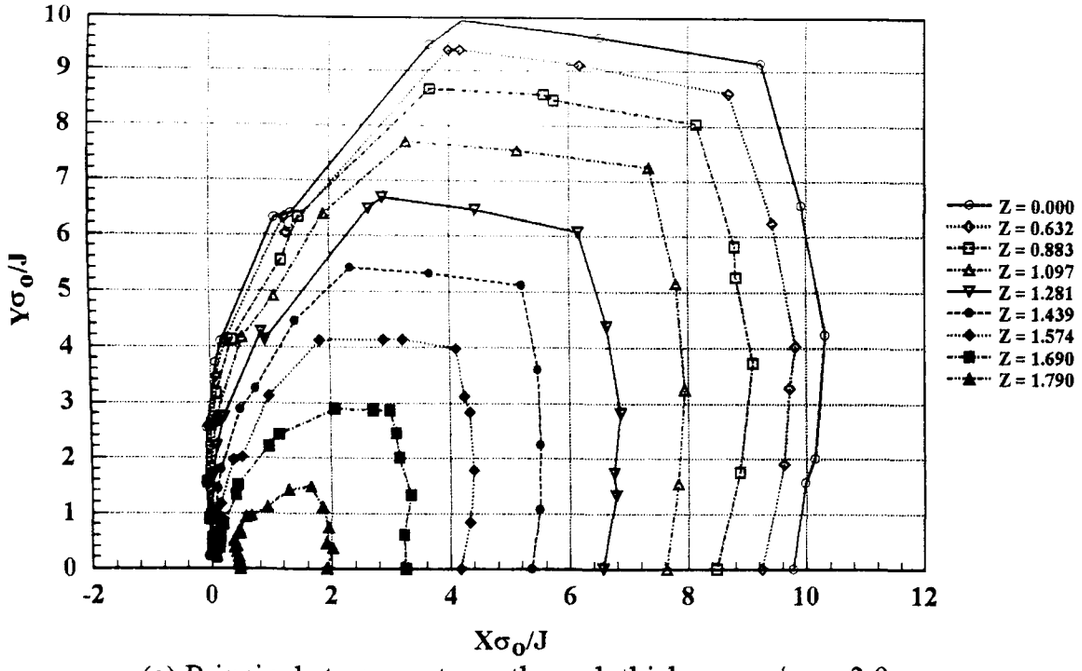

(a) Principal stress contours through thickness; $\sigma/\sigma_o = 2.0$

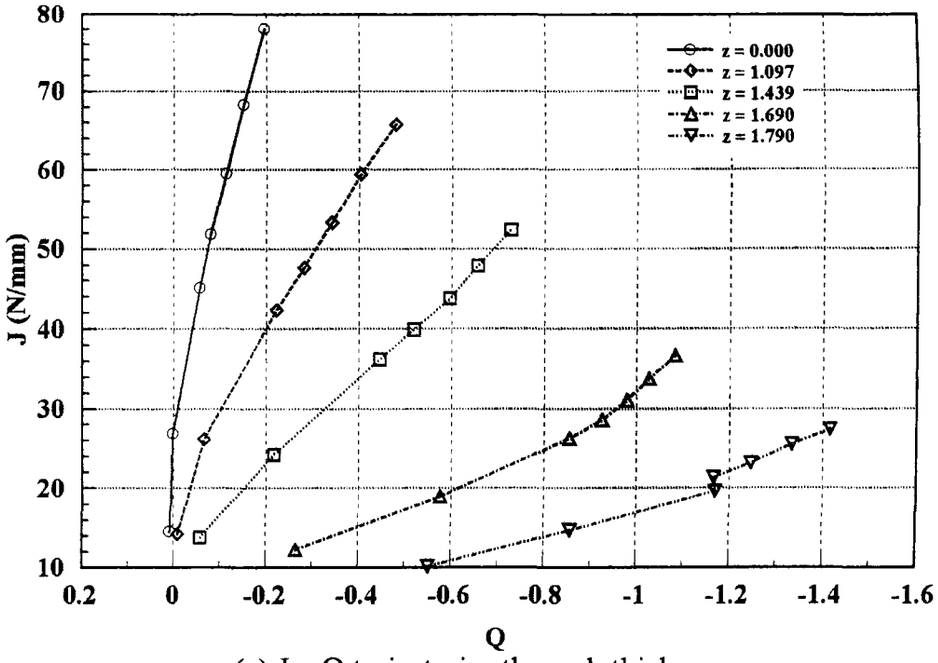

(c) J – Q trajectories through thickness

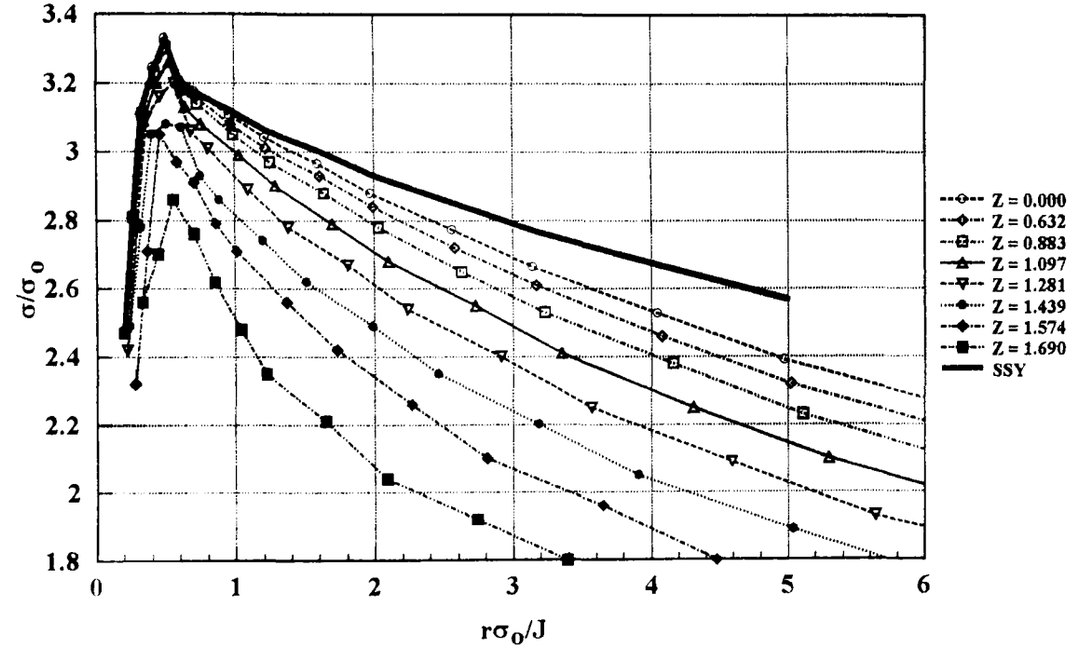

(b) Crack line opening mode stress

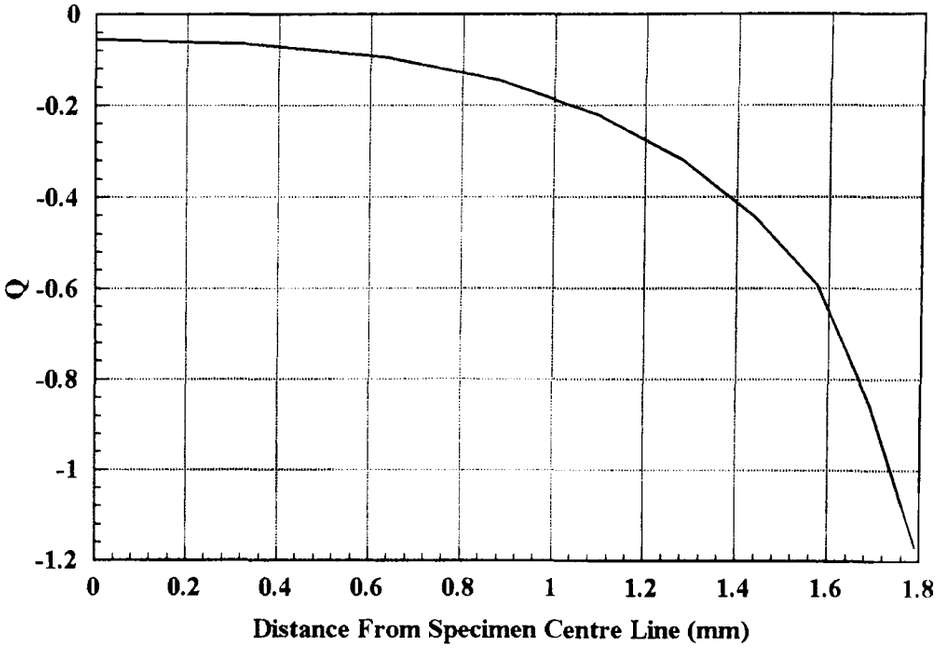

(d) Variation of Q through thickness

Fig 6.24 Analysis results 3.75 mm thick specimen

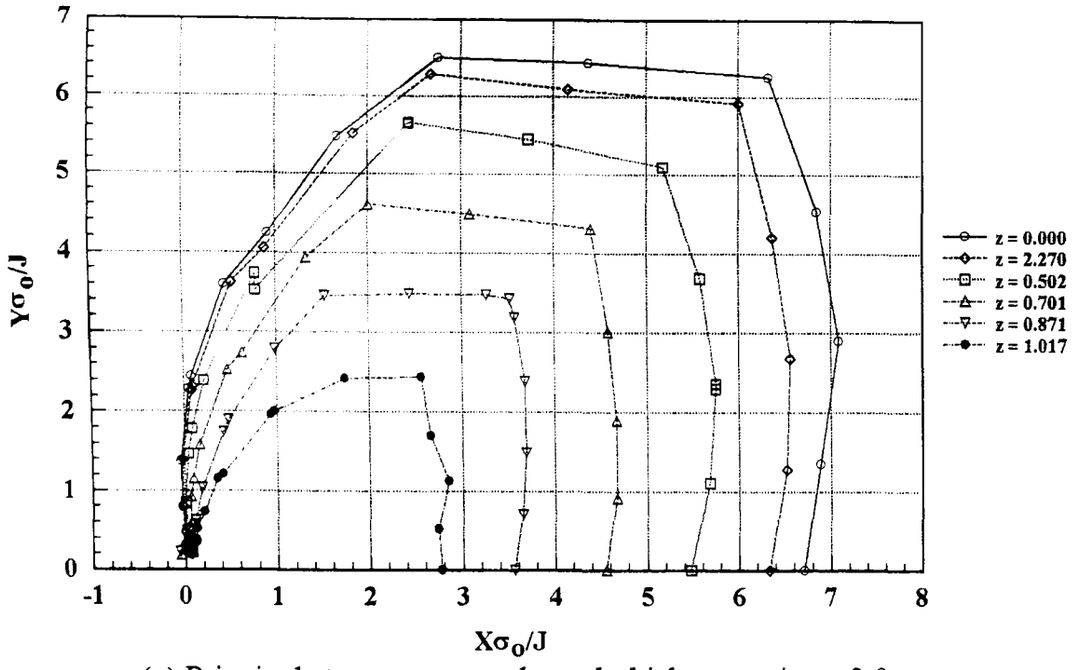

(a) Principal stress contours through thickness; $\sigma/\sigma_o = 2.0$

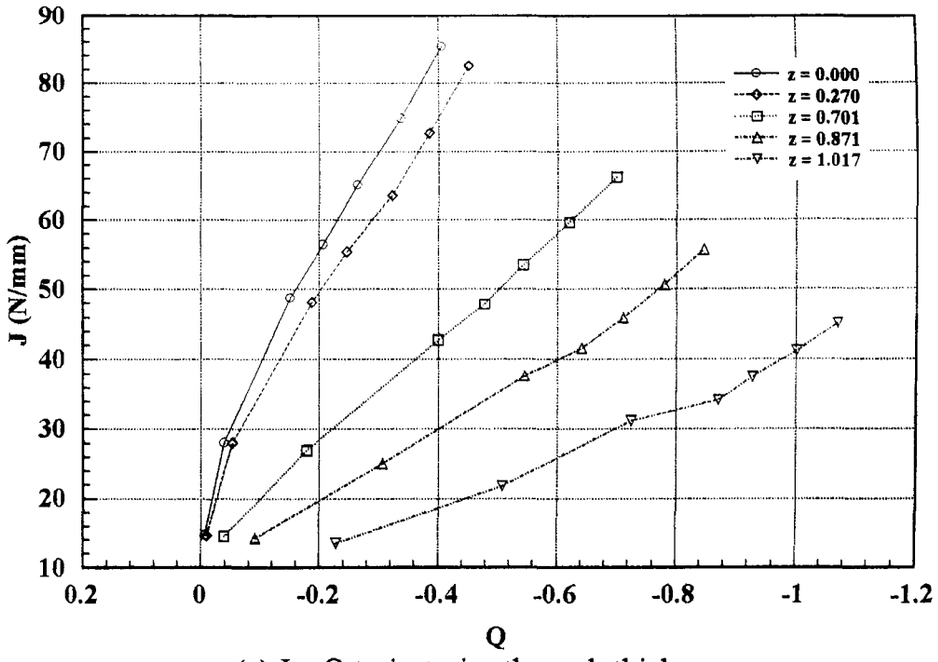

(c) J – Q trajectories through thickness

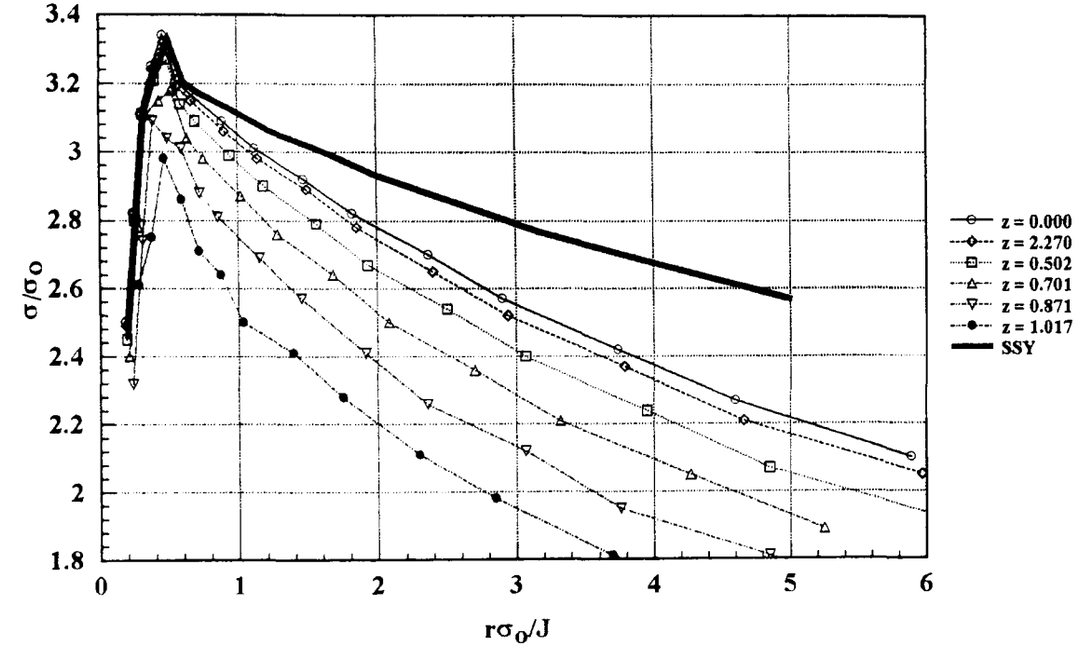

(b) Crack line opening mode stress

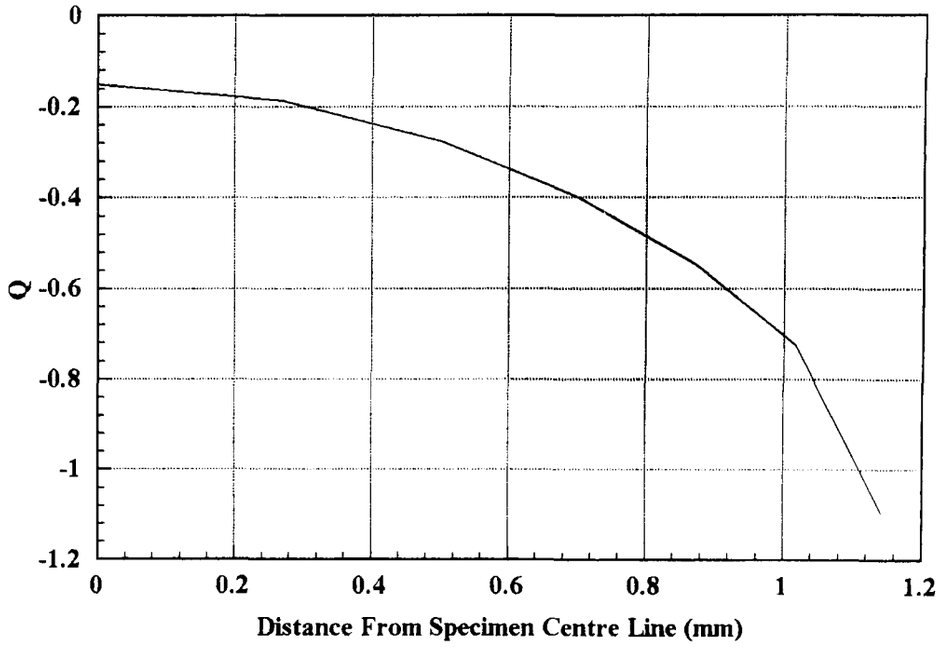

(d) Variation of Q through thickness

Fig 6.25 Analysis results 2.5 mm thick specimen

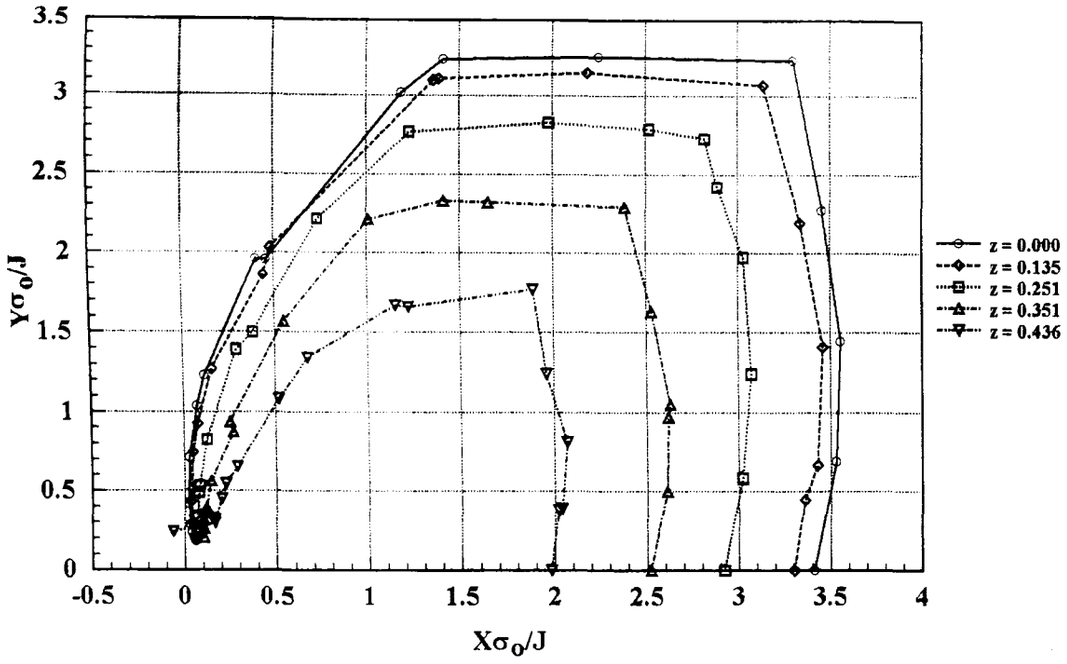

(a) Principal stress contours through thickness; $\sigma/\sigma_o = 2.0$

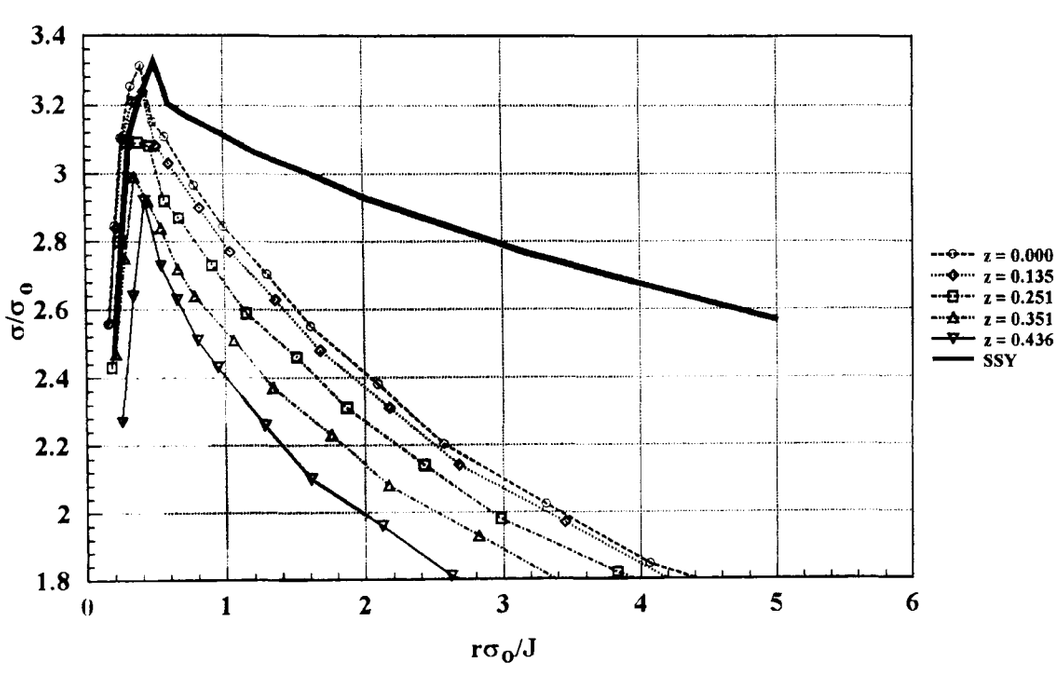

(b) Crack line opening mode stress

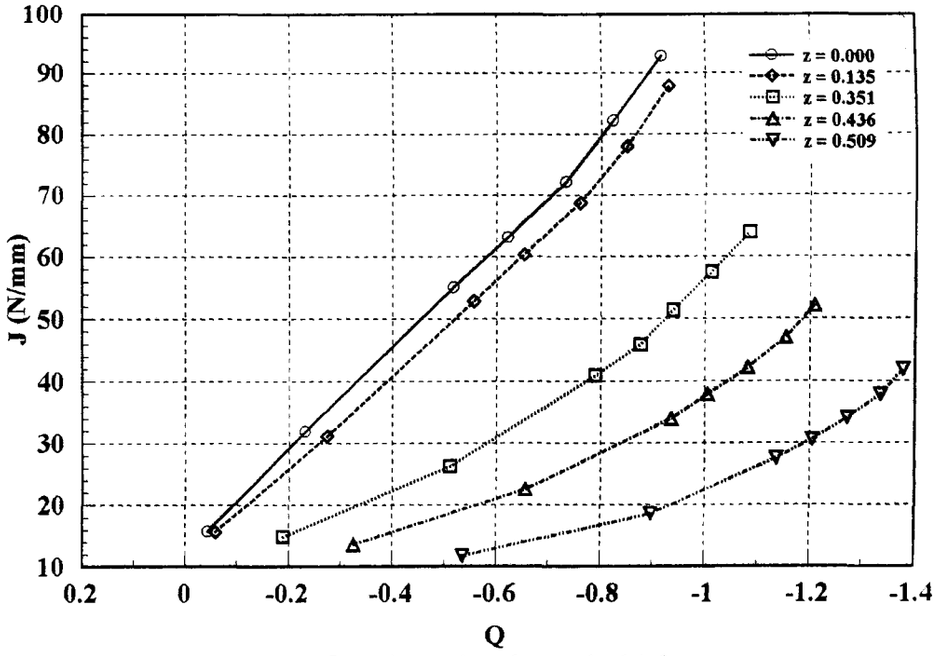

(c) J – Q trajectories through thickness

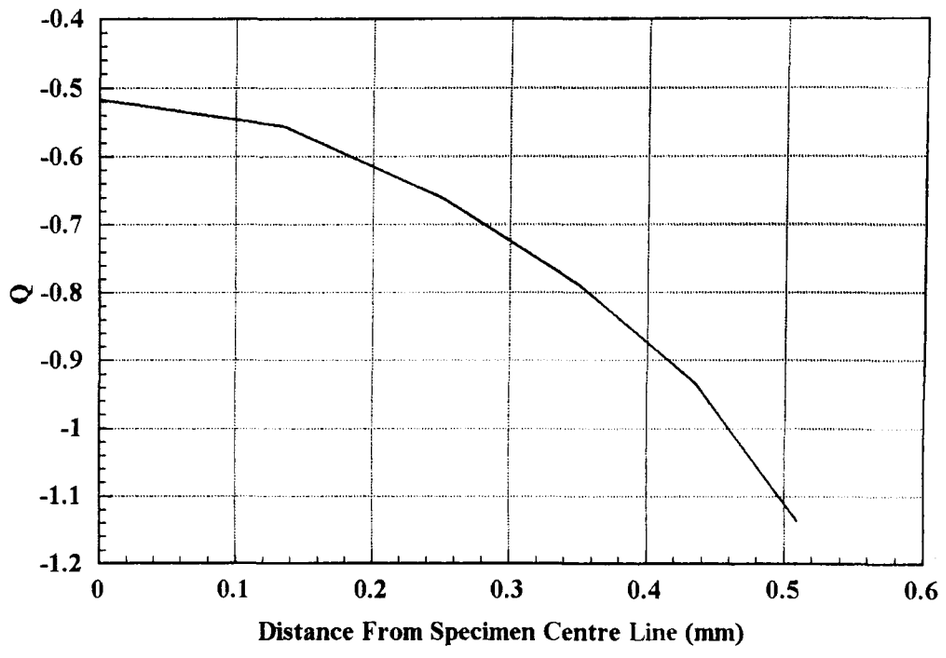

(d) Variation of Q through thickness

Fig 6.26 Analysis results 1.25 mm thick specimen

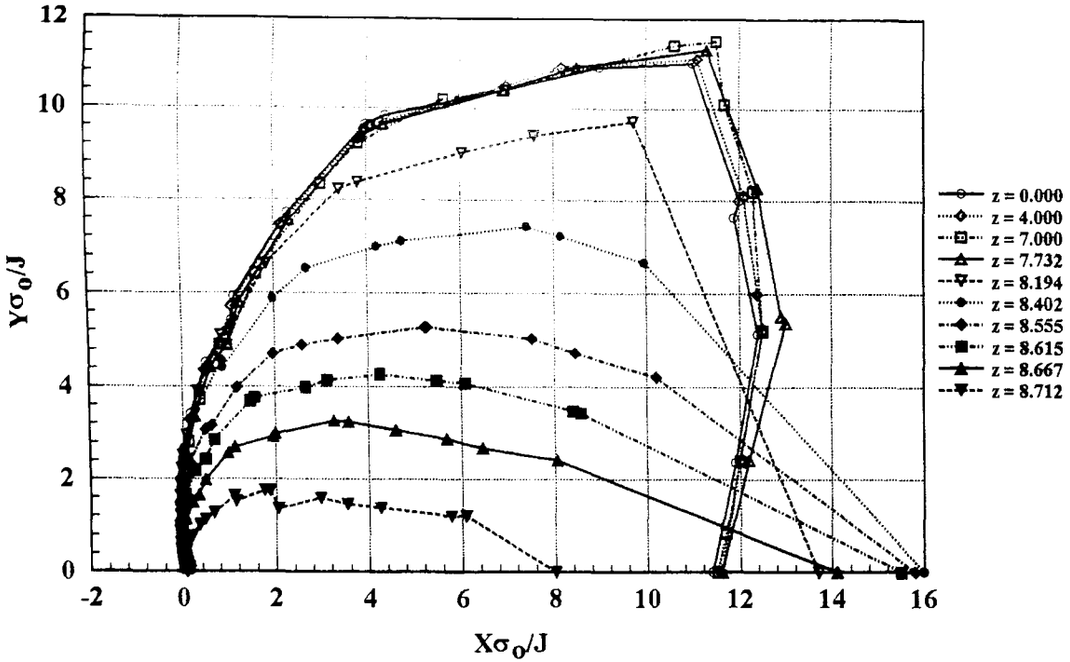

(a) Principal stress contours through thickness; $\sigma/\sigma_o = 2.0$

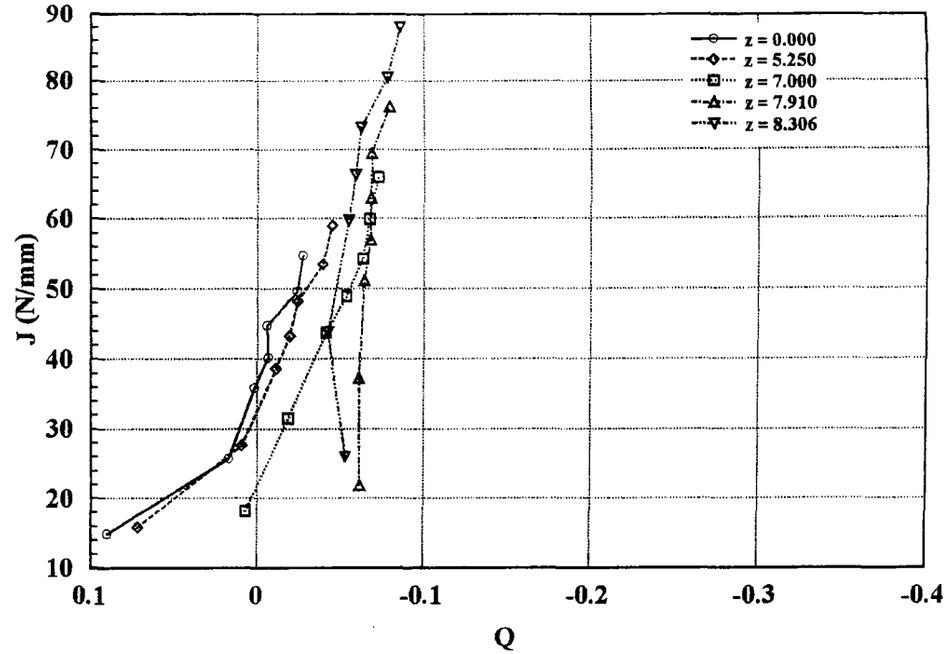

(c) J – Q trajectories through thickness

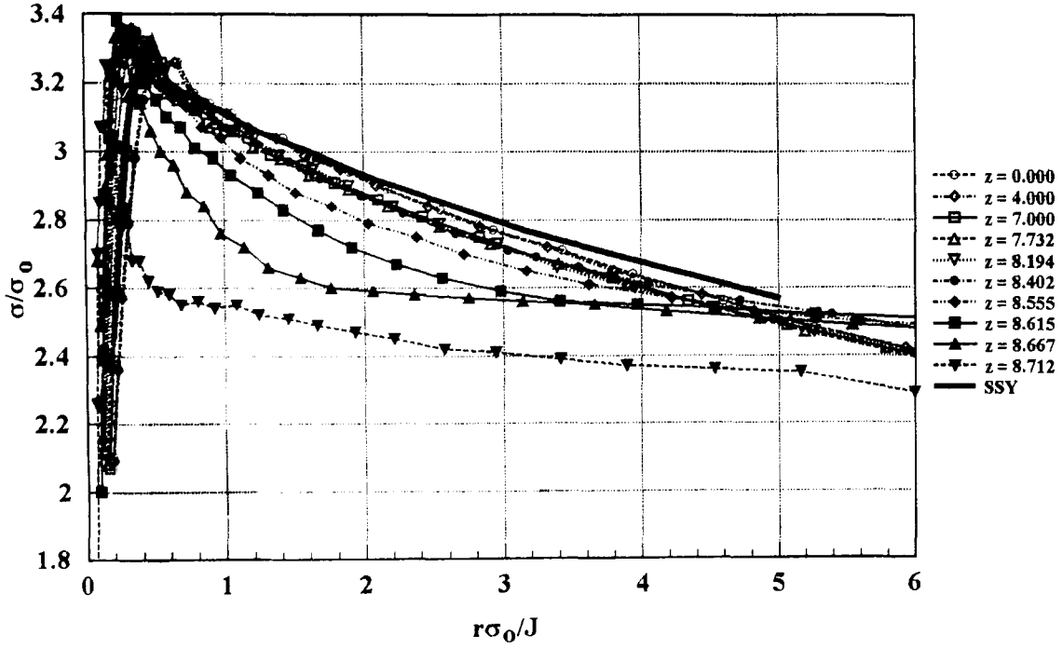

(b) Crack line opening mode stress

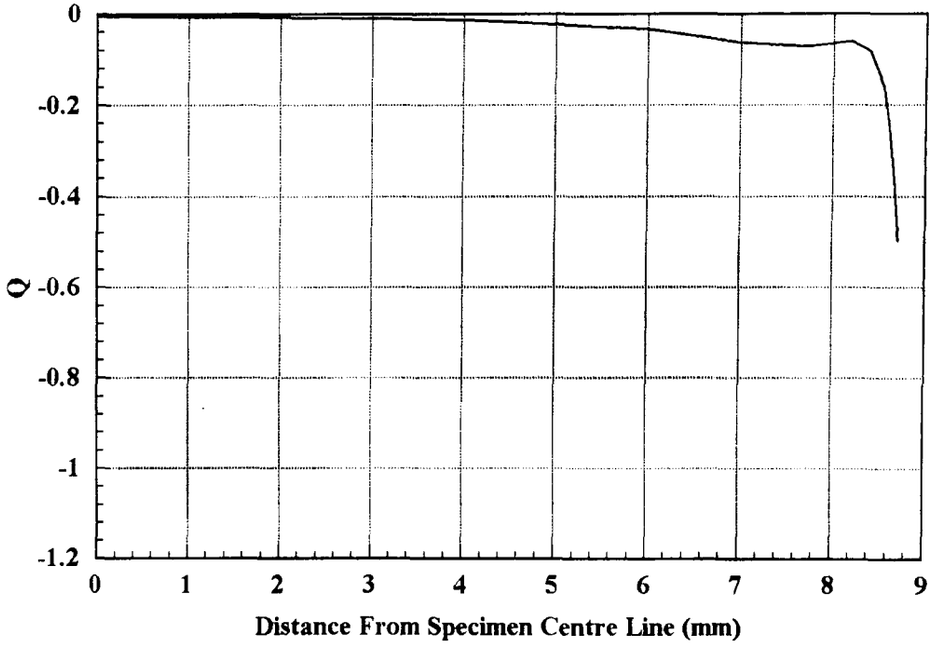

(d) Variation of Q through thickness

Fig 6.27 Analysis results; 25 mm thick side grooved specimen

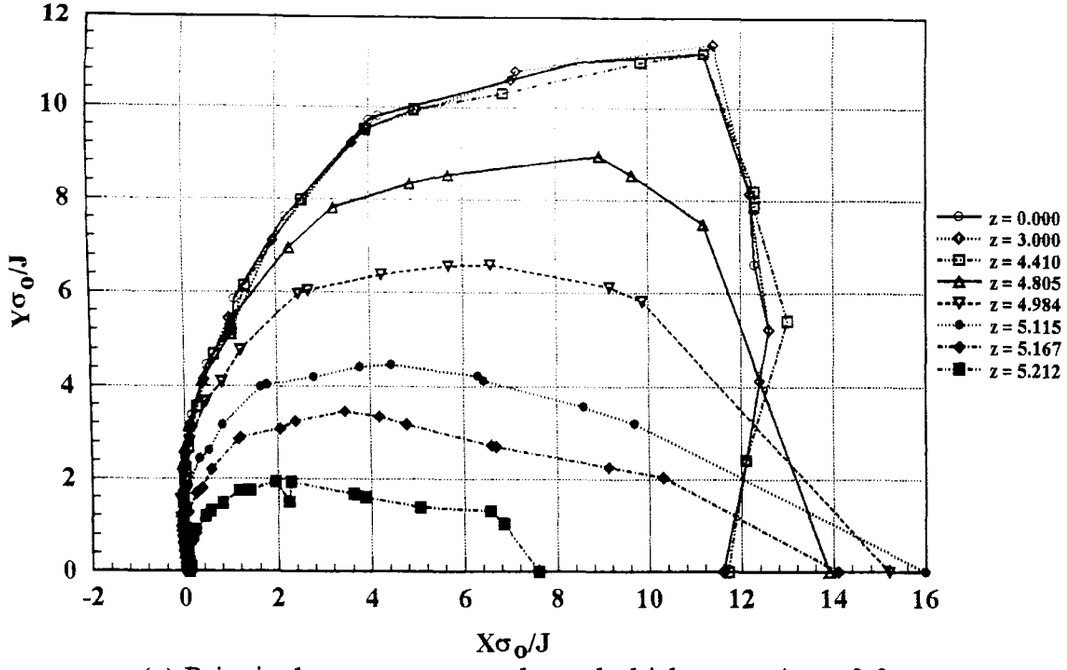

(a) Principal stress contours through thickness; $\sigma/\sigma_o = 2.0$

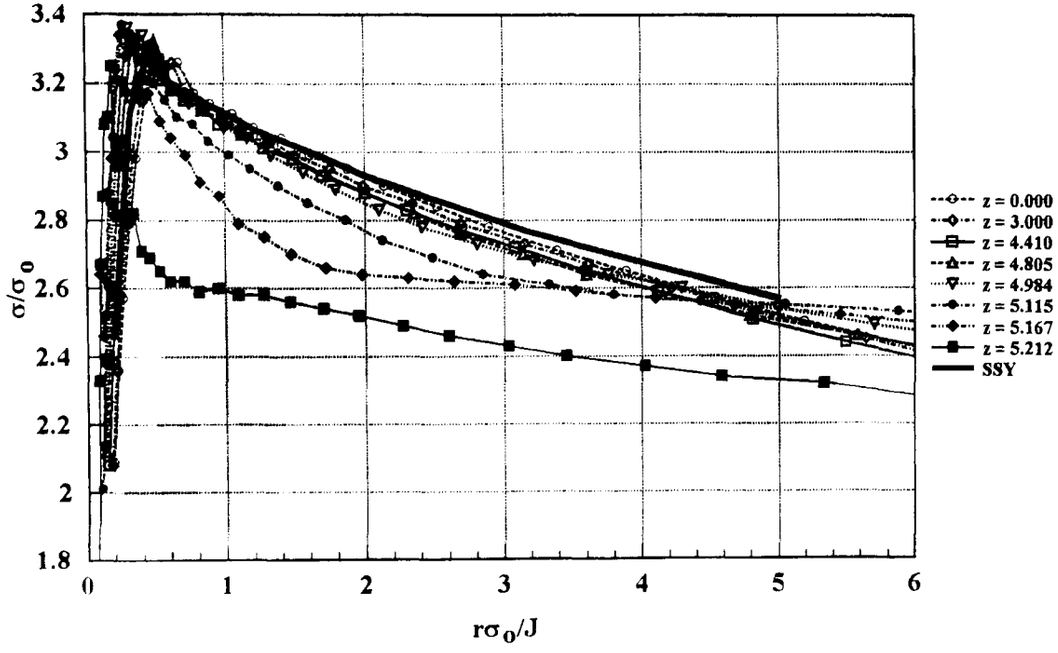

(b) Crack line opening mode stress

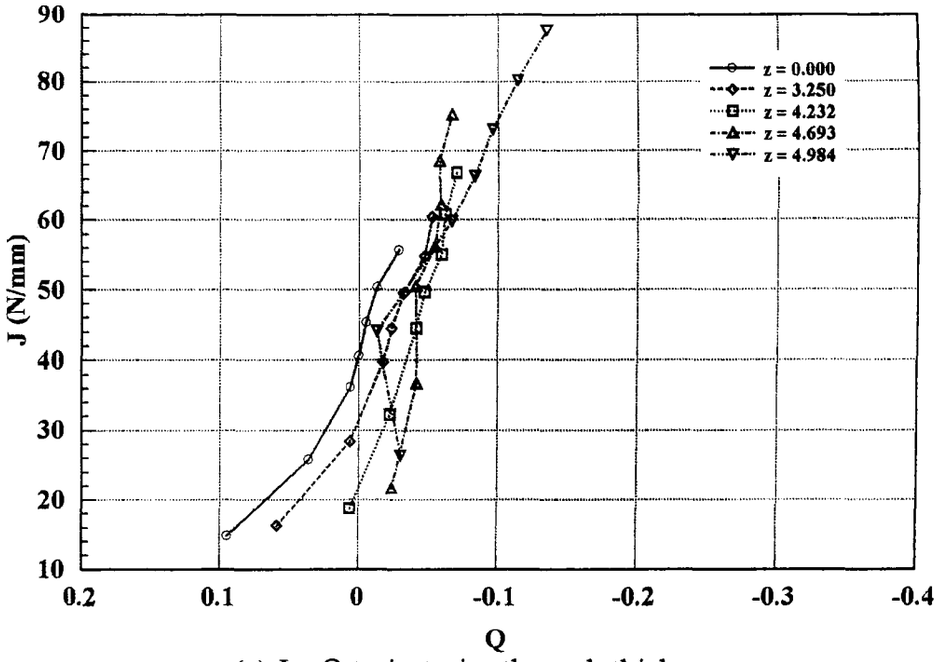

(c) J – Q trajectories through thickness

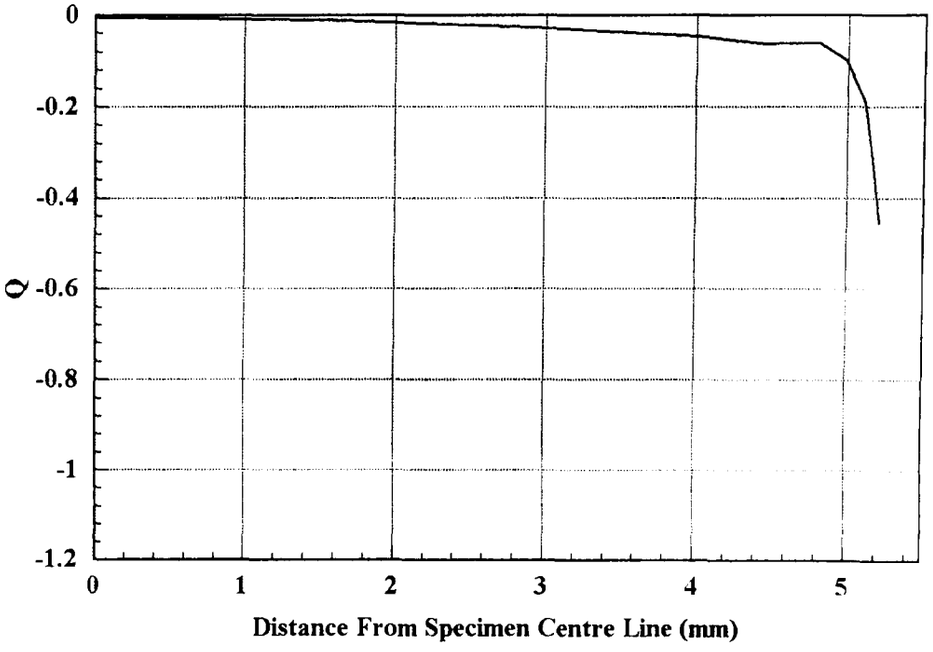

(d) Variation of Q through thickness

Fig 6.28 Analysis results; 15 mm thick side grooved specimen

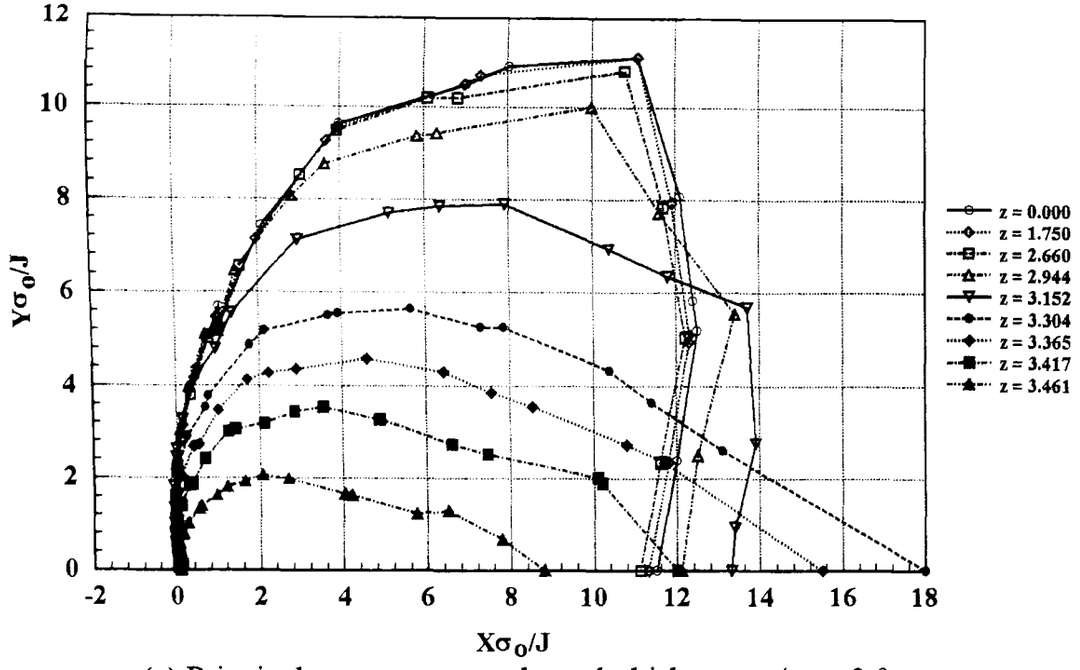

(a) Principal stress contours through thickness; $\sigma/\sigma_o = 2.0$

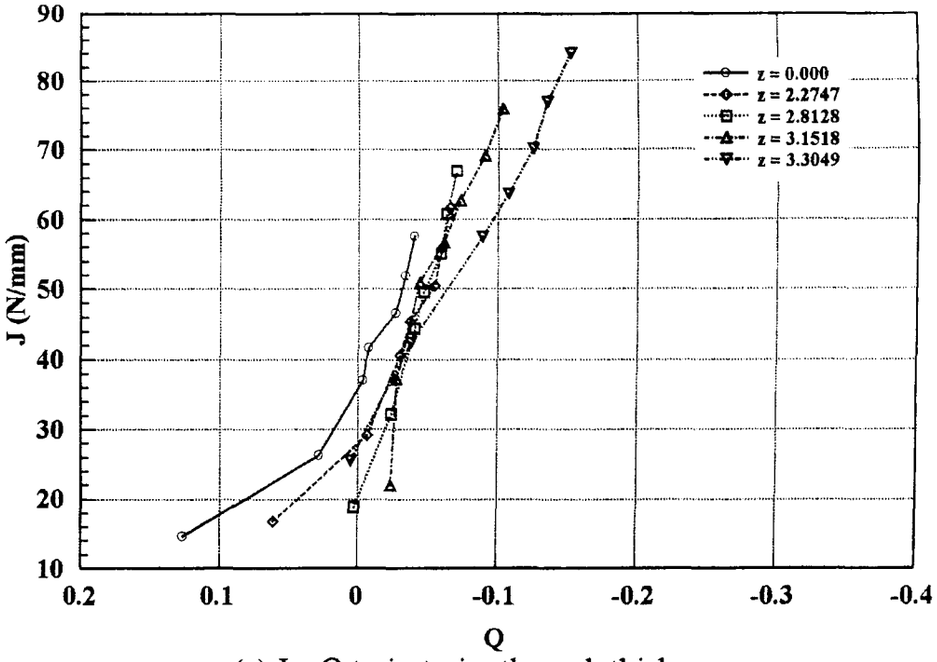

(c) J – Q trajectories through thickness

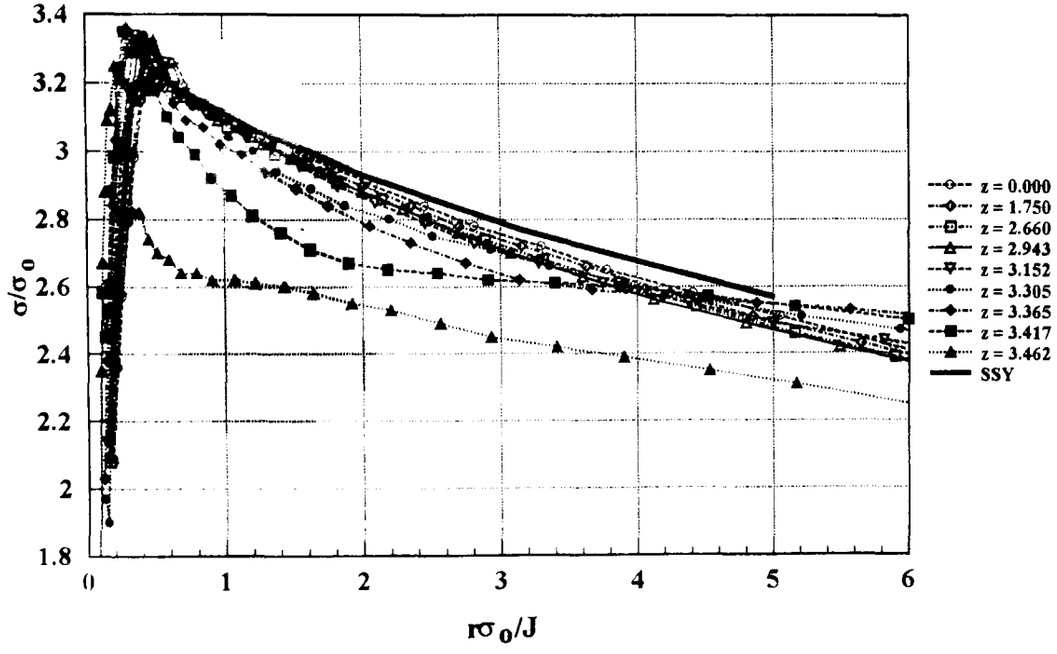

(b) Crack line opening mode stress

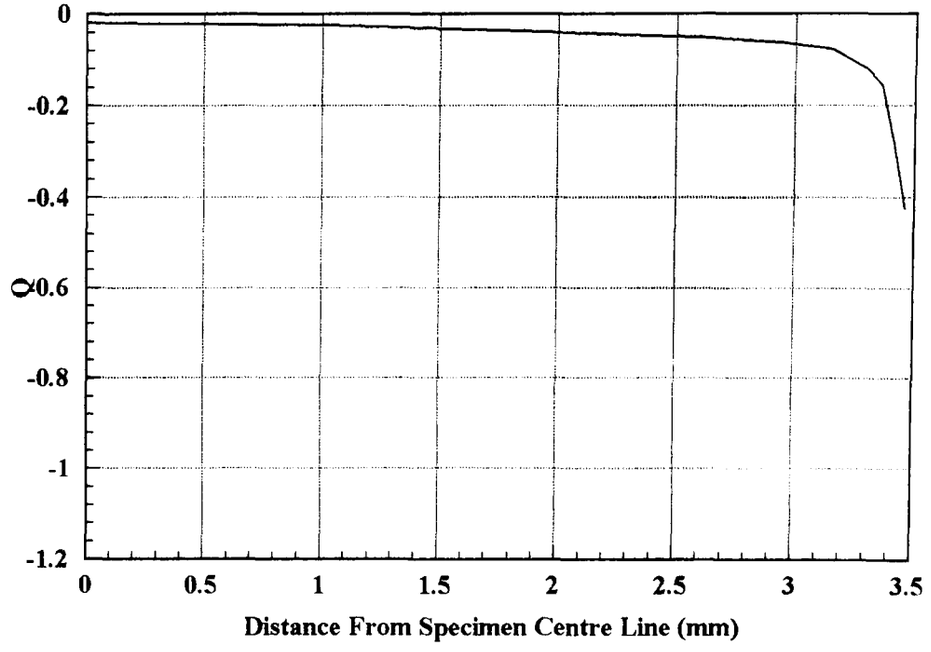

(d) Variation of Q through thickness

Fig 6.29 Analysis results; 10 mm thick side grooved specimen

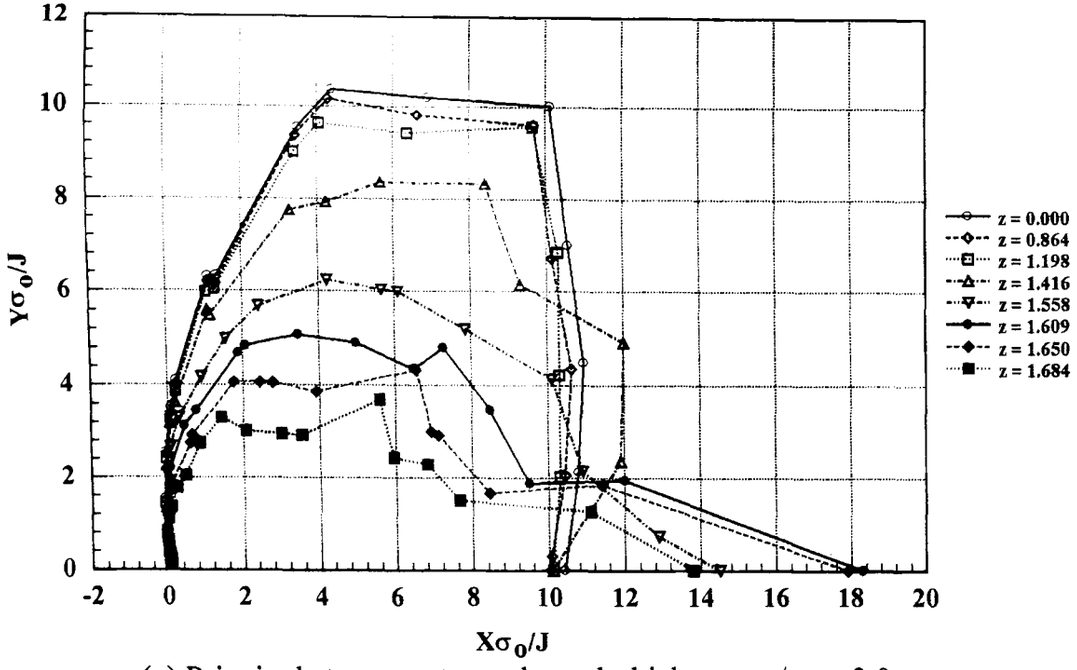

(a) Principal stress contours through thickness; $\sigma/\sigma_o = 2.0$

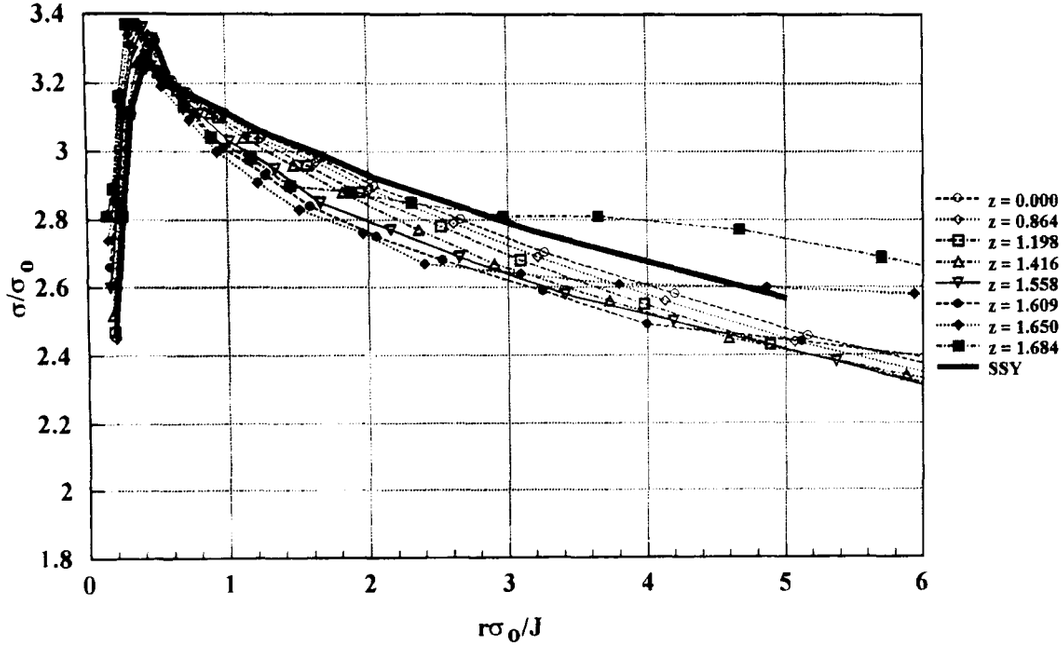

(b) Crack line opening mode stress

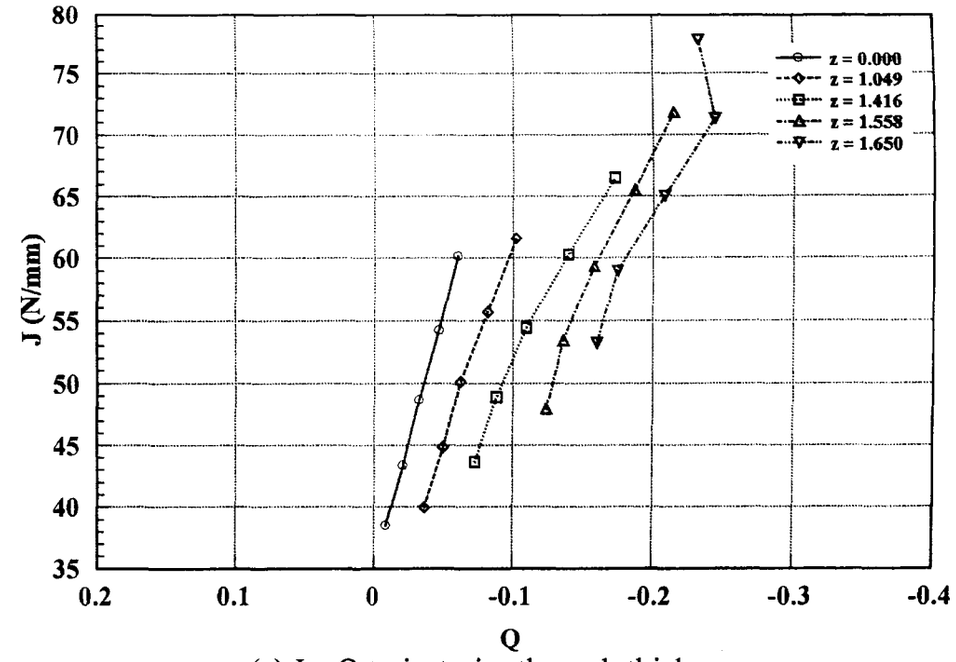

(c) J – Q trajectories through thickness

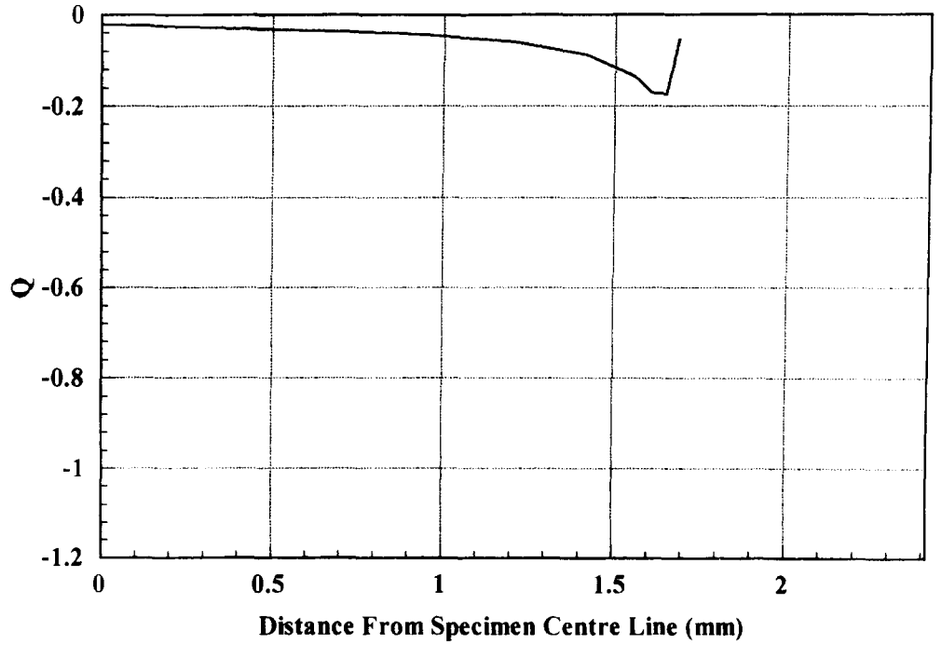

(d) Variation of Q through thickness

Fig 6.30 Analysis results; 5 mm thick side grooved specimen

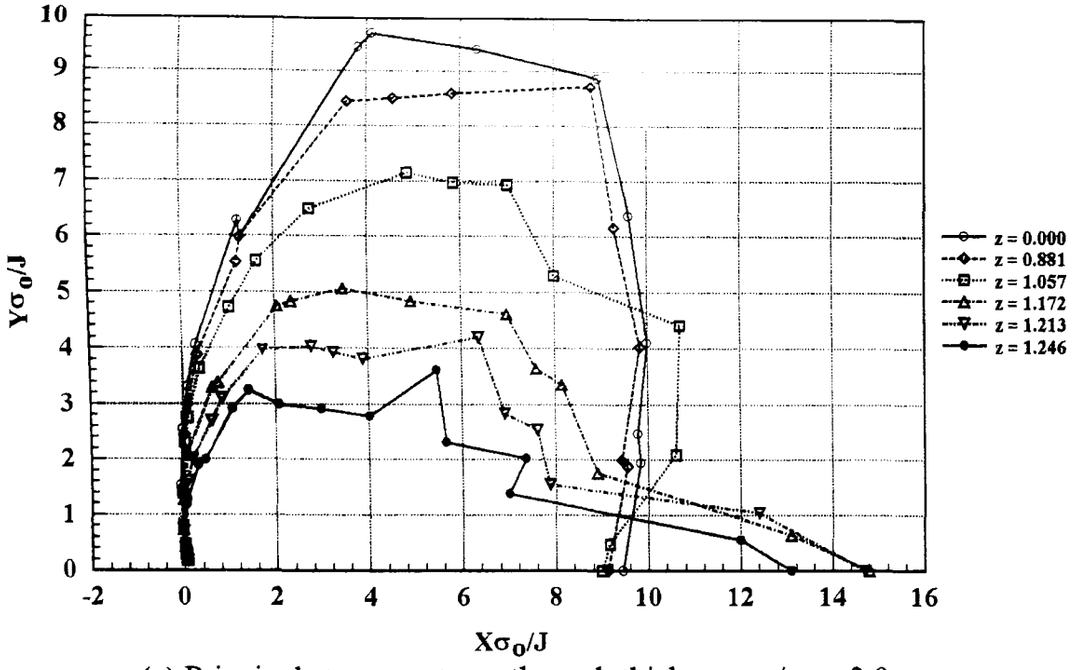

(a) Principal stress contours through thickness; $\sigma/\sigma_o = 2.0$

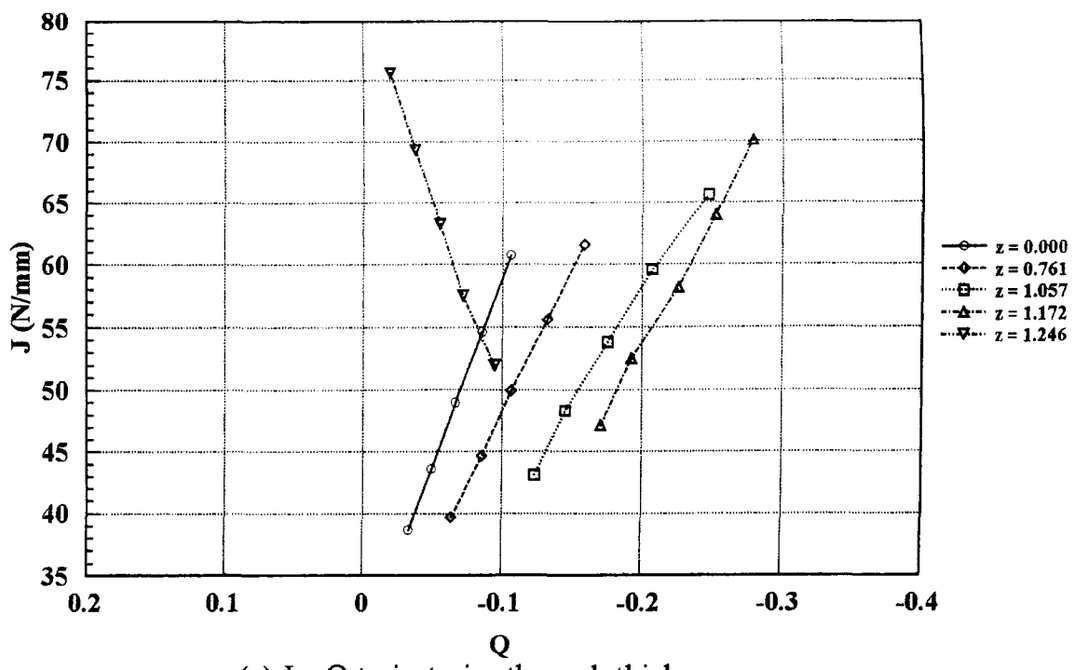

(c) J – Q trajectories through thickness

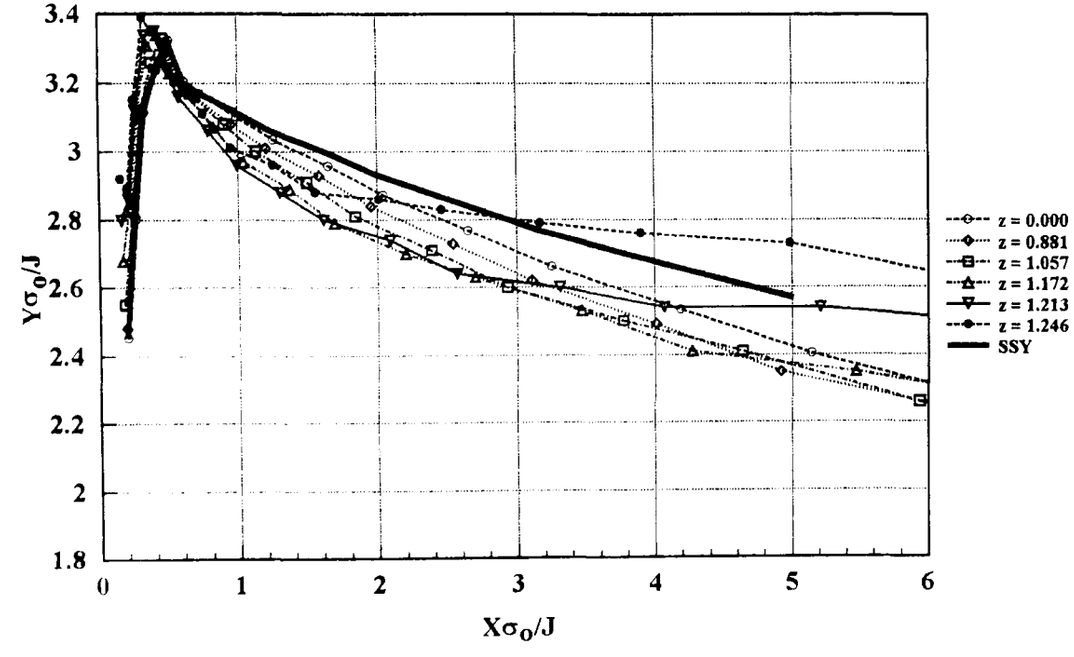

(b) Crack line opening mode stress

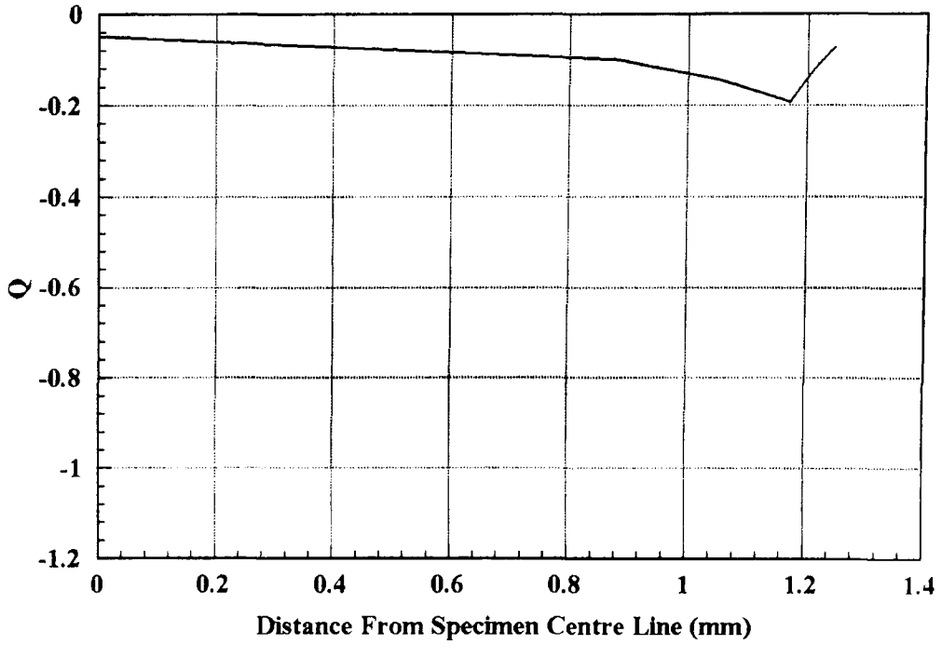

(d) Variation of Q through thickness

Fig 6.31 Analysis results; 3.75 mm thick side grooved specimen

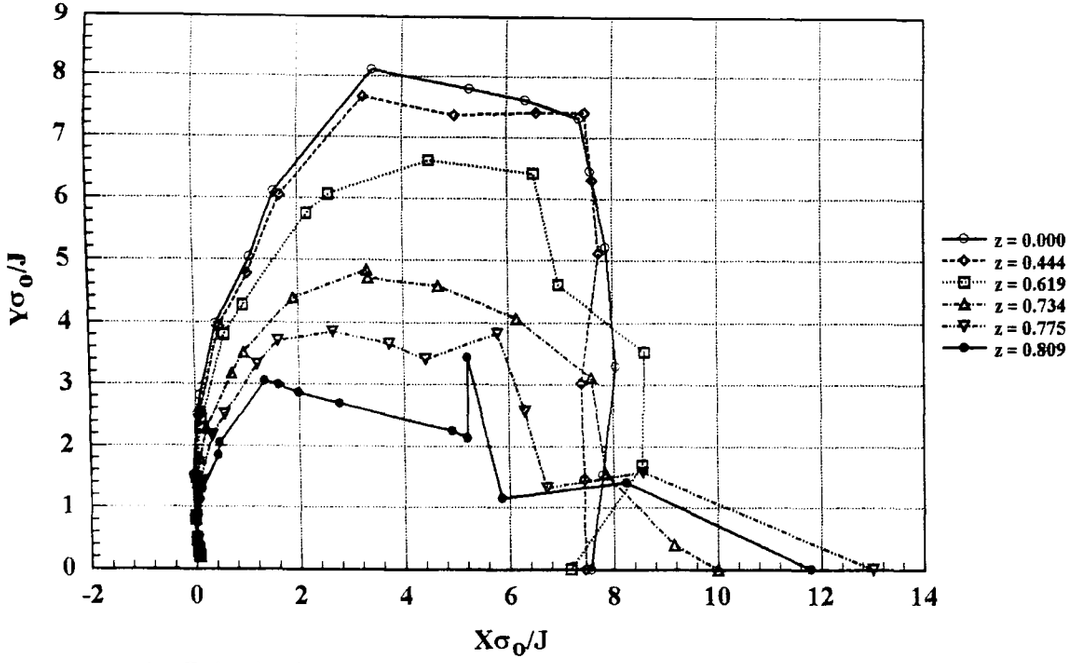

(a) Principal stress contours through thickness; $\sigma/\sigma_o = 2.0$

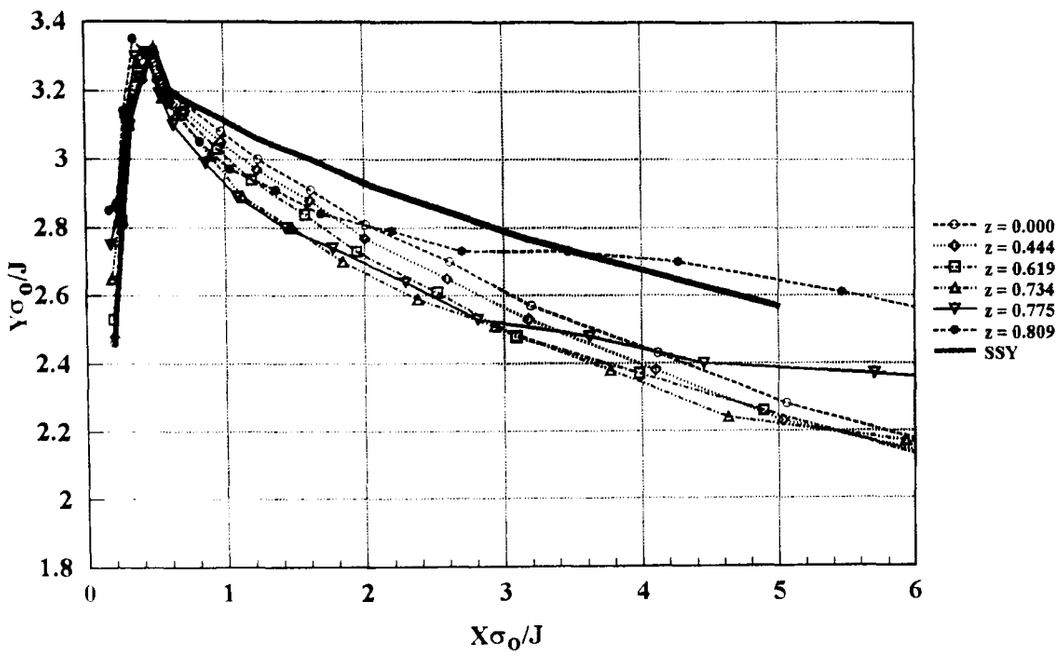

(b) Crack line opening mode stress

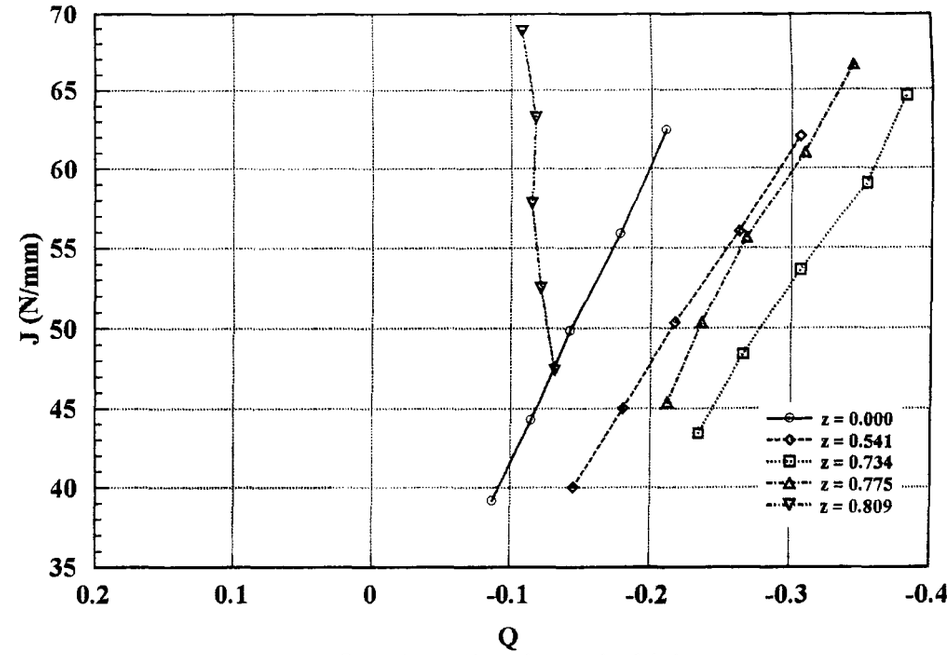

(c) J – Q trajectories through thickness

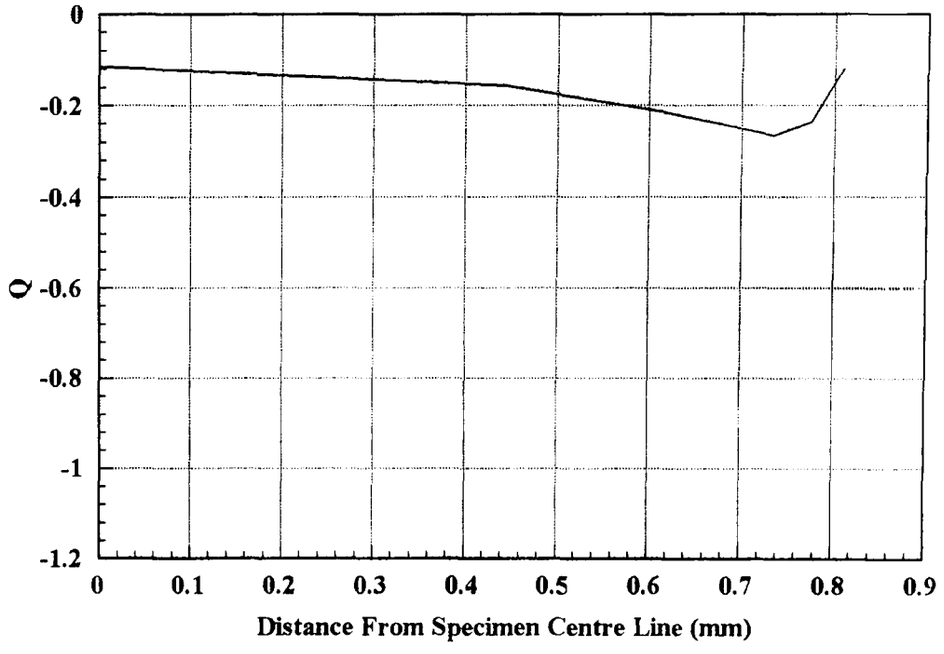

(d) Variation of Q through thickness

Fig 6.32 Analysis results; 2.5 mm thick side grooved specimen

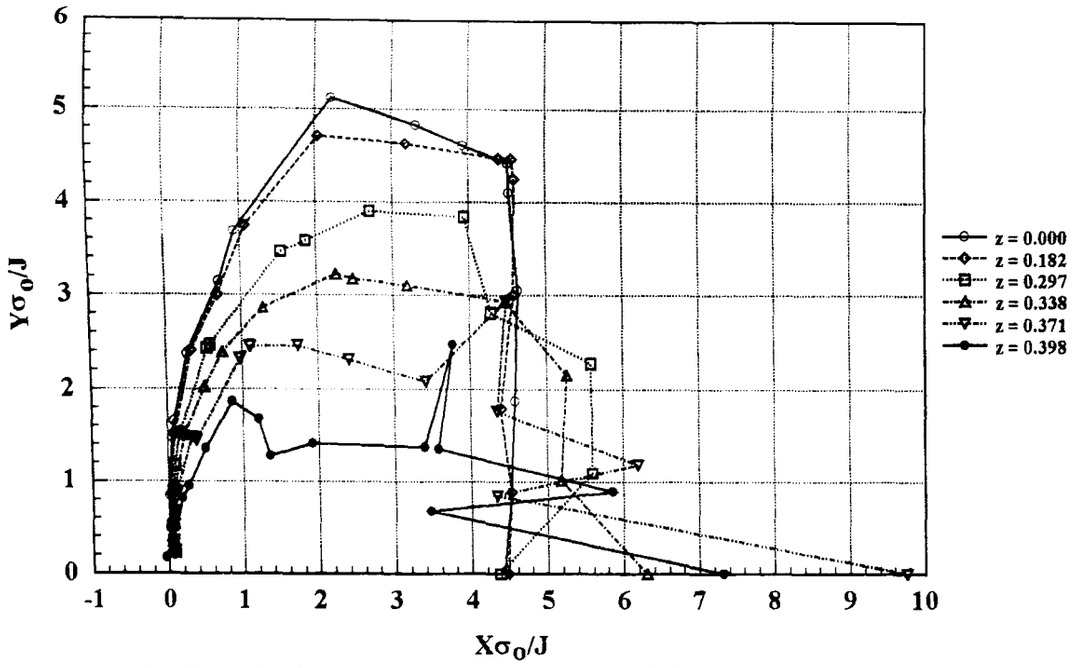

(a) Principal stress contours through thickness; $\sigma/\sigma_o = 2.0$

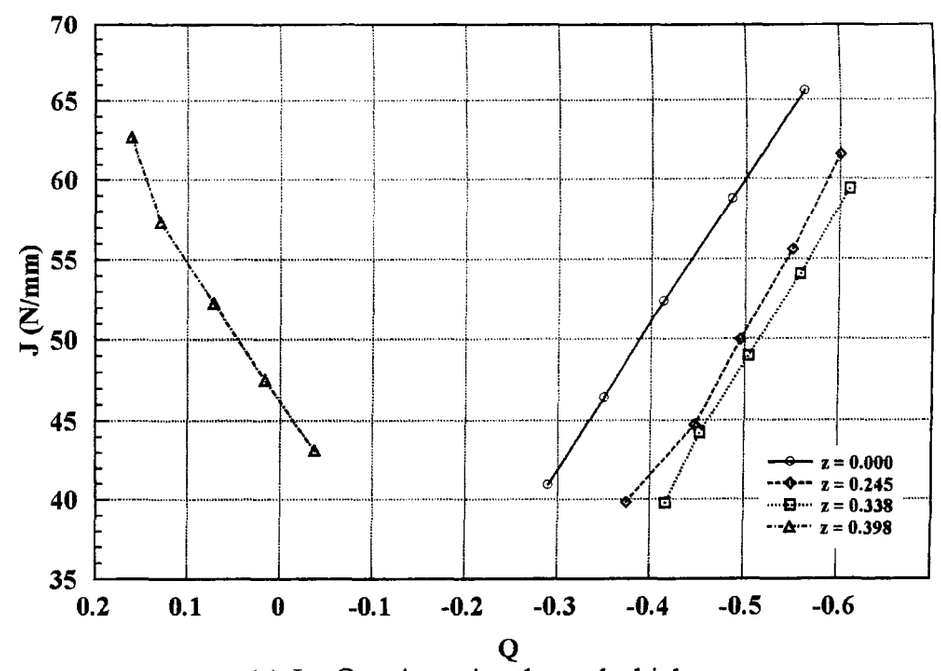

(c) J – Q trajectories through thickness

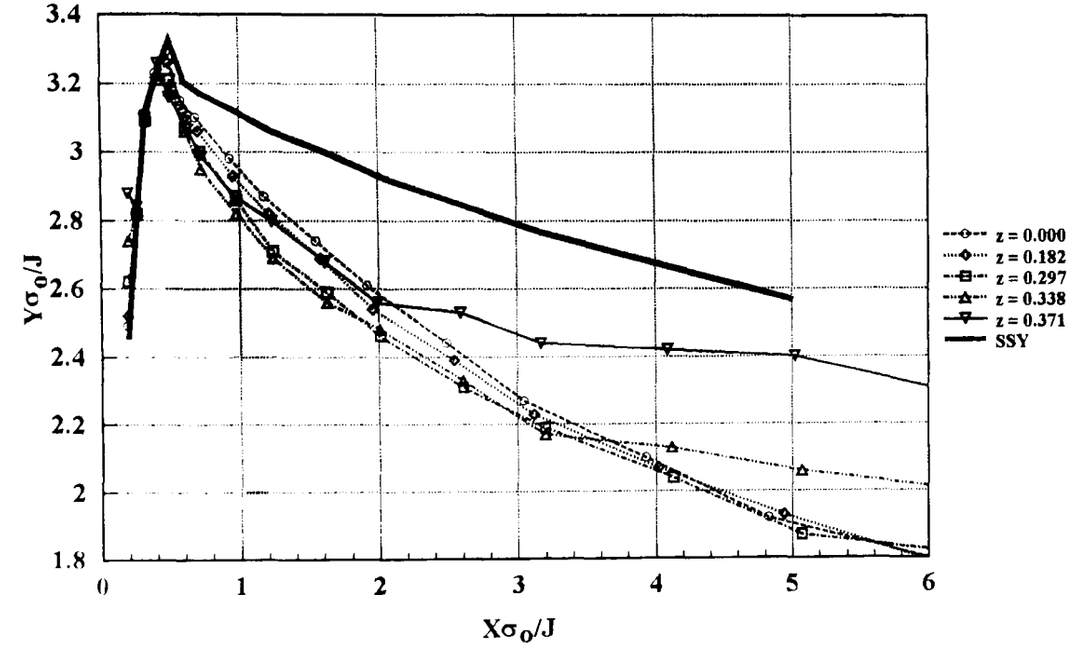

(b) Crack line opening mode stress

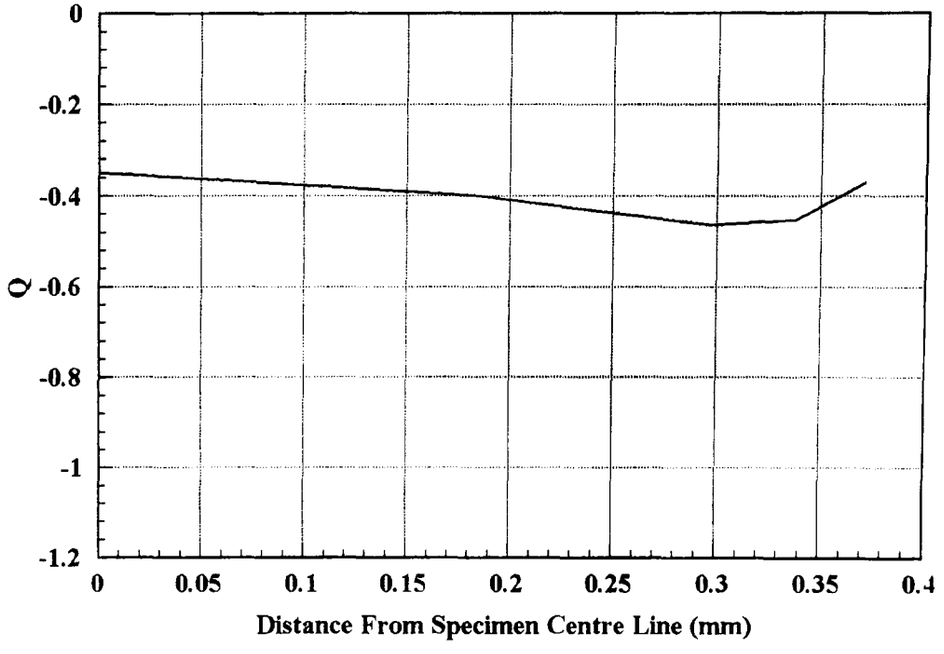

(d) Variation of Q through thickness

Fig 6.33 Analysis results; 1.25 mm thick side grooved specimen

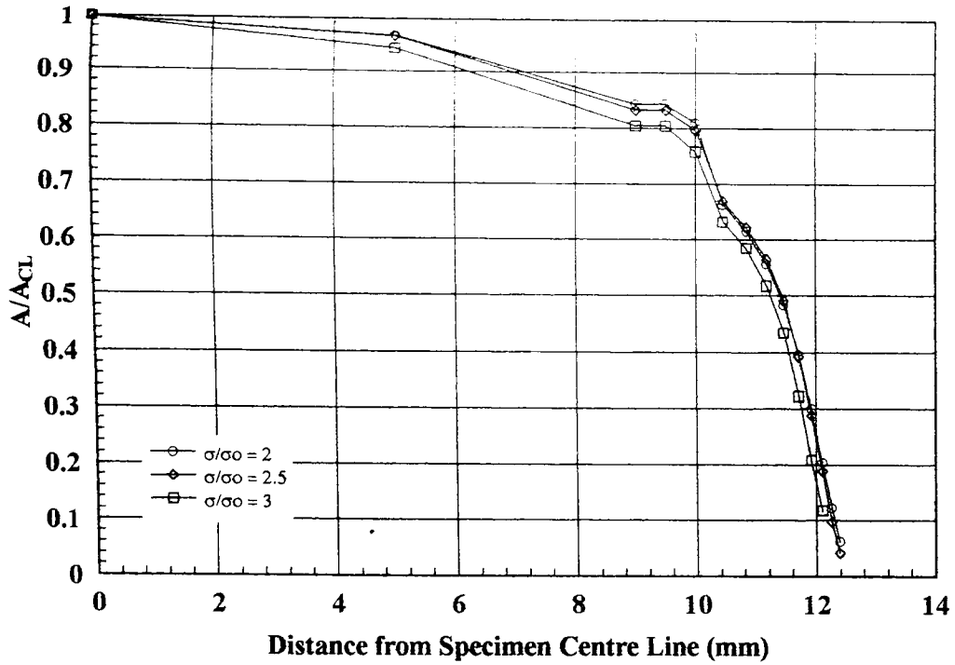

Fig. 6.34 Variation of A/A_{CL} through specimen thickness 25 mm thick specimen

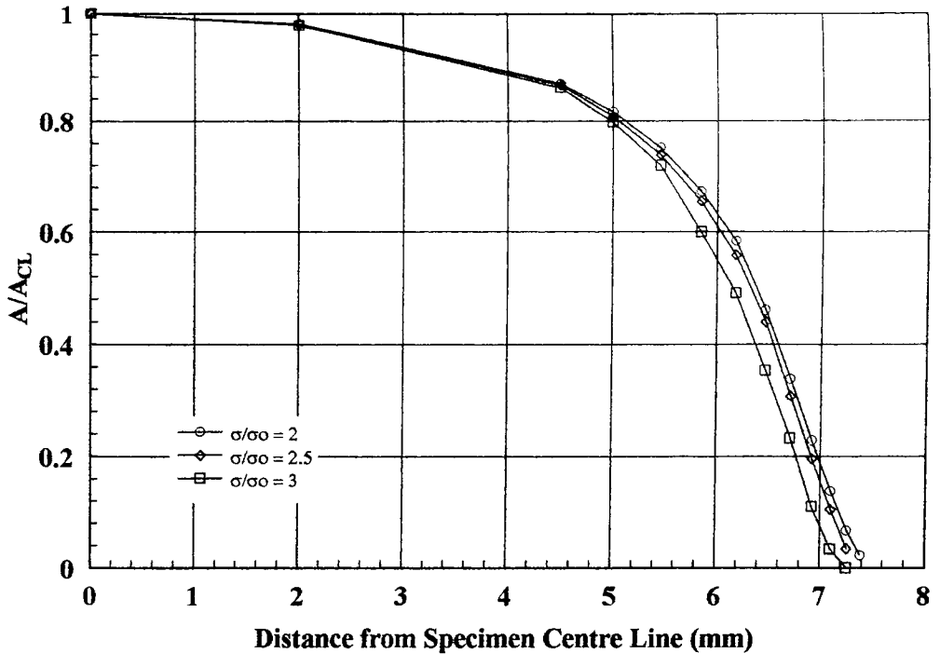

Fig. 6.35 Variation of A/A_{CL} through specimen thickness 15 mm thick specimen

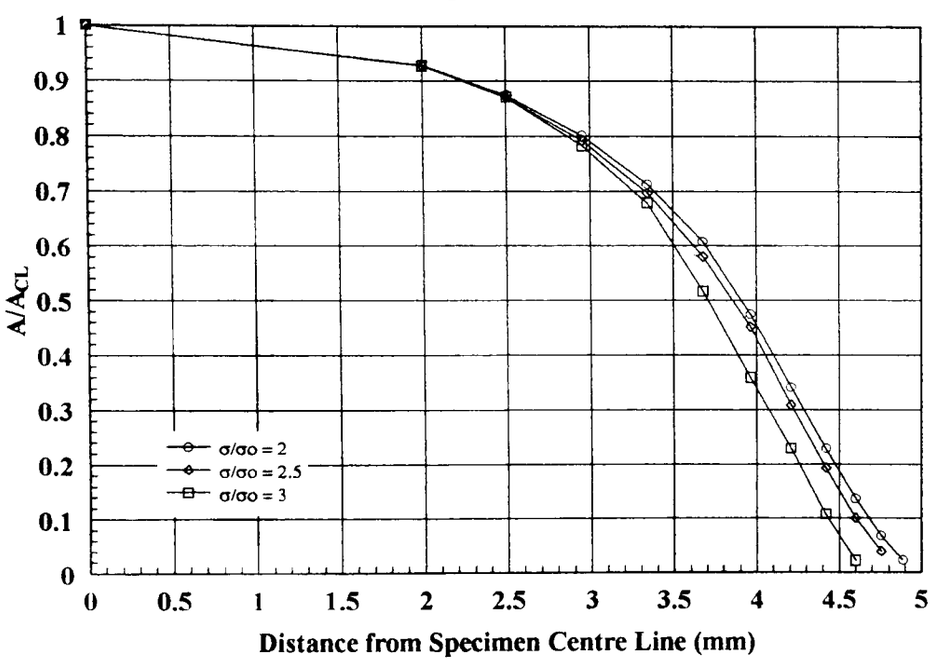

Fig. 6.36 Variation of A/A_{CL} through specimen thickness 10 mm thick specimen

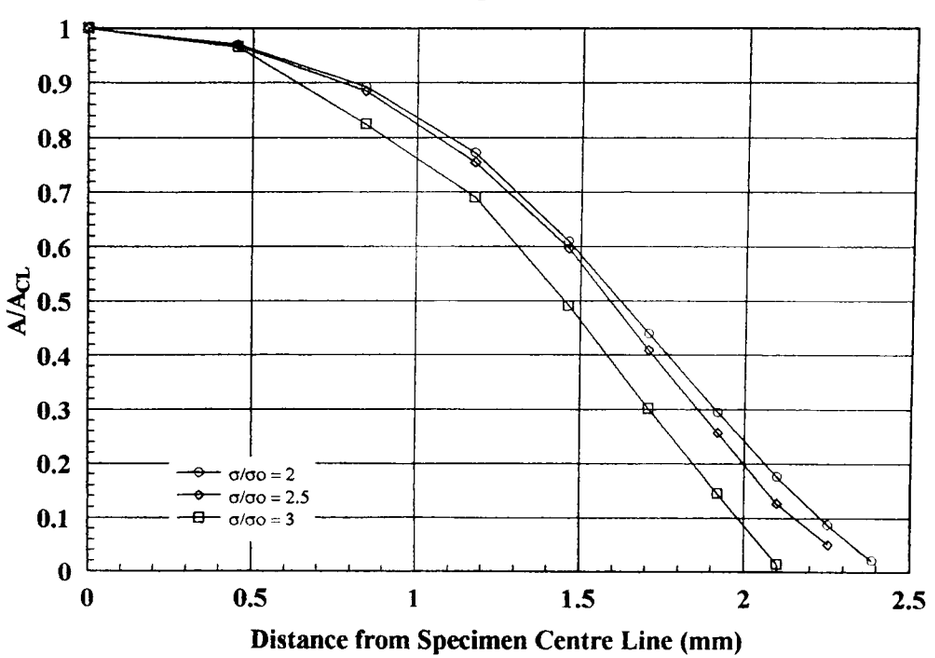

Fig. 6.37 Variation of A/A_{CL} through specimen thickness 5 mm thick specimen

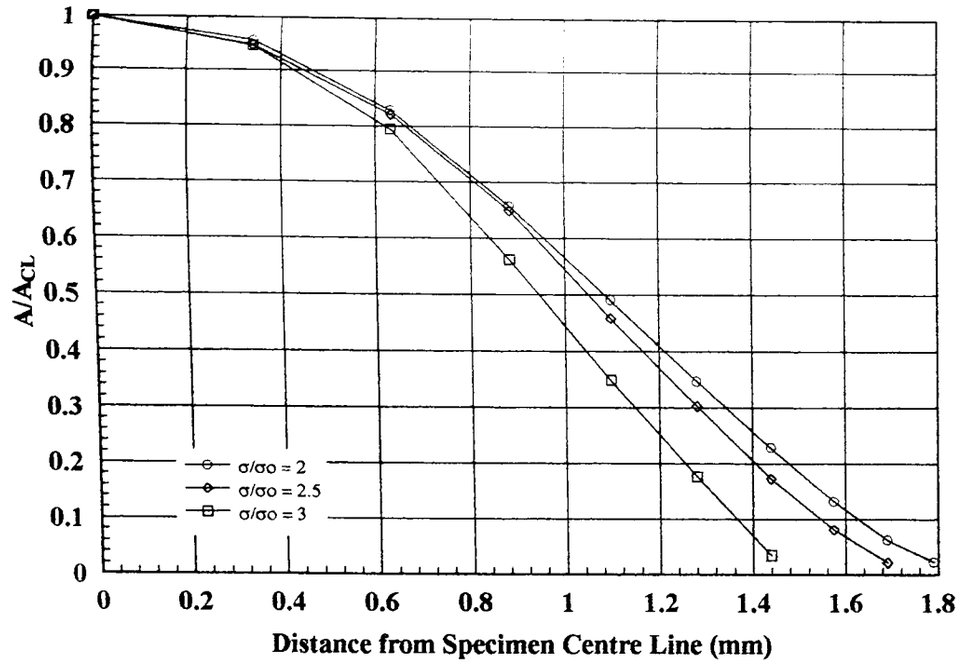

Fig. 6.38 Variation of A/A_{CL} through specimen thickness 3.75 mm thick specimen

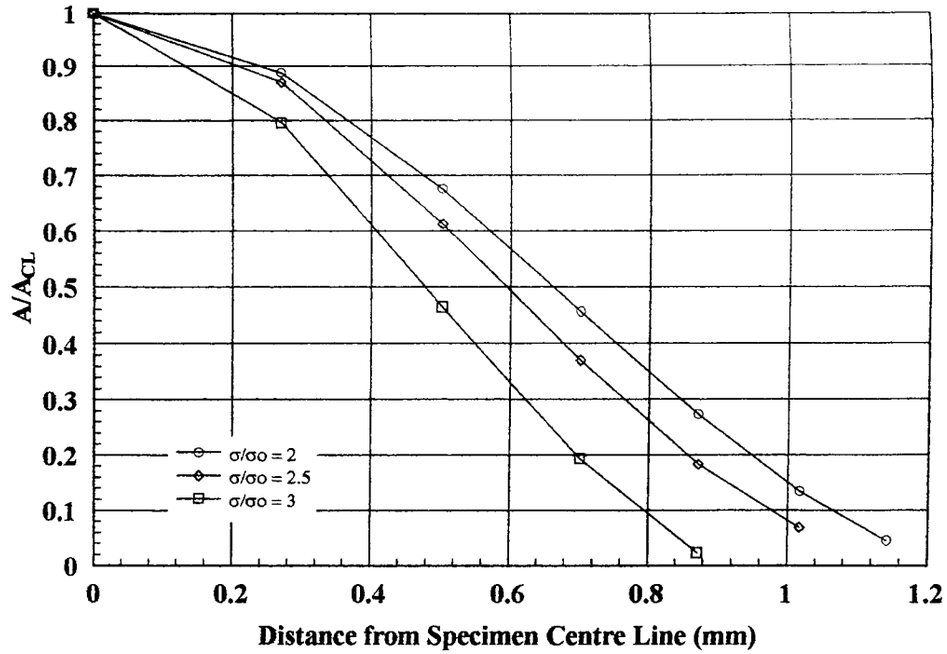

Fig. 6.39 Variation of A/A_{CL} through specimen thickness 2.5 mm thick specimen

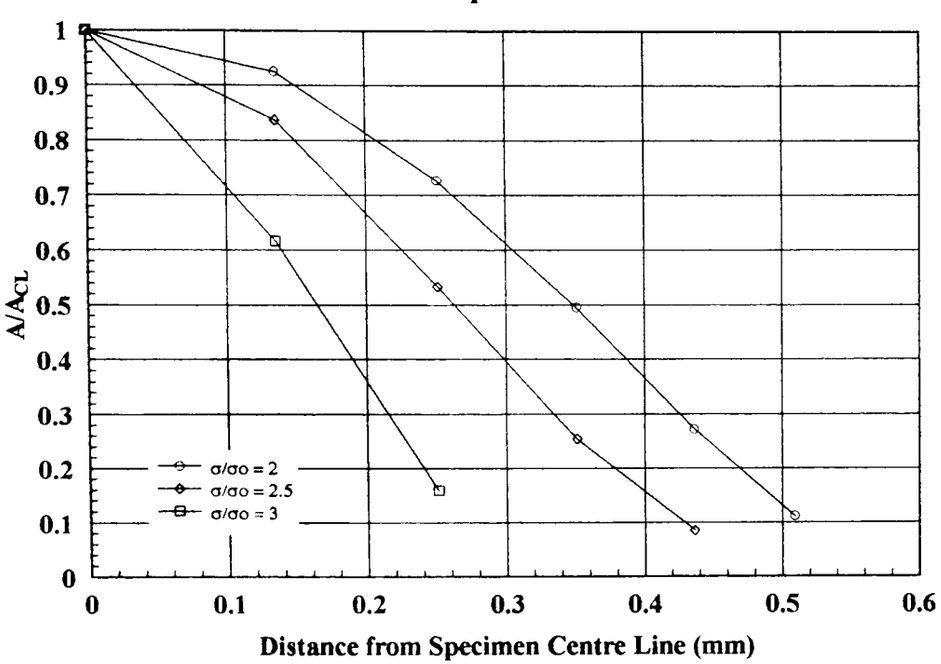

Fig. 6.40 Variation of A/A_{CL} through specimen thickness 1.25 mm thick specimen

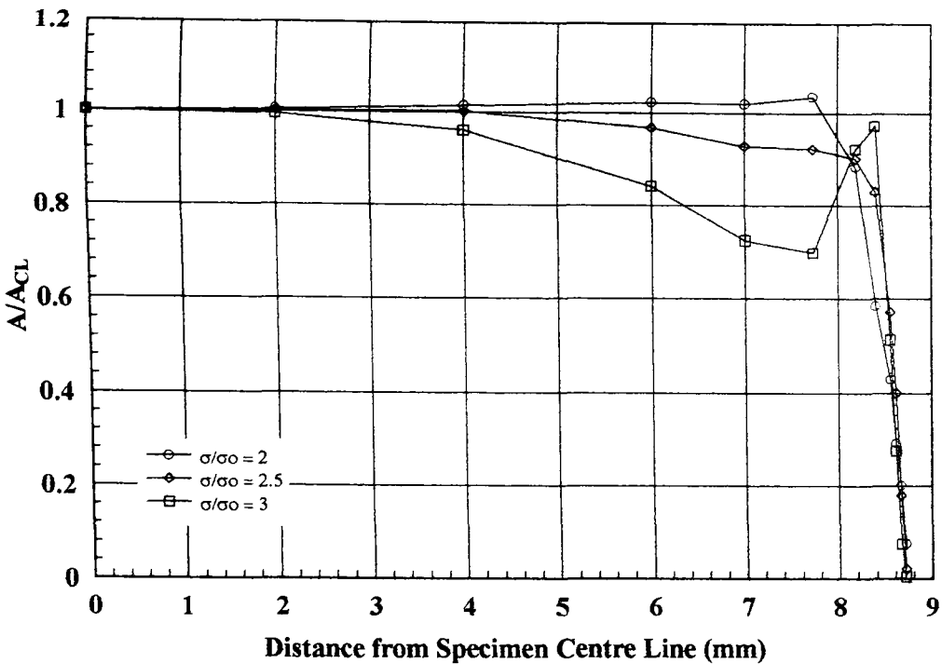

Fig. 6.41 Variation of A/A_{CL} through specimen thickness 25 mm thick side grooved specimen

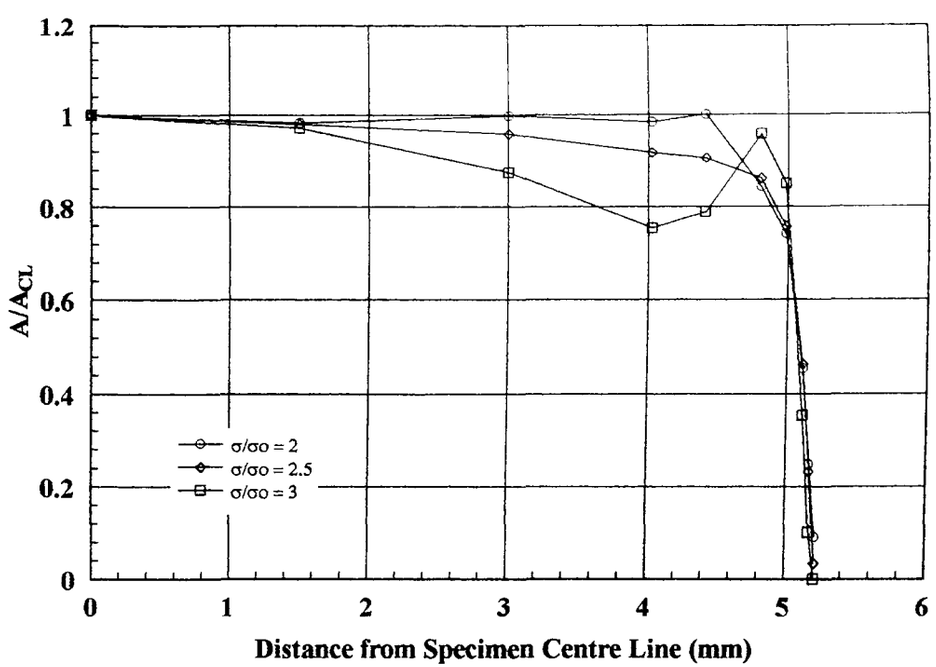

Fig. 6.42 Variation of A/A_{CL} through specimen thickness 15 mm thick side grooved specimen

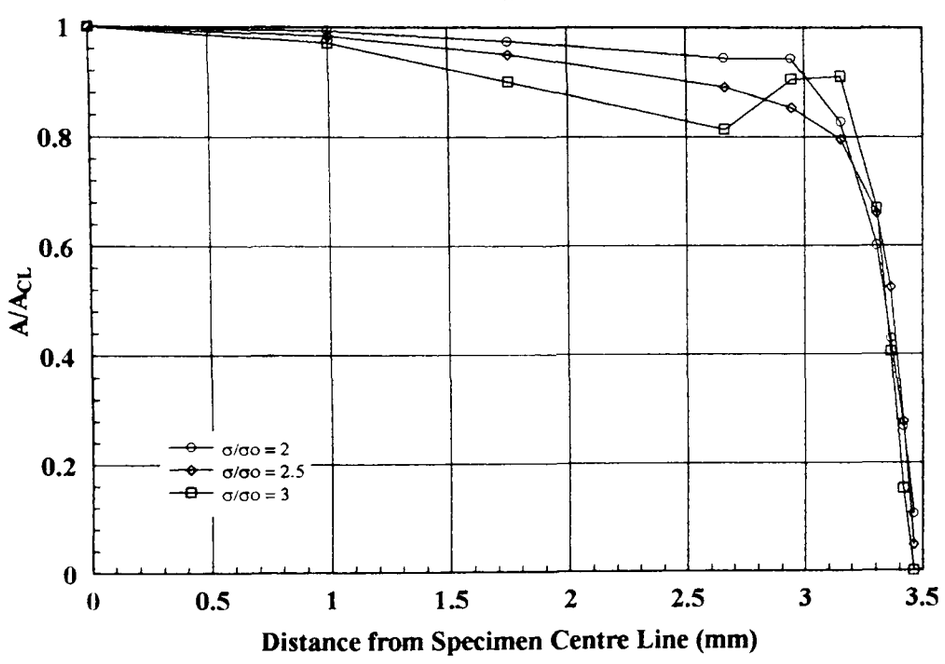

Fig. 6.43 Variation of A/A_{CL} through specimen thickness 10 mm thick side grooved specimen

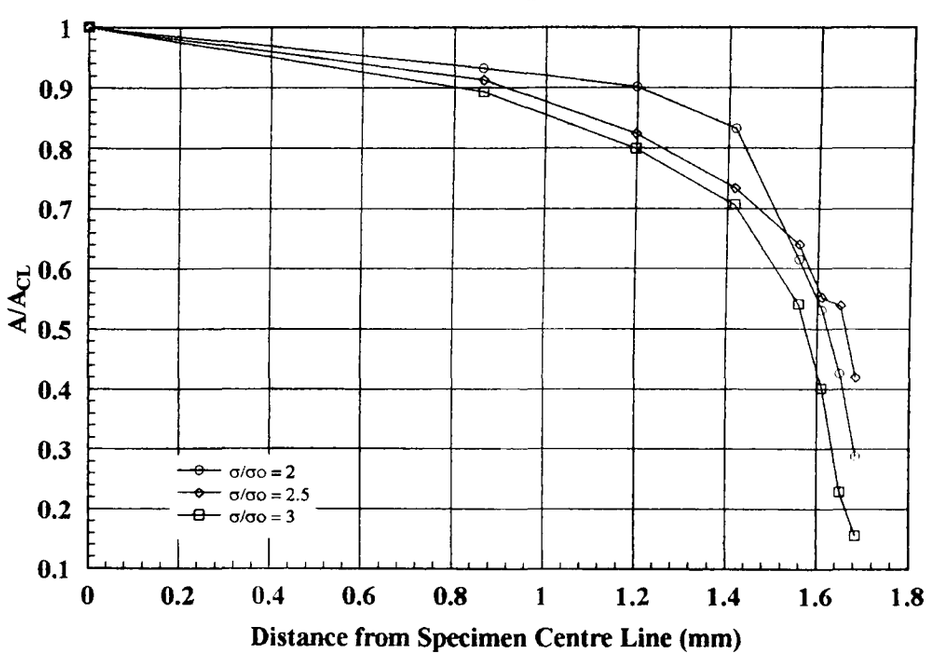

Fig. 6.44 Variation of A/A_{CL} through specimen thickness 5 mm thick side grooved specimen

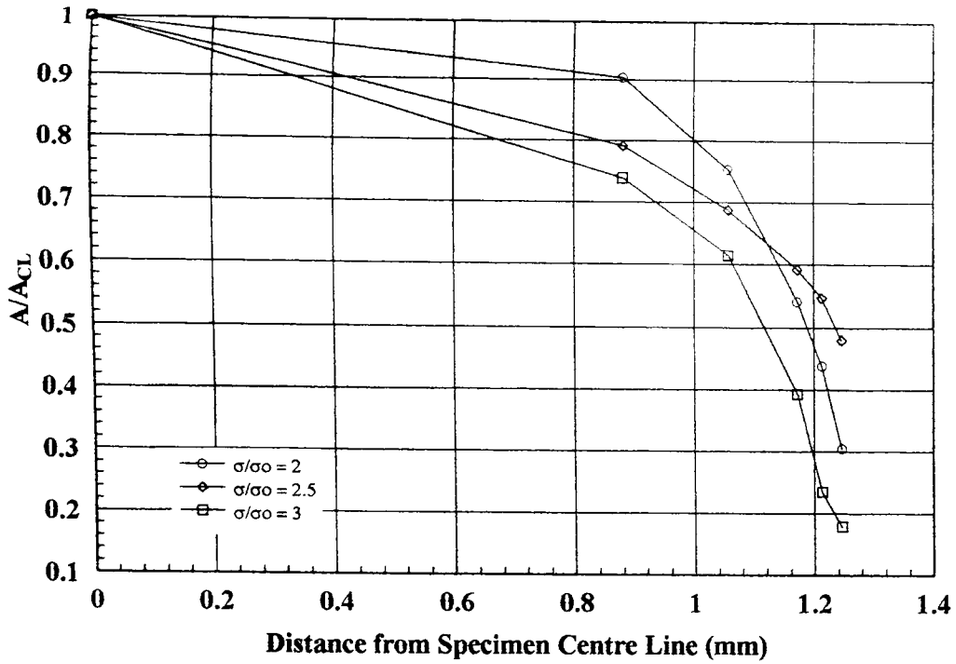

Fig. 6.45 Variation of A/A_{CL} through specimen thickness 3.75 mm thick side grooved specimen

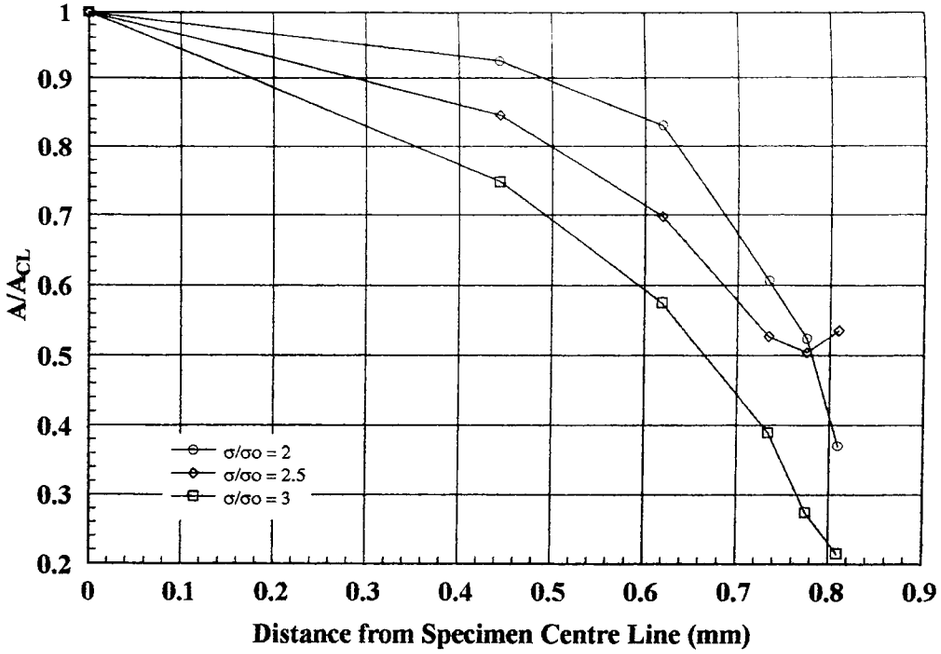

Fig. 6.46 Variation of A/A_{CL} through specimen thickness 2.5 mm thick side grooved specimen

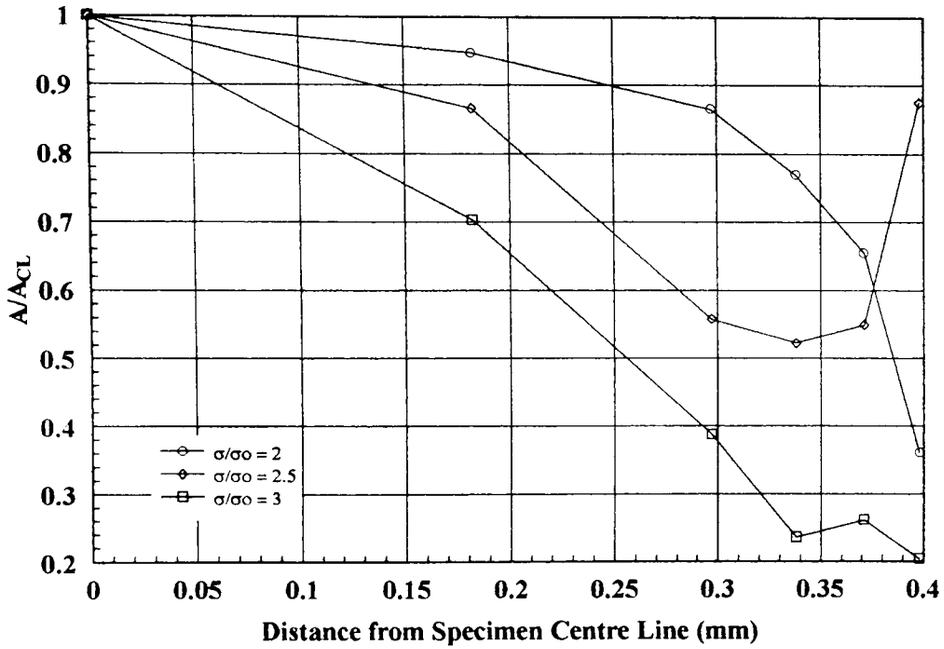

Fig. 6.47 Variation of A/A_{CL} through specimen thickness 1.25 mm thick side grooved specimen

In comparison the through thickness variation of Q for side grooved specimens, although remaining relatively constant across the crack front for a wider range of thicknesses is always negative. It is interesting to note that the value of Q falls away at the root of the side groove for specimen thicknesses of 10 mm and above, but is slightly elevated at the root of the side groove for specimens below 10 mm thick. The reason for this observation is not clear but it is probably due to slightly different mesh refinements being used immediately adjacent to the side groove root. Even though the centre line value of Q is always negative, consideration of average Q values as given in table 6.1 indicates that they are much closer to zero over a wide range of thicknesses than those obtained for the plain specimens. Comparison of results for the 5 mm thick plain and side grooved specimens gives an indication of the increased constraint provided by the introduction of side grooves, the results obtained for the plain specimen being -0.173 with the result from the side grooved specimen being -0.056.

Specimen Type	**Thickness (mm)**	**J_{AVE}/J_{CL}**	**Q_{AVE}**
Plain	25	0.930	0.0038
	15	0.934	-0.0378
	10	0.925	-0.0787
	5	0.895	-0.1726
	3.75	0.868	-0.2676
	2.5	0.811	-0.3971
	1.25	0.727	-0.7164
Side Grooved	25	1.136	-0.0336
	15	1.129	-0.0360
	10	1.111	-0.0483
	5	1.073	-0.0559
	3.75	1.062	-0.0930
	2.5	1.039	-0.1692
	1.25	0.980	-0.4048

Table 6.1 – Average J and Q values for plain and side grooved specimens

J-Q trajectories obtained from the analysis indicate that for plain sided specimens trajectories are steep within the interior of the specimen but become shallow towards the specimen edge for the full thickness specimen. As the specimen thickness reduces the J-Q trajectories become progressively more shallow even within the interior of the specimen. Results for the side grooved specimens, however, remain steep across a greater proportion of the crack front and for a wider range of thicknesses. It is interesting to note that the trajectory obtained closest to the side groove root for specimens of less than 5 mm thick exhibits an opposite slope to all other J-Q trajectories, this again suggests that the influence of side grooving in the region adjacent to the groove root is strong. Figs. 6.48 and 6.49 show crack front average trajectories for both plain sided and side grooved specimens. The results presented in this form give a good indication of the performance of side grooves in increasing the general level of constraint across the crack front, with trajectories remaining steep for all side grooved specimens greater than 2.5 mm thick.

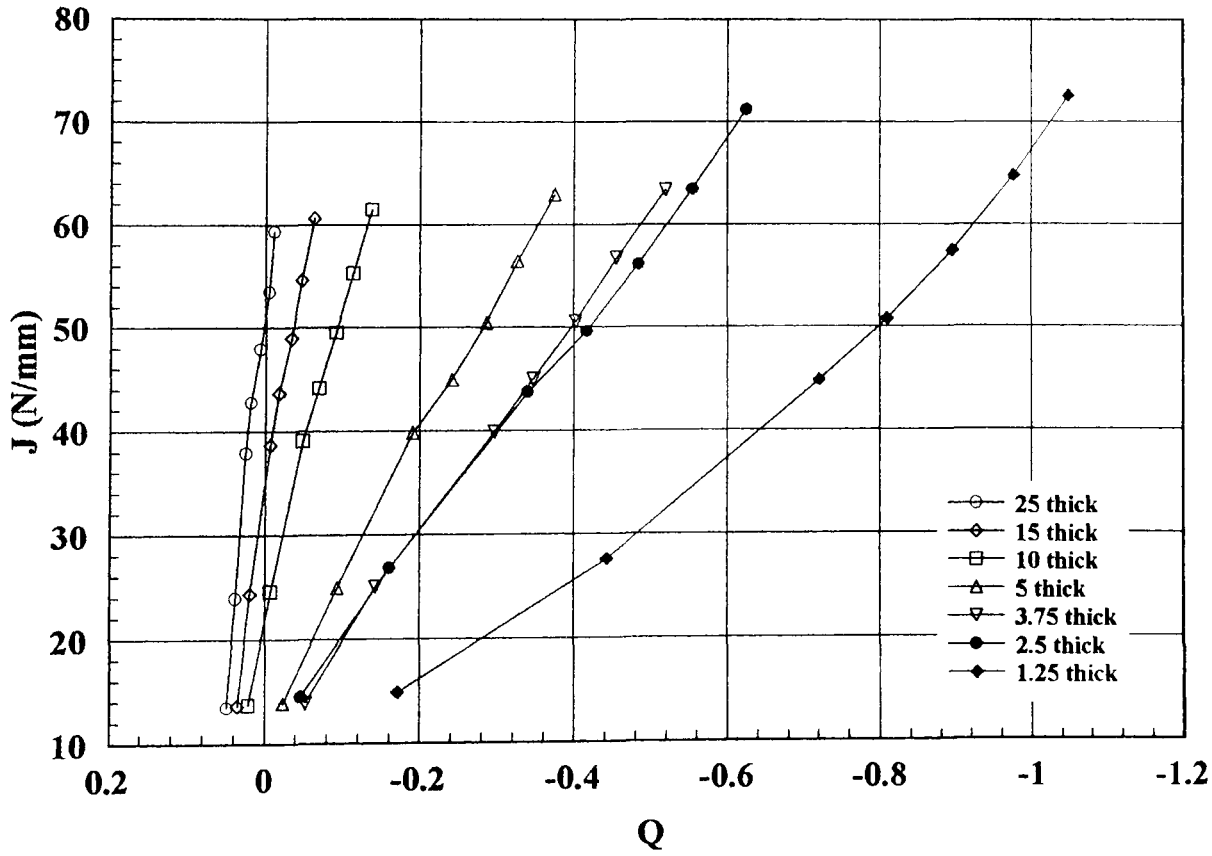

Fig. 6.48 Average J-Q trajectories plain specimens

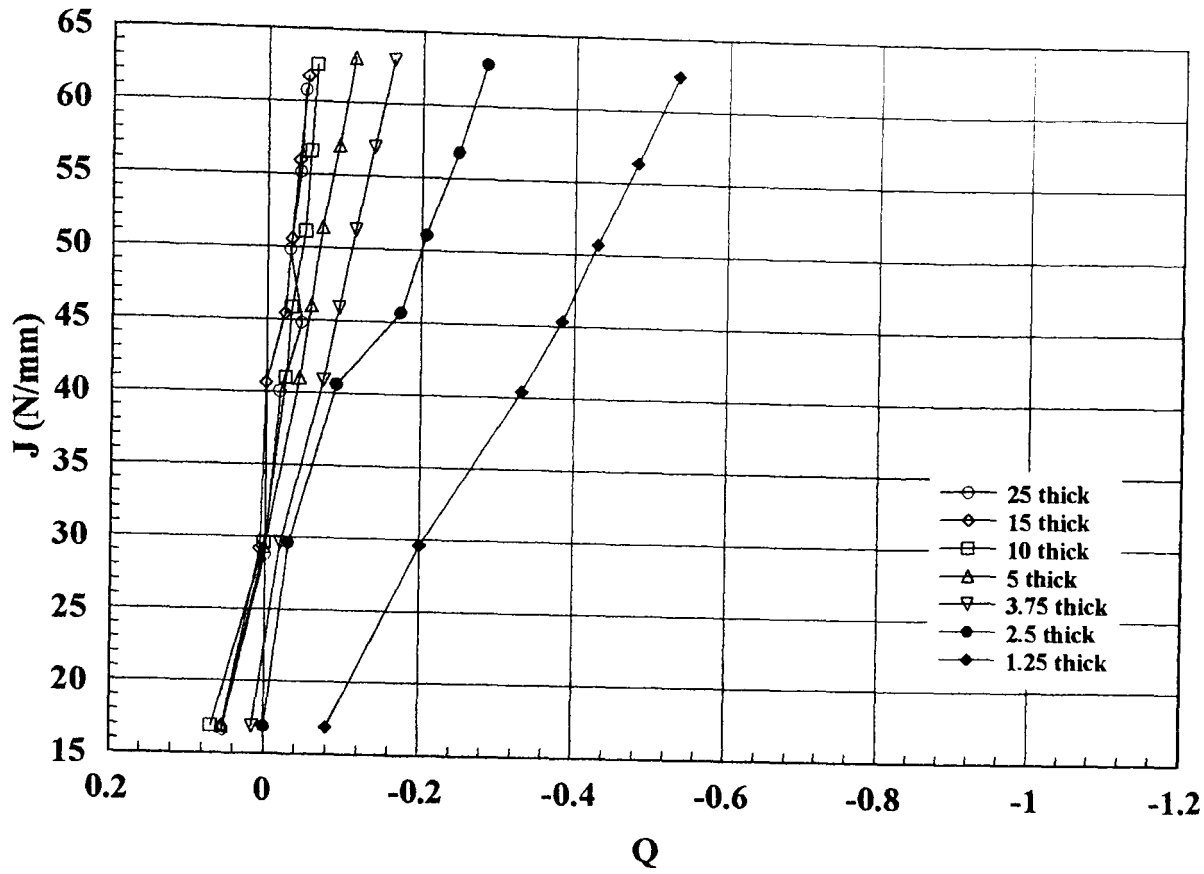

Fig. 6.49 Average J-Q trajectories side grooved specimens

The results presented relating to J-Q methodology strongly suggest that benefits obtained from side grooving have the potential to yield valid fracture toughness values from specimens that are significantly thinner than called for by both British and American Standards [26, 27].

Area scaling results presented in the form of principal stress contours for $\sigma/\sigma_0 = 2$ in figs. 6.20 – 6.33 give an indication of the volume of material contained within each specimen subjected to a stress level at or above $2\sigma_0$. Each contour represents the area subjected to such a stress level at a particular crack front location, the results indicate that the area is a maximum at the specimen centre line diminishing to zero at the specimen edge. The volume of material contained at or above a particular stress level can be easily obtained for each specimen and is presented for both plain and side grooved specimens in table 6.2 for $\sigma/\sigma_0 = 2$, 2.5 and 3. Figs. 6.34 – 6.40 illustrate the ratio of slice area to centre line area for the full thickness range of plain sided specimens for $\sigma/\sigma_0 = 2$, 2.5 and 3. The results indicate only a weak dependence on the stress contour level for the majority of thicknesses, only for specimen thicknesses of 5 mm and below does any significant dependence present itself. Similar results for side grooved specimens are presented in figs. 6.41 – 6.46 again for stress ratio of $\sigma/\sigma_0 = 2$, 2.5

Specimen Type	Gross Thickness (mm)	Net Thickness (mm)	$\sigma/\sigma_0 = 2.0$			$\sigma/\sigma_0 = 2.5$			$\sigma/\sigma_0 = 3.0$		
			Volume (units^3)	Centre Line Area (units^2)	Average Area (units^2)	Volume (units^3)	Centre Line Area (units^2)	Average Area (units^2)	Volume (units^3)	Centre Line Area (units^2)	Average Area (units^2)
Plain	25	25	1117.300	130.700	89.384	193.700	22.670	15.496	10.630	1.289	0.850
	15	15	707.000	119.500	94.267	121.100	20.670	16.147	6.610	1.157	0.881
	10	10	396.900	108.870	79.380	67.830	18.880	13.566	3.705	1.064	0.741
	5	5	133.400	85.430	53.360	22.200	14.600	8.880	1.140	0.828	0.456
	3.75	3.75	73.000	65.540	38.933	11.990	11.700	6.395	0.590	0.641	0.315
	2.5	2.5	25.610	39.300	20.488	4.190	7.080	3.352	0.201	0.424	0.161
	1.25	1.25	3.310	9.830	5.296	0.499	1.910	0.798	0.020	0.128	0.032
Side Grooved	25	17.5	946.220	110.640	108.139	141.530	16.920	16.175	5.464	0.702	0.624
	15	10.5	568.390	114.080	108.265	84.460	17.410	16.088	3.243	0.705	0.618
	10	7	362.110	112.260	103.460	53.090	16.860	15.169	2.034	0.663	0.581
	5	3.5	143.810	96.260	82.177	22.360	15.390	12.777	1.037	0.742	0.593
	3.75	2.625	87.110	79.830	66.370	13.260	12.830	10.103	0.617	0.641	0.470
	2.5	1.75	37.890	53.960	43.303	5.840	8.910	6.674	0.268	0.462	0.306
	1.25	0.875	6.780	19.260	15.497	1.030	3.300	2.354	0.046	0.186	0.104

Table 6.2 Process zone volumes

and 3. Consideration of those results for side grooved specimens show slightly more dependence on the chosen stress level with respect to the slice area obtained. For side grooved specimens above 5 mm thick there is a marked increase in the proportion of specimen thickness when the slice area is at the same level as the specimen centre line. At specimen thicknesses of 5 mm and below the slice area to centre line area falls away towards the specimen edge, as is the case with the plain sided specimens.

As with the results for J-Q methodology the consideration of material volumes at stress levels above that which cleavage is likely, i.e. in the lower shelf region, strongly suggests that the introduction of side grooves has the potential to yield valid fracture toughness values for sub thickness specimens. The applicability of area scaling methodology in the prediction of cleavage failure for three dimensional finite element models will be further considered in section 6.6.

6.4 FRACTURE TOUGHNESS TESTING

Fracture toughness testing of the EN24 material was undertaken using the compact tension configuration shown in fig. 6.1 and described in section 6.2. This configuration of specimen allows either K or J results to be obtained. As with the aluminium specimens described in section 4.4 testing was done using an Instron servo-hydraulic test machine of 50 kN dynamic and 100 kN static load capacity in accordance with BS7448 part 1, 1991 [26] for K determination and ASTM E813-88 [104] for J determination.

6.4.1 SPECIMEN PREPARATION

All specimens were prepared in accordance with BS7448, part 1, 1991 [26], section 6. The specimens were first machined to a plain sided condition and then heat treated as described in section 5.3. The specimens were then fatigue pre-cracked to give a ratio of a/W between 0.45 – 0.55. Crack length during the pre-cracking process was monitored by the use of a travelling microscope. Pre-cracking was in accordance with clause 6.4.6 of BS7448 [26] as described in section 4.4.1 and hence equations (4.12), (4.13) and (4.14). These requirements are more stringent than those laid down in ASTM E813-88 [104] and hence satisfy all of the requirements therein.

Table 6.3 gives details of all pre-cracking data and maximum pre-cracking force conditions according to clause 6.4.6 of BS7448 [26]. All of the requirements of clause 6.4.6 were met by all of the specimens under consideration.

Further conditions as laid down by clause 6.4.7(a) and (b) of BS 7448 [26] which states that the maximum stress intensity factor during the initial fatigue pre-crack extension shall not exceed 1.3 K_f, where K_f is defined by equation (4.15) and that the fatigue force ratio shall be in the range 0 – 0.1, were also satisfied by all specimens. Clause 6.4.7(c), (d) and (e) which relate to pre-crack shape and size were also satisfied.

As with the aluminium specimens the side grooves were machined after pre-cracking due to the difficulty in determining the fatigue crack length at the root of the side groove, this procedure is also recommended in ASTM E813-88 [104] in order to produce a straight fatigue pre-crack front.

6.4.2 TEST PROCEDURE

Some preliminary testing was undertaken in order to establish the fracture characteristics of the complete range of specimens both plain sided and side grooved. The test records from this preliminary testing revealed that a wide difference could be expected in the test records obtained.

As could be expected the results of these preliminary tests showed that the results obtained for full thickness plain sided specimens exhibited flat fracture across the width of the specimen with typical test records in terms of load v load line displacement similar to that illustrated in fig. 6.50(a). Sub thickness plain sided specimens varied considerably in the way they behaved. Both 15 mm thick and 10 mm thick specimens still exhibited a flat fracture surface across the width of the specimen but the load v load line displacement test record exhibited an increasing number of 'pop ins' as the thickness reduced. Typical results obtained from the 10 mm thick specimens are similar to those illustrated in fig. 6.50(b). Specimens of 5 mm thickness and below exhibited a transition from flat fracture surfaces to slanted fracture surfaces indicating a greater amount of shear. Typical load v load line displacement test records for these specimens are as illustrated in fig. 6.50(c), in all cases, for these thin specimens there was evidence of stable crack growth.

Specimen No	Side Groove Type	Pre-cracking Data								Pre-cracking force conditions		
		Initial Cycles				Final Cycles				F_f(kN)	Condition	F_f(kN)
		Mean Load (kN)	Amplitude (kN)	No of Cycles	Crack length (mm)	Mean Load (kN)	Amplitude (kN)	No of Cycles	Crack length (mm)	eq 4.12	eq 4.13	eq 4.14
25P1	None	14.00	13.00	4000	0.2	13.00	11.00	7000	1.99	98.50	1.89218E-07	36.29
25P2	None	14.00	13.00	5700	0.2	13.00	11.00	3000	1.59	100.81	1.85401E-07	40.02
25P3	None	14.00	13.00	5850	0.2	13.00	11.00	3750	1.91	99.03	1.88372E-07	37.92
25P4	None	14.00	13.00	5100	0.2	13.00	11.00	4200	1.83	99.42	1.87652E-07	38.88
15P1	None											
15P2	None											
15P3	None	9.00	8.00	3800	0.3	7.00	6.00	1000	1.71	60.07	1.68333E-07	25.02
15P4	None	9.00	8.00	4600	0.2	7.00	6.00	1300	1.19	61.76	1.64043E-07	24.54
10P1	None	6.00	5.00	6000	0.2	4.50	4.00	3200	1.34	40.84	1.62101E-07	17.82
10P2	None	6.00	5.00	5900	0.2	4.50	4.00	2600	1.24	41.08	1.6124E-07	15.78
10P3	None	6.00	5.00	6000	0.2	4.50	4.00	3500	1.34	40.84	1.62101E-07	17.04
10P4	None	6.00	5.00	7000	0.2	4.50	4.00	500	1.33	40.88	1.6195E-07	16.32
5P1	None	3.00	2.60	2200	0.2	2.60	2.30	5000	1.94	19.77	1.92654E-07	8.82
5P2	None	3.00	2.60	2200	0.2	2.60	2.30	5000	2.26	19.42	1.95791E-07	12.30
5P3	None	3.00	2.60	2200	0.3	2.60	2.30	5000	2.13	19.56	1.94467E-07	12.00
5P4	None	3.00	2.60	2200	0.3	2.60	2.30	5000	2.24	19.44	1.95601E-07	10.26
5P5	None	3.00	2.60	2200	0.3	2.60	2.30	5000	2.24	19.43	1.95663E-07	9.18
5P6	None	3.00	2.60	2200	0.3	2.60	2.30	5000	2.24	19.43	1.95663E-07	9.84
5P7	None	3.00	2.60	2200	0.3	2.60	2.30	5000	2.26	19.42	1.95803E-07	9.24
5P8	None	3.00	2.60	2200	0.2	2.60	2.30	5000	2.08	19.61	1.94054E-07	9.60
5P9	None	3.00	2.60	2200	0.2	2.60	2.30	5000	1.76	19.96	1.9088E-07	10.20
5P10	None	3.00	2.60	2200	0.2	2.60	2.30	5000	1.93	19.77	1.92554E-07	10.80
5P11	None	3.00	2.60	2200	0.2	2.60	2.30	5000	2.04	19.66	1.93568E-07	11.40
5P12	None	3.00	2.60	2200	0.2	2.60	2.30	5000	1.55	20.19	1.88869E-07	12.00
5P13	None	3.00	2.60	2200	0.2	2.60	2.30	5000	2.04	19.65	1.93618E-07	9.00
5P14	None	3.00	2.60	2200	0.2	2.60	2.30	5000	1.98	19.92	1.91208E-07	9.90
5P15	None	3.00	2.60	2200	0.2	2.60	2.30	5000	1.83	19.88	1.9155E-07	10.50
5P16	None	3.00	2.60	2200	0.2	2.60	2.30	5000	1.84	19.87	1.91672E-07	11.10
5P17	None	3.00	2.60	2200	0.2	2.60	2.30	5000	1.10	20.69	1.8464E-07	11.70
2-5p1	None											
2-5p2	None											
2-5p3	None	1.50	1.30	2200	0.2	1.30	1.15	5000	1.44	10.16	1.88E-07	5.10
2-5p4	None	1.50	1.30	2200	0.2	1.30	1.15	5000	1.72	10.00	1.91E-07	5.40
2-5p5	None	1.50	1.30	2200	0.2	1.30	1.15	5000	2.09	9.80	1.94E-07	5.70
2-5p6	None	1.50	1.30	2200	0.2	1.30	1.15	5000	1.45	10.15	1.88E-07	6.00
2-5p7	None	1.50	1.30	2200	0.2	1.30	1.15	5000	1.89	9.91	1.92E-07	6.30
2-5p8	None	1.50	1.30	2200	0.2	1.30	1.15	5000	1.61	10.06	1.89E-07	6.60
2-5p9	None	1.50	1.30	2200	0.2	1.30	1.15	5000	1.65	10.04	1.90E-07	4.80
2-5p10	None	1.50	1.30	2200	0.2	1.30	1.15	5000	1.09	10.35	1.85E-07	5.10
2-5p11	None	1.50	1.30	2200	0.2	1.30	1.15	5000	1.61	10.07	1.89E-07	5.40
2-5p12	None	1.50	1.30	2200	0.2	1.30	1.15	5000	1.97	9.87	1.93E-07	5.70
2-5p13	None	1.50	1.30	2200	0.2	1.30	1.15	5000	1.39	10.18	1.87E-07	6.00
25SG1	Vee 30%	14.00	13.00	12000	0.2	13.00	11.00	8000	1.18	97.52	1.91E-07	32.40
25SG2	Vee 30%	14.00	13.00	9000	0.22	13.00	11.00	7000	1.60	95.27	1.95E-07	26.94
15SG1	Vee 30%	9.00	8.00	10000	0.19	7.00	6.00	7000	1.29	58.16	1.73E-07	16.85
10SG1	Vee 30%	6.00	5.00	10000	0.1	4.50	4.00	7000	0.78	61.98	1.07E-07	12.55
10SG2	Vee 30%	6.00	5.00	10000	0.2	4.50	4.00	7000	1.63	64.82	1.03E-07	13.34
5SG1	Vee 30%	3.00	2.60	11000	0.3	2.60	2.30	9000	1.24	19.44	1.96E-07	5.97
5SG2	Vee 30%	3.00	2.60	11000	0.42	2.60	2.30	9000	1.90	19.81	1.92E-07	5.78
5SG3	Vee 30%	3.00	2.60	11000	0.25	2.60	2.30	9000	2.08	19.61	1.94E-07	6.85
5SG4	Vee 30%	3.00	2.60	11000	0.3	2.60	2.30	9000	2.02	19.68	1.93E-07	5.54
5SG5	Vee 30%	3.00	2.60	11000	0.31	2.60	2.30	9000	1.77	19.95	1.91E-07	6.41
5SG6	Vee 30%	3.00	2.60	11000	0.52	2.60	2.30	9000	2.27	19.41	1.96E-07	5.50
5SG7	Vee 30%	3.00	2.60	11000	0.54	2.60	2.30	9000	2.26	19.42	1.96E-07	5.40
2-5SG1	Vee 30%	1.50	1.30	11000	0.53	1.30	1.15	6000	2.23	8.65	2.18E-07	3.12
2-5SG2	Vee 30%	1.50	1.30	11000	0.32	1.30	1.15	6000	1.70	10.01	1.90E-07	3.15
2-5SG3	Vee 30%	1.50	1.30	11000	0.52	1.30	1.15	6000	1.43	10.16	1.88E-07	3.45
2-5SG4	Vee 30%	1.50	1.30	11000	0.23	1.30	1.15	6000	1.35	10.21	1.87E-07	2.90
2-5SG5	Vee 30%	1.50	1.30	11000	0.1	1.30	1.15	6000	0.85	10.48	1.82E-07	3.39
2-5SG6	Vee 30%	1.50	1.30	11000	0.23	1.30	1.15	6000	1.08	10.36	1.84E-07	3.24

Table 6.3 Pre-cracking data

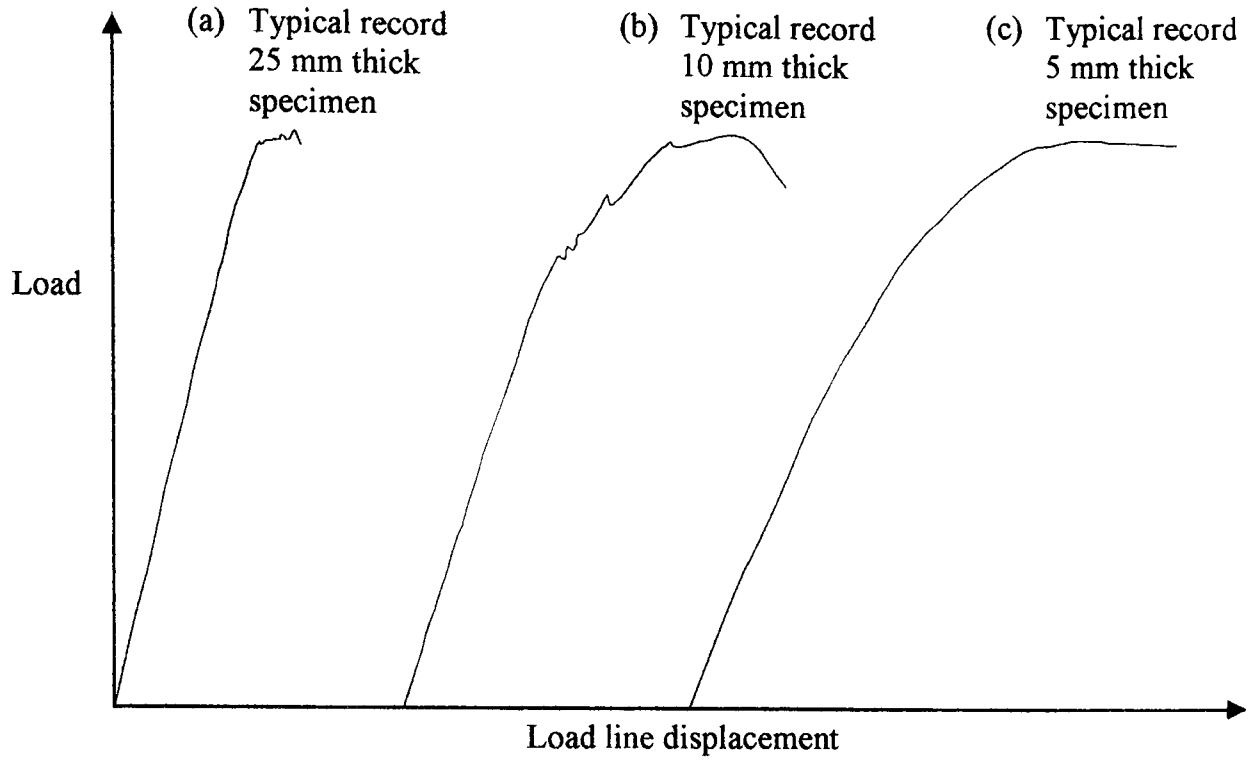

Fig. 6.50 Typical test records for plain and side grooved specimens

Preliminary results obtained from the side grooved specimens varied significantly from those obtained from the plain sided specimens. In all cases the fracture surfaces were flat even at thicknesses of 2.5 mm and all load v load line displacement test records were of the type illustrated in fig. 6.50(a) and (b).

As a result of the preliminary testing it was decided that plain sided specimens of 10 mm thickness and above should be subjected to a standard K test in accordance with BS 7448 pt 1 [26]. Specimens below 10 mm thick would be subjected to J testing in accordance with ASTM E813-88 [104] with K values being determined from the resulting J values according to equation (2.22). All side grooved specimens were subjected to standard K tests in accordance with BS 7448 pt 1 [26].

Procedure for K testing

The procedure for K testing was identical to that described in section 4.4.2 for aluminium specimens with the exception that stepped notched specimens were used rather than straight notched.

All specimens were tested under displacement control such that a nominal loading rate of 1.0 MPa $\sqrt{m}$/s was achieved for all specimens based on a nominal a/W of 0.5 which again complies with Clause 8.5 of BS 7448 of a loading rate between

0.5 and 3.0 MPa √m/s. The specimen geometry was of the stepped notched compact tension type as illustrated in fig. 6.1. Load line displacement was measured by the use of a standard Instron clip gauge mounted on inward facing knife edges of thickness 0.5 mm. All other aspects of the test procedure were in accordance with clause 8 of BS 7448 [26].

Procedure for J testing

The original experimental method for the determination of J was published by Begley and Landes [107] in 1972 with an alternative method being proposed by Rice et al [108] in 1973. It is this alternative method that forms the basis of the method specified in BS 7448 pt 1 and ASTM E813-88. Using equation (2.22) as a starting point, Rice showed that for a compact tension specimen:

$$J = \frac{2}{B(W-a)} \int_0^{v_c} P dv_c \quad \ldots\ldots (6.2)$$

Equation (6.2) effectively states that:

$$J = \frac{2U_c}{B(W-a)} \quad \ldots\ldots (6.3)$$

where U_c is the area under the P – v curve owing to the introduction of the crack. Hence J can be determined by examination of the load – load line displacement test record. However, in a J test the total displacement v_t is measured where v_t comprises two components v_{uc} which is the displacement resulting from loading of an uncracked specimen and v_c which is the contribution that the presence of the crack has to total displacement. Consequently the area under the P - v curve represents a total energy condition U_t rather than U_c. However, owing to the fact that for deep cracks the energy absorption due to the presence of the crack is very much greater than that of an uncracked body it is normal to assume that the energy contained in the cracked body U_c is equal to the total energy U_t and equation (6.3) becomes:

$$J = \frac{2U_t}{B(W-a)} \quad \ldots\ldots (6.4)$$

Further to the above assumption, if the crack is deep, v_c and hence v_t will contain both elastic and plastic contributions. It follows, therefore, that the total energy U_t is divided into elastic and plastic components U_{el} and U_{pl} respectively, see fig. 6.51. It then follows that:

$$J = J_{el} + J_{pl} \quad .....(6.5)$$

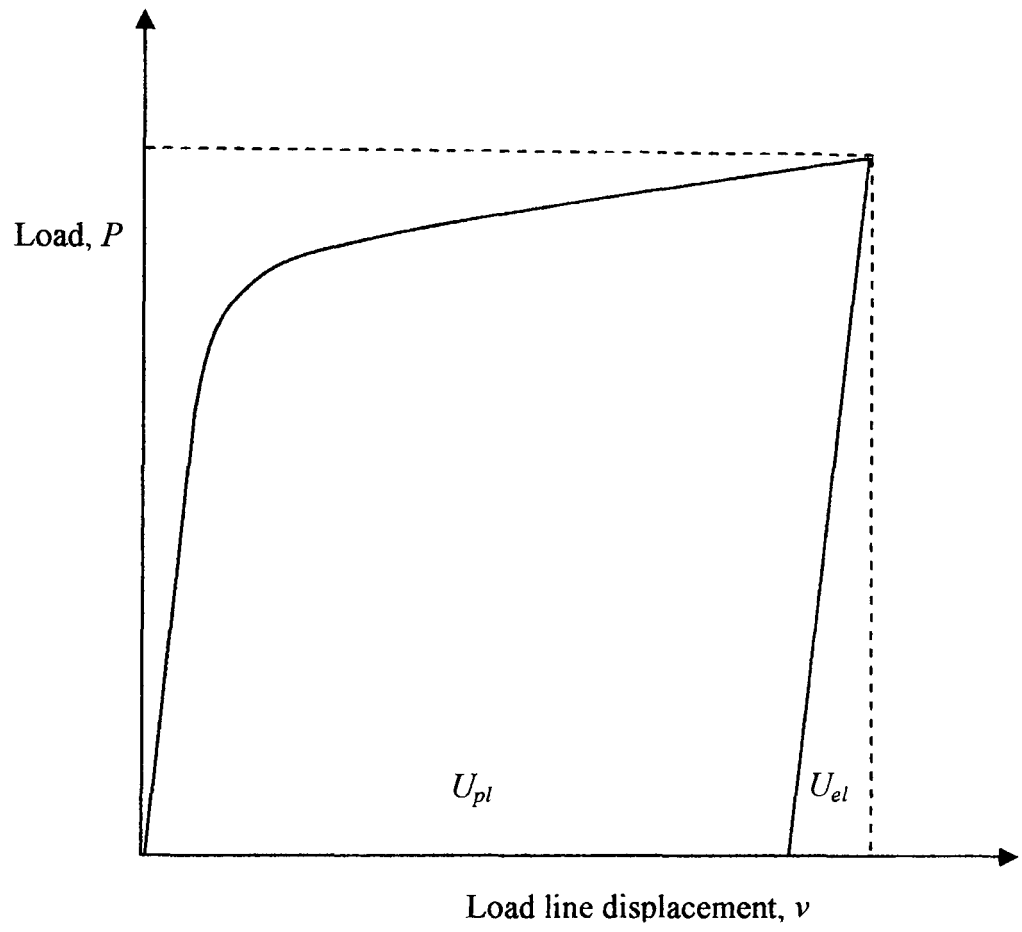

Fig. 6.51 Elastic and plastic energy components of area under $P-v$ curve

The relative magnitude of the elastic and plastic contributions is dependent on specimen geometry, in general we can write:

$$J = \frac{\eta U_t}{B(W-a)} \quad .....(6.6)$$

where η is a dimensionless constant dependent on geometry. By combining equation (6.5) and (6.6) we arrive at a general expression for J separated into elastic and plastic components:

$$J = \frac{\eta_{el} U_{el}}{B(W-a)} + \frac{\eta_{pl} U_{pl}}{B(W-a)} \quad \text{.....(6.7)}$$

As was shown in equation 2.23 for linear elastic behaviour J is equivalent to G, hence.

$$J = \frac{K_I^{\,2}}{E} + \frac{\eta_{pl} U_{pl}}{B(W-a)} \; for \; plane \; stress \quad (6.8)$$

and

$$J = \frac{K_I^{\,2}\left(1-\nu^2\right)}{E} + \frac{\eta_{pl} U_{pl}}{B(W-a)} \; for \; plane \; strain \quad (6.9)$$

Hence J can be found experimentally from the load displacement records for specimens of known geometry. This method forms the basis of all current standards for the experimental determination of J. However, the standards do vary in their interpretation of the results obtained. The two standards used in this work use essentially the same method to define crack extension and to derive J but differ in their definition of critical fracture toughness. BS 7448 pt 1 uses the fracture appearance of the specimen and the slope of the local displacement in terms of 'pop in' behaviour to define J, whereas ASTM E813-88 uses a regression analysis to define J_{IC} as the critical J value at stable crack initiation. As stated in section 6.4.2 all of the results presented here, in terms of J testing are in accordance with ASTM E813-88.

The objective of the test method described in ASTM E813-88 is to determine J as a function of crack growth. Load versus load line displacement is recorded and plotted with J being calculated in accordance with equation (6.9). This calculated J value is then plotted against estimated or physical crack growth using at least four data points within specified limits of crack growth. The resulting curve reflects the materials resistance to crack growth. The critical value of J at crack initiation, defined as J_{IC}, can be established by approximating the crack growth behaviour by a best fit power law relationship. A blunting line is calculated from material properties and an offset line at 0.2 mm from the blunting line is constructed. It is the intersection of this 0.2 mm offset line and the power law regression line that determines J_{IC}, see fig. 6.52.

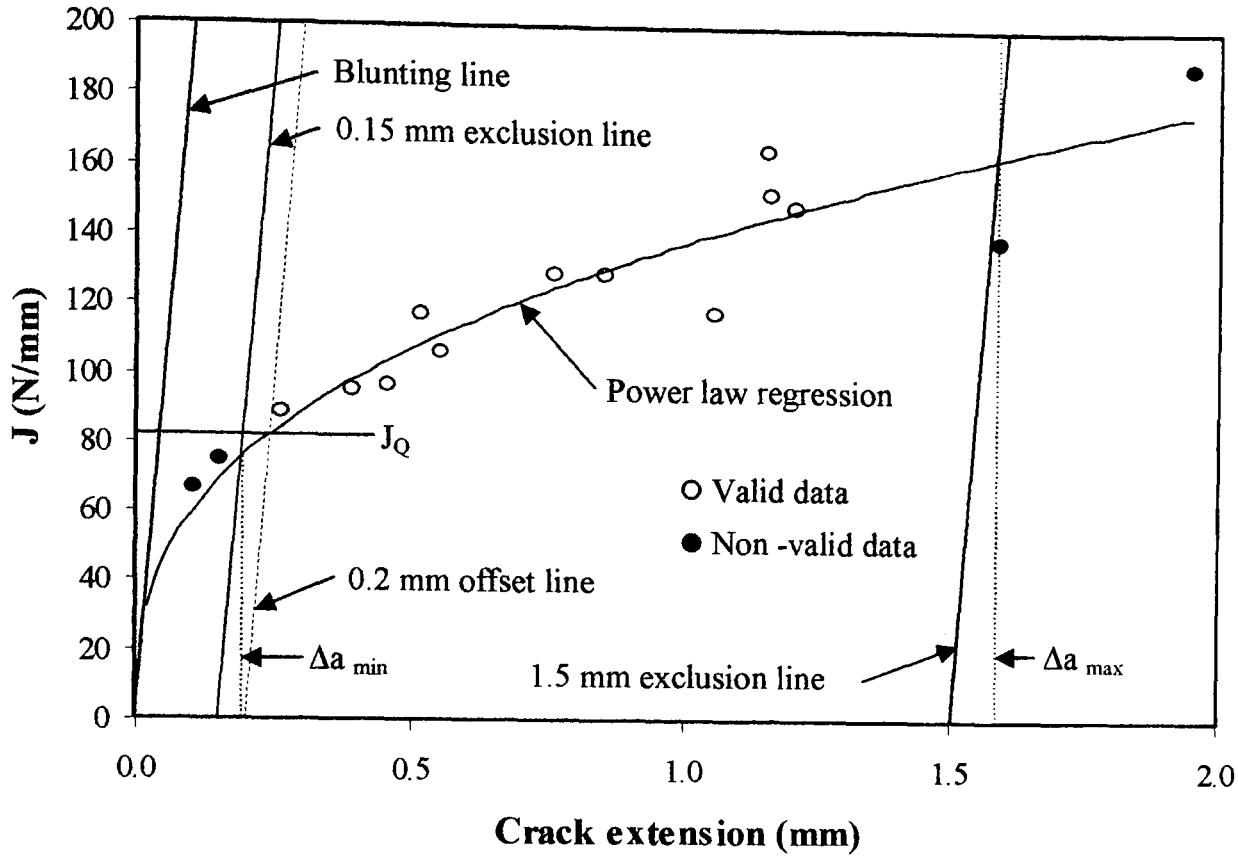

Fig. 6.52 Definitions for data qualification

ASTM E813-88 describes two techniques that can be used to obtain J as a function of crack growth. The first technique is a multi-specimen technique which requires at least four identically prepared specimens to be tested to different crack opening displacements and plotted on a single curve to obtain the required power law regression plot. The actual crack growth is used as determined post fracture using a heat tinting method. The second technique is a single specimen technique and uses elastic compliance or an equivalent indirect method to evaluate the crack length. Elastic compliance measurements are taken from a series of unloading/reloading segments spaced along the load versus load line displacement record.

The multi-specimens technique was used in the work presented here, mainly due to the fact that single specimen testing could not be undertaken with the available Instron control interface.

Once the plot of J versus Δa has been constructed ASTM E813-88 required that some data is excluded from the determination of the power law regression line. Hence exclusion lines are constructed, outside of which data is not valid, as follows:

i) The blunting line is constructed in accordance with $J = 2\sigma_y \Delta a$. This blunting line takes account of the apparent increase in crack length due to crack tip blunting.

ii) Maximum and minimum data lines are drawn parallel to the blunting line which intersect the crack extension axis at 1.5 mm and 0.15 mm respectively.

iii) An upper capping line is added in accordance with $J_{max} = \frac{(W-a)\sigma_y}{15}$.

All of the above constructions are illustrated in fig. 6.51 together with the region of valid data.

Data within the valid region must be suitably distributed in order to yield valid J_{IC} results. ASTM E813-88 demands that one data point must lie within a band between the 0.15 mm exclusion line and an offset line 0.5 mm from the blunting line. Similarly one data point must lie within a band between an offset line 1.0 mm from the blunting line and the 1.5 mm exclusion line.

A provisional value of J_{IC} can now be determined for the qualifying data by finding the intersection of the power law regression line and the 0.2 mm offset line. The following procedure is recommended in ASTM E813-88 for accurate determination of J_{IC}.

i) An estimated $J_{Q(1)} - J_{Q(i)}$ value is read for the graphical plot.

ii) $\Delta a_{(i)}$ is evaluated using:

$$\Delta a_{(i)} = \frac{J_{Q(i)}}{2\sigma_y} + 0.2\ mm \quad \ldots\ldots (6.10)$$

iii) An interim value $J_{Q(i+1)}$ is derived for the power law hardening relationship as follows:

$$J_{Q(i+1)} = C_1 \left(\Delta a_{(i)}\right)^{C_2} \quad \ldots\ldots (6.11)$$

iv) The integer *i* is incremented and fed back into equation (6.10) and (6.11) to obtain successive values of $\Delta a_{(i)}$ and interim $J_{Q(i+1)}$ until the J_Q results converge within ±2%.

v) Maximum and minimum crack extensions valid for J_{IC} qualifications are determined by projection down the crack extension axis of the intercepts between the power law curve and the 0.15 mm and 1.5 mm exclusion lines, see fig. 6.52.

6.4.3 TEST RESULTS

As with the aluminium specimens described in section 4.4.3, P_Q was calculated by using the 5% offset rule specified in clause 9.2.2 of BS 7448 [26] (see fig. 4.23) for all specimens subjected to a K_{IC} test. This procedure is performed automatically within the K_{IC} Instron program but as with the aluminium specimens several results were manually checked. Typical fracture surfaces are illustrated in fig. 6.53 for a range of plain sided and side grooved specimens. There was no evidence of stable crack growth in any of the specimens subjected to this type of test. The final fatigue pre-crack length was determined by the use of a travelling microscope with digital electronic readout. Test records obtained from both plain and side grooved specimens were similar to those described for the preliminary tests in section 6.4.2 and illustrated in fig 6.50.

For plain sided specimens K_Q was calculated from P_Q in accordance with equation (4.4) and (4.5) and post fracture validity checks were performed in accordance with Clause 10 in BS 7448 [26]. In total four full thickness specimens were tested from which three valid K_{IC} results were obtained, the other specimen (25P2) failed the $P_{max}/P_Q < 1.1$ check but only marginally with a value of 1.14 being obtained. Hence the average value of fracture toughness, K_{IC} obtained was 95.6 MPa $m^{0.5}$. In the case of sub thickness specimens K_Q could not be designated K_{IC} due not only to the thickness requirements being met but also because the $P_{max}/P_Q < 1.1$ condition was increasingly violated as the thickness reduced. Values of P_Q and K_Q can be seen for all plain sided specimens in table 6.4 and a complete set of test records can be seen in Appendix II.

(a) 25 Thick plain

(b) 10 Thick plain

(c) 25 Thick side grooved

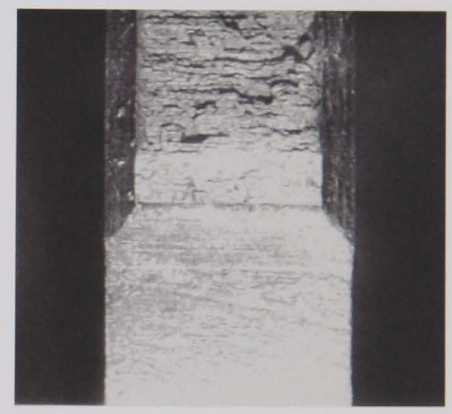

(d) 10 Thick side grooved

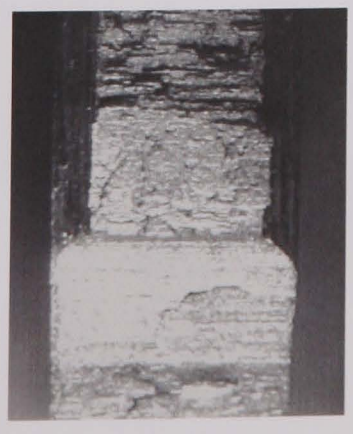

(e) 5 Thick side grooved

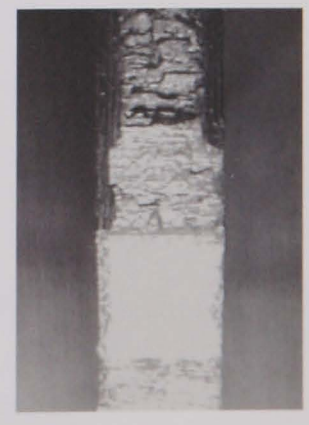

(f) 2.5 Thick side grooved

Fig. 6.53 Typical fracture surfaces – specimens subjected to K tests

In the case of side grooved specimens K_Q was calculated from P_Q in the same way as for plain specimens based on the actual specimen thickness. Corrected fracture toughness values were then calculated by using equation (2.29) for values of $m = 0.5$ and $m = 0.7$. Values of P_Q, K_Q and corrected K_Q can be seen in table 6.4 and a complete set of records for side grooved specimens can be seen in Appendix III.

Results for plain sided specimens subjected to J testing in accordance with ASTM E813-88 [104] can be seen in fig. 6.54 for 5 mm thick specimens and fig. 6.55 for 2.5 mm thick specimens. Stable crack growth was observed in all of these specimens and was marked by heat tinting by placing the specimens in an oven preheated to approximately 300°C and left for at least 20 minutes. The specimens were then broken open using the Instron test machine set at a rapid steady displacement.

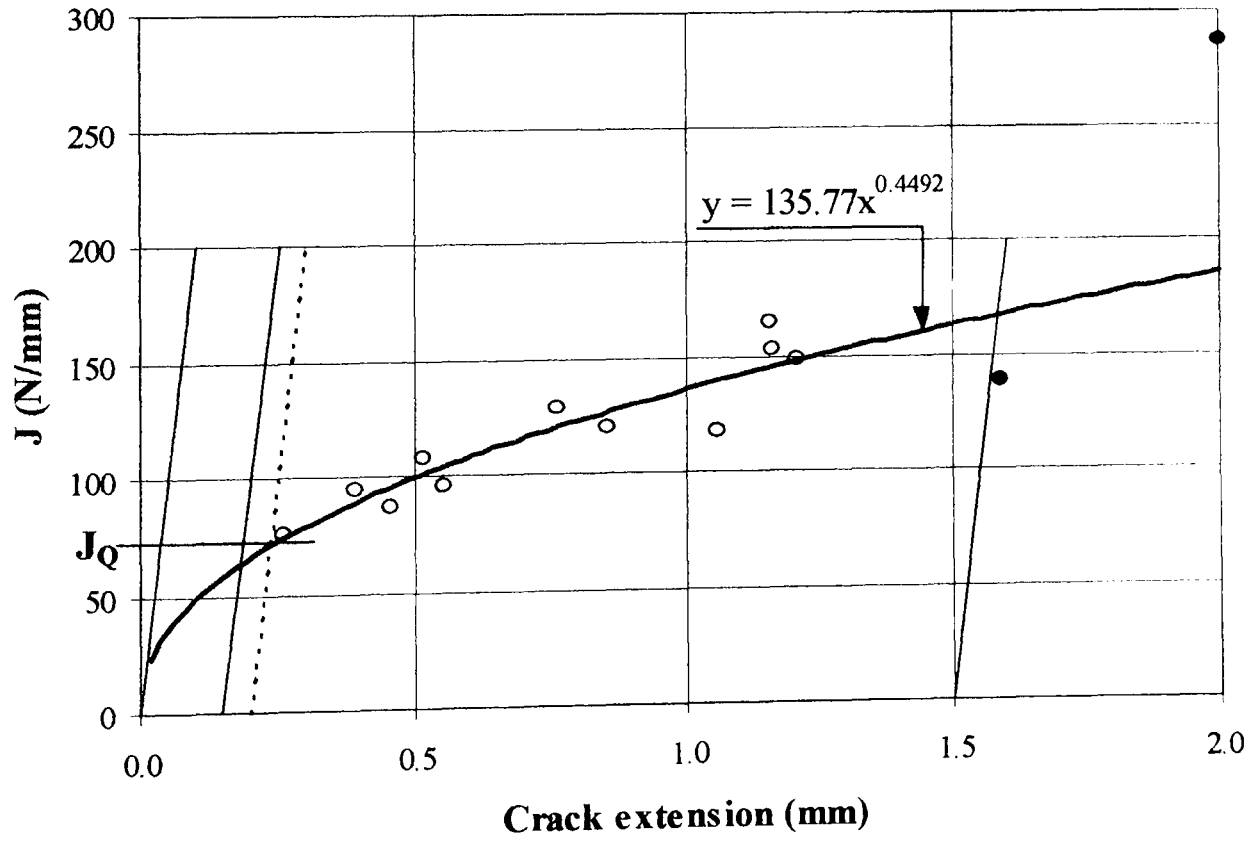

Fig. 6.54 J - Δa for 5mm thick specimens

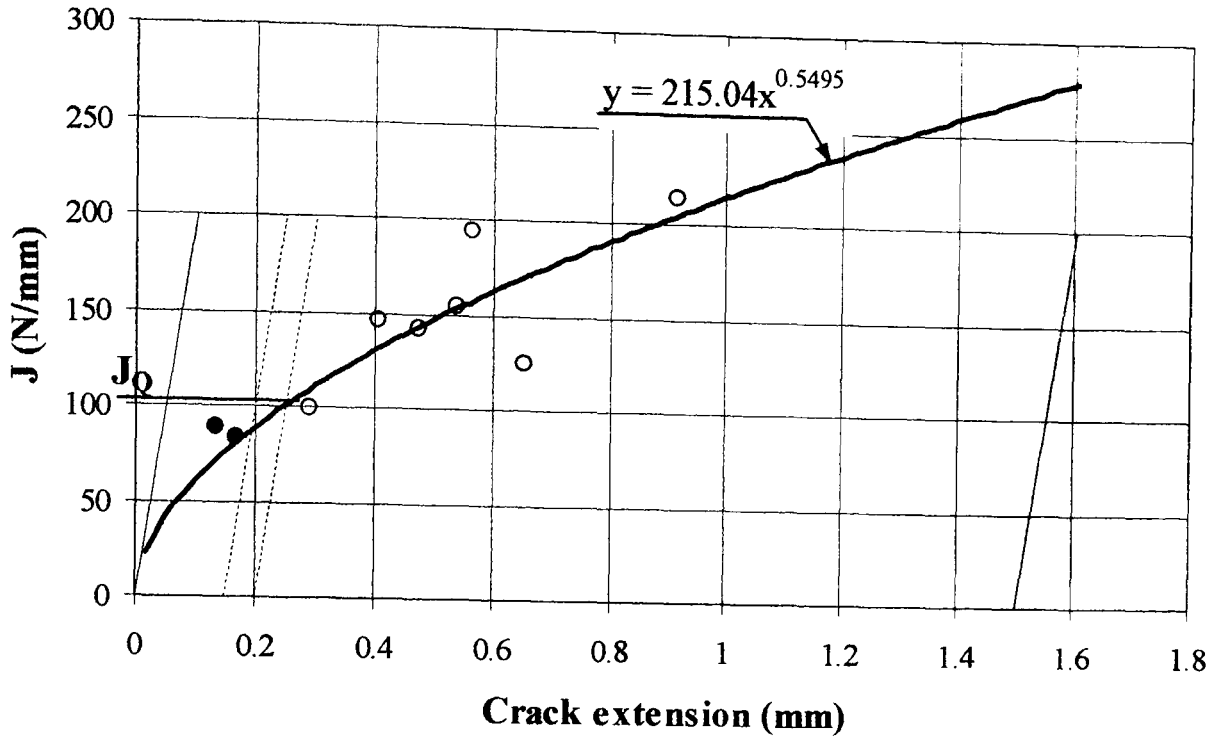

Fig. 6.55 J - Δa for 2.5mm thick specimens

Results obtained from the tests were J_Q = 71.0 N/mm for the 5 mm thick specimens and J_Q = 100.8 N/mm for the 2.5 mm thick specimens these results were then converted into K_Q values using equation (2.14) to give K_Q = 119.2 MPa $m^{0.5}$ for the 5 mm thick specimens and K_Q = 142.0 MPa $m^{0.5}$ for the 2.5 mm thick specimens.

Typical fracture surfaces are illustrated in fig. 6.56 for a range of crack extensions. Stable crack growth was measured in the same way as for fatigue pre-crack measurement. Final K_Q values were obtained from the J_Q values using equation (6.8) and added to table 6.3. A complete set of records can be seen in Appendix II. None of the J_Q values obtained could be designated as J_{IC} values due to failure to comply with clause 9.4.1.6 of ASTM E 813-88 [104] which states that the two near surface crack extension measurements shall not differ from the centre line value by more than +/- 0.02 W. In all cases crack tunnelling prevented this condition being met.

A sample of specimens, both plain and side grooved, were examined by scanning electron microscope with some typical results being shown in fig. 6.57. In all cases the failure mechanism was microvoid coalescenece.

(a) Specimen 5P1

(b) Specimen 5P4

(c) Specimen 5P3

(d) Specimen 5P2

Fig. 6.56 Typical fracture surfaces – specimens subjected to J tests

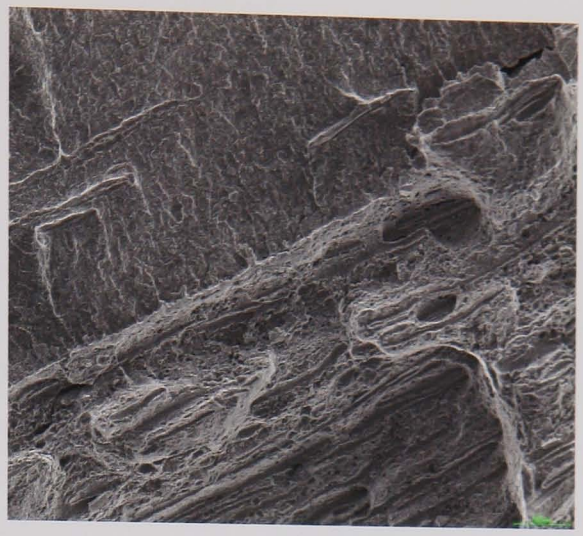

(a) Fatigue crack – fracture area interface, magnification = 120

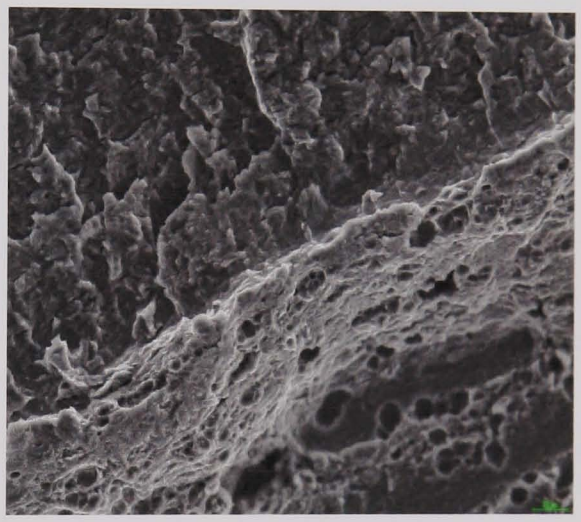

(b) Fatigue crack – fracture area interface, magnification = 750

(c) Ductile failure region, magnification = 2200

Fig. 6.57 Scanning electron microscope fractographs

Specimen No	Side Groove Type	Gross Thickness	Net Thickness	P_Q (kN)	K_Q (Mpa.m$^{0.5}$) Full thickness	K_Q (Mpa.m$^{0.5}$) Based on $K_{IC} = K_{NOM}(B/B_N)^m$	
						m = 0.5	m = 0.7
25P1	None	25		60.5	95.4		
25P2	None	25		62.3	96.3		
25P3	None	25		60.7	95.2		
25P4	None	25		61.5	96.2		
15P3	None	15		39.6	102.5		
15P4	None	15		38.9	98.2		
10P1	None	10		29.7	113.3		
10P2	None	10		26.3	99.8		
10P3	None	10		28.4	108.3		
10P4	None	10		27.2	103.7		
All J tests	None	5			119.2		
All J tests	None	2.5			142.0		
25SG1	30% Vee	25	17.5	54.0	85.96	102.74	110.34
25SG2	30% Vee	25	17.5	44.9	73.05	87.31	93.77
15SG1	30% Vee	15	10.5	28.1	74.95	89.58	96.21
10SG1	30% Vee	10	7	20.9	78.9	94.30	101.28
10SG2	30% Vee	10	7	22.2	80.5	96.22	103.33
5SG1	30% Vee	5	3.5	9.9	79.44	94.95	101.97
5SG2	30% Vee	5	3.5	9.6	75.62	90.38	97.07
5SG3	30% Vee	5	3.5	11.4	90.44	108.10	116.09
5SG4	30% Vee	5	3.5	9.2	72.94	87.18	93.63
5SG5	30% Vee	5	3.5	10.6	83.32	99.59	106.95
5SG6	30% Vee	5	3.5	9.2	73.26	87.56	94.04
5SG7	30% Vee	5	3.5	9.0	71.92	85.96	92.32
2-5SG1	30% Vee	2.5	1.75	5.2	92.41	110.45	118.62
2-5SG2	30% Vee	2.5	1.75	5.3	81.55	97.47	104.68
2-5SG3	30% Vee	2.5	1.75	5.8	88.12	105.32	113.11
2-5SG4	30% Vee	2.5	1.75	4.8	73.86	88.28	94.81
2-5SG5	30% Vee	2.5	1.75	5.6	84.11	100.53	107.96
2-5SG6	30% Vee	2.5	1.75	5.4	81.3	97.17	104.36

Table 6.4 Summary of experimental results

6.5 COMPARISON OF FINITE ELEMENT AND EXPERIMENTAL RESULTS

Comparison of finite element and experimental results can only be undertaken based on J-Q theory due to the dominant room temperature failure mode being microvoid coalescence.

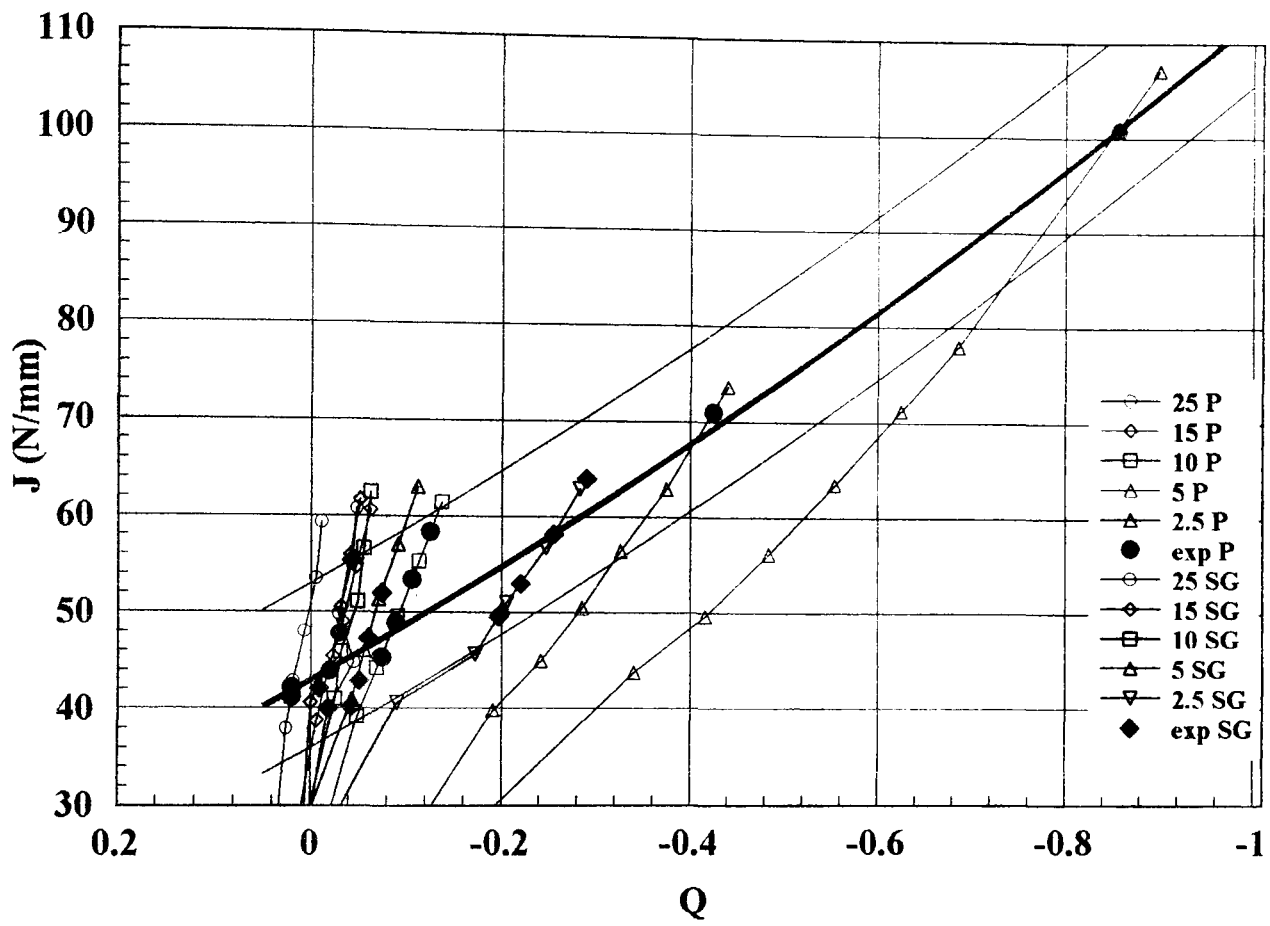

Fig. 6.58 Comparison of FE and experimental results based on J – Q theory

Fig. 6.58 shows the experimental results superimposed on the J-Q trajectories from figs 6.48 and 6.49 for both plain sided and side grooved specimens. Each set of experimental results is plotted on the appropriate J-Q trajectory for the specimen size and type in question. Experimental results obtained from K_{IC} tests have been converted into J values by using equation (2.23). A trend line has been added to fig. 6.58 of average experimental results obtained from the plain sided specimens together with scatter limits based on the results plotted. Consideration of fig. 6.58 illustrates the effectiveness of side grooving in terms of increased constraint and fracture performance particularly for thin specimens. J-Q trajectories for the plain sided specimens become progressively shallower as the thickness reduces with both the 5 mm thick and 2.5 mm thick plain specimens exhibiting very shallow J-Q trajectories together with high values of fracture toughness associated with stable crack growth. In contrast the introduction of side grooves produces steep J-Q trajectories and much lower measured values of

fracture toughness with no stable crack growth. The experimental fracture toughness values plotted for side grooved specimens in fig. 6.58 are based on m = 0.7 in equation (2.29). It is interesting to note that the 5 mm thick side grooved specimen performs better than the 10 mm thick plain sided specimen and almost as well as the 15 mm thick plain sided specimen.

The intersection of the J-Q trajectory for the 5 mm thick side grooved specimen with the trend line based on plain sided experimental results can be used to predict the likely performance of the specimen under test conditions. The result of such an analysis would be an expected, measured, fracture toughness of 100.6 MPa $m^{0.5}$. This compares well with the average experimental result obtained with m = 0.7 of 100.3 MPa $m^{0.5}$. It is, however, approximately 5% higher than the measured fracture toughness based on the average result obtained from full thickness specimens.

The results obtained in this study using J-Q theory are consistent with the principles illustrated in fig. 3.21.

6.6 LOWER SHELF CLEAVAGE FAILURE PREDICTION

Prediction of the likely influence of side grooves on fracture toughness values obtained at lower shelf temperatures where the dominant failure mode is cleavage can be made by the application of the area scaling method.

Application of area scaling is however problematic in 3D cases in that the use of equation 3.37 is dependent upon an appropriate choice of reference area, h_0, which in 2D studies is normally taken to be the area associated with a Q = 0 situation. Since area scaling is essentially a 2D method its extension into 3D is open to some interpretation particularly when considering what constitutes an appropriate reference area [109]. Consideration of the results shown in table 6.2 indicate that for the 25 mm thick specimen the centre line slice area is 130.7 $units^2$ compared to the small scale yielding value obtained from boundary layer analysis of 143.2 $units^2$. Away from the specimen centre line the area decreases as indicated in fig. 6.34 giving an average area across the specimen of 89.38 $units^2$. Clearly the 25 mm thick specimen yields a plane strain fracture toughness result in accordance with the relevant standards even though the small scale yielding slice area, h_0, is not achieved anywhere through the thickness of the specimen. It is with this in mind that the average area across the 25 mm thick specimen

was selected as the plane strain reference area, h_{PS}. Hence combining equations 3.37 and 2.23 a constraint corrected fracture toughness value can be calculated for each specimen thickness in accordance with:

$$K = K_{PS} \sqrt[4]{\frac{h_{PS}\left(\sigma_1/\sigma_0\right)}{h\ \left(\sigma_1/\sigma_0\right)}} \quad \text{..... (6.12)}$$

where K_{PS} is the plane strain fracture toughness.

It is further assumed that if the ratio obtained of $K_{PS}/K > 1$ that the specimen will fail at the plane strain value. This assumption would seem reasonable because the volume of material ahead of the crack tip subjected to a stress level at which cleavage fracture could occur will be greater than for the specimen yielding a plane strain fracture toughness value. Results of the finite element predictions based on equation 6.12 and the above assumption for $\sigma/\sigma_0 = 2$ are shown in fig. 6.59. The results suggest that side grooving would also improve the performance of CT specimens at lower shelf temperatures where the dominant failure load is cleavage.

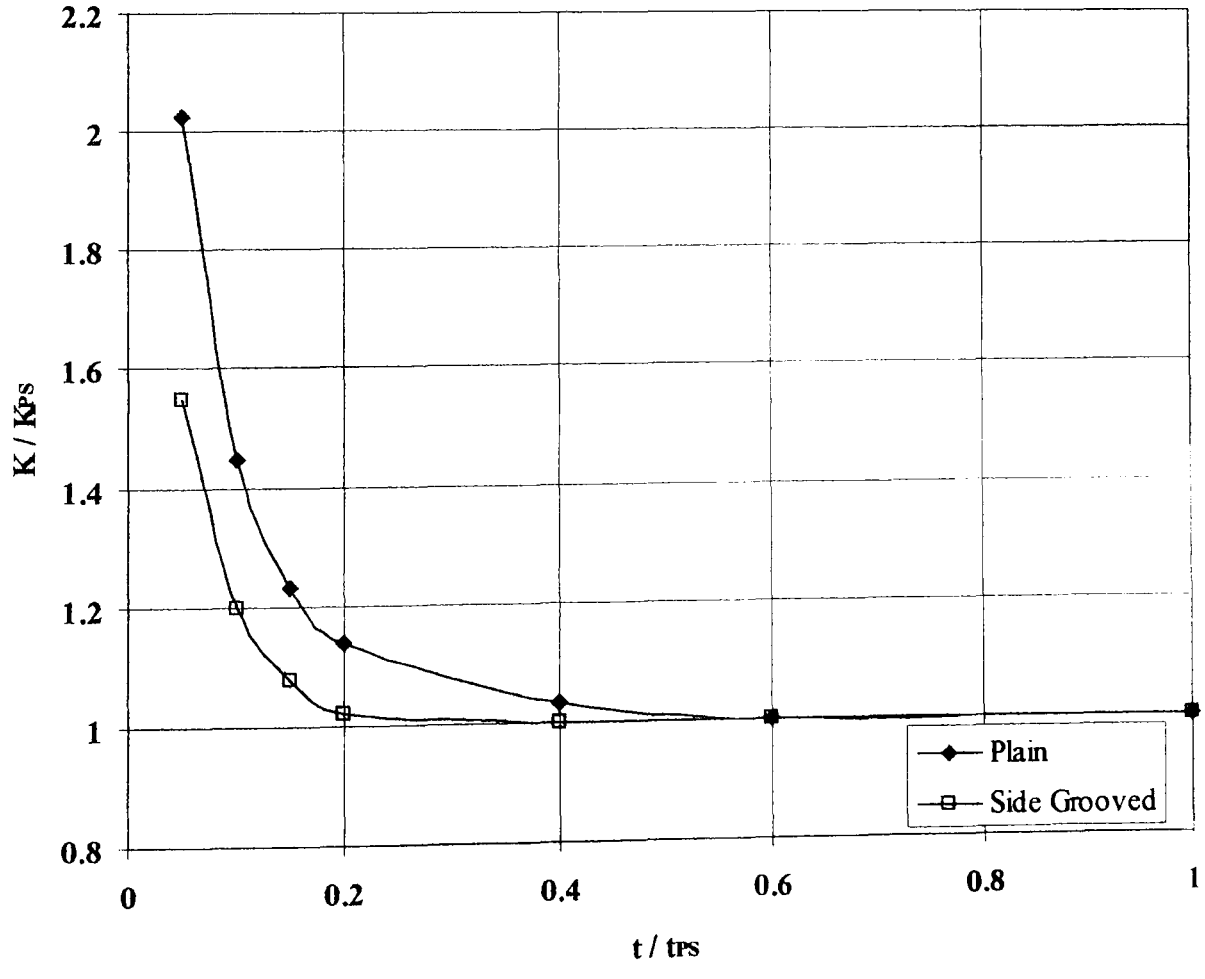

Fig. 6.59 Finite element predictions for cleavage failure based on area scaling

6.7 DISCUSSION OF RESULTS AND CLOSURE

The results presented in this chapter suggest that crack tip constraint is sufficiently enhanced by the introduction of side grooves as to allow near minimum (i.e. plane strain) fracture toughness values to be obtained from sub thickness fracture specimens under both ductile conditions where failure is by microvoid coalescence and brittle conditions where cleavage is the prime failure mechanism. In the case of cleavage this is based upon theoretical considerations alone, but in the case of microvoid coalescence is supported by both theoretical (finite element) and experimental evidence.

Table 6.5 gives some key average experimental and finite element results for ductile fracture, as can be seen the experimental results for m = 0.7 give good agreement with the finite element predictions obtained by taking the intersection of the J-Q trajectory for each side grooved specimen thickness with the trend line based on plain sided experimental results. The percentage difference from the measured plane strain fracture toughness value of 95.6 MPa $m^{0.5}$ is also given.

Although good agreement is obtained between the experimental results for m = 0.7 and the finite element results they are, in all cases, slightly elevated from the plane strain value obtained from the 25 mm thick specimen. As would be expected the deviation from the plane strain value increases as the specimen thickness reduces, the average value of 102.3 MPa $m^{0.5}$ obtained from the 10 mm thick specimens is based on the results from two tests only which may explain the larger experimental deviation compared with the finite element prediction. All other experimental results for 5 mm thick and 2.5 mm thick specimens are the average of a least six results.

Specimen Thickness	K (MPa $m^{0.5}$)		
25 mm Plain	95.6		
	m = 0.5	m = 0.7	FE Prediction
10 mm Side Grooved	95.26 (-0.3%)	102.3 (+7.0%)	99.12 (+3.6%)
5 mm Side Grooved	93.38 (-2.3%)	100.29 (+4.9%)	100.6 (+5.2%)
2.5 mm Side Grooved	99.87 (+4.5%)	107.25 (+11.9%)	105.8 (+10.6%)

Table 6.5

Consideration of the 5 mm thick specimen results indicate that the expected increase in fracture toughness for the side grooved specimen is approximately 5% from both the experimental results based on m = 0.7 and finite element predictions. In comparison the increase in fracture toughness obtained experimentally for the plain sided specimen was in the order of 25%.

Although BS 7448 [26] allows the use of side grooves under certain conditions it makes no provision for the calculation of results based on side grooved specimens, ASTM E 399 [27] on the other hand does make such provision in the form of equation (6.13)

$$K_I = \frac{P_Q}{\left(B B_N W\right)^{0.5}} \cdot f\left(\frac{a}{W}\right) \quad \ldots.(6.13)$$

where the symbols have the same meaning as in equations (2.29) and (4.8).

It is recognised that equation (6.13) is identical to equation (2.29) with m = 0.5, hence from the results presented in table 6.5 conservative results would be obtained for side grooved specimens down to 5 mm in thickness, i.e. one fifth of the recommended thickness required to yield plane strain results. Results obtained from the 2.5 mm thick specimens proved to be non conservative even with m = 0.5. It is therefore recommended that, although m = 0.7 gives the best fit between experimental results and finite element predictions, if sub thickness side grooved specimens are used for fracture testing a value of m = 0.5 should be used to ensure conservative results. This leads to a thickness limit for side grooved specimens based on the results presented here for EN24 of:

$$B \geq 0.5\left(\frac{K_{IC}}{\sigma_Y}\right)^2 \quad \ldots.(6.14)$$

Although the results presented give a positive indication of the benefits of side grooving only one material has been investigated and the observations made here may not be applicable across a wide range of materials. Although results have been published in the open literature for side grooved specimens they are often limited to the effects of side grooving on full thickness specimens. Very little has been published on the effects of

side grooving on sub thickness specimens hence the difficulty in comparing the results presented here with others. This lack of published data is probably due to the fact that fracture testing is expensive and that the detailed 3D finite element analysis required demands powerful computers and long runtimes. Further work to investigate the effects of hardening and different material toughness characteristics would be beneficial particularly in consideration of the potential benefit to many industries where the materials employed often can not provide specimens of the standard thickness required by current fracture toughness test methods.

CHAPTER 7

CIRCUMFERENTIALLY CRACKED ROUND BAR SPECIMENS

7.1 INTRODUCTION

In previous chapters side grooving of compact tension specimens has been investigated as a possible way of obtaining essentially plane strain fracture toughness values from sub thickness specimens. However the planar dimensions of such specimens can still be considerable and the accuracy of machining required to produce the specimens is high. An alternative to the compact tension and single edge notched bend specimen that is the subject of increasing interest is the circumferentially cracked round bar (CRB) specimen. Reasons for this increased interest are due to the low machining costs of the specimen and perceived weaker size requirement. The argument in support of this weaker size requirement stems around the fact that for CRB specimens the circumferential crack tip has no free surface and that the required crack depth and minimum diameter need only to ensure that the crack tip plastic zone is not influenced by the free surface of the cylinder or the specimen axis of symmetry.

The work presented in this chapter aims to investigate the above claims by considering crack tip constraint and size requirements for this type of specimen by again using a J-Q approach. In this way a direct comparison can be made of the performance of the CRB specimen and side grooved compact tension specimens.

Three materials have been investigated, the aluminium alloy from chapter 4, EN24 steel from chapters 5/6 and HY-130 steel. Material properties for the aluminium alloy and EN24 are as defined previously, properties for the HY-130 steel are taken from published literature.

7.1.1 AIMS AND OBJECTIVES

The aims and objectives of the work described in this chapter are as follows:

i) To investigate crack tip constraint provided by CRB specimens for a variety of diameters and crack depths.

ii) To define specimen size requirements for CRB specimens in terms of material properties.

iii) To compare the effectiveness of the CRB specimen with that of side grooved compact tension specimen for EN24 steel.

7.2 SPECIMEN GEOMETRY AND SIZE REQUIREMENTS

No recognized test procedure for precracked CRB specimens exists, hence there is an unreliability inherent in reported fracture toughness values obtained from such tests. E602-81 [110] defines a test method for sharp–notched cylindrical tension specimens but only allows the use of two standard diameters, i.e. $^1/_2$" and $1^1/_{16}$" as indicated in fig. 7.1. Donoso and Labbe [111] used a modified form of this specimen with a diameter of 12 mm and a notch root radius of 0.0625 mm to evaluate Q stresses and constraint behaviour of bi-metallic specimens. Wilson [112], Shabara et al [113] and Toribio [114] also used this type of specimen but with a variety of notch radii, whilst other investigators Li and Bakker [115]; Itoh, Murakami and Kashiwaya[116]; Giovanola, Homma, Lichtenberger, Crocker and Klopp [117] have used fatigue precracked versions of this specimen type.

When considering size requirements for CRB specimens the published literature presents conflicting views. For CT specimens it is generally accepted that the minimum size requirements to achieve minimum values of K_{IC} occurs when the specimen thickness and uncracked ligament size are eight times the plane stress plastic zone size, see 4.2.

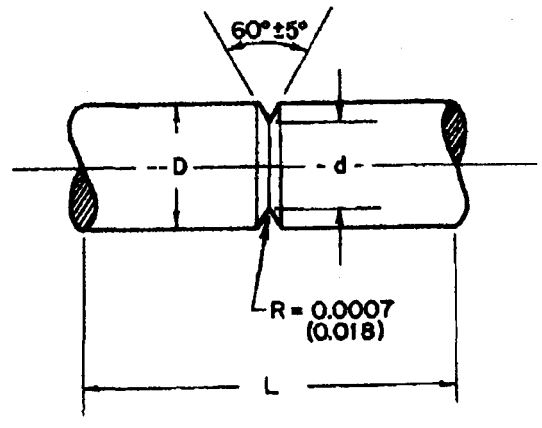

NOTE 1—Dimensions are in inches and (millimetres).
NOTE 2— *d* must be concentric with *D* within 0.001 in. (0.025 mm).

Nominal Size	*D*	*d*	*L*, minimum
½ in.	0.500 ± 0.005 (12.7 ± 0.13)	0.353 ± 0.005 (8.96 ± 0.13)	1.00 (25.4)
1 1/16 in.	1.060 ± 0.005 (26.9 ± 0.13)	0.750 ± 0.005 (19.0 ± 0.13)	2.13 (54.1)

Fig. 7.1 Standard notched specimen according to E 602-81

It can be argued that for CRB specimens the circumferential crack tip has no free surface and that the required crack depth and minimum diameter need only to ensure that the crack tip plastic zone is not influenced by the free surface of the cylinder or the specimen axis of symmetry. Ibrahim and Kotousov [118] then used the Irwin plastic zone size in plane strain as given in equation (7.1) to determine the minimum specimen diameter based on a crack depth to radius ratio of 0.5 to be 32 r_Y as given by equation (7.2)

$$r_Y = \frac{1}{6\pi}\left(\frac{K_{IC}}{\sigma_Y}\right)^2 \quad .....(7.1)$$

$$D \geq 32\, r_Y \; or \; D \geq 1.7\left(\frac{K_{IC}}{\sigma_Y}\right)^2 \quad .....(7.2)$$

Other earlier studies by Shen et al [119], Lucon et al [120] and Ibrahim et al [121] all suggested that less stringent size requirements were appropriate with the crack length, uncracked ligament required being given by:

$$a, b \geq 0.27\left(\frac{K_{IC}}{\sigma_Y}\right)^2 \quad from\,[120\ \&\ 121] \quad .....(7.3)$$

and

$$a, b \geq 0.38\left(\frac{K_{IC}}{\sigma_Y}\right)^2 \quad from\,[119] \quad .....(7.4)$$

This leads to a specimen diameter requirement for a crack depth to radius ratio 0.5 of:

$$D \geq 1.08\left(\frac{K_{IC}}{\sigma_Y}\right)^2 \quad from\,[120\ \&\ 120] \quad .....(7.5)$$

and

$$D \geq 1.52\left(\frac{K_{IC}}{\sigma_Y}\right)^2 \quad from\,[119] \quad .....(7.6)$$

Scibetta [122] undertook an experimental and finite element study of CRB specimens but concluded that the minimum specimen size requirement is more stringent than any of the above and was equivalent to twice the ASTM limit for CT specimens, i.e.

$$D \geq 5\left(\frac{K_{IC}}{\sigma_Y}\right)^2 \quad .....(7.7)$$

Scibetta's reasoning was based on both constraint loss as defined by J-Q theory [82, 83] and by the area scaling method of Anderson and Dodds [91].

The analysis matrix for this study is given in table 7.1, the specimen diameters were chosen to give a spread of results in the range of $0.92\left(\frac{K_{IC}}{\sigma_Y}\right)^2$ to $13.3\left(\frac{K_{IC}}{\sigma_Y}\right)^2$ for the EN24, aluminium alloy and cleavage dominated HY-130 steel.

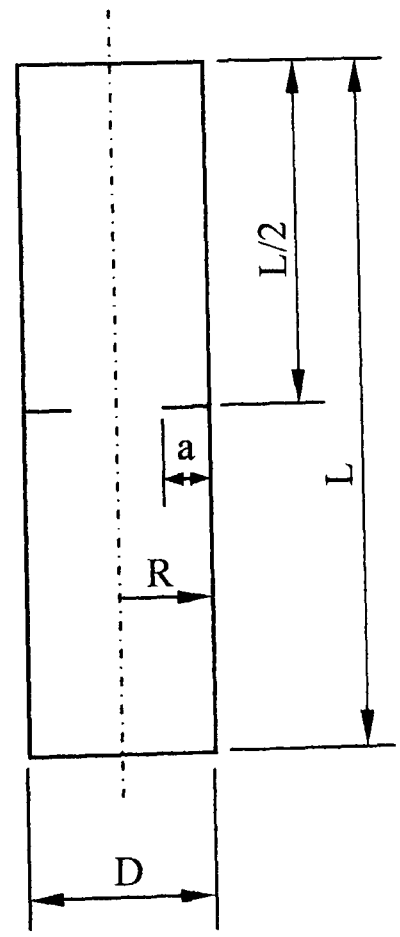

Fig. 7.2 Schematic of specimen

Due to the fact that experimental results have been well published for HY-130 information is available for both the brittle cleavage dominated low temperature region and the ductile upper shelf region thereby giving the opportunity of studying both failure

modes. The specimen range for ductile behaviour is from $0.18\left(\frac{K_{IC}}{\sigma_Y}\right)^2$ to $0.72\left(\frac{K_{IC}}{\sigma_Y}\right)^2$.

From a manufacturing point of view it was considered unlikely that specimens smaller than 8 mm diameter could be manufactured and successfully precracked so this was taken as a lower limit. A schematic of the specimen is shown in fig. 7.2. For the EN24 and HY-130 specimens three crack depths were considered a/R = 0.3, 0.5 and 0.7 for the aluminium alloy specimen only a/R = 0.5 was considered.

7.3 MATERIAL PROPERTIES

Material properties for the aluminium alloy and EN24 were taken from the experimental results presented in chapters 4 and 5. For EN24 a Ramberg Osgood material model as given by equation (5.2) had already been defined, see fig. 5.9, to have the parameters of n = 50, $\alpha = 0.15$, $\varepsilon_o = 0.0048$, $\sigma_o = 970$ MPa and E = 200 GPa.

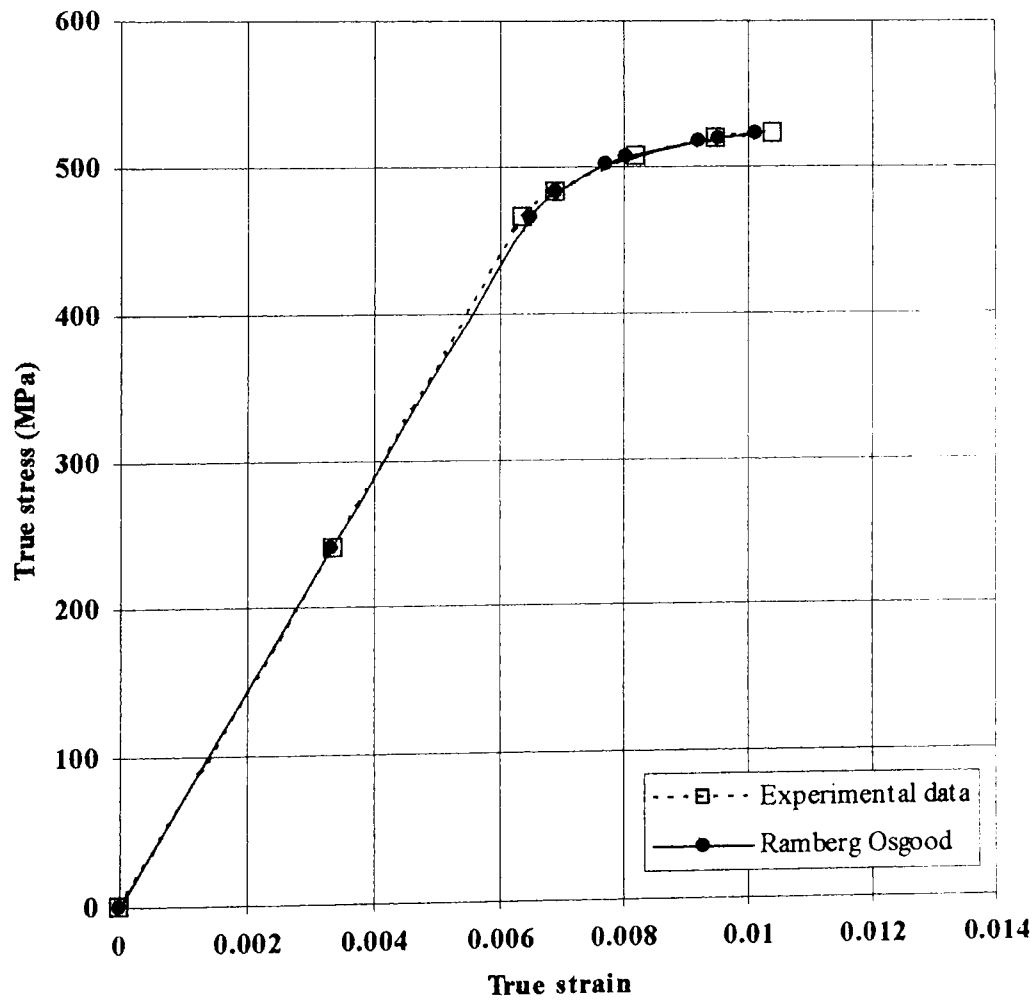

Fig 7.3 Aluminium alloy stress strain curve

Material properties for the aluminium alloy, although presented in fig. 4.21 were only used for linear elastic finite element analysis in chapter 4. Fig. 7.3 shows the stress strain data from fig. 4.21 re-plotted as true stress – true strain together with the appropriate Ramberg Osgood material curve. The values used in the material description are n = 32, $\alpha = 0.02$, $\varepsilon_o = 0.00659$, $\sigma_o = 475$ MPa and E = 72 GPa.

HY-130 steel was chosen because it is well characterized in published literature [123, 124], it is a ductile quenched and tempered steel that requires elastic-plastic fracture test methods at room temperature where failure is essentially by microvoid coalescence. Data is also available for this material at low temperatures where failure is essentially by cleavage. Joyce and Hasson [123] present results for a full temperature range with the J_{IC} versus temperature curve from [123] being shown in fig. 7.4. Measured values from [123] are K_{IC} = 51.5 to 81.3 MPa $\sqrt{m}$ at -192°C and J_{IC} = 139 to 174.7 KPa m at room temperature. All tests were conducted using 25 mm thick compact tension specimens with a/W = 0.65 and a/W = 0.8.

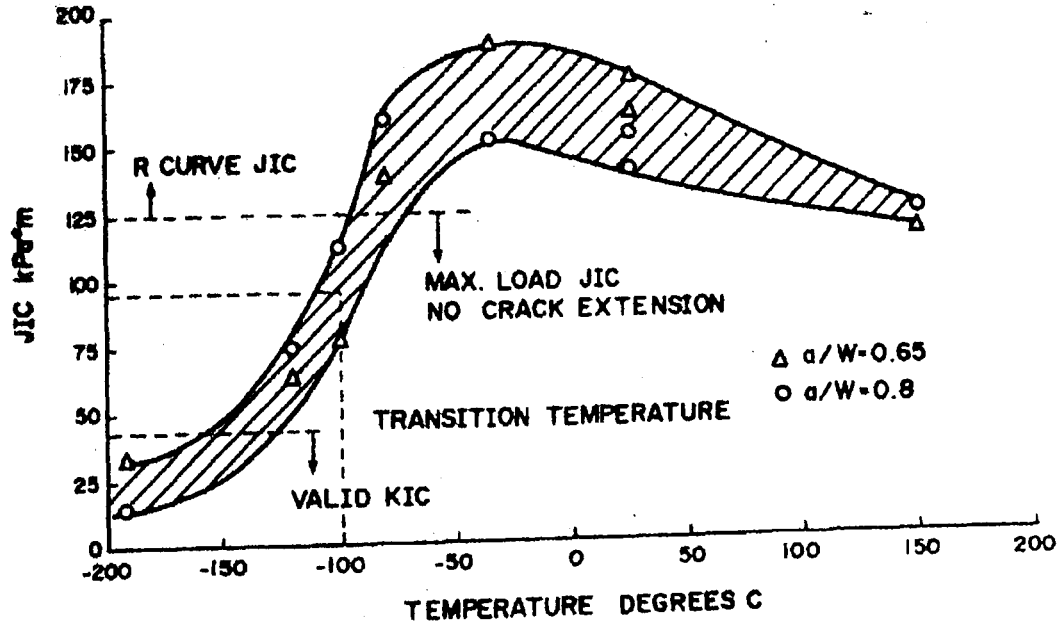

Fig. 7.4 J_{IC} vs temperature HY 130 steel.
After Joyce and Hasson [123]

Giovanola et al [117] tested CRB specimens in a variety of materials including HY-130 steel at room temperature. In addition to the normally expected ductile form of the material at room temperature which required elastic-plastic test procedures Giovanola also obtained the material in an embrittled form.

Material	EN24		HY-130 (Cleavage)		HY-130 (Ductile)		Aluminium alloy	
K_{IC} (MPa $m^{0.5}$)	96		55		190		22	
σ_Y (MPa)	970		873		873		475	
K_{IC}/σ_Y	0.099		0.063		0.210		0.049	
Specimen Diameter	9mm	$0.92\left(\frac{K_{IC}}{\sigma_Y}\right)^2$	8mm	$2.00\left(\frac{K_{IC}}{\sigma_Y}\right)^2$	8mm	$0.18\left(\frac{K_{IC}}{\sigma_Y}\right)^2$	8mm	$3.30\left(\frac{K_{IC}}{\sigma_Y}\right)^2$
	18mm	$1.83\left(\frac{K_{IC}}{\sigma_Y}\right)^2$	16mm	$4.00\left(\frac{K_{IC}}{\sigma_Y}\right)^2$	16mm	$0.36\left(\frac{K_{IC}}{\sigma_Y}\right)^2$	16mm	$6.60\left(\frac{K_{IC}}{\sigma_Y}\right)^2$
	36mm	$3.67\left(\frac{K_{IC}}{\sigma_Y}\right)^2$	32mm	$8.00\left(\frac{K_{IC}}{\sigma_Y}\right)^2$	32mm	$0.72\left(\frac{K_{IC}}{\sigma_Y}\right)^2$	32mm	$13.3\left(\frac{K_{IC}}{\sigma_Y}\right)^2$
	72mm	$7.34\left(\frac{K_{IC}}{\sigma_Y}\right)^2$						

Table 7.1

Although the reasons for embrittlement were not known the material cleaved at room temperature and effectively measured values of fracture toughness were similar to the lower shelf values obtained in [123]. Measured values from this test programme were K at initiation for the embrittled material of 50.9 – 59.8 MPa$\sqrt{m}$ without bending eccentricity correction and 51.1 to 61.2MPa$\sqrt{m}$ with correction. Results for the ductile HY-130 material were J = 150-157 KPa m for a crack depth, a/R, of 0.65 and 190 KPa m for a crack depth a/R, of 0.37.

Giovanola et al [117] also performed finite element analysis on two of the specimens tested, one manufactured from the embrittled material which was 16 mm diameter and had a crack depth, a/R, of 0.62 and one manufactured from the ductile material which was 6.4 mm in diameter with a/R = 0.37. A power law fit material model was used for the finite element analysis of the form.

$$\frac{\varepsilon}{\varepsilon_o} = \alpha \left(\frac{\sigma}{\sigma_o} \right)^n \quad .....(7.7)$$

with $\varepsilon_o = \sigma_o/E$ and $\sigma_o = 873$ MPa , n = 13.9 and $\alpha = 1.0044$.

The implementation of a true power law hardening material as in equation (7.7) is not possible with the ABAQUS package used for this study, hence a Ramberg Osgood model with the parameters of n = 13.9, $\alpha = 1.0044$, $\varepsilon_o = 0.0043$, $\sigma_o = 873$ MPa and E = 200 GPa was used. The effect of this change is indicated in fig. 7.5 which shows the true power law hardening material model together with the Ramberg Osgood material model. Also indicated is the elastic slope line. As can be seen from fig. 7.5 the Ramberg Osgood model provides a far better fit to the elastic portion of the curve than the true power law hardening curve. This is important, particularly when considering constrained plasticity as is the case early in the loading sequence applied to the CRB specimens. The Ramberg Osgood model is also in reasonable agreement with the power law hardening model for the plastic portion of the curve. It is not clear from [117] how the power law hardening model was implemented in the bespoke finite element package

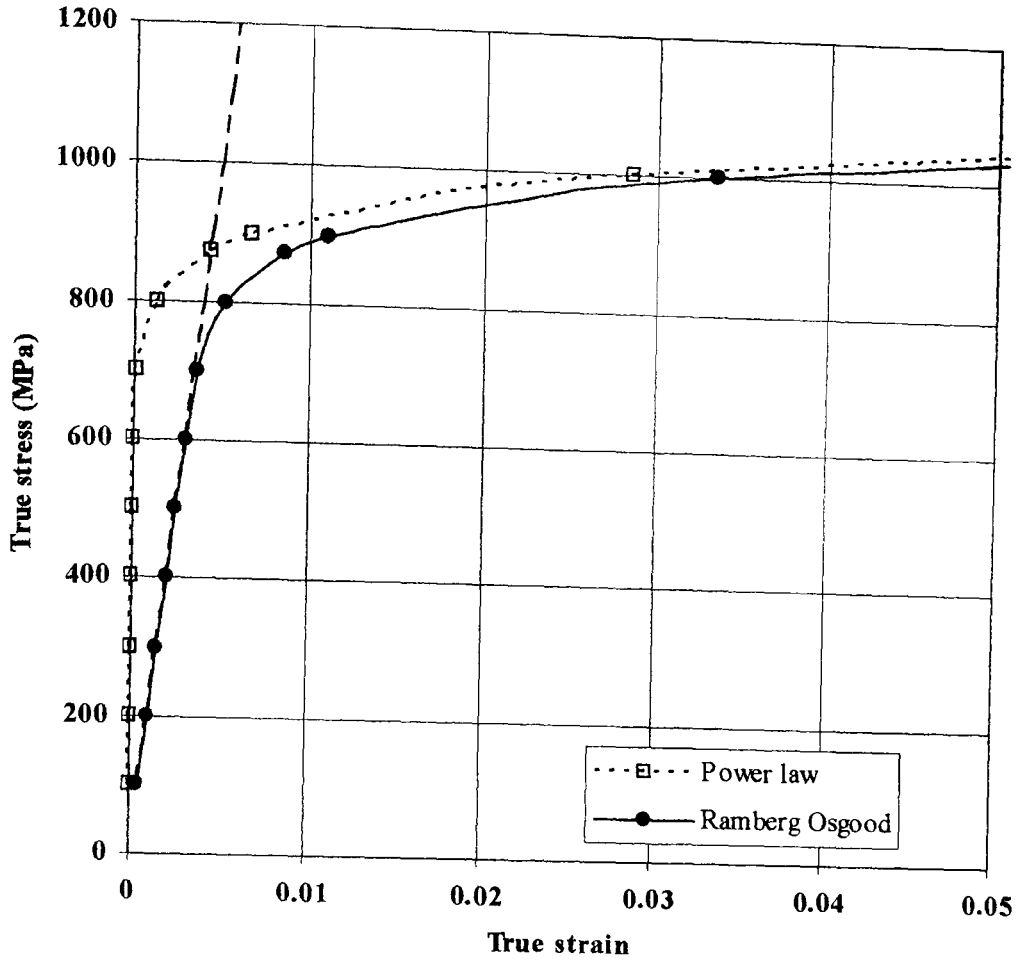

Fig. 7.5 HY-130 stress strain curve

used, NIKE2D, it is likely that the elastic behaviour was specified elsewhere in the material description in which case the two curves would become virtually identical.

7.4 FINITE ELEMENT ANALYSIS

Again the finite element analysis was undertaken using the ABAQUS package [99] together with the FEMGV graphical pre/post processor [100] and ABAQUS post [101].

First a modified boundary layer analysis was performed for the aluminium alloy and HY-130 materials as described in section 5.2 for EN24. A near crack tip region was modelled as a circular domain of outer radius R and initial, blunted, crack tip radius, r_o, of 10^{-5} times the outer radius R. Boundary conditions were applied in accordance with fig. 5.1, equation (5.1) and table 5.2. The mesh was similar to that illustrated in fig. 5.2 and had a high degree of refinement consisting of eight noded plane strain reduced integration elements concentric to the crack tip, the element size being arranged in an approximate geometric progression getting coarser away from the crack tip. As in chapter 5 a small strain formulation was used throughout. The small scale yielding results for each material were subsequently used as reference stress fields for Q stress evaluation.

Finite element modeling of the CRB specimens was done using an axisymetric model as shown in fig. 7.6 a symmetry boundary condition was applied along the crack tip and the aspect ratio of the specimen was 5:1 in all cases. Loading was applied in the form of prescribed displacements on the top edge of the specimen so as to allow the analysis to proceed to full section plasticity without convergence difficulties.

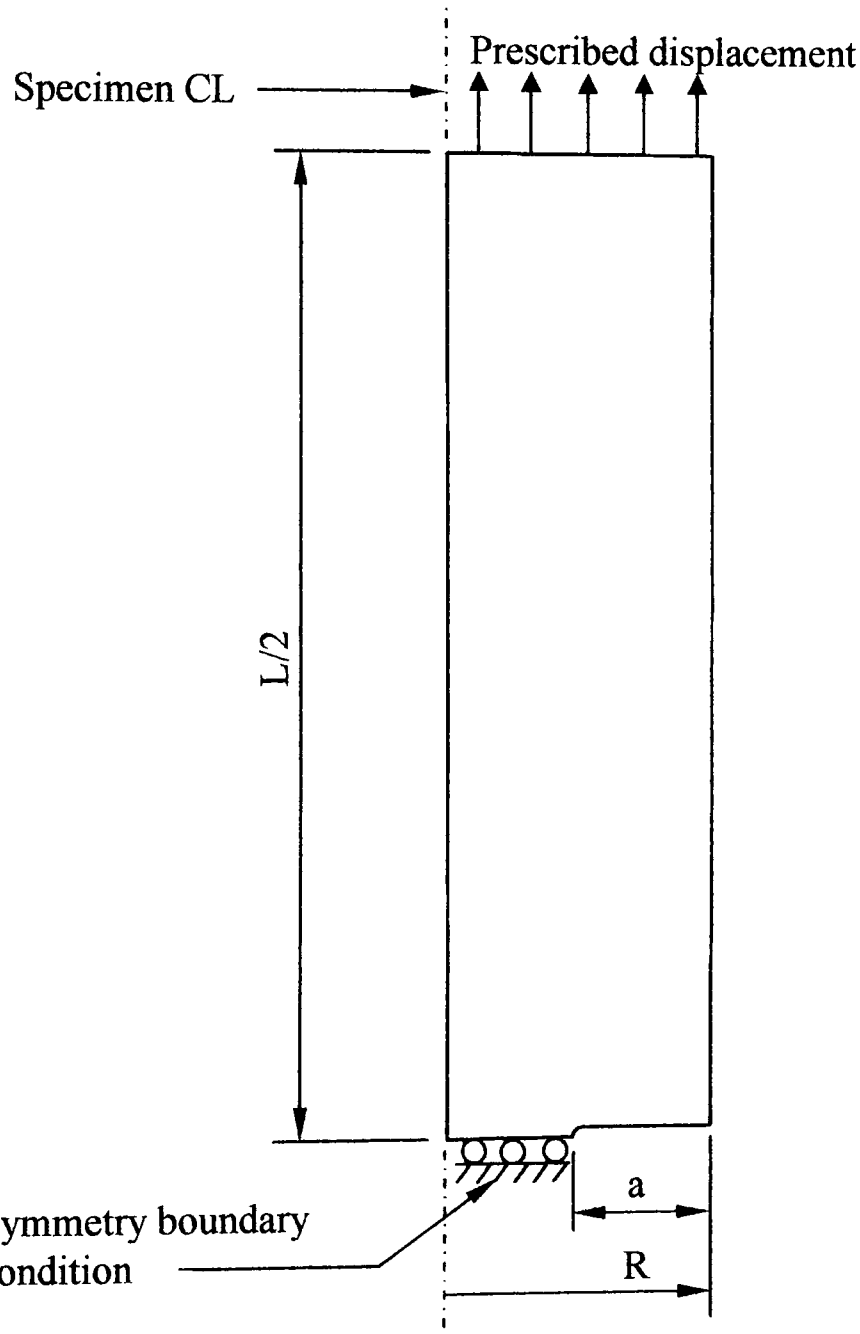

Fig. 7.6 Finite element boundary conditions and loading

The prescribed displacements were applied in approximately 20 load steps for all specimens through to full plasticity, the automatic time stepping routine in ABAQUS was used to overcome any convergence difficulties and this lead to the number of load steps being increased to 25 in some instances.

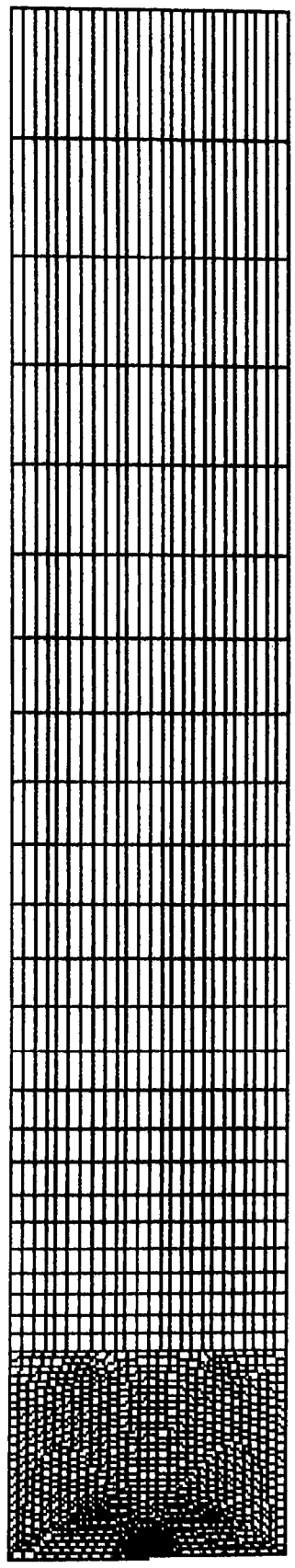

(a) Full mesh

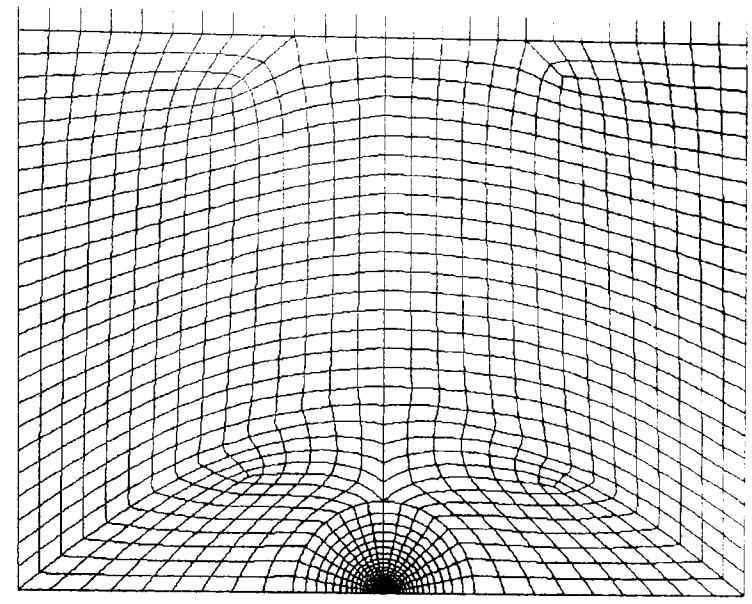

(b) Base region

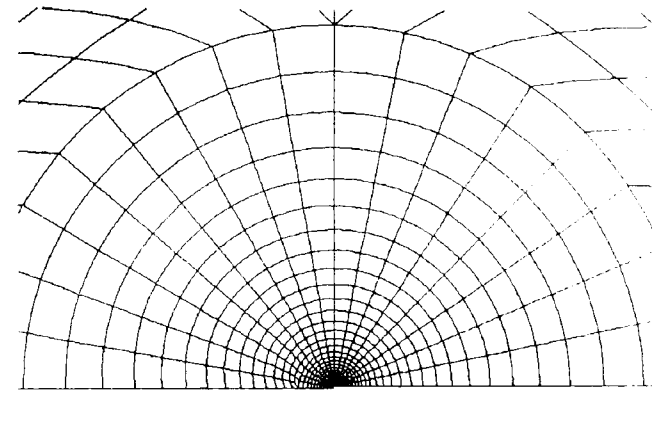

(c) Crack tip region

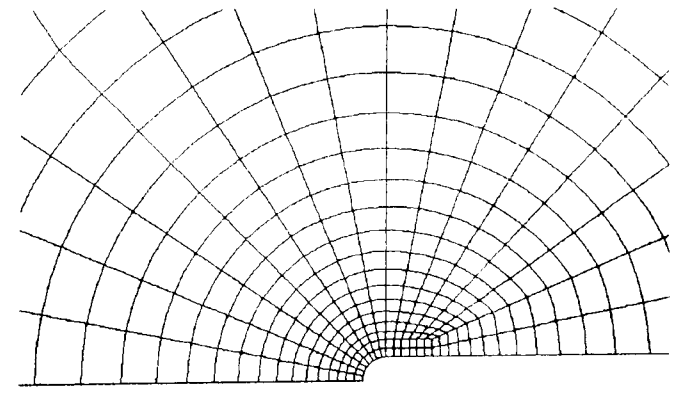

(d) Crack tip detail

Fig. 7.7 Finite element mesh

The finite element mesh consisted of quadratic axisymetric reduced integration elements arranged as shown in fig. 7.7. As with the EN24 compact tension specimens the crack tip was modelled as being blunted with a radius of 0.005 mm. Due to the fact that the analysis was in 2D and would run relatively quickly a great deal of mesh refinement was used in the region of the crack tip.

7.5 FINITE ELEMENT ANALYSIS RESULTS

The finite element analysis results will be considered for each material separately.

7.5.1 EN24

J integral development with load together with J-Q trajectories can be seen for the full range of EN24 specimens in figs. 7.8 to 7.15. Consideration of J-Q trajectories for the EN24 material indicate that both crack depth and specimen size have a strong influence. The smallest diameter specimen, 9 mm (see fig. 7.9), exhibits J-Q trajectories that develop in a very shallow, almost flat, manner at low load but become steeper as the load is increased. For the shallow cracked specimen, a/R = 0.3, this steepening of the J-Q trajectory is less than for the other crack depths with Q becoming progressively more negative with increasing load. For the a/R = 0.5 specimen however a point is reached where the J-Q trajectory exhibits a turning point after which the trajectory becomes almost vertical for a significant load increase before finally returning to a trajectory where Q becomes progressively more negative with increased load. The a/R = 0.7 specimen J-Q trajectory also reaches a turning point but for this specimen the value of Q becomes progressively more positive with increasing load. This behaviour for deeply cracked CRB specimens was also observed by Giovanola et al [117] for HY-130 specimens and by Scribetta [122] for a hypothetical $E/\sigma_Y = 500$ material.

Similar, but less pronounced, effects are observed for all of the other specimen sizes as can be seen in figs. 7.11, 7.13 and 7.15. Due to the fact that these figures are plotted to a different horizontal, Q, axis scale it is difficult to observe the full effects of specimen size.

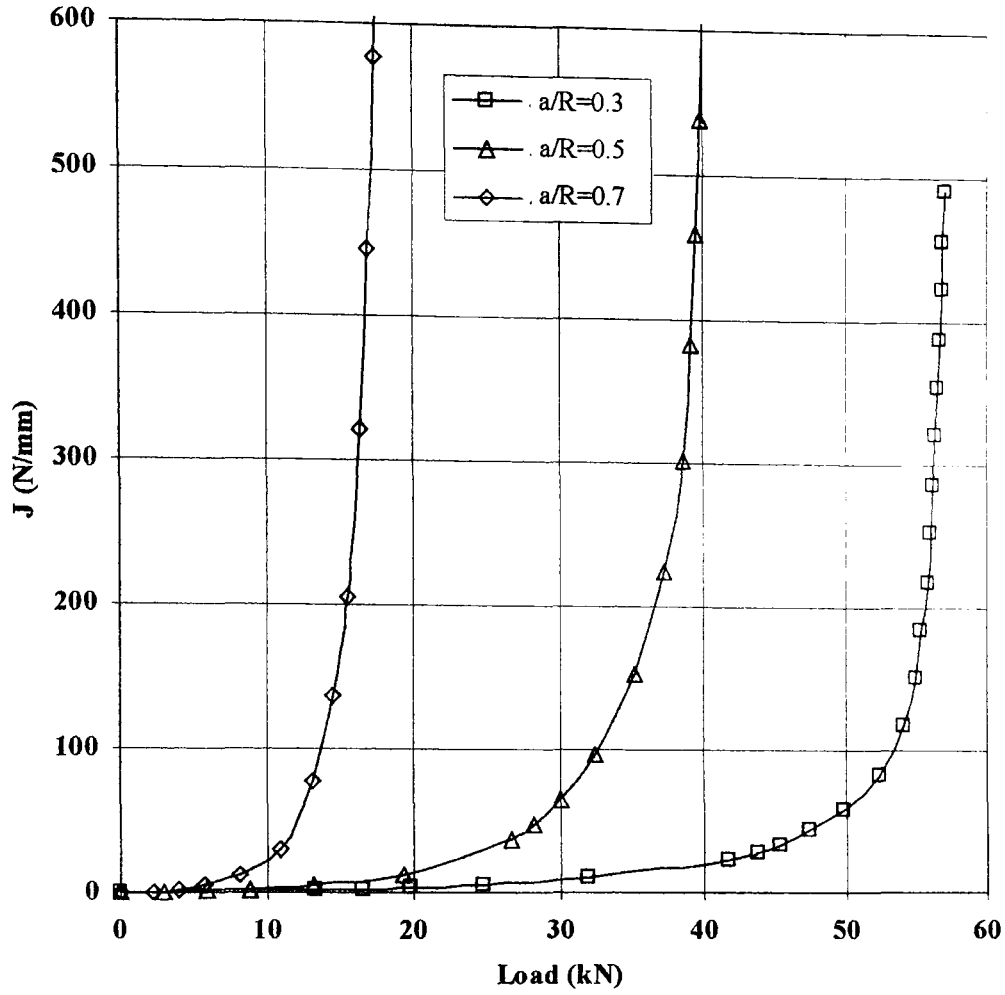

Fig. 7.8 J v load 9 mm diameter EN24 specimens

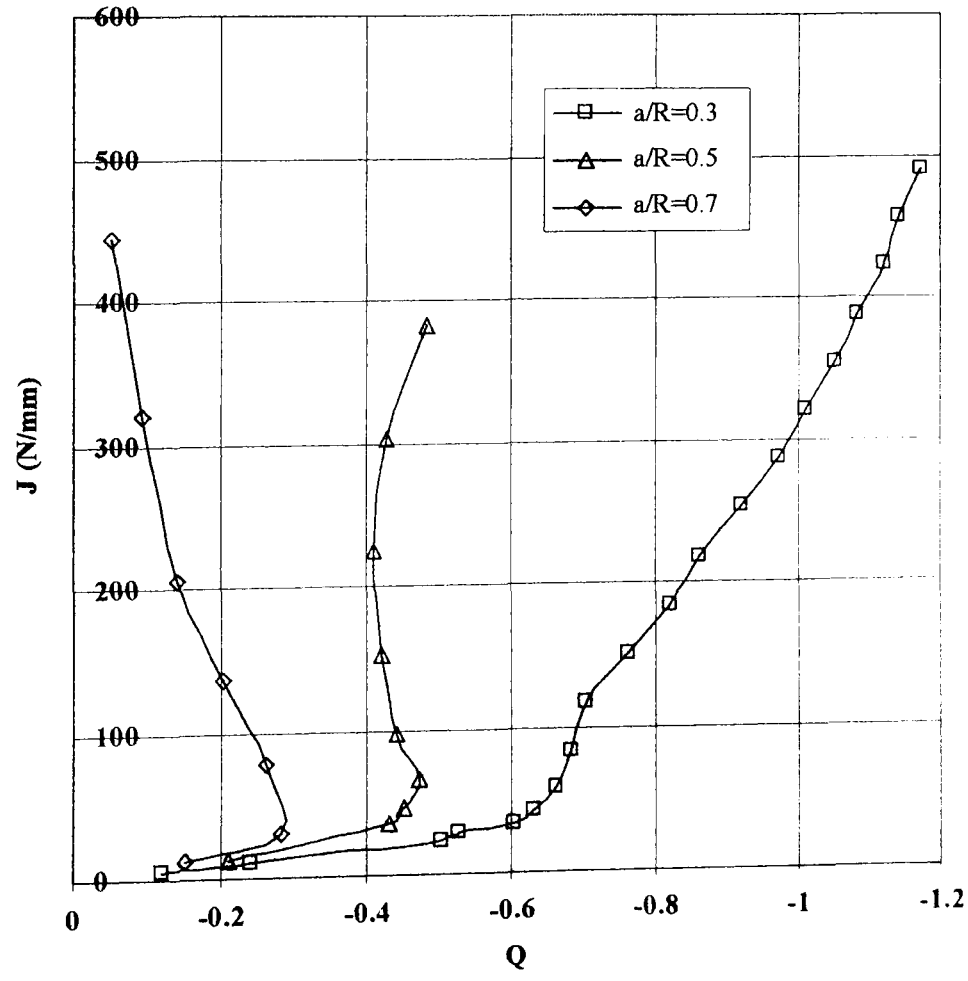

Fig. 7.9 J – Q trajectories 9 mm diameter EN24 specimens

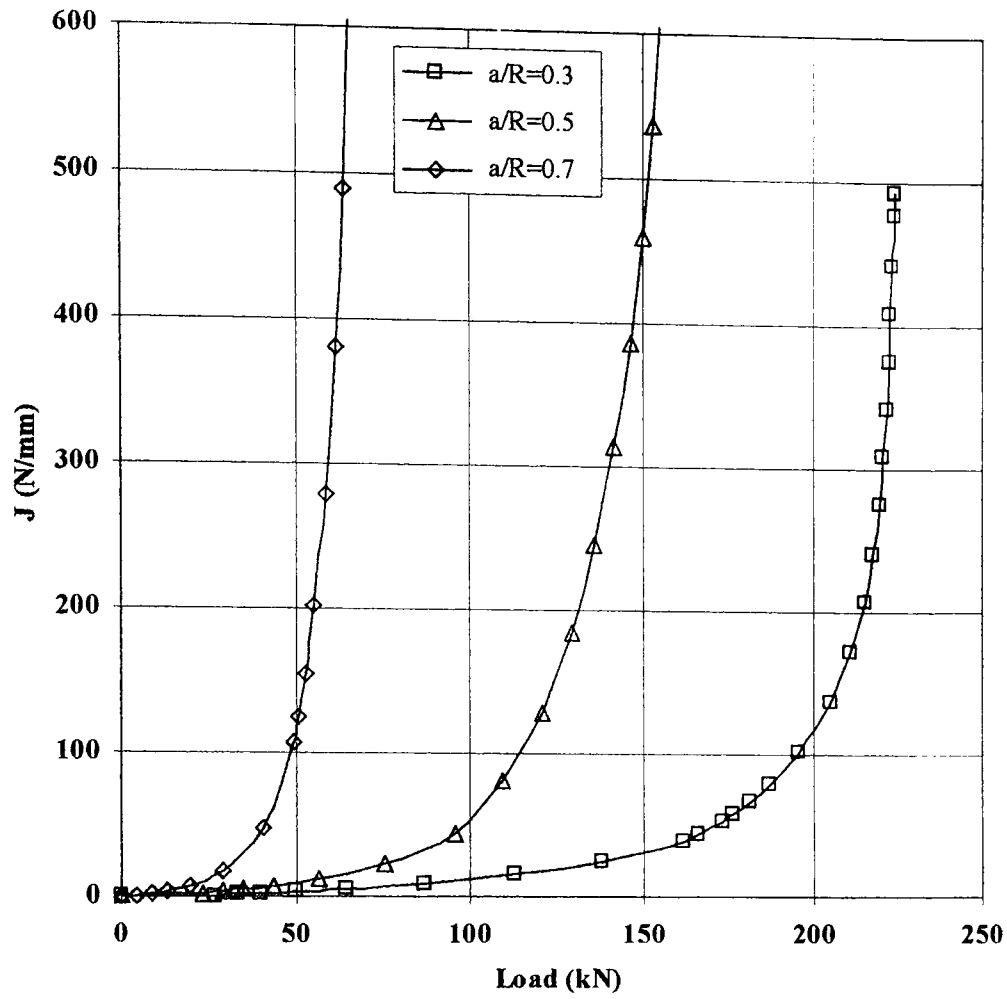

Fig. 7.10 J v load 18 mm diameter EN24 specimens

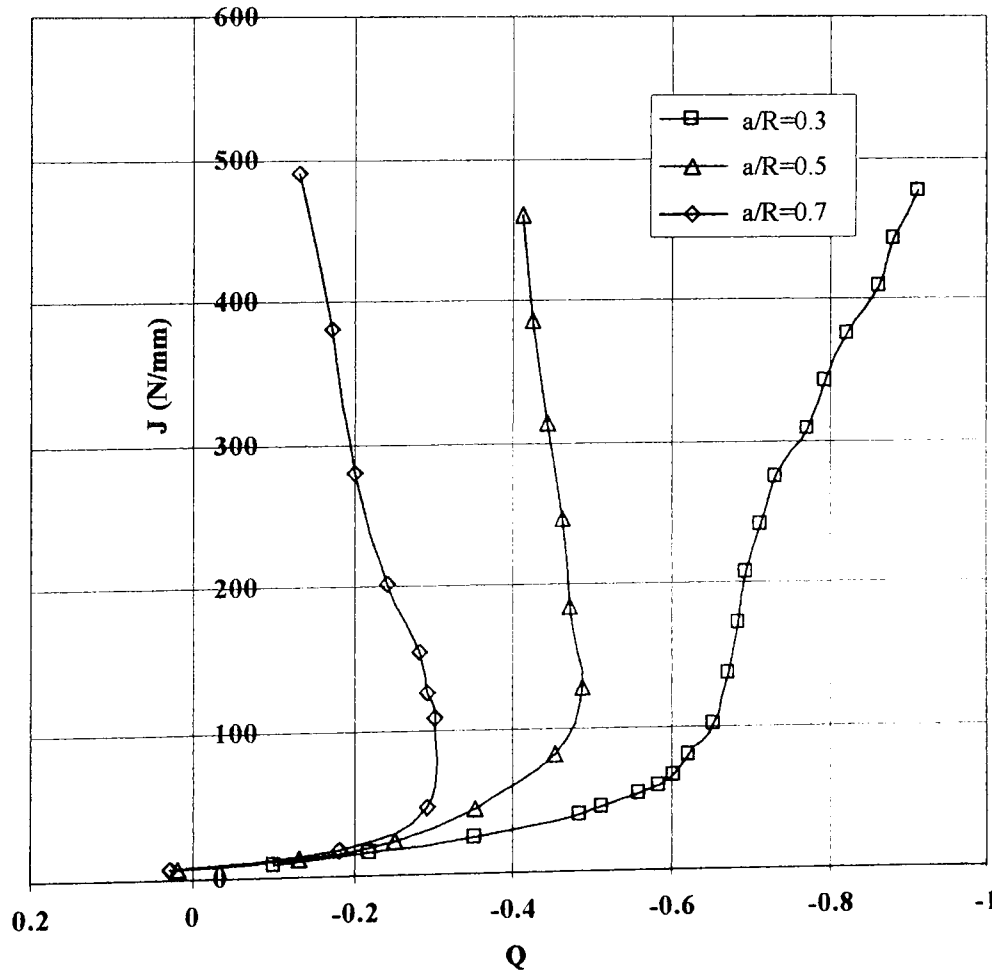

Fig. 7.11 J – Q trajectories18 mm diameter EN24 specimens

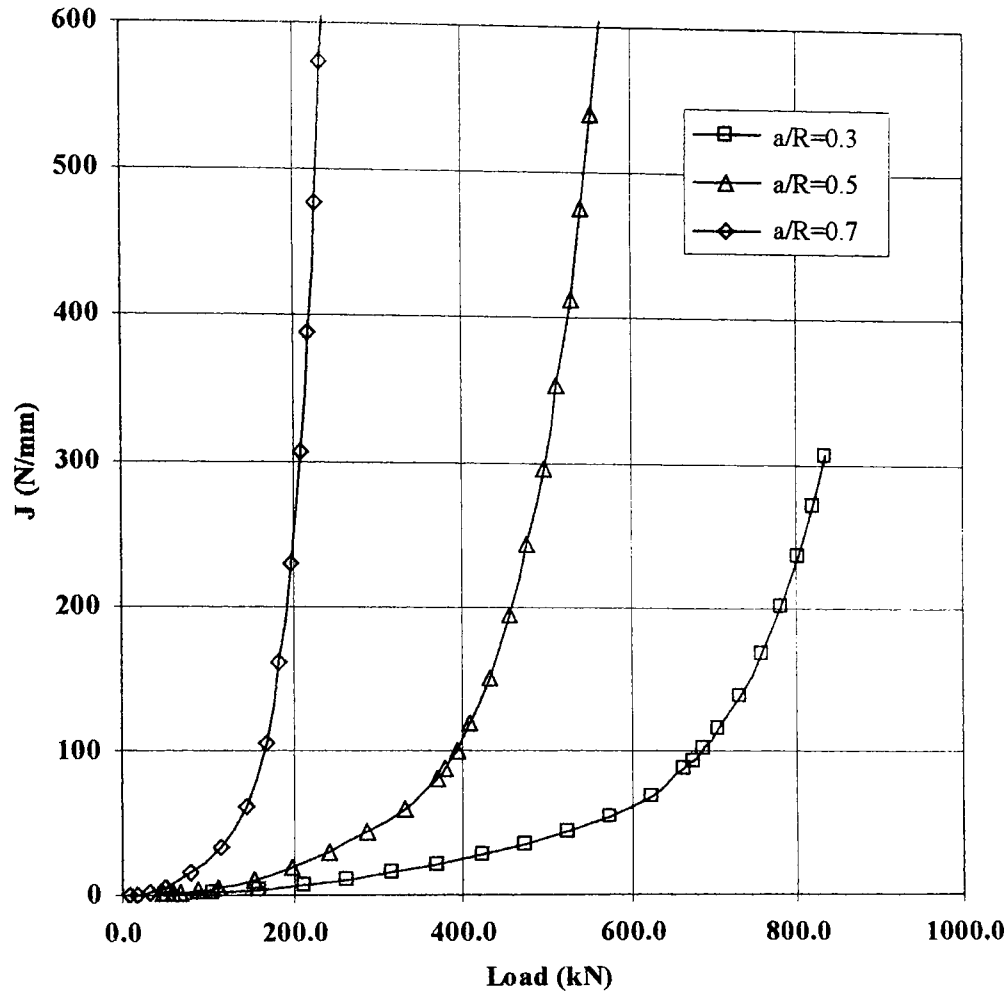

Fig 7.12 J v load 36 mm diameter specimens

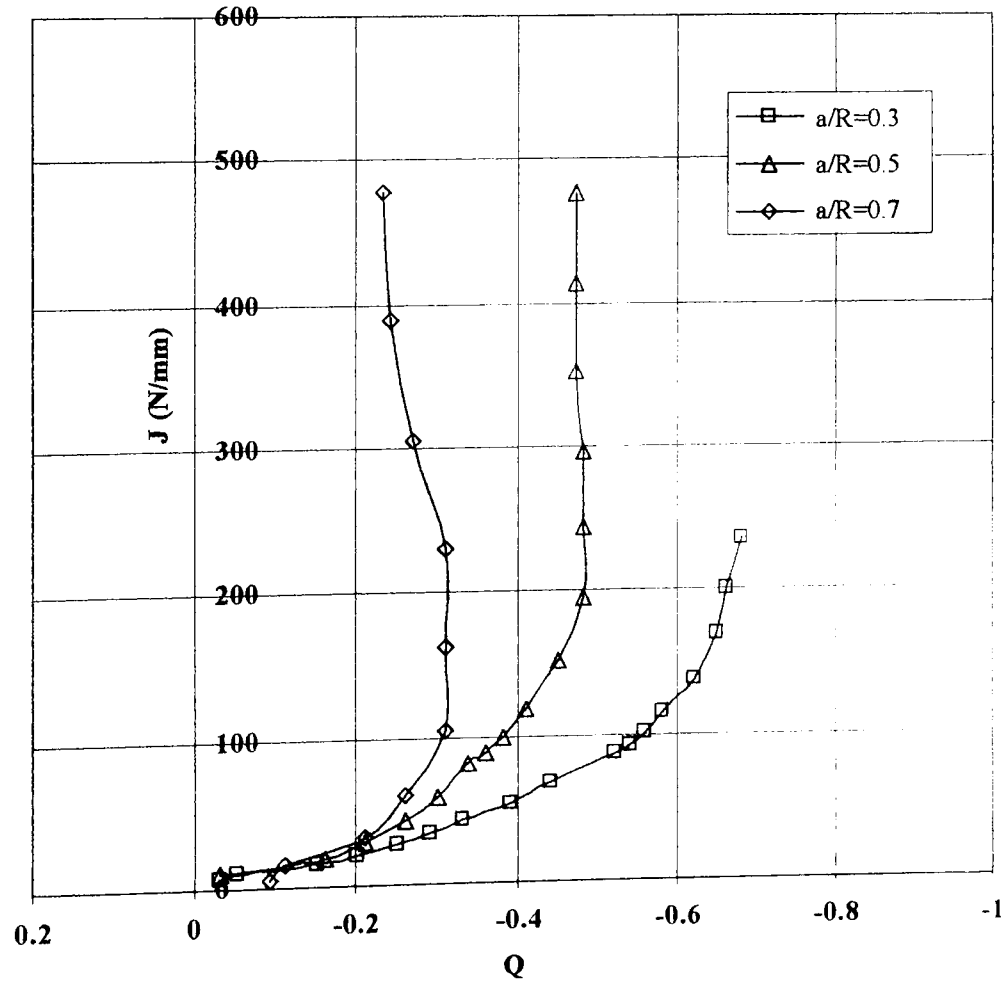

Fig. 7.13 J – Q trajectories 36 mm diameter specimens

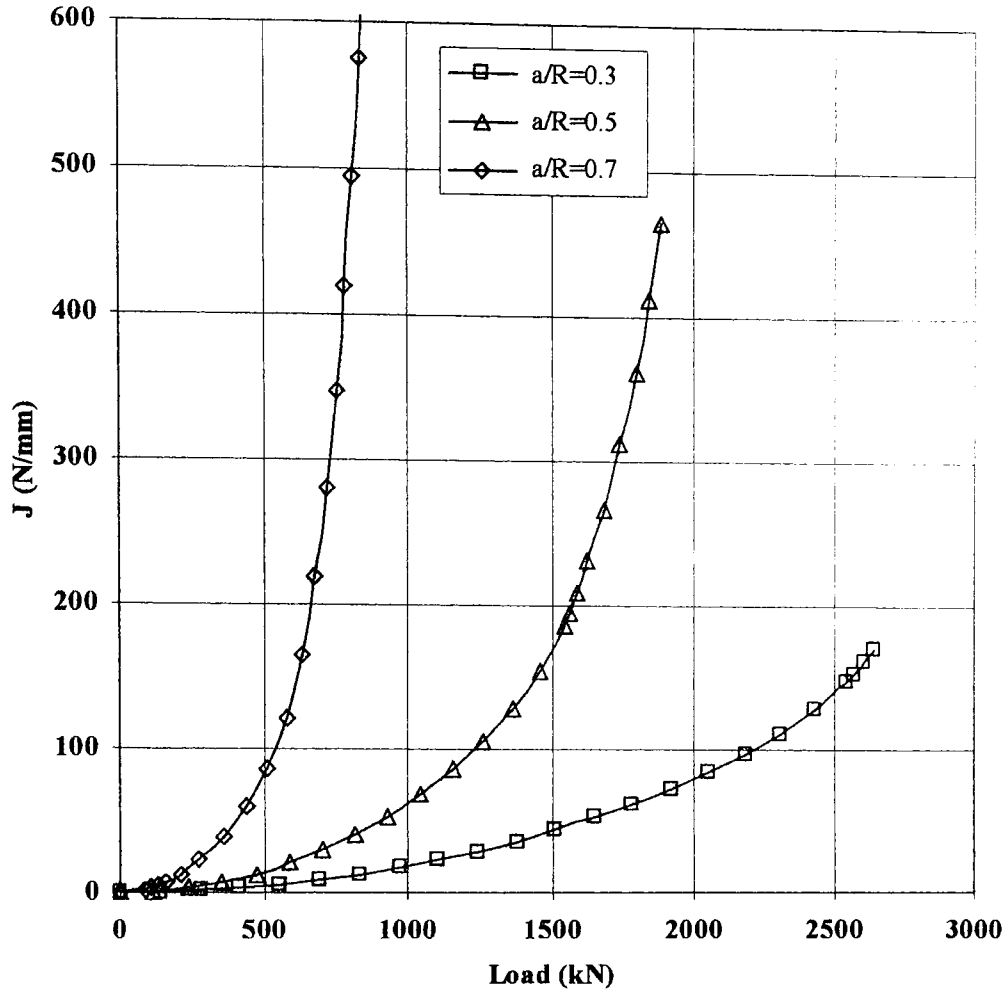

Fig. 7.14 J v load 72 mm diameter EN24 specimens

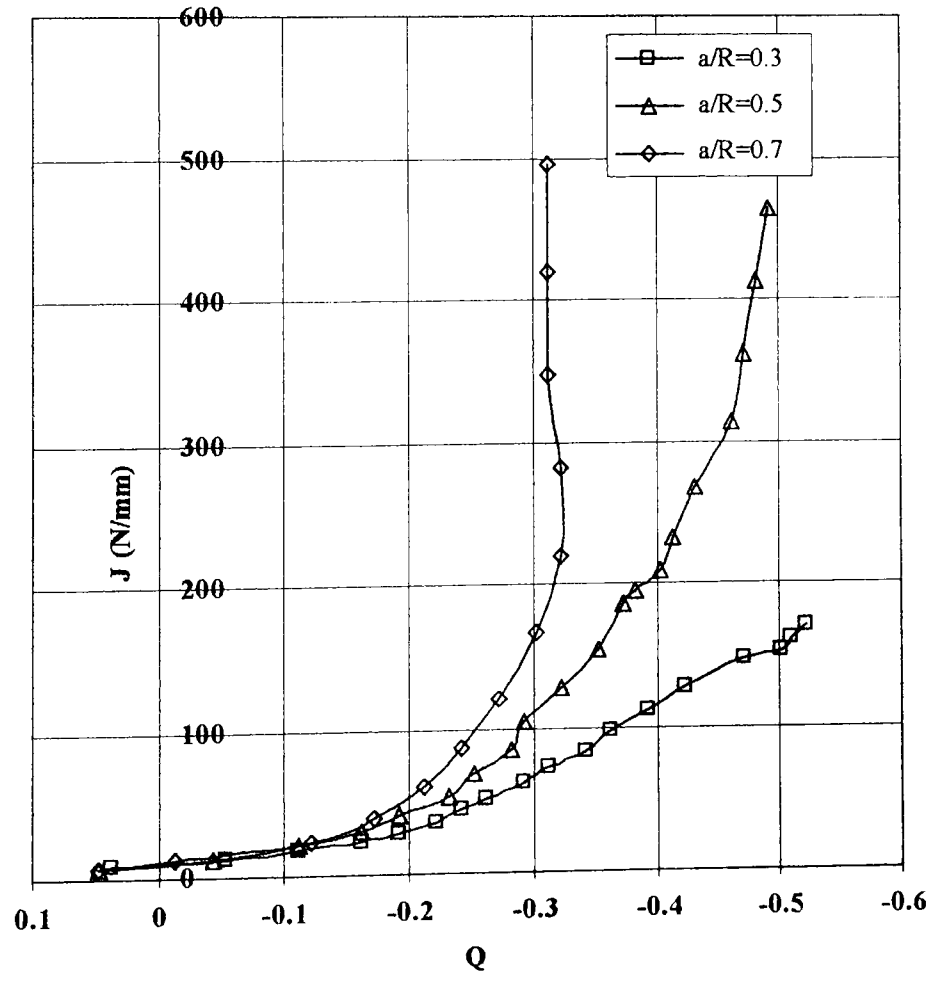

Fig. 7.15 J – Q trajectories 72 mm diameter EN24 specimens

Fig. 7.16 provides a summary of the J-Q trajectory envelopes for each specimen diameter. Each envelope represents the range of J-Q trajectories that can be expected for a/R in the range 0.3 to 0.7. When plotted on a single graph the effect of specimen size can be clearly seen, as the specimen diameter increases the J-Q trajectory range is reduced and, most importantly, the trajectory at low load becomes much steeper.

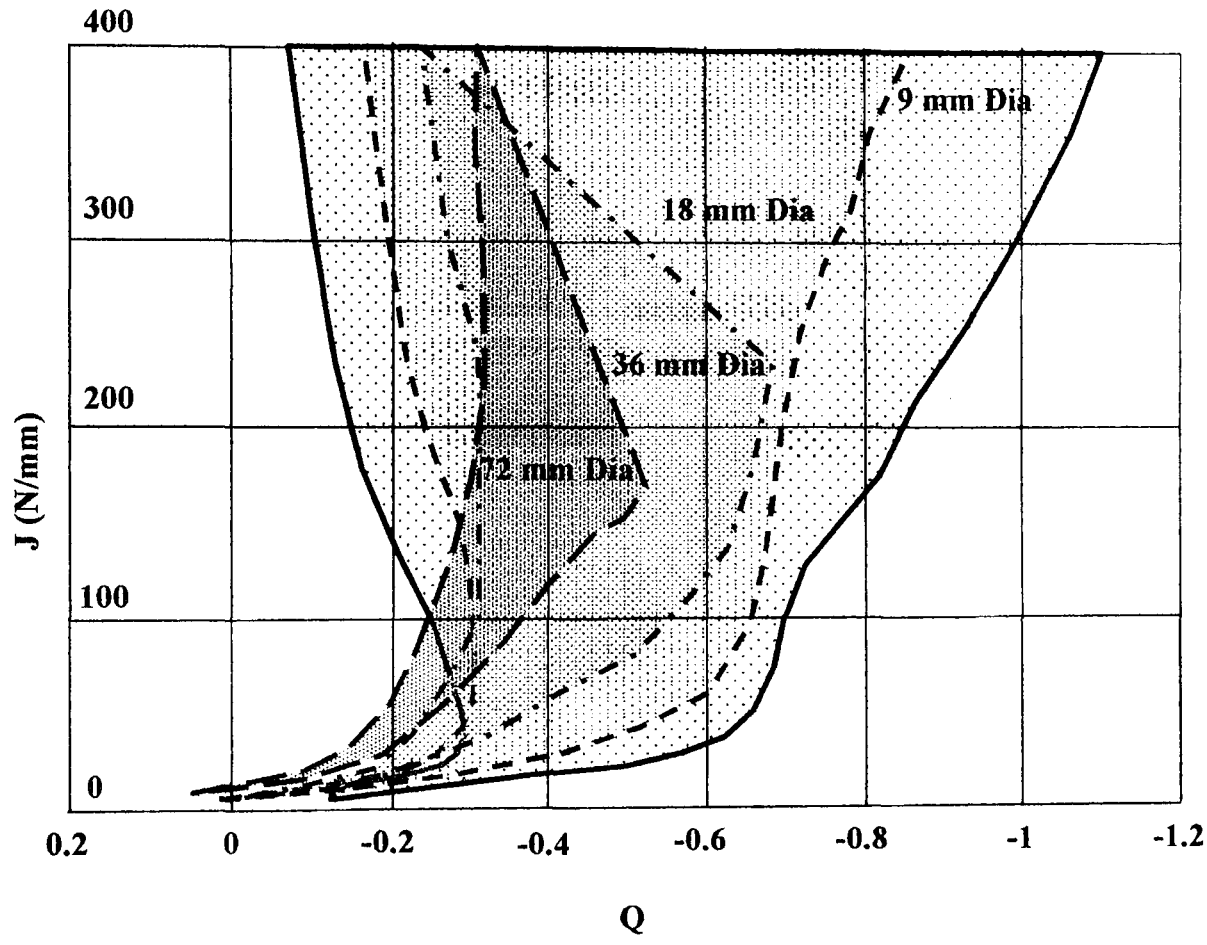

Fig. 7.16 J-Q envelopes for EN24 specimens

The above observations have a fundamental effect on CRB specimen design. For EN24 with a fracture toughness of K_{IC} = 95 MPa $\sqrt{m}$, i.e. J_{IC} = 41N/mm an unacceptably low value of constraint would be provided by all of the specimens considered, even for the 72 mm diameter specimen Q ≈ -0.2 at a/R = 0.7. Further consider that the load required at this level of J can be estimated from fig. 7.14 to be in the order of 380 kN for a/R = 0.7 and 820 kN for a/R = 0.5 then it becomes apparent that the CRB specimen would not be a practical proposition. However, for high toughness materials tested under elastic plastic conditions the use of CRB specimens may have some merit because of the increase in constraint, particularly for smaller diameter specimens, as loading progresses into the fully plastic region.

For EN24 it is possible to estimate J at fracture for the CRB specimens under consideration here by using the FE and experimental data generated in chapter 6 and plotted in fig. 6.58. Fig. 7.17 shows selected data from fig. 6.58 together with the J-Q trajectories for each diameter of CRB specimen with a/R = 0.5 and 0.7. As can be seen the best performance could be expected from the 72 mm diameter, a/R = 0.7, specimen but the expected J at failure would be approximately 55 N/mm which is considerably elevated from the plain strain fracture toughness value for the material. The worst performance specimen, 9 mm diameter, a/R = 0.5, could be expected to yield a value of J at failure of approximately 73 N/mm. Clearly this would be unacceptable.

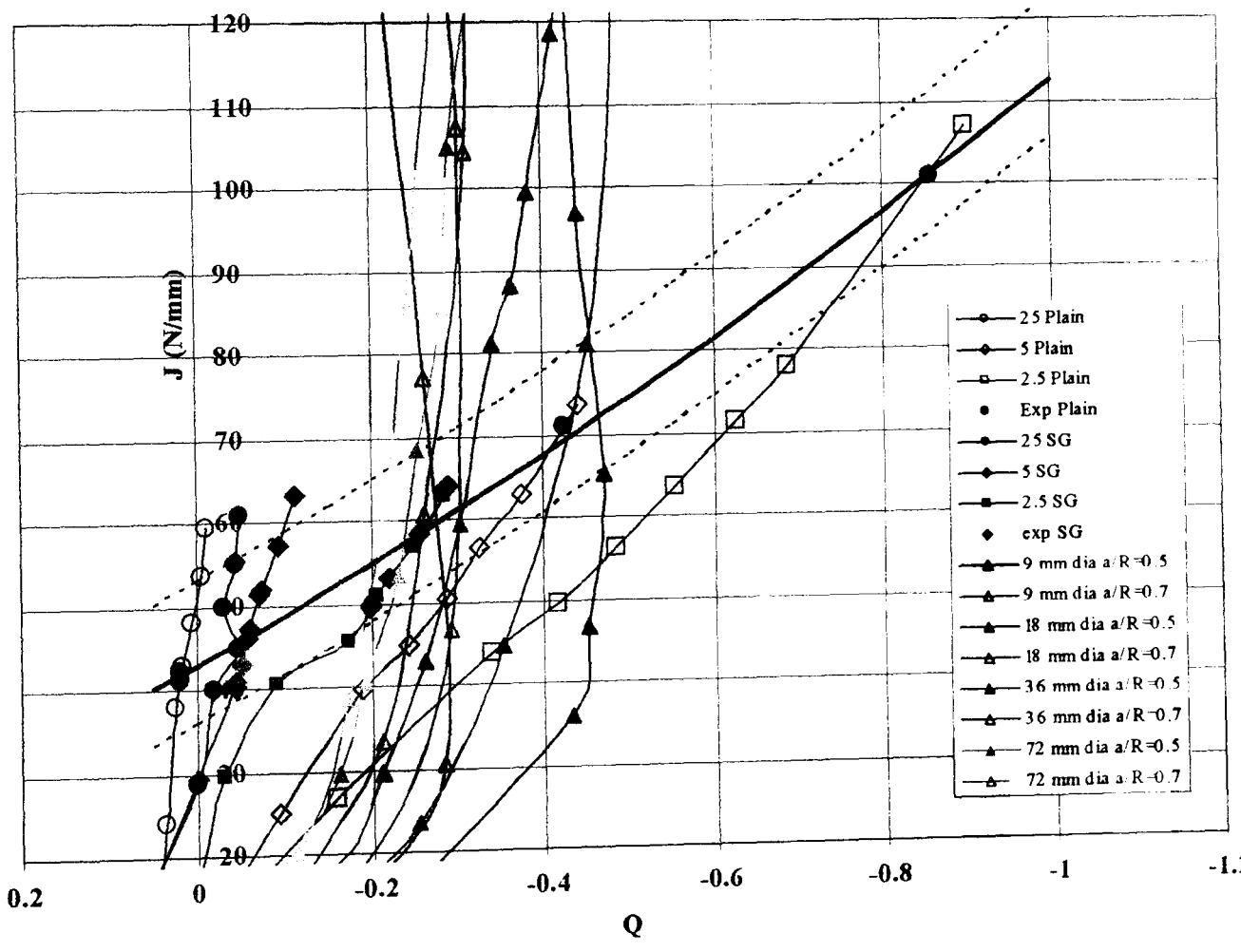

Fig. 7.17 Comparison of CRB and CT specimen performance EN24

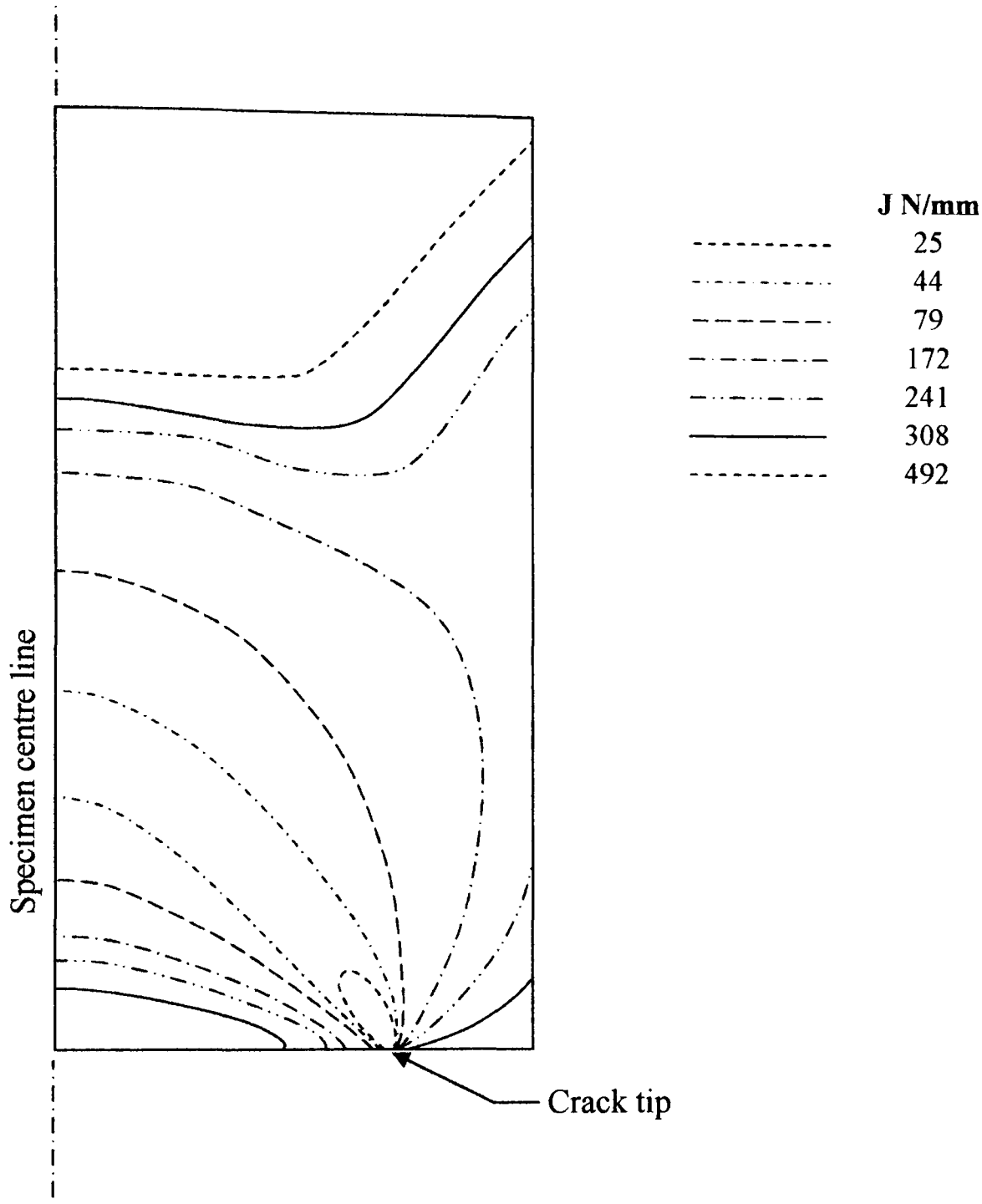

Fig. 7.18 Development of plastic zone with increasing J EN24 specimen 18 mm diameter a/R = 0.3

Plastic zone development has also been studied for the EN24 specimens, figs. 7.18 to 7.20 show the effect of crack depth for the 18 mm diameter specimens. As can be seen, plastic zone sizes are large in comparison to the length of the uncracked ligament even for the a/R = 0.5 case, at J = 44 N/mm which is the closest contour available to the material fracture toughness the plastic zone stretches half way to the specimen centre line.

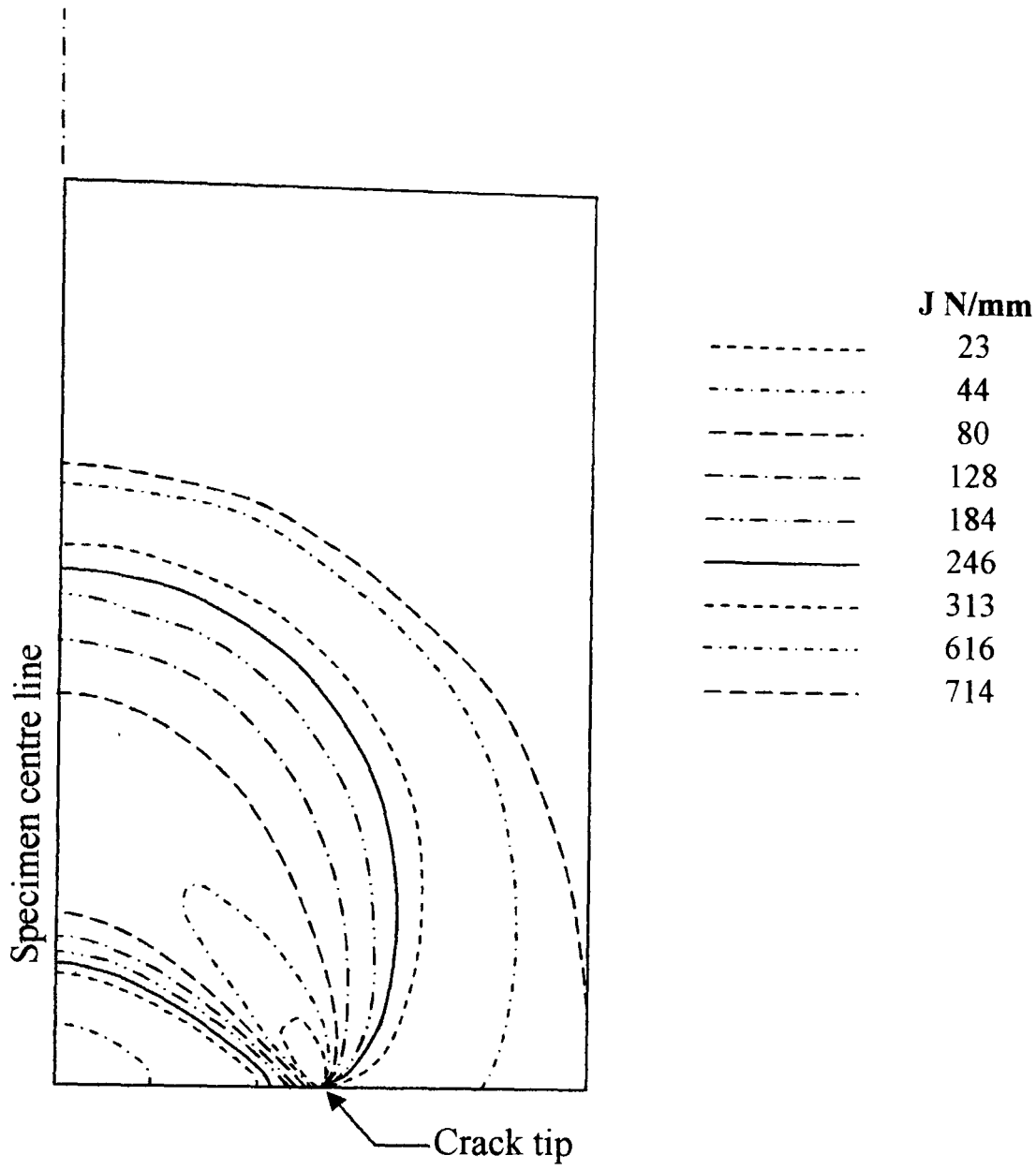

Fig. 7.19 Development of plastic zone with increasing J
EN24 specimen 18mm diameter a/R = 0.5

For shallow crack depths the plastic zone quickly spreads to the surface of the specimen and is probably the largest contributory factor in the observed loss of constraint. For the deeply cracked specimen, a/R = 0.7, the plastic zone quickly spreads to the specimen centre line, indeed at the nearest contour to the material fracture toughness, J = 46 N/mm, the contour has already intersected the centre line. Hence it is concluded that from plastic zone development view point a/R should be limited to say $0.45 \leq a/R \leq 0.55$ if the plastic zone is to be confined to reasonable proportions at the crack tip.

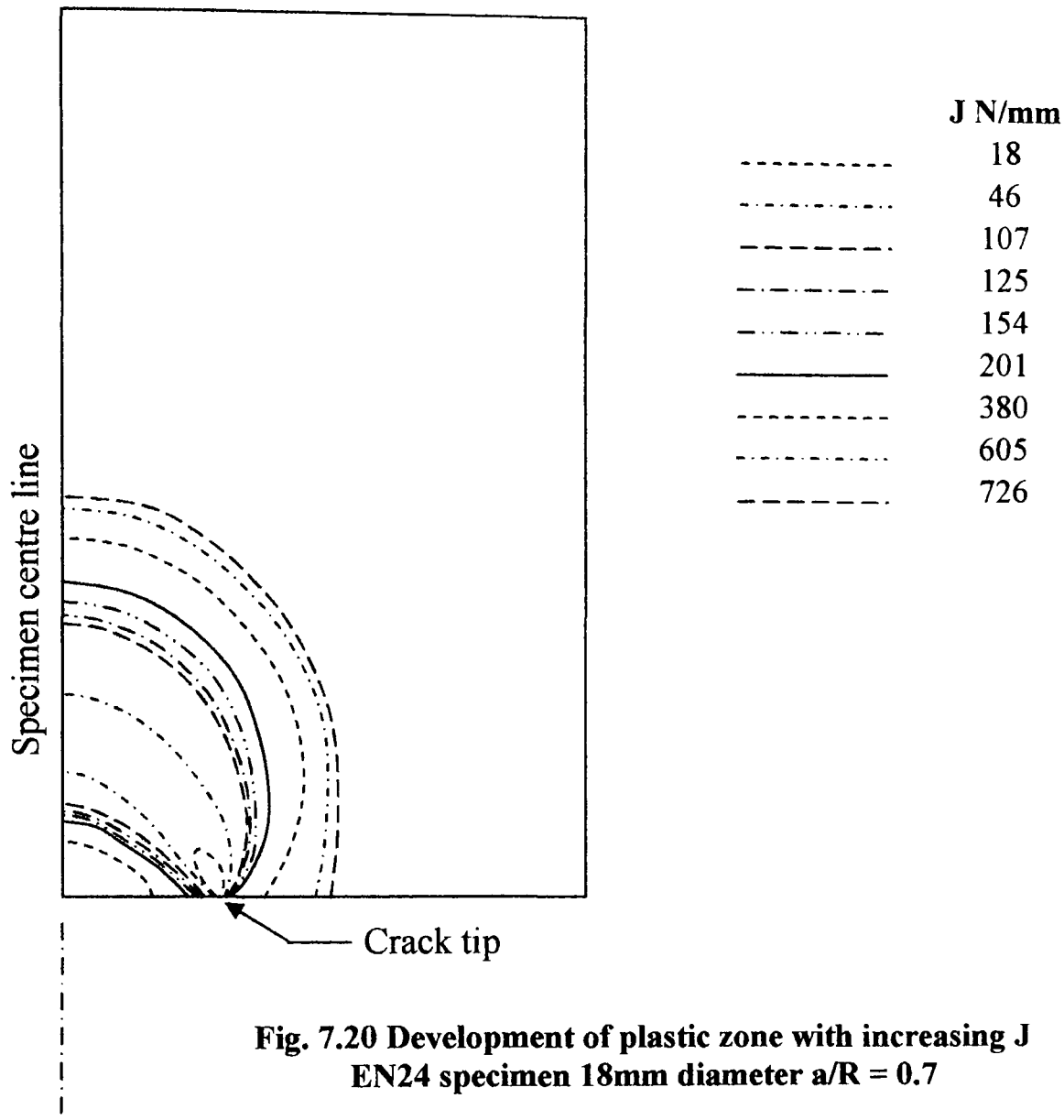

Fig. 7.20 Development of plastic zone with increasing J EN24 specimen 18mm diameter a/R = 0.7

This conclusion is broadly in line with the work of Scribetta [122] who estimated the optimum a/R range by plotting the J level at which plasticity reaches a specific bound for a moderately hardening material with $E/\sigma_Y = 500$, see fig. 7.21.

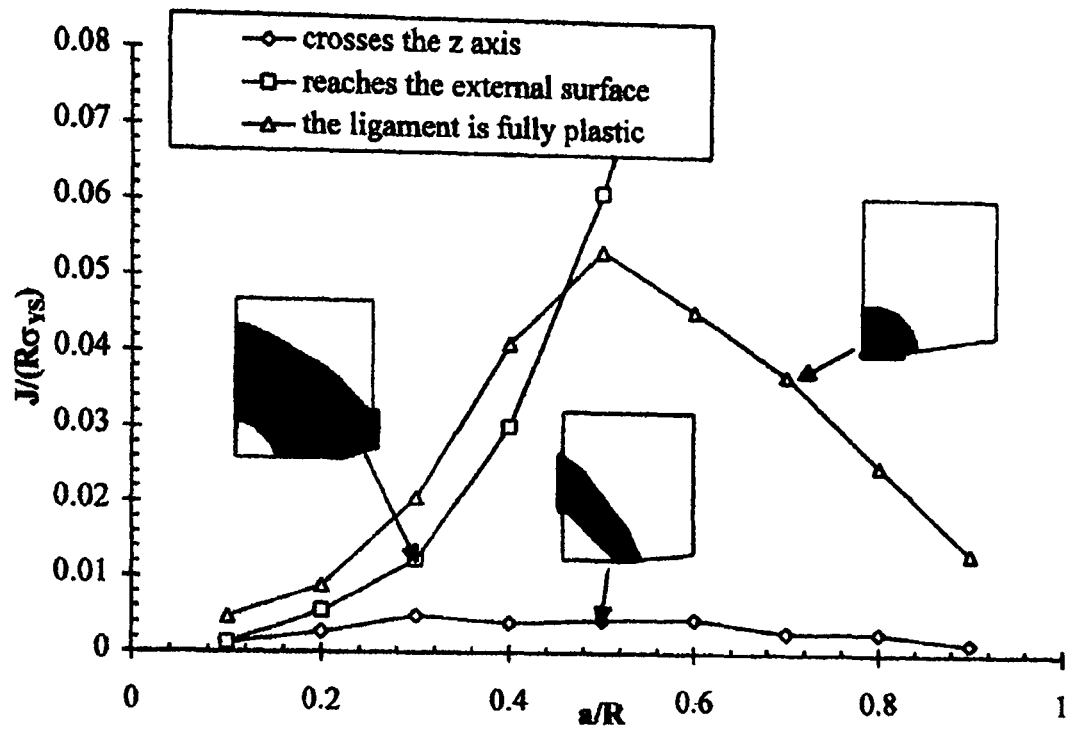

Fig. 7.21 Plastic zone size evolution for different a/R ratios for $E/\sigma_Y = 500$. After Scribetta [122]

Scribetta concluded from these results that $0.4 \leq a/R \leq 0.6$ could be an appropriate range, however, a slightly more conservative approach as suggested above is justified even when considering fig. 7.21 due to the fact that the line representing the J level at which the plastic zone reaches the specimen external surface and that representing the J level at which the ligament is fully plastic cross at approximately $a/R = 0.45$.

Fig. 7.22 to 7.24 show the effect of specimen size on plastic zone development for a crack depth of $a/R = 0.5$ for the 9 mm,32 mm and 72 mm diameter specimens. By considering the contour for the J level closest to the material fracture toughness in each case it is observed that only the 72 mm diameter specimen provides what could be considered to be a suitable ratio of plastic zone size to uncracked ligament length for linear elastic fracture mechanics testing.

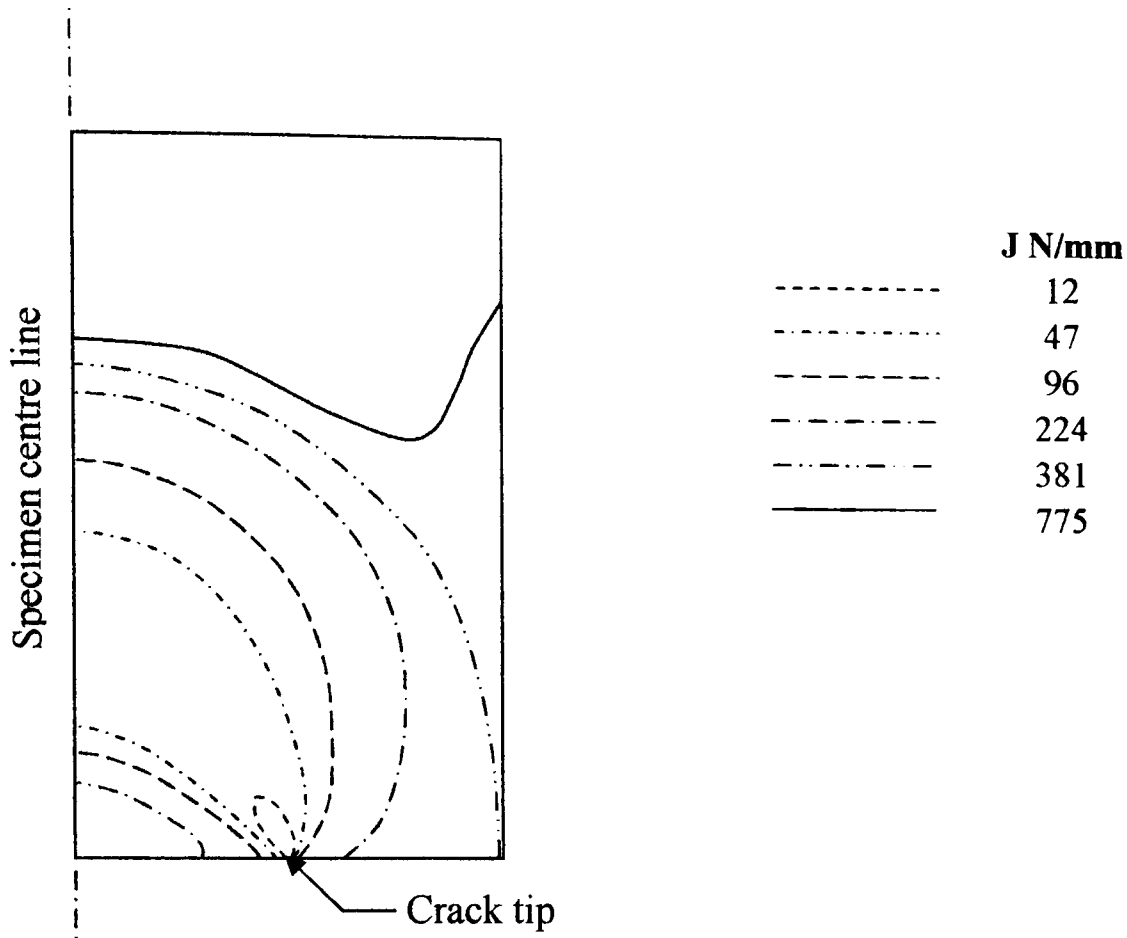

Fig. 7.22 Development of plastic zone with increasing J
EN24 specimen 9mm diameter a/R = 0.5

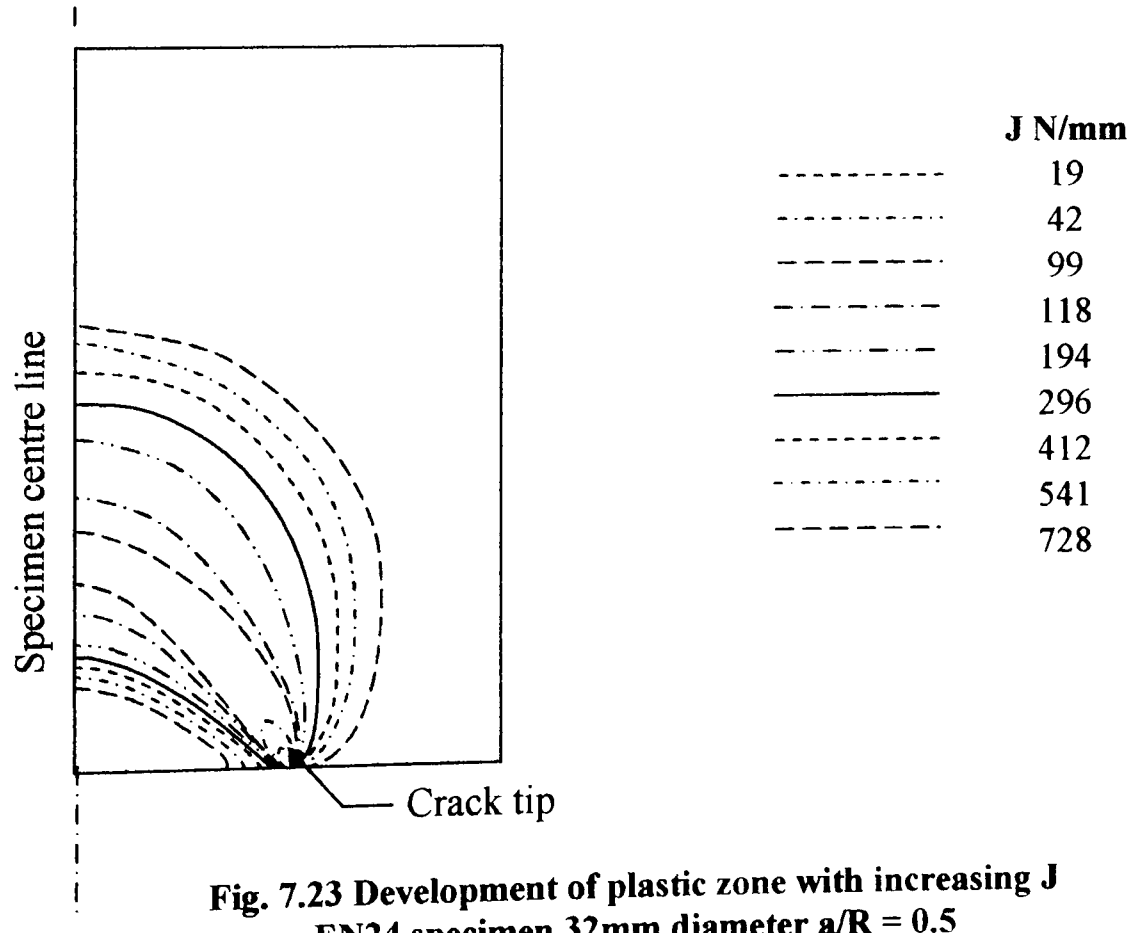

Fig. 7.23 Development of plastic zone with increasing J
EN24 specimen 32mm diameter a/R = 0.5

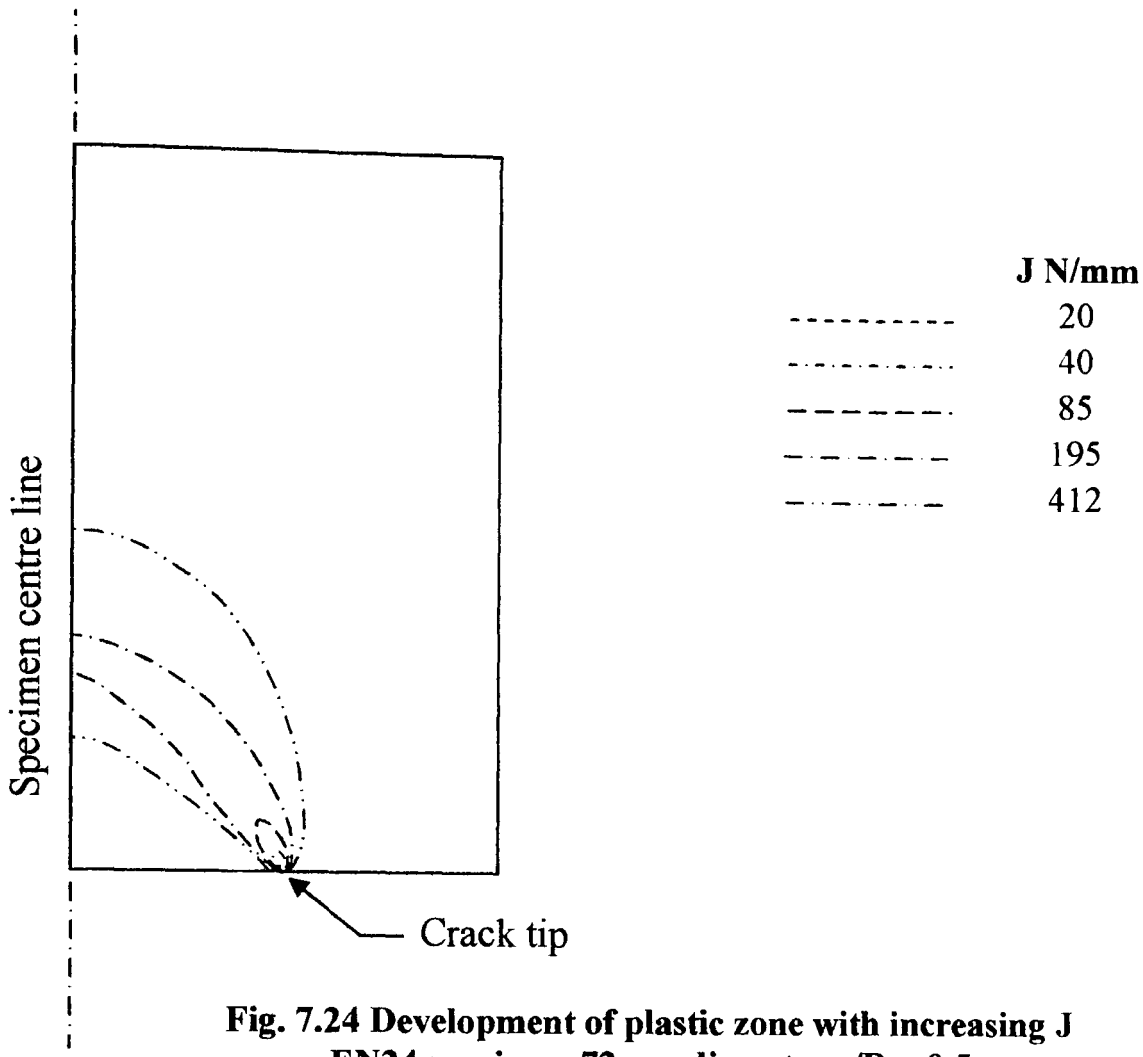

Fig. 7.24 Development of plastic zone with increasing J EN24 specimen 72mm diameter a/R = 0.5

7.5.2 ALUMINIUM ALLOY

J integral development with load together with J-Q trajectories for the aluminium alloy specimens can be seen in figs. 7.25 and 7.26. Table 7.1 indicates that for the aluminium alloy under consideration the smallest, 8 mm diameter, specimen $D = 3.3 (K_{IC}/\sigma_Y)^2$ which is equivalent to the condition achieved by the 36 mm diameter EN24 specimen. Hence all of the J-Q trajectories are relatively steep in comparison to those obtained for EN24 at low levels of applied load. However at the material fracture toughness of $K_{IC} = 22$ MPa $\sqrt{M}$, i.e. $J_{IC} = 6.1$ N/mm only the 16 mm and 32 mm diameter specimens exhibit what would be considered to be an acceptable level of constraint, i.e. $Q \leq -0.1$, with $Q \approx -0.06$ and $Q \approx -0.01$ respectively. The performance of the 8 mm diameter specimen would be considered to be unacceptable at $Q \approx -0.18$. Further, even though the J-Q trajectories are steep in comparison to those obtained for the EN24 specimens they are shallow in comparison to the near vertical J-Q trajectory expected from a CT or bend specimen at the same level of applied J.

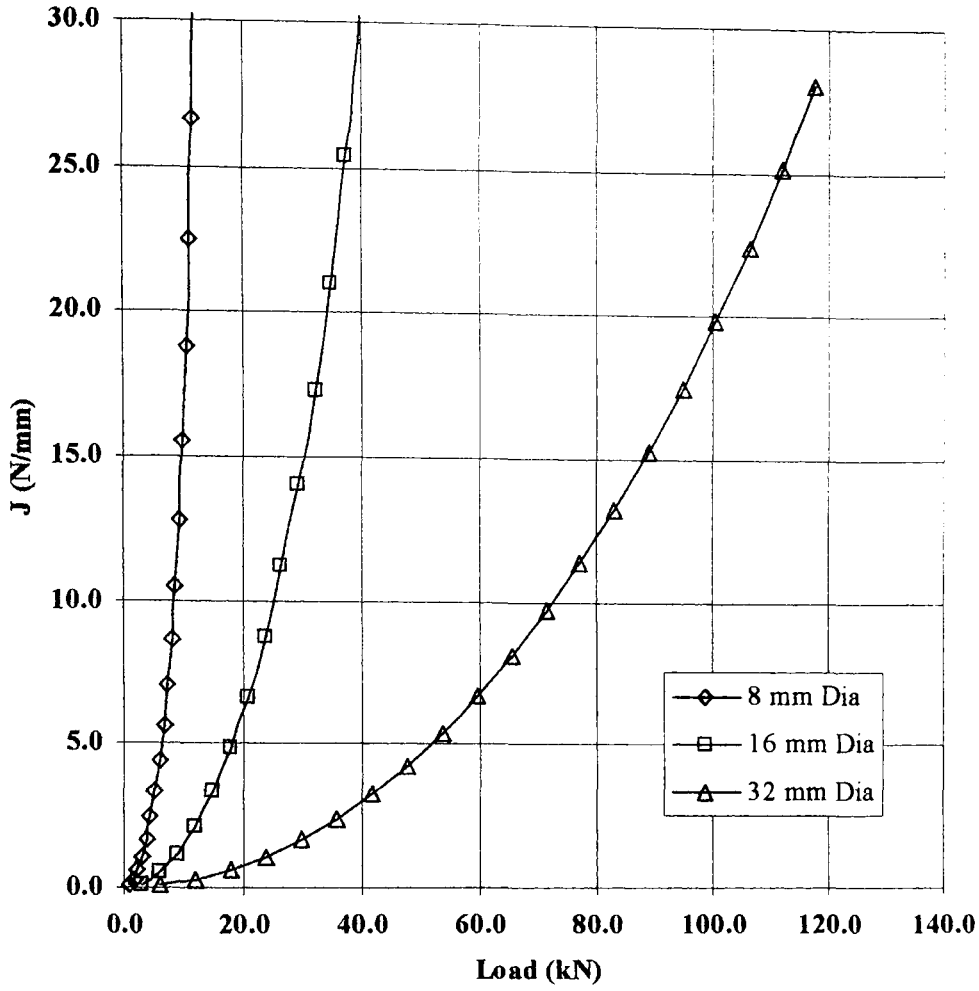

Fig 7.25 J v load Aluminium alloy specimens a/R = 0.5

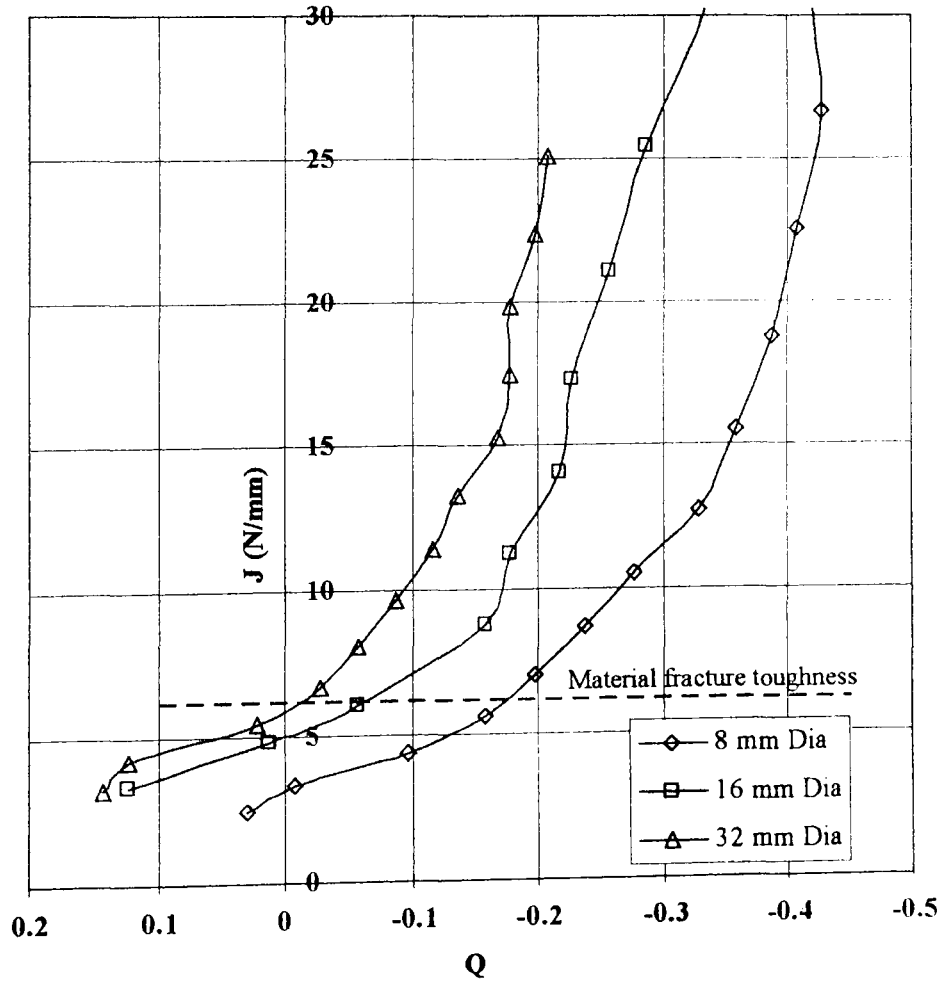

Fig. 7.26 J – Q trajectories Aluminium alloy specimens a/R = 0.5

Hence due to the shallow nature of the J-Q trajectory even though acceptable levels of constraint are achieved for both the 16 mm and 32 mm diameter specimens this constraint can vary considerably even within the normal statistical scatter bands expected from fracture testing. This is illustrated by the curve for the 16 mm diameter specimen in particular, consider a variation on fracture toughness of 10% which would not be unreasonable then the value of Q could range from $Q \approx -0.02$ to $Q \approx -0.1$. The situation is slightly better for the 32 mm diameter specimen. Hence even at the largest diameter tested with $D = 13.3 (K_{IC}/\sigma_Y)^2$, though the level of constraint at the material fracture toughness could be deemed acceptable, the CRB specimen could not be relied upon to yield consistent results due to the shallow nature of the J-Q trajectory. Also for the 32 mm diameter specimen the load at failure can be estimated from fig. 7.23 to be in the region of 60 kN in comparison to the failure load of 2.97 kN reported in section 4.4.3 for a CT specimen.

7.5.3 HY-130

J integral development with load together with J-Q trajectories for the HY-130 specimens are shown in figs. 7.27 to 7.32. The results obtained for these specimens are particularly interesting in that material properties are available for both lower and upper shelf, i.e. brittle and ductile behaviour.

In general the results exhibit similar trends in terms of specimen size effects as those exhibited by the EN24 specimens, this is clearly seen in fig. 7.33, J-Q envelopes for the HY-130 specimens. However the HY-130 results clearly illustrate the difference in performance that can be expected from CRB specimens under linear elastic and elastic plastic test conditions.

Both the cleavage and ductile toughness ranges from [123] are illustrated on fig.'s 7.28, 7.30 and 7.32. The toughness ranges indicated were obtained from compact tension specimens and hence the scatter is due to statistical effects only and not as a result of changes in constraint conditions. The low levels of constraint exhibited by the CRB specimens under linear elastic conditions is separate from the scatter in the toughness range shown and will potentially lead to a further increase in the measured fracture toughness values under test conditions.

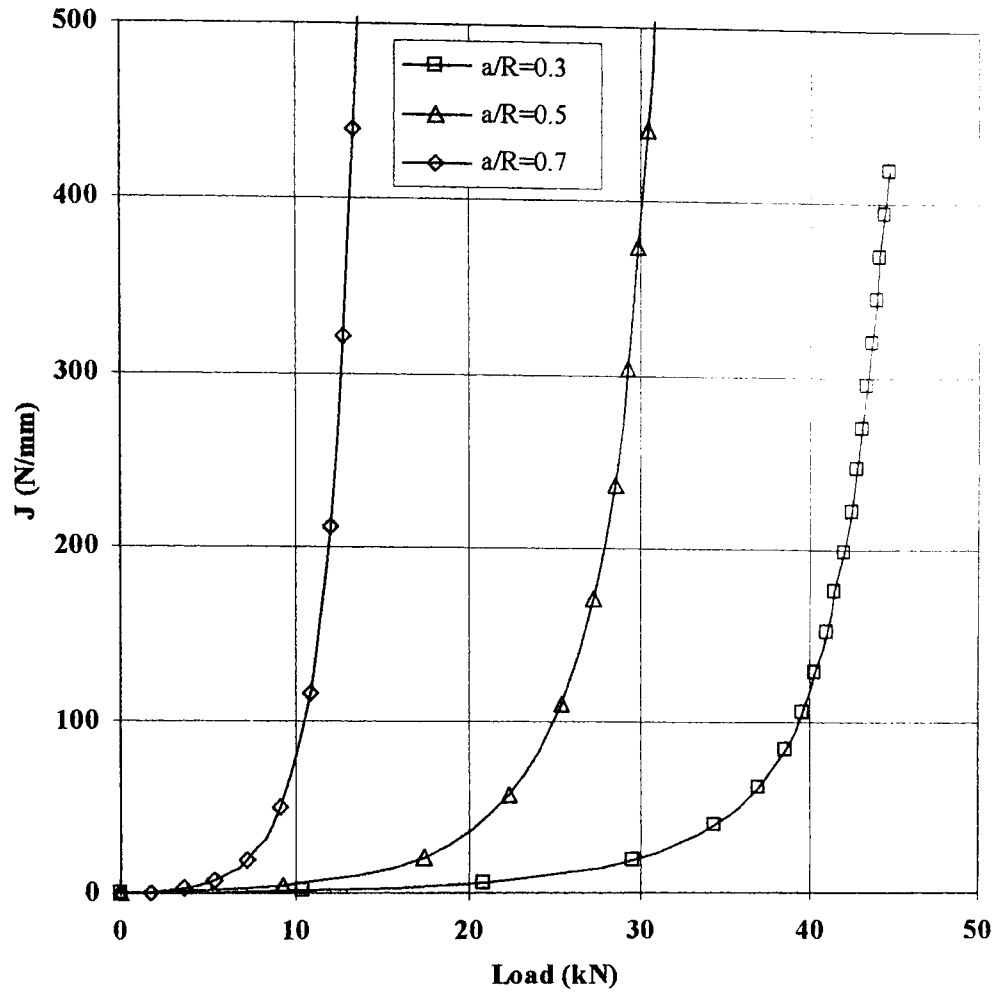

Fig 7.27 J v load 8 mm diameter HY-130 specimens

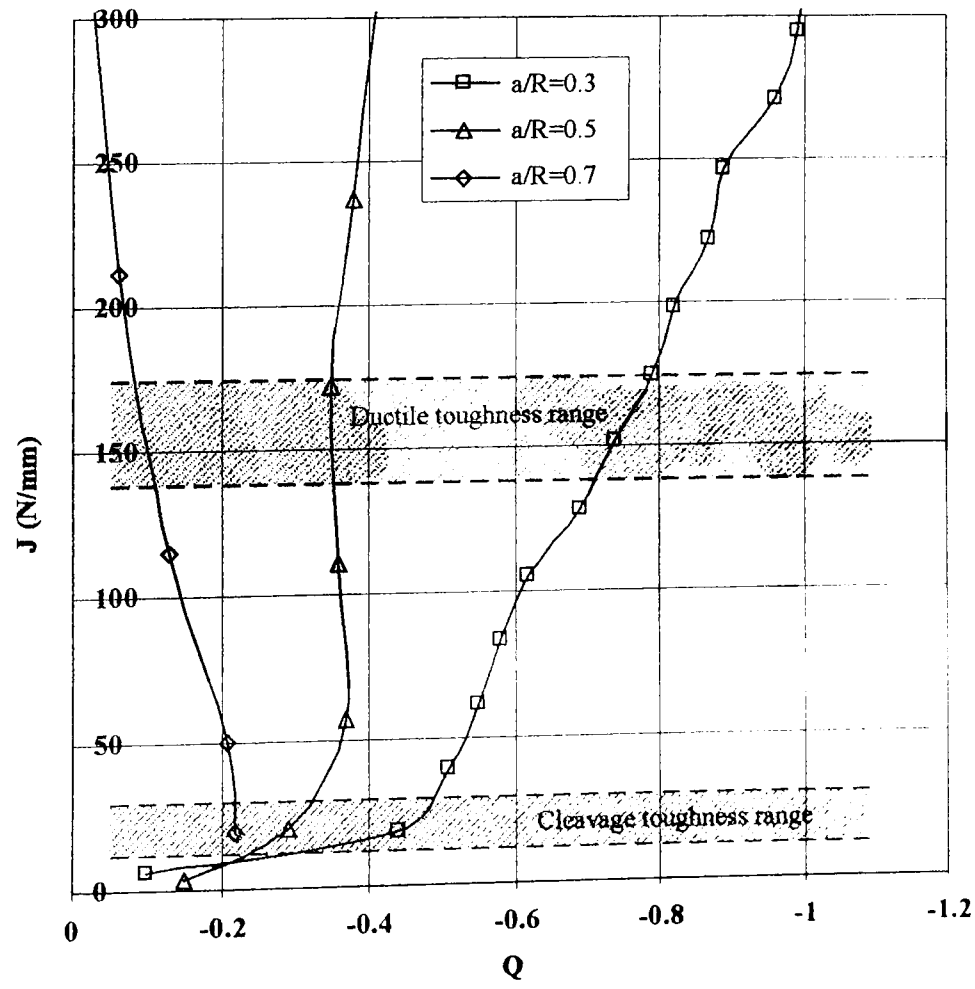

Fig. 7.28 J – Q trajectories 8 mm diameter HY-130 specimens

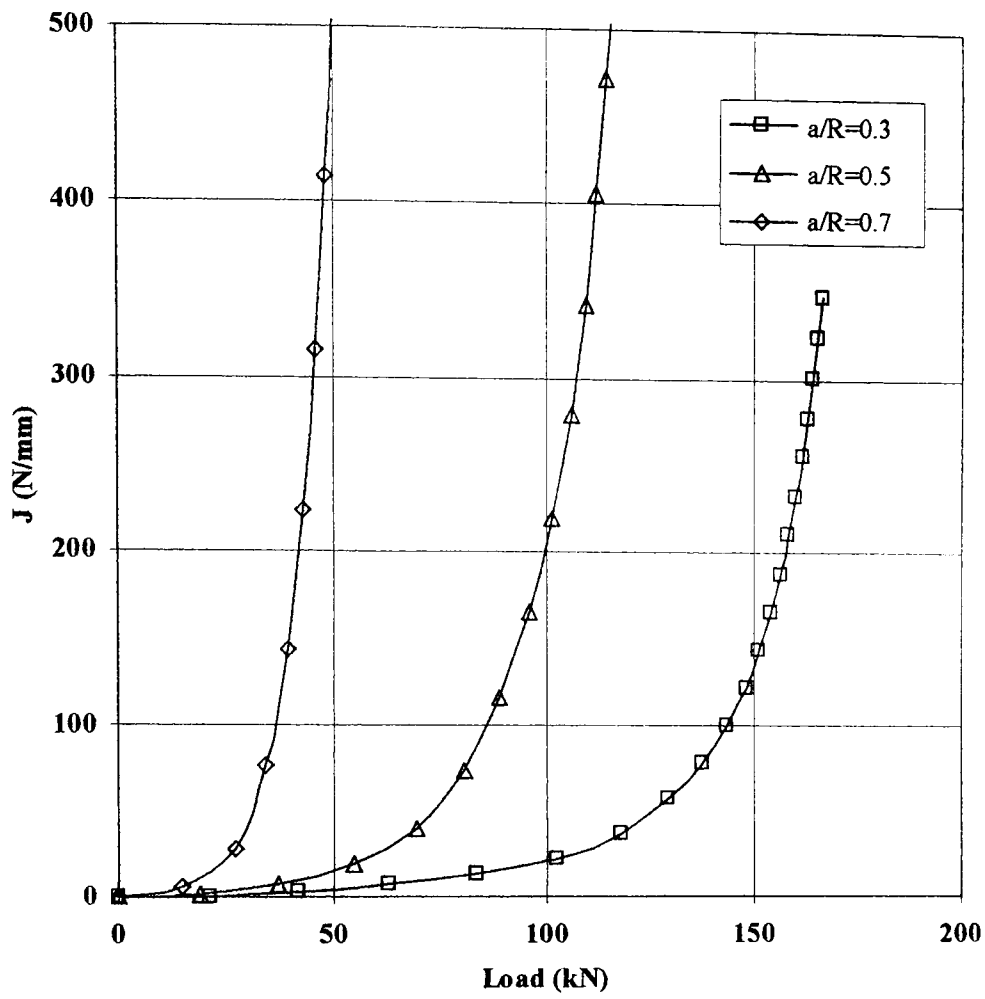

Fig 7.29 J v load 16 mm diameter HY-130 specimens

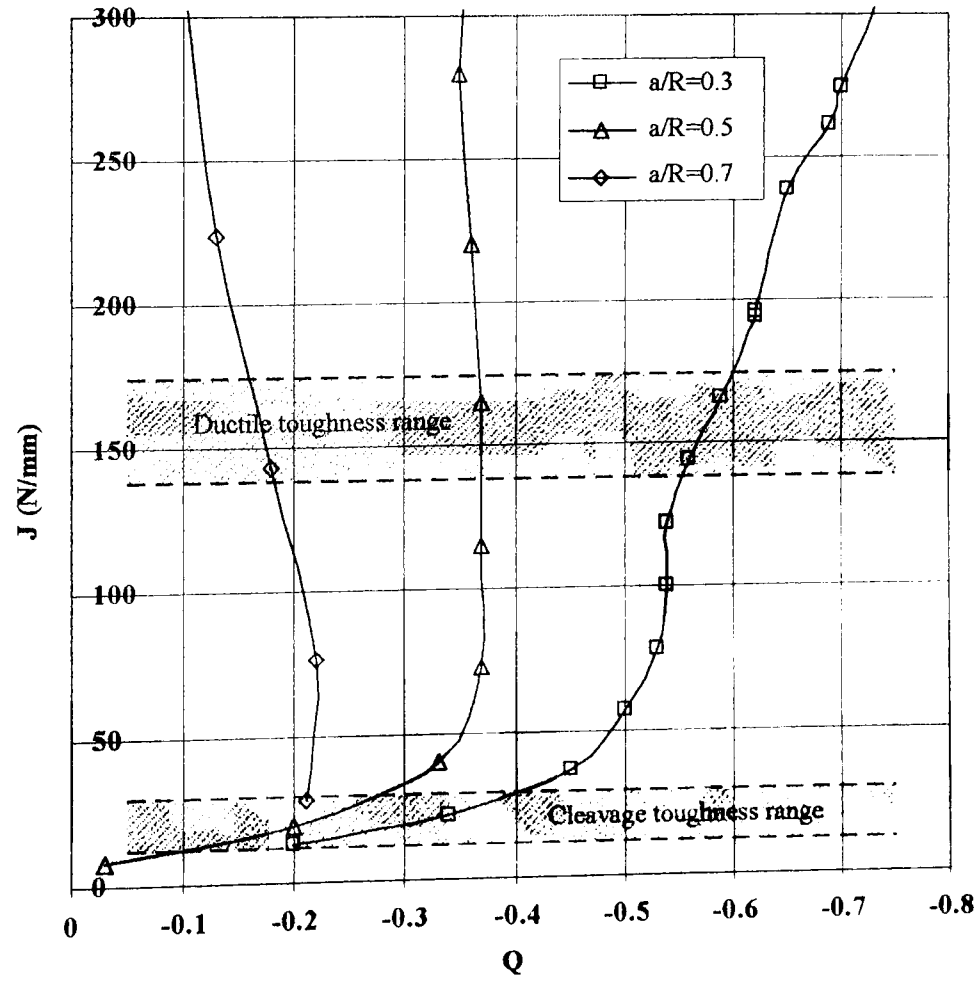

Fig. 7.30 J – Q trajectories 16 mm diameter HY-130 specimens

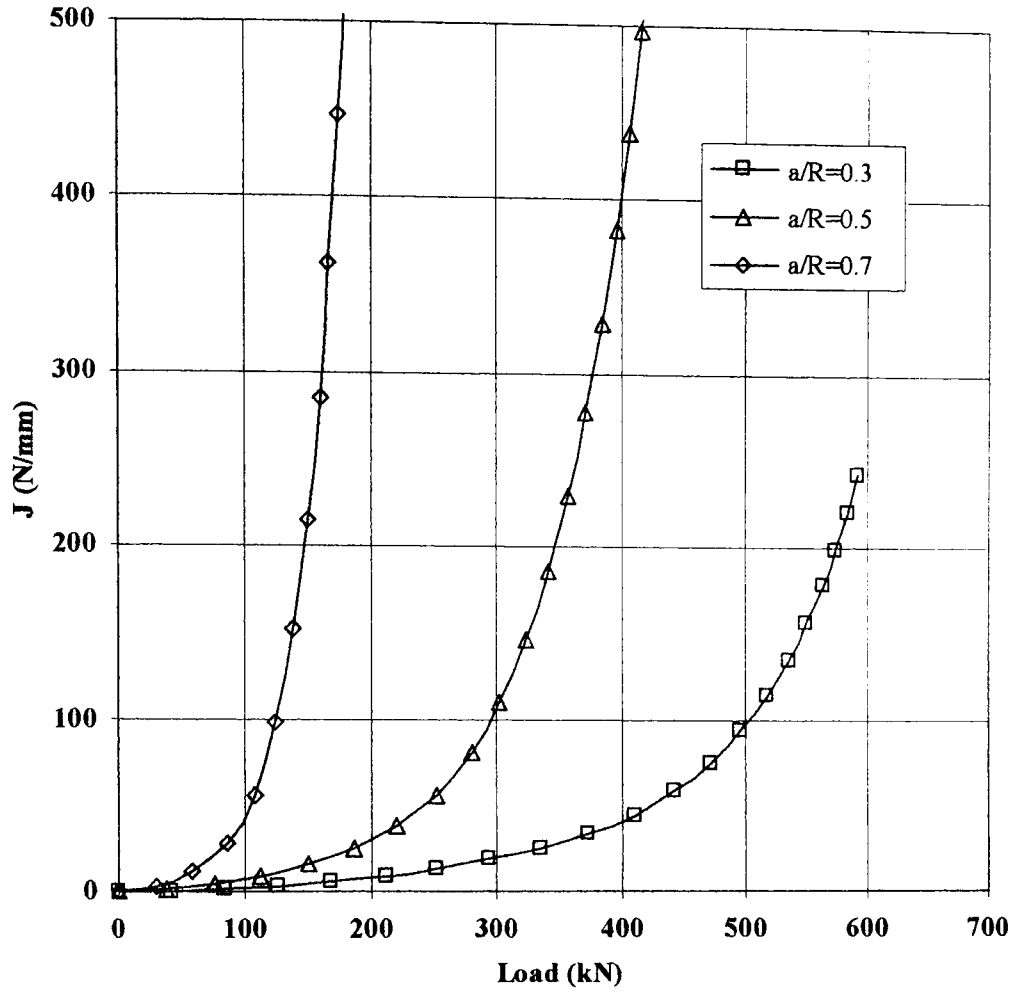

Fig 7.31 J v load 32 mm diameter HY-130 specimens

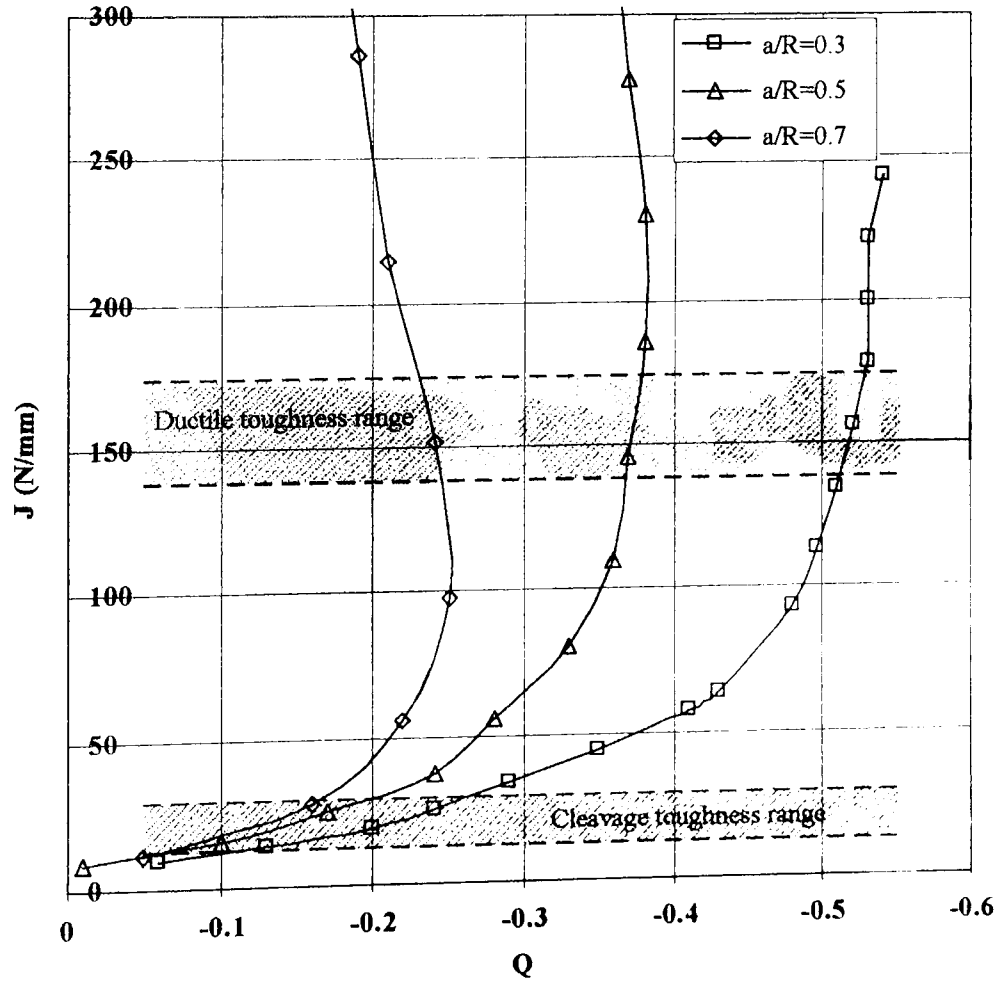

Fig. 7.32 J – Q trajectories 32 mm diameter HY-130 specimens

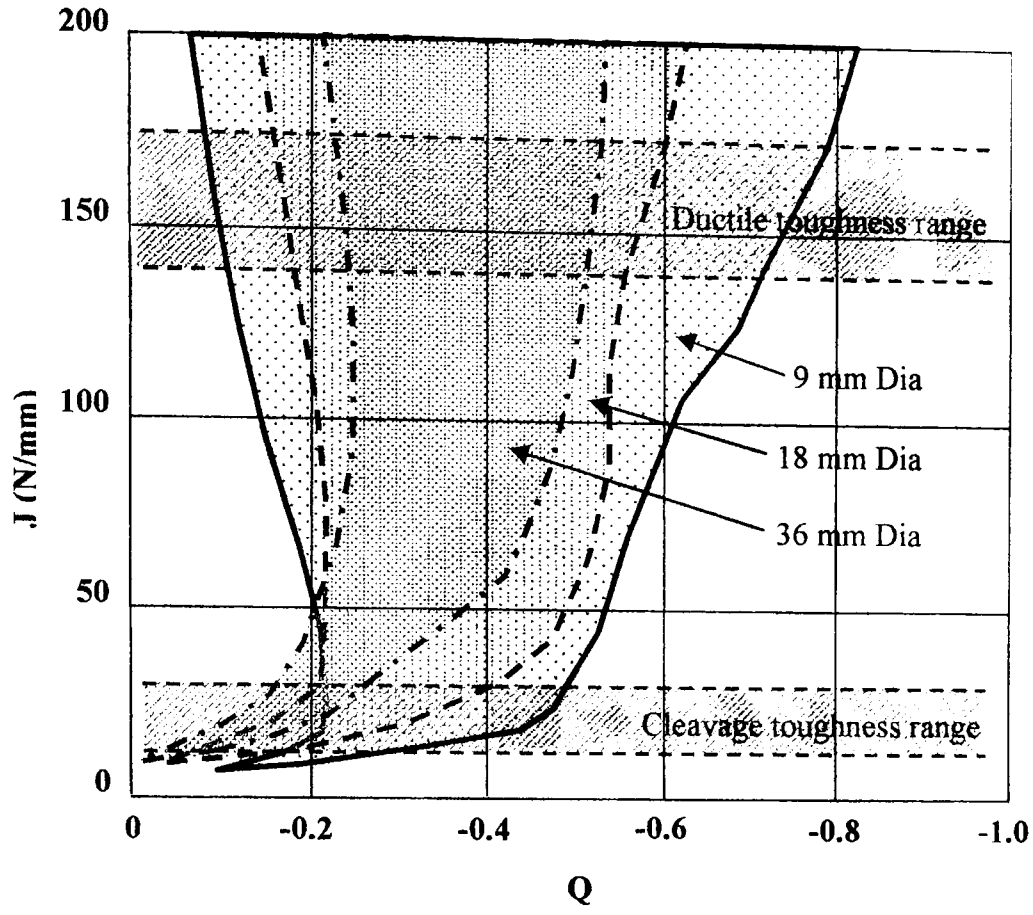

Fig 7.33 J-Q envelopes for HY 130 specimens

In the cleavage toughness range that can be expected from this material the J-Q trajectories are again shallow indicating the unsuitability of the CRB specimen for linear elastic testing. The largest diameter specimen tested corresponded to $D = 8\,(K_{IC}/\sigma_Y)^2$ with a load at failure, estimated from fig. 7.31, in excess of 200kN for $a/R = 0.5$.

Under elastic plastic conditions however the J-Q trajectories presented are much steeper and therefore more likely to produce consistent test results. Indeed, small deeply cracked specimens would appear to offer the best performance under these conditions. Consider, for example, the 8 mm diameter specimen with $a/R = 0.7$ which provides a steady increase in constraint as the specimen loading increases, with $Q \approx -0.1$ within the expected ductile toughness range. This is consistent with the results obtained by Giovanola et al [117] who observed that, for a 16 mm diameter specimen of the same material with $a/R = 0.62$, Q increased steadily under conditions of full but confined plasticity. Hence, in contrast to compact tension and bend specimens, where constraint levels decrease with the spread of plasticity, the CRB specimen appears to exhibit increased constraint with increasing J for small diameter deeply cracked specimens.

7.6 DISCUSSION OF RESULTS AND CLOSURE

The results presented in this chapter give an indication of the performance characteristics of CRB specimens for a range of materials. The results suggest that previously defined minimum specimen size requirements from published literature [118 to 122] are not stringent enough to guarantee minimum values of fracture toughness. Indeed, the current results suggest that even the most stringent of these previously defined requirements due to Scribetta [122] equivalent to twice the ASTM limit for CT specimens of $D \geq 5\left(\frac{K_{IC}}{\sigma_Y}\right)^2$ is not conservative enough to guarantee minimum values. Comparisons made with plain sided and side grooved EN24 specimens suggest that fracture toughness values significantly above plane strain values obtained from appropriately sized CT specimens would be obtained from CRB specimens with a diameter as high as $D = 7.34\left(\frac{K_{IC}}{\sigma_Y}\right)^2$.

The J-Q trajectories obtained for all of the materials under consideration suggest that due to the shallow nature of the trajectories at low load the CRB specimen does not present a viable alternative to the compact tension or bend specimen for linear elastic fracture mechanics testing. It is observed that even within the normal statistical scatter bands expected for this type of test, constraint values can vary considerably. Although the J-Q trajectories do become steeper as the specimen diameter increases the test load required soon becomes prohibitive.

Within the elastic plastic test range however the J-Q trajectories become much steeper and therefore more likely to produce consistent test results particularly for small diameter deeply cracked specimens.

Hence this type of specimen, although limited for linear elastic testing, has good potential for elastic plastic testing and is a viable alternative to compact tension and bend specimens within this regime.

CHAPTER 8

CONCLUSION AND FUTURE WORK

8.1 CONCLUSION

The work presented in this thesis has examined the validity of using sub sized fracture specimens to determine minimum, i.e. plane strain fracture toughness values. Two such approaches have been considered, firstly the use of side grooves to increase crack front constraint in reduced thickness compact tension specimens and secondly the use of circumferentially cracked round bar specimens.

Linear elastic fracture mechanics analysis of aluminium alloy specimens was undertaken in order to establish the effects of side groove depth and geometry on crack front stress intensity factor and constraint for full thickness specimens. It was concluded that Vee grooves with a depth of 30% of the specimen thickness provided an optimum configuration, i.e. an effective thickness at the root of the side groove, B_N, of 0.7 times the specimen thickness, B. The linear elastic investigations also gave analytical and experimental support to Freed and Krafft's idea of effective thickness with the actual material fracture toughness, K_{IC}, being related to the nominal fracture toughness obtained by testing side grooved specimens, K_{NOM}, by $K_{IC} = K_{NOM}\left(\frac{B}{B_N}\right)^m$. The exponent, m, was evaluated by finite element analysis to be between 0.62 and 0.66, and experimentally to be 0.71 for the specimen configuration in question.

A two parameter elastic plastic fracture mechanics analysis was performed to investigate the effects of 30% Vee side grooving on sub thickness compact tension specimens manufactured from EN24 steel. J-Q theory was used to quantify crack tip constraint for various specimen thicknesses in order to predict thickness effects in plain sided specimens and the effects of side grooving. The reference stress field used in the J-Q predictions was first obtained from a modified boundary layer analysis. The results from this analysis indicated that side grooves were very effective at increasing the level of constraint along the crack front, to the extent that near minimum fracture toughness values could be expected from specimens of one fifth the recommended thickness.

An experimental programme was also undertaken to investigate the effects of thickness and side grooving on EN24 specimens, with good agreement being found between the finite element predictions and experimental results for m = 0.7 in the Freed and Krafft equation. Fracture toughness values elevated by only 5% above the plane strain fracture toughness for the material were obtained from specimens of one fifth the recommended thickness. By using m = 0.5 in the Freed and Krafft equation, as demanded by ASTM E 399 the experimental results obtained were found to be conservative, being approximately 2% lower than plane strain results from specimens of one fifth the recommended thickness. It is proposed therefore that for side grooved specimens a thickness limit as low as $B \geq 0.5\left(\frac{K_{IC}}{\sigma_Y}\right)^2$ could be appropriate if m = 0.5 is used in the Freed and Krafft equation, this is subject to further work on other materials.

As an alternative to side grooved compact tension specimens circumferentially cracked round bar specimens have also been investigated for a range of materials, these being, the aluminium alloy from chapter 3, EN24 and HY-130 steel. Again J-Q theory was used to evaluate crack tip constraint for a variety of crack depths for each material. The J-Q trajectories obtained for all of the materials considered suggest that due to the shallow nature of the trajectories at low load the CRB specimen does not present a viable alternative to the compact tension or bend specimen for linear elastic fracture mechanics testing. Comparisons made with plain sided and side grooved EN24 specimens suggest that fracture toughness values significantly above plane strain values obtained from appropriately sized CT specimens would be obtained from CRB specimens with a specimen diameter as high as $D = 7.34\left(\frac{K_{IC}}{\sigma_Y}\right)^2$.

Within the elastic plastic test range however the J-Q trajectories become much steeper and therefore more likely to produce consistent test results particularly for small diameter deeply cracked specimens. Hence this type of specimen, although limited for linear elastic testing, has good potential for elastic plastic testing and is a viable alternative to compact tension and bend specimens within this regime.

8.2 FUTURE WORK

The greatest potential for future work is in the area of sub thickness side grooved specimens. The results presented for EN24 give a positive indication of the benefits of side grooving but only one material has been investigated and the observations made here may not be applicable across a wide range of materials. Further work to investigate the effects of hardening and different material toughness characteristics would be beneficial, particularly in consideration of the potential benefit to many industries where the materials employed often can not provide specimens of the standard thickness required by current fracture toughness test methods.

Lack of investigation in this area has almost certainly been due to two reasons:

- That the detailed finite element analysis required demands powerful computers and long run times.

- That fracture testing is expensive and to investigate tougher materials than those considered here large specimens and hence large testing machines will be required.

With the introduction of ever more powerful computers the first restriction to further work is no longer a problem. However, J-Q theory although providing good agreement with experimental results can not be used alone as a predictive tool, the method relies on experimental data being available for specimens tested under different constraint conditions in order to develop a toughness locus for a particular material. Only when this toughness locus is available can specimens of differing constraint be evaluated, hence the real obstacle to future work is the requirement for large test machines and expensive muti-specimen test programmes.

Future work on circumferentially cracked round bar specimens is really limited to their performance under elastic plastic fracture testing conditions where they could provide benefits due to the simplified and less expensive machining requirements. They do not seem to provide any benefits for linear elastic testing.

REFERENCES

1. Ewalds H.L. & Wanhill R.J.H., **FRACTURE MECHANICS**, Arnold, third edition (1989).

2. Broek D., **ELEMENTARY ENGINEERING FRACTURE MECHANICS**, Kluwer, fourth edition (1986).

3. Atkins A.G. & Mai Y.W., **ELASTIC AND PLASTIC FRACTURE**, Ellis Horwood (1988).

4. Knott J., **FUNDAMENTALS OF FRACTURE MECHANICS**, Buterworths (1973).

5. Griffith A.A., **THE PHENOMENA OF RUPTURE AND FLOW IN SOLIDS**, Phil. Trans. Roy. Soc. of London, A221, pp 163–197 (1921).

6. Griffith A.A., **THE THEORY OF RUPTURE**, Proc. 1st Int. Congress Appl. Mech. (1924) pp 55–63. Biezeno and Burgers Ed. Waltman (1925).

7. Inglis C.E., **STRESSES IN A PLATE DUE TO THE PRESENCE OF CRACKS AND SHARP CORNERS**, Trans. Inst. Nav. Arch., 55, (1), pp 219 – 230 (1913).

8. Irwin G. R., **FRACTURE DYNAMICS**, Fracturing of Metals, pp 147–166, ASM publ. (1948).

9. Orowan E., **ENERGY CRITERIA FOR FRACTURE**, Welding Journal, 34, pp 1575–1605 (1955).

10. Irwin G. R., **ANALYSIS OF STRESSES AND STRAINS NEAR THE END OF A CRACK TRAVERSING A PLATE**, J. Appl. Mech., (24), pp 361 – 364 (1957).

11. Westergaard H.M., **BEARING PRESSURES AND CRACKS**, Trans. ASME, Vol 61, pp A49-A53 (1939).

12. Rooke D. P. & Cartwright D.J., **A COMPENDIUM OF STRESS INTENSITY FACTORS**, HMSO, London (1976).

13. Irwin G. R., **PLASTIC ZONE NEAR A CRACK AND FRACTURE TOUGHNESS**, Proc. 7th Sagamore Conf., pp IV – 63(1960).

14. Rooke D.P., **ELASTIC YIELD ZONE ROUND A CRACK TIP**, Royal Aircraft Est., Farnborough, Tech. Note CPM 29 (1963).

15. Wells A.A, **UNSTABLE CRACK PROPAGATION IN METALS: DAMAGE AND FAST FRACTURE**, Proceedings of the Crack Propagation Symposium, Cranfield, The College of Aeronautics, Vol. 1, pp 210–230 (1962).

16. Burdekin F. M. & Stone D.E.W., **THE CRACK OPENING DISPLACEMENT APPROACH TO FRACTURE MECHANICS IN YIELDING**, J. Strain Analysis, 1, pp 145–153 (1966).

17. Dugdale D. S., **YIELDING OF STEEL SHEETS CONTAINING SLITS**, J. Mech. Phys. Sol., 8, pp 100–108 (1960)

18. Rice J.R., **A PATH INDEPENDENT INTEGRAL AND THE APPROXIMATE ANALYSIS OF STRAIN CONCENTRATIONS BY NOTCHES AND CRACKS**, J. Appl. Mech., pp 379–386 (1968).

19. Eshelby J. D., **CALCULATION OF ENERGY RELEASE RATE**, Prospects of Fracture Mechanics, pp 69–84, Sih, Van Elst, Broek, Eds.,Noordhoff (1974).

20. Bluhm J. I., **A MODEL FOR THE EFFECT OF THICKNESS ON FRACTURE TOUGHNESS**, ASTM Proc. 61, pp 1324-1331 (1961).

21. Repko A. J., Jones M.H., Brown W.F., **INFLUENCE OF SHEET THICKNESS ON THE SHARPE-EDGE-NOTCH PROPERTIES OF A β TITANIUM ALLOY AT ROOM AND LOW TEMPERATURES**, Symposium on Evaluation of Metallic Materials in Design for Low-Temperature Service, ASTM STP No. 302, Am. Soc. Testing Mats. pp 213 (1962).

22. Broek D. & Vlieger H., **THE THICKNESS EFFECT IN PLANE STRESS FRACTURE TOUGHNESS**, Nat. Aerospace Inst., Amsterdam, Rept. 74032 (1974).

23. Isherwood D. P. & Williams J. G., **THE EFFECT OF STRESS-STRAIN PROPERTIES ON NOTCHED TENSILE FAILURE IN PLANE STRESS**, Eng. Fract. Mech., 2, pp 19-35 (1970).

24. Sih G. C. & Hartranft R. J., **VARIATION OF STRAIN ENERGY RELEASE RATE WITH PLATE THICKNESS**, Int. J. Fract. Mech., 9, pp 75-82 (1973).

25. Anderson W. E., **SOME DESIGNER-ORIENTED VIEWS ON BRITTLE FRACTURE**, Battelle North West Rept. SA-2290 (1969).

26. BS 7448: Pt. 1: 1991, **FRACTURE MECHANICS TOUGHNESS TESTS METHOD FOR DETERMINATION OF K_{IC} CRITICAL COD AND CRITICAL J VALUES OF METALLIC MATERIALS**.

27. ASTM E399-83, **STANDARD TEST METHOD FOR PLANE STRAIN FRACTURE TOUGHNESS OF MATALLIC MATERIALS, 1984**.

28. Freed C.N. & Krafft J. M., **EFFECT OF SIDE GROOVING ON MEASUREMENTS OF PLANE STRAIN FRACTURE TOUGHNESS**, Journal of Materials, 1, pp 770-790 (1966).

29. Paris P.C. & Sih S.C.M., **STRESS ANALYSIS OF CRACKS, FRACTURE TOUGHNESS TESTING AND ITS APPLICATIONS**, ASTM STP381, pp 30 (1965).

30. Macdonald D. & Pajot J.J., **STRESS INTENSITY FACTORS FOR SIDE GROOVED FRACTURE SPECIMENS**, Journal of Testing and Evaluation, Vol. 18, No. 4, pp 281-285 (1990).

31. Delorenzi H.G. & Shih C.F., **3D ELASTIC PLASTIC INVESTIGATION OF FRACTURE PARAMETERS IN SIDE GROOVED COMPACT SPECIMEN**, Int. Jnl. of Fracture, 21, pp 105-220 (1983).

32. Shih C. F., Delorenzi H. G. & Andrews W.R., **ELASTIC PLASTIC FRACTURE**, ASTM STP 668, pp 65-120 (1979).

33. Andrews W. R. & Shih C. F., **ELASTIC PLASTIC FRACTURE**, ASTM STP 668, pp 426-450 (1979).

34. Shih C. F., Delorenzi H.G. & Andrews W. R., **ELASTIC COMPLIANCES AND STRESS INTENSITY FACTORS FOR SIDE GROOVED COMPACT SPECIMENS,** Int. Jnl. of Fracture, 13, pp 544-548 (1977).

35. Owen D. R. J. & Fawkes A. J., **ENGINEERING FRACTURE MECHANICS,** Pineridge Press Swansea, first edition (1988).

36. Rice J. & Tracey D., **COMPUTATIONAL FRACTURE MECHANICS IN NUMERICAL AND COMPUTER METHODS IN STRUCTURAL MECHANICS,** S. J. Fennes et al, Eds. Academic Press, NY, pp 555-624 (1973).

37. Gallagher R. H., **A REVIEW OF FINITE ELEMENT TECHNIQUES IN FRACTURE MECHANICS**, Proc. 1st Int. Conf. on Num. Meth. in Fracture Mechanics, A. R. Luxmore & D. R. J. Owen, Eds. Swansea (1978).

38. Chan S. K., Tuba J. S. & Wilson W. K., **ON THE FINITE ELEMENT METHOD IN LINEAR FRACTURE MECHANICS**, Engineering Fracture Mechanics, 2, pp 1-17 (1970).

39. Tracey D. M., **FINITE ELEMENTS FOR THE DETERMINATION OF CRACK TIP ELASTIC STRESS INTENSITY FACTORS**, Engineering Fracture Mech., 3, pp 255-266 (1971).

40. Tracey D. M. & Cook T. S., **ANALYSIS OF POWER TYPE SINGULARITIES USING FINITE ELEMENTS**, Int. J. Num. Meth. Engng, 11, No. 8, pp 1225-1235 (1977).

41. Blackburn W. S., **CALCULATION OF STRESS INTENSITY FACTORS AT CRACK TIP USING SPECIAL FINITE ELEMENTS**, Mathematics of Finite Elements, J. R. Witeman Ed., Academic Press, N.Y., pp 327-336 (1973).

42. Benzley S. E., **REPRESENTATION OF SINGULARITIES WITH ISOPARAMETRIC FINITE ELEMENTS**, Int. J. Num. Method Engng., 8, No. 3, pp 537-545 (1974).

43. Barsoum R. S., **ON THE USE OF ISOPARAMETRIC FINITE ELEMENTS IN LINEAR FRACTURE MECHANICS**, Int. J. Num. Meth. Engng, 10, No. 1, pp 25-37 (1976).

44. Henshell R. D. & Shaw K. G., **CRACK TIP ELEMENTS ARE UNNECESSARY**, Int. J. Num. Meth. Engng, 9, pp 495-509 (1975).

45. Shih C. F., Delorenzi H. G. & German M. D., **CRACK EXTENSION MODELLING WITH SINGULAR QUADRATIC ISOPARAMETRIC ELEMENTS**, Int. J. Fract., 12, pp 647-651 (1976).

46. Parks D. M., **A STIFFNESS DERIVATIVE FINITE ELEMENT TECHNIQUE FOR DETERMINATION OF CRACK TIP STRESS INTENSITY FACTORS**, Int. J. Fract., Vol. 10, pp 487-502 (1974).

47. Helen T. K., **ON THE METHOD OF VIRTUAL CRACK EXTENSIONS**, Int. J. Num. Meths. Engng., Vol. 9, pp 187-207 (1975).

48. Parks D. M., **VIRTUAL CRACK EXTENSION A GENERAL FINITE ELEMENT TECHNIQUE FOR J-INTEGRAL EVALUATION**, Int. Conf. Num. Meth. in Fracture Mechanics, pp 464-478 (1978).

49. Hutchinson J. W., **SINGULAR BAHAVIOUR AT THE END OF A TENSILE CRACK IN A HARDENING MATERIAL**, J. Mech. Phys. Sol., 16, pp 13-31 (1968).

50. Hutchinson J. W., **PLASTIC STRESS AND STRAIN FIELDS AT A CRACK TIP**, J. Mech. Phys. Sol., 16, pp 337-347 (1968).

51. Rice J. R. & Rosengren G. F., **PLANE STRAIN DEFORMATION NEAR A CRACK TIP IN A POWER LAW HARDENING MATERIAL**, J. Mech. Phys. Sol., 16, pp 1-12 (1968).

52. Rice J. R., **MATHEMATICAL ANALYSIS IN THE MECHANICS OF FRACTURE**, In Fracture An Advanced Treatise (ed H. Liebowitz), Vol 2, Academic Press, pp 191-311 (1968).

53. Shih C. F., **SMALL SCALE YIELDING ANALYSIS OF MIXED MODE PLANE STRAIN CRACK PROBLEMS**, ASTM STP 560, pp 187-210 (1974).

54. Shih C. F., **TABLES OF HUTCHINSON-RICE-ROSENGREN SINGULAR FIELD QUANTITIES**, Brown University Report MRLE-147 (1983).

55. Ritchie R.O., Knott J. F., Rice J. R., **ON THE RELATIONSHIP BETWEEN CRITICAL TENSILE STRESS AND FRACTURE TOUGHNESS IN MILD STEEL**, J. Mech. Phys. Sol., 21, pp 395-410 (1973).

56. Smith E., **PHYSICAL BASIS OF YIELD AND FRACTURE,** Conf. Proc., Institute of Physics and Physical Society, London, p 36 (1966).

57. Smith E., **CLEAVAGE FRACTURE IN MILD STEEL** Int. J. Fracture Mech., 4, pp 131-145 (1968).

58. Rice J. R. & Johnson M. A., **INELASITIC BEHAVIOUR OF SOLIDS**, pp 641, McGraw Hill (1970).

59. Orowan E., **FRACTURE AND STRENGTH OF SOLIDS** Rep. Prog. Phys., 12, pp 185-232 (1948).

60. Knott J. F., **SOME EFFECTS OF HYDROSTATIC TENSION ON THE FRACTURE BEHAVIOUR OF MILD STEEL,** J. Iron and Steel, Inst. 204, p 104 (1966).

61. Hill R., **THE MATHEMATICAL THEORY OF PLASTICITY**, Oxford University Press (1950).

62. Richie R.O. & Thompson A. W., **ON MACROSCOPIC AND MICROSCOPIC ANALYSIS FOR CRACK INITIATION AND CRACK GROWTH TOUGHNESS IN DUCTILE ALLOYS**, Metallurgical Transactions, Vol. 16A, pp 233-248 (1985).

63. Curry D. A.,**CLEAVAGE MICROMECHANISMS OF CRACK EXTENSION IN STEELS**, Met. Sci., Vol. 14, pp 319-326 (1980).

64. Ritchie R. O., Sever W. L. and Wullaert R. A., **CRITICAL FRACTURE STRESS AND FRACTURE STRAIN MODELS FOR THE PREDICTION OF UPPER SHELF TOUGHNESS IN NUCLEAR PRESSURE VESSEL STEELS**, Met. Trans. A, Vol. 10a, pp 1557-1570 (1979).

65. McClintock F. A., **IN PHYSICS OF STRENGTH AND PLASTICITY**, A. S. Argon ed., MIT Press, Cambridge MA, pp 307-326 (1969).

66. Rice J. R. & Tracey D. M., **ON THE DUCTILE ENLARGEMENT OF VOIDS IN TRIAXIAL STRESS FIELDS**, J. Mech., Phys. Solids, Vol. 17, pp 201-217 (1969).

67. McClintock F. A., **A CRITERION FOR DUCTILE FRACTURE BY THE GROWTH OF HOLES**, J. Applied Mech., Trans. ASME Series E, Vol. 35, pp 363-371 (1968).

68. Mackenzie A. C., Hancock J. W. and Brown D. K., **ON THE INFLUENCE OF STATE OF STRESS ON DUCTILE FAILURE INITIATION IN HIGH STRENGTH STEELS**, Eng. Fract., Mech. Vol 9, pp 167-188 (1977).

69. McMeeking R. M., **FINITE DEFORMATION ANALYSIS OF CRACK TIP OPENING IN ELASTIC-PLASTIC MATERIALS AND IMPLICATIONS FOR FRACTURE**, J. Mech. Phys. Solids,Vol 25,pp 357-381 (1977).

70. Bates R. C., **METALLURGICAL TREATISES**, ed J. K. Tien & J. F. Elliott, TMS-AIME, Warrendale, PA, pp 551-570 (1982).

71. Begley J. A. and Landes J. D., **THE J INTEGRAL AS A FRACTURE CRITERION**, Fracture Toughness, ASTM STP 514, pp 1-23 (1972).

72. Paris P.C., Written discussion of ref [71] in Fracture Toughness, ASTM STP 514, pp 21-22 (1972).

73. McMeeking R. M. & Parks D. M., **ON CRITERIA FOR J-DOMINANCE OF CRACK-TIP FIELDS IN LARGE-SCALE YIELDING**, ASTM STP 668, pp 175-193 (1979).

74. Shih C. F. & German M. D., **REQUIREMENTS FOR A ONE PARAMETER CHARACTERISATION OF CRACK TIP FIELDS BY THE HRR SINGULARITY**, Int. J. Fract., 17, No. 1, pp 27-43 (1981).

75. Williams M. L., **ON THE STRESS DISTRIBUTION AT THE BASE OF A STATIONARY CRACK**, ASME Jrn. Of App. Mech., Vol. 24, pp 111-114 (1957).

76. Larsson S. G. & Carlsson A. J., **INFLUENCE OF NON-SINGULAR STRESS TERMS AND SPECIMEN GEOMETRY ON SMALL-SCALE YIELDING AT CRACK TIPS IN ELASTIC-PLASTIC MATERIAL,** Jrn. of Mech. Phys. Solids, Vol. 21, pp 263-278 (1973).

77. Rice J. R., **LIMITATIONS TO THE SMALL SCALE YIELDING APPROXIMATION FOR CRACK TIP PLASTICITY**, Jrn. of Mech. Phys. Solids, Vol. 22, pp 17-26 (1974).

78. Leevers P. S. & Radon J. C., **INHERENT STRESS BIAXILITY IN VARIOUS FRACTURE SPECIMEN GEOMETRIES**, Int. Jrn. Fract., Vol. 19, pp 311-325 (1983).

79. Betegon C. & Hancock J. W., **TWO-PARAMETER CHARACTERIZATION OF ELASTIC-PLASTIC CRACK-TIP FIELDS**, Jrn. of App. Mech., Vol. 58, pp 104-110 (1991).

80. Du Z. Z. & Hancock J. W., **THE EFFECT OF NON-SINGULAR STRESSES ON CRACK TIP CONSTRAINT**, Jrn. Mech. Phys. Solids, Vol 39, No. 4, pp 555-567 (1991).

81. Al-Ani A. M. & Hancock J. W., **J-DOMINANCE OF SHORT CRACKS IN TENSION AND BENDING**, Jrn. Mech. Phys. Solids, Vol. 39, No.1, pp 23-43 (1991).

82. O'Dowd N. P. & Shih C. F., **FAMILY OF CRACK-TIP FIELDS CHARACTERISED BY A TRIAXIALITY PARAMETER – I. STRUCTURE OF FIELDS**, Jrn. Mech. Phys. Solids, Vol. 39, No. 8, pp 989-1015 (1991).

83. O'Dowd N. P. & Shih C. F., **FAMILY OF CRACK-TIP FIELDS CHARACTERISED BY A TRIAXIALITY PARAMETER – II. FRACTURE APPLICATIONS**, Jrn. Mech. Phys. Solids, Vol. 40, No. 5, pp 939-963 (1992).

84. Shih C. F., O'Dowd N. P. & Kirk M. T., **A FRAMEWORK FOR QUANTIFYING CRACK TIP CONSTRAINT**, proc. Symposium on constraint effects in fracture, Indianapolis, Indiana, May 8-9, (1991)

85. Xia L., Wang T. C. & Shih C. F., **HIGHER-ORDER ANALYSIS OF CRACK TIP FIELDS IN ELASTIC POWER LAW HARDENING MATERIALS**, Jrn. Mech. Phys. Solids, Vol 41, No 6, pp 665-687 (1993).

86. Li Y. C. & Wang T. C., Scientia Sinica (Series A), Vol. 29, pp 941-955 (1986).

87. Sharma S. M. & Aravas N., **DETERMINATION OF HIGHER ORDER TERMS IN ASYMPTOTIC ELASTOPLASTIC CRACK TIP SOLUTIONS**, Jrn. Mech. Phys. Solids, Vol. 39, pp 1043-1072 (1991).

88. Shih C. F. & O'Dowd N. P., **A FRACTURE MECHANICS APPROACH BASED ON A TOUGHNESS LOCUS**, Shallow Crack Fracture Mechanics, Toughness Tests and Applications, Cambridge UK (1982).

89. Dodds R. H., Shih C. F. & Anerson T. L., **CONTINUUM AND MICROMECHANICS TREATMENT OF CONSTRAINT IN FRACTURE**, Int. Jrn. Fract., Vol. 64, pp 101-133 (1993).

90. Dodds R. H., Anderson T. L. & Kirk M. T., **A FRAMEWORK TO CORRELATE a/W RATIO EFFECTS ON ELASTIC-PLASTIC FRACTURE TOUGHNESS**, Int. Jrn. Fract., Vol. 48, pp 1-22 (1991).

91. Anderson T. L. & Dodds P. H., **SPECIMEN SIZE REQUIREMENTS FOR FRACTURE TOUGHNESS TESTING IN THE TRANSITION REGION**, Jrn. Test. & Eval. pp 123 –134 (1991).

92. Engineering Mechanics Research Corporation, **NISA Users Manual**, Troy, Michigan, Version 92 (1992).

93. Engineering Mechanics Research Corporation, **ENDURE Users Manual**, Troy, Michigan, Version 92 (1992).

94. Engineering Mechanics Research Corporation, **DISPLAY III Users Manual**, Troy, Michigan, Version 92 (1992).

95. NAFEMS, **2D TEST CASES IN LINEAR ELASTIC FRACTURE MECHANICS**, Ref R0014 (1990).

96. Tada H., Paris P. C. & Irwin G. R., **THE STRESS ANALYSIS OF CRACKS HANDBOOK**, Third Edition, ASME (2000).

97. Irwin G. R. & Kies J. A., **CRITICAL ENERGY RATE ANALYSIS OF FRACTURE STRENGTH**, Welding Institute Jrnl Supplement, Vol 19, p193 (1954).

98. Paris P. C. & Sih S. C. M., **STRESS ANALYSIS OF CRACKS**, Fracture toughness testing and its applications, ASTM, p30 (1965).

99. Hibbitt, Karlsson & Sorensen Inc, **ABAQUS Users Manual**, Ver 5.7, Pawtucket (1997).

100. Femsys Ltd, **FEMGV Users Manual,** Leicester, Ver 5, (1997)

101. Hibbitt, Karlsson & Sorensen Inc, **ABAQUS POST Users Manual**, Ver 5.7, Pawtucket (1997).

102. Wang Y. Y. & Parks D. M., **CHARACTERISATION OF CONSTRAINT EFFECTS ON CLEAVAGE FRACTURE USING T-STRESS**, Shallow crack fracture mechanics toughness tests and applications, Cambridge, 22-24 Sept (1992).

103. O,Dowd N. P., **APPLICATIONS OF TWO PARAMETER APPROACHES IN ELASTIC —PLASTIC FRACTURE MECHANICS**, Eng. Fract., Mech. Vol 52, pp 445-465 (1995).

104. ASTM E813-88, **STANDARD TEST METHOD FOR J_{IC}, A MEASURE OF FRACTURE TOUGHNESS.**

105. NAFEMS, **THREE DIMENSIONAL TEST CASES IN LINEAR ELASTIC FRACTURE MECHANICS**, Ref R0028, (1993).

106. Nakumara K. & Parks P. C., **MODIFIED CRACK CLOSURE INTEGRAL (MCCI) USING 12 NODED ISOPARAMETRIC BRICK ELEMENTS FOR 3-D CRACK PROBLEMS**, Int. Conf. Numerical Methods in Fracture Mechanics, Ed. Luxmore & Owen, (1990).

107. Begley J. A. and Landes J. D., **THE INFLUENCE OF SPECIMEN GEOMETRY ON J_{IC}, FRACTURE TOUGHNESS,** Fracture Toughness, ASTM STP 514, pp 24-39 (1972).

108. Rice J. T., Paris P. C. & Merkle J. G., **SOME FURTHER RESULTS OF J INTEGRAL ANALYSIS AND ESTIMATES**, Progress in Flaw Growth and Fracture Toughness Testing, ASTM STP 536, pp 231-245 (1973).

109. Dodds R. H., Private communication, (2001).

110. ASTM E602-81 (Reapproved 1986), **STANDARD METHOD FOR SHARP-NOTCH TENSION TESTING WITH CYLINDRICAL SPECIMENS.**

111. Donoso J. R. & Labbe F., **Q-STRESS AND CONSTRAINT BEHAVIOR OF THE NOTCHED CYLINDRICAL TENSILE SPECIMEN**, Eng. Fract., Mech. Vol 68, pp 487-496 (2001).

112. Wilson C. D., **FRACTURE TOUGHNESS TESTING WITH NOTCHED ROUND BARS**, PhD Thesis, University of Tennessee, Knoxville, 1997.

113. Shabara M. A. N., El-Domiaty A. A. & Al-Ansary M. D., **ESTIMATION OF PLANE STRAIN FRACTURE TOUGHNESS FROM CIRCUMFERENTIALLY BLUNTLY NOTCHED ROUND-BAR SPECIMENS**. Eng. Fract., Mech. Vol 54, pp 533-541 (1996).

114. Toribio J., **A FRACTURE CRITERION FOR HIGH-STRENGTH STEEL NOTCHED BARS**, Eng. Fract., Mech. Vol 57, pp 391-404 (1997).

115. Li D.M. & Bakker A., **FRACTURE TOUGHNESS EVALUATION USING CIRCUMFERENTIALLY-CRACKED CYLINDRICAL BAR SPECIMENS**, Eng. Fract., Mech. Vol 57, pp 1-11 (1997).

116. Itoh Y. Z., Murakami T. & Kashiwaya H., **APPROXIMATE FORMULAE FOR ESTIMATING THE J-INTEGRAL OF A CIRCUMFERENTIALLY CRACKED ROUND BAR UNDER TENSION OR TORSION**, Eng. Fract., Mech. Vol 31, pp 967-975 (1988).

117. Giovanola J.H., Homma H., Lichtenberger M., Crocker J. E. & Klopp W., **FRACTURE TOUGHNESS MEASUREMENTS USING SMALL CRACKED ROUND BARS**, Constraint Effects in Fracture Theory and Applications: 2nd Vol, ASTM STP 1244, Philadelphia (1995).

118. Ibrahim R. N. & Kotousov A., **ECCENTRICITY CORRECTION FOR THE EVALUATION OF FRACTURE TOUGHNESS FROM CYLINDRICAL NOTCHED TEST SMALL SPECIMENS**, Eng. Fract., Mech. Vol 64, pp 49-58 (1999).

119. Shen W., Zhao T., Gao D., Li D., Li P., Qui X., **FRACTURE TOUGHNESS MEASUREMENT BY CYLINDRICAL SPECIMEN WITH RING SHAPED CRACK**, Eng. Fract., Mech. Vol 16, pp 69-82 (1982).

120. Lucon E., **CYLINDRICAL SPECIMENS FOR EVALUATING A SERVICED COMPONENTS FRACTURE TOUGHNESS PROPERTIES**, 9th European Conf on Fracture, ECF9, Varna (1992).

121. Ibrahim R. N. & Stark H. L., **VALIDITY REQUIREMENTS FOR FRACTURE TOUGHNESS MEASUREMENTS OBTAINED FROM SMALL CIRCUMFERENTIALLY NOTCHED CYLINDRICAL SPECIMENS**, Eng. Fract., Mech. Vol 28, pp 455-460 (1987).

122. Scibetta M., **CONTRIBUTION TO THE EVALUATION OF THE CIRCUMFERENTIALLY-CRACKED ROUND BAR FOR FRACTURE TOUGHNESS DETERMINATION OF REACTOR PRESSURE VESSEL STEELS**, PhD Thesis, Universite de Liege (1999).

123. Joyce J. A.. & Hasson D. F., **CHARACTERIZATION OF TRANSITION TEMPERATURE BEHAVIOUR OF HY-130 STEEL**, Eng. Fract., Mech. Vol 13, pp 417-430 (1980).

124. Hasson D. F. & Joyce J. A., **THE EFFECT OF A HIGHER LOADING RATE ON THE J_{IC} FRACTURE TOUGHNESS TRANSITION TEMPERATURE OF HY STEELS,** Jrn of Engineering Materials and Technology, Vol 103, pp 133-141 (1981).

APPENDIX I

MATLAB FILES

SORT3DPLAIN.m

```
%%%
```

```
 inp=[lcoords(:,1:3),layer7(:,2)];
 end
%
 if numm==8
 load lcoord8.dat
 lcoords=lcoord8;
 load layer8.dat
 inp=[lcoords(:,1:3),layer8(:,2)];
 end
%
 if numm==9
 load lcoord9.dat
 lcoords=lcoord9;
 load layer9.dat
 inp=[lcoords(:,1:3),layer9(:,2)];
 end
%
 if numm==10
 load lcoord10.dat
 lcoords=lcoord10;
 load layer10.dat
 inp=[lcoords(:,1:3),layer10(:,2)];
 end
%
 if numm==11
 load lcoord11.dat
 lcoords=lcoord11;
 load layer11.dat
 inp=[lcoords(:,1:3),layer11(:,2)];
 end
%
 if numm==12
 load lcoord12.dat
 lcoords=lcoord12;
 load layer12.dat
 inp=[lcoords(:,1:3),layer12(:,2)];
 end
%

 if numm==13
 load lcoord13.dat
 lcoords=lcoord13;
 load layer13.dat
 inp=[lcoords(:,1:3),layer13(:,2)];
 end
%
 if numm==14
 load lcoord14.dat
 lcoords=lcoord14;
 load layer14.dat
 inp=[lcoords(:,1:3),layer14(:,2)];
 end
%
 if numm==15
 load lcoord15.dat
 lcoords=lcoord15;
 load layer15.dat
 inp=[lcoords(:,1:3),layer15(:,2)];
 end
%
 if numm==16
 load lcoord16.dat
 lcoords=lcoord16;
 load layer16.dat
 inp=[lcoords(:,1:3),layer16(:,2)];
 end
%
 if numm==17
 load lcoord17.dat
 lcoords=lcoord17;
```

```
 load layer17.dat
 inp=[lcoords(:,1:3),layer17(:,2)];
 end
%
 if numm==18
 load lcoord18.dat
 lcoords=lcoord18;
 load layer18.dat
 inp=[lcoords(:,1:3),layer18(:,2)];
 end
%
 if numm==19
 load lcoord19.dat
 lcoords=lcoord19;
 load layer19.dat
 inp=[lcoords(:,1:3),layer19(:,2)];
 end
%
 if numm==20
 load lcoord20.dat
 lcoords=lcoord20;
 load layer20.dat
 inp=[lcoords(:,1:3),layer20(:,2)];
 end
%%%
```

```
 load layer17.dat
 inp=[lcoords(:,1:3),layer17(:,2)];
 end
%
 if numm==18
 load lcoord18.dat
 lcoords=lcoord18;
 load layer18.dat
 inp=[lcoords(:,1:3),layer18(:,2)];
 end
%
 if numm==19
 load lcoord19.dat
 lcoords=lcoord19;
 load layer19.dat
 inp=[lcoords(:,1:3),layer19(:,2)];
 end
%
 if numm==20
 load lcoord20.dat
 lcoords=lcoord20;
 load layer20.dat
 inp=[lcoords(:,1:3),layer20(:,2)];
 end
%%%
```

```
% also check if x(p) equals x(p+1) but not x(p+2), if so then include
% x(p+1)
% and associated row data in temp also
%
%%%
```

```
srtbk(q,1)=st((position(1,1)),1);
srtbk(q,2)=st((position(1,1)),2);
srtbk(q,3)=st((position(1,1)),3);
srtbk(q,4)=st((position(1,1)),4);
stcoords=[st(1:(position(1,1)-1),:);st((position(1,1)+1):lengthst,:)];
st=stcoords;
end
%%%
```

CONT3DPLAIN.m

```
%%%
```

CONT3DPLAIN.m

```
%%%
```

```
    ninc=1;
    elseif loop==2
    start=(35*count)-11;
    finish=(35*count)-1;
    inc=1;
    ninc=1;
    elseif loop==3
    start=2*count;
    finish=(2*count)+175;
    inc=35;
    ninc=35;
    end
%%%
```

```
sc(q,2)=c((position(1,1)),2);   % position
d=[c(1:(position(1,1)-1),:);c((position(1,1)+1):sizec,:)];
c=d;
end
%%%
```

```
%
% maximum2 is a matrix which gives the maximum value in each column of
% sortc2 and position is a matrix which gives the position of the
% maximum value in each column.
% count2 then defines the limit of data that needs to be re-arranged
% in y order and puts data into a matrix temp2 for sorting.
%
%%%
```

```
%%%
```

```
save cont14a.dat sortca -ascii -tabs
end
if numm==15
save cont15.dat sortc -ascii -tabs
save cont15a.dat sortca -ascii -tabs
end
if numm==16
save cont16.dat sortc -ascii -tabs
save cont16a.dat sortca -ascii -tabs
end
if numm==17
save cont17.dat sortc -ascii -tabs
save cont17a.dat sortca -ascii -tabs
end
if numm==18
save cont18.dat sortc -ascii -tabs
save cont18a.dat sortca -ascii -tabs
end

if numm==19
save cont19.dat sortc -ascii -tabs
save cont19a.dat sortca -ascii -tabs
end
if numm==20
save cont20.dat sortc -ascii -tabs
save cont20a.dat sortca -ascii -tabs
end
```

Q3DPLAIN.m

```
%%%
```

```
 inp=[lcoords(:,1:3),layer6(:,4)];
 end
%
 if numm==7
 load lcoord7.dat
 lcoords=lcoord7;
 load layer7.dat
 inp=[lcoords(:,1:3),layer7(:,4)];
 end
%
 if numm==8
 load lcoord8.dat
 lcoords=lcoord8;
 load layer8.dat
 inp=[lcoords(:,1:3),layer8(:,4)];
 end
%
 if numm==9
 load lcoord9.dat
 lcoords=lcoord9;
 load layer9.dat
 inp=[lcoords(:,1:3),layer9(:,4)];
 end
%
 if numm==10
 load lcoord10.dat
 lcoords=lcoord10;
 load layer10.dat
 inp=[lcoords(:,1:3),layer10(:,4)];
 end
%
 if numm==11
 load lcoord11.dat
 lcoords=lcoord11;
 load layer11.dat
 inp=[lcoords(:,1:3),layer11(:,4)];
 end
%
 if numm==12
 load lcoord12.dat
 lcoords=lcoord12;
 load layer12.dat
 inp=[lcoords(:,1:3),layer12(:,4)];
 end
%
 if numm==13
 load lcoord13.dat
 lcoords=lcoord13;
 load layer13.dat
 inp=[lcoords(:,1:3),layer13(:,4)];
 end
%
 if numm==14
 load lcoord14.dat
 lcoords=lcoord14;
 load layer14.dat
 inp=[lcoords(:,1:3),layer14(:,4)];
 end
%
 if numm==15
 load lcoord15.dat
 lcoords=lcoord15;
 load layer15.dat
 inp=[lcoords(:,1:3),layer15(:,4)];
 end
%
 if numm==16
 load lcoord16.dat
 lcoords=lcoord16;
 load layer16.dat
```

```
 inp=[lcoords(:,1:3),layer16(:,4)];
 end
%
 if numm==17
 load lcoord17.dat
 lcoords=lcoord17;
 load layer17.dat
 inp=[lcoords(:,1:3),layer17(:,4)];
 end
%
 if numm==18
 load lcoord18.dat
 lcoords=lcoord18;
 load layer18.dat
 inp=[lcoords(:,1:3),layer18(:,4)];
 end
%
 if numm==19
 load lcoord19.dat
 lcoords=lcoord19;
 load layer19.dat
 inp=[lcoords(:,1:3),layer19(:,4)];
 end
%
 if numm==20
 load lcoord20.dat
 lcoords=lcoord20;
 load layer20.dat
 inp=[lcoords(:,1:3),layer20(:,4)];
 end
%%%
```

```
%%%
```

```
lengthst=size(st);
[maximum,position]=max(st);
 if lengthst==[1,4]
 position=[1,1];
 end
srtbk(q,1)=st((position(1,1)),1);
srtbk(q,2)=st((position(1,1)),2);
srtbk(q,3)=st((position(1,1)),3);
srtbk(q,4)=st((position(1,1)),4);
stcoords=[st(1:(position(1,1)-1),:);st((position(1,1)+1):lengthst,:)];
st=stcoords;
end
%%%
```

```
%Interpolation of stress profiles to allow Q evaluation
%
%%%
```

```
save qsts12.dat inter -ascii -tabs
end
if numm==13
save qsts13.dat inter -ascii -tabs
end
if numm==14
save qsts14.dat inter -ascii -tabs
end
if numm==15
save qsts15.dat inter -ascii -tabs
end
if numm==16
save qsts16.dat inter -ascii -tabs
end
if numm==17
save qsts17.dat inter -ascii -tabs
end
if numm==18
save qsts18.dat inter -ascii -tabs
end
if numm==19
save qsts19.dat inter -ascii -tabs
end
if numm==20
save qsts20.dat inter -ascii -tabs
end
```

APPENDIX II

TEST RECORDS – PLAIN SPECIMENS

Fracture Toughness Test Data - K_{IC} Test

Specimen Data

Specimen Thickness:	25 mm
Specimen Width:	60 mm
Material:	EN24
Yield Stress:	970 MPa
Specimen No:	25P1
Side Groove Type:	None
Side Groove Depth:	0 mm
Effective Thickness:	25 mm

Precracking Data

Initial Cycles	
Mean Load:	14 kN
Amplitude:	13 kN
Max Load:	27 kN
No Cycles:	4000
Force Ratio:	0.04
Final Cycles	
Mean Load:	13 kN
Amplitude:	11 kN
Max Load:	24 kN
No Cycles:	7000
Force Ratio:	0.08

Post Fracture Data

Dist from edge	Crack length
1.0%	29.50
12.5%	29.90
25.0%	30.25
37.5%	30.25
50.0%	30.25
62.5%	30.25
75.0%	30.25
87.5%	29.60
99.0%	28.90
Ave	**29.99**

$K_Q = [F_Q/(BW^{0.5})].f(a/W)$

where f(a/W) is given by 9.2.3.2 of BS7448:pt1

FQ =	60.48 kN	(from Instron)
B =	25 mm	
W =	60 mm	
a/W =	0.4999	
f(a/W) =	9.6560	
KQ =	**95.37 MPa.m^0.5**	

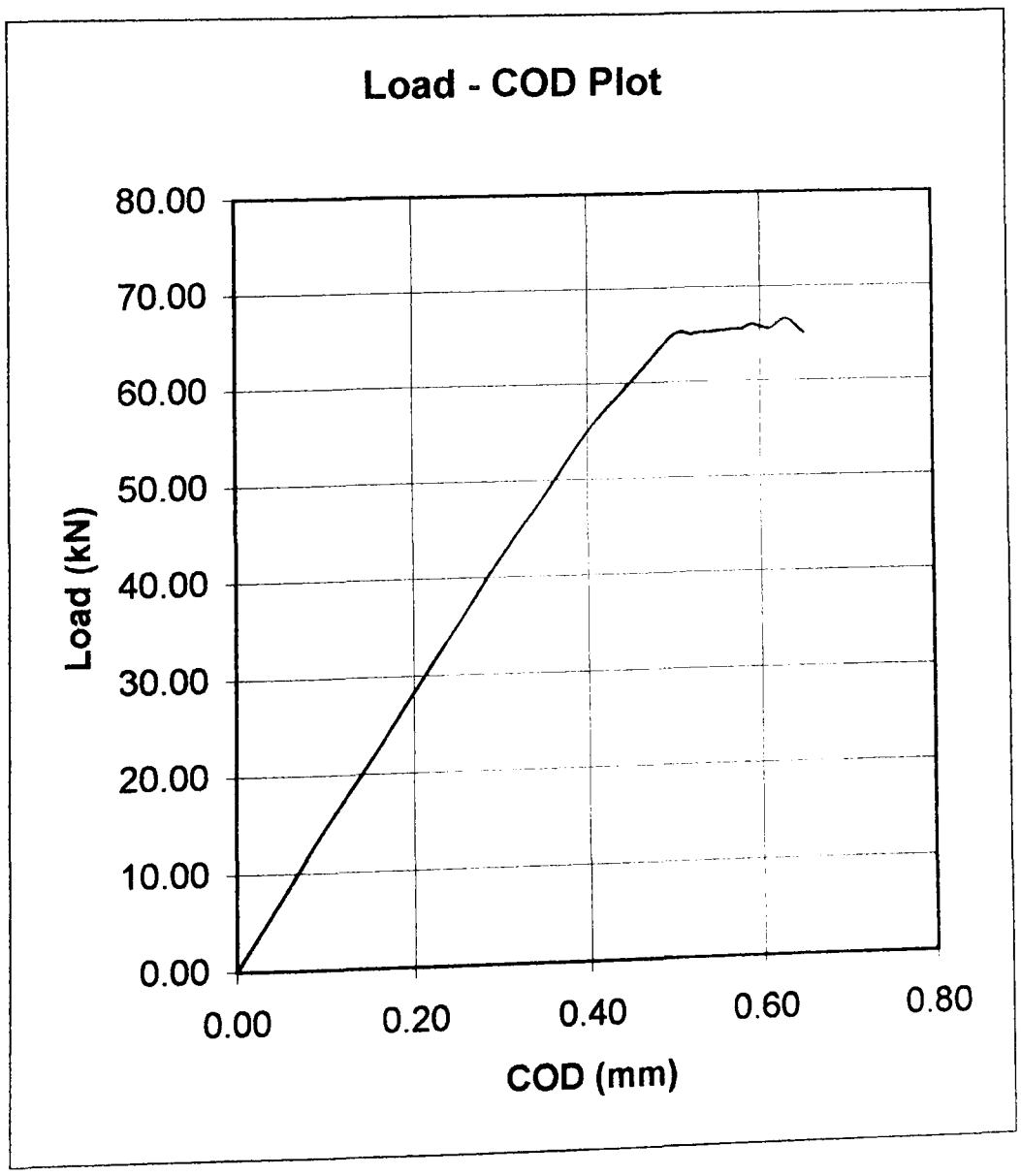

Fracture Toughness Test Data - K_{IC} Test

Specimen Data	
Specimen Thickness:	25 mm
Specimen Width:	60 mm
Material:	EN24
Yield Stress:	970 MPa
Specimen No:	25P2
Side Groove Type:	None
Side Groove Depth:	0 mm
Effective Thickness:	25 mm

Precracking Data	
Initial Cycles	
Mean Load:	14 kN
Amplitude:	13 kN
Max Load:	27 kN
No Cycles:	5700
Force Ratio:	0.04
Final Cycles	
Mean Load:	13 kN
Amplitude:	11 kN
Max Load:	24 kN
No Cycles:	3000
Force Ratio:	0.08

Post Fracture Data

Dist from edge	Crack length
1.0%	29.20
12.5%	29.40
25.0%	29.60
37.5%	29.80
50.0%	29.90
62.5%	29.80
75.0%	29.60
87.5%	29.45
99.0%	29.20
Ave	**29.59**

$K_Q = [F_Q/(BW^{0.5})].f(a/W)$
where f(a/W) is given by 9.2.3.2 of BS7448:pt1

FQ =	62.3 kN	(from Instron)
B =	25 mm	
W =	60 mm	
a/W =	0.4932	
f(a/W) =	9.4612	
KQ =	**96.25 MPa.m^0.5**	

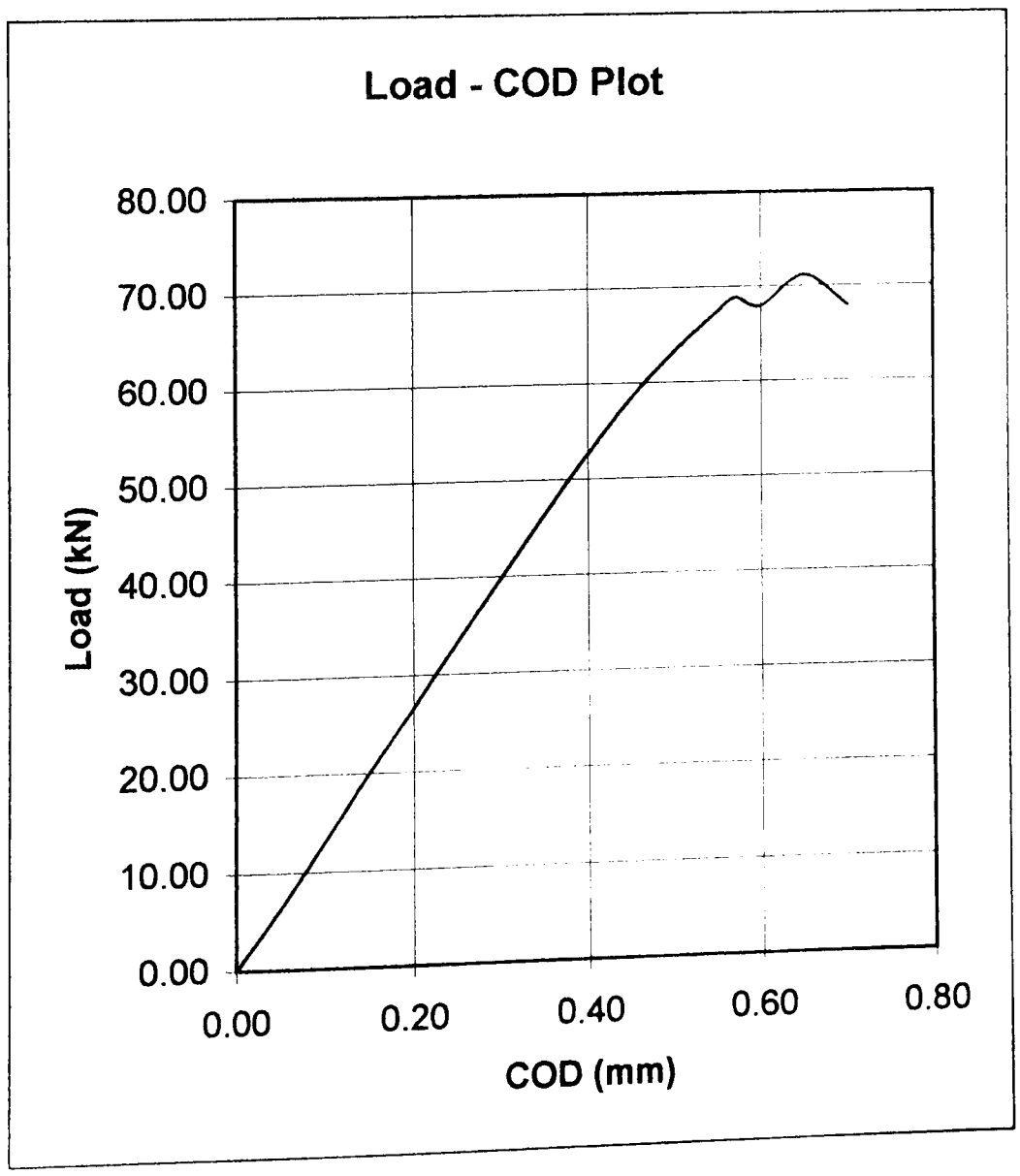

Fracture Toughness Test Data - K_{IC} Test

Specimen Data

Specimen Thickness:	25 mm
Specimen Width:	60 mm
Material:	EN24
Yield Stress:	970 MPa
Specimen No:	25P3
Side Groove Type:	None
Side Groove Depth:	0 mm
Effective Thickness:	25 mm

Precracking Data

Initial Cycles	
Mean Load:	14 kN
Amplitude:	13 kN
Max Load:	27 kN
No Cycles:	5850
Force Ratio:	0.04
Final Cycles	
Mean Load:	13 kN
Amplitude:	11 kN
Max Load:	24 kN
No Cycles:	3750
Force Ratio:	0.08

Post Fracture Data

Dist from edge	Crack length
1.0%	29.50
12.5%	29.70
25.0%	30.20
37.5%	30.25
50.0%	30.20
62.5%	30.10
75.0%	30.00
87.5%	29.50
99.0%	29.10
Ave	**29.91**

$K_Q = [F_Q/(BW^{0.5})].f(a/W)$

where f(a/W) is given by 9.2.3.2 of BS7448:pt1

FQ =	60.67 kN	(from Instron)
B =	25 mm	
W =	60 mm	
a/W =	0.4984	
f(a/W) =	9.6128	
KQ =	**95.24 MPa.m^0.5**	

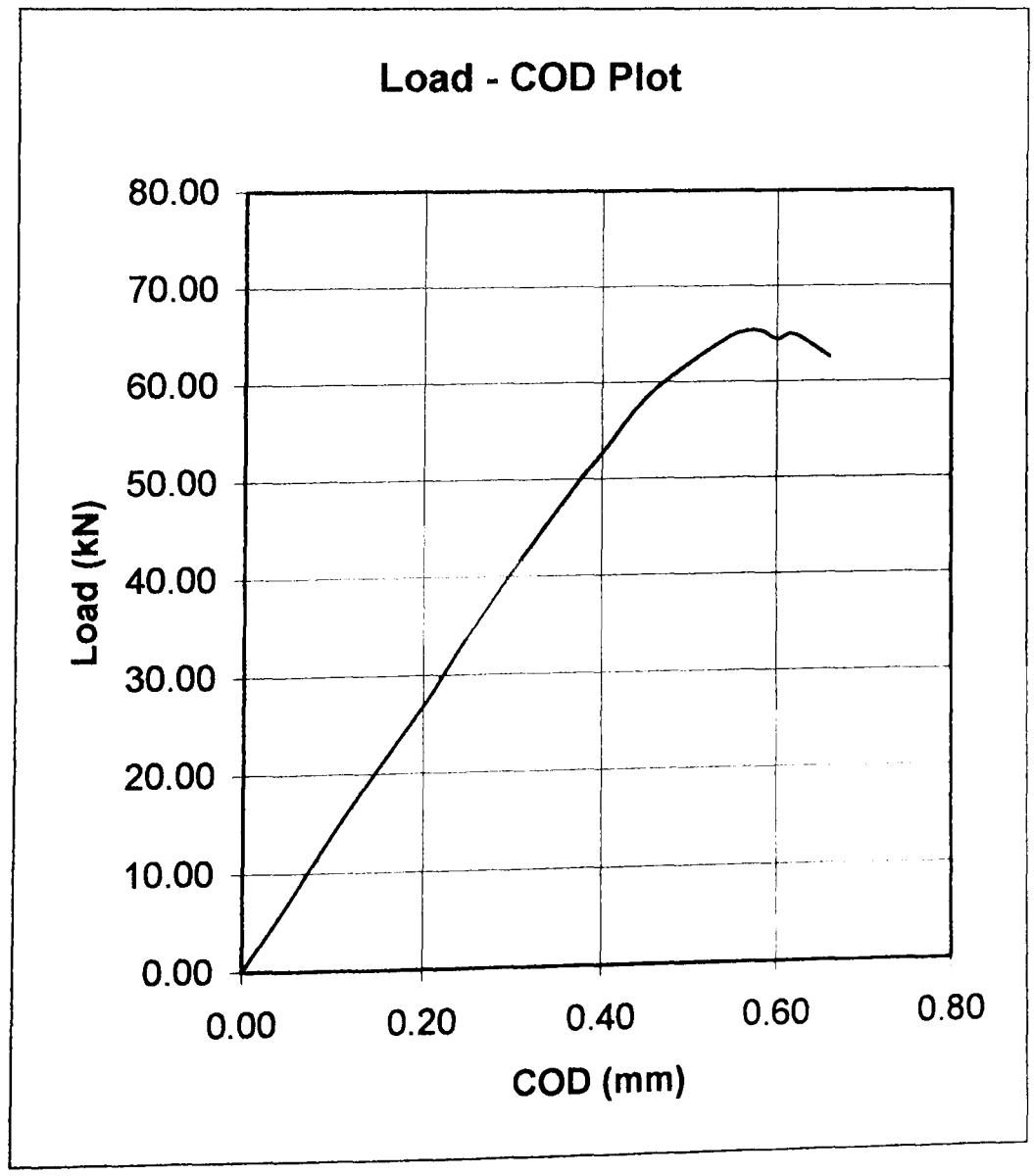

Fracture Toughness Test Data - K_{IC} Test

Specimen Data

Specimen Thickness:	25 mm
Specimen Width:	60 mm
Material:	EN24
Yield Stress:	970 MPa
Specimen No:	25P4
Side Groove Type:	None
Side Groove Depth:	0 mm
Effective Thickness:	25 mm

Precracking Data

Initial Cycles	
Mean Load:	14 kN
Amplitude:	13 kN
Max Load:	27 kN
No Cycles:	5100
Force Ratio:	0.04
Final Cycles	
Mean Load:	13 kN
Amplitude:	11 kN
Max Load:	24 kN
No Cycles:	4200
Force Ratio:	0.08

Post Fracture Data

Dist from edge	Crack length
1.0%	29.30
12.5%	29.60
25.0%	30.00
37.5%	30.00
50.0%	30.00
62.5%	30.00
75.0%	30.00
87.5%	29.70
99.0%	29.40
Ave	**29.83**

$K_Q = [F_Q/(BW^{0.5})].f(a/W)$

where f(a/W) is given by 9.2.3.2 of BS7448:pt1

FQ =	61.5 kN	(from Instron)
B =	25 mm	
W =	60 mm	
a/W =	0.4972	
f(a/W) =	9.5761	
KQ =	**96.17 MPa.m^0.5**	

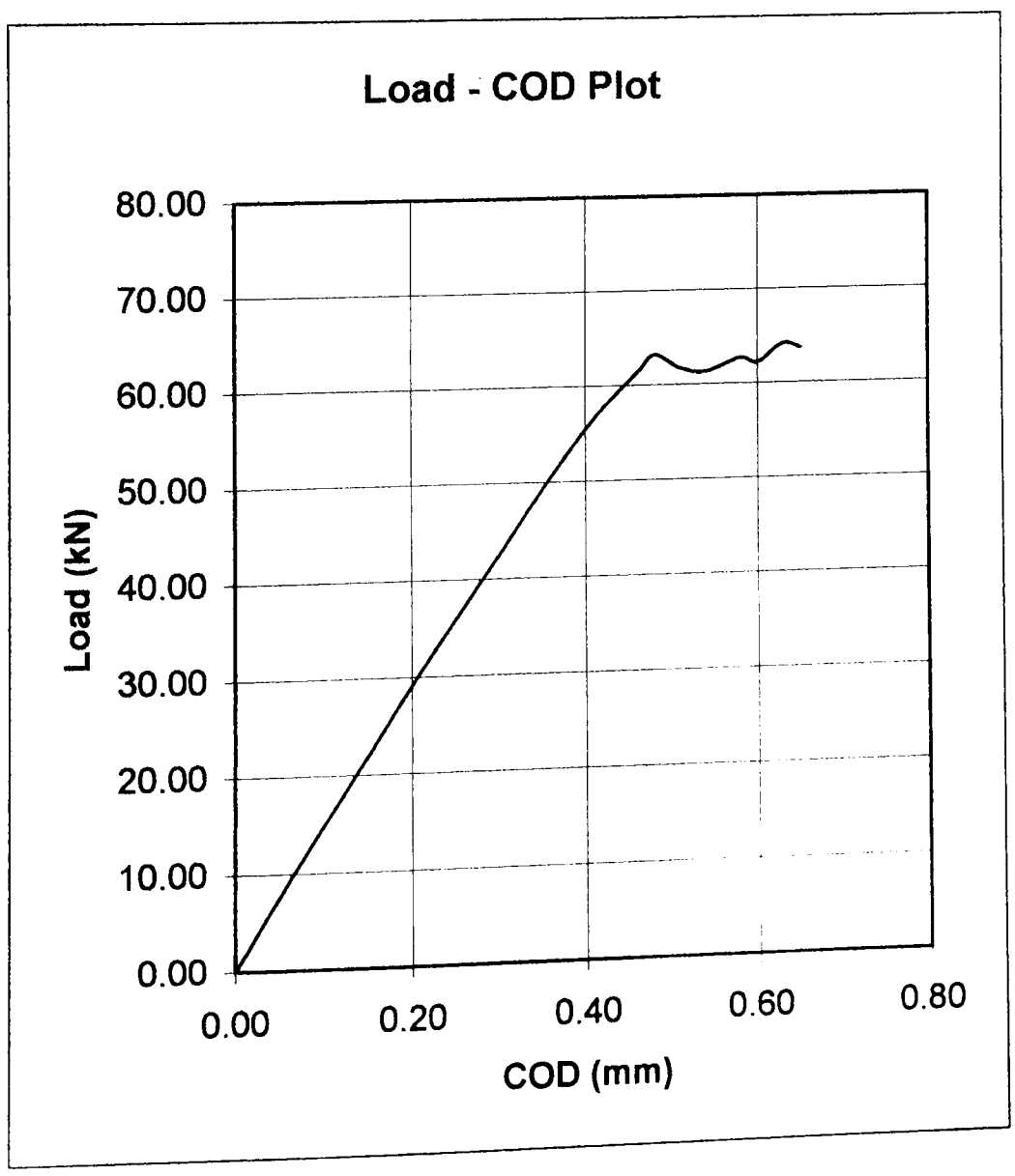

Fracture Toughness Test Data - K_{IC} Test

Specimen Data

Specimen Thickness:	15 mm
Specimen Width:	60 mm
Material:	EN24
Yield Stress:	970 MPa
Specimen No:	15P3
Side Groove Type:	None
Side Groove Depth:	0 mm
Effective Thickness:	15 mm

Precracking Data

Initial Cycles	
Mean Load:	9 kN
Amplitude:	8 kN
Max Load:	17 kN
No Cycles:	3800
Force Ratio:	0.06
Final Cycles	
Mean Load:	7 kN
Amplitude:	6 kN
Max Load:	13 kN
No Cycles:	1000
Force Ratio:	0.08

Post Fracture Data

Dist from edge	Crack length
1.0%	28.70
12.5%	29.40
25.0%	30.00
37.5%	30.10
50.0%	30.10
62.5%	29.90
75.0%	29.70
87.5%	29.50
99.0%	29.20
Ave	**29.71**

$K_Q = [F_Q/(BW^{0.5})].f(a/W)$

where f(a/W) is given by 9.2.3.2 of BS7448:pt1

FQ =	39.6 kN	(from Instron)
B =	15 mm	
W =	60 mm	
a/W =	0.4951	
f(a/W) =	9.5153	
KQ =	**102.55 MPa.m^0.5**	

Note:- Part of precrack was due to quenching rather than fatigue

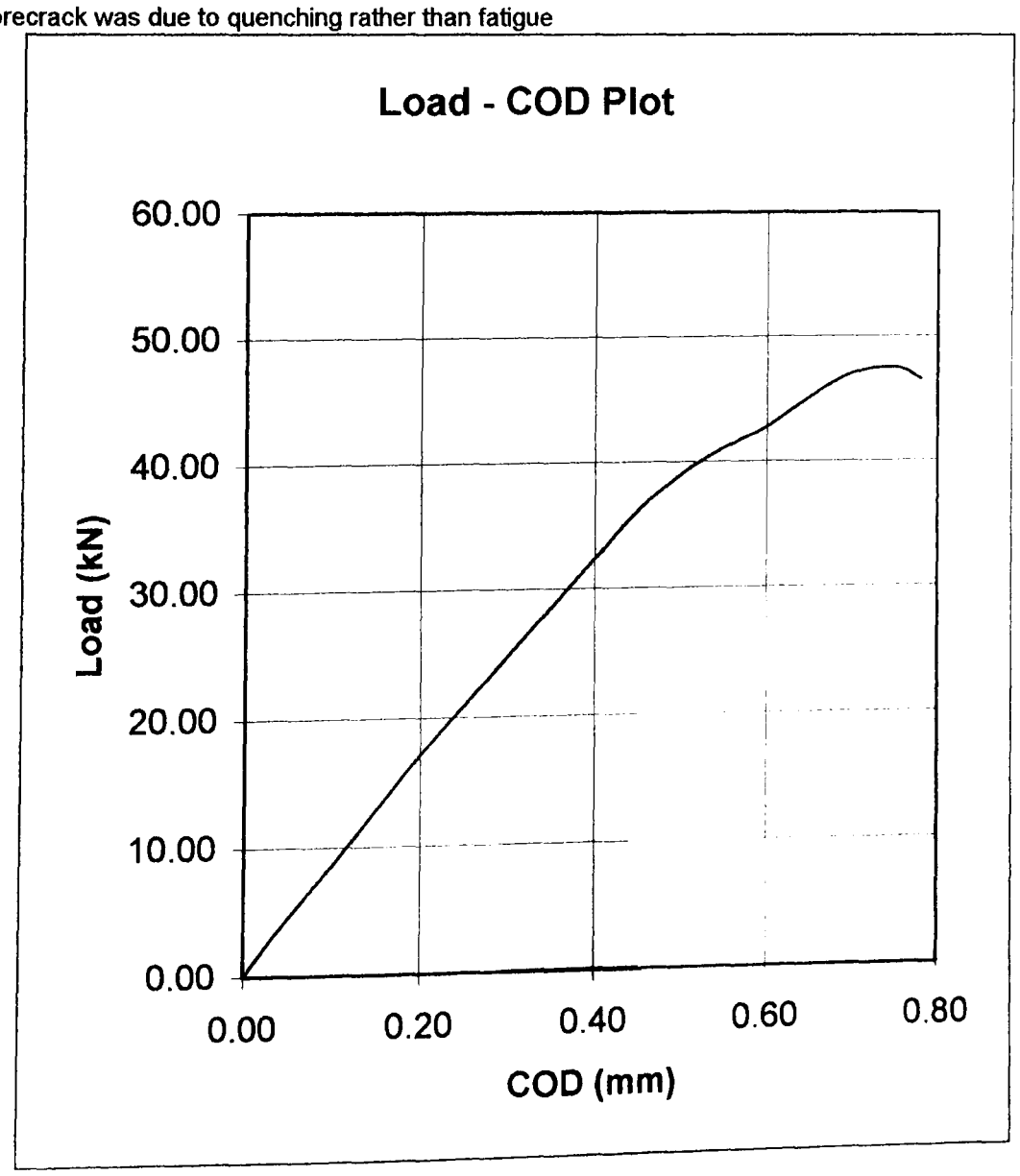

Fracture Toughness Test Data - K_{IC} Test

Specimen Data

Specimen Thickness:	15 mm
Specimen Width:	60 mm
Material:	EN24
Yield Stress:	970 MPa
Specimen No:	15P4
Side Groove Type:	None
Side Groove Depth:	0 mm
Effective Thickness:	15 mm

Precracking Data

Initial Cycles	
Mean Load:	9 kN
Amplitude:	8 kN
Max Load:	17 kN
No Cycles:	4600
Force Ratio:	0.06
Final Cycles	
Mean Load:	7 kN
Amplitude:	6 kN
Max Load:	13 kN
No Cycles:	1300
Force Ratio:	0.08

Post Fracture Data

Dist from edge	Crack length
1.0%	29.40
12.5%	29.40
25.0%	29.40
37.5%	29.30
50.0%	29.20
62.5%	29.20
75.0%	29.10
87.5%	29.00
99.0%	28.50
Ave	**29.19**

$K_Q = [F_Q/(BW^{0.5})].f(a/W)$

where f(a/W) is given by 9.2.3.2 of BS7448:pt1

FQ =	38.9 kN	(from Instron)
B =	15 mm	
W =	60 mm	
a/W =	0.4866	
f(a/W) =	9.2728	
KQ =	**98.17 MPa.m^0.5**	

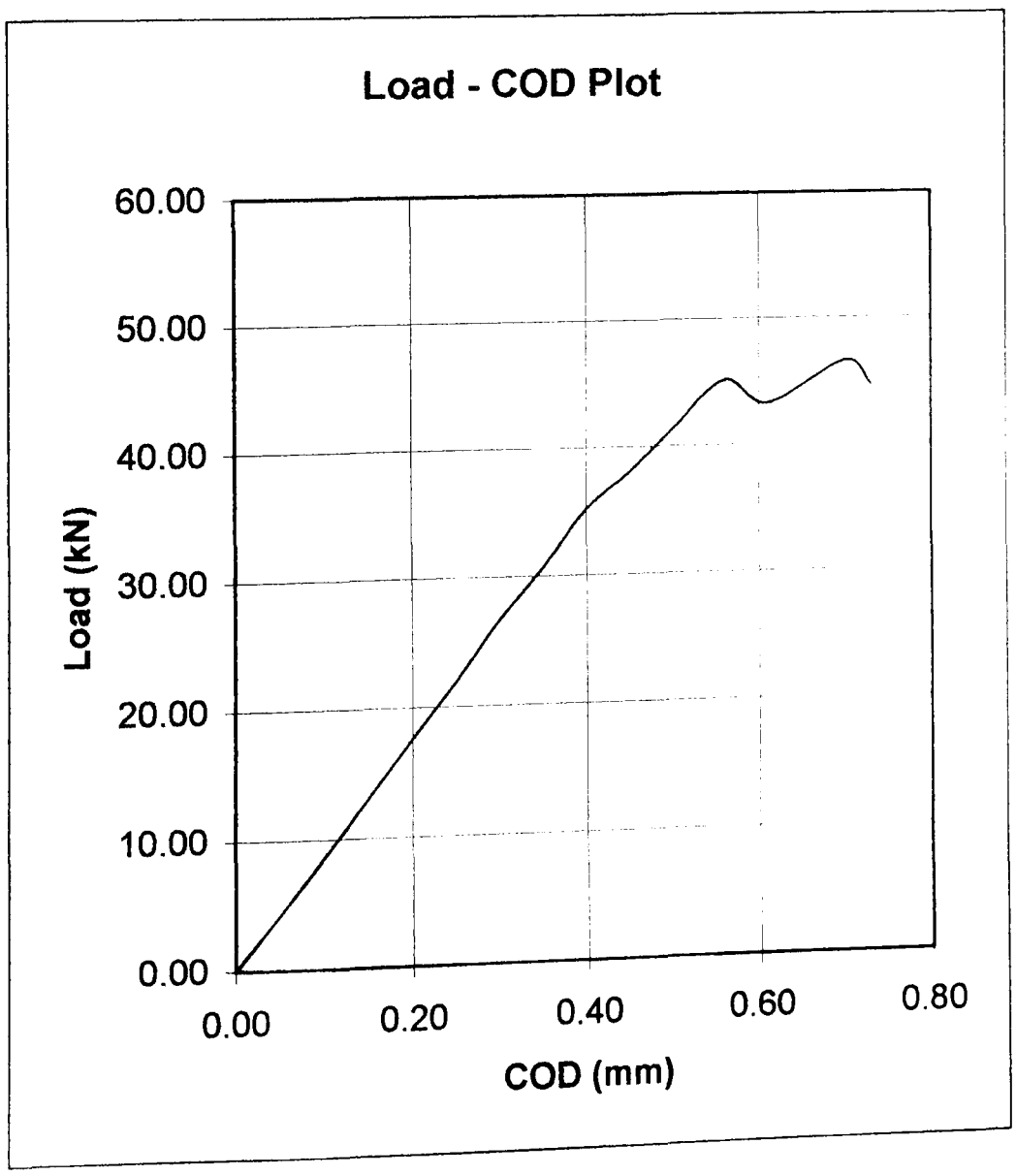

Fracture Toughness Test Data - K_{IC} Test

Specimen Data

Specimen Thickness:	10 mm
Specimen Width:	60 mm
Material:	EN24
Yield Stress:	970 MPa
Specimen No:	10P1
Side Groove Type:	None
Side Groove Depth:	0 mm
Effective Thickness:	10 mm

Precracking Data

Initial Cycles	
Mean Load:	6 kN
Amplitude:	5 kN
Max Load:	11 kN
No Cycles:	6000
Force Ratio:	0.09
Final Cycles	
Mean Load:	4.5 kN
Amplitude:	4 kN
Max Load:	8.5 kN
No Cycles:	3200
Force Ratio:	0.06

Post Fracture Data

Dist from edge	Crack length
1.0%	28.90
12.5%	29.30
25.0%	29.50
37.5%	29.50
50.0%	29.40
62.5%	29.45
75.0%	29.30
87.5%	29.25
99.0%	29.20
Ave	**29.34**

$K_Q = [F_Q/(BW^{0.5})].f(a/W)$

where f(a/W) is given by 9.2.3.2 of BS7448:pt1

FQ =	29.7 kN	(from Instron)
B =	10 mm	
W =	60 mm	
a/W =	0.4891	
f(a/W) =	9.3427	
KQ =	**113.28 MPa.m^0.5**	

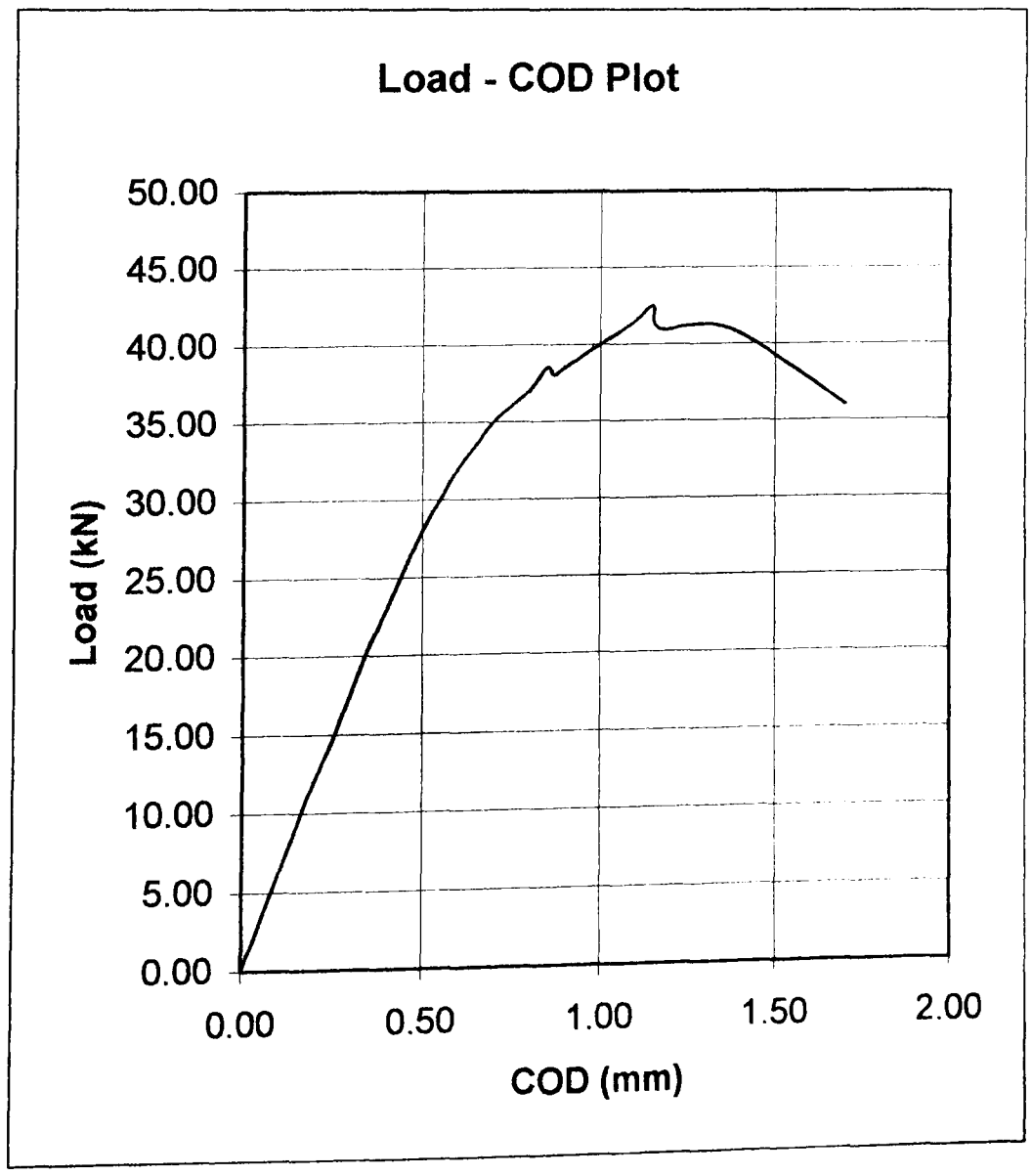

Fracture Toughness Test Data - K_{IC} Test

Specimen Data

Specimen Thickness:	10	mm
Specimen Width:	60	mm
Material:	EN24	
Yield Stress:	970	MPa
Specimen No:	10P2	
Side Groove Type:	None	
Side Groove Depth:	0	mm
Effective Thickness:	10	mm

Precracking Data

Initial Cycles		
Mean Load:	6	kN
Amplitude:	5	kN
Max Load:	11	kN
No Cycles:	5900	
Force Ratio:	0.09	
Final Cycles		
Mean Load:	4.5	kN
Amplitude:	4	kN
Max Load:	8.5	kN
No Cycles:	2600	
Force Ratio:	0.06	

Post Fracture Data

Dist from edge	Crack length
1.0%	29.20
12.5%	29.30
25.0%	29.40
37.5%	29.40
50.0%	29.30
62.5%	29.30
75.0%	29.20
87.5%	29.00
99.0%	28.80
Ave	**29.24**

$K_Q = [F_Q/(BW^{0.5})].f(a/W)$

where f(a/W) is given by 9.2.3.2 of BS7448:pt1

FQ =	26.3	kN	(from Instron)
B =	10	mm	
W =	60	mm	
a/W =	0.4873		
f(a/W) =	9.2931		
KQ =	**99.78**	**MPa.m^0.5**	

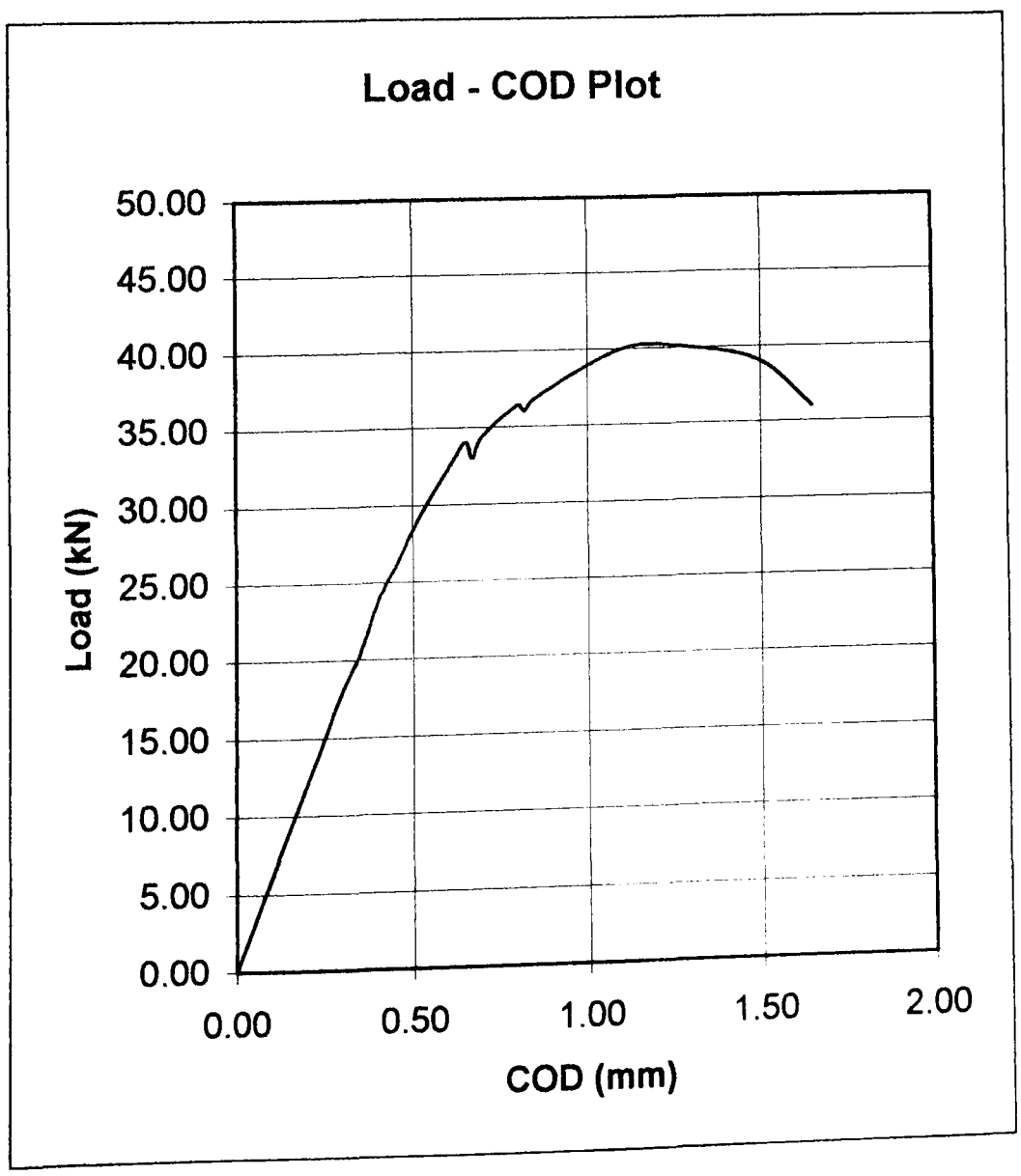

Fracture Toughness Test Data - K_{IC} Test

Specimen Data

Specimen Thickness:	10 mm
Specimen Width:	60 mm
Material:	EN24
Yield Stress:	970 MPa
Specimen No:	10P3
Side Groove Type:	None
Side Groove Depth:	0 mm
Effective Thickness:	10 mm

Precracking Data

Initial Cycles	
Mean Load:	6 kN
Amplitude:	5 kN
Max Load:	11 kN
No Cycles:	6000
Force Ratio:	0.09
Final Cycles	
Mean Load:	4.5 kN
Amplitude:	4 kN
Max Load:	8.5 kN
No Cycles:	3500
Force Ratio:	0.06

Post Fracture Data

Dist from edge	Crack length
1.0%	29.10
12.5%	29.20
25.0%	29.40
37.5%	29.45
50.0%	29.50
62.5%	29.40
75.0%	29.40
87.5%	29.30
99.0%	29.10
Ave	**29.34**

$K_Q = [F_Q/(BW^{0.5})].f(a/W)$

where f(a/W) is given by 9.2.3.2 of BS7448:pt1

FQ =	28.4 kN	(from Instron)
B =	10 mm	
W =	60 mm	
a/W =	0.4891	
f(a/W) =	9.3427	
KQ =	**108.32 MPa.m^0.5**	

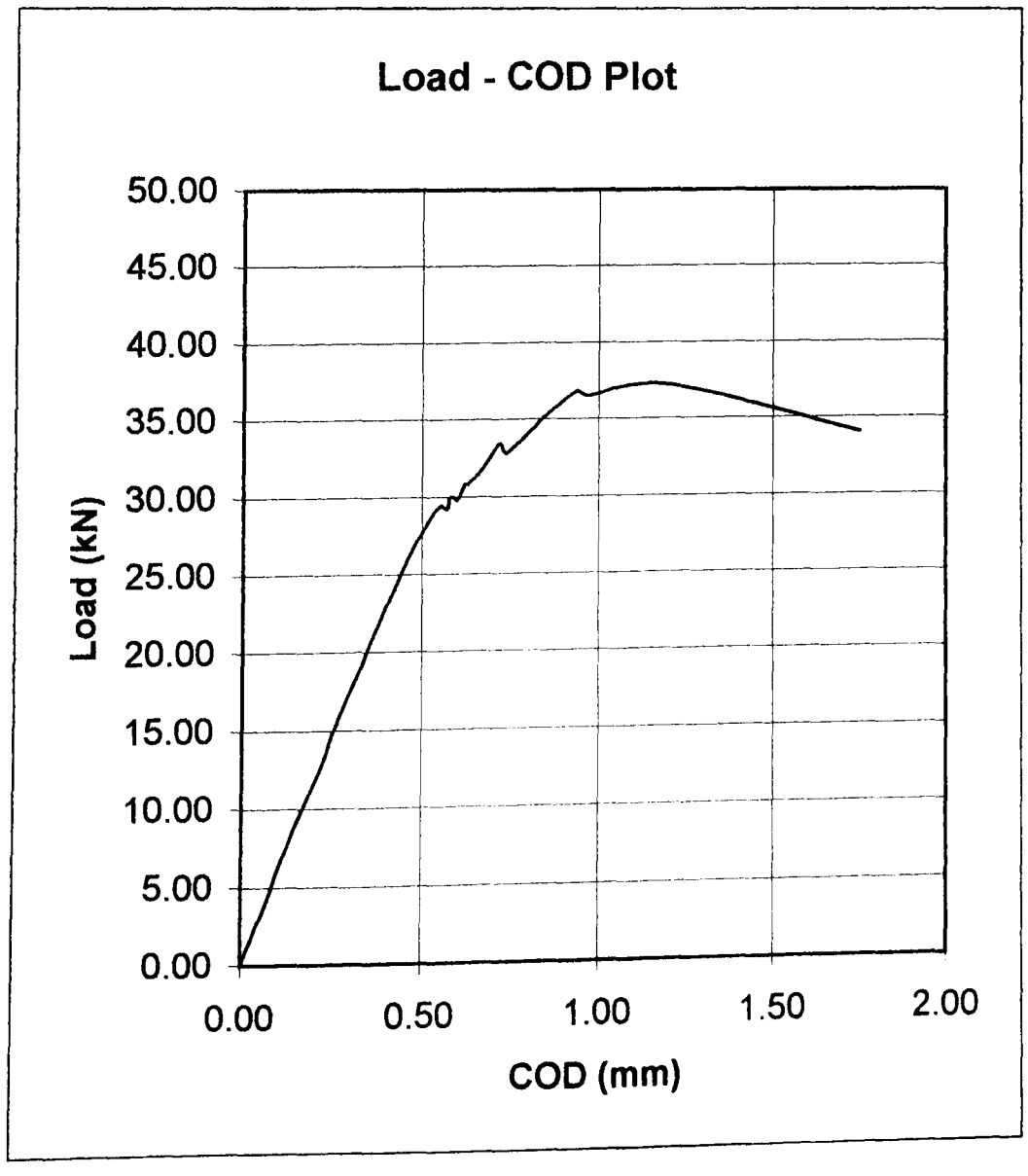

Fracture Toughness Test Data - K_{IC} Test

Specimen Data

Specimen Thickness:	10 mm
Specimen Width:	60 mm
Material:	EN24
Yield Stress:	970 MPa
Specimen No:	10P4
Side Groove Type:	None
Side Groove Depth:	0 mm
Effective Thickness:	10 mm

Precracking Data

Initial Cycles	
Mean Load:	6 kN
Amplitude:	5 kN
Max Load:	11 kN
No Cycles:	7000
Force Ratio:	0.09
Final Cycles	
Mean Load:	4.5 kN
Amplitude:	4 kN
Max Load:	8.5 kN
No Cycles:	500
Force Ratio:	0.06

Post Fracture Data

Dist from edge	Crack length
1.0%	29.00
12.5%	29.20
25.0%	29.40
37.5%	29.45
50.0%	29.50
62.5%	29.45
75.0%	29.40
87.5%	29.20
99.0%	29.00
Ave	**29.33**

$K_Q = [F_Q/(BW^{0.5})].f(a/W)$

where f(a/W) is given by 9.2.3.2 of BS7448:pt1

FQ =	27.2 kN	(from Instron)
B =	10 mm	
W =	60 mm	
a/W =	0.4888	
f(a/W) =	9.3340	
KQ =	**103.65 MPa.m^0.5**	

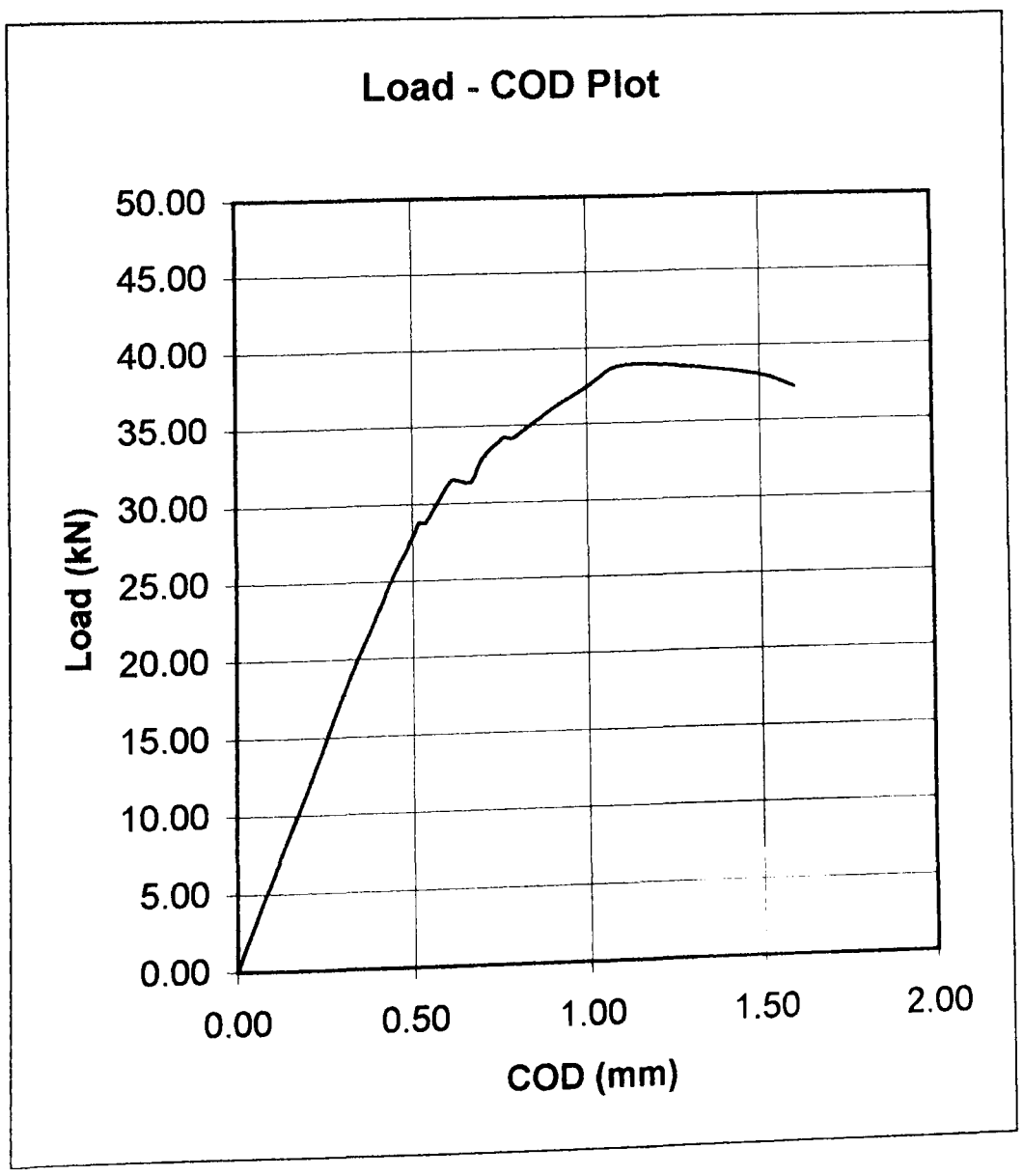

Fracture Toughness Test Data - J_{IC} Test

Specimen Data

Specimen Thickness:	5 mm
Specimen Width:	60 mm
Material:	EN24
Yield Stress:	970 MPa
Specimen No:	5P1
Side Groove Type:	None
Side Groove Depth:	0 mm
Effective Thickness:	5 mm

Precracking Data

Initial Cycles	
Mean Load:	3 kN
Amplitude:	2.6 kN
Max Load:	5.6 kN
No Cycles:	2200
Force Ratio:	0.07
Final Cycles	
Mean Load:	2.6 kN
Amplitude:	2.3 kN
Max Load:	4.9 kN
No Cycles:	5000
Force Ratio:	0.06

Post Fracture Data

Dist from edge	Crack length	Stable Crack
1.0%	29.62	0
12.5%	29.74	0
25.0%	29.86	0
37.5%	29.93	0.73
50.0%	30.00	0.73
62.5%	30.05	0.43
75.0%	30.10	0.18
87.5%	30.05	0
99.0%	30.00	0
Ave	**29.94**	**0.259**

$J = \{[F/(BW^{0.5})].f(a/W)\}^2 [(1-\nu^2)/E] + [(\eta_p U_p)/B(W-a)]$

where f(a/W) is given by 9.2.3.2 of BS7448:pt1

and $\eta_p = 2+0.522.(1-a/W)$

F =	14.7 kN	η_p =	2.2615
B =	5 mm	Up =	0.970813
W =	60 mm		
a/W =	0.4990		
f(a/W) =	9.6307		
J=	**75.40 N/mm**		

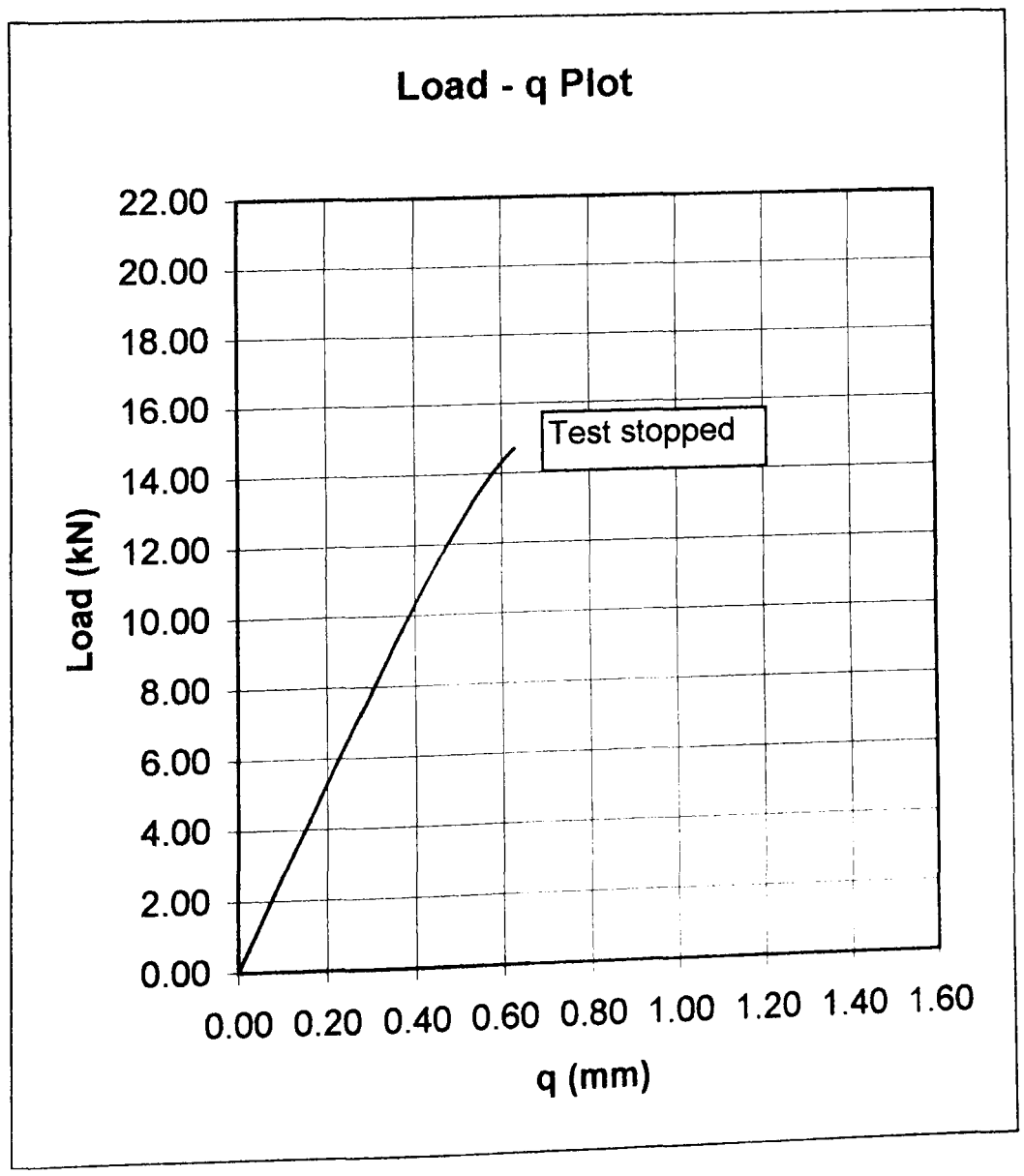

Fracture Toughness Test Data - J_{IC} Test

Specimen Data

Specimen Thickness:	5 mm
Specimen Width:	60 mm
Material:	EN24
Yield Stress:	970 MPa
Specimen No:	5P2
Side Groove Type:	None
Side Groove Depth:	0 mm
Effective Thickness:	5 mm

Precracking Data

Initial Cycles	
Mean Load:	3 kN
Amplitude:	2.6 kN
Max Load:	5.6 kN
No Cycles:	2200
Force Ratio:	0.07
Final Cycles	
Mean Load:	2.6 kN
Amplitude:	2.3 kN
Max Load:	4.9 kN
No Cycles:	5000
Force Ratio:	0.06

Post Fracture Data

Dist from edge	Crack length	Stable Crack
1.0%	30.05	0.00
12.5%	30.25	0.85
25.0%	30.30	1.90
37.5%	30.30	2.85
50.0%	30.30	3.55
62.5%	30.30	3.15
75.0%	30.25	2.40
87.5%	30.25	1.30
99.0%	30.15	0.00
Ave	**30.26**	**2.000**

$J = \{[F/(BW^{0.5})].f(a/W)\}^2 [(1-\nu^2)/E]+[(\eta_p U_p)/B(W-a)]$

where f(a/W) is given by 9.2.3.2 of BS7448:pt1

and $\eta_p = 2+0.522.(1-a/W)$

F =	20.5 kN	η_p =	2.258771
B =	5 mm	Up =	10.85327
W =	60 mm		
a/W =	0.5043		
f(a/W) =	9.7875		
J=	**286.96 N/mm**		

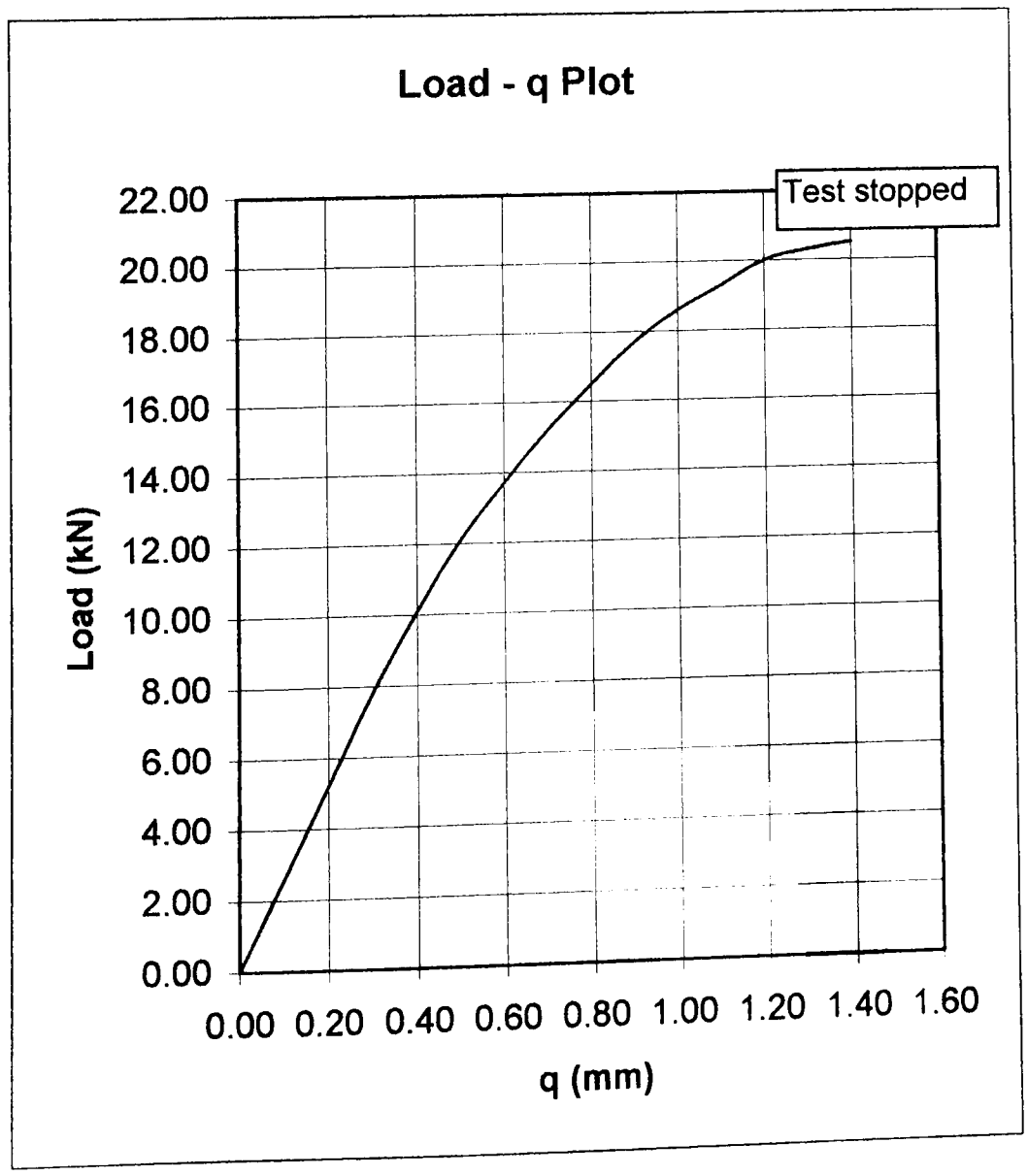

Fracture Toughness Test Data - J_{IC} Test

Specimen Data

Specimen Thickness:	5 mm
Specimen Width:	60 mm
Material:	EN24
Yield Stress:	970 MPa
Specimen No:	5P3
Side Groove Type:	None
Side Groove Depth:	0 mm
Effective Thickness:	5 mm

Precracking Data

Initial Cycles	
Mean Load:	3 kN
Amplitude:	2.6 kN
Max Load:	5.6 kN
No Cycles:	2200
Force Ratio:	0.07
Final Cycles	
Mean Load:	2.6 kN
Amplitude:	2.3 kN
Max Load:	4.9 kN
No Cycles:	5000
Force Ratio:	0.06

Post Fracture Data

Dist from edge	Crack length	Stable Crack
1.0%	29.70	0.00
12.5%	30.00	0.15
25.0%	30.15	0.70
37.5%	30.25	1.85
50.0%	30.25	2.50
62.5%	30.25	2.50
75.0%	30.15	1.45
87.5%	30.15	0.40
99.0%	29.90	0.00
Ave	**30.13**	**1.194**

$J = \{[F/(BW^{0.5})].f(a/W)\}^2 [(1-\nu^2)/E] + [(\eta_p U_p)/B(W-a)]$

where f(a/W) is given by 9.2.3.2 of BS7448:pt1

and $\eta_p = 2+0.522.(1-a/W)$

F =	20 kN	η_p =	2.259913
B =	5 mm	Up =	6.04
W =	60 mm		
a/W =	0.5021		
f(a/W) =	9.7213		
J=	**206.05 N/mm**		

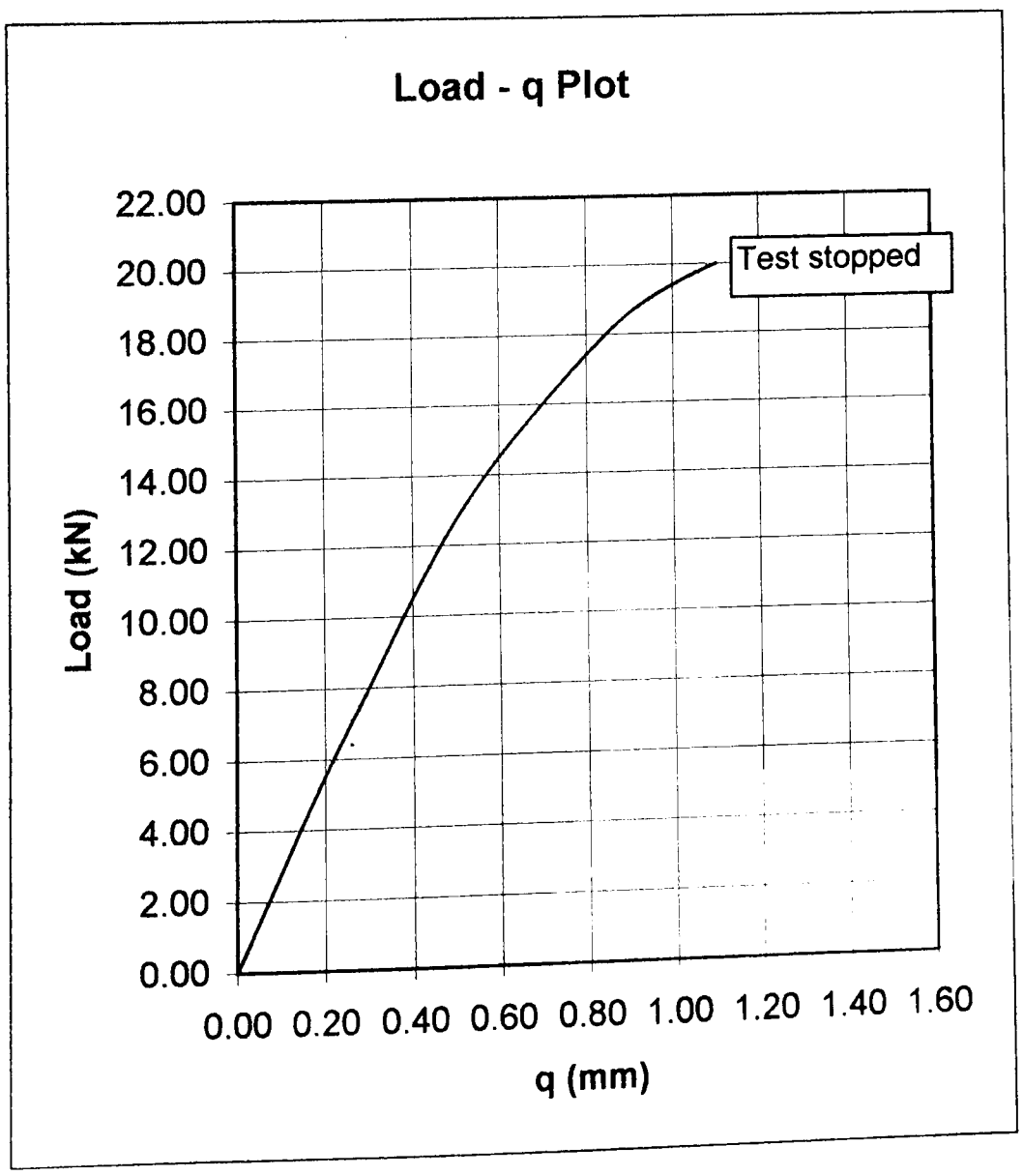

Fracture Toughness Test Data - J_{IC} Test

Specimen Data

Specimen Thickness:	5 mm
Specimen Width:	60 mm
Material:	EN24
Yield Stress:	970 MPa
Specimen No:	5P4
Side Groove Type:	None
Side Groove Depth:	0 mm
Effective Thickness:	5 mm

Precracking Data

Initial Cycles	
Mean Load:	3 kN
Amplitude:	2.6 kN
Max Load:	5.6 kN
No Cycles:	2200
Force Ratio:	0.07
Final Cycles	
Mean Load:	2.6 kN
Amplitude:	2.3 kN
Max Load:	4.9 kN
No Cycles:	5000
Force Ratio:	0.06

Post Fracture Data

Dist from edge	Crack length	Stable Crack
1.0%	30.10	0.00
12.5%	30.20	0.30
25.0%	30.35	0.90
37.5%	30.35	1.45
50.0%	30.35	1.70
62.5%	30.30	1.45
75.0%	30.15	0.90
87.5%	30.15	0.15
99.0%	30.00	0.00
Ave	**30.24**	**0.856**

$J = \{[F/(BW^{0.5})].f(a/W)\}^2 [(1-\nu^2)/E] + [(\eta_p U_p)/B(W-a)]$

where f(a/W) is given by 9.2.3.2 of BS7448:pt1

and $\eta_p = 2+0.522.(1-a/W)$

F =	17.1 kN	η_p =	2.258934
B =	5 mm	Up =	2.272313
W =	60 mm		
a/W =	0.5040		
f(a/W) =	9.7780		
J=	**119.30 N/mm**		

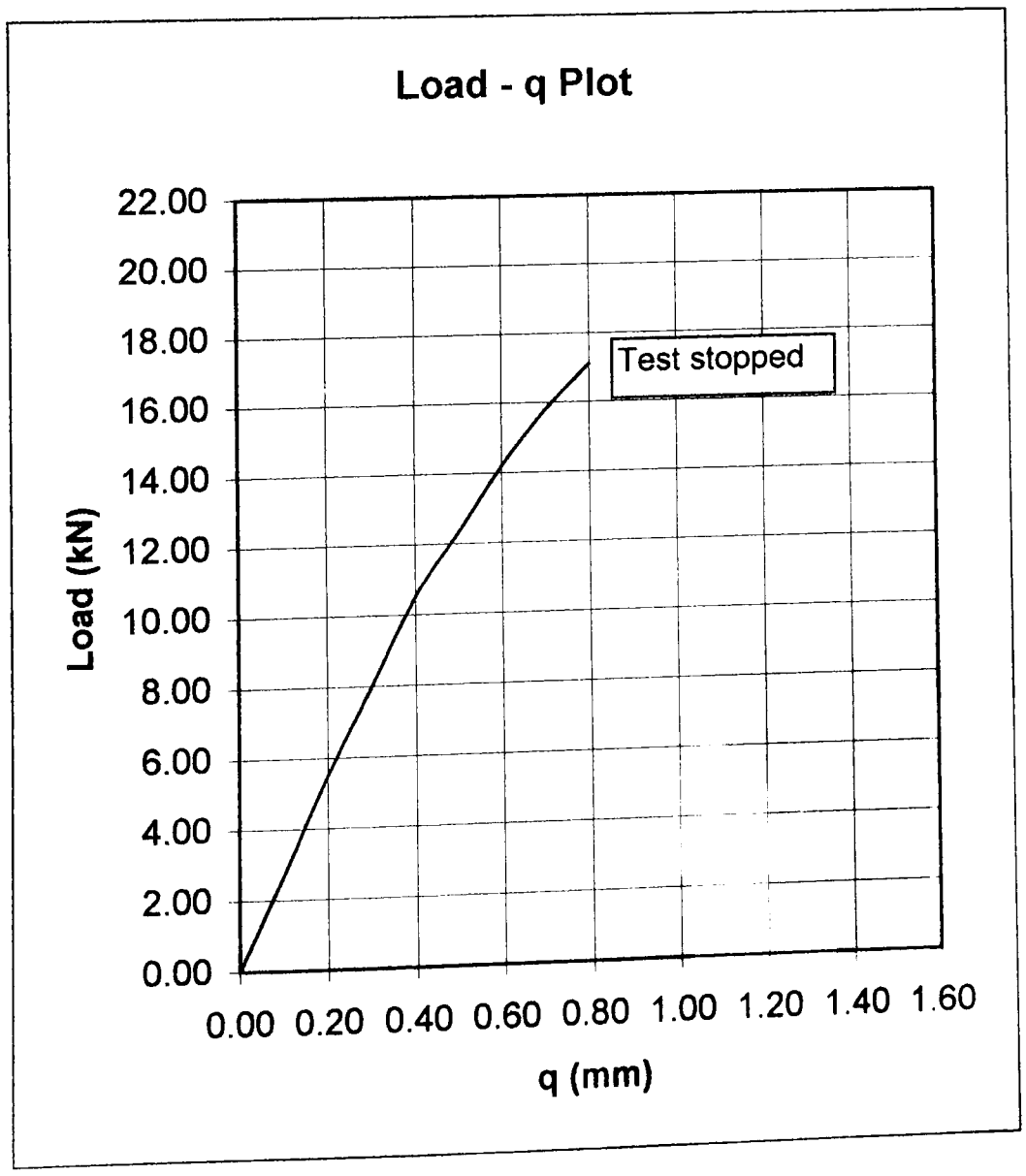

Fracture Toughness Test Data - J_{IC} Test

Specimen Data

Specimen Thickness:	5 mm
Specimen Width:	60 mm
Material:	EN24
Yield Stress:	970 MPa
Specimen No:	5P5
Side Groove Type:	None
Side Groove Depth:	0 mm
Effective Thickness:	5 mm

Precracking Data

Initial Cycles	
Mean Load:	3 kN
Amplitude:	2.6 kN
Max Load:	5.6 kN
No Cycles:	2200
Force Ratio:	0.07
Final Cycles	
Mean Load:	2.6 kN
Amplitude:	2.3 kN
Max Load:	4.9 kN
No Cycles:	5000
Force Ratio:	0.06

Post Fracture Data

Dist from edge	Crack length	Stable Crack
1.0%	30.20	0.00
12.5%	30.55	0.05
25.0%	30.55	0.35
37.5%	30.55	0.65
50.0%	30.20	0.90
62.5%	30.15	1.05
75.0%	30.00	0.65
87.5%	29.95	0.00
99.0%	29.80	0.00
Ave	**30.24**	**0.456**

$J = \{[F/(BW^{0.5})].f(a/W)\}^2 [(1-\nu^2)/E] + [(\eta_p U_p)/B(W-a)]$

where f(a/W) is given by 9.2.3.2 of BS7448:pt1

and $\eta_p = 2+0.522.(1-a/W)$

F =	15.3 kN	η_p =	2.258879
B =	5 mm	Up =	1.224208
W =	60 mm		
a/W =	0.5041		
f(a/W) =	9.7811		
J=	**86.52 N/mm**		

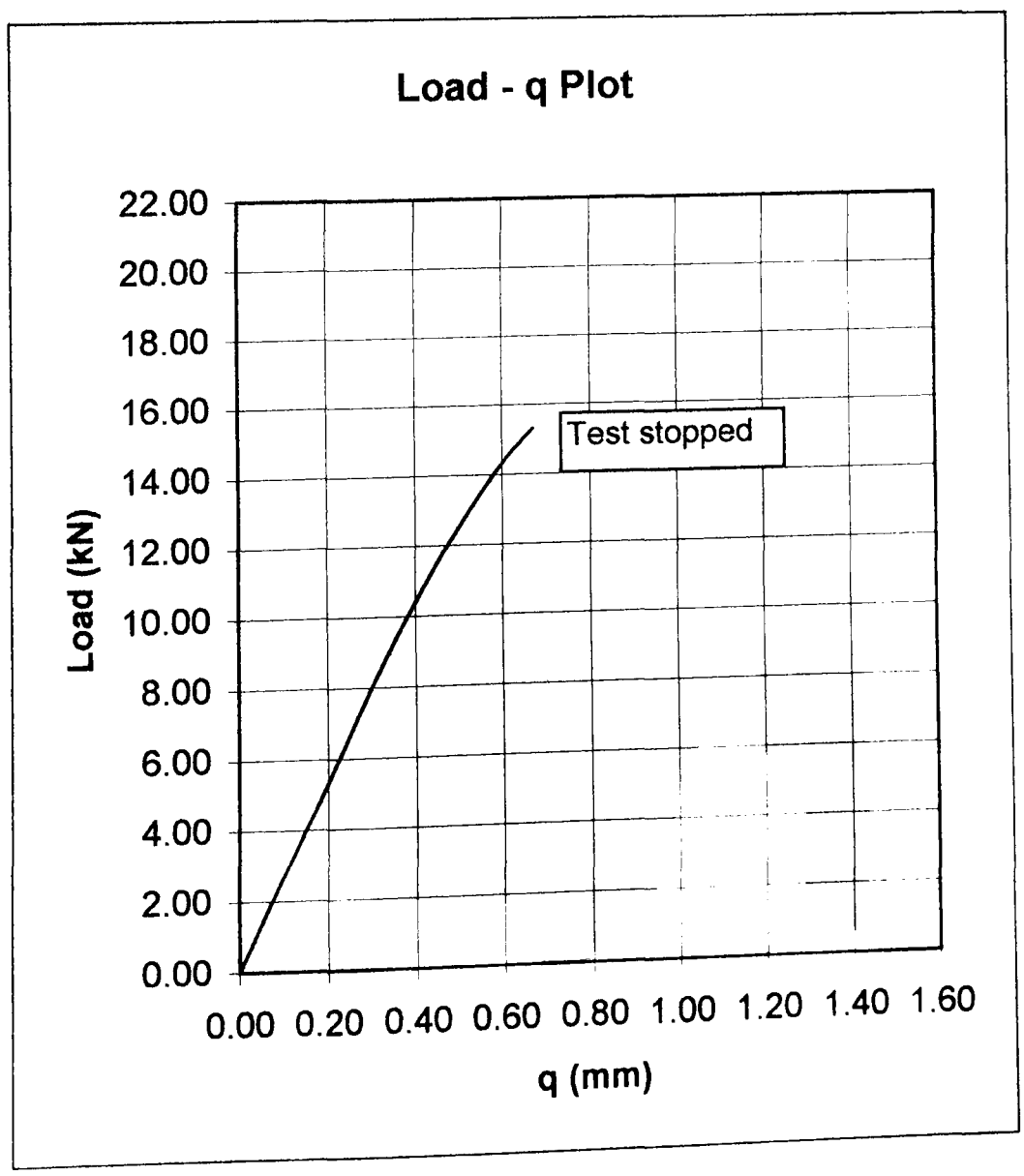

Fracture Toughness Test Data - J_{IC} Test

Specimen Data

Specimen Thickness:	5 mm
Specimen Width:	60 mm
Material:	EN24
Yield Stress:	970 MPa
Specimen No:	5P6
Side Groove Type:	None
Side Groove Depth:	0 mm
Effective Thickness:	5 mm

Precracking Data

Initial Cycles	
Mean Load:	3 kN
Amplitude:	2.6 kN
Max Load:	5.6 kN
No Cycles:	2200
Force Ratio:	0.07
Final Cycles	
Mean Load:	2.6 kN
Amplitude:	2.3 kN
Max Load:	4.9 kN
No Cycles:	5000
Force Ratio:	0.06

Post Fracture Data

Dist from edge	Crack length	Stable Crack
1.0%	29.95	0.00
12.5%	30.15	0.00
25.0%	30.25	0.55
37.5%	30.30	0.90
50.0%	30.35	1.15
62.5%	30.35	1.00
75.0%	30.30	0.50
87.5%	30.25	0.00
99.0%	30.05	0.00
Ave	**30.24**	**0.513**

$J = \{[F/(BW^{0.5})].f(a/W)\}^2 [(1-\nu^2)/E] + [(\eta_p U_p)/B(W-a)]$

where f(a/W) is given by 9.2.3.2 of BS7448:pt1

and $\eta_p = 2+0.522.(1-a/W)$

F =	16.4 kN	η_p =	2.258879
B =	5 mm	Up =	1.943818
W =	60 mm		
a/W =	0.5041		
f(a/W) =	9.7811		
J=	**107.56 N/mm**		

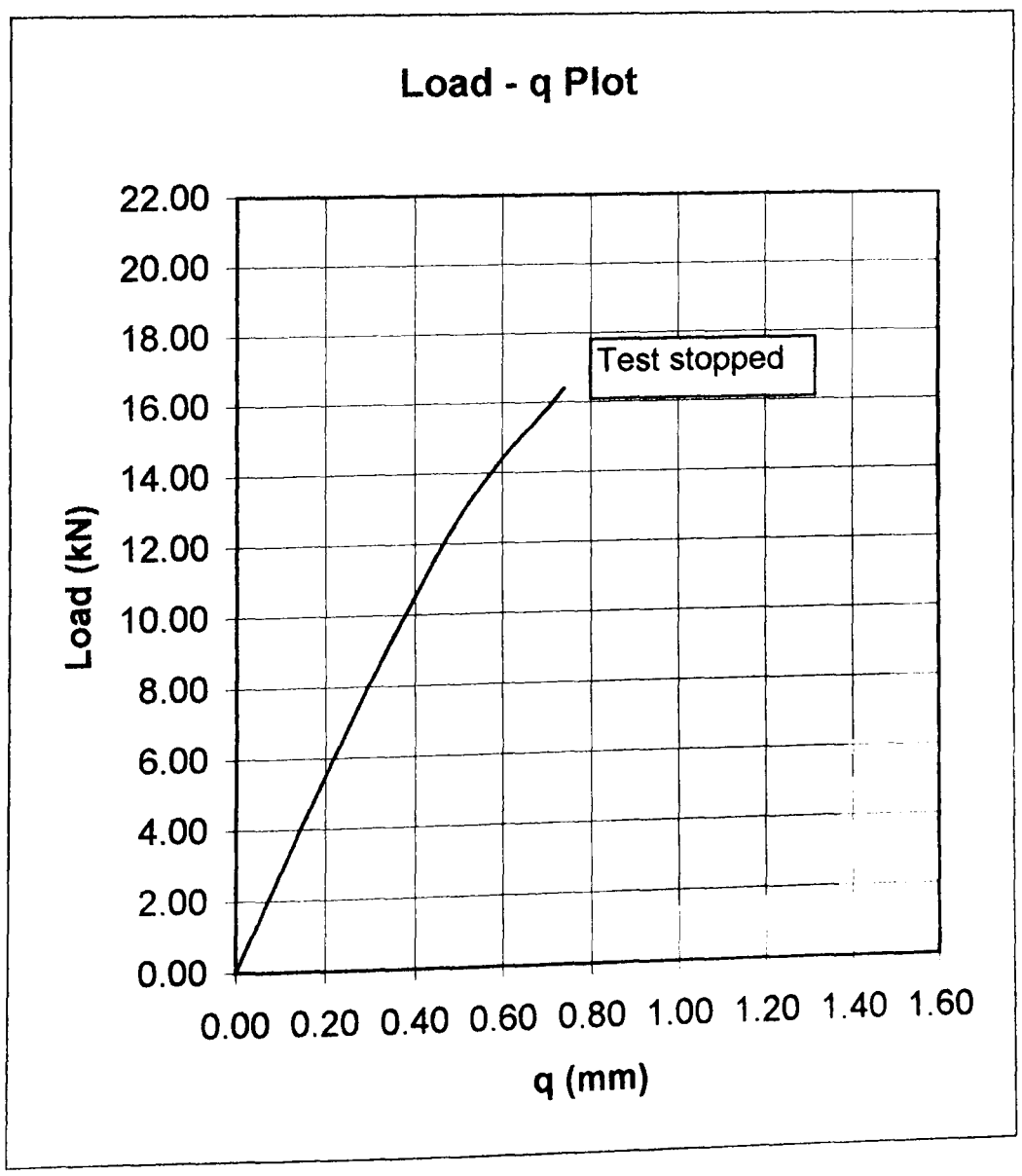

Fracture Toughness Test Data - J_{IC} Test

Specimen Data

Specimen Thickness:	5 mm
Specimen Width:	60 mm
Material:	EN24
Yield Stress:	970 MPa
Specimen No:	5P7
Side Groove Type:	None
Side Groove Depth:	0 mm
Effective Thickness:	5 mm

Precracking Data

Initial Cycles	
Mean Load:	3 kN
Amplitude:	2.6 kN
Max Load:	5.6 kN
No Cycles:	2200
Force Ratio:	0.07
Final Cycles	
Mean Load:	2.6 kN
Amplitude:	2.3 kN
Max Load:	4.9 kN
No Cycles:	5000
Force Ratio:	0.06

Post Fracture Data

Dist from edge	Crack length	Stable Crack
1.0%	29.72	0.040
12.5%	29.96	0.100
25.0%	30.12	0.670
37.5%	30.25	1.460
50.0%	30.38	1.340
62.5%	30.39	1.350
75.0%	30.48	0.600
87.5%	30.48	0.020
99.0%	30.28	0.000
Ave	**30.26**	**0.695**

$J = \{[F/(BW^{0.5})].f(a/W)\}^2 [(1-\nu^2)/E] + [(\eta_p U_p)/B(W-a)]$

where f(a/W) is given by 9.2.3.2 of BS7448:pt1

and $\eta_p = 2+0.522.(1-a/W)$

F =	15.4 kN	η_p =	2.25876
B =	5 mm	Up =	1.505034
W =	60 mm		
a/W =	0.5043		
f(a/W) =	9.7881		
J=	**91.78 N/mm**		

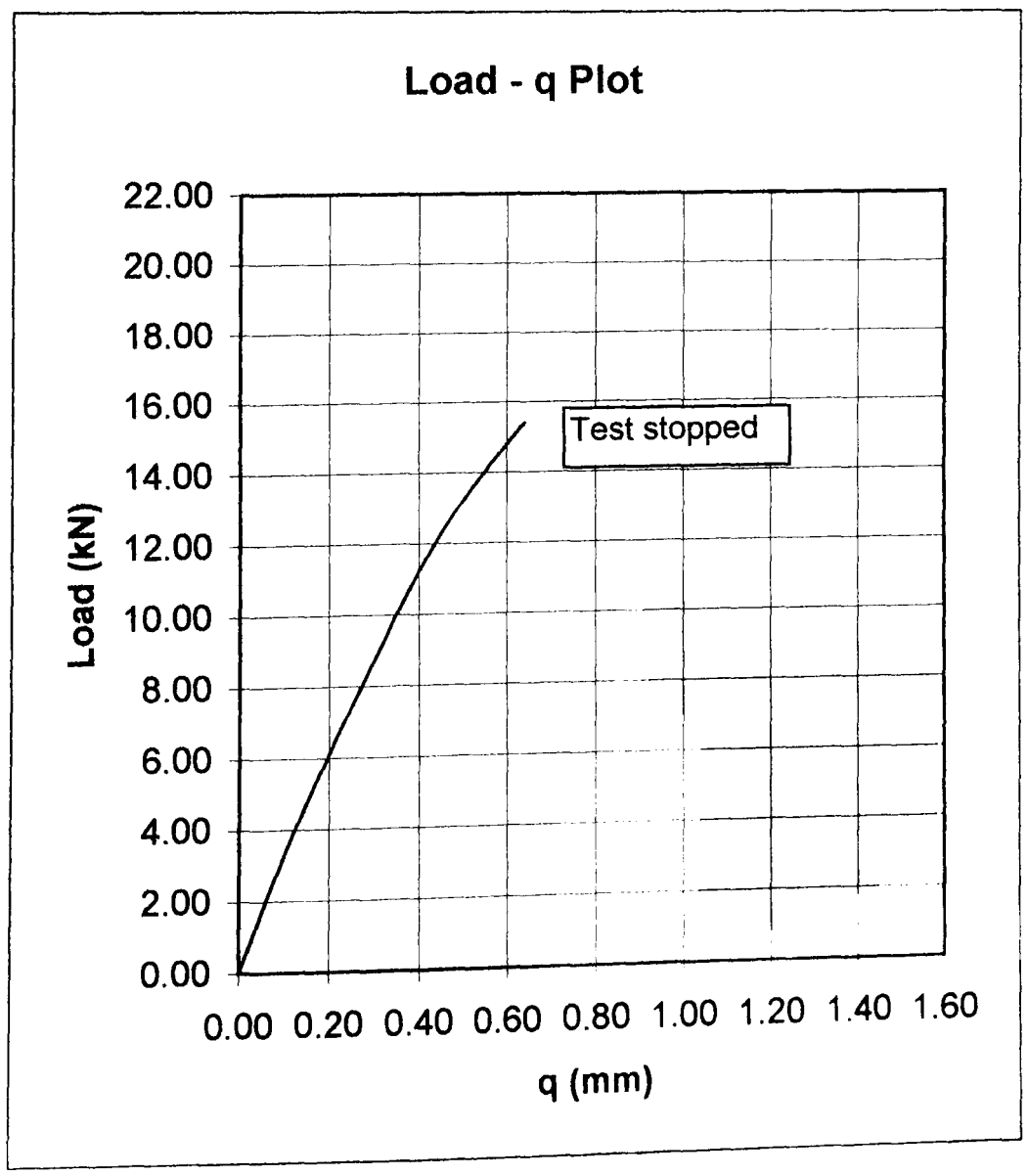

Fracture Toughness Test Data - J_{IC} Test

Specimen Data

Specimen Thickness:	5 mm
Specimen Width:	60 mm
Material:	EN24
Yield Stress:	970 MPa
Specimen No:	5P8
Side Groove Type:	None
Side Groove Depth:	0 mm
Effective Thickness:	5 mm

Precracking Data

Initial Cycles	
Mean Load:	3 kN
Amplitude:	2.6 kN
Max Load:	5.6 kN
No Cycles:	2200
Force Ratio:	0.07
Final Cycles	
Mean Load:	2.6 kN
Amplitude:	2.3 kN
Max Load:	4.9 kN
No Cycles:	5000
Force Ratio:	0.06

Post Fracture Data

Dist from edge	Crack length	Stable Crack
1.0%	29.93	0.000
12.5%	30.11	0.070
25.0%	30.15	0.550
37.5%	30.18	1.010
50.0%	30.19	1.030
62.5%	30.12	1.100
75.0%	30.09	0.500
87.5%	29.97	0.120
99.0%	29.79	0.040
Ave	**30.08**	**0.550**

$J = \{[F/(BW^{0.5})].f(a/W)\}^2 [(1-\nu^2)/E] + [(\eta_p U_p)/B(W-a)]$

where f(a/W) is given by 9.2.3.2 of BS7448:pt1

and $\eta_p = 2+0.522.(1-a/W)$

F =	16 kN	η_p =	2.260271
B =	5 mm	Up =	1.508667
W =	60 mm		
a/W =	0.5014		
f(a/W) =	9.7007		
J=	**95.87 N/mm**		

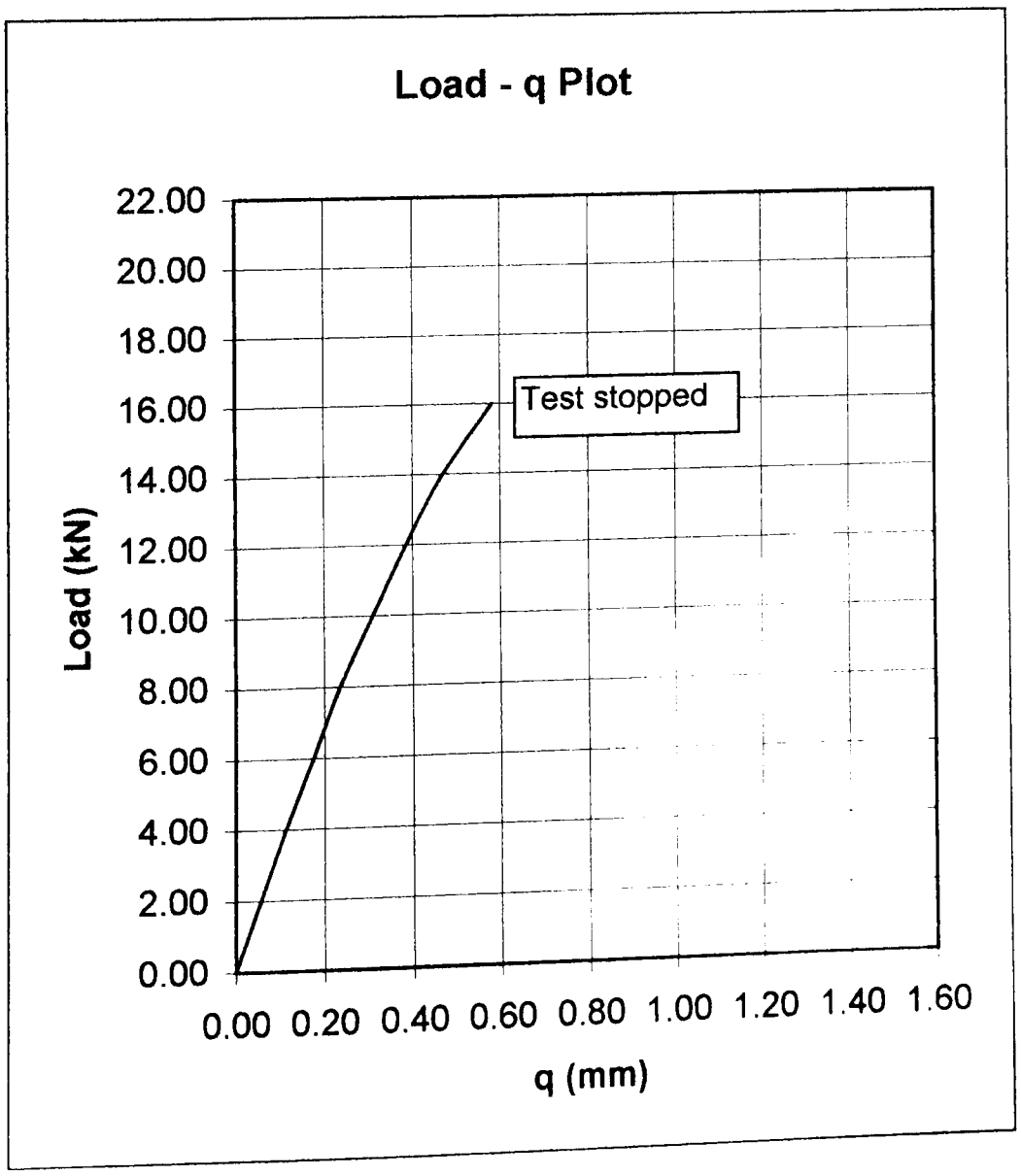

Fracture Toughness Test Data - J_{IC} Test

Specimen Data

Specimen Thickness:	5 mm
Specimen Width:	60 mm
Material:	EN24
Yield Stress:	970 MPa
Specimen No:	5P9
Side Groove Type:	None
Side Groove Depth:	0 mm
Effective Thickness:	5 mm

Precracking Data

Initial Cycles	
Mean Load:	3 kN
Amplitude:	2.6 kN
Max Load:	5.6 kN
No Cycles:	2200
Force Ratio:	0.07
Final Cycles	
Mean Load:	2.6 kN
Amplitude:	2.3 kN
Max Load:	4.9 kN
No Cycles:	5000
Force Ratio:	0.06

Post Fracture Data

Dist from edge	Crack length	Stable Crack
1.0%	29.39	0.030
12.5%	29.56	0.270
25.0%	29.71	1.100
37.5%	29.78	1.670
50.0%	29.86	2.060
62.5%	29.92	1.900
75.0%	29.89	0.990
87.5%	29.83	0.330
99.0%	29.69	0.060
Ave	**29.76**	**1.046**

$J = \{[F/(BW^{0.5})].f(a/W)\}^2 [(1-\nu^2)/E] + [(\eta_p U_p)/B(W-a)]$

where f(a/W) is given by 9.2.3.2 of BS7448:pt1

and $\eta_p = 2+0.522.(1-a/W)$

F =	17 kN	η_p =	2.263077
B =	5 mm	Up =	1.623083
W =	60 mm		
a/W =	0.4960		
f(a/W) =	9.5420		
J=	**104.11 N/mm**		

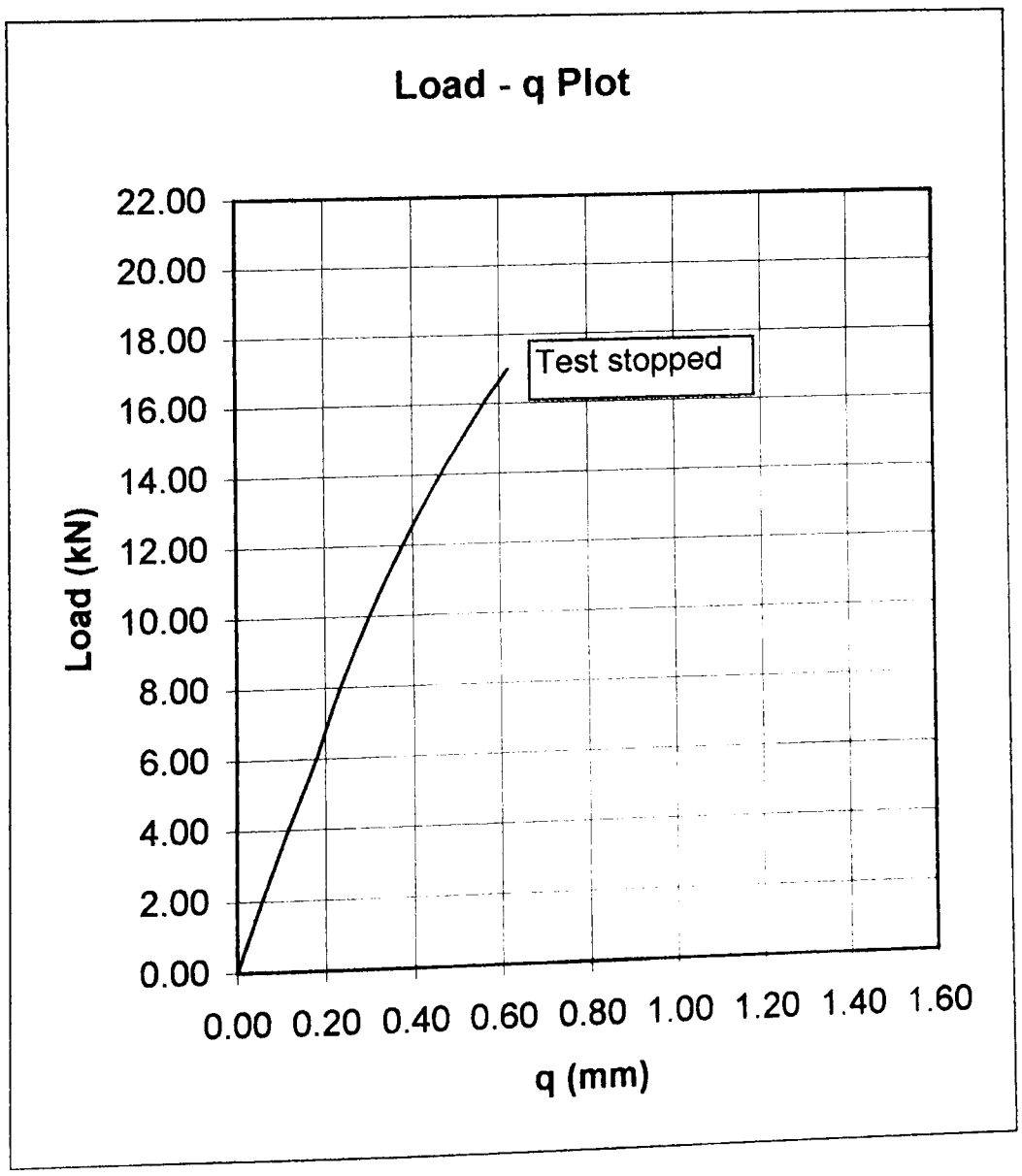

Fracture Toughness Test Data - J_{IC} Test

Specimen Data

Specimen Thickness:	5 mm
Specimen Width:	60 mm
Material:	EN24
Yield Stress:	970 MPa
Specimen No:	5P10
Side Groove Type:	None
Side Groove Depth:	0 mm
Effective Thickness:	5 mm

Precracking Data

Initial Cycles	
Mean Load:	3 kN
Amplitude:	2.6 kN
Max Load:	5.6 kN
No Cycles:	2200
Force Ratio:	0.07
Final Cycles	
Mean Load:	2.6 kN
Amplitude:	2.3 kN
Max Load:	4.9 kN
No Cycles:	5000
Force Ratio:	0.06

Post Fracture Data

Dist from edge	Crack length	Stable Crack
1.0%	29.62	0.040
12.5%	29.83	0.480
25.0%	29.96	1.460
37.5%	29.98	2.880
50.0%	30.03	3.330
62.5%	30.02	2.920
75.0%	30.00	1.300
87.5%	29.94	0.290
99.0%	29.78	0.040
Ave	**29.93**	**1.588**

$J = \{[F/(BW^{0.5})].f(a/W)\}^2 [(1-\nu^2)/E] + [(\eta_p U_p)/B(W-a)]$

where f(a/W) is given by 9.2.3.2 of BS7448:pt1

and $\eta_p = 2+0.522.(1-a/W)$

F =	18 kN	η_p =	2.261587
B =	5 mm	Up =	3.14
W =	60 mm		
a/W =	0.4989		
f(a/W) =	9.6257		
J=	**138.30 N/mm**		

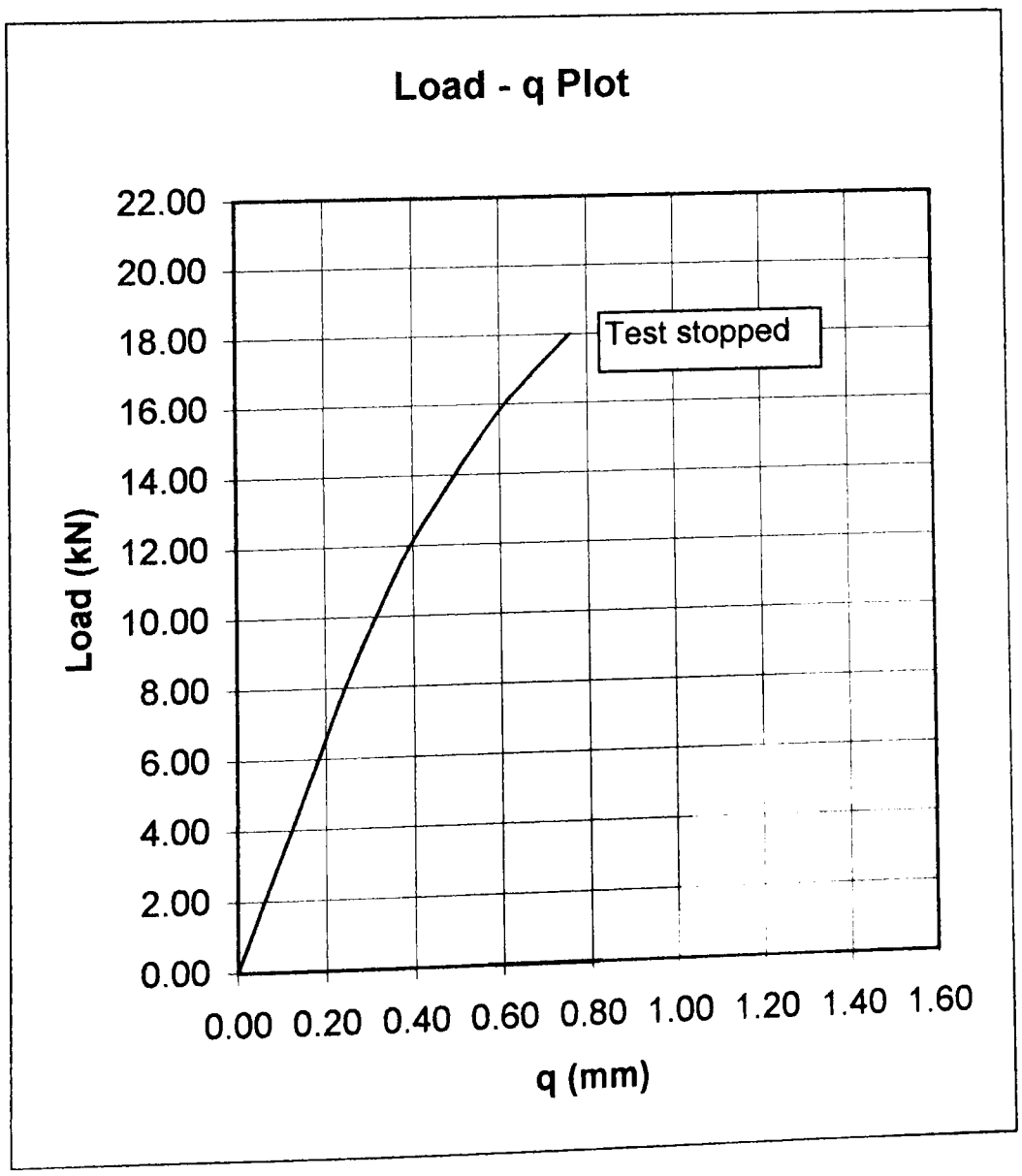

Fracture Toughness Test Data - J_{IC} Test

Specimen Data

Specimen Thickness:	5 mm
Specimen Width:	60 mm
Material:	EN24
Yield Stress:	970 MPa
Specimen No:	5P11
Side Groove Type:	None
Side Groove Depth:	0 mm
Effective Thickness:	5 mm

Precracking Data

Initial Cycles	
Mean Load:	3 kN
Amplitude:	2.6 kN
Max Load:	5.6 kN
No Cycles:	2200
Force Ratio:	0.07
Final Cycles	
Mean Load:	2.6 kN
Amplitude:	2.3 kN
Max Load:	4.9 kN
No Cycles:	5000
Force Ratio:	0.06

Post Fracture Data

Dist from edge	Crack length	Stable Crack
1.0%	29.91	0.040
12.5%	30.07	0.520
25.0%	30.13	1.200
37.5%	30.14	2.160
50.0%	30.10	2.650
62.5%	30.06	1.970
75.0%	30.03	0.570
87.5%	29.92	0.200
99.0%	29.75	0.000
Ave	**30.04**	**1.161**

$J = \{[F/(BW^{0.5})].f(a/W)\}^2 [(1-\nu^2)/E] + [(\eta_p U_p)/B(W-a)]$

where f(a/W) is given by 9.2.3.2 of BS7448:pt1

and $\eta_p = 2+0.522.(1-a/W)$

F =	19 kN	η_p =	2.260696
B =	5 mm	Up =	3.317083
W =	60 mm		
a/W =	0.5006		
f(a/W) =	9.6764		
J=	**152.58 N/mm**		

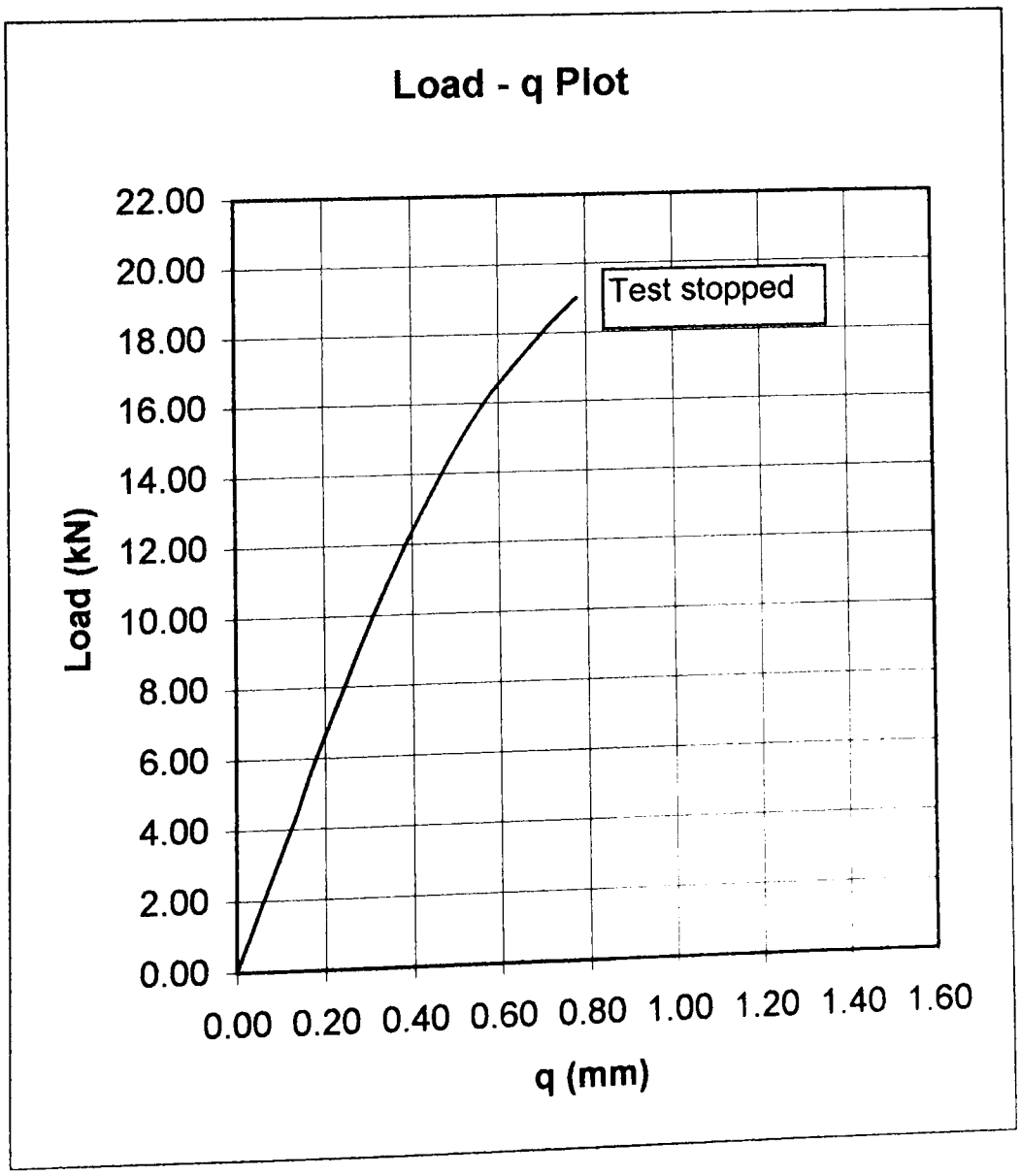

Fracture Toughness Test Data - J_{IC} Test

Specimen Data

Specimen Thickness:	5 mm
Specimen Width:	60 mm
Material:	EN24
Yield Stress:	970 MPa
Specimen No:	5P12
Side Groove Type:	None
Side Groove Depth:	0 mm
Effective Thickness:	5 mm

Precracking Data

Initial Cycles	
Mean Load:	3 kN
Amplitude:	2.6 kN
Max Load:	5.6 kN
No Cycles:	2200
Force Ratio:	0.07
Final Cycles	
Mean Load:	2.6 kN
Amplitude:	2.3 kN
Max Load:	4.9 kN
No Cycles:	5000
Force Ratio:	0.06

Post Fracture Data

Dist from edge	Crack length	Stable Crack
1.0%	29.16	0.000
12.5%	29.34	0.280
25.0%	29.48	0.850
37.5%	29.61	2.170
50.0%	29.64	2.680
62.5%	29.68	2.070
75.0%	29.69	0.890
87.5%	29.63	0.260
99.0%	29.54	0.100
Ave	**29.55**	**1.156**

$J = \{[F/(BW^{0.5})].f(a/W)\}^2 [(1-\nu^2)/E] + [(\eta_p U_p)/B(W-a)]$

where f(a/W) is given by 9.2.3.2 of BS7448:pt1

and $\eta_p = 2+0.522.(1-a/W)$

F =	20 kN	η_p =	2.264893
B =	5 mm	Up =	3.798867
W =	60 mm		
a/W =	0.4925		
f(a/W) =	9.4415		
J=	**164.68 N/mm**		

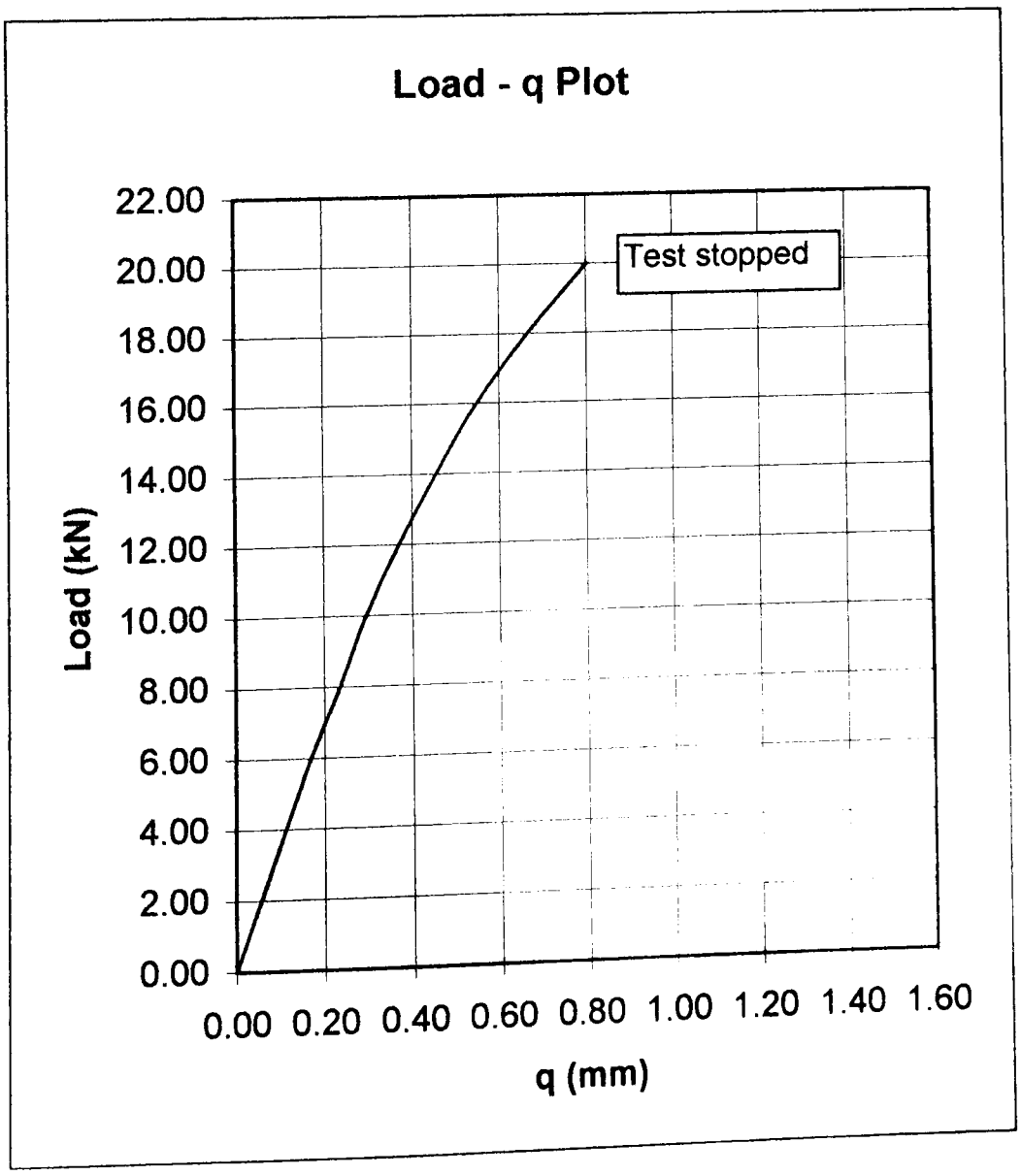

Fracture Toughness Test Data - J_{IC} Test

Specimen Data

Specimen Thickness:	5 mm
Specimen Width:	60 mm
Material:	EN24
Yield Stress:	970 MPa
Specimen No:	5P13
Side Groove Type:	None
Side Groove Depth:	0 mm
Effective Thickness:	5 mm

Precracking Data

Initial Cycles	
Mean Load:	3 kN
Amplitude:	2.6 kN
Max Load:	5.6 kN
No Cycles:	2200
Force Ratio:	0.07
Final Cycles	
Mean Load:	2.6 kN
Amplitude:	2.3 kN
Max Load:	4.9 kN
No Cycles:	5000
Force Ratio:	0.06

Post Fracture Data

Dist from edge	Crack length	Stable Crack
1.0%	29.96	0.000
12.5%	30.10	0.220
25.0%	30.17	0.800
37.5%	30.18	1.310
50.0%	30.11	1.580
62.5%	30.03	1.270
75.0%	29.98	0.600
87.5%	29.92	0.130
99.0%	29.70	0.000
Ave	**30.04**	**0.739**

$J = \{[F/(BW^{0.5})].f(a/W)\}^2 [(1-\nu^2)/E] + [(\eta_p U_p)/B(W-a)]$

where f(a/W) is given by 9.2.3.2 of BS7448:pt1

and $\eta_p = 2+0.522.(1-a/W)$

F =	15 kN	η_p =	2.260652
B =	5 mm	Up =	1.20145
W =	60 mm		
a/W =	0.5007		
f(a/W) =	9.6789		
J=	**82.07 N/mm**		

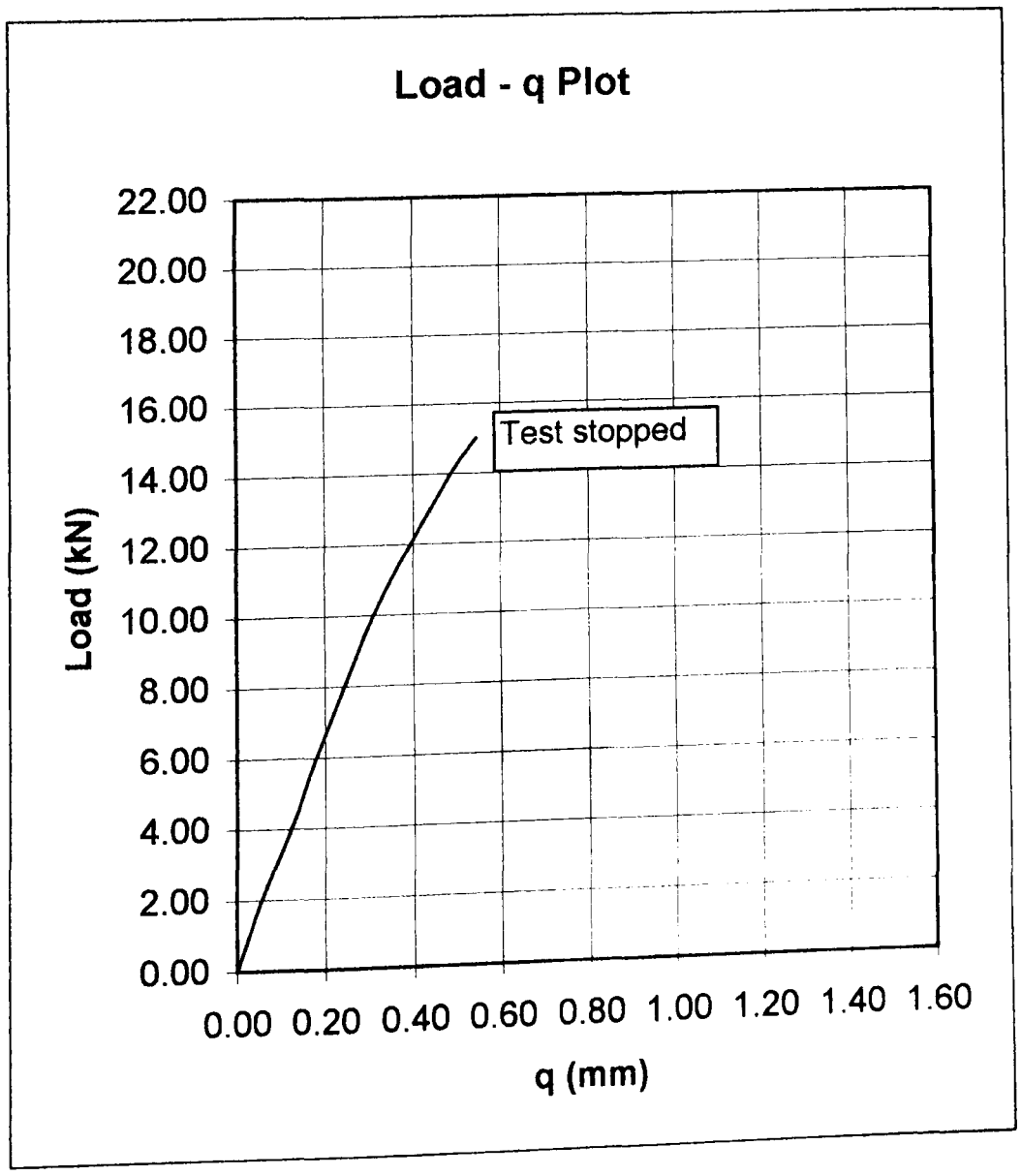

Fracture Toughness Test Data - J_{IC} Test

Specimen Data

Specimen Thickness:	5 mm
Specimen Width:	60 mm
Material:	EN24
Yield Stress:	970 MPa
Specimen No:	5P14
Side Groove Type:	None
Side Groove Depth:	0 mm
Effective Thickness:	5 mm

Precracking Data

Initial Cycles	
Mean Load:	3 kN
Amplitude:	2.6 kN
Max Load:	5.6 kN
No Cycles:	2200
Force Ratio:	0.07
Final Cycles	
Mean Load:	2.6 kN
Amplitude:	2.3 kN
Max Load:	4.9 kN
No Cycles:	5000
Force Ratio:	0.06

Post Fracture Data

Dist from edge	Crack length	Stable Crack
1.0%	29.53	0.000
12.5%	29.68	0.000
25.0%	29.81	0.450
37.5%	29.85	0.830
50.0%	29.87	0.760
62.5%	29.91	0.740
75.0%	29.86	0.300
87.5%	29.80	0.030
99.0%	29.63	0.000
Ave	**29.80**	**0.389**

$J = \{[F/(BW^{0.5})].f(a/W)\}^2 [(1-\nu^2)/E] + [(\eta_p U_p)/B(W-a)]$

where f(a/W) is given by 9.2.3.2 of BS7448:pt1

and $\eta_p = 2+0.522.(1-a/W)$

F =	16.5 kN	η_p =	2.262784
B =	5 mm	Up =	1.300325
W =	60 mm		
a/W =	0.4966		
f(a/W) =	9.5584		
J=	**94.93 N/mm**		

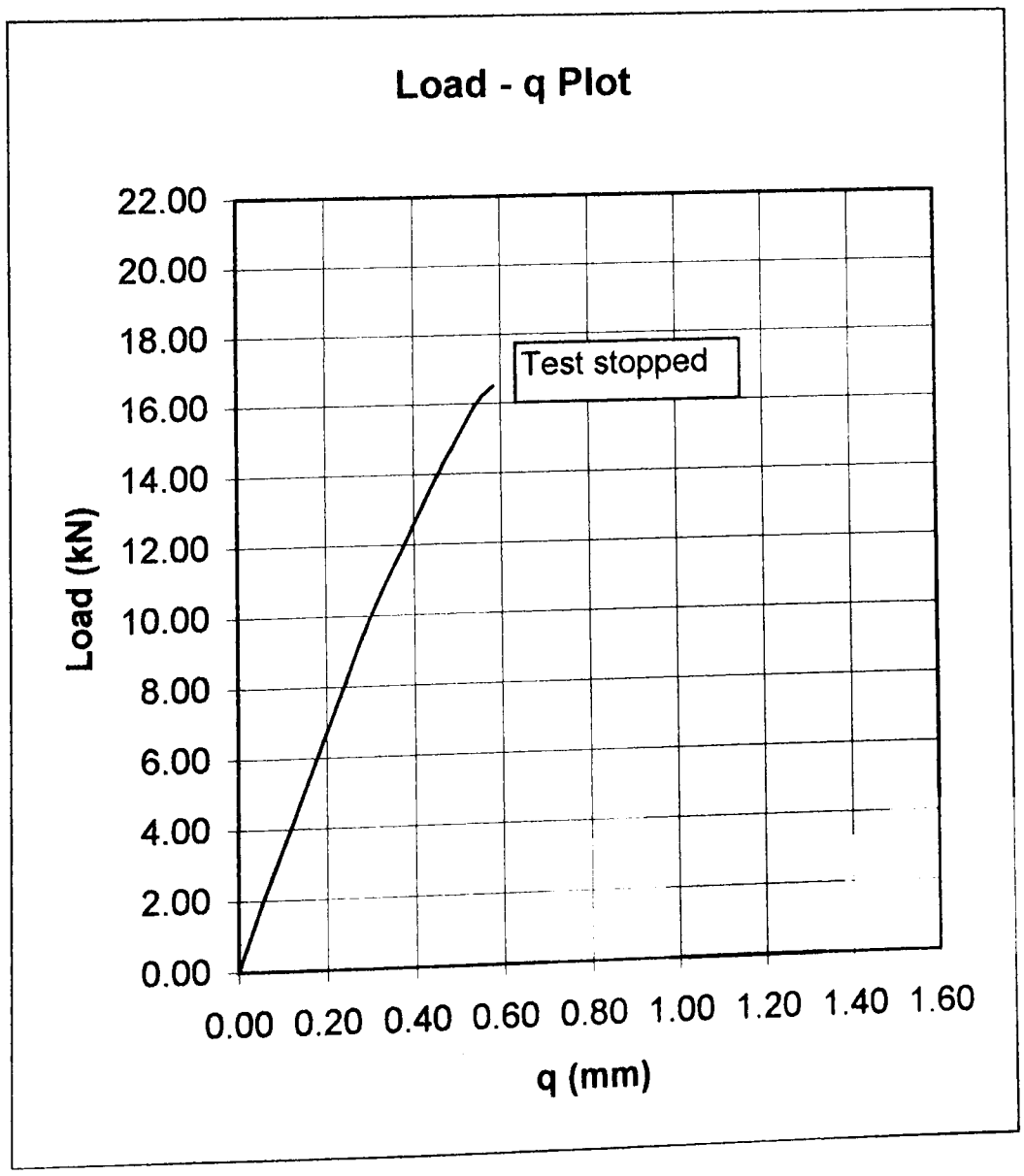

Fracture Toughness Test Data - J_{IC} Test

Specimen Data

Specimen Thickness:	5 mm
Specimen Width:	60 mm
Material:	EN24
Yield Stress:	970 MPa
Specimen No:	5P15
Side Groove Type:	None
Side Groove Depth:	0 mm
Effective Thickness:	5 mm

Precracking Data

Initial Cycles	
Mean Load:	3 kN
Amplitude:	2.6 kN
Max Load:	5.6 kN
No Cycles:	2200
Force Ratio:	0.07
Final Cycles	
Mean Load:	2.6 kN
Amplitude:	2.3 kN
Max Load:	4.9 kN
No Cycles:	5000
Force Ratio:	0.06

Post Fracture Data

Dist from edge	Crack length	Stable Crack
1.0%	29.51	0.000
12.5%	29.67	0.280
25.0%	29.73	1.060
37.5%	29.86	2.290
50.0%	29.91	2.540
62.5%	29.93	1.670
75.0%	29.94	0.600
87.5%	29.91	0.030
99.0%	29.87	0.020
Ave	**29.83**	**1.060**

$J = \{[F/(BW^{0.5})].f(a/W)\}^2 [(1-\nu^2)/E] + [(\eta_p U_p)/B(W-a)]$

where f(a/W) is given by 9.2.3.2 of BS7448:pt1

and $\eta_p = 2+0.522.(1-a/W)$

F =	17.5 kN	η_p =	2.262479
B =	5 mm	Up =	2.164221
W =	60 mm		
a/W =	0.4972		
f(a/W) =	9.5755		
J=	**117.63 N/mm**		

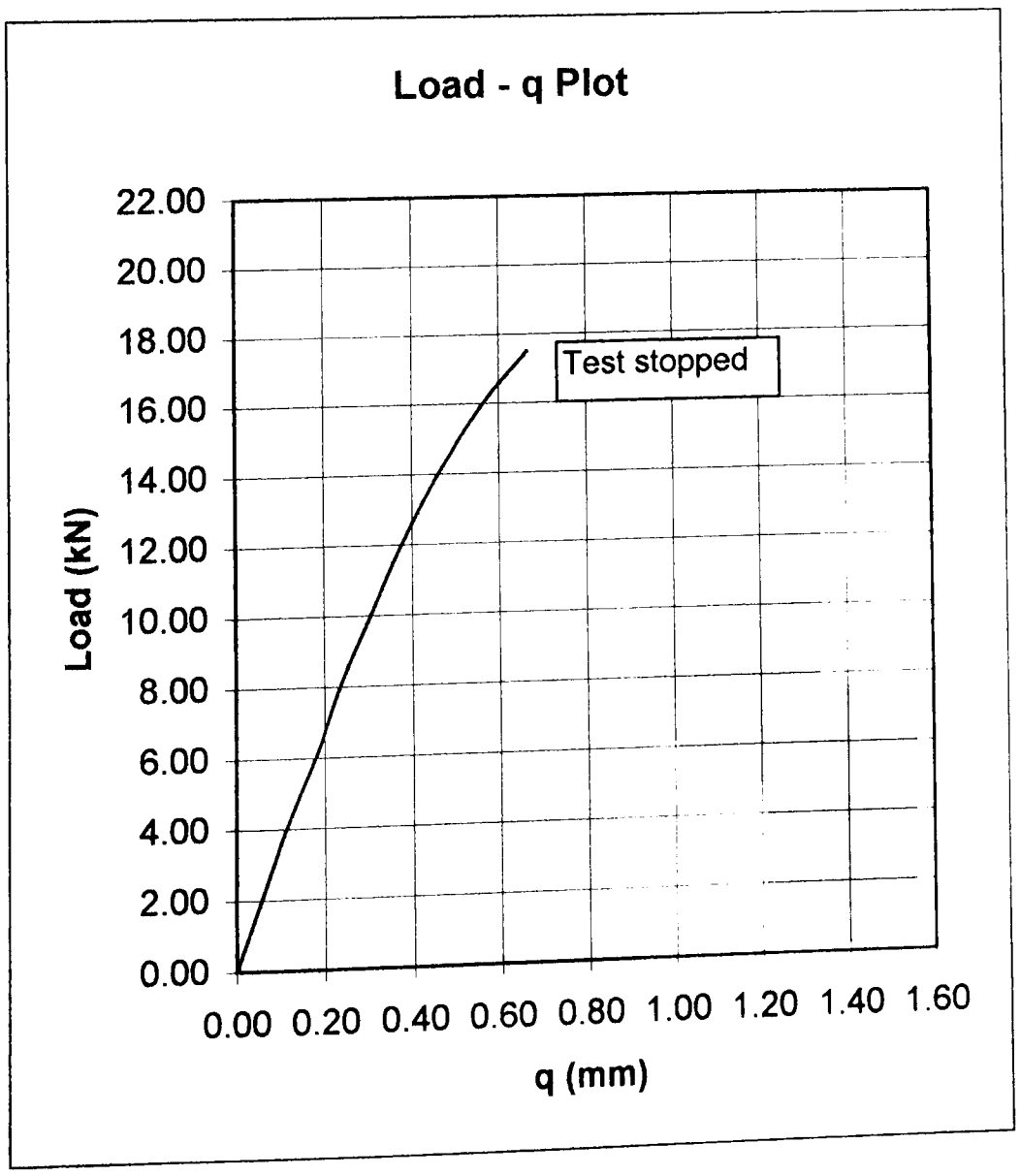

Fracture Toughness Test Data - J_{IC} Test

Specimen Data

Specimen Thickness:	5 mm
Specimen Width:	60 mm
Material:	EN24
Yield Stress:	970 MPa
Specimen No:	5P16
Side Groove Type:	None
Side Groove Depth:	0 mm
Effective Thickness:	5 mm

Precracking Data

Initial Cycles	
Mean Load:	3 kN
Amplitude:	2.6 kN
Max Load:	5.6 kN
No Cycles:	2200
Force Ratio:	0.07
Final Cycles	
Mean Load:	2.6 kN
Amplitude:	2.3 kN
Max Load:	4.9 kN
No Cycles:	5000
Force Ratio:	0.06

Post Fracture Data

Dist from edge	Crack length	Stable Crack
1.0%	29.54	0.180
12.5%	29.68	0.150
25.0%	29.87	0.350
37.5%	29.89	0.760
50.0%	29.92	1.330
62.5%	29.96	1.370
75.0%	29.91	0.830
87.5%	29.89	0.800
99.0%	29.70	0.830
Ave	**29.84**	**0.762**

$J = \{[F/(BW^{0.5})].f(a/W)\}^2 [(1-\nu^2)/E] + [(\eta_p U_p)/B(W-a)]$

where f(a/W) is given by 9.2.3.2 of BS7448:pt1

and $\eta_p = 2+0.522.(1-a/W)$

F =	18.5 kN	η_p =	2.26237
B =	5 mm	Up =	2.223625
W =	60 mm		
a/W =	0.4974		
f(a/W) =	9.5816		
J=	**128.67 N/mm**		

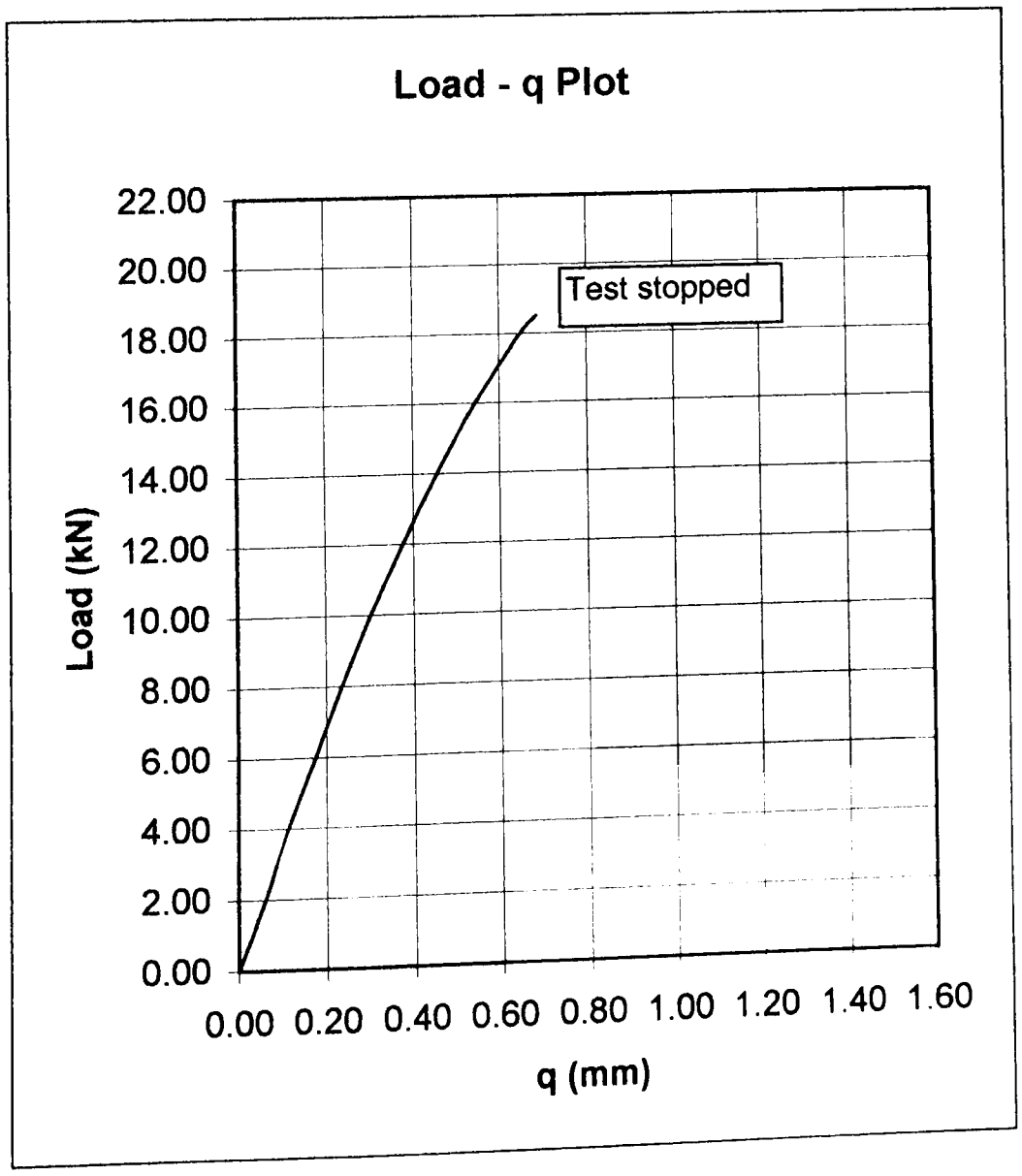

Fracture Toughness Test Data - J_{IC} Test

Specimen Data

Specimen Thickness:	5 mm
Specimen Width:	60 mm
Material:	EN24
Yield Stress:	970 MPa
Specimen No:	5P17
Side Groove Type:	None
Side Groove Depth:	0 mm
Effective Thickness:	5 mm

Precracking Data

Initial Cycles	
Mean Load:	3 kN
Amplitude:	2.6 kN
Max Load:	5.6 kN
No Cycles:	2200
Force Ratio:	0.07
Final Cycles	
Mean Load:	2.6 kN
Amplitude:	2.3 kN
Max Load:	4.9 kN
No Cycles:	5000
Force Ratio:	0.06

Post Fracture Data

Dist from edge	Crack length	Stable Crack
1.0%	28.80	0
12.5%	28.89	0.37
25.0%	29.00	1.06
37.5%	29.09	1.87
50.0%	29.15	2.61
62.5%	29.19	2.19
75.0%	29.25	1.22
87.5%	29.27	0.32
99.0%	29.14	0
Ave	**29.10**	**1.205**

$J = \{[F/(BW^{0.5})].f(a/W)\}^2 [(1-\nu^2)/E] + [(\eta_p U_p)/B(W-a)]$

where f(a/W) is given by 9.2.3.2 of BS7448:pt1

and $\eta_p = 2+0.522.(1-a/W)$

F =	19.5 kN	η_p =	2.268819
B =	5 mm	Up =	3.443763
W =	60 mm		
a/W =	0.4850		
f(a/W) =	9.2301		
J=	**148.84 N/mm**		

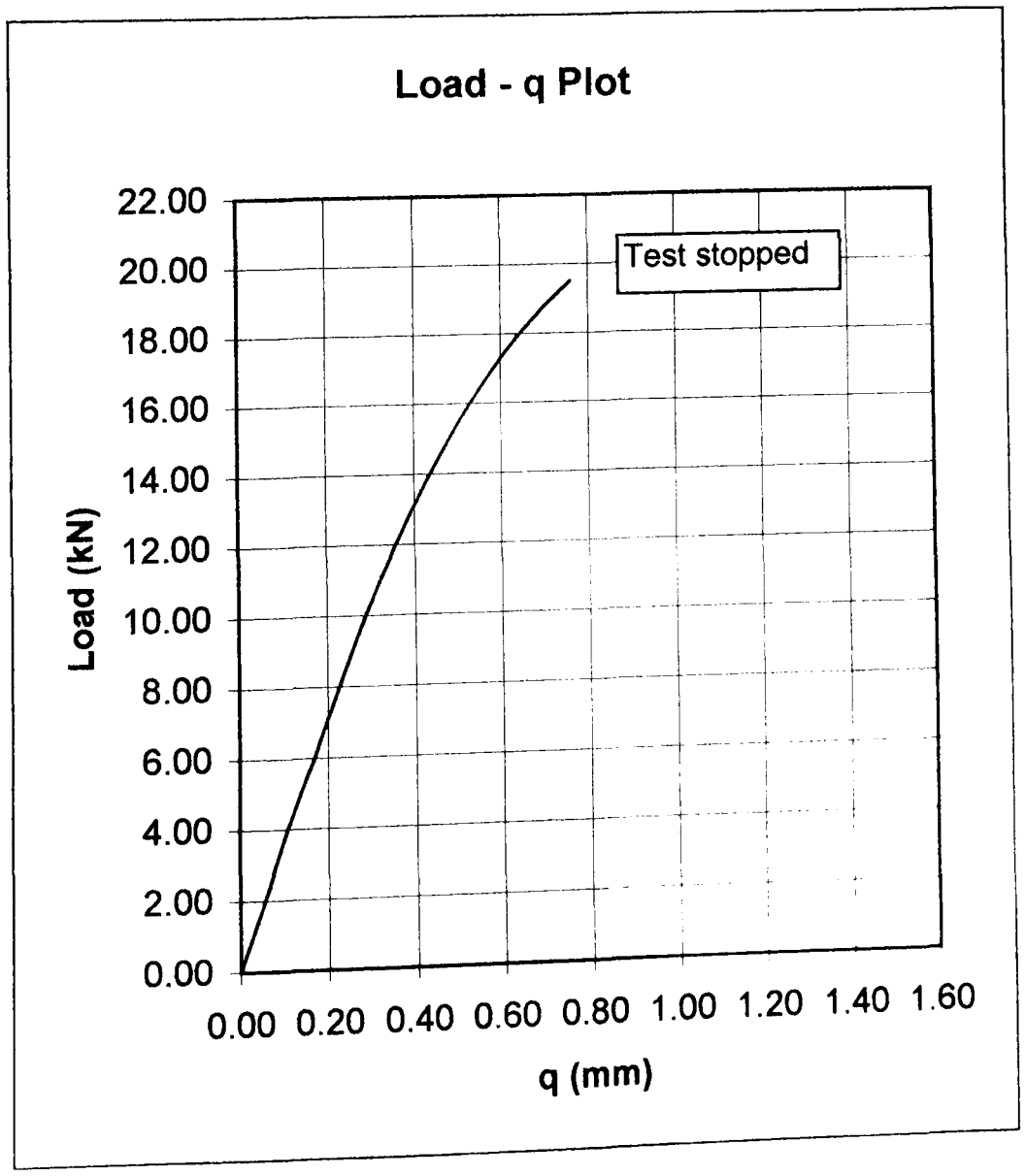

Fracture Toughness Test Data - J_{IC} Test

Specimen Data

Specimen Thickness:	2.5 mm
Specimen Width:	60 mm
Material:	EN24
Yield Stress:	970 MPa
Specimen No:	2-5P3
Side Groove Type:	None
Side Groove Depth:	0 mm
Effective Thickness:	2.5 mm

Precracking Data

Initial Cycles	
Mean Load:	1.5 kN
Amplitude:	1.3 kN
Max Load:	2.8 kN
No Cycles:	2200
Force Ratio:	0.07
Final Cycles	
Mean Load:	1.3 kN
Amplitude:	1.15 kN
Max Load:	2.45 kN
No Cycles:	5000
Force Ratio:	0.06

Post Fracture Data

Dist from edge	Crack length	Stable Crack
1.0%	29.38	0
12.5%	29.47	0.03
25.0%	29.50	0.32
37.5%	29.49	0.61
50.0%	29.47	0.68
62.5%	29.49	0.41
75.0%	29.44	0.14
87.5%	29.38	0.11
99.0%	29.25	0.04
Ave	**29.44**	**0.290**

$J = \{[F/(BW^{0.5})].f(a/W)\}^2 [(1-\nu^2)/E] + [(\eta_p U_p)/B(W-a)]$

where f(a/W) is given by 9.2.3.2 of BS7448:pt1

and $\eta_p = 2+0.522.(1-a/W)$

F =	8.5 kN	η_p =	2.265834
B =	2.5 mm	Up =	0.752167
W =	60 mm		
a/W =	0.4907		
f(a/W) =	9.3901		
J=	**99.61 N/mm**		

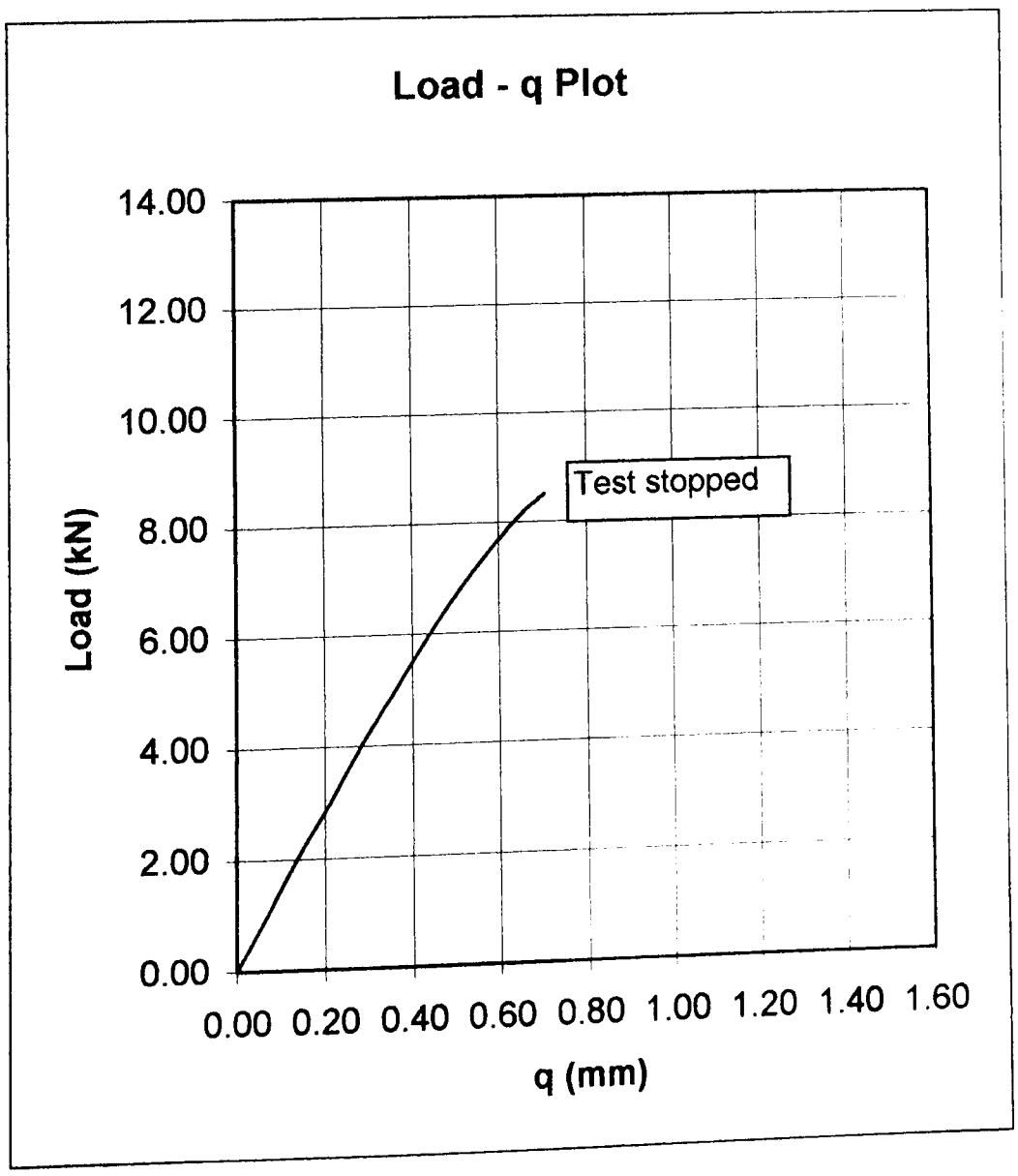

Fracture Toughness Test Data - J_{IC} Test

Specimen Data

Specimen Thickness:	2.5 mm
Specimen Width:	60 mm
Material:	EN24
Yield Stress:	970 MPa
Specimen No:	2-5P4
Side Groove Type:	None
Side Groove Depth:	0 mm
Effective Thickness:	2.5 mm

Precracking Data

Initial Cycles	
Mean Load:	1.5 kN
Amplitude:	1.3 kN
Max Load:	2.8 kN
No Cycles:	2200
Force Ratio:	0.07
Final Cycles	
Mean Load:	1.3 kN
Amplitude:	1.15 kN
Max Load:	2.45 kN
No Cycles:	5000
Force Ratio:	0.06

Post Fracture Data

Dist from edge	Crack length	Stable Crack
1.0%	29.56	0
12.5%	29.66	0.02
25.0%	29.74	0.46
37.5%	29.76	0.98
50.0%	29.77	0.98
62.5%	29.79	0.6
75.0%	29.75	0.33
87.5%	29.72	0.13
99.0%	29.63	0
Ave	**29.72**	**0.438**

$J = \{[F/(BW^{0.5})].f(a/W)\}^2 [(1-\nu^2)/E] + [(\eta_p U_p)/B(W-a)]$

where f(a/W) is given by 9.2.3.2 of BS7448:pt1

and $\eta_p = 2+0.522.(1-a/W)$

F =	9 kN	η_p =	2.263409
B =	2.5 mm	Up =	0.888
W =	60 mm		
a/W =	0.4954		
f(a/W) =	9.5235		
J=	**115.69 N/mm**		

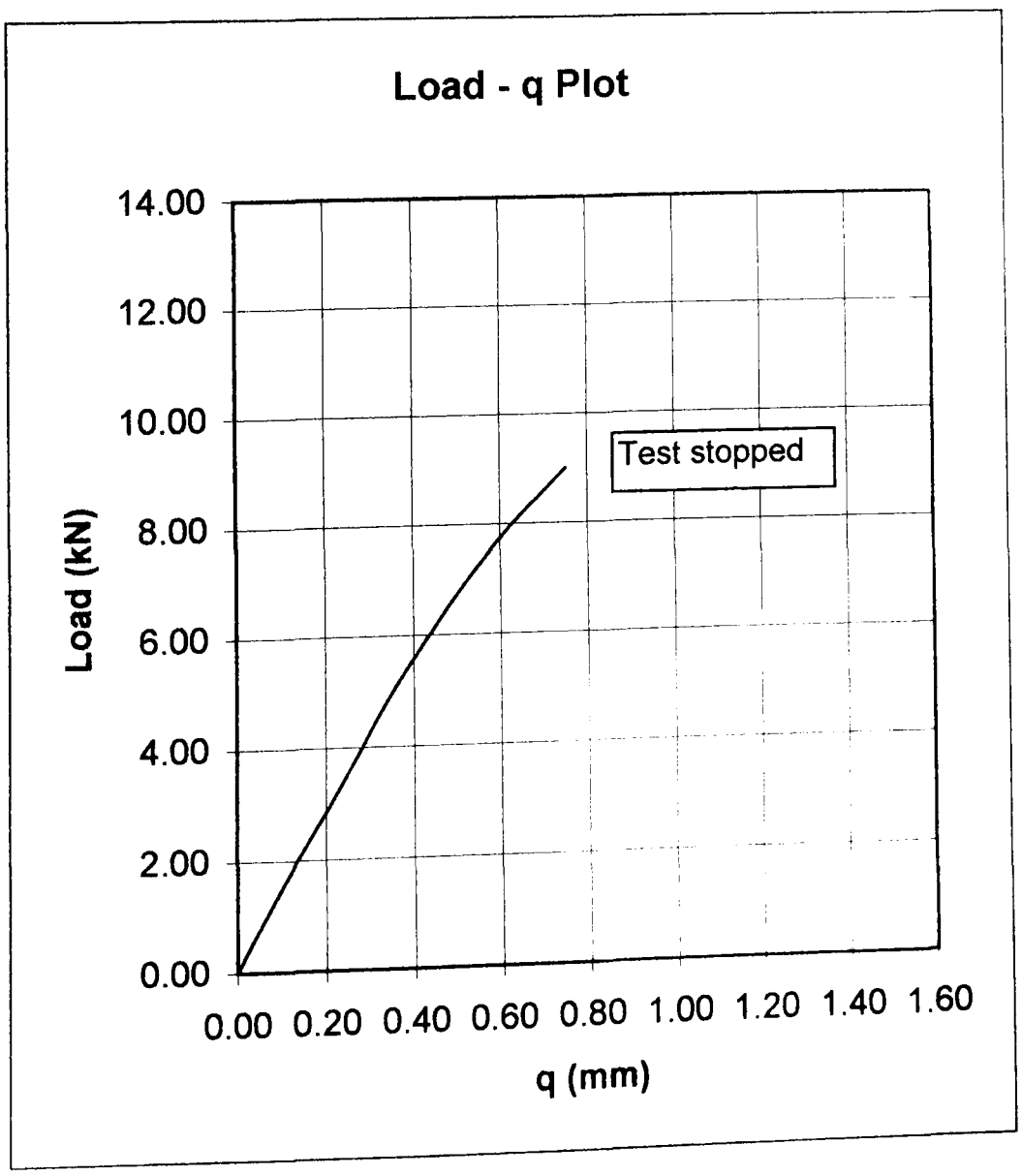

Fracture Toughness Test Data - J_{IC} Test

Specimen Data

Specimen Thickness:	2.5 mm
Specimen Width:	60 mm
Material:	EN24
Yield Stress:	970 MPa
Specimen No:	2-5P5
Side Groove Type:	None
Side Groove Depth:	0 mm
Effective Thickness:	2.5 mm

Precracking Data

Initial Cycles	
Mean Load:	1.5 kN
Amplitude:	1.3 kN
Max Load:	2.8 kN
No Cycles:	2200
Force Ratio:	0.07
Final Cycles	
Mean Load:	1.3 kN
Amplitude:	1.15 kN
Max Load:	2.45 kN
No Cycles:	5000
Force Ratio:	0.06

Post Fracture Data

Dist from edge	Crack length	Stable Crack
1.0%	29.92	0.05
12.5%	30.05	0.09
25.0%	30.13	0.3
37.5%	30.15	0.83
50.0%	30.16	1.16
62.5%	30.17	0.92
75.0%	30.12	0.43
87.5%	30.03	0.04
99.0%	29.93	0
Ave	**30.09**	**0.474**

$J = \{[F/(BW^{0.5})].f(a/W)\}^2 [(1-\nu^2)/E] + [(\eta_p U_p)/B(W-a)]$

where f(a/W) is given by 9.2.3.2 of BS7448:pt1

and $\eta_p = 2+0.522.(1-a/W)$

F =	9.5 kN	η_p =	2.260201
B =	2.5 mm	Up =	1.322042
W =	60 mm		
a/W =	0.5015		
f(a/W) =	9.7048		
J=	**143.10 N/mm**		

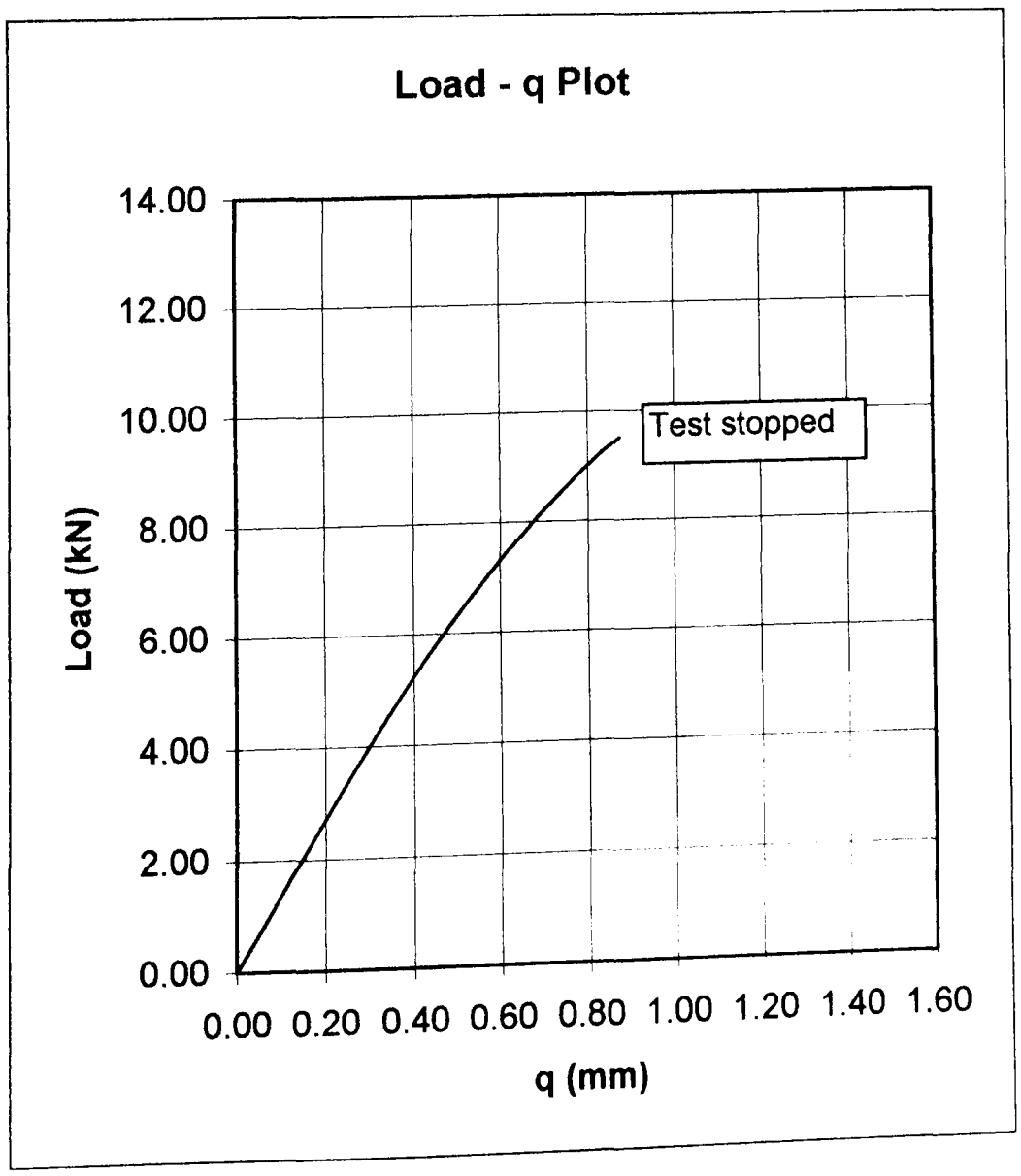

Fracture Toughness Test Data - J_{IC} Test

Specimen Data

Specimen Thickness:	2.5 mm
Specimen Width:	60 mm
Material:	EN24
Yield Stress:	970 MPa
Specimen No:	2-5P6
Side Groove Type:	None
Side Groove Depth:	0 mm
Effective Thickness:	2.5 mm

Precracking Data

Initial Cycles	
Mean Load:	1.5 kN
Amplitude:	1.3 kN
Max Load:	2.8 kN
No Cycles:	2200
Force Ratio:	0.07
Final Cycles	
Mean Load:	1.3 kN
Amplitude:	1.15 kN
Max Load:	2.45 kN
No Cycles:	5000
Force Ratio:	0.06

Post Fracture Data

Dist from edge	Crack length	Stable Crack
1.0%	29.13	0.08
12.5%	29.27	0.31
25.0%	29.36	0.55
37.5%	29.48	0.89
50.0%	29.53	1.02
62.5%	29.57	0.78
75.0%	29.58	0.46
87.5%	29.55	0.21
99.0%	29.45	0.05
Ave	**29.45**	**0.536**

$J = \{[F/(BW^{0.5})].f(a/W)\}^2 [(1-\nu^2)/E] + [(\eta_p U_p)/B(W-a)]$

where f(a/W) is given by 9.2.3.2 of BS7448:pt1

and $\eta_p = 2+0.522.(1-a/W)$

F =	10 kN	η_p =	2.265752
B =	2.5 mm	Up =	1.606667
W =	60 mm		
a/W =	0.4909		
f(a/W) =	9.3946		
J=	**154.76 N/mm**		

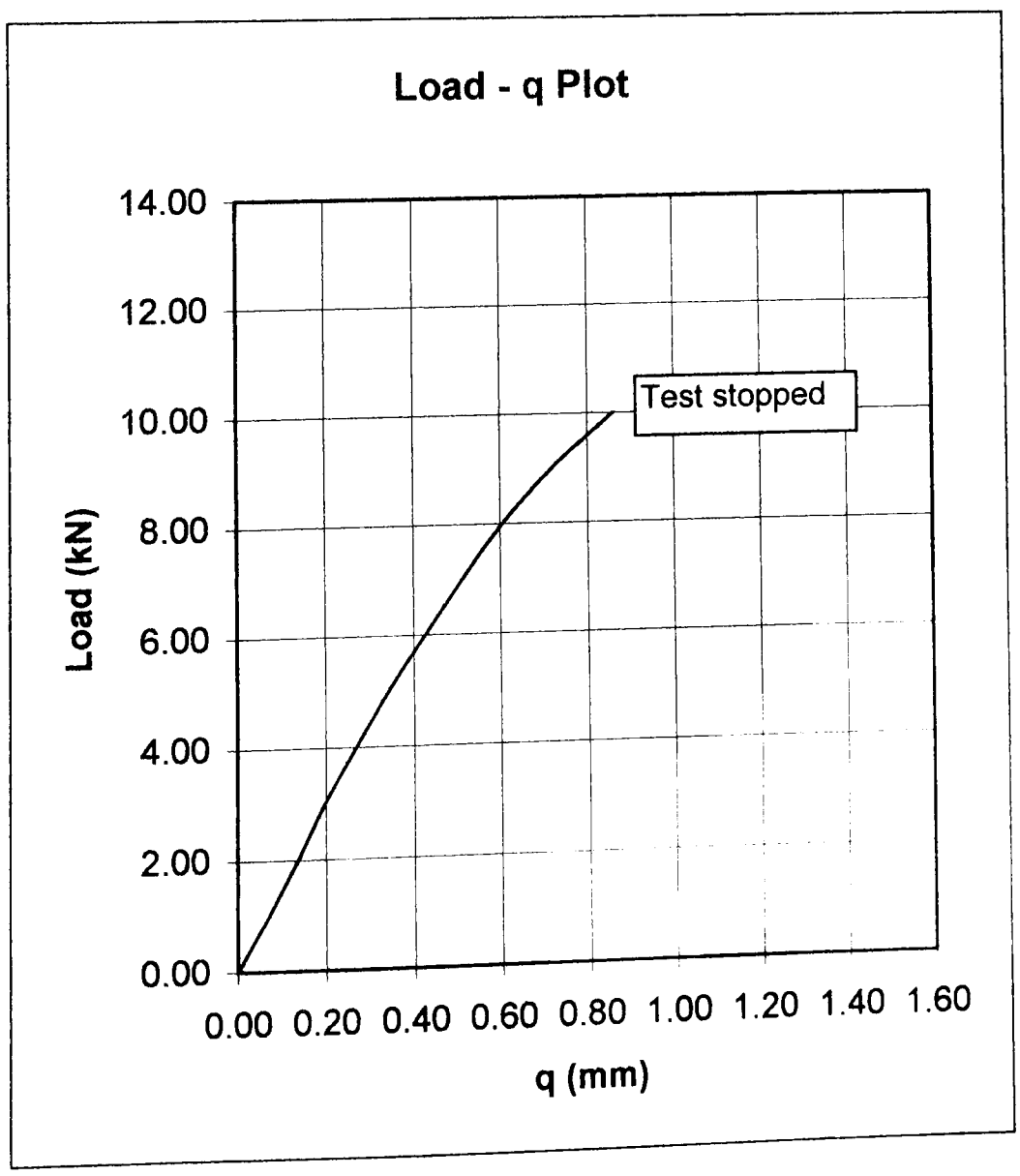

Fracture Toughness Test Data - J_{IC} Test

Specimen Data

Specimen Thickness:	2.5 mm
Specimen Width:	60 mm
Material:	EN24
Yield Stress:	970 MPa
Specimen No:	2-5P7
Side Groove Type:	None
Side Groove Depth:	0 mm
Effective Thickness:	2.5 mm

Precracking Data

Initial Cycles	
Mean Load:	1.5 kN
Amplitude:	1.3 kN
Max Load:	2.8 kN
No Cycles:	2200
Force Ratio:	0.07
Final Cycles	
Mean Load:	1.3 kN
Amplitude:	1.15 kN
Max Load:	2.45 kN
No Cycles:	5000
Force Ratio:	0.06

Post Fracture Data

Dist from edge	Crack length	Stable Crack
1.0%	29.67	0.15
12.5%	29.79	0.16
25.0%	29.92	0.33
37.5%	29.95	1.21
50.0%	29.96	1.3
62.5%	29.94	1.08
75.0%	29.94	0.18
87.5%	29.91	0.12
99.0%	29.77	0.12
Ave	**29.89**	**0.564**

$J = \{[F/(BW^{0.5})].f(a/W)\}^2 [(1-\nu^2)/E] + [(\eta_p U_p)/B(W-a)]$

where f(a/W) is given by 9.2.3.2 of BS7448:pt1

and $\eta_p = 2+0.522.(1-a/W)$

F =	10.5 kN	η_p =	2.261946
B =	2.5 mm	Up =	2.3545
W =	60 mm		
a/W =	0.4982		
f(a/W) =	9.6054		
J=	**194.18 N/mm**		

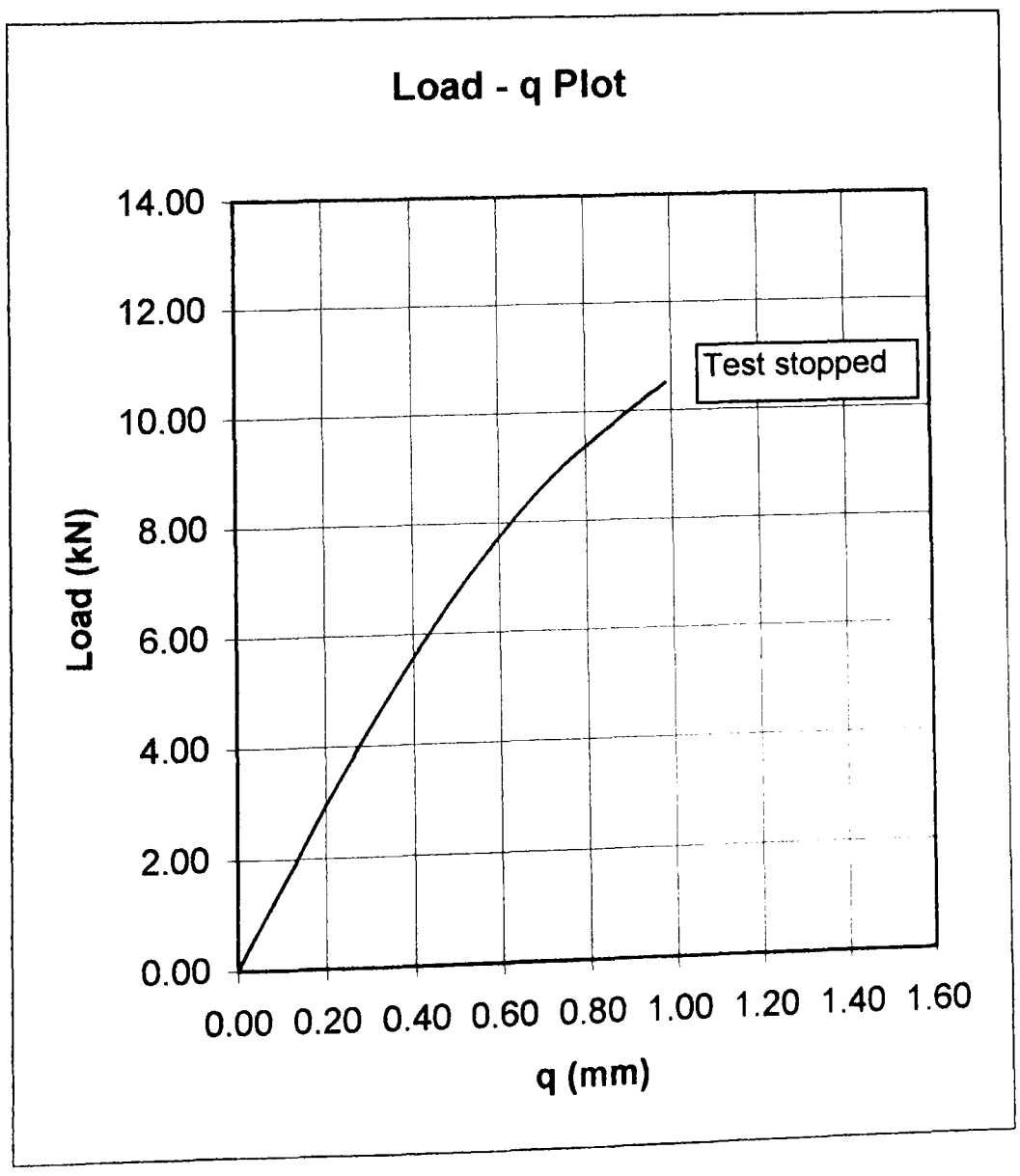

Fracture Toughness Test Data - J_{IC} Test

Specimen Data

Specimen Thickness:	2.5 mm
Specimen Width:	60 mm
Material:	EN24
Yield Stress:	970 MPa
Specimen No:	2-5P8
Side Groove Type:	None
Side Groove Depth:	0 mm
Effective Thickness:	2.5 mm

Precracking Data

Initial Cycles	
Mean Load:	1.5 kN
Amplitude:	1.3 kN
Max Load:	2.8 kN
No Cycles:	2200
Force Ratio:	0.07
Final Cycles	
Mean Load:	1.3 kN
Amplitude:	1.15 kN
Max Load:	2.45 kN
No Cycles:	5000
Force Ratio:	0.06

Post Fracture Data

Dist from edge	Crack length	Stable Crack
1.0%	29.54	0.1
12.5%	29.62	0.48
25.0%	29.68	0.81
37.5%	29.68	1.44
50.0%	29.67	1.79
62.5%	29.64	1.32
75.0%	29.61	1.02
87.5%	29.53	0.31
99.0%	29.42	0.18
Ave	**29.61**	**0.914**

$J = \{[F/(BW^{0.5})].f(a/W)\}^2 [(1-\nu^2)/E] + [(\eta_p U_p)/B(W-a)]$

where f(a/W) is given by 9.2.3.2 of BS7448:pt1

and $\eta_p = 2+0.522.(1-a/W)$

F =	11 kN	η_p =	2.26436
B =	2.5 mm	Up =	2.801
W =	60 mm		
a/W =	0.4936		
f(a/W) =	9.4708		
J=	**215.18 N/mm**		

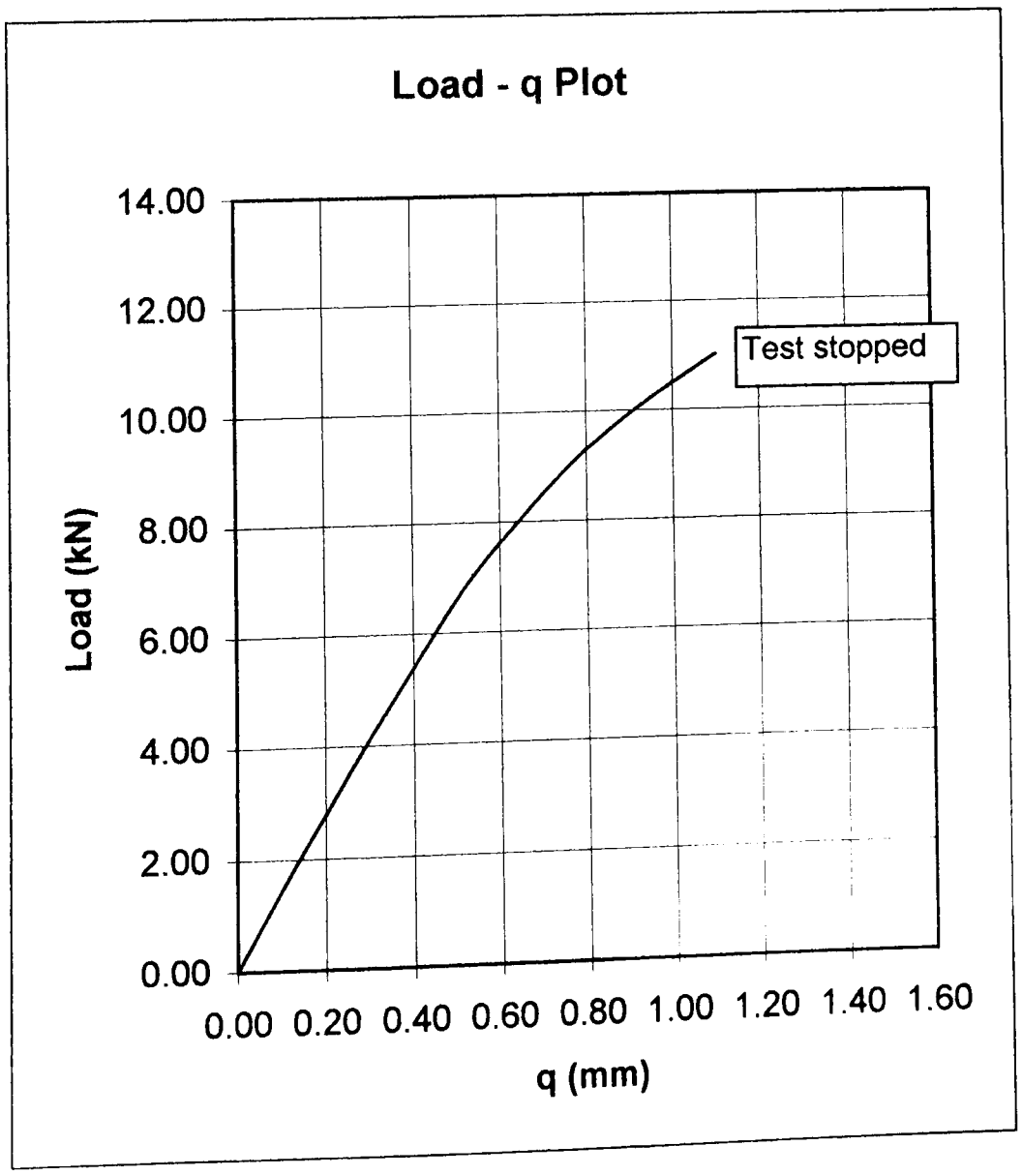

Fracture Toughness Test Data - J_{IC} Test

Specimen Data

Specimen Thickness:	2.5 mm
Specimen Width:	60 mm
Material:	EN24
Yield Stress:	970 MPa
Specimen No:	2-5P9
Side Groove Type:	None
Side Groove Depth:	0 mm
Effective Thickness:	2.5 mm

Precracking Data

Initial Cycles	
Mean Load:	1.5 kN
Amplitude:	1.3 kN
Max Load:	2.8 kN
No Cycles:	2200
Force Ratio:	0.07
Final Cycles	
Mean Load:	1.3 kN
Amplitude:	1.15 kN
Max Load:	2.45 kN
No Cycles:	5000
Force Ratio:	0.06

Post Fracture Data

Dist from edge	Crack length	Stable Crack
1.0%	29.45	0
12.5%	29.61	0
25.0%	29.74	0
37.5%	29.77	0.3
50.0%	29.76	0.45
62.5%	29.69	0.31
75.0%	29.62	0.22
87.5%	29.58	0.04
99.0%	29.44	0.05
Ave	**29.65**	**0.168**

$J = \{[F/(BW^{0.5})].f(a/W)\}^2 [(1-\nu^2)/E] + [(\eta_p U_p)/B(W-a)]$

where f(a/W) is given by 9.2.3.2 of BS7448:pt1

and $\eta_p = 2+0.522.(1-a/W)$

F =	8 kN	η_p =	2.264029
B =	2.5 mm	Up =	0.462167
W =	60 mm		
a/W =	0.4942		
f(a/W) =	9.4891		
J=	**83.71 N/mm**		

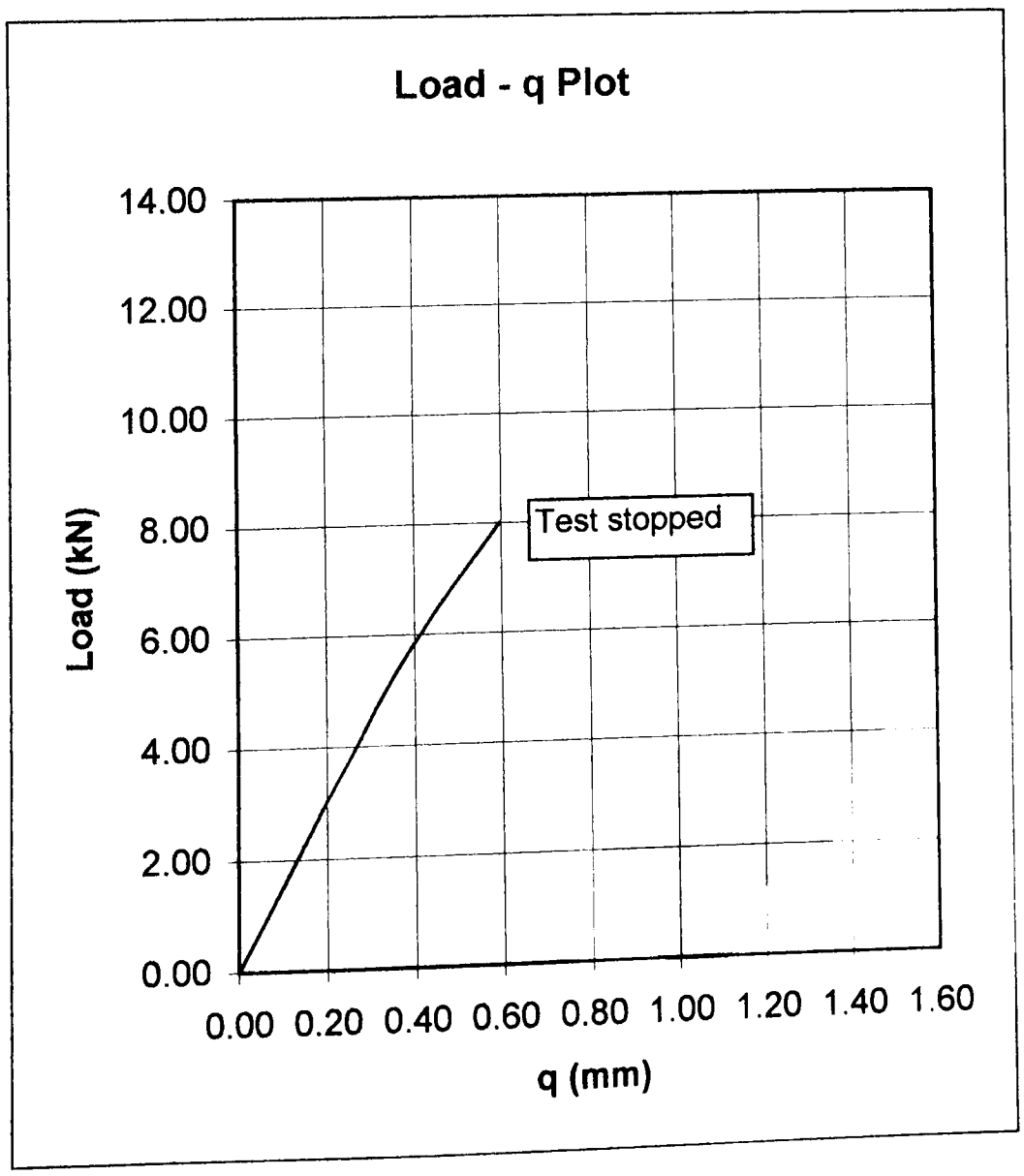

Fracture Toughness Test Data - J_{IC} Test

Specimen Data

Specimen Thickness:	2.5 mm
Specimen Width:	60 mm
Material:	EN24
Yield Stress:	970 MPa
Specimen No:	2-5P10
Side Groove Type:	None
Side Groove Depth:	0 mm
Effective Thickness:	2.5 mm

Precracking Data

Initial Cycles	
Mean Load:	1.5 kN
Amplitude:	1.3 kN
Max Load:	2.8 kN
No Cycles:	2200
Force Ratio:	0.07
Final Cycles	
Mean Load:	1.3 kN
Amplitude:	1.15 kN
Max Load:	2.45 kN
No Cycles:	5000
Force Ratio:	0.06

Post Fracture Data

Dist from edge	Crack length	Stable Crack
1.0%	29.04	0
12.5%	29.07	0
25.0%	29.09	0.11
37.5%	29.12	0.25
50.0%	29.12	0.35
62.5%	29.12	0.26
75.0%	29.10	0.08
87.5%	29.06	0
99.0%	29.00	0
Ave	**29.09**	**0.131**

$J = \{[F/(BW^{0.5})].f(a/W)\}^2 [(1-\nu^2)/E] + [(\eta_p U_p)/B(W-a)]$

where f(a/W) is given by 9.2.3.2 of BS7448:pt1

and $\eta_p = 2+0.522.(1-a/W)$

F =	8.5 kN	η_p =	2.268939
B =	2.5 mm	Up =	0.487667
W =	60 mm		
a/W =	0.4848		
f(a/W) =	9.2238		
J=	**88.90 N/mm**		

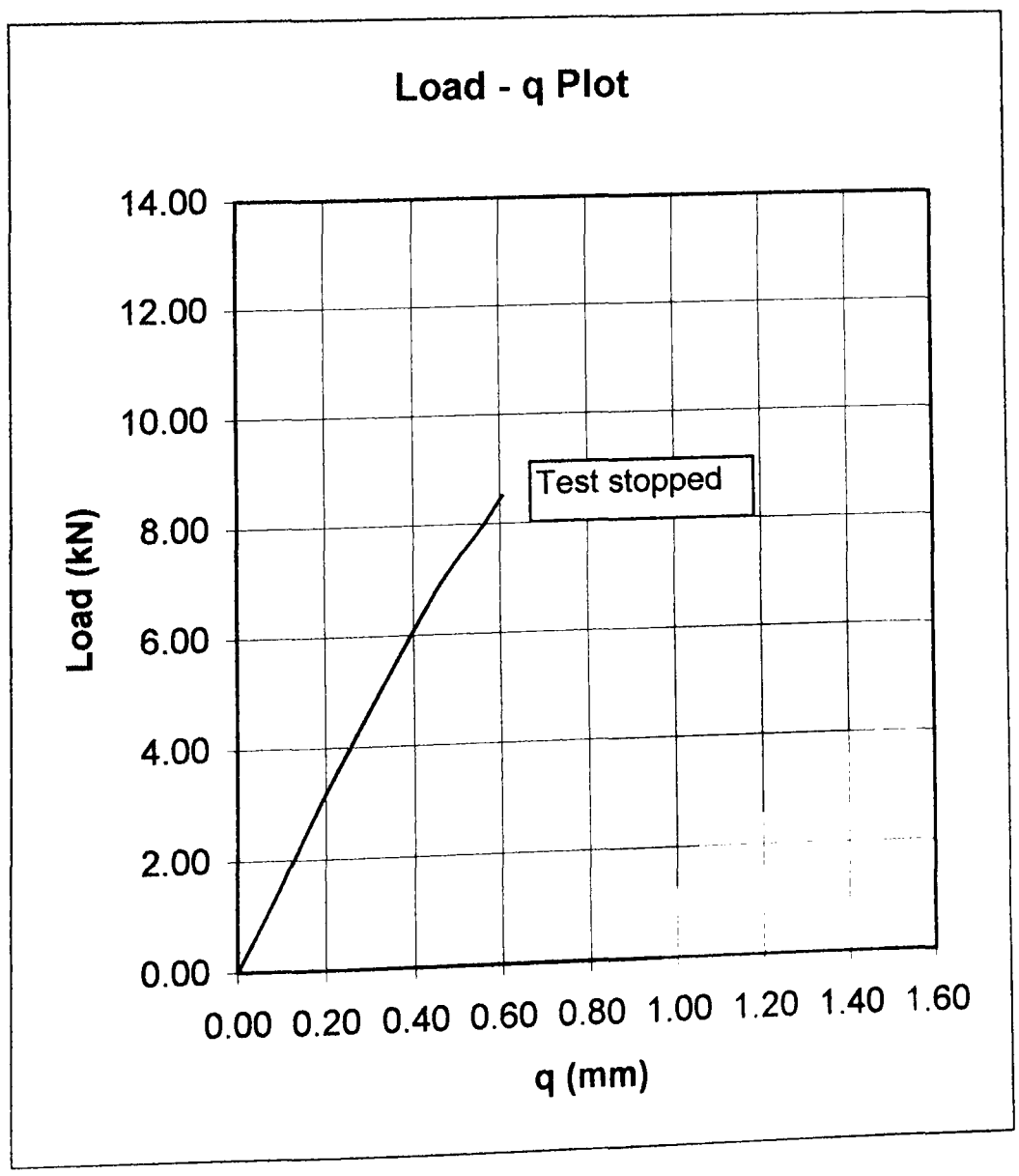

Fracture Toughness Test Data - J_{IC} Test

Specimen Data

Specimen Thickness:	2.5 mm
Specimen Width:	60 mm
Material:	EN24
Yield Stress:	970 MPa
Specimen No:	2-5P11
Side Groove Type:	None
Side Groove Depth:	0 mm
Effective Thickness:	2.5 mm

Precracking Data

Initial Cycles	
Mean Load:	1.5 kN
Amplitude:	1.3 kN
Max Load:	2.8 kN
No Cycles:	2200
Force Ratio:	0.07
Final Cycles	
Mean Load:	1.3 kN
Amplitude:	1.15 kN
Max Load:	2.45 kN
No Cycles:	5000
Force Ratio:	0.06

Post Fracture Data

Dist from edge	Crack length	Stable Crack
1.0%	29.45	0.060
12.5%	29.56	0.160
25.0%	29.56	0.840
37.5%	29.62	1.320
50.0%	29.68	1.240
62.5%	29.69	1.000
75.0%	29.66	0.510
87.5%	29.59	0.110
99.0%	29.51	0.000
Ave	**29.61**	**0.651**

$J = \{[F/(BW^{0.5})].f(a/W)\}^2 [(1-\nu^2)/E] + [(\eta_p U_p)/B(W-a)]$

where f(a/W) is given by 9.2.3.2 of BS7448:pt1

and $\eta_p = 2+0.522.(1-a/W)$

F =	9 kN	η_p =	2.264437
B =	2.5 mm	Up =	1.234
W =	60 mm		
a/W =	0.4934		
f(a/W) =	9.4666		
J=	**124.85 N/mm**		

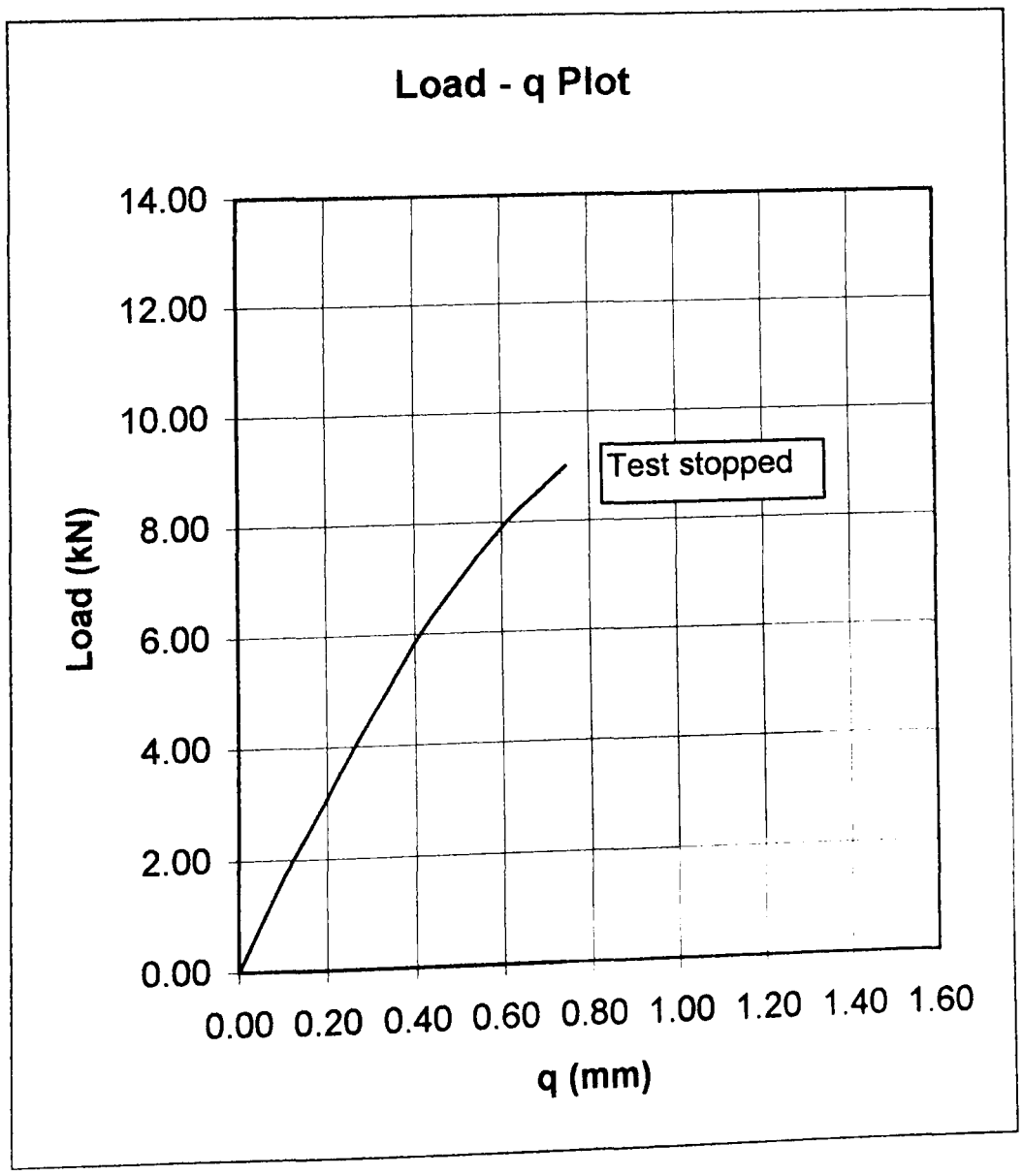

Fracture Toughness Test Data - J_{IC} Test

Specimen Data

Specimen Thickness:	2.5 mm
Specimen Width:	60 mm
Material:	EN24
Yield Stress:	970 MPa
Specimen No:	2-5P12
Side Groove Type:	None
Side Groove Depth:	0 mm
Effective Thickness:	2.5 mm

Precracking Data

Initial Cycles	
Mean Load:	1.5 kN
Amplitude:	1.3 kN
Max Load:	2.8 kN
No Cycles:	2200
Force Ratio:	0.07
Final Cycles	
Mean Load:	1.3 kN
Amplitude:	1.15 kN
Max Load:	2.45 kN
No Cycles:	5000
Force Ratio:	0.06

Post Fracture Data

Dist from edge	Crack length	Stable Crack
1.0%	29.71	0.000
12.5%	29.83	0.130
25.0%	29.93	0.660
37.5%	30.02	0.960
50.0%	30.04	0.970
62.5%	30.05	0.590
75.0%	30.05	0.310
87.5%	29.99	0.180
99.0%	29.98	0.000
Ave	**29.97**	**0.475**

$J = \{[F/(BW^{0.5})].f(a/W)\}^2 [(1-\nu^2)/E] + [(\eta_p U_p)/B(W-a)]$

where f(a/W) is given by 9.2.3.2 of BS7448:pt1

and $\eta_p = 2+0.522.(1-a/W)$

F =	9.5 kN	η_p =	2.261266
B =	2.5 mm	Up =	1.375708
W =	60 mm		
a/W =	0.4995		
f(a/W) =	9.6439		
J=	**143.28 N/mm**		

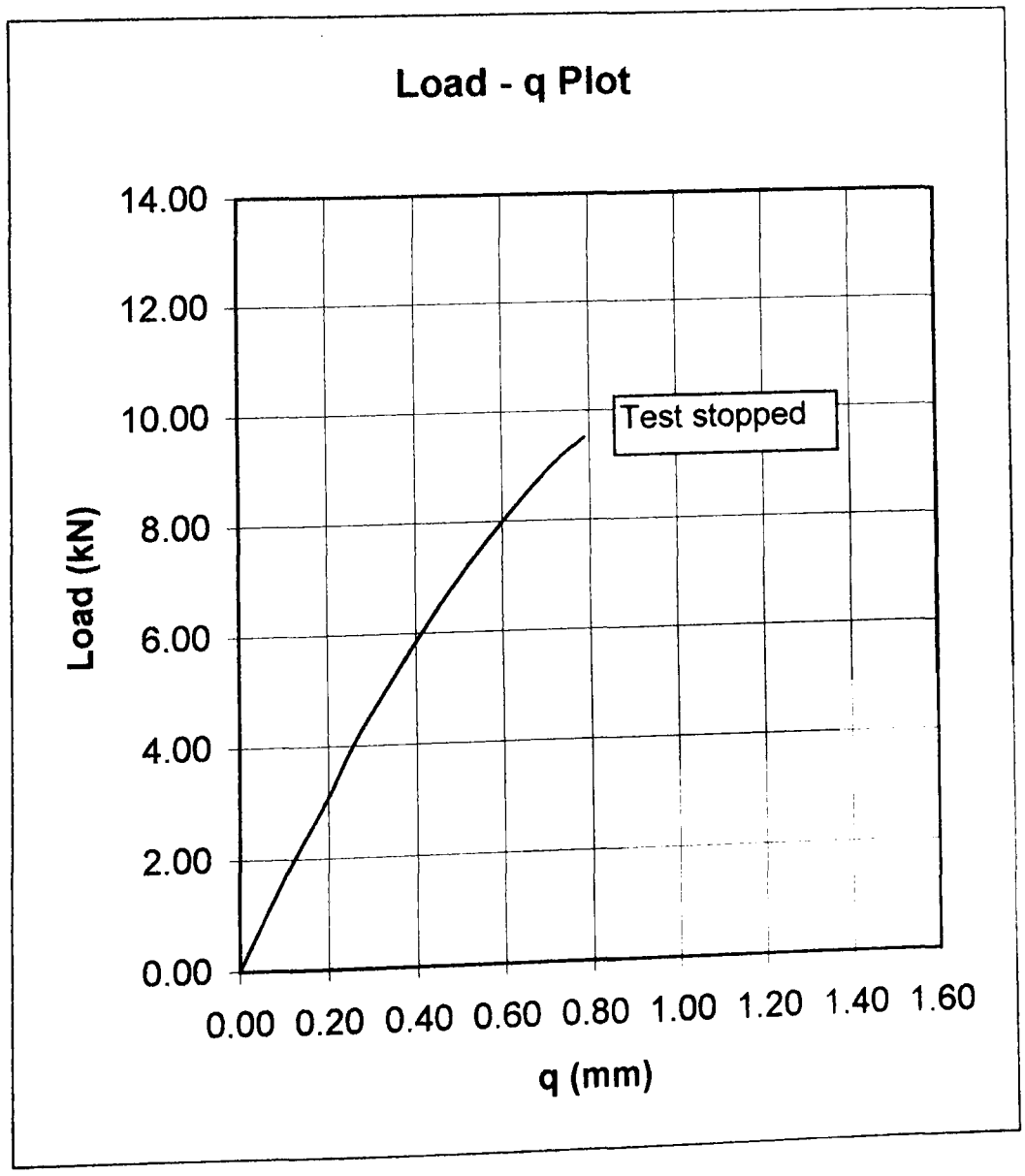

Fracture Toughness Test Data - J_{IC} Test

Specimen Data

Specimen Thickness:	2.5 mm
Specimen Width:	60 mm
Material:	EN24
Yield Stress:	970 MPa
Specimen No:	2-5P13
Side Groove Type:	None
Side Groove Depth:	0 mm
Effective Thickness:	2.5 mm

Precracking Data

Initial Cycles	
Mean Load:	1.5 kN
Amplitude:	1.3 kN
Max Load:	2.8 kN
No Cycles:	2200
Force Ratio:	0.07
Final Cycles	
Mean Load:	1.3 kN
Amplitude:	1.15 kN
Max Load:	2.45 kN
No Cycles:	5000
Force Ratio:	0.06

Post Fracture Data

Dist from edge	Crack length	Stable Crack
1.0%	29.21	0.030
12.5%	29.30	0.130
25.0%	29.38	0.350
37.5%	29.44	0.660
50.0%	29.49	0.970
62.5%	29.48	0.760
75.0%	29.44	0.330
87.5%	29.38	0.030
99.0%	29.28	0.000
Ave	**29.39**	**0.406**

$J = \{[F/(BW^{0.5})].f(a/W)\}^2 [(1-\nu^2)/E] + [(\eta_p U_p)/B(W-a)]$
where f(a/W) is given by 9.2.3.2 of BS7448:pt1
and $\eta_p = 2+0.522.(1-a/W)$

F =	10 kN	η_p =	2.266269
B =	2.5 mm	Up =	1.368667
W =	60 mm		
a/W =	0.4899		
f(a/W) =	9.3665		
J=	**146.99 N/mm**		

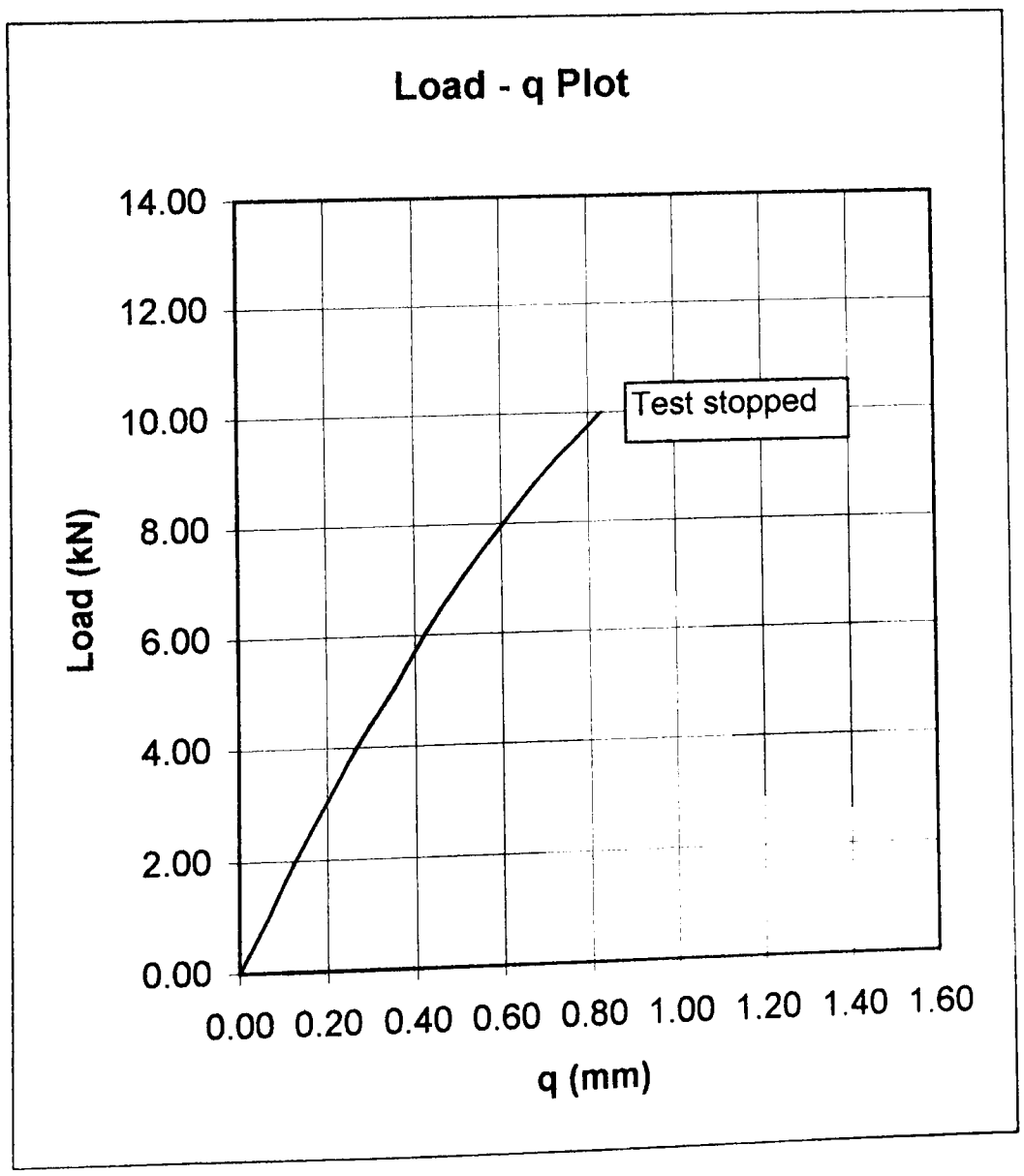

APPENDIX III

TEST RECORDS – SIDE GROOVED SPECIMENS

Fracture Toughness Test Data - K_{IC} Test

Specimen Data

Specimen Thickness:	25 mm
Specimen Width:	60 mm
Material:	EN24
Yield Stress:	970 MPa
Specimen No:	25SG1
Side Groove Type:	Vee
Side Groove Depth:	3.75 mm
Groove Base Thickness	17.5 mm

Precracking Data

Initial Cycles	
Mean Load:	14 kN
Amplitude:	13 kN
Max Load:	27 kN
No Cycles:	12000
Force Ratio:	0.04
Final Cycles	
Mean Load:	13 kN
Amplitude:	11 kN
Max Load:	24 kN
No Cycles:	8000
Force Ratio:	0.08

Post Fracture Data

Dist from edge	Crack length
1.0%	29.95
12.5%	30.10
25.0%	30.23
37.5%	30.29
50.0%	30.28
62.5%	30.28
75.0%	30.23
87.5%	30.09
99.0%	29.90
Ave	**30.18**

$K_Q = [F_Q/(BW^{0.5})].f(a/W)$

where f(a/W) is given by 9.2.3.2 of BS7448:pt1

FQ =	54 kN	(from Instron)
B =	25 mm	
W =	60 mm	
a/W =	0.5030	
f(a/W) =	9.7480	
KQ =	**85.96 MPa.m^0.5**	

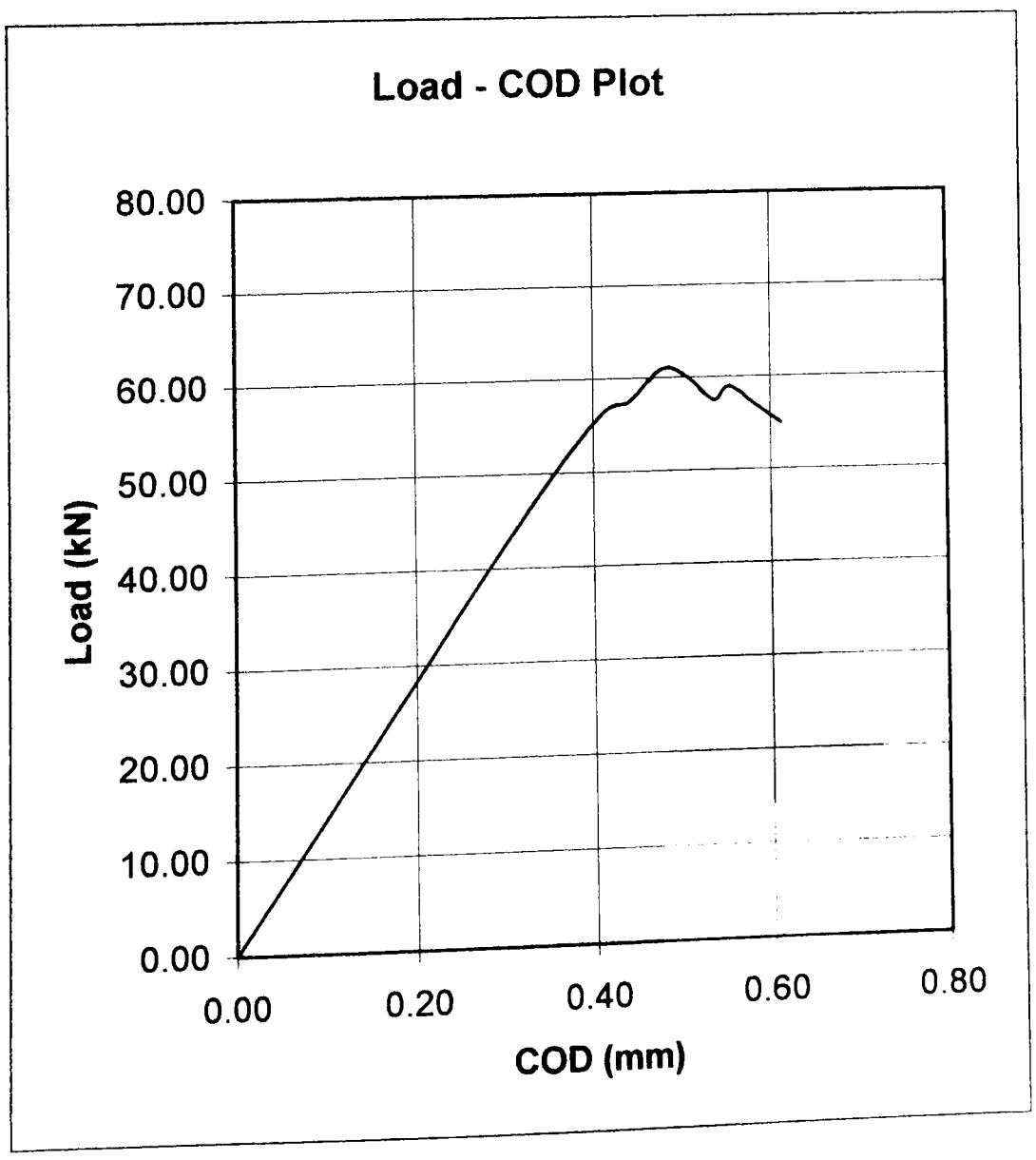

Fracture Toughness Test Data - K_{IC} Test

Specimen Data

Specimen Thickness:	25 mm
Specimen Width:	60 mm
Material:	EN24
Yield Stress:	970 MPa
Specimen No:	25SG2
Side Groove Type:	Vee
Side Groove Depth:	3.75 mm
Groove Base Thickness	17.5 mm

Precracking Data

Initial Cycles	
Mean Load:	14 kN
Amplitude:	13 kN
Max Load:	27 kN
No Cycles:	9000
Force Ratio:	0.04
Final Cycles	
Mean Load:	13 kN
Amplitude:	11 kN
Max Load:	24 kN
No Cycles:	7000
Force Ratio:	0.08

Post Fracture Data

Dist from edge	Crack length
1.0%	30.44
12.5%	30.52
25.0%	30.66
37.5%	30.72
50.0%	30.70
62.5%	30.66
75.0%	30.64
87.5%	30.49
99.0%	30.33
Ave	**30.60**

$K_Q = [F_Q/(BW^{0.5})].f(a/W)$

where f(a/W) is given by 9.2.3.2 of BS7448:pt1

FQ =	44.9 kN	(from Instron)
B =	25 mm	
W =	60 mm	
a/W =	0.5099	
f(a/W) =	9.9626	
KQ =	**73.05 MPa.m^0.5**	

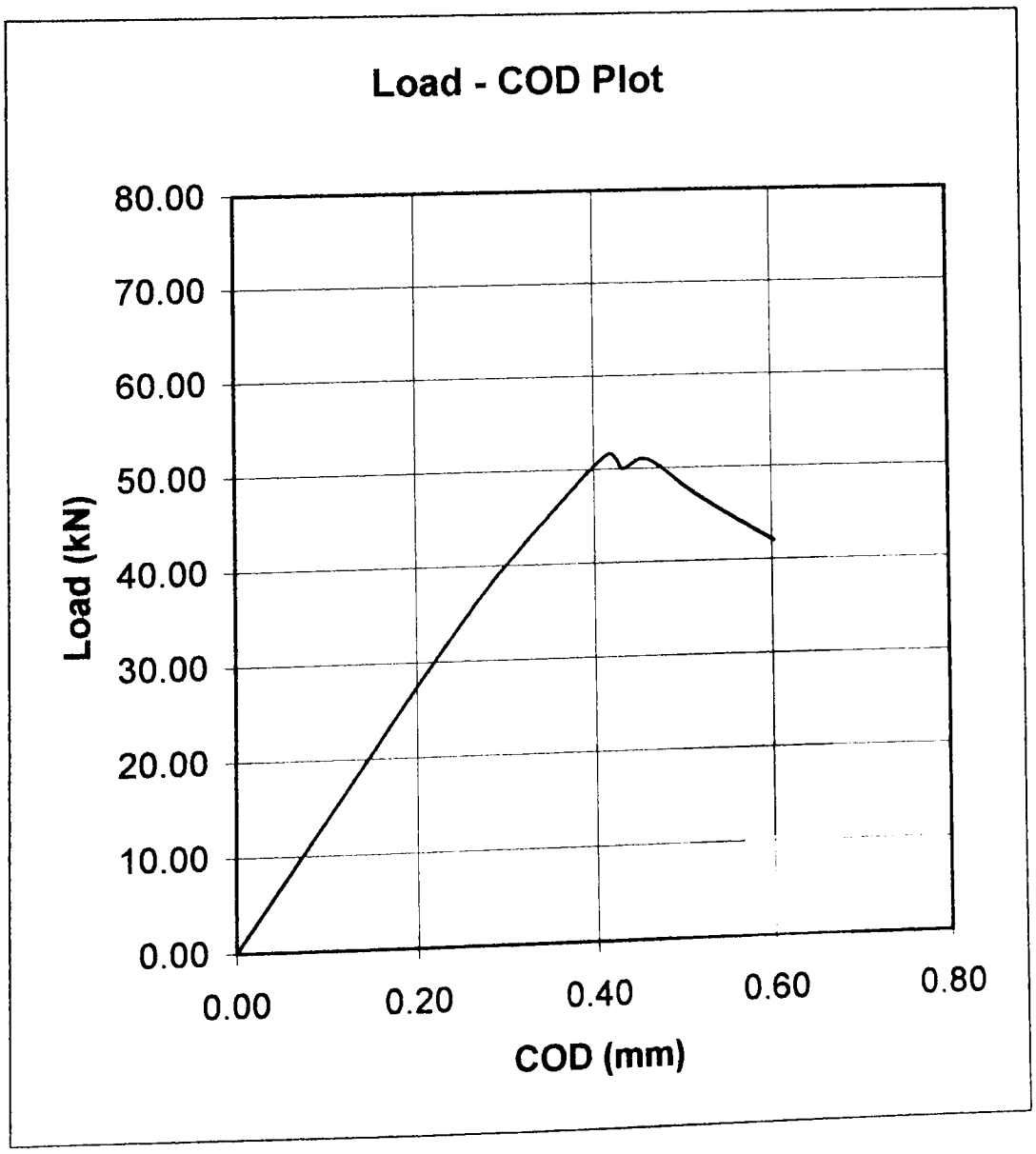

Fracture Toughness Test Data - K_{IC} Test

Specimen Data

Specimen Thickness:	15 mm
Specimen Width:	60 mm
Material:	EN24
Yield Stress:	970 MPa
Specimen No:	15SG1
Side Groove Type:	Vee
Side Groove Depth:	2.25 mm
Groove Base Thickness	10.5 mm

Precracking Data

Initial Cycles	
Mean Load:	9 kN
Amplitude:	8 kN
Max Load:	17 kN
No Cycles:	10000
Force Ratio:	0.06
Final Cycles	
Mean Load:	7 kN
Amplitude:	6 kN
Max Load:	13 kN
No Cycles:	7000
Force Ratio:	0.08

Post Fracture Data

Dist from edge	Crack length
1.0%	29.82
12.5%	30.00
25.0%	30.14
37.5%	30.25
50.0%	30.38
62.5%	30.48
75.0%	30.48
87.5%	30.45
99.0%	30.42
Ave	**30.29**

$K_Q = [F_Q/(BW^{0.5})].f(a/W)$

where f(a/W) is given by 9.2.3.2 of BS7448:pt1

FQ =	28.09 kN	(from Instron)
B =	15 mm	
W =	60 mm	
a/W =	0.5048	
f(a/W) =	9.8033	
KQ =	**74.95 MPa.m^0.5**	

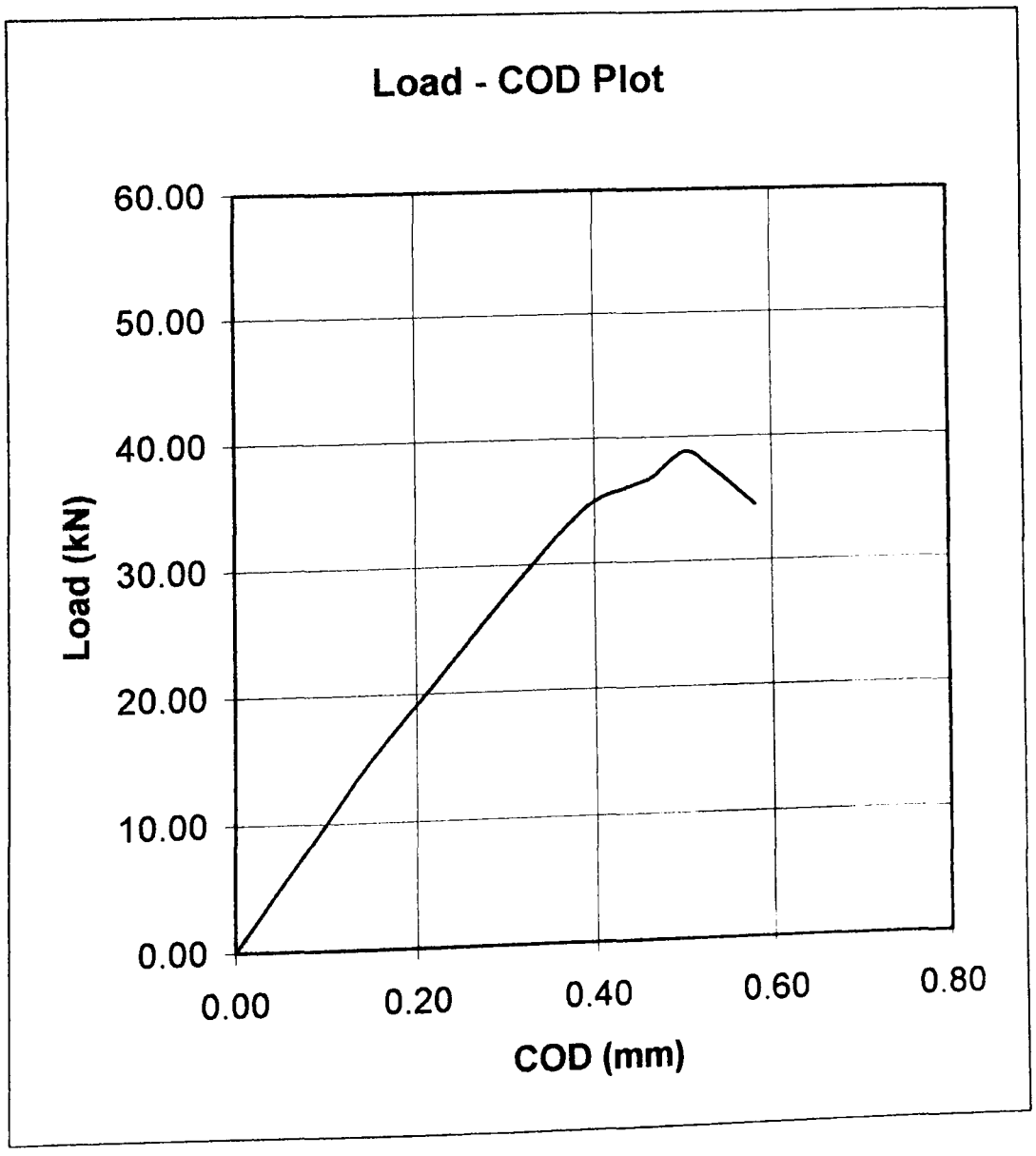

Fracture Toughness Test Data - K_{IC} Test

Specimen Data

Specimen Thickness:	10 mm
Specimen Width:	60 mm
Material:	EN24
Yield Stress:	970 MPa
Specimen No:	10SG1
Side Groove Type:	Vee
Side Groove Depth:	1.5 mm
Groove Base Thickness	7 mm

Precracking Data

Initial Cycles	
Mean Load:	6 kN
Amplitude:	5 kN
Max Load:	11 kN
No Cycles:	10000
Force Ratio:	0.09
Final Cycles	
Mean Load:	4.5 kN
Amplitude:	4 kN
Max Load:	8.5 kN
No Cycles:	7000
Force Ratio:	0.06

Post Fracture Data

Dist from edge	Crack length
1.0%	29.10
12.5%	29.12
25.0%	29.14
37.5%	29.15
50.0%	29.16
62.5%	29.16
75.0%	29.14
87.5%	29.12
99.0%	29.00
Ave	**29.13**

$K_Q = [F_Q/(BW^{0.5})].f(a/W)$

where f(a/W) is given by 9.2.3.2 of BS7448:pt1

FQ =	20.91 kN	(from Instron)
B =	10 mm	
W =	60 mm	
a/W =	0.4855	
f(a/W) =	9.2434	
KQ =	**78.91 MPa.m^0.5**	

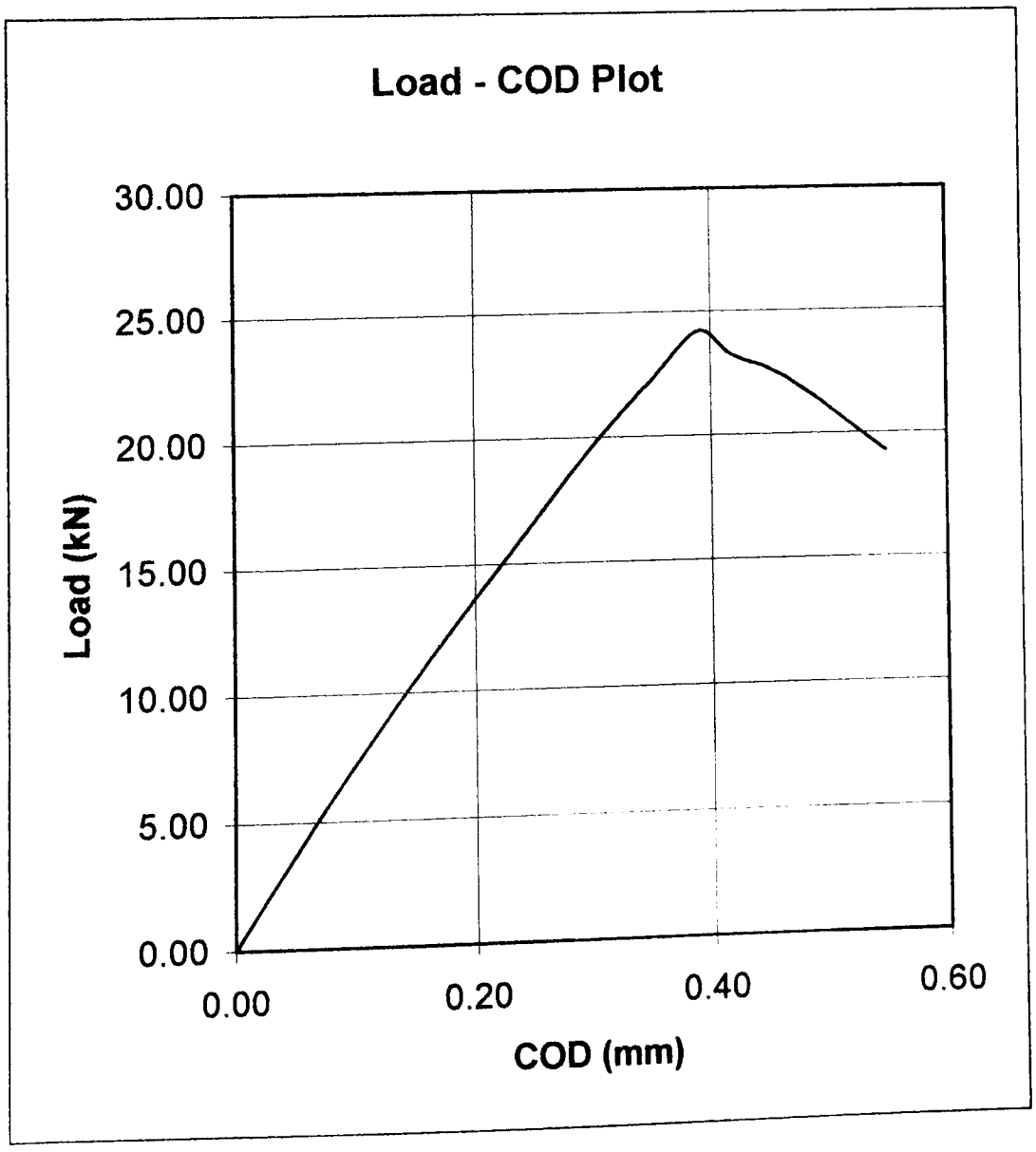

Fracture Toughness Test Data - K_{IC} Test

Specimen Data

Specimen Thickness:	10 mm
Specimen Width:	60 mm
Material:	EN24
Yield Stress:	970 MPa
Specimen No:	10SG2
Side Groove Type:	Vee
Side Groove Depth:	1.5 mm
Groove Base Thickness	7 mm

Precracking Data

Initial Cycles	
Mean Load:	6 kN
Amplitude:	5 kN
Max Load:	11 kN
No Cycles:	10000
Force Ratio:	0.09
Final Cycles	
Mean Load:	4.5 kN
Amplitude:	4 kN
Max Load:	8.5 kN
No Cycles:	7000
Force Ratio:	0.06

Post Fracture Data

Dist from edge	Crack length
1.0%	28.20
12.5%	28.27
25.0%	28.28
37.5%	28.32
50.0%	28.32
62.5%	28.33
75.0%	28.30
87.5%	28.29
99.0%	28.10
Ave	**28.28**

$K_Q = [F_Q/(BW^{0.5})].f(a/W)$

where f(a/W) is given by 9.2.3.2 of BS7448:pt1

FQ =	22.24 kN	(from Instron)
B =	10 mm	
W =	60 mm	
a/W =	0.4714	
f(a/W) =	8.8658	
KQ =	**80.50 MPa.m^0.5**	

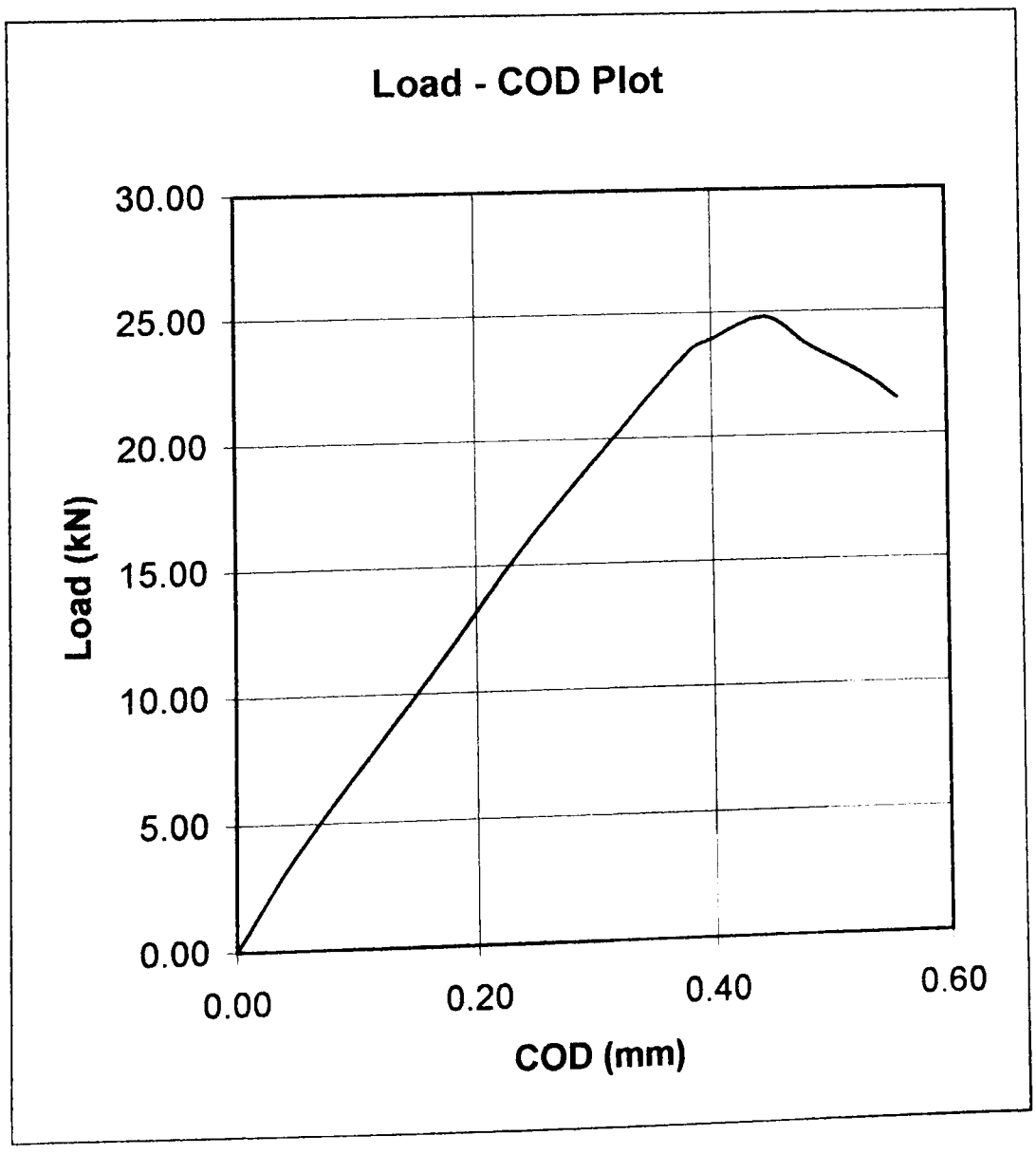

Fracture Toughness Test Data - K_{IC} Test

Specimen Data

Specimen Thickness:	5 mm
Specimen Width:	60 mm
Material:	EN24
Yield Stress:	970 MPa
Specimen No:	5SG1
Side Groove Type:	Vee
Side Groove Depth:	0.75 mm
Groove Base Thickness	3.5 mm

Precracking Data

Initial Cycles	
Mean Load:	3 kN
Amplitude:	2.6 kN
Max Load:	5.6 kN
No Cycles:	11000
Force Ratio:	0.07
Final Cycles	
Mean Load:	2.6 kN
Amplitude:	2.3 kN
Max Load:	4.9 kN
No Cycles:	9000
Force Ratio:	0.06

Post Fracture Data

Dist from edge	Crack length
1.0%	30.24
12.5%	30.27
25.0%	30.26
37.5%	30.27
50.0%	30.29
62.5%	30.27
75.0%	30.19
87.5%	30.16
99.0%	30.15
Ave	**30.24**

$K_Q = [F_Q/(BW^{0.5})].f(a/W)$

where f(a/W) is given by 9.2.3.2 of BS7448:pt1

FQ =	9.95 kN	(from Instron)
B =	5 mm	
W =	60 mm	
a/W =	0.5040	
f(a/W) =	9.7783	
KQ =	**79.44 MPa.m^0.5**	

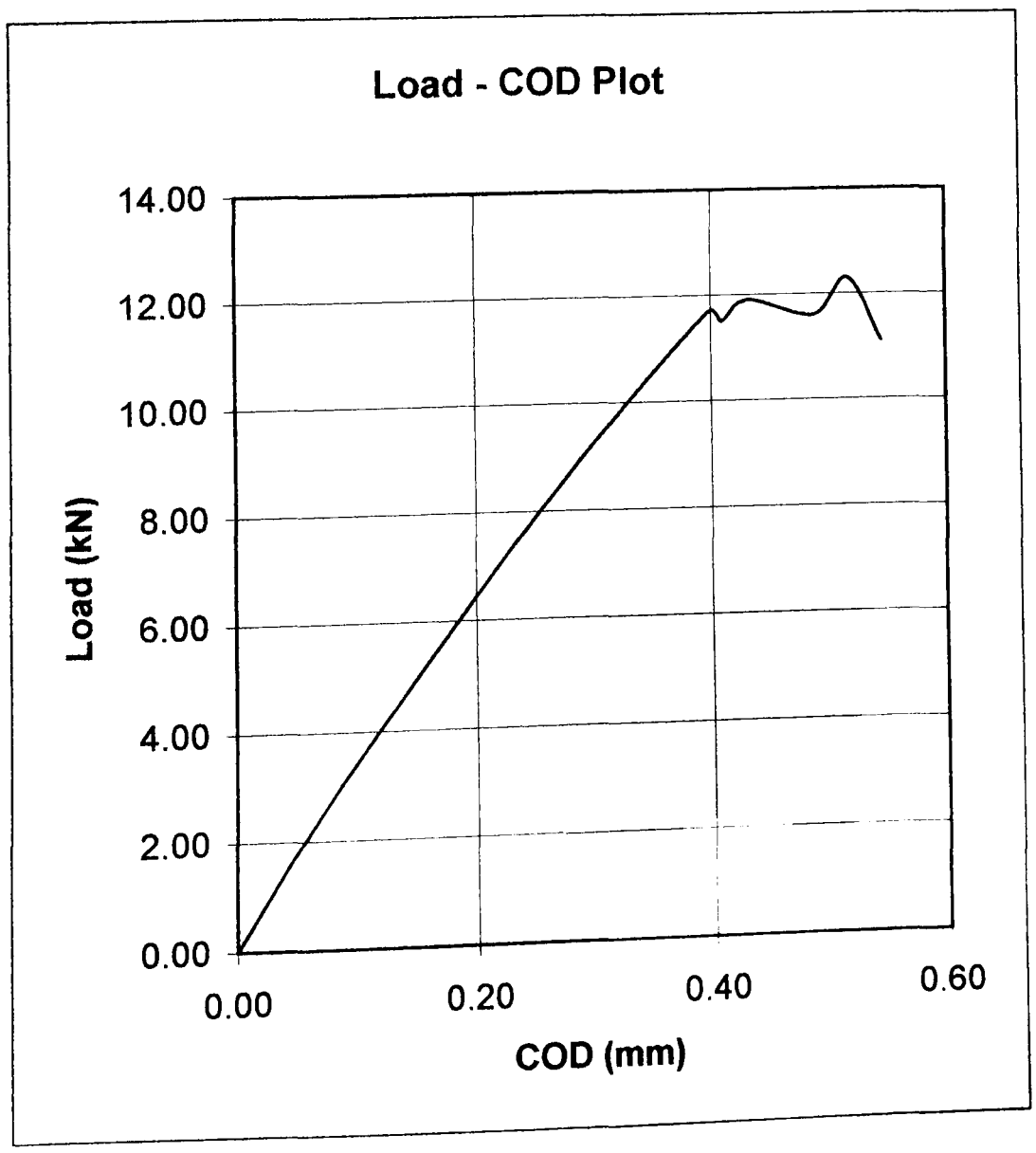

Fracture Toughness Test Data - K_{IC} Test

Specimen Data	
Specimen Thickness:	5 mm
Specimen Width:	60 mm
Material:	EN24
Yield Stress:	970 MPa
Specimen No:	5SG2
Side Groove Type:	Vee
Side Groove Depth:	0.75 mm
Groove Base Thickness	3.5 mm

Precracking Data	
Initial Cycles	
Mean Load:	3 kN
Amplitude:	2.6 kN
Max Load:	5.6 kN
No Cycles:	11000
Force Ratio:	0.07
Final Cycles	
Mean Load:	2.6 kN
Amplitude:	2.3 kN
Max Load:	4.9 kN
No Cycles:	9000
Force Ratio:	0.06

Post Fracture Data

Dist from edge	Crack length
1.0%	29.65
12.5%	29.74
25.0%	29.83
37.5%	29.87
50.0%	29.94
62.5%	29.96
75.0%	30.00
87.5%	30.01
99.0%	29.99
Ave	**29.90**

$K_Q = [F_Q/(BW^{0.5})].f(a/W)$

where f(a/W) is given by 9.2.3.2 of BS7448:pt1

FQ =	9.64 kN	(from Instron)
B =	5 mm	
W =	60 mm	
a/W =	0.4983	
f(a/W) =	9.6079	
KQ =	**75.62 MPa.m^0.5**	

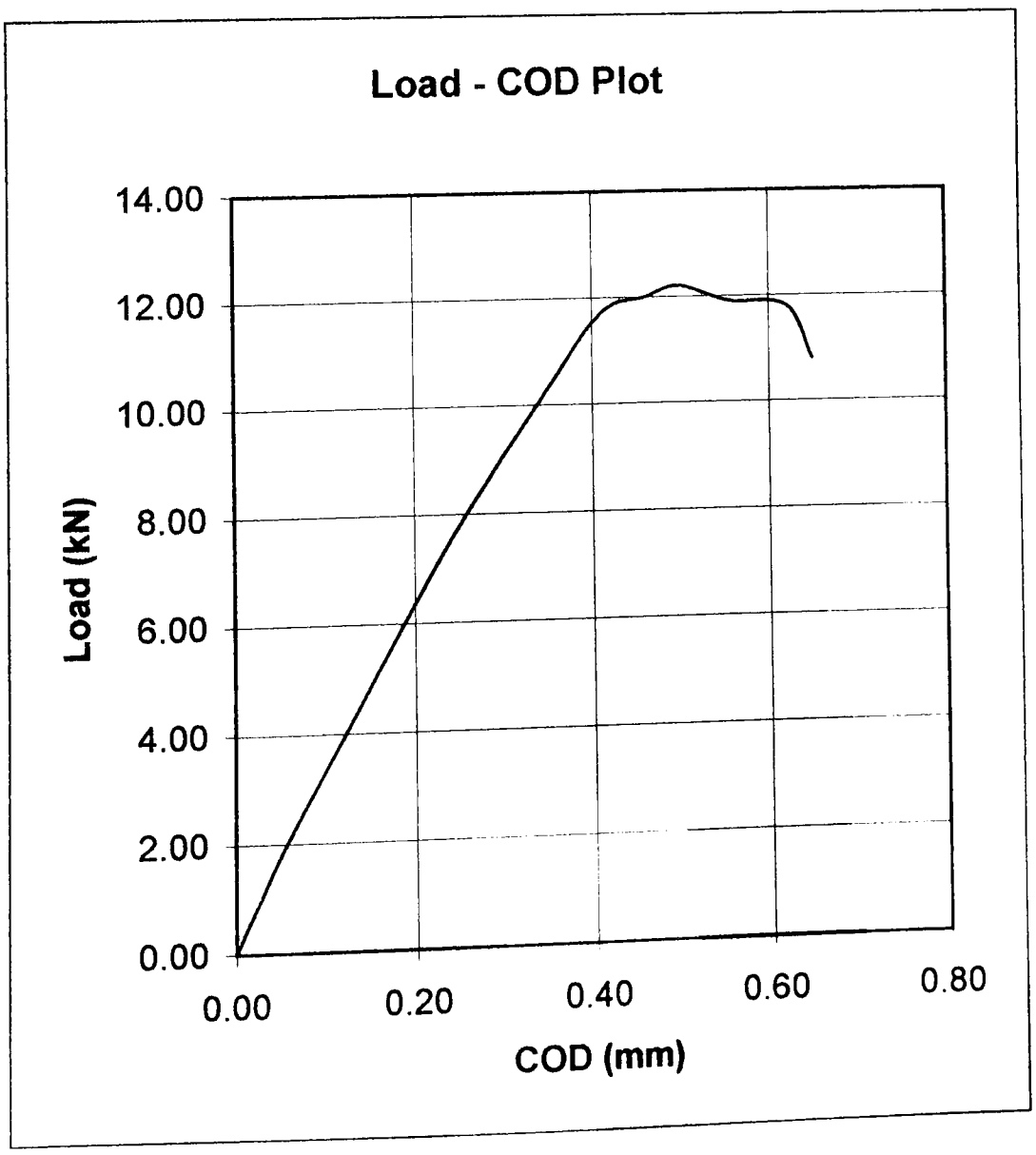

Fracture Toughness Test Data - K_{IC} Test

Specimen Data

Specimen Thickness:	5 mm
Specimen Width:	60 mm
Material:	EN24
Yield Stress:	970 MPa
Specimen No:	5SG3
Side Groove Type:	Vee
Side Groove Depth:	0.75 mm
Groove Base Thickness	3.5 mm

Precracking Data

Initial Cycles	
Mean Load:	3 kN
Amplitude:	2.6 kN
Max Load:	5.6 kN
No Cycles:	11000
Force Ratio:	0.07
Final Cycles	
Mean Load:	2.6 kN
Amplitude:	2.3 kN
Max Load:	4.9 kN
No Cycles:	9000
Force Ratio:	0.06

Post Fracture Data

Dist from edge	Crack length
1.0%	29.98
12.5%	30.03
25.0%	30.05
37.5%	30.10
50.0%	30.10
62.5%	30.10
75.0%	30.13
87.5%	30.12
99.0%	30.07
Ave	**30.08**

$K_Q = [F_Q/(BW^{0.5})].f(a/W)$

where f(a/W) is given by 9.2.3.2 of BS7448:pt1

FQ =	11.42 kN	(from Instron)
B =	5 mm	
W =	60 mm	
a/W =	0.5014	
f(a/W) =	9.6998	
KQ =	**90.44 MPa.m^0.5**	

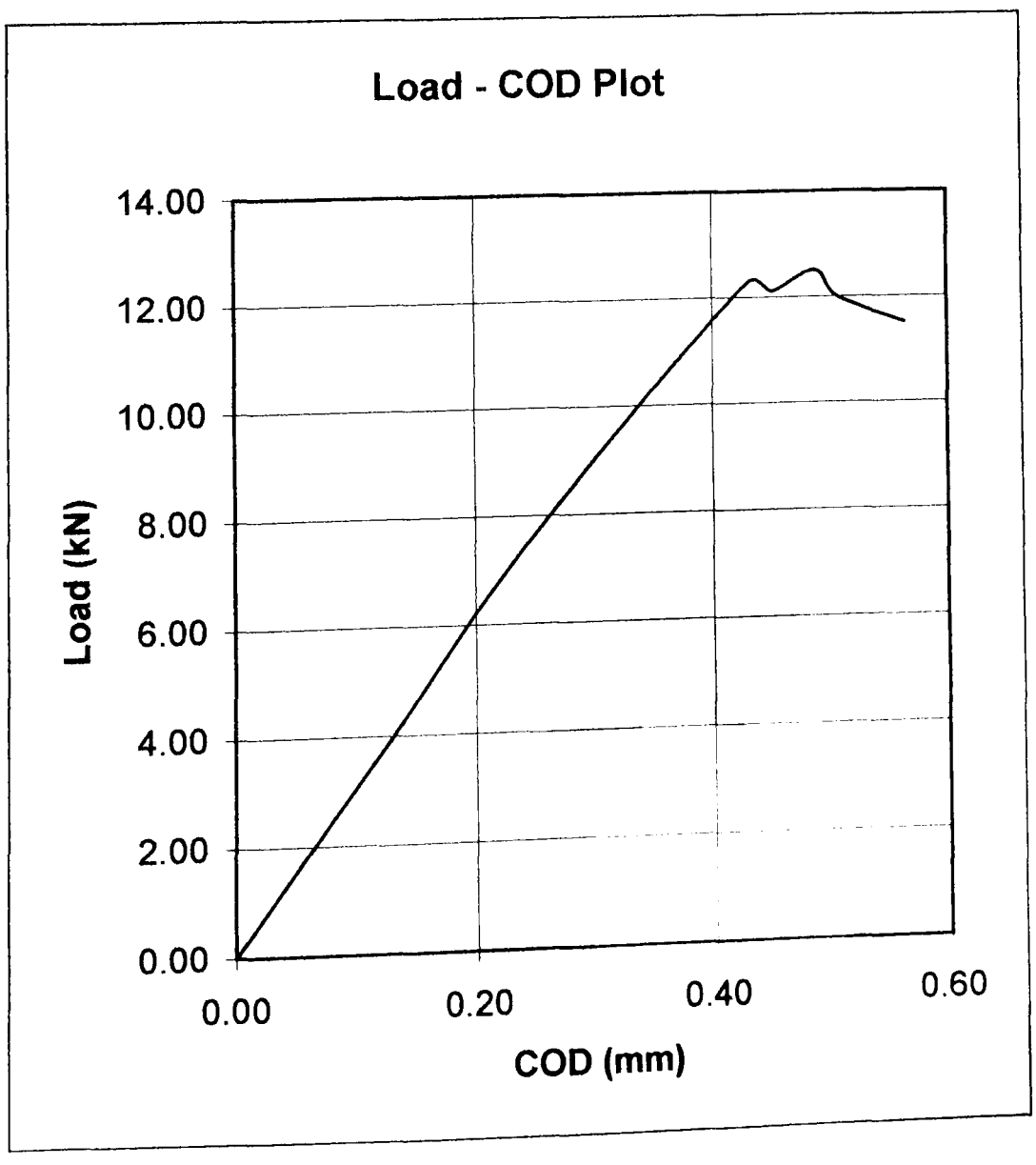

Fracture Toughness Test Data - K_{IC} Test

Specimen Data

Specimen Thickness:	5 mm
Specimen Width:	60 mm
Material:	EN24
Yield Stress:	970 MPa
Specimen No:	5SG4
Side Groove Type:	Vee
Side Groove Depth:	0.75 mm
Groove Base Thickness	3.5 mm

Precracking Data

Initial Cycles	
Mean Load:	3 kN
Amplitude:	2.6 kN
Max Load:	5.6 kN
No Cycles:	11000
Force Ratio:	0.07
Final Cycles	
Mean Load:	2.6 kN
Amplitude:	2.3 kN
Max Load:	4.9 kN
No Cycles:	9000
Force Ratio:	0.06

Post Fracture Data

Dist from edge	Crack length
1.0%	30.05
12.5%	30.04
25.0%	30.05
37.5%	30.04
50.0%	30.03
62.5%	30.01
75.0%	29.99
87.5%	29.99
99.0%	29.92
Ave	**30.02**

$K_Q = [F_Q/(BW^{0.5})].f(a/W)$

where f(a/W) is given by 9.2.3.2 of BS7448:pt1

FQ =	9.24 kN	(from Instron)
B =	5 mm	
W =	60 mm	
a/W =	0.5003	
f(a/W) =	9.6674	
KQ =	**72.94 MPa.m^0.5**	

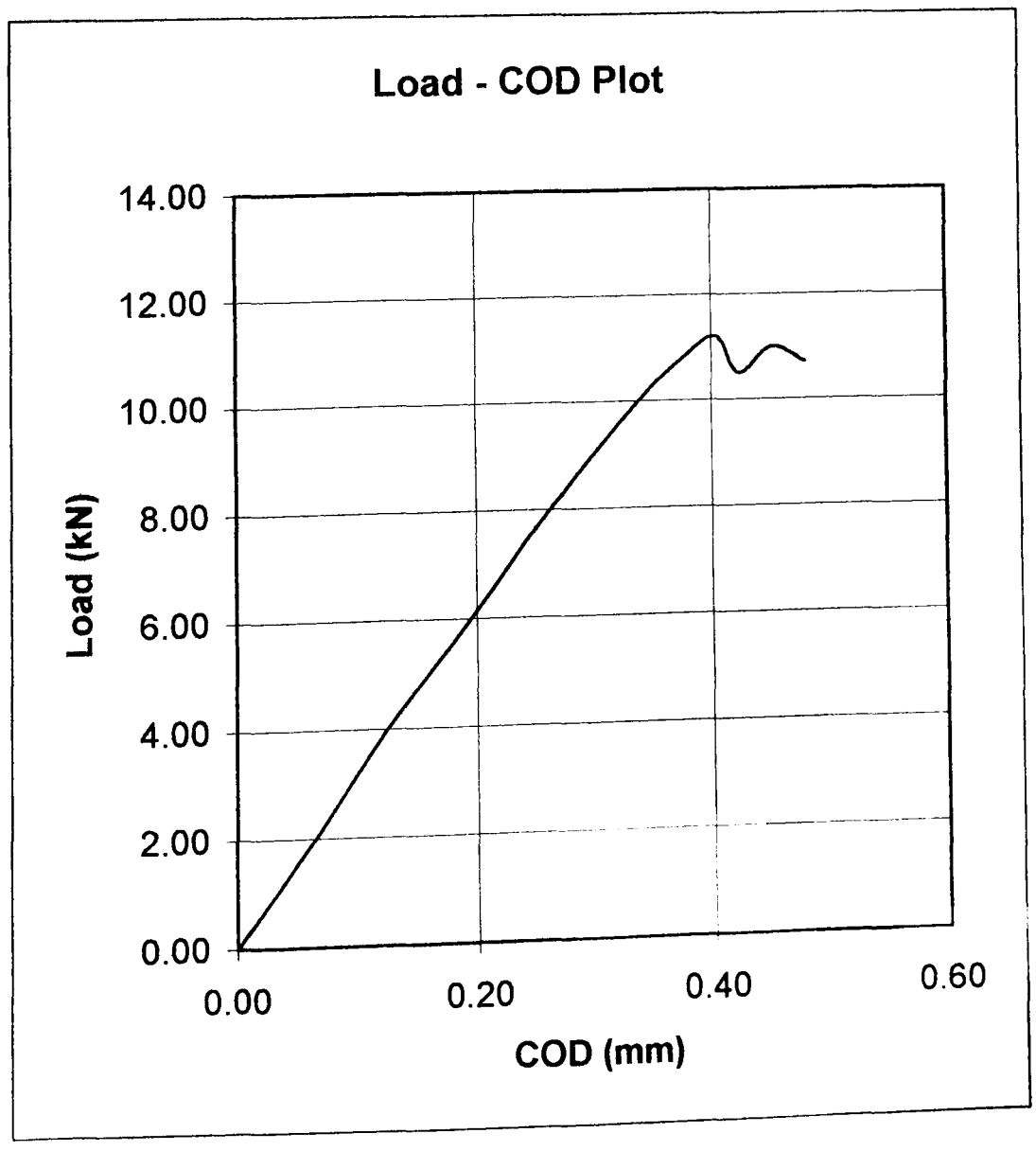

Fracture Toughness Test Data - K_{IC} Test

Specimen Data	
Specimen Thickness:	5 mm
Specimen Width:	60 mm
Material:	EN24
Yield Stress:	970 MPa
Specimen No:	5SG5
Side Groove Type:	Vee
Side Groove Depth:	0.75 mm
Groove Base Thickness	3.5 mm

Precracking Data	
Initial Cycles	
Mean Load:	3 kN
Amplitude:	2.6 kN
Max Load:	5.6 kN
No Cycles:	11000
Force Ratio:	0.07
Final Cycles	
Mean Load:	2.6 kN
Amplitude:	2.3 kN
Max Load:	4.9 kN
No Cycles:	9000
Force Ratio:	0.06

Post Fracture Data

Dist from edge	Crack length
1.0%	29.56
12.5%	29.61
25.0%	29.63
37.5%	29.76
50.0%	29.82
62.5%	29.84
75.0%	29.87
87.5%	29.90
99.0%	29.89
Ave	**29.77**

$K_Q = [F_Q/(BW^{0.5})].f(a/W)$

where f(a/W) is given by 9.2.3.2 of BS7448:pt1

FQ =	10.69 kN	(from Instron)
B =	5 mm	
W =	60 mm	
a/W =	0.4962	
f(a/W) =	9.5459	
KQ =	**83.32 MPa.m^0.5**	

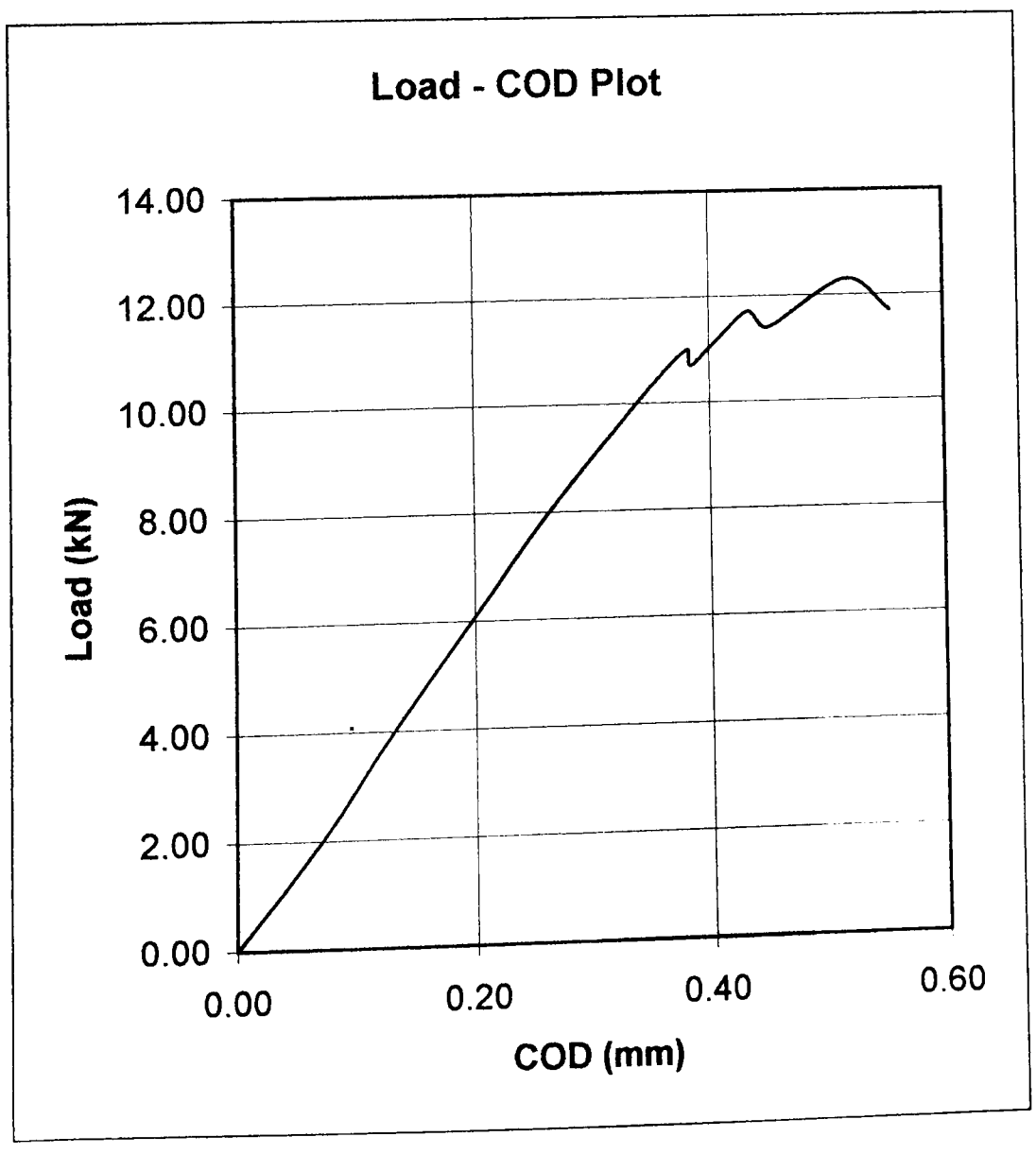

Fracture Toughness Test Data - K_{IC} Test

Specimen Data	
Specimen Thickness:	5 mm
Specimen Width:	60 mm
Material:	EN24
Yield Stress:	970 MPa
Specimen No:	5SG6
Side Groove Type:	Vee
Side Groove Depth:	0.75 mm
Groove Base Thickness	3.5 mm

Precracking Data	
Initial Cycles	
Mean Load:	3 kN
Amplitude:	2.6 kN
Max Load:	5.6 kN
No Cycles:	11000
Force Ratio:	0.07
Final Cycles	
Mean Load:	2.6 kN
Amplitude:	2.3 kN
Max Load:	4.9 kN
No Cycles:	9000
Force Ratio:	0.06

Post Fracture Data

Dist from edge	Crack length
1.0%	30.06
12.5%	30.09
25.0%	30.15
37.5%	30.27
50.0%	30.31
62.5%	30.34
75.0%	30.36
87.5%	30.42
99.0%	30.39
Ave	**30.27**

$K_Q = [F_Q/(BW^{0.5})].f(a/W)$

where f(a/W) is given by 9.2.3.2 of BS7448:pt1

FQ =	9.16 kN	(from Instron)
B =	5 mm	
W =	60 mm	
a/W =	0.5045	
f(a/W) =	9.7947	
KQ =	**73.26 MPa.m^0.5**	

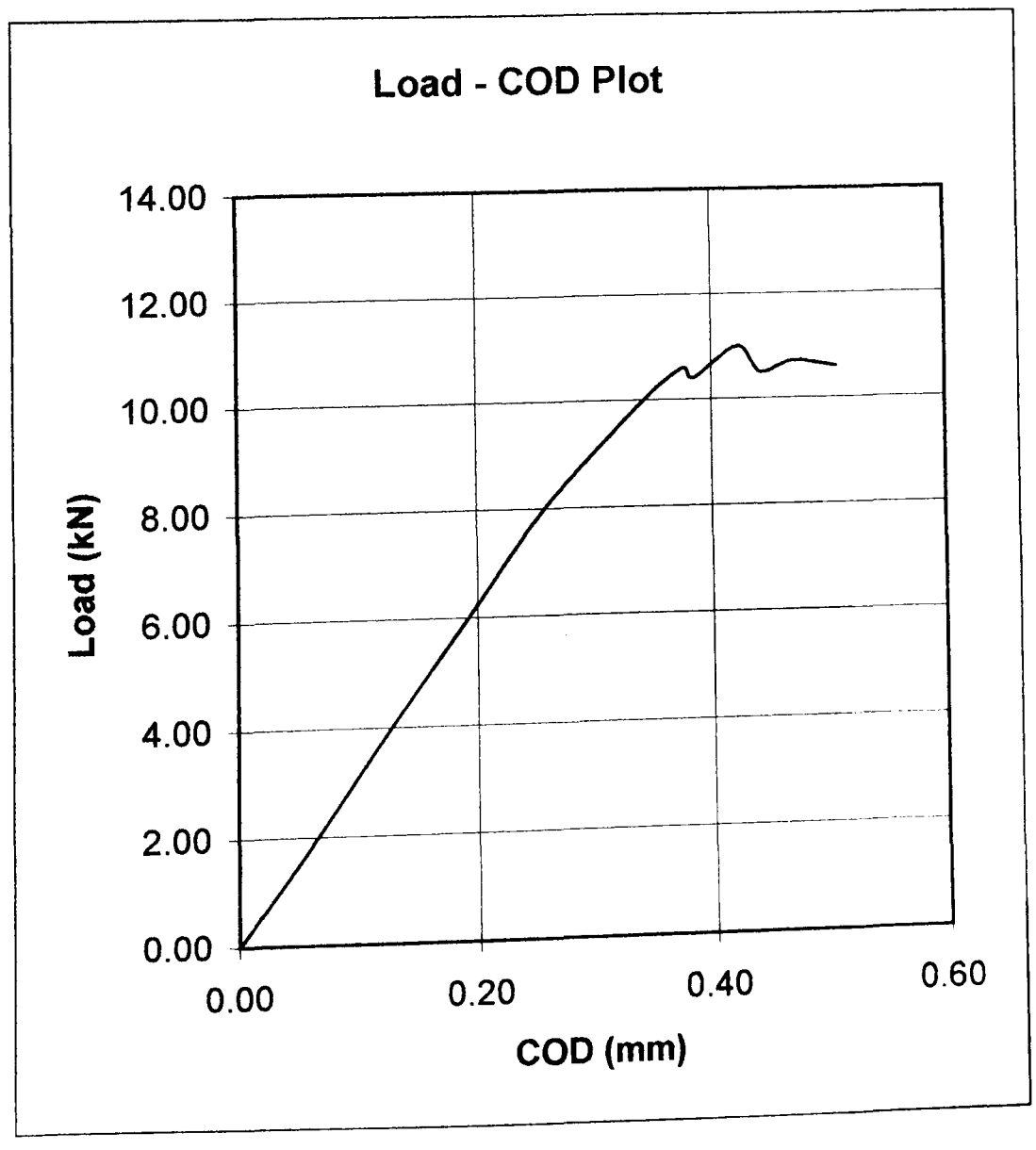

Fracture Toughness Test Data - K_{IC} Test

Specimen Data

Specimen Thickness:	5 mm
Specimen Width:	60 mm
Material:	EN24
Yield Stress:	970 MPa
Specimen No:	5SG7
Side Groove Type:	Vee
Side Groove Depth:	0.75 mm
Groove Base Thickness	3.5 mm

Precracking Data

Initial Cycles	
Mean Load:	3 kN
Amplitude:	2.6 kN
Max Load:	5.6 kN
No Cycles:	11000
Force Ratio:	0.07
Final Cycles	
Mean Load:	2.6 kN
Amplitude:	2.3 kN
Max Load:	4.9 kN
No Cycles:	9000
Force Ratio:	0.06

Post Fracture Data

Dist from edge	Crack length
1.0%	30.25
12.5%	30.29
25.0%	30.30
37.5%	30.29
50.0%	30.30
62.5%	30.29
75.0%	30.23
87.5%	30.19
99.0%	30.08
Ave	**30.26**

$K_Q = [F_Q/(BW^{0.5})].f(a/W)$

where f(a/W) is given by 9.2.3.2 of BS7448:pt1

FQ =	9 kN	(from Instron)
B =	5 mm	
W =	60 mm	
a/W =	0.5043	
f(a/W) =	9.7876	
KQ =	**71.92 MPa.m^0.5**	

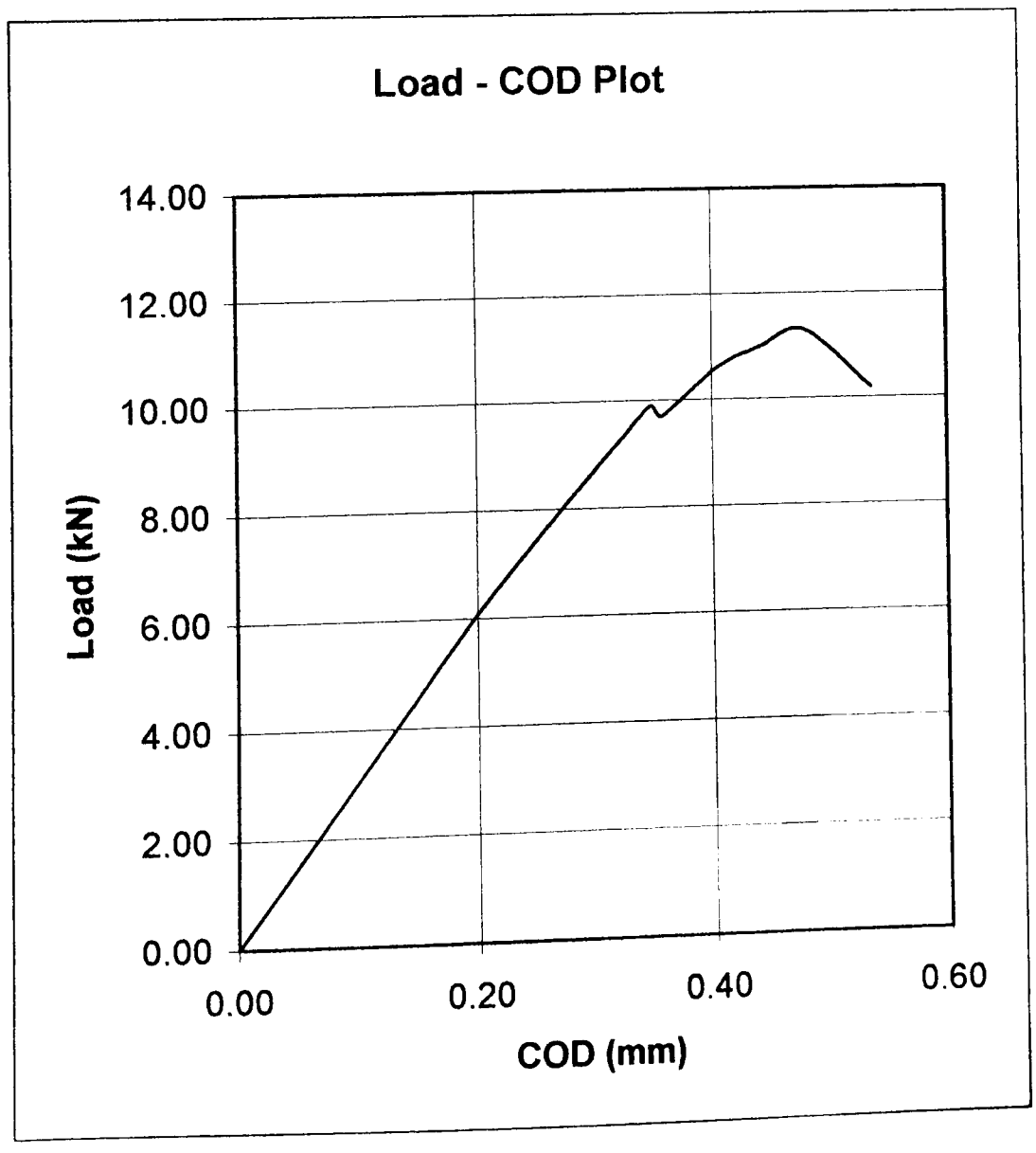

Fracture Toughness Test Data - K_{IC} Test

Specimen Data		
Specimen Thickness:	2.5	mm
Specimen Width:	60	mm
Material:	EN24	
Yield Stress:	970	MPa
Specimen No:	2-5SG1	
Side Groove Type:	Vee	
Side Groove Depth:	0.375	mm
Groove Base Thickness	1.75	mm

Precracking Data		
Initial Cycles		
Mean Load:	1.5	kN
Amplitude:	1.25	kN
Max Load:	2.75	kN
No Cycles:	11000	
Force Ratio:	0.09	
Final Cycles		
Mean Load:	1.3	kN
Amplitude:	1.15	kN
Max Load:	2.45	kN
No Cycles:	6000	
Force Ratio:	0.06	

Post Fracture Data

Dist from edge	Crack length
1.0%	32.24
12.5%	32.28
25.0%	32.29
37.5%	32.28
50.0%	32.28
62.5%	32.27
75.0%	32.18
87.5%	32.13
99.0%	32.08
Ave	**32.23**

$K_Q = [F_Q/(BW^{0.5})].f(a/W)$

where f(a/W) is given by 9.2.3.2 of BS7448:pt1

FQ =	5.2 kN	(from Instron)
B =	2.5 mm	
W =	60 mm	
a/W =	0.5372	
f(a/W) =	10.8827	
KQ =	**92.41 MPa.m^0.5**	

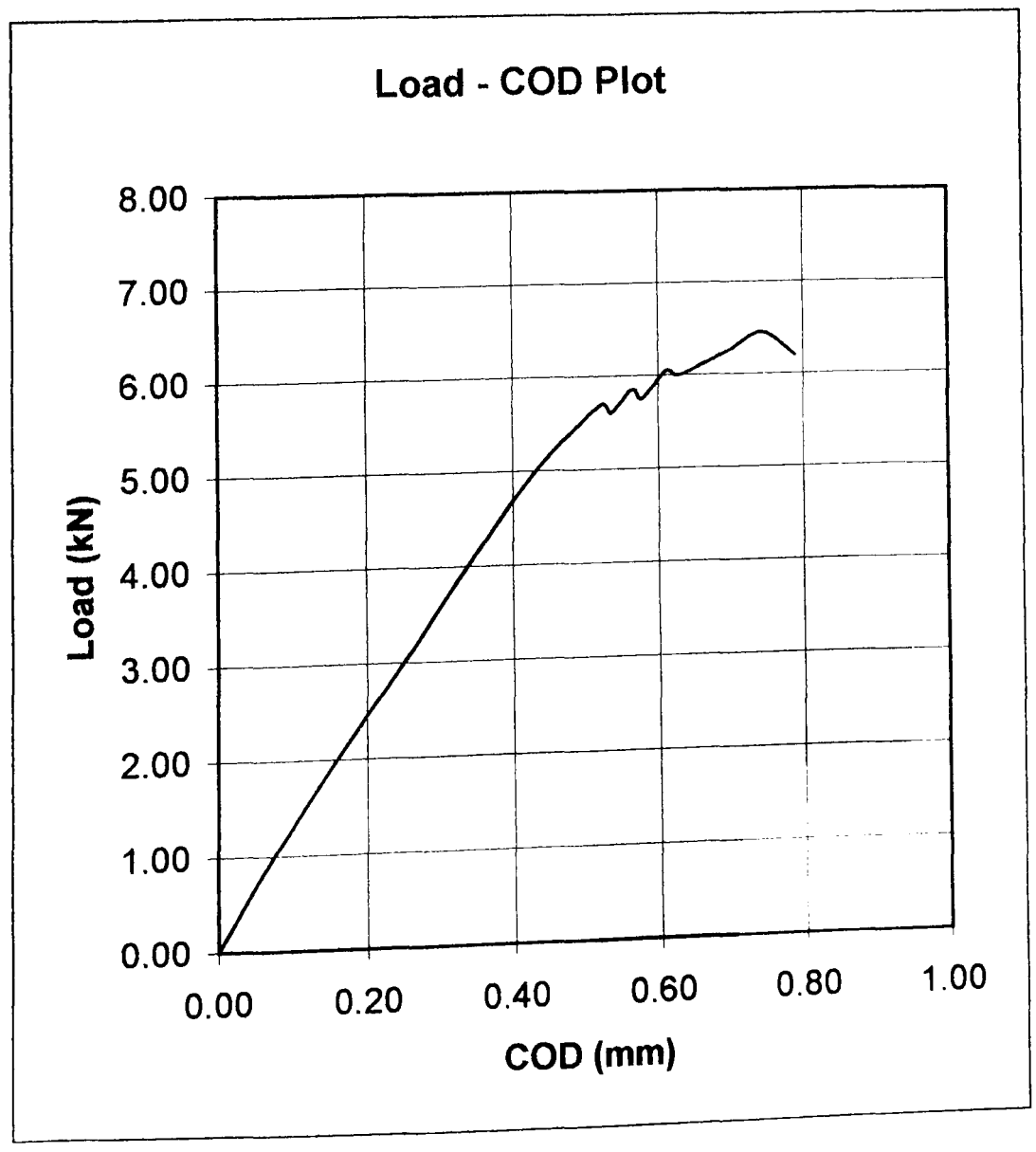

Fracture Toughness Test Data - K_{IC} Test

Specimen Data

Specimen Thickness:	2.5 mm
Specimen Width:	60 mm
Material:	EN24
Yield Stress:	970 MPa
Specimen No:	2-5SG2
Side Groove Type:	Vee
Side Groove Depth:	0.375 mm
Groove Base Thickness	1.75 mm

Precracking Data

Initial Cycles	
Mean Load:	1.5 kN
Amplitude:	1.25 kN
Max Load:	2.75 kN
No Cycles:	11000
Force Ratio:	0.09
Final Cycles	
Mean Load:	1.3 kN
Amplitude:	1.15 kN
Max Load:	2.45 kN
No Cycles:	6000
Force Ratio:	0.06

Post Fracture Data

Dist from edge	Crack length
1.0%	29.64
12.5%	29.69
25.0%	29.76
37.5%	29.77
50.0%	29.77
62.5%	29.71
75.0%	29.65
87.5%	29.63
99.0%	29.60
Ave	**29.70**

$K_Q = [F_Q/(BW^{0.5})].f(a/W)$

where f(a/W) is given by 9.2.3.2 of BS7448:pt1

FQ =	5.25 kN	(from Instron)
B =	2.5 mm	
W =	60 mm	
a/W =	0.4950	
f(a/W) =	9.5123	
KQ =	**81.55 MPa.m^0.5**	

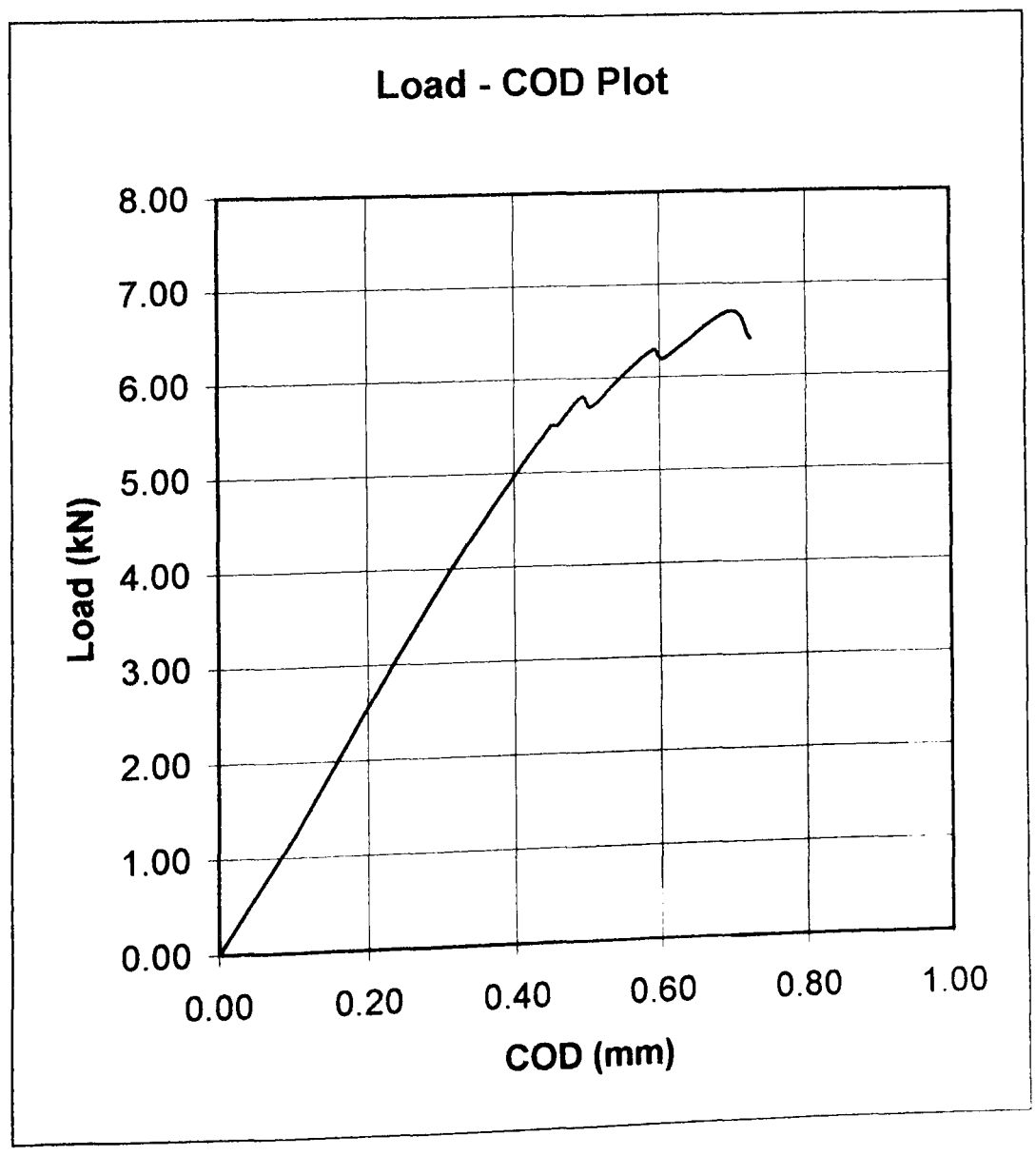

Fracture Toughness Test Data - K_{IC} Test

Specimen Data

Specimen Thickness:	2.5 mm
Specimen Width:	60 mm
Material:	EN24
Yield Stress:	970 MPa
Specimen No:	2-5SG3
Side Groove Type:	Vee
Side Groove Depth:	0.375 mm
Groove Base Thickness	1.75 mm

Precracking Data

Initial Cycles	
Mean Load:	1.5 kN
Amplitude:	1.25 kN
Max Load:	2.75 kN
No Cycles:	11000
Force Ratio:	0.09
Final Cycles	
Mean Load:	1.3 kN
Amplitude:	1.15 kN
Max Load:	2.45 kN
No Cycles:	6000
Force Ratio:	0.06

Post Fracture Data

Dist from edge	Crack length
1.0%	29.38
12.5%	29.42
25.0%	29.45
37.5%	29.47
50.0%	29.46
62.5%	29.45
75.0%	29.43
87.5%	29.40
99.0%	29.39
Ave	**29.43**

$K_Q = [F_Q/(BW^{0.5})].f(a/W)$

where f(a/W) is given by 9.2.3.2 of BS7448:pt1

FQ =	5.75 kN	(from Instron)
B =	2.5 mm	
W =	60 mm	
a/W =	0.4906	
f(a/W) =	9.3848	
KQ =	**88.12 MPa.m^0.5**	

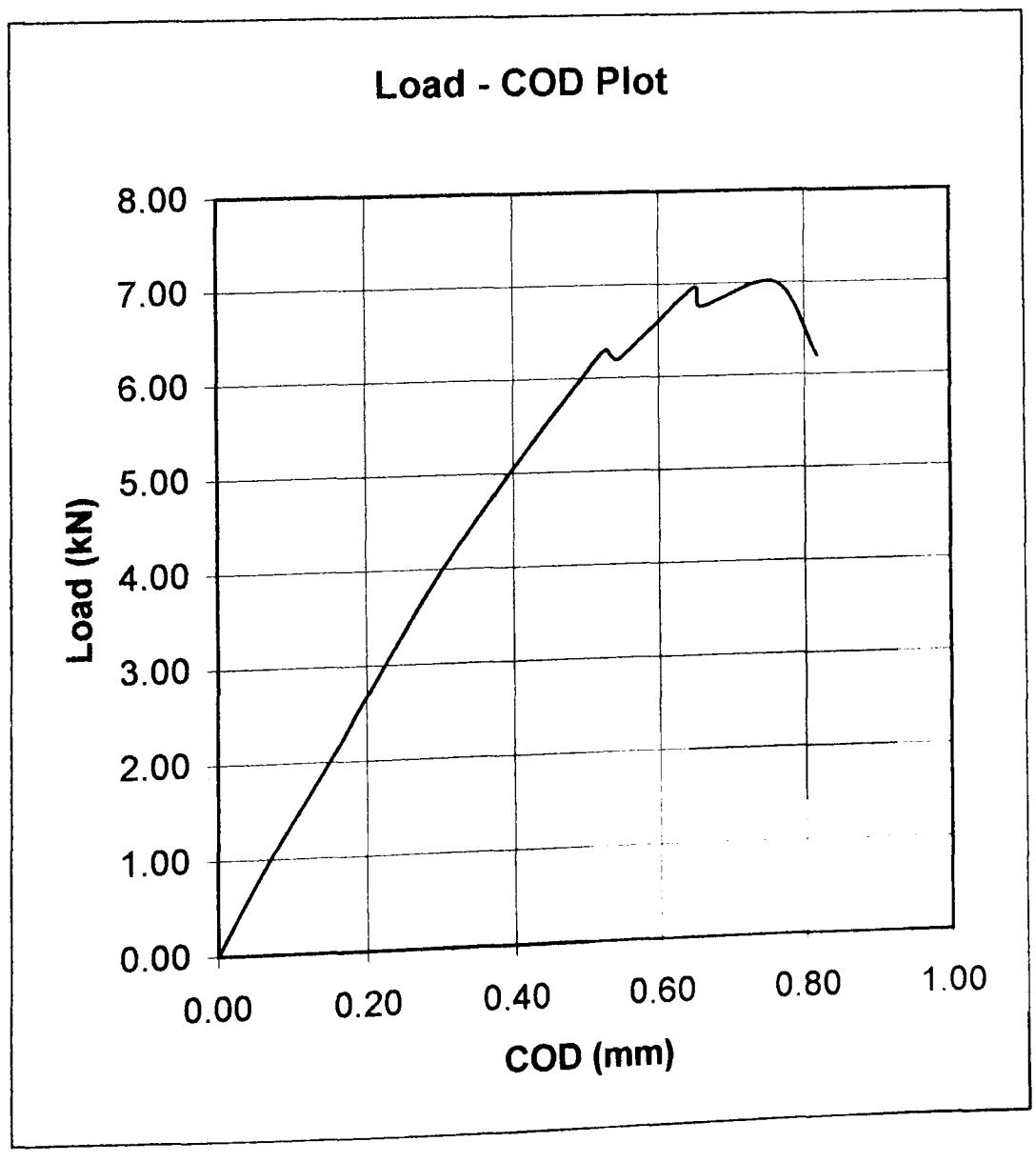

Fracture Toughness Test Data - K_{IC} Test

Specimen Data

Specimen Thickness:	2.5 mm
Specimen Width:	60 mm
Material:	EN24
Yield Stress:	970 MPa
Specimen No:	2-5SG4
Side Groove Type:	Vee
Side Groove Depth:	0.375 mm
Groove Base Thickness	1.75 mm

Precracking Data

Initial Cycles	
Mean Load:	1.5 kN
Amplitude:	1.25 kN
Max Load:	2.75 kN
No Cycles:	11000
Force Ratio:	0.09
Final Cycles	
Mean Load:	1.3 kN
Amplitude:	1.15 kN
Max Load:	2.45 kN
No Cycles:	6000
Force Ratio:	0.06

Post Fracture Data

Dist from edge	Crack length
1.0%	29.33
12.5%	29.33
25.0%	29.37
37.5%	29.37
50.0%	29.35
62.5%	29.36
75.0%	29.36
87.5%	29.34
99.0%	29.29
Ave	**29.35**

$K_Q = [F_Q/(BW^{0.5})].f(a/W)$

where f(a/W) is given by 9.2.3.2 of BS7448:pt1

FQ =	4.84 kN	(from Instron)
B =	2.5 mm	
W =	60 mm	
a/W =	0.4891	
f(a/W) =	9.3451	
KQ =	**73.86 MPa.m^0.5**	

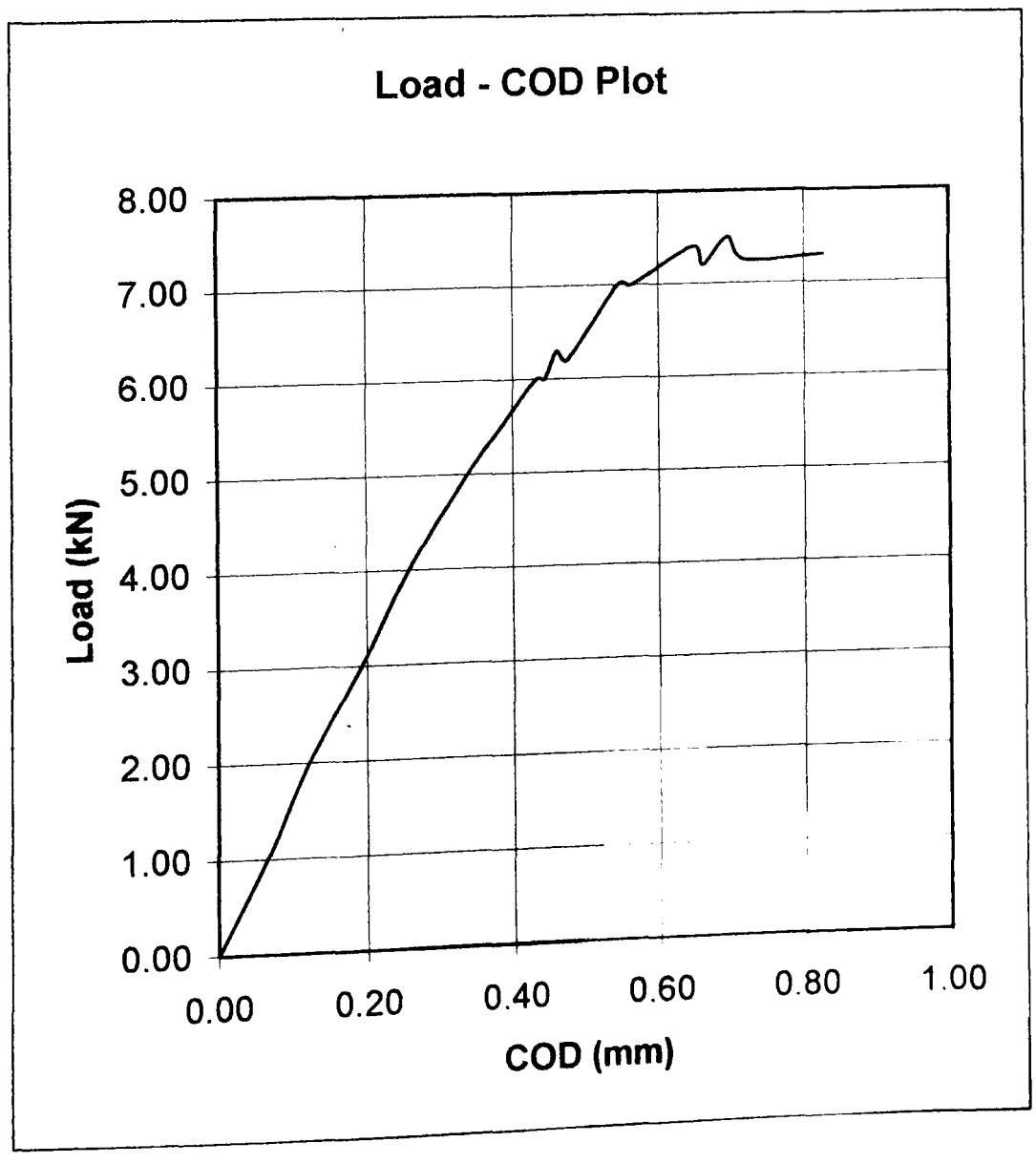

Fracture Toughness Test Data - K_{IC} Test

Specimen Data		
Specimen Thickness:	2.5	mm
Specimen Width:	60	mm
Material:	EN24	
Yield Stress:	970	MPa
Specimen No:	2-5SG5	
Side Groove Type:	Vee	
Side Groove Depth:	0.375	mm
Groove Base Thickness	1.75	mm

Precracking Data		
Initial Cycles		
Mean Load:	1.5	kN
Amplitude:	1.25	kN
Max Load:	2.75	kN
No Cycles:	11000	
Force Ratio:	0.09	
Final Cycles		
Mean Load:	1.3	kN
Amplitude:	1.15	kN
Max Load:	2.45	kN
No Cycles:	6000	
Force Ratio:	0.06	

Post Fracture Data

Dist from edge	Crack length
1.0%	28.85
12.5%	28.82
25.0%	28.89
37.5%	28.92
50.0%	28.87
62.5%	28.84
75.0%	28.85
87.5%	28.83
99.0%	28.74
Ave	**28.85**

$K_Q = [F_Q/(BW^{0.5})].f(a/W)$
where f(a/W) is given by 9.2.3.2 of BS7448:pt1

FQ =	5.65	kN	(from Instron)
B =	2.5	mm	
W =	60	mm	
a/W =	0.4809		
f(a/W) =	9.1166		
KQ =	**84.11**	**MPa.m^0.5**	

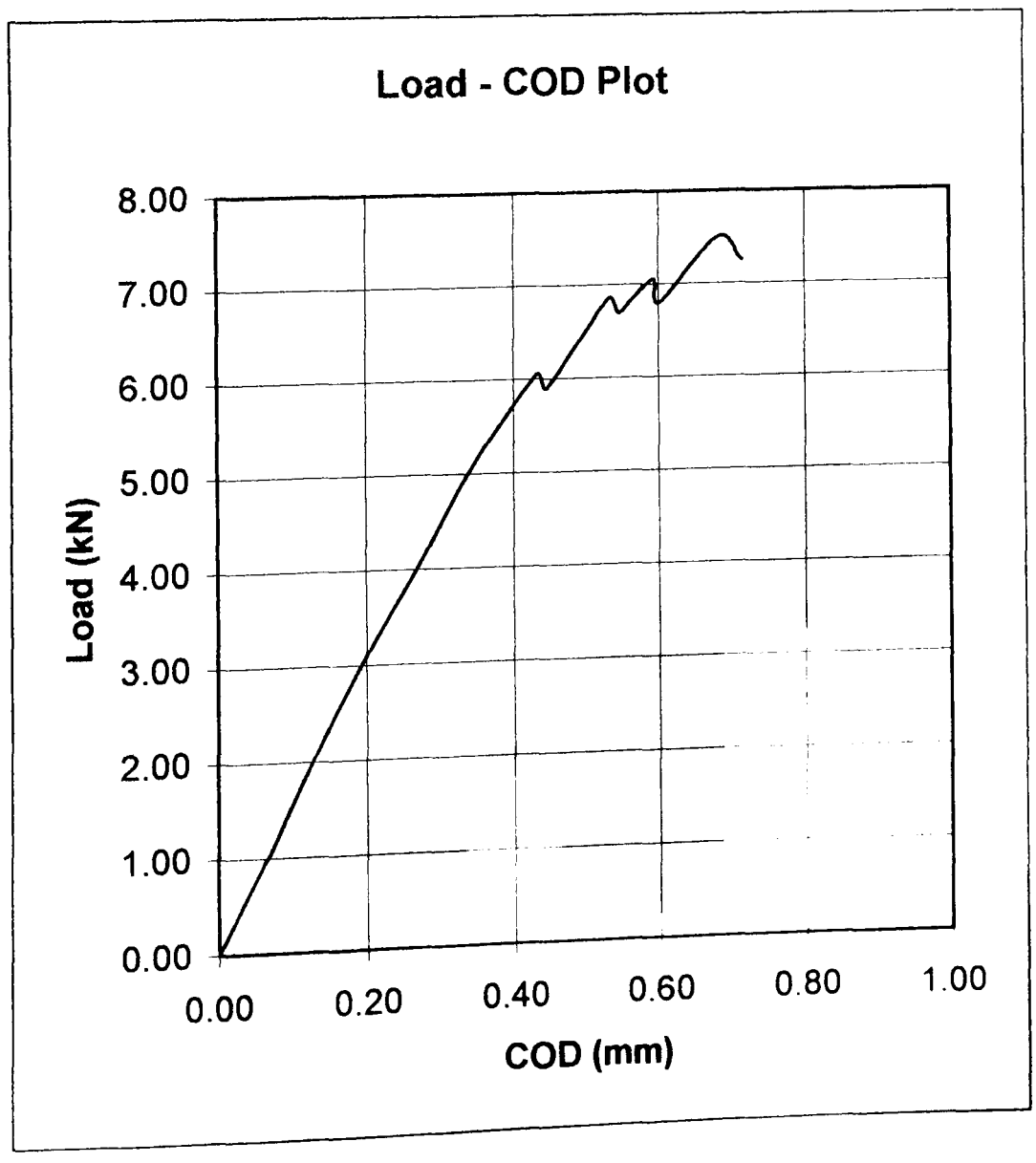

Fracture Toughness Test Data - K_{IC} Test

Specimen Data		
Specimen Thickness:	2.5	mm
Specimen Width:	60	mm
Material:	EN24	
Yield Stress:	970	MPa
Specimen No:	2-5SG6	
Side Groove Type:	Vee	
Side Groove Depth:	0.375	mm
Groove Base Thickness	1.75	mm

Precracking Data		
Initial Cycles		
Mean Load:	1.5	kN
Amplitude:	1.25	kN
Max Load:	2.75	kN
No Cycles:	11000	
Force Ratio:	0.09	
Final Cycles		
Mean Load:	1.3	kN
Amplitude:	1.15	kN
Max Load:	2.45	kN
No Cycles:	6000	
Force Ratio:	0.06	

Post Fracture Data

Dist from edge	Crack length
1.0%	29.11
12.5%	29.11
25.0%	29.12
37.5%	29.13
50.0%	29.12
62.5%	29.14
75.0%	29.04
87.5%	28.96
99.0%	28.90
Ave	**29.08**

$K_Q = [F_Q/(BW^{0.5})].f(a/W)$

where f(a/W) is given by 9.2.3.2 of BS7448:pt1

FQ =	5.4	kN	(from Instron)
B =	2.5	mm	
W =	60	mm	
a/W =	0.4846		
f(a/W) =	9.2195		
KQ =	**81.30**	**MPa.m^0.5**	

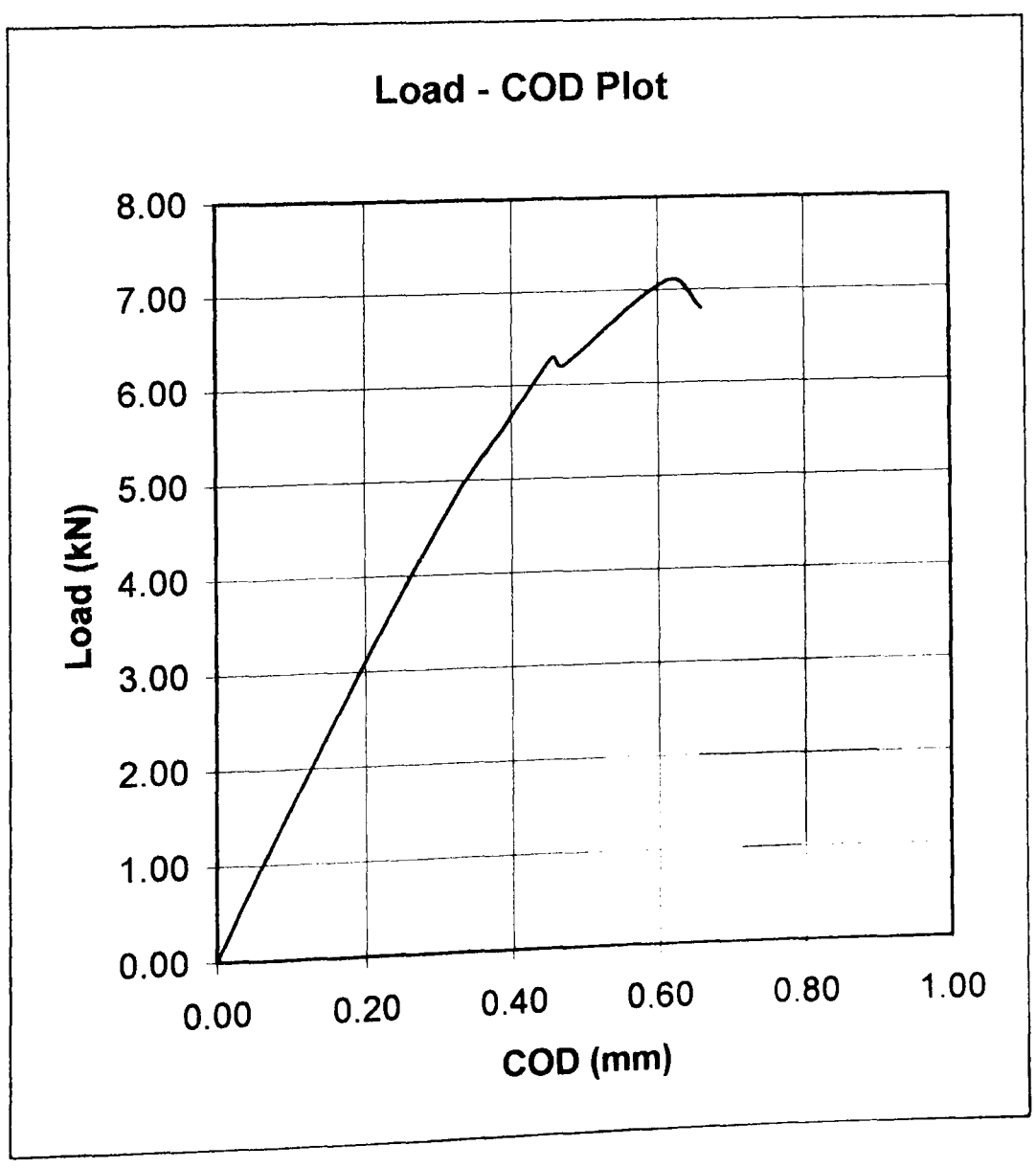

Fracture Toughness Test Data - K_{IC} Test

Specimen Data

Specimen Thickness:	2.5 mm
Specimen Width:	60 mm
Material:	EN24
Yield Stress:	970 MPa
Specimen No:	2-5SG6
Side Groove Type:	Vee
Side Groove Depth:	0.375 mm
Groove Base Thickness	1.75 mm

Precracking Data

Initial Cycles	
Mean Load:	1.5 kN
Amplitude:	1.25 kN
Max Load:	2.75 kN
No Cycles:	11000
Force Ratio:	0.09
Final Cycles	
Mean Load:	1.3 kN
Amplitude:	1.15 kN
Max Load:	2.45 kN
No Cycles:	6000
Force Ratio:	0.06

Post Fracture Data

Dist from edge	Crack length
1.0%	29.11
12.5%	29.11
25.0%	29.12
37.5%	29.13
50.0%	29.12
62.5%	29.14
75.0%	29.04
87.5%	28.96
99.0%	28.90
Ave	**29.08**

$K_Q = [F_Q/(BW^{0.5})].f(a/W)$
where f(a/W) is given by 9.2.3.2 of BS7448:pt1

FQ =	5.4 kN	(from Instron)
B =	2.5 mm	
W =	60 mm	
a/W =	0.4846	
f(a/W) =	9.2195	
KQ =	**81.30 MPa.m^0.5**